UNIVERSITY OF HULL

Exploring the use of Arginine Methylation Inhibitors Against Brain Tumours in an ex vivo Perfusion System

A thesis submitted in partial fulfilment of the requirements for the degree of

Doctor of Philosophy

to the University of Hull

by

Antonia Barry

BSc (Hons) University of Leicester

MPhil University of Newcastle

AFHEA University of Hull

PGCert University of Hull

September 2024

Abstract

Glioblastoma (GBM) is the most common primary malignancy in the central nervous system and the most devastating, with a median survival of 18 months from diagnosis. The development of models to research and understand GBM tumourigenesis and progression, as well as for drug screening is paramount to tackling this disease and determining new and effective therapeutic interventions. Microfluidics models have been developing over the past several years with the aim of maintaining tissue viability over several days and presenting a more patient-personalised and clinically relevant model of GBM. The University of Hull have driven the manufacture of a novel perfusion device which allows a micro-biopsy of the tissue to be maintained for up to 8 days for drug screening and evaluation of aspects of the tumour microenvironment.

Type I protein arginine methyltransferases (PRMTs) are responsible for the deposition of asymmetric dimethyl marks on arginine residues of both histones and proteins, whereas type II PRMTs deposit symmetric dimethylation marks and type III perform monomethylation, solely. Methylation is a very common and stable post-translational modification and can alter protein expression and function. PRMTs are upregulated in and have been associated with dysregulation of a variety of pathways in GBM and have been involved in clinical trials for a variety of cancers, including GBM. The overarching hypothesis for this study was that GSK3368715 could cause cell death in GBM patient tissues in the novel perfusion device. This was investigated by evaluating cell death through histology and cellular stress assays, determining transcriptomic changes as a result of treatment and comparing the outcomes of these results to healthy mouse brains maintained in the novel perfusion device.

Type I PRMT inhibition using GSK3368715 was evaluated in U87-MG cells and in GBM patient tissue in the novel perfusion device throughout this research. No significant cellular stress was found between individual time points in control GBM and healthy mouse or cichlid brain tissues, maintained in the perfusion device for 8- (GBM, $F = 1.11$, df = 7, $p = 0.37$; Mouse, F=1.45, df=5, p=0.22) or 12- days (GBM, $F = 1.38$, df =11 , $p = 0.22$) after the first 48 hours. Similarly, no significant changes in apoptosis were determined between pre- and 8- (cleaved PARP: GBM, w=38, p=0.151, Mouse, t = 0.020, df = 2, p = 0.99; Annexin V: GBM, t = -0.064, df = 13.76, p = 0.95, Mouse, t = -0.23, df = 6, p = 0.8), or 12-day (cleaved PARP: GBM, t = -0.40, df = 4.75, p-value = 0.71; Annexin V: t = -0.064, df = 13.76, p = 0.95) post-perfused

tissue in GBM, or healthy mouse brain tissues. Together with the presence of mitoses in histological staining and cytokine profile shifts, which showed greater changes in cytokine profiles after 12 days, this indicated that tissues could be maintained for up to 8 days on chip, but further optimization would be required to extend perfusion to 12 days. Cichlid brain tissues were also found to be able to maintained in the perfusion device through no significant change in cellular stress for up to 6 days ($F=1.73$, $df=1$, $p=0.21$), lack of significant cellular death up to 4 days ($X^2=5.50$, $df = 3$, $p = 0.14$) and presence of live cells seen through histology.

GSK3368815 was found to cause a 2.17-fold increase in apoptotic cleaved PARP expression in GBM tissue in the perfusion device, after 8 days ($t = -4.52$, $df = 9$, $p = 0.001$), but did not show synergy with other drugs ($X^2 = -0.41$, $df = 14{,}42$, $p = 0.69$). This was not recapitulated with the Annexin V apoptotic marker ($t = -0.41$, $df = 14.42$, $p = 0.69$). Variation between GBM response to treatment, as well as extension of time on-chip beyond 8 days requires further exploration and optimisation. GSK3368715 and TMZ also caused changes to cytokines, including decreased expression of matrix metalloproteinase 9 (logFC=-0.07, t=-43.32, padj=0.0046) and vascular endothelial growth factor (logFC=-0.08, t=-4.25, padj=0.0004), as well as an increase in mesenchymal cell phenotype marker chitinase 3 like 1 (logFC=0.05, t=-2.97, padj=0.0088), which has been implicated in successful treatment of GBM. Differential gene expression of treated tissue was also determined, with gene ontology indicating reductions in protein synthesis capacity and increase in cell death with GSK3368715 treatment, supporting apoptotic marker expression in the tissue. Hundreds of alternatively spliced genes and links with fused in sarcoma (FUS) suggested that this may be a mechanism by which PRMT inhibition functions to cause apoptosis. This data was then compared to healthy mouse brain controls, in which GSK3368715 did not cause any apoptotic effects (cleaved PARP: t=-1.20, df=5, p=0.28; Annexin V: t=-0.47, df=6, p=0.65).

In conclusion, GSK3368715 was found to cause apoptosis in 8-day post-perfused GBM patient tissue. This could be caused by PRMT-inhibition induced alternative splicing and involvement of FUS, which may lead cells to be driven to a more differentiated phenotype, resensitisation of cells to TMZ and reduction of tumour microenvironmental factors associated with aggressive GBM phenotypes.

Acknowledgements

A huge thanks to Yorkshire's Brain Tumour Charity for funding this project and to the patients and their families whose generosity and understanding has made this project a possibility. Thank you to my supervisor Pedro for being a constant source of guidance, positivity, grounding and most of all, patience, throughout the entire process and to Mark and Lucy for always being there with your support, expertise and help.

This project could not have been completed without the help of the amazing staff at HRI, including Shailendra Achawal and Chittoor Rajaraman; Amr, who has been a fantastic M.D. to work with; Ian, for his histology expertise and insight; Ricky, for his help with the mouse brains; Lauric, for his bioinformatics help; Domino, for care and provision of the cichlids and Vicky and John, who have always helped me out when things have gone wrong. Also, thank you to Andrew, Lynsey, Ellie, Lydia, Ines and Andy who have helped immensely with training and troubleshooting.

To Quentin, Lucie, Tom, Danielle, Karen, Sabrina, Alistair, Rebecca and everyone else - thank you for making turning up on the difficult days an absolute pleasure.

My friends, amazing family and Liam, as always, you make me work hard, play hard and laugh hard. You are my cheerleaders, my never-ending support you have been and still are my role models and inspiration. Thank you for picking me up and dusting me off when it got hard, I promise to make you all a thank you cake!

"Angels up above you are peeping at you deary from the sky."

Publications and Conferences

Publications

- Barry, A., Samuel, S.F., Hosni, I., Moursi, A., Feugere, L., Sennett, C.J., Deepak, S., Achawal, S., Rajaraman, C., Iles, A., Valero, K.C.W., Scott, I.S., Green, V., Stead, L.F., Greenman, J., Wade, M.A. and Beltran-Alvarez, P. (2023). Investigating the effects of arginine methylation inhibitors on micro-dissected brain tumour biopsies maintained in a miniaturised perfusion system. *Lab on a Chip*, 23(11), pp.2664-2682.
- Marsden, A. J.; Riley, D.; Barry, A.; Khalil, J.S.; Guinn, B.; Kemp, N.T.; Rivero, F.; Beltran-Alvarez, P. (2021) Inhibition of Arginine Methylation Impairs Platelet Function. *ACS Pharmacol. Transl. Sci.*, 4(5), 1567-1577.
- Samuel, S. F., Barry, A., Greenman, J. & Beltran-Alvarez, P. (2021) Arginine methylation: the promise of a 'silver bullet' for brain tumours? *Amino Acids*, 53, pp.489-506

Conferences

- Organ-on-a-chip conference, April 2021, 5-minute flash talk
- Allam Lecture, April 2021, Poster Presentation 1st prize winner
- BNOS (British Neuro Oncology Society) Conference, June 2022, 10-minute presentation
- Yorkshire's Brain Tumour Charity symposium, July 2022, 45-minute presentation
- Research Celebration Event, April 2022, poster
- Allam Lecture, May 2023, 10-minute presentation,
- BNOS (British Neuro Oncology Society) Conference, June 2023, 3-minute presentation and poster
- Hradec-Kralove Conference, November 2023, 10-minute presentation

Contents

List of Figures

List of Tables

Abbreviations

+7/-10	Chromosome 7 gain and chromosome 10 loss
μ	Viscosity
μg	Micrograms
μM	Micromolar
2D	2 dimensional
2-HG	2-hydroxyglutarate
3D	3-dimensional
3'UTR	3' untranslated region
5-ALA	5-aminolevulinic acid
A	Area
aa	Amino acid
ABCG2	ATP-binding cassette G2
AC	Astrocyte cell like
ADAMTS9-AS2	Disintegrin and metalloproteinase with thrombospondin type 1 motif 9 antisense RNA 2
ADC	Apparent diffusion coefficients
aDMA	Asymmetric dimethylation of arginine
AdOx	Adenosine-2,3-dialdehyde
ADP	Adenosine diphosphate
AGXT2	Alanine:glycoxylate aminotransferase 2
AICc	Akaike criterion with small sample compensation
ALK	Anti-anaplastic lymphoma kinase
ALS	Amyotrophic lateral sclerosis
AML	Acute myeloid leukaemia
ANOVA	Analysis of variance
ANT	Adenine nucleotide transporter
AP	Apyrimidine
APAF1	Apoptotic peptidase activating factor 1
APC	Adenomatosis polyposis coli tumour suppressor
APE1/2	AP endonucleases
ARF/p14	ADP-ribosylation factor/p14
ATF4	Activating transcription factor 4
ATM	Ataxia telangiectasia mutated
ATP	Adenosine triphosphate
ATR	Ataxia telangiectasia and rad3 related
ATRIP	ATR-interacting protein
ATRX	Alpha-thalassaemia syndrome X-linked
AU	Arbitrary units
B cell	Bone marrow lymphocyte
BAD	Bcl2-antagonist of cell death
BAK1	Bcl2 antagonist killer 1
BBB	Blood brain barrier

BBTB	Blood brain tumour barrier
BCA	Bicinchoninic acid
BCL2	B cell CLL/lymphoma 2
BCLX	B cell lymphoma X
BCNU	1-3-bis(2-chloroethyl)-1-nitrosourea
BDNF	Brain derived neurotrophic factor
BER	Base excision repair
BID	Bcl2 interacting protein
BLM	Bloom syndrome protein
BOLA2B	*Bola-like protein-2B*
BRAF	Serine threonine kinase protooncogene
BRCA1/2	*Breast cancer gene 1/2*
C&F	Lamellae clubbing and fusion
C15orf39	Chromosome 15 open reading frame 39
C3L1	Chitinase 3 like 1
Ca^{2+}	Calcium ion
CAD	Carbamoyl-phosphate synthetase 2
cAMP	Cyclic adenosine monophosphate
CARM1	Coactivator associated arginine methyltransferase 1
CAR-T	Chimeric antigen receptor-T cell
Cbl	Casitas B-lineage lymphoma
CBP	CREB binding protein
CCL2	Chemokine ligand 2
CCNU	1-(2-chloroethyl)-3-cyclohexyl-1-nitrosourea
CD4/8/44	Cluster of differentiation4/8/44
CDC20/25A/C	Cell division cycle 20/25A/25C
CDK1/2/4/6	Cyclin dependent kinase1/2/4/6
CDKN1A/2A/B	Cyclin-dependent kinase inhibitor 1A/2A/2B
cDNA	Complementary DNA
ceRNETs	Certain competing endogenous RNA regulator network
CETN2	Centrin-2
cGAS	GMP-AMP synthase
CH_3	Methyl group
CHIP	Hsc70-interacting protein
ChIP	Chromatin immunoprecipitation
Chk1/2	Checkpoint kinase 1/2
CIAP1	Cellular inhibitor of apoptosis-1
cIMPACT-NOW	Consortium to Inform Molecular and Practical Approaches to CNS Tumour Taxonomy
CK1α	Casein kinase 1 alpha
CL	Classical
CLC	Chloride cell
CLDN5	Claudin-1
cm	Centimetres

CMPD-1	Campomelic dysplasia 1
CNS	Central nervous system
CO_2	Carbon dioxide
Cobl	Cordon-bleu
coeff. est.	Coefficient estimate
COL3A1	*Collagen III alpha subunit 1*
COL6A3	*Collagen IV alpha subunit 3*
COP9	Constitutive photomorphogenesis 9
COX1	Cytochrome c oxidase subunit 1
CREB	Camp-response element binding protein
CRISPR	Clustered regularly interspaced short palindromic repeats
CRUK	Cancer research UK
CSA/B	Cockayne syndrome group A/B
CSN6	COP9 signalosome complex subunit
CT	Computed tomography
CTCs	Circulating tumour cells
CTLA4	Cytotoxic T lymphocyte-associated antigen-4
CTRL	DMSO control
Cu^{+}	Cuprous ions
Cu^{2+}	Cupric ions
CXCL12	Cytokine-chemokine ligand 12
CXCL4	Cytokine-chemokine receptor 4
d	Diameter
DAB	3, 3'-diaminobenzidine
DAPI	4′,6-diamidino-2-phenylindole
DDAH	Dimethylarginine dimethylaminohydrolase
ddH_2O	Double distilled water
DDR	DNA damage response
DED	Death effector domain
DEGs	Differentially expressed genes
DEX	Dexamethasone
DIABLO	Direct inhibitor of apoptosis-binding protein with low pi
diH_2O	Deionised water
DKK1	*Dickkopf WNT signalling pathway inhibitor-1*
DMEM	Dulbecco's modified eagle's medium
DMSO	Dimethyl sulfoxide
DNA	Deoxyribose nucleic acid
DNA-PK	DNA protein kinase
DOCK7	Dedicator of cytokinesis 1
dRP	Deoxyribose phosphate
DSB	Double strand breaks
dTTP	Deoxythymidine triphosphate
dUTP	2′-deoxyuridine, 5′-triphosphate

DWI	Diffusion weighted imaging
E	Erythrocytes
Eu2F	Eukaryotic transcription factor 2
E2F	E2 promoter binding factor
ECL	Enhanced chemiluminescence
ECM	Extracellular matrix
EDTA	Ethylenediaminetetraacetic acid
EGF/R	Epithelial growth factor/receptor
EGFRvIII	Epithelial growth factor receptor splice variant 8
EID3	EP300-interacting inhibitor of differentiation 3
eIF2α	Eukaryotic initiator factor 2 alpha
ELISA	Enzyme-linked immunosorbent assays
EMBL-EBI	European molecular biology laboratory-European bioinformatics institute
EMC9	Endoplasmic reticulum membrane protein complex subunit 9
EMMPRIN	Extracellular matrix metalloproteinase inducer
EMT	Epithelial to mesenchymal transition
EPL	Epithelium lifting
ER	Endoplasmic reticulum
ERCC1	Excision repair protein
ERK	Extracellular signal-related kinase
ERα	Oestrogen receptor-α
EVs	Extracellular vesicles
EWS	Ewing sarcoma
Exo1	Exonuclease 1
EZH2	Enhancer of zeste 2
FADD	Fas associated via death domain
FasL	Fas ligand
FC	Fold change
FDA	Food and drug administration
FDR	False discovery rate
Fen1	Flap structure specific endonuclease 1
FET	FUS/EWRS1/TAF15 family
FFPE	Formalin fixed paraffin embedded
FGF/R	Fibroblast growth factor/receptor
FHA	Fork head-associated
FIH	Factor-inhibiting HIF
FLIP	Fas-associated death domain protein-like interleukin-1α-converting enzyme-like inhibitory protein
FRG1	FSHD region gene 1
FSHD	Facioscapulohumeral muscular dystrophy
FTD	Frontotemporal dementia
FTMU	Fotemustine
FUS	Fused in sarcoma
g	Gravity

G1/2	Gap phase 1/2
G3BP1	GAP SH3 domain-binding protein 1
$GABA_A$	Gamma-aminobutyric acid
GADD34	Growth arrest and DNA damage-inducible protein 34
GAP	Ras GTPase accelerating protein
GBM	Glioblastoma multiforme
GCN5	General control non-depressible 5
GEF	Guanine nucleotide exchange factor
GEO	Gene expression omnibus
GFAP	Glial fibrillary acidic protein
GFP	Green fluorescent protein
GG/TC/NER	Global genome/transcription-coupled/nucleotide excision repair
GLASS	Glioma longitudinal analysis consortium
GLICOs	Cerebral organoid gliomas
GLM	General linear modelling
GLUT1	Glucose transporter
GMP	Guanosine monophosphate
GMT	Glial to mesenchymal transition
GO	Gene ontology
GSC	Glioma stem cells
GSK	1μm GSK3368715
GSK3α/β	Glycogen synthase kinase-3 alpha/beta
GTP	Guanosine triphosphate
GTR	Gross total resection
Gy	Grays
h	Hours
H&E	Haematoxylin and eosin
H_2O_2	Hydrogen peroxide
H3K27	Histone 3 lysine 27
H4R3me2a	Histone 4 arginine 3 asymmetric dimethylation
H4R3me2s	Histone 4 arginine 3 symmetric dimethylation
HAT	Histone acetyl transferases
HCl	Hydrochloric acid
HDAC	Histone deacetyl transferases
HDL	High density lipoprotein
HECT3	Homologous to the E6-AP carboxyl terminus
hg38	Human reference genome version 38
HIF1/α	Hypoxia inducible factor 1/alpha
HISAT	Hierarchical indexing for spliced alignment of transcripts
HIV1	Human immunodeficiency virus-1
HLA-DRA	Histocompatibility complex, class II, DR alpha
HMG	High mobility group
HNPCC	Hereditary nonpolyposis colorectal cancer
hnRNP/A1/P2	Heterogenous nuclear ribonucleoprotein A2/P2

HOXA	*Homeobox protein A*
HR	Homologous recombination
HRI	Hull royal infirmary
HRP	*Horseradish peroxidase*
Hsc70	Heat shock chaperone 70
HSP70	Heat shock protein 70
HTRA2/Omi	Htra serine peptidase 2
IAP	Inhibitor of apoptosis
IC_{50}	50% inhibitory concentration
ICAD	Inhibitor of caspase-activated DNase
Id2/4	Inhibitor of differentiation/DNA binding 2/4
IDH1/2	Isocitrate dehydrogenase 1/2
IFNα/γ	Interferon alpha/gamma
IGFBP-2	Insulin-like growth factor binding protein-2
IHC	Immunohistochemistry
IL1β/6/8/10	Interleukin 1 beta/6/8/10
ING4	Inhibitor of growth family member 4
INT	Tetrazolium salt
IP	Immunoprecipitate
iPSCs	Induced-pluripotent stem cells
IRAS	Integrated research application system
IRE1α	Inositol-requiring protein 1 α
iTRAQ	Isobaric tags for relative and absolute quantitation
IκB	Inhibitor of nfκb
IκK	Iκb kinase
JAK	Janus kinase
JMY	Junction-mediating and regulatory protein
JNK	C-Jun N-terminal kinase
Kapβ2	Karyopherin- β2
KAT	Lysine acetyltransferases
kDa	Kilodaltons
KDAC	Lysine deacetyltransferases
KDM1A/6A	Histone demethylase 1A/6A
KEGG	Kyoto Encyclopaedia of Genes and Genomes
kg	Kilograms
Ki67	Antigen Kiel 67
KISS1/R	Kisspeptin-1/receptor
KRAS	Kirsten rat sarcoma virus
KRT5/17/19	Keratin
LDH	Lactate dehydrogenase
LITT	Laser interstitial thermal therapy
LMF1	*Lipase maturation factor-1*
lncRNA	Long non-coding RNA
Log	Logarithm

Log2FC	Lof2 fold change
LogFC	Log fold change
LREC	Local research ethics committee
LXRα	Liver X receptor alpha
LYZ	*Lysozyme*
M	Mitosis
m	Metres
M.D.	Doctor of Medicine
m^6A	N6-methyladenosine
MAP1B	Microtubule-associated protein 1B
MAPK	Mitogen activated protein kinase
MC	Mucous cell
MCP1	Monocyte chemoattractant protein-1
MDM2	Mouse double minute 2
ME	Mesenchymal
MEK	Mitogen-activated protein kinase
MEKK	Mitogen-activated protein kinase kinase
MEP50	Methylosome protein 50
MES	Mesenchymal cell like
MET	Mesenchymal to epithelial transition
METTL3	Methyltransferase-like 3
mg	Milligrams
Mg^{2+}	Magnesium ion
MGMT	O6-methylguanine-methyltransferase
MIF	Macrophage migration inhibitory factor
min	Minute
miRNA	Micro RNA
MitoMP	Mitochondrial membrane permeabilisation
MLL	Mixed lineage leukaemia
mM	Millimolar
mm	Millimetres
mMA	Monomethylation of arginine
MMP/7/9	Matrix metalloproteinase7/9
MMR	Mismatch repair
MND	Motor neuron disease
MR	Magnetic resonance
MRE11	Meiotic recombination 11
MRI	Magnetic resonance imaging
MRN	MRE11-RAD50-Nijmegen breakage syndrome 1
mRNA	Messenger RNA
MS	Mass spectrometry
MSc	Master of Science
MSCC	Methyl-sensitive cut counting analysis
MTA	2-methyladenosine

MTAP	Methyladenosine phosphorylase
MTIC	Monomethyl triazene 5-(3-methyltriazen-1-yl)-imidazole-4-carboxamide
MTND2P28	*Mitochondrially encoded NADH:ubiquinone oxidoreductase core subunit 2 pseudogene 28*
mTOR	Mammalian target if rapamycin
MTR	Maximum tumour resection
MTS	3-(4,5-dimethylthiazol-2-yl)-5-(3-carboxymethoxyphenyl)-2-(4-sulfophenyl)-2H-tetrazolium
Myc	Myelocytomatosis oncogene
Myr	Myristylation
$N^{+}H$	Cationic guanidino group
NaCl	Sodium chloride
NAD+	Nicotinamide adenine dinucleotide
NADH	Nicotinamide adenine dinucleotide
NADP+	Nicotinamide adenine dinucleotide phosphate ion
NADPH	Nicotinamide adenine dinucleotide phosphate
Na_v	Voltage gated sodium channel
NBA	Neurobasal A medium
Nd1-L	Kelch family gene
NES	Nuclear export sequence
Nf1	Neurofibromatosis 1
NFAT	Tonicity-responsive enhancer binding protein
NFκB	Nuclear factor kappa-light-chain-enhancer of activated B cells
ng	Nanograms
NHEJ/1	*Non-homologous end-joining/1*
NHS	National health service
NIFK	FHA domain of Ki-67
NIHR	National Institute for Health and Care Research
NLS	Nuclear localisation sequence
nM	Nanomolar
nm	Nanometres
No.	Number
NPC	Neural progenitor cell like
NSC	Neural stem cells
NTK	Natural killer cells
$O^{6}meG$	*O6-methylguanine*
OCT	Optimal Cutting Temperature compound
OCT4	Octamer-binding transcription factor 4
ODDD	Oxygen-dependent degradation domains
-OH	Hydroxyl group
OLIG2	Oligodendrocyte transcription factor 2
OPC	Oligodendrocyte progenitor cell like
OS	Overall survival
PABPC1	PolyA binding protein cytoplasmic 1

padj	Adjusted p value
PAR	Poly-ADP ribose
PARP1	Poly (ADP-ribose) polymerase 1
PBR	Peripheral-type benzodiazepine receptor
PBS	Phosphate buffered saline
PC1/2/3	Principal component 1/2/3
PCA	Principal component analysis
PCAF	GCN5/P300/CBP-associated factor
PCNA	Proliferating cell nuclear antigen
PD-1	Programmed cell death protein-1
PDGF/R/α	Platelet-derived growth factor/receptor/alpha
PDX	Patient derived xenografts
PERMANOVA	Permutation Analysis of Variance
PFA	Paraformaldehyde
PFS	Progression free survival
PHD	Prolyl hydroxylase
PI3K	Phosphoinositide 3-kinase
PI4K2A	Phosphatidylinositol 4-kinase type 2A
PIAS	Inhibitor of activated STAT
pICln	Ion chloride nucleotide-sensitive protein
PIK3CA	PI3K catalytic subunit alpha
PIP2	Phosphatidylinositol-3, 5-bisphosphate
PIP3	Phosphatidylinositol-3, 4, 5-bisphosphate
PKB/AKT	Protein kinase B
PKC	Protein kinase C
PL	Primary lamellae
PLCγ	Phospholipase C gamma
PLS-DA	Partial least square discriminant analysis
PmMA	Polymethyl methacrylate
PN	Proneural
POIs	Proteins of interest
POLD1	DNA polymerase D1
POLR2A	RNA polymerase II subunit A
PolyA	Poly adenylate
PolyT	Poly-thymidine
Polβ/δ/ε/μ/λ	DNA polymerase beta/delta/epsilon/mu/lambda
PRC	Polycomb repressive complexes
PRIDE	Proteomics identification database EMBL-EBI
PRMT/1/2/3/4/5/6/7/8/9	Protein arginine methyltransferase/1/2/3/4/5/6/7/8/9
PRMT1v2	PRMT1 splice variant 2
PROTAC	Proteolysis-targeting chimera
PTB	Polypyrimidine tracts-binding protein
PTEN	Phosphatase and tensin homolog
PTM	Post translational modification

PTPC	Permeability transition pore complex
PUMA	P53-upregulated modulator of apoptosis
PVC	Pavement cell
PVDF	Polyvinylidene difluoride
PY	Proline-tyrosine
Q	Flow rate
QC	Quality control
R&D	Research and Development
RAD51	Radiation sensitive protein 51
RAF	Rapidly accelerated fibrosarcoma
RanBP2	Ran binding protein 2
RAS	Rat sarcoma
Rb1	Retinoblastoma 1
RCC1	Regulator of chromatin condensation 1
Re	Reynold's number
RFC	Replication factor C
RGG3	Three repeat RGG/RG-rich domain
RIN	RNA integrity number
RIP1	Receptor-interacting protein-1
RIPA	Radioimmunoprecipitation assay
RNA	Ribose nucleic acid
RNAPII	RNA polymerase II
RNP	Ribonucleoprotein
ROCK2	Regulatory protein rho-kinase 2
ROS	Reactive oxygen species
RPA/C	Replication protein A/C
RRM	RNA recognition motif
rRNA	Ribosomal RNA
RTK	Receptor tyrosine kinase
S	Synthesis
s	Seconds
SAE1/2	SUMO-activating enzyme 1/2
SAH/AdoHcy	S-adenosyl-L-homocysteine
SAM/AdoMet	S-adenosyl-L-methionine
SAM68	Src associated in mitosis of 68 kDa
SAP145	Spliceosome-associated protein 145
SD	Standard Deviation
sDMA	Symmetric dimethylation of arginine
SDS	Sodium dodecyl sulphate
SDS-PAGE	Sodium dodecyl sulphate – poly-acrylamide gel electrophoresis
SE	Standard error
SERPIN E1	Serine protease inhibitor clade E member 1
SF3B2	Splicing factor 3B subunit 2
SFPQ	Splicing factor proline and glutamine-rich

SH3	*Src homology 3*
Shh	Sonic hedgehog
SHP1	Src homology region 2 domain-containing phosphatase-1
SL	Secondary lamellae
SMAC	Second mitochondria-derived activator of caspase
SMAD7	Mothers against decapentaplegic homolog 7
SMR	Supramaximal resection
SNF	Sucrose non-fermentable
SNHG16	Small Nucleolar RNA host gene 16
SNP	Single nucleotide polymorphism
snRNP	Small nuclear ribonuclease proteins
SNRPB	Small nuclear ribonucleoprotein-associated proteins B
SOX2	SRY-related HMG-box transcription factor 2
SRC	Non-receptor tyrosine kinase
SRY	Sex determining region
ssDNA	Single stranded DNA
STAT/3	Signal transducer and activator of transcription /3
STI1	Stress-inducible phosphoprotein 1
STRAP	Stress-responsive activator of p300
STRING	Search Tool for the Retrieval of Interacting Genes/Proteins
SUMO	Small ubiquitin-like modifier
SWI	Switch
T cell	Thyroid lymphocyte
TAD1	Trans-aconitate decarboxylase
TAF15	TATA-box binding protein associated factor 15
TAM	Tumour associated macrophages
TBC1D3K	TBC1 domain family member 3K
TBS	Tris-buffered saline
TCGA	The cancer genome atlas
TdT	Terminal deoxynucleotidyl
TEE	Thromboembolic event
TEMED	N, N, N’, N’-Tetramethylethan-1,2diamine
TERT	Telomerase reverse transcriptase
TET	Ten-eleven translocation
TFIID/H	Transcription factor IID/H
TGFβ	Transforming growth factor beta
Th1/2	T helper cell 1/2
TIE2	Tyrosine kinase with immunoglobin and EGF homology domains
TIMP3	Tissue inhibitor of metalloproteinase-3
TLS	Translocated in liposarcoma
TMZ	Temozolomide
TNF/R/α	Tumour necrosis factor/receptor/alpha
TNPO1	Transportin 1
TOPBP1	DNA topoisomerase II binding protein 1

TP53	Tumour protein 53
TRADD	TNFR1 associated death domain
TRAF2/6	TNF receptor associated factor 2/6
TRAIL	Tumour necrosis factor-related apoptosis-inducing ligand
Treg	T regulator cells
TRIM11	Tripartite motif containing 11
TRIP13	Thyroid receptor interacting protein-13
Tri-TPR	*Tetratricopeptide*
TTBS	Tween-20 with TBS
TTFIELDS	Tumour treating fields
TUNEL	Terminal deoxynucleotidyl transferase biotin-dUTP nick end labelling
u	Velocity
U	Units
UBC9	SUMO-specific conjugating enzyme
UK	United Kingdom
USP15	Ubiquitin carboxyl-terminal hydrolase 15
UV	Ultraviolet
V	Vacuole
VDAC	Voltage dependent anion channel
VDAC1	Voltage-dependent anion channel 1
VEGF/R	Vascular endothelial growth factor/receptor
VHL	Von Hippel Lindau
W	Watt
WDR5	WD repeat domain 5
WGS	Whole genome sequencing
WHO	World health organisation
Wnt	Wingless/integrated
XLF	XRCC4-like factor
XPC/G	Xeroderma pigmentosum complementation group C /G
XRCC1/4	X-ray repair cross-complementing protein 1/4
XRN2	Exoribonuclease 2
YTHDF2	YTH N6-methyladenosine RNA binding protein 2
YY1	Ying-yang 1
Znf	Zinc finger
αKG	Alpha-ketoglutarate
β-ME	B-mercaptoethanol
γH2AX	Gamma-histone2-
μm	Micrometres
ρ	Density

List of Equations

List of Appendices

CHAPTER 1: GENERAL INTRODUCTION

1.1. Aetiology and Epidemiology of Glioblastoma multiforme

Gliomas are cancers of glial cells, which make up the supportive tissue located in the brain and spinal cord and are the most common cancers of the central nervous system (CNS) (Cancer Research UK, 2021). Gliomas can arise in three types of glial tissue: astrocytes, forming astrocytomas, which are the most common; oligodendrocytes, forming oligodendrogliomas and ependymal cells, forming ependymomas (Weller *et al.*, 2015). Astrocytes contribute to 50% of overall brain mass (Kimelberg and Norenberg, 1989) and are essential for CNS homeostasis. Star-like projections, astrocytes form interactions with other neural cells and mediate response to external stimuli (Vasile *et al.*, 2017), being involved in regulation of blood pH and ion concentrations, glycogen and energy substrate synthesis and maintaining neurotransmission (Verkhratsky and Semyanov, 2022).

Glioblastoma (GBM) is a Grade 4, diffuse adult astrocytic glioma (Louis *et al.*, 2021) and the most common form of glioma, with 32% of primary brain tumour diagnoses in England being GBM, between 1995 and 2017 (Cancer Research UK, 2021). It is the most aggressive and therefore most devastating form of glioma, with a median survival of 1.5 years from initial diagnosis (Ostrom *et al.*, 2021). Prior to the 2021 reclassification (Louis *et al.*, 2021), gliomas which arose from neuronal, or glial stem cells at various stages of differentiation, were also classed as GBM (Phillips *et al.*, 2006). *De novo* disease is present in 90% of cases, with only 5% of patients having progression from lower WHO grade II/III gliomas (Janjua *et al.*, 2021). Ionising radiation has been shown to stimulate development of GBM. Relatively little else is known about the causes of GBM (Ellor *et al.*, 2014), although there are several theories. Germline predisposition occurs in less than 5% of cases, with syndromes such as *Neurofibromatosis I (Nf1)* (D'Angelo *et al.*, 2019); Li-Fraumeni, characterised by mutations in the *tumour protein (TP53)* gene (Shinagare *et al.*, 2011); Turcot, with mutations in *adenomatosis polyposis coli tumour suppressor* (*APC)* and *hereditary nonpolyposis colorectal cancer* (*HNPCC)* genes (Harned *et al.*, 1991) and Ollier (Hori *et al.*, 2010). There is also some debate as to whether traumatic brain injury may drive development of GBM, due to the infiltration of inflammatory factors, progenitor cells, or astrocytic dedifferentiation (Al-Kharboosh *et al.*, 2020, An *et al.*, 2024).

There are several recognised variants of GBM, including: giant cell, characterised by large multinucleated cells; gliosarcoma, with sarcomatous tissue and epithelioid, which have an eosinophilic cytoplasm and vesicular chromatin (Louis *et al.*, 2021). It is widely accepted that GBM cells can exist in at least three subtypes, in different clonal regions, in different patients, determined using data from The Cancer Genome Atlas (TCGA): classical (CL), proneural (PN) and mesenchymal (ME) (Neftel *et al.*, 2019). These subtypes contain varying proportions of GBM cells in four transcriptional states, indicated by single cell ribonucleic acid (RNA) sequencing: oligodendrocyte progenitor cell like (OPCs), astrocyte like (ACs), neural progenitor cell like (NPCs) and mesenchymal cell like (MES) (Wang *et al.*, 2017, Verhaak *et al.*, 2010). The classical subtype is more associated with ACs and some MES cells, the ME subtype is characterised by MES cells and the proneural subtype contains more NPCs and OPCs (Neftel *et al.*, 2019). Each of the cell states is characterised by different biological markers. ACs display *epithelial growth factor receptor* (*EGFR)* aberrations and chromosome 7 gain/chromosome 10 loss (+7/-10), whereas NPCs and OPCs contain high levels of *platelet-derived growth factor receptor (PDGFRA)* and *cyclin dependent kinase (CDK4)* and MES cell states are associated with loss of function *Nf1* mutations and chromosome 5q deletions (Neftel *et al.*, 2019), as well as presence of *chitinase-3-like-1 (C3L1)* and *cluster of differentiation 44 (CD44)* (Kanderi *et al.*, 2024). There are several hypotheses on the developmental origin of GBM. The hierarchical theory suggests that glioma stem cells (GSCs) are responsible for gliomagenesis, whereas the dedifferentiation model hypothesises that OPCs, ACs and NPCs are responsible (Jovcevska, 2019).

Akin to many cancers, GBM is a disease of age, with the mean age of patients being 62 years. Men also appear to be more affected by GBM than women, with men being ~60% more likely to develop a primary GBM tumour and women tending to have increased survival (Carrano *et al.*, 2021). There is a higher incidence of left-sided, frontal primary tumour presentation in men (Li *et al.*, 2018), with higher androgen levels being associated with having a transcriptional effect on neural stem cells (NSCs), and inhibition of androgen receptor signalling being found to cause GBM cell death (Bao *et al.*, 2017a, Bramble *et al.*, 2016). An anti-inflammatory environment, more often seen in men, is also associated with worse prognosis (Sorensen *et al.*, 2018) and greater tumour growth is associated with expression of genes such as *sonic hedgehog*

(shh), which is linked with tumour invasion and progression (Buczkowicz *et al.*, 2014) (Kfoury *et al.*, 2018). Conversely, women more commonly appear to develop secondary GBM tumours (those resulting from lower grade gliomas) in the right temporal lobe (Li *et al.*, 2018), with the effect of oestrogen found to be protective in mobilising NSCs (He *et al.*, 2015), therefore displaying longer survival in pre-menopausal women (Altinoz *et al.*, 2019). The pro-inflammatory environment, interestingly, is associated with longer survival, with oestrogen exhibiting a sex-specific effect on interleukin-1β (IL1β), subsequently producing opposing inflammatory effects on microglia in the different sexes (Gold *et al.*, 2019). *Nf1* inactivation and *retinoblastoma 1* (*Rb1)* have also been seen to reduce tumour growth, driving cells more towards the mesenchymal phenotype and causing a sexually dimorphic effect, whereby CDK inhibitors p16, p21 and p27 are increased, thereby reducing tumour growth in females, but not in males (Kfoury *et al.*, 2018, Buczkowicz *et al.*, 2014). There is also a higher prevalence of O6-methylguanine-methyltransferase (MGMT) promoter methylation in women (80%), *vs* men (27%), which conveys better prognosis (Franceschi *et al.*, 2018).

As well as differences in sexes and higher prevalences in older age groups, GBM incidence and survival varies between ethnicities. After adjustments for age, gender, primary tumour site, tumour size and surgical implications, patients from Asian and Pacific Island backgrounds were generally found to have a prognostic advantage, followed by those with Hispanic heritage, Black African and Black Caribbean backgrounds and then by those of a Caucasian ethnic origin, with 3-year survival rates being 36.6%, 32.3%, 28.8% and 27.7%, respectively (Crimmins *et al.*, 2021, Bohn *et al.*, 2018). The reasons behind these figures have been speculated to be socioeconomic, with those from Asian and Pacific Island backgrounds due to the general presence of extended family, who may notice neurological changes quicker than those in the stereotypical nuclear family associated with Caucasian communities, therefore leading to earlier diagnosis, conferring better survival outcomes (Patel *et al.*, 2019). A lower incidence (-42%) of GBM has also been found in people with diabetes (Kitahara *et al.*, 2014) and individuals from Black and South Asian origins are at an increased risk of developing earlier onset type II diabetes, therefore potentially conveying a reduced risk of developing GBM (Whyte *et al.*, 2019). Further research would be required to elucidate ethnic differences in GBM occurrence.

1.2. Clinical Presentation and Diagnosis

Patient presentation of GBM is dependent upon the location of the tumour. Patients with suspected lesions within the frontal, or temporal lobes and the corpus callosum (Figure 1.1) usually present with mood disorders and some memory loss, whilst patients with tumours in other areas may suffer from seizures, compromised vision, or motor function (Kanderi *et al.*, 2024). Computed Tomography (CT) scans may indicate irregular thick margins, with a dense necrotic centre and surrounding oedema from loose gap junctions (Gaillard, 2008). Magnetic resonance imaging (MRI) scans confirm GBM through identifications of a ring-enhancing lesion with central necrosis, surrounded by a ring of peri-tumoural oedema (Alexander and Cloughesy, 2017). Figure 1.1.2(taken from (Melhem *et al.*, 2022)) shows several MRI imaging techniques of a patient with a left frontal GBM tumour.

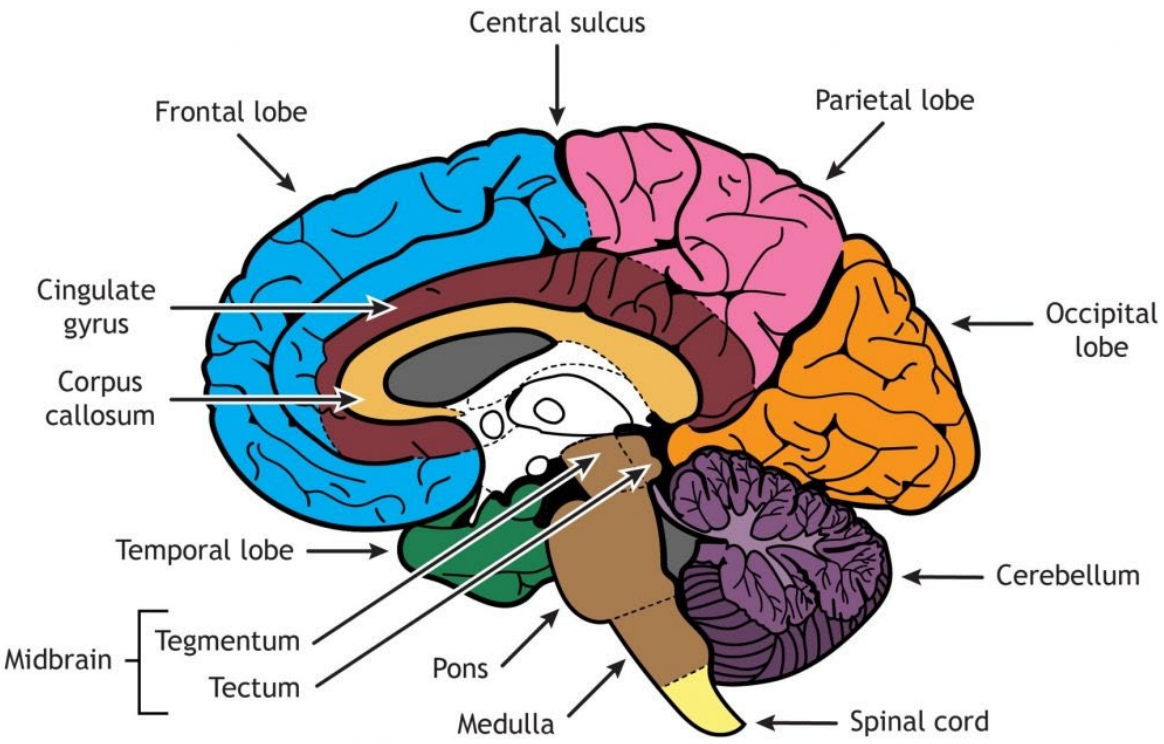

Figure 1.1.1.: Schematic of the lobes of the brain

Midsagittal diagram indicating the main features and lobes of the brain. Figure taken from 'Internal Brain Regions' by Casey Henley *and is licensed under a* Creative Commons Attribution Non-Commercial Share-Alike *(CC BY-NC-SA) 4.0 International License. ~(https://openbooks.lib.msu.edu/introneuroscience1/chapter/external-brain-anatomy/).*

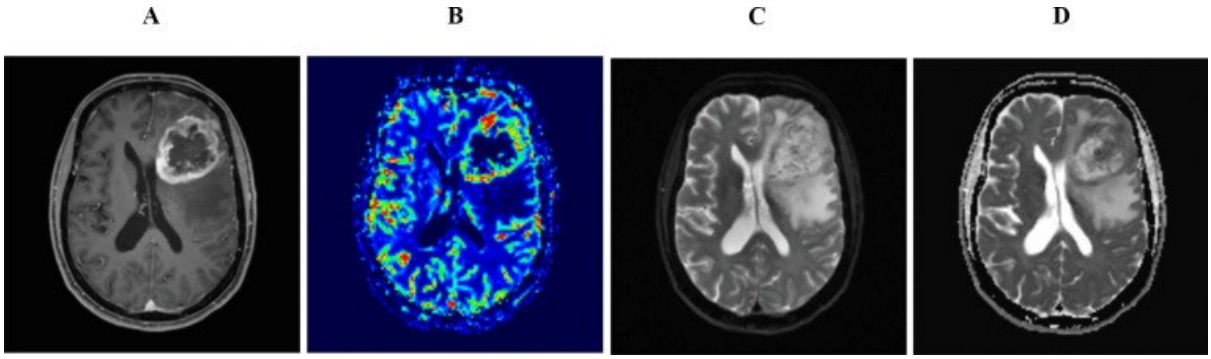

Figure 1.1.2.: Contrast-enhanced T1 imaging of patient with IDH-wildtype GBM.

A) *T1-W1 dynamic susceptibility contrast MRI of a large necrotic mass in left frontal region.* ***B)*** *Elevated cerebral blood volume on magnetic resonance (MR) perfusion correlates to areas of enhancement in MRI.* ***C)*** *Compared to diffusion weighted imaging (DWI) map,* ***D)*** *cellular heterogeneity is evident within the tumour fields as more hypercellular areas demonstrates higher signal drop on the apparent diffusion coefficients (ADC) map (GBM has a lower ADC compared to gliomas of lower grades). Image taken from (Melhem et al., 2022).*

Histopathology of GBM sections may indicate high mitotic and angiogenic marker expression; microvasculature; central necrosis, or multiple foci surrounded by pseudopalisading cells and Weibel-Palade bodies, which contribute to inflammation and angiogenesis (Kanderi *et al.*, 2024). Magnetic resonance (MR) spectroscopy indicating an elevated choline peak also confirms changes in brain metabolism, including necrosis and increased cellular proliferation (Di Costanzo *et al.*, 2006). Histopathological analysis is also performed on patient tissues for IDH-wildtype status, glial fibrillary acidic protein (GFAP) and prognostic MGMT promoter methylation (Stoyanov *et al.*, 2019). GFAP is a cytoskeletal protein which is highly expressed in GBM, but not in other primary brain tumours, or brain metastases (Jung *et al.*, 2007). Various other genetic testing also determines confounding molecular biomarkers present in the tumours of patients, which aid towards diagnosis and prognosis of the patient.

1.2.1. Classification

During the course of this work, GBM has been reclassified by the WHO (Louis *et al.*, 2016, Louis *et al.*, 2021) and therefore the threshold for the types of tissue that this project has

received has altered slightly. There are a few GBM tissue samples which fall under the realm of the pre-2021 molecular classification; however, the majority of tissues adhere to the new definition of GBM.

Pre-2021, GBM was defined as a grade IV astrocytoma and could be *isocitrate dehydrogenase 1* (*IDH1)* wildtype, or mutated. Grade II was labelled diffuse astrocytoma, Grade III anaplastic astrocytoma and Grade IV GBM, which may or may not have alpha-thalassaemia syndrome X-linked (*ATRX)* loss, *TP53* mutation and Cyclin-dependent kinase inhibitor 2A/B (*CDKN2A/B)* loss (Louis *et al.*, 2016). Reclassification means that GBM has been defined as a diffuse astrocytic adult glioma, which now must display *IDH1* wildtype homozygosity, as well as histone 3 lysine 27 (H3K27) wildtype status, whereby H3K27 is trimethylated. GBM may also display: telomerase reverse transcriptase (*TERT)* promoter alterations, +7/-10, *EGFR* amplification, *CDKN2A/B* homozygous deletion. Necrosis, or microvascular proliferation may also be present, but this is not a necessity, if the molecular pre-requisites are met (Sareen *et al.*, 2022, Louis *et al.*, 2021). Any glioma which meets the 2021 molecular classification requirements is automatically classified at Grade 4 GBM, replacing the Grade II-IV of the 2016 revision (Louis *et al.*, 2021). *MGMT* promoter methylation remains an important predictive and prognostic biomarker (Park *et al.*, 2023). GBM is highly genetically heterogenous, both between patients and in within the tumour of an individual patients and therefore, there are several molecular markers associated with GBM (Miranda *et al.*, 2017).

1.2.1.1. *IDH1* and *IDH2*

IDH1 and IDH2 are involved in the production of alpha-ketoglutarate (α-KG), from isocitrate, *via* reduction of nicotinamide adenine dinucleotide phosphate (NADP+) to NADPH, in the Krebs cycle. The former carries out this reaction in the cytoplasm, whilst the latter carries out this reaction within the mitochondria . Prior to WHO 2021 classification, *IDH1* mutation, IDH1_R132H formed a subtype of GBM, associated with better overall survival, than in patients with the wildtype *IDH1* gene (Khan *et al.*, 2017). This mutation is cause by a single nucleotide polymorphism (SNP) (G to A) at the codon encoding for arginine at position 132, changing the residue to a histidine (Machida *et al.*, 2020). This mutation causes a decreased binding affinity for isocitrate and increased binding affinity for NADPH, causing a reduction in α-KG production and an increase in 2-hydroxyglutarate (2-HG) production, which differs

only in a hydroxyl group, in place of the carbonyl group and acts as a competitive inhibitor of α-KG reactions. This leads to dysregulation in deoxyribose nucleic acid (DNA) and histone methylation, as well as hypoxia, which in turn leads to hypoxia inducible factor 1α (*HIF1α)* upregulation and differentiation inhibition. *IDH1* mutation is also generally reported in younger GBM patients, giving them a 25% overall increase in life expectancy, over patients with wildtype *IDH1* (Ahmadipour *et al.*, 2019). *IDH1* mutation also occurs early in the glioma forming process and is therefore present in lower grade gliomas, as well as GBM, therefore it is not the only biomarker utilised to clinically diagnose GBM (Watanabe *et al.*, 2009). *IDH2* R172H/S mutation occurs at arginine residue 172 of the *IDH2* gene. It is less common than its *IDH1* R132H counterpart in gliomas, but is generally mutually exclusive to *IDH1* mutation and also confers better prognostic outcome to patients (Cho et al., 2021b). On the recommendation of the Consortium to Inform Molecular and Practical Approaches to CNS Tumour Taxonomy (cIMPACT-NOW) (Tesileanu *et al.*, 2020), in 2021, the WHO reconsidered *IDH1/2* mutant tumours to be alternative gliomas to GBM, with GBM being classified as only having wildtype *IDH1/2,* which may have several other molecular biomarkers (Louis *et al.*, 2021).

1.2.1.2. *TERT Promoter Alterations*

TERT are nucleoprotein complexes, found at the ends of telomeres and are responsible for maintaining telomere integrity to allow accurate cellular division, until telomeres shorten enough to lead to senescence, or cell death (Kim *et al.*, 1994). *TERT* promoter alterations are a common feature in many cancers which do not have an abundance of self-renewing tissue, including GBM (Yuan *et al.*, 2019). Mutually exclusive cytidine to thymidine dypyrimide transition in *TERT* promoters occur at 124bp (C228T) and 146bp (C250T) upstream of the translational start site, in the promoter region (Olympios *et al.*, 2021). Other alterations, including tandem nucleotide duplications and methylation occur much less frequently, but many of these *TERT* promoter variants are gain of function and cause upregulation in the production of *TERT* (Pierini *et al.*, 2020). Activation of TERT is essential in tumourigenesis, as it allows cancers to develop the characteristic "immortality" cancer hallmark (Hanahan and Weinberg, 2000, Hanahan and Weinberg, 2011). Due to the activation of *TERT,* telomeres are repaired and cells acquire the ability to replicate, without entering senescence, or leading to cell death and this makes them more susceptible to chemotherapy which targets rapidly

dividing cancer cells, over healthy cells which replicate at a normal rate (Bell *et al.*, 2016). In IDH-wildtype gliomas, *TERT* promoter alteration has been linked with a more clinically and biologically aggressive phenotype (Arita *et al.*, 2020).

1.2.1.3. *Chromosomal abnormalities*

Several losses and gains of chromosomes, resulting in copy number variation, are found in GBM. The most common are: loss of heterozygosity of chromosome 10 which is associated with phosphatase and tensin homolog (PTEN) (10q23.31) and phosphatidylinositol 4-kinase type 2A (PI4K2A) (10q24) loss; this happens in concurrence with polysomy of chromosome 7, which is associated with EGFR (7p12) and mesenchymal-epithelial transition (MET) (7q31) copy number amplification and homozygous 9p21 loss is associated with CDKN2A loss (Brennan *et al.*, 2013, Verhaak *et al.*, 2010).

Other, less frequent alterations in chromosome number occur in chromosomes: 4q12 leading to PDGFRα amplification; 7q21 polysomy increasing CDK6 expression; 12q resulting in the increase of CDK4 (12q14) and murine double minute 2 (MDM2) (12q15); 13q14 which is associated with loss of Rb1 and 17q11.2 hemizygous deletion containing *Nf1* (Verhaak *et al.*, 2010).

1.2.1.4. *EGFR signalling*

EGFR is a transmembrane receptor tyrosine kinase (RTK) and key regulator of epithelial cell development and homeostasis and is often dysregulated in many cancers, including in GBM (Sigismund *et al.*, 2018), being associated more with classical GBM subtype (Verhaak *et al.*, 2010). In a study by Higa *et al.* (2023), copy number amplification and subsequent overexpression of EGFR, associated with chromosome 7p gain, occurred in approximately 23.9% GBM patients and 10% had other EGFR mutations. Other sources report a prevalence of EGFR alteration in ~50% of patients (Brennan *et al.*, 2013). EGFR alteration leads to increased signalling and activation of transcriptional pathways responsible for proliferation, differentiation and survival (An *et al.*, 2018).

EGFR triggers a series of signalling pathways (Higa *et al.*, 2023) (Figure 1.1.3). The rat sarcoma (RAS) (*e.g. Nf1*)/mitogen activated protein kinase (MAPK)/extracellular signal-related kinase (ERK) pathway, leads to transcription factor motility (Deschenes-Simard *et al.*, 2014). After ligand binding, EGFR may also bind phosphoinositide 3-kinase (PI3K), which causes a phosphorylation cascade, converting phosphatidylinositol-3, 5-bisphosphate (PIP2) into phosphatidylinositol-3, 4, 5-bisphosphate (PIP3), which subsequently phosphorylates protein kinase B (PKB/Akt), involved in the mammalian target if rapamycin (mTOR) signalling cascade and proliferative and metabolic regulation (Lemmon *et al.*, 2014, Thorpe *et al.*, 2015). This pathway is also negatively regulated by *PTEN*, which has been found to be lost with chromosome 10 deletion in GBM, thereby preventing inhibition of the PI3K/Akt pathway (Ozawa *et al.*, 2014). EGFR also initiates the Janus kinase (JAK)/signal transducer and activator of transcription (STAT) pathway, which facilitates inflammation-associated tumourigenesis and migration (O'Shea *et al.*, 2015). STAT proteins can also be motivated by EGFR-mediated Akt activation, mediating DNA methylation (Kim *et al.*, 2013). The presence of EGFRvIII drives *PTEN* loss-induced malignant transformation of astrocytes, which is otherwise repressed by transcription factor STAT3 activation (de la Iglesia *et al.*, 2008, Hashemi *et al.*, 2023). The protein kinase C (PKC) pathway is associated with angiogenesis and inflammation (Garg *et al.*, 2014), with high levels of PKC denominations being associated with poor survival (Mawrin *et al.*, 2003). EGFR can also affect signalling molecules, including DNA protein kinase (DNA-PK) and histone H4. EGFR oncogenic variant EGFRvIII is formed when there is a deletion of *EGFR* exons 2-7, which renders the variant constitutively active, as do other point mutations, such as R108K and G598D (Furnari *et al.*, 2015).

There has been some debate as to whether EGFR amplification in GBM displays a more aggressive phenotype and is associated with reduced survival (Guo *et al.*, 2022), or has the opposite effect on prognosis (Higa *et al.*, 2023). Interestingly, Guo *et al. (2022)* determined that constitutively high expression of EGFR ligand results in small hyper-proliferating, but non-invasive tumours and thereby becoming tumour-suppressive *via* inhibiting a dedicator of cytokinesis 7 (DOCK7)-regulated Rho guanosine triphosphate(GTP)ase pathway. Several drugs have been trialled to target EGFR overexpression, *via* tyrosine kinase inhibitors, including gefitinib, erlotinib and afatinib (An *et al.*, 2018) with limited success (Vivanco *et al.*, 2012).

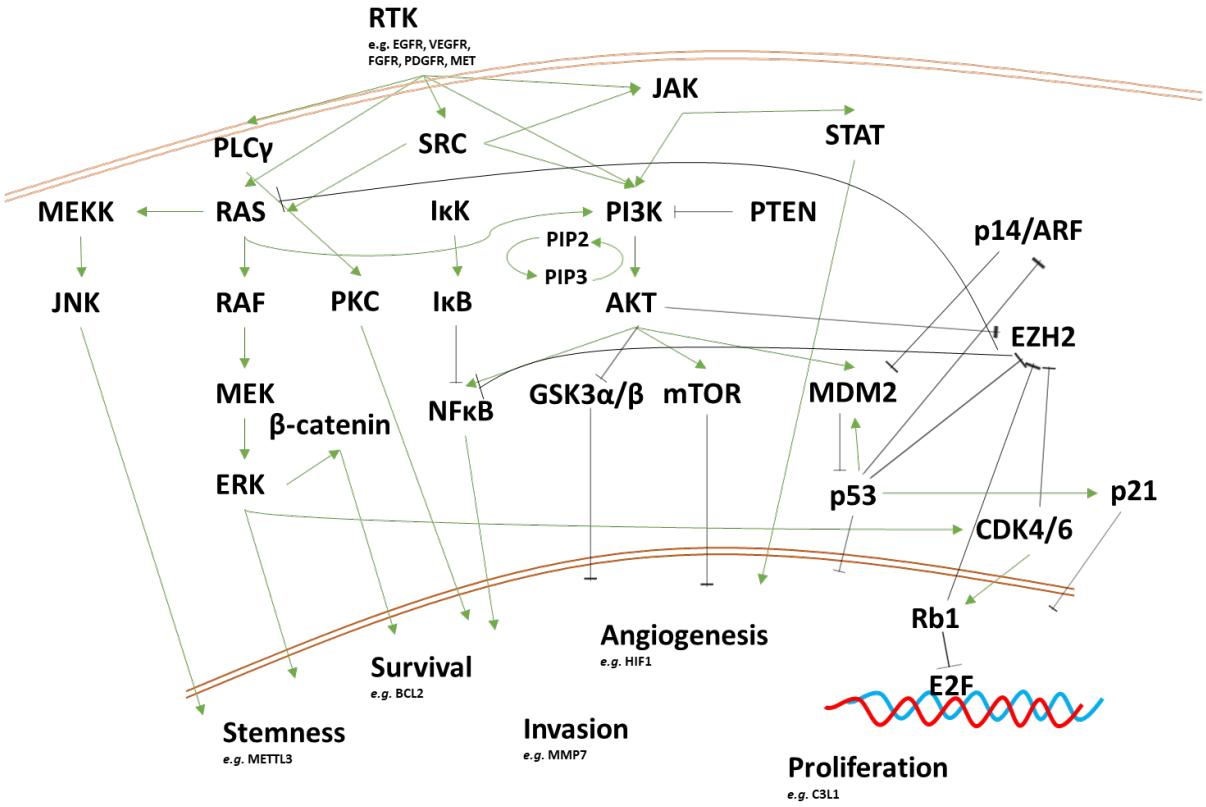

Figure 1.1.3.: Receptor tyrosine kinase (RTK) signalling pathways

RTKs include: epidermal growth factor receptor (EGFR); vascular endothelial growth factor receptor (VEGFR); fibroblast growth factor receptor (FGFR); platelet-derived growth factor receptor (PDGFR) and mesenchymal epithelial transition (MET). Mitogen-activated protein kinase kinase (MEKK); c-Jun N-terminal kinase (JNK); phospholipase C gamma (PLCγ); rat sarcoma GTPase (RAS); rapidly accelerated fibrosarcoma (RAF); mitogen-activated protein kinase (MEK); extracellular signal-related kinase (ERK); beta-catenin (β-catenin); non-receptor tyrosine kinase (SRC); nuclear factor kappa B (NFκB); IκB kinase (IκK); inhibitor of NFκB (IκB); Janus kinase (JAK); phosphoinositide 3 kinase (PI3K); phosphatidyl inositol 4, 5-bisphosphate (PIP2); phosphatidyl inositol 3, 4, 5-trisphosphate (PIP3); protein kinase B (AKT); glycogen synthase kinase α/β (GSKα/β); mammalian target if rapamycin (mTOR); phosphatase and tensin homolog (PTEN); signal transducer and activator of transcription (STAT); mouse double minute protein 2 (MDM2); ADP-ribosylation factor (ARF); enhancer of zeste homolog 2 (EZH2); cyclin-dependent kinase 4/6 (CDK4/6); p21; retinoblastoma 1 (Rb1) and eukaryotic transcription factor 2 (E2F). Resulting downstream effects and potential effectors include: stemness, methyltransferase-like 3 (METTL3); survival, B cell lymphoma 2

(BCL2); invasion, matrix metalloproteinase 7 (MMP7); angiogenesis, hypoxia inducible factor 1 (HIF1) and proliferation, chitinase 3-like 1 (C3L1).

1.2.1.5. *Other receptor tyrosine kinase signalling*

Fibroblast growth factor (FGF), platelet-derived growth factor (PDGF) and vascular endothelial growth factor (VEGF) RTK signalling have also been described in the progression of GBM (Figure 1.1.3). FGF modulates tissue repair and regeneration though proliferation, GSC self-renewal and morphogenesis, *via* the RAS/MAPK, PI3K/Akt, phospholipase C gamma (PLCγ) and STAT pathways, by stimulating production of *e.g.* matrix metalloproteinase 7 (MMP7), causing angiogenesis (Farooq *et al.*, 2021, Pollard *et al.*, 2009). PDGF mediates signalling through PDGFRα, which is responsible for intertumour heterogeneity and is enriched in the proneural subtype and PDGFRβ, which informs intratumour heterogeneity and is expressed in GSCs in the proneural and mesenchymal subgroups (Verhaak *et al.*, 2010). High PDGF expression has been linked to PTEN loss in wildtype GBM, as well as simultaneous mutations in other RTKs, such as EGFR and MET. VEGF is a mediator of hypoxia-induced glioma progression and is found to be expressed with the necrotic core of GBM, stimulating pro-angiogenic activity (Chi *et al.*, 2009, Ahir *et al.*, 2020). N6-methyladenosine (m^6A) is a transcriptional modification, which accumulates in GSCs, induced by PDGF signalling, as well as EGFR and VEGF signalling (Yue *et al.*, 2015). m^6A helps to target mRNA for splicing, export and translation and its regulators have been reported to be positively correlated with VEGFR, EGFR and PDGFR signalling pathways and negatively correlated with enhancer of zeste homolog 2 (EZH2). m^6A accumulation as a result of constitutive PDGF signalling and *via* methyltransferase-like 3 (METTL3) has been linked to GSC proliferation and stemness (Lv *et al.*, 2022). This has been recapitulated by Lane *et al.* (2022) who found that inhibition of PDGFR induces differentiation of GSCs into neural-like cells, slowing proliferation and invasion, *via* the Akt/MAPK pathway. Neurotrophic RTK oncogenic gene fusions have also been found in GBM, albeit at a lower rate than some other RTKs at 1.69%, (Wang *et al.*, 2020b) again allowing dysregulation of the PI3K/AKT/mTOR, PLCγ/PKC and RAS/RAF/ mitogen-activated protein kinase (MEK)/ERK pathways (Cocco *et al.*, 2018).

1.2.1.6. *p53 pathway*

P53 is a transcription factor that is widely mutated in many cancers, including GBM, where mutations appear in approximately 84% of patients (Brennan *et al.*, 2013). Gain of function of oncogenic variants causes dysregulation of the p53/p14/MDM2 axis, leading to genomic instability, angiogenesis and evasion of apoptosis (Zhang *et al.*, 2018b). P53 is generally activated in response to cellular stress, such as hypoxia and DNA damage and mutational variants result in p53 inactivation (England *et al.*, 2013). Dysregulation of the p53 pathway (Figure 1.1.4) is linked to CDKNA2/p14 locus deletion, which then inhibits the degradation of MDM2, therefore allowing degradation of p53 and leading to a suppression of the DNA damage response (DDR) (Figure 1.1.5) and apoptotic response associated with p53-regulated genes (Leroy *et al.*, 2013). Adenosine diphosphate (ADP) ribosylation factor (ARF)/p14 has also been shown to upregulate tissue inhibitor of metalloproteinase-3 (TIMP3), therefore dysregulation of this pathway leads to GBM cell migration (Zerrouqi *et al.*, 2012). TP53 loss of functions mutations are mutually exclusive to MDM2 amplifications (Ghimenti *et al.*, 2003). The p53 pathway is also linked to Rb1, whereby eukaryotic transcription factor 2 (E2F) dissociation from Rb1 and subsequent activation is stimulated by the MAPK/CDK4/6 pathway, leading to stimulation of p14 to inhibit MDM2 (Dono *et al.*, 2021). Rb1 mutations have been found to convey improved progression-free survival in GBM patients, with decreased frequency of CDKN2A/B loss and EGFR amplification. Loss of function of Rb1 leads to replication stress and initiation of the DDR, leading to GBM cell death (Dono *et al.*, 2021).

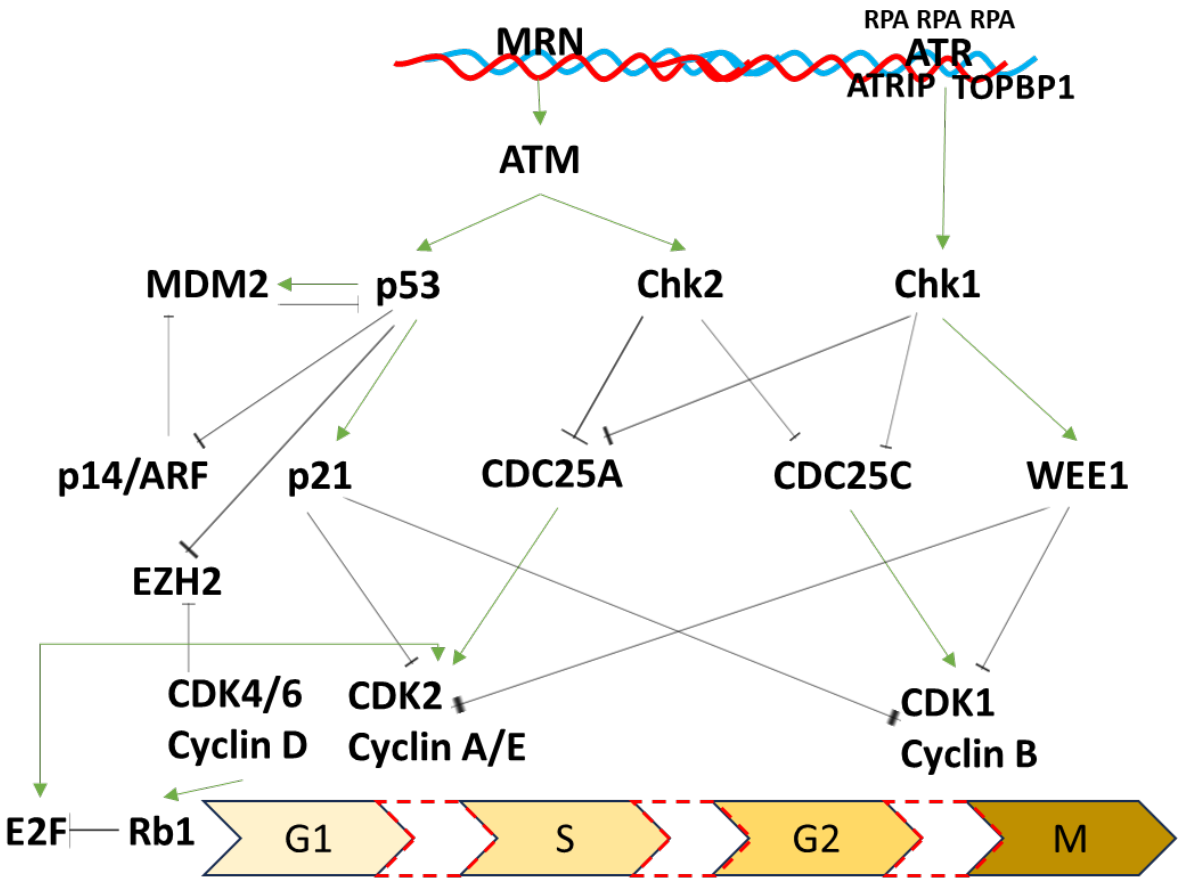

Figure 1.1.4.: P53 pathway

Meiotic recombination 11-RAD50-Nijmegen breakage syndrome 1 (MRN) recognises double strand breaks (DSBs) and recruits ataxia telangiectasia mutated (ATM). The phosphorylation cascade affects: p53, which induces p21 to inhibit cyclin dependent kinase 2 (CDK2) and cyclin A/E, arresting the cell cycle at the gap phase (G)1/synthesis (S) transition; or checkpoint 2 (Chk2), which inhibits phosphatase cell division cycle 25 homolog A (CDC25A) through ubiquitination and degradation, which would otherwise continue the G2/mitosis (M) transition. P53 also inhibits enhancer of zeste homolog 2 (EZH2), preventing histone methyltransferase activity and p14/ADP-ribosylation factor (ARF), which inhibits MDM2. Cyclin-dependent kinase 4/6 (CDK4/6) and cyclin D also inhibit EZH2, as well as encouraging dissociation of inhibitory retinoblastoma 1 (Rb1) from eukaryotic transcription factor 2 (E2F), allowing transcription. E2F is also activated by CDK2/Cyclin E at the G1/S transition and activates CDK2/Cyclin A. Ataxia telangiectasia and rad3 related (ATR) is recruited to replication protein A (RPA)-coated single stranded DNA overhangs, alongside ATR-interacting protein (ATRIP) and DNA topoisomerase II binding protein 1 (TOPBP1), leading to checkpoint protein

1 (Chk1) phosphorylation and subsequent inhibition of phosphatase cell division cycle 25 homolog C (CDC25C) and activation of phosphatase WEE1, which prevents cyclin dependent kinase 1 (CDK1) and cyclin B for progressing the G2/M cell cycle transition. The pathways also cause cross inhibition of cell cycle phases (Ding et al. 2020)(Kung and Weber, 2022)(Choi and Lee, 2022).

1.3. Treatment

1.3.1. Current Methods

Upon diagnosis of a patient with a brain tumour, patients are immediately put on Dexamethasone (DEX), a synthetic glucocorticoid, to reduce inflammation and cerebral oedema at the tumour site, thereby alleviating cranial pressure and often, some of the symptoms that the patient may have been experiencing (Cenciarini *et al.*, 2019). DEX is given twice per day, at the time of initial diagnosis and through imaging. Standard procedure is that patients receive 8 mg Dex for at least 48 hours, which is then reduced to between 2–4 mg until the day of surgery. Dose is then increased back to 8 mg on the day of surgery for 48 hours, and then again reduced to 2 mg (Barry *et al.*, 2023). Gross total resection (GTR) is the preferred outcome of surgery, where possible, with progression-free survival (PFS) increasing by 50% over supramaximal resection (SMR) and maximum tumour resection (MTR) of more than 89% also leading to a better prognosis (Wang *et al.*, 2019a). Resection is guided by intraoperative imaging with 5-aminolevulinic acid (5-ALA), which identifies the infiltrative margin of the tumour to get as close to GTR as possible (McCracken *et al.*, 2022). Awake craniotomy is preferred, should the patient tolerate it, to reduce further damage to areas of the brain which may impact quality of life, such as the motor cortex, or speech centre (Ramakrishnan *et al.*, 2024). The diffuse nature of GBM, however, makes GTR and MTR very difficult, therefore recurrence after resection is highly likely (The GLASS Consortium, 2018).

Surgery is followed by adjuvant radiotherapy and chemotherapy with alkylating agent temozolomide (TMZ) (Kaina, 2023), known as the Stupp Regimen. Ionising photon radiotherapy is generally given at 60 Grays (Gy) over the course of 6 weeks, or between 25-40Gy in 5-15 daily fractions, depending on the tolerance of the patient (Perry *et al.*, 2017, Minniti *et al.*, 2019). Radiation causes single and double stranded DNA breaks in the rapidly

dividing cells, which cannot then be repaired by the DDR (Figure 1.1.5), therefore the cells are marked for senescence, or apoptosis. Ionising radiation triggers a cascade involving ataxia telangiectasia mutated (ATM) protein and p53, which induces apoptosis by p21-mediated inhibition of CDKs and also by stimulating apoptotic B-cell lymphoma 2 (Bcl-2) and Bcl-2-associated X protein (Bax) expression, preventing gap phase (G)1 to synthesis (S) phase transition (Jonathan *et al.*, 1999).

TMZ has many advantages that lend itself to being a good first line chemotherapy for GBM. These include oral administration and excellent bioavailability, allowing almost 100% of the drug to enter circulation; stability in high acidity environment, allowing spontaneous breakdown into its active form monomethyl triazene 5-(3-methyltriazen-1-yl)-imidazole-4-carboxamide (MTIC) with the increasing pH of the GBM tumour microenvironment (TME) (Zhang *et al.*, 2012); and in conjunction with other drugs and its ability to penetrate the blood brain barrier (BBB) (Hu *et al.*, 2020b). TMZ adds an alkyl group to guanine N7 residues, within guanine-rich regions, as well as less frequently at O6 residues and N3 adenine residues. Alkylation induces adducts in the DNA, which are then repaired by base excision repair (BER) (Figure 1.1.5) and MGMT enzyme repair (Figure 1.1.6) (Bobola *et al.*, 2012). TMZ is S-phase dependent, as it causes mispairing of bases which is then detected by mismatch repair (MMR) proteins, resulting in double stranded breaks through S-phase development, therefore performing its cytotoxic effect (Kaina, 2023, Kaina and Christmann, 2019).

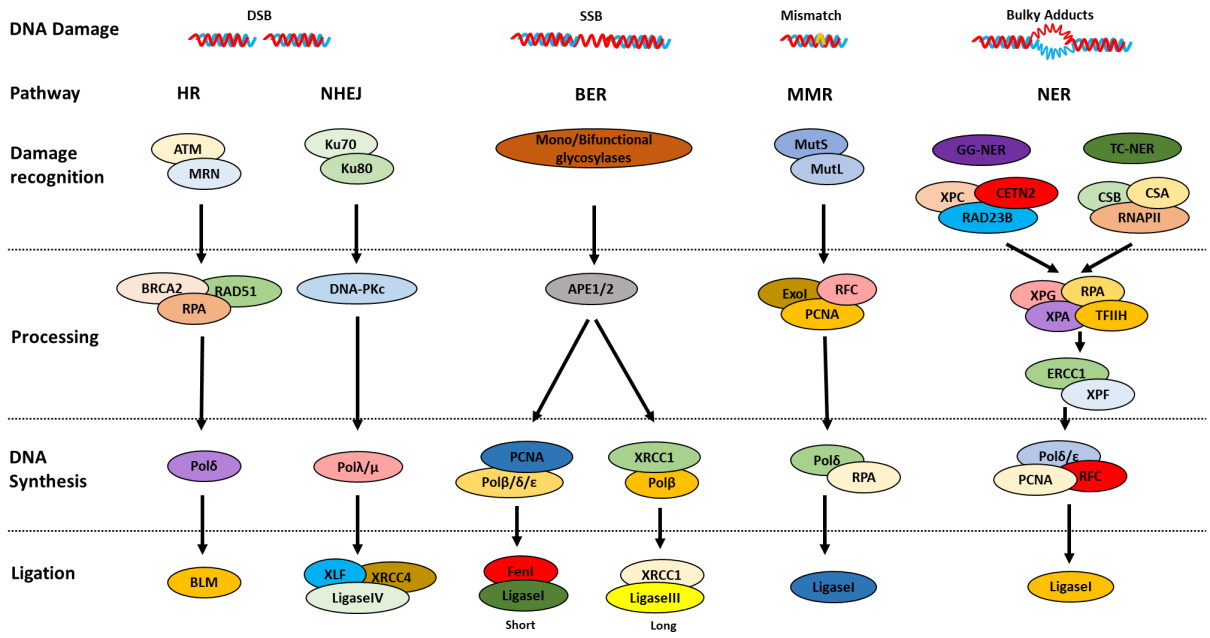

Figure 1.1.5.: DNA damage response (DDR) pathways.

DNA damage by double strand breaks (DSB) is repaired by homologous recombination (HR), or non-homologous end-joining (NHEJ). For HR to occur, the sister chromatid is used. Upon DSB, ataxia telangiectasia mutated (ATM) is recruited by the meiotic recombination 11-RAD50-Nijmegen breakage syndrome 1 (MRN) complex, which stabilises the chromatin. Ataxia telangiectasia and rad3 related (ATR) is recruited to replication protein A (RPA)-coated single stranded DNA overhangs. (BRCA2) then recruits radiation sensitive protein 51 (RAD51) to the DSB and replaces RPA, forming a D-loop with the invading 3' ssDNA and homologous chromosome. Strands are repaired by DNA polymerase δ (polδ) and ligated by Bloom syndrome protein (BLM) helicase (Ranjha et al. 2018). NHEJ is less accurate but is quicker as the broken ends are ligated together. The DNA-binding regulatory subunits Ku70 and Ku80 dimers recognise the DSB and recruits DNA-dependent protein kinase catalytic subunits (DNA-PKc), which autophosphorylate and recruits further factors, including Polλ/μ to synthesise DNA to repair the gap and ends are then joined by X-ray repair cross-complementing protein 4 (XRCC4), XRCC4-like factor (XLF) and ligase IV (Lieber, 2010). The base excision repair (BER) pathway repairs single strand breaks (SSB), caused by reactive oxygen species (ROS), or alkylating agents, by short- (1 nucleotide), or long-patch (2-10 nucleotides) repair. Aberrant bases are excised by mono- or bi-functional glycosylases, leaving an apyrimidine (AP) site. This is recognised by AP endonucleases (APE1/2) which cleave the

site, leaving a 5'deoxyribose phosphate (dRP) termini, which is cleaved by Polβ/δ/ε, aided by proliferating cell nuclear antigen (PCNA) and the nick repaired by ligase I with flap structure specific endonuclease 1 (Fen1) for short-path repair, or XRCC1 and ligase III for long-patch repair (Caldecott 2014). (MutS) and (MutL) detect DNA base mismatches caused during replication and lead to cleavage of DNA. Exonuclease I (ExoI), replication factor C (RFC) and PCNA ensure cleavage of the nascent strand and Polδ and RPA fill the resulting gap. Ligase I then completes the mismatch repair (MMR) (Jiricny 2006). Bulky adducts, such as thymine dimers, through ultraviolet light (UV) exposure, are detected using xeroderma pigmentosum complementation group C (XPC), centrin-2 (CETN2) and RAD23B in the global genome NER (GG-NER), or Cockayne syndrome group B (CSB), CSA and RNA Polymerase II (RNAPII) in the transcription-coupled NER (TC-NER). These converge through the processing complex, which includes XPG endonuclease, RPA, XPA and transcription factor IIH (TFIIH) and then excision repair protein (ERCC1) and XPF, removing the bulky adduct. Polδ/ε, PCNA and RFC synthesise the DNA to fix the bulky adduct and Ligase I completes the nucleotide excision repair (NER) (Scharer, 2013) (Moon et al., 2023).

MGMT is a DNA repair enzyme which has been associated with resistance to alkylating chemotherapy reagents, such as TMZ. MGMT removes O6-guanine residues from alkyl adducts from DNA, placed there by alkylating chemotherapy agents and irreversibly sequester it to cysteine-145 within its own active site, allowing replication to continue (Mansouri *et al.*, 2019, Raghavan *et al.*, 2020). *MGMT* suppression occurs though the methylation of cytidine-phosphate-guanine (CpG) islands in the promoter region of glioma cells (Figure 1.1.6) (Bobola *et al.*, 2015). *MGMT* promoter methylation switches off the *MGMT* gene, located on chromosome 10q26, involved in the repair of DNA damage, caused by TMZ (Alexander and Cloughesy, 2017, Binabaj *et al.*, 2018). Upon *MGMT* promoter silencing, unrepaired O6-guanine residues are mismatched with thymine, which is excised by the MMR, however leaving behind the original lesion. The cycle continues until the replication fork collapses and the DNA begins to break, leading to replicative arrest and apoptosis (Mojas *et al.*, 2007).

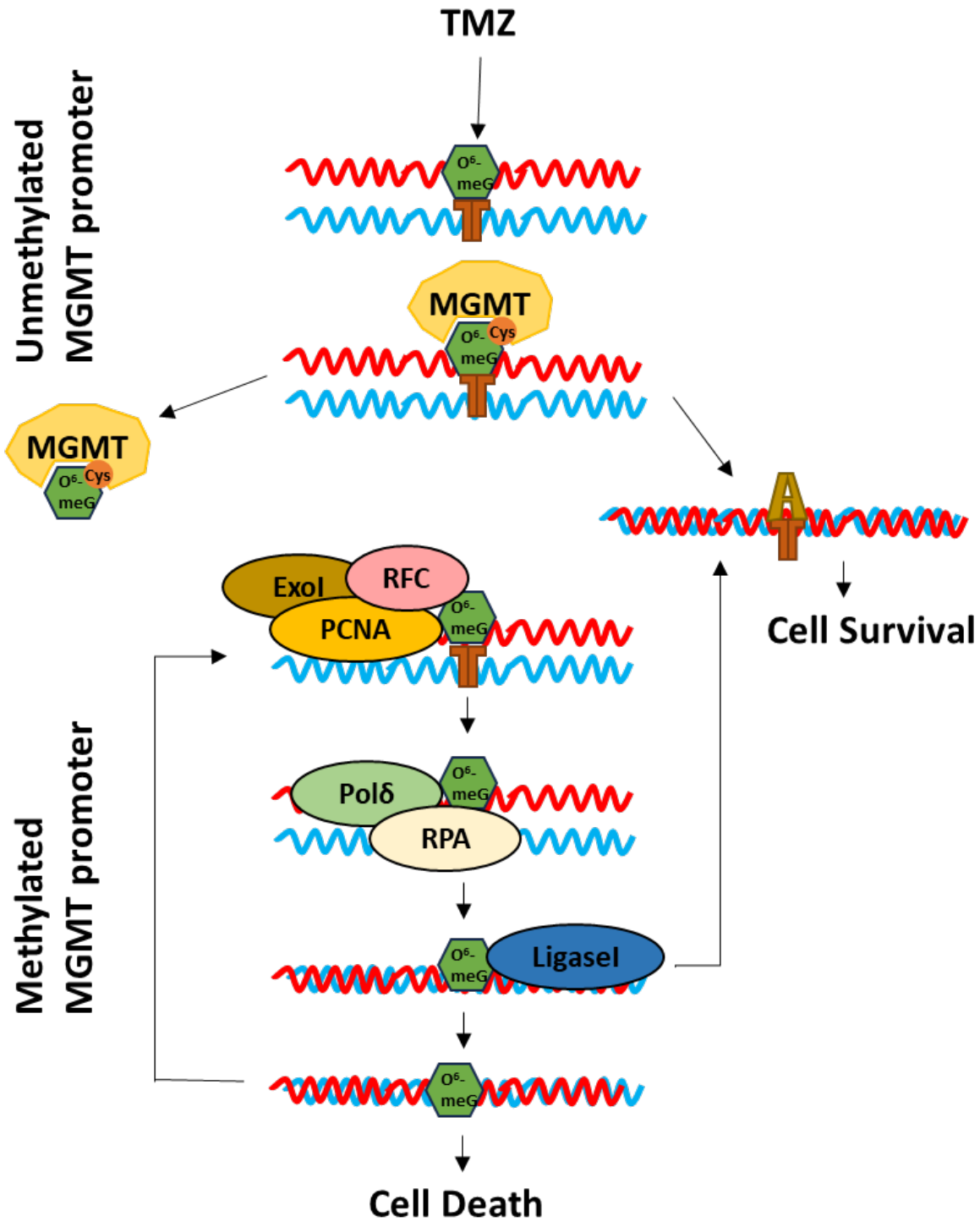

Figure 1.1.6.: MGMT repair pathway

Alkyl adducts (O6-methylguanine (O^6-meG)) are added to DNA by temozolomide (TMZ) and mismatched with thymine residues (orange T). If the O6-Methylguanine-SNA methyltransferase (MGMT) promoter is unmethylated, MGMT sequesters the adduct to cysteine-145 (c) in its active site, allowing continuation of DNA replication and cell survival.

If the MGMT gene is silenced by methylation, the mismatch repair (MMR) pathway attempts to remove the adduct. Exonuclease I (ExoI), replication factor C (RFC) and proliferating cell nuclear antigen (PCNA) ensure cleavage of the nascent strand and DNA polymerase (Polδ) and replication protein A (RPA) fill the resulting gap. Ligase I then completes the MMR (Mojas et al., 2007). If the lesion remains, the futile cycle repeats until replication fork collapse and arrest and cell death (Fan et al., 2013).

MGMT is also affected by chromosome 10q deletion and patients who have this alteration and *MGMT* promoter methylation have an improved response rate to TMZ and radiation than those who have one aberration or the other (Chiang *et al.*, 2019). In a study performed to determine the prognostic effect of *MGMT* promoter methylation, patients with methylation had increased survival of 21.2 months, compared to 14 months in the non-methylated group (Gilbert *et al.*, 2013). Survival has also been linearly correlated with the number of methylated CpG sites (Siller *et al.*, 2021). Meta-analysis studies have also indicated that patients with *MGMT* promoter methylation, and therefore suppressed MGMT expression, have longer overall survival and a generally better prognosis than patients with unmethylated *MGMT* promoter regions (Binabaj *et al.*, 2018). There is, as of yet, no optimal cutoff for promoter methylation for the best overall survival, with a study by Nguyen *et al.* (2021) suggesting 21%. Clinically, different National Health Service (NHS) trusts stratify *MGMT* promoter-methylated GBMs at various levels of methylation, with some trusts utilising a threshold of 8.7% (Khor, 2017); whereas Hull NHS Teaching Hospitals Trust regards methylation between 10-15% as equivocal and anything over this as positive for *MGMT* promoter methylation. Patients with *IDH1* mutations also have longer overall survival when in conjunction when the mutations appear alongside *MGMT* promoter methylation (Chai *et al.*, 2021), although this no longer applies to GBM under the new definition (Louis *et al.*, 2021).

Extending median life expectancy after diagnosis from 12.2 to 14.6 months (Stupp *et al.*, 2009), this meagre improvement in survival has largely been attributed to *MGMT* promoter methylation as a prognostic biomarker (Alexander and Cloughesy, 2017). Despite this improvement, the prognosis for GBM patients remains poor. This has become the driving force for identifying, not only new therapies for GBM, but also biomarkers for earlier diagnosis.

1.3.2. Monitoring, Metastasis and Recurrent GBM

Due to the inevitability of recurrence in GBM, patients living with GBM are monitored frequently for pseudoprogression, recurrence and metastasis, with scans every 8-12 weeks (Gaillard, 2008). Extracranial GBM metastasis is very rare, occurring in less than 2% of patients (Türkeş and Sağmen, 2018). Despite this, GBM can undergo glial to mesenchymal transition (GMT), equivalent to epithelial to mesenchymal transition (EMT), which stimulates MMP upregulation and inhibits E-cadherins, which loosen gap junctions and facilitate GBM cell invasion (Kim *et al.*, 2022). It is associated with cerebrospinal fluid dissemination and is the only primary CNS tumour that can produce metastasis (Stoyanov *et al.*, 2023). GBM can metastasise to the peritoneum (Fecteau *et al.*, 1998), lungs (Türkeş and Sağmen, 2018), lymph nodes (Wassati *et al.*, 2016), bones (Conte *et al.*, 2022) and other soft tissues (Lewis *et al.*, 2017). The rarity of metastases could potentially be down to the comparatively short period of time that patients survive with GBM, in comparison with other cancers in which metastatic disease in more prevalent (Stoyanov *et al.*, 2023).

Complications is monitoring recurrence are hindered by the incidence of pseudoprogression and radionecrosis. Pseudoprogression is when tumour bulk increases, usually 3 months post-therapy and then stabilizes, or reduces and is seen in around 30% of patients. Radionecrosis, as mentioned previously, is an unwanted side effect of radiotherapy, where cells necrose instead of undergoing apoptosis and being cleared by the body, occurring up to 12 months after chemoradiation (Zikou *et al.*, 2018). Recurrence is much more likely than metastasis and occurs in all GBM patients who survive beyond the primary tumour and treatment. If tolerated by the patient, recurrence can again be resectioned, improving prognosis should GMR again be achieved (Brown *et al.*, 2016). Unfortunately, recurrent tumours tend to have become more heterogenous than their primary counterparts and clonal expansion post-treatments means that these tumours are often resistant to first line TMZ chemotherapy (Wang *et al.*, 2016).

There are also several second line therapies which have been implemented in other countries. Lomustine (1-(2-chloroethyl)-3-cyclohexyl-1-nitrosourea (CCNU)), Fotemustine (FTMU) and Carmustine ((1-3-bis(2-chloroethyl)-1-nitrosourea (BCNU)) are lipid soluble, alkylating

nitrosourea drugs, which work similarly to and in combination with TMZ, particularly with *MGMT* promotor methylated tumours. They are generally administered locally, as wafers, in a resection site, which then reduces the effects of side effects, such as pulmonary fibrosis and liver toxicity (Herrlinger *et al.*, 2019, Weller and Le Rhun, 2020, Xiao *et al.*, 2020, Reithmeier *et al.*, 2010). Bevacizumab is a VEGF inhibitor and is used to combat angiogenesis. Despite improvements PFS, oedema, oxygenation and reduction in necrosis associated with radiation treatment, Bevacizumab has been linked to haemorrhaging and thromboembolism (Fu *et al.*, 2023, Gil-Gil *et al.*, 2013).

1.3.3. Treatment Resistance

Around 70% of GBMs recur with *de novo* or treatment-acquired resistance (Seystahl *et al.*, 2020), leading to poor prognosis, with median overall survival at around 9.9 months (Robin *et al.*, 2017). There are several methods of resistance employed by GBM to evade surgical, radio- and chemotherapeutic cells death. The first is the physical ability for drugs to cross the selectively permeable BBB and the blood brain tumour barrier (BBTB), with 98% of developed drugs, including recombinant proteins, adenovirus and antibodies being unable to permeate the endothelial cell tight junctions (Pandit *et al.*, 2020) and many lipophilic substances having limited diffusion due to polarised efflux transporters (Abbott *et al.*, 2010). In cases where the BBB and BBTB are weakened by GBM invasion, pro-oncogenic chemokine, cytokine and immune cells, such as prostaglandin E2, interleukin-10 (IL10), tumour associated macrophages (TAMs) and natural killer cells (NTKs) can infiltrate the normally immune-distinct site, causing an immune suppressive environment in which GBM thrives (Goenka *et al.*, 2021). GBM cells also avoid immune surveillance through modulators, such as transforming growth factor-β (TGF-β), which stimulates CD4+ thymus lymphocyte (T cell) differentiation into regulator T cells (Treg) cells, inhibiting production of T helper Th1 and Th2 cytokines, as well as normal T cell proliferation. Cytolytic gene products, such as Fas ligand and interferon-γ (IFN-γ) are also inhibited, preventing CD8+ T cell cytotoxicity (Rocha Pinheiro *et al.*, 2023). In tumours which do have a high mutational, or MMR burden, tumour antigens which are sometime present in GBM cells, are reduced, therefore inhibiting effective drug targeting as well as conveying immune evasion (Wang, 2021). Tumour microtubes, which extend into the surrounding brain tissue and enable to development of multicellular networks, such as

vasculature, aiding in the progression of neoplastic lesions and contribute to the diffusiveness of GBM (Weil *et al.*, 2017).

Clonal expansion theory dictates that selective pressures in the TME, including hypoxia, immune evasion and treatment allow the rapid expansion of clonal colonies of cells containing cumulative mutations which support their development (Marjanovic *et al.*, 2013). Some of these cells include GSCs, which contribute to the multiple lineages of cells, post-recurrence and have been linked to cytotoxic agent and radiation resistance *via* mechanisms like the G2/mitosis (M) DNA damage checkpoint, nuclear factor kappa B (NFκB), EZH2, PARP and wingless/integrated (Wnt)/β-catenin signalling pathway (Dymova *et al.*, 2021). The dysregulation of various RTKs, including EGFR and PDGFR may also be responsible for development of resistance, due to their multiple modalities of signalling, ensuring that there are a multitude of alternative pathways that could be disrupted, as outlined previously (1.2.1.4 and 0) entering cells into a state of disequilibrium (Tilak *et al.*, 2021).

Suppression of long non-coding RNAs (lncRNAs), such as SLC26A4-AS1, has also been associated with pro-angiogenesis in GBM (Li *et al.*, 2021a). Post-treatment hypermutation is hypothesized to be linked to DNA polymerase, leading to aberrant expression and MMR defects, whereby treatment induces double stranded DNA breaks which MMR fails to detect, therefore causing base mismatch tolerance and hypermutation, driving acquired resistance (Garnier *et al.*, 2018, Daniel *et al.*, 2019). Alternative splicing is a system which is dysregulated in many cancers, altering functionality and expression of transcriptional variant proteins (Larionova *et al.*, 2022). Alterations in expression of small nuclear ribonucleoprotein-associated proteins B (SNRPB), heterogenous nuclear ribonucleoproteins (hnRNPs) and polypyrimidine tracts-binding protein (PTB) have been shown to be involved in alternative splicing and tumour progression (Correa *et al.*, 2016). Micro RNAs (miRNAs) have been shown to degrade messenger RNA (mRNA) and therefore decrease expression of target proteins, for examples, miR-1271 targets apoptotic factor Bcl-2 for degradation, thereby impacting the apoptotic pathway in GBM (Yang *et al.*, 2018). Certain competing endogenous RNA regulator network (ceRNETs) is a promising new mechanism of post-transcriptional gene regulation, driven my miRNAs which may lead to methods of earlier diagnosis (Dymova *et al.*, 2021, Bryant *et al.*, 2021).

1.3.4. Emerging Therapies

Due to high prevalence of treatment resistance in GBM to first and second-line therapies, it is paramount that research into the mechanisms behind this resistance endeavours in order to employ alternative methods of therapy. There are several niches of alternative treatment discovery occurring in this area, ranging from targeting the TME (Rocha Pinheiro *et al.*, 2023), RTK pathways (Vaz-Salgado *et al.*, 2023) and radiation techniques (Angom *et al.*, 2023).

1.3.4.1. *Immunotherapies*

In order to counteract the immunosuppressive TME of GBM, studies into pro-inflammatory cytokines, such as IFN-α, tumour necrosis factor (TNF)-α and IL12 have indicated increased activity of T cells and improved chimeric antigen receptor-T cell (CAR-T) efficacy, as well as reduced tumour growth in mouse models. There are currently, however, systemic toxicity and associated negative side effects of these therapies and they require further development (Enderlin *et al.*, 2009, Agliardi *et al.*, 2021, Birocchi *et al.*, 2022). Immune checkpoint inhibitors, for which receptors are found on immune cells, such as T and bone marrow lymphocytes (B), NTK and dendritic cells, have also been highlighted as a potential therapeutic alternative. The aim of these drugs is to intercept interactions between GBM cells and the immune cells, which enable checkpoint inhibition, thereby maintaining immune cell activation. Resistance to immune checkpoint inhibitors, through programmed cell death protein-1 (PD-1) and cytotoxic T lymphocyte-associated antigen-4 (CTLA-4) prevent the negative regulation of the immune cell checkpoint of T cell activation (Zhang *et al.*, 2021). The PD-1 receptor, for example, in bound by PD-L1 expressed by GBM cells, leading to T cell apoptosis and inflammatory mediator production prevention (Ghouzlani *et al.*, 2021). Mouse models treated with anti-PD-1 immune checkpoint inhibitor, nivolumab, displayed good anti-tumour efficacy, but this was not recapitulated in the CheckMate-548 (Lim *et al.*, 2022), -498 (Omuro *et al.*, 2023) and -143 (Reardon *et al.*, 2020) phase III clinical trials in humans (Park *et al.*, 2019a, Reardon *et al.*, 2020).

Cancer vaccines have also been developed which aim to stimulate effector T-cell recruitment to target the antigens (Saxena *et al.*, 2021) presented on GBM cells. Peptide vaccines, such as

rindopepimut (against EGFRvIII), mimic antigens presented on GBM cells, therefore eliciting an innate immune response from the host, which will them target the cancer cells (Calvo Tardon *et al.*, 2019). Dendritic cell vaccines, such as DCVax-L (Liau *et al.*, 2023), take the patient's own dendritic cells, culture them with haematopoietic progenitor cells or monocytes and cytokines to stimulate dendritic cell differentiation before loading the tumour antigen (Xiong *et al.*, 2024). The dendritic cells are then injected back into the patient to elicit an adaptive immune response (Palucka and Banchereau, 2012) and phase I clinical trials of DCVax-L have shown that it is well tolerated in patients and overall survival compared favourably with historical controls (Hu *et al.*, 2022). mRNA vaccines have gained traction in the last few years and aim to introduce the mRNA of GBM antigens into the host and again stimulate an immune response (Hu *et al.*, 2022). Ongoing clinical trials have not yet come to a conclusion (NCT04573140 and NCT04573140), however, trials into mRNA vaccines for similar antigens in other cancers have shown favourable patient outcomes (Rittig *et al.*, 2011). There are, however, drawbacks to vaccine therapy in the heterogeneity of GBM and therefore of the antigens and requirement for customisation (Zhao et al., 2022a). CAR-T cell therapy involves the reprogramming of T lymphocyte immune functions, using synthetic receptors (Brown *et al.*, 2024) and has displayed positive results in blood-bourne malignancies (Rocha Pinheiro *et al.*, 2023). CAR-T treatment against EGFRvIII is being explored and although it has not shown anti-tumour efficacy, due to inducing an immunosuppressive cascade, it has displayed successful trafficking to the tumour and lack of toxicity (O'Rourke *et al.*, 2017).

Oncolytic viruses, such as adenovirus and reovirus, are also in clinical trials and are weak pathogenic viruses which can be manipulated to selectively infect tumour cells, delivering therapeutic genes, or replicate, inducing the host's innate immune system to promote cell lysis and adaptive immune system to cancer antigens (Peruzzi and Chiocca, 2018, Rong *et al.*, 2022). Phase I and II trials into oncolytic virus DNX-2401, in combination with PD-1 immune checkpoint inhibitor pembrolizumab in recurrent GBM indicated that there was a prolonged survival in patients receiving this dual therapy (Nassiri *et al.*, 2023).

1.3.4.2. *Tyrosine Kinase Inhibitors*

As mentioned previously, tyrosine kinase receptor elevation and their dysregulation are heavily involved in the malignancy of GBM. A well as VEGF inhibitor bevacizumab, this has led to the development of several multi-kinase inhibitors, such as regorafenib, cediranib and sunitinib, which have been explored further in clinical trials. Regorafenib indicated a median overall survival of 1.8 months longer than patients treated with Lomustine, in a phase II trial (Lombardi *et al.*, 2019), however, both cediranib (Batchelor *et al.*, 2023)and sunitinib (Kreisl *et al.*, 2013) did not show any significant improvements in progression free survival over current second-line therapies. First and second-generation EGFR inhibitors, such as erlotinib (van den Bent *et al.*, 2009) and afatinib (Reardon *et al.*, 2015) have shown limited activity in both primary and recurrent GBMs. Third generation pan-EGFR inhibitors, however, remain under investigation with Osimertinib being able to cross the BBB, block ERK signaling in pre-clinical models (Liu *et al.*, 2019) and showing long-lasting benefits in a subgroup of GBM patients (Cardona *et al.*, 2021). EGFR-targeting, tumour-specific antibody-drug conjugate depatuxizumab-mafodotin produced a 1.4-month median overall survival in recurrent GBM patients, when used in combination with TMZ, compared with the TMZ treatment only (Van Den Bent *et al.*, 2020), but this was not recapitulated in a phase III trial with newly diagnosed GBM patients (Lassman *et al.*, 2023). Carbozatinib targets both MET and VEGFR2 receptors and had a progression free survival response rate of 17.6% in recurrent GBM patients, over the control in a phase II trial (Wen *et al.*, 2018), where crizotinib, an anti-anaplastic lymphoma kinase (ALK) and anti-MET compound showed promising overall survival of 22.6 months (Martinez-Garcia *et al.*, 2022). Due to the ability of GBM to evade EGFR and MET inhibition *via* FGFR pathways (Day *et al.*, 2020), FGFR inhibitors, such as igrafitinib (Lassman *et al.*, 2022) and erdafitinib (Di Stefano *et al.*, 2015) are also being trialed with minor improvements in patient survival and stable disease. Larotrectinib is a pan-RTK, food and drug administration (FDA)-approved drug against neurotrophic tyrosine kinase gene oncogenic fusions, which has produced prolonged responses in GBM patients (Doz *et al.*, 2022) and second-generation inhibitors, such as repotrectinib are being developed with reduced induction of treatment resistance (Drilon *et al.*, 2018).

1.3.4.3. *Radiation, Laser and Tumour Treating Fields Therapy*

Use of the gamma knife increases precision of stereotactic radiotherapy delivery to GBM, thereby reducing the chance of radiation injury, such as radionecrosis mentioned previously, to neighbouring healthy tissue and requires only one session (Sanders *et al.*, 2019). Brachytherapy can be delivered *via* implant at the time of surgery, again improving precision of radiotherapy, whilst the cesium-131 isotope has displayed improved survival rates and reduced radionecrosis when used in conjunction with bevacizumab (Wernicke *et al.*, 2020). Laser interstitial thermal therapy (LITT) is a minimally invasive technique, whereby heat is used to destroy tumor cells and is highly useful for treating patients with GBM located deep into the brain. The lasers, guided by MRI, will also damage the BBB, leading to more effective delivery of a wider range of chemotherapeutic drugs. Proton beam therapy has also been suggested as an alternative to photon beam therapy as the larger protons are able to decelerate more quickly at the depth site of the tumour and deposit higher proportions of energy at the specific site, rather than the dispersal that is seen with photon beam therapy. This also reduces the dose of radiation to which the surrounding healthy tissue is exposed (Weber *et al.*, 2020) (LaRiviere *et al.*, 2019). There are currently only two centres in the United Kingdom (UK) offering proton bean therapy, due to the cost (Cancer Research UK, 2021). The NovoTTF-100A System is a tumour treating fields (TTFIELDS) therapy which is FDA approved for recurrent GBM and employs alternating electric fields to the tumour, at low intensity. This disrupts the rapid formation of polar mitotic spindles, thereby forcing cells into mitotic arrest and cell death. Limitations include that the therapy should be administered for around 18 hours per day, per 4-week cycle, with transducers placed ion the patient's shaved scalp. (Fabian *et al.*, 2019). TTFIELDS have, however, been shown to be comparable to chemotherapy in prolonging patient survival, with increased safety profiles and patient quality of life and when used in conjunction with TMZ, overall survival (OS) increased by a further 4.9 months over TMZ alone (Stupp *et al.*, 2017).

1.3.4.4. *Other therapies*

PARP inhibitors are widely used in other cancers and clinical trials into PARP1 and PARP2 inhibitors, veliparib (Robins *et al.*, 2016) and Olaparib (Hanna *et al.*, 2020), have indicated a slight increase in PFS of around 2 months. Voltage-gated calcium channels are often

overexpressed and dysregulated in GBM, leading to disruption to the cell cycle and resistance to TMZ function (Valerie *et al.*, 2013). "Time sequential therapy" can be employed, whereby T-type calcium channel inhibitors, such as Cav3.3-specific inhibitor Mibefradil, are given concurrently with TMZ to force GBM cells into S phase and resensitise cells to TMZ, leading to GBM cell apoptosis (Zhang *et al.*, 2017b). Type III, or T-type voltage gated calcium channels are low-voltage and therefore low-calcium and transiently activated *via* inhibitory post-synaptic potentials and activation of potassium channels. They allow regulation of neuronal excitation around resting membrane potential (Lory *et al.*, 2020) and calcium entry causes GSC renewal and entry into the cell cycle through the expression of early genes (Zhang *et al.*, 2017b).

1.4. Modelling GBM

In order to understand biological characteristics and pathology of GBM, it is imperative that accurate models of the disease are developed which aid, not only in the characterisation of the genesis and progression of GBM, but in its response to various treatments (Purshouse *et al.*, 2024). Despite the fact that tumours of the CNS are relatively isolated from the rest of the body, there are still many complex factors which affect how GBM responds to treatment and therefore, there is not one specific pre-clinical model which is able to entirely and accurately recapitulate GBM behaviour in the human body and mirroring patient biology in brain tumours in particularly complex (Rominiyi *et al.*, 2019). This is due to aspects of brain biology, such as the BBB and the TME and the complex heterogenous nature of GBM. There are, therefore, several models which are routinely used in pre-clinical research, from which data can be collated to better understand GBM and several more models which are being developed to better represent GBM and its environment (Purshouse *et al.*, 2024) and initiatives such as GlioModel aiming to bring institutions together for a more collaborative approach to tacking GBM (GlioModel., 2012).

1.4.1. Cell Lines

Immortalised and patient-derived cell lines are routinely used for pre-clinical studies, as they carry very few ethical implications and are relatively cheap compared to other models (Notarangelo *et al.*, 2014). Immortalised cell lines are originally taken from patients and

undergo an immortalisation process, such as telomere lengthening. GBM- cell lines include U87-MG and U-251 cells, which can be easily grown in serum-containing medium; however, the serum in the medium induces differentiation of the cells, meaning that they no longer accurately represent the GBM from which they came from and are not the most relevant model (Lathia *et al.*, 2015, Timerman and Yeung, 2014, Freedman *et al.*, 2015). They are, however, a good starting point for early-stage experiments into GBM. Patient-derived cells, or glioma stem cells (GSCs) are more difficult to propagate than immortalised cell lines but are a much better representation of GBM (Paolillo *et al.*, 2021). They are generally cultured in serum-free medium, meaning they do not differentiate as readily; although, they do fluctuate gene expression patterns dependent on culture and treatment conditions (Prager *et al.*, 2020). GSCs also have a shorter passage life than immortalised cell lines. Cell lines in generally do have the drawback that they are comprised of one cell type and do not reflect the heterogeneity of GBM, nor the infiltrative nature and therefore, multiple cell lines should be used and compared alongside other models (Ding, 2000, Gomez-Oliva *et al.*, 2020).

1.4.2. Organoids

Organoids are comprised of multiple cell types and aim to better reflect the 3-dimensional (3D) structure of organs and the interactions between various cells within that organ. Earlier organoid, or tumouroid, models consisted of patient-derived tumours minced and implanted into a matrigel (Hubert *et al.*, 2016), which, when orthotopically implanted into mice, displayed very similar features and responses to treatment as the patients from whence they were derived (Goff *et al.*, 2019). Brain organoids can also be generated from induced-pluripotent stem cells (iPSCs), and tumorigenesis encouraged using clustered regularly interspaced short palindromic repeats (CRISPR) techniques (Bian *et al.*, 2018, Wang *et al.*, 2024), presenting as a brain organoid with an invading tumouroid. Using this technique, however, does potentially limit the scope of heterogeneity displayed by GBMs in the native environment (Rybin *et al.*, 2021). Cerebral organoid gliomas (GLICOs) are also generated iPSCs and cocultured with patient derived GBM cells, which then form invasive microtubules and differential sensitivities to treatment, reminiscent of GBM (Osswald *et al.*, 2015, Linkous *et al.*, 2019). Although GLICOs benefit from being patient-specific, they do not recapitulate the immune environment, or vascularisation (Rybin *et al.*, 2021); however, implantation into mice allows these interactions to be visualised (Wang *et al.*, 2023b). Other cells can also be introduced to these organoids,

such as microglia, which reflects the immune system of the brain and can be used to help understand the TME (Zhang *et al.*, 2023).

1.4.3. Animal Models

Mouse models are the current gold standard when it comes to testing drug efficacy as the effects of a drug can be seen interacting throughout the entire mammalian system. It is possible to track potential side effects of the drug, as well as how well drugs permeate the BBB and the efficiency with which they reduce tumour burden (Haddad *et al.*, 2021). Syngenic mouse models are immunocompetent mice, which can also help to understand the host's anti-tumour immune response and have been used to test out immune-targeting therapies, such as the PD-1 immune checkpoint inhibitors mentioned previously (Genoud *et al.*, 2018). Patient derived xenografts (PDXs) are patient-derived tumour spheres which are subcutaneously, or orthotopically injected into immunodeficient mice and propagated through generations, reflecting patient histology and genetics (William *et al.*, 2017, Hidalgo *et al.*, 2014); however, this is not a standardised process and not all tumours propagate within the mice (Kim *et al.*, 2016). Genetically engineered mouse models are also ideal for targeting specific genetic alterations within GBM, but this does not reflect the clonal heterogeneity, particularly of recurrent tumours (Huszthy *et al.*, 2012). Zebrafish have also been used as models of GBM due to similarities in tumourigenesis pathways (Huang *et al.*, 2016). Fluorescent tumour cells are injected into zebrafish embryos and invasion tracked, or cells are implanted into zebrafish brains, similarly to murine models (Eden *et al.*, 2015). Animal systems are not exactly the same as human systems (Wong *et al.*, 2023, Kalueff *et al.*, 2014) and it is often the case that great efficacy of drugs in animal models is not translated to human clinical practise, or there may be intolerable side effects in human patients (El Meskini *et al.*, 2015). There are also impracticalities with drug screening at scale and ethical implications in the use of animal models and there are ongoing efforts to replace, and reduce the number of, animals used in medical research (Olubajo *et al.*, 2020).

Mouse, PDX and organoid models are costly and time consuming and do not provide the personalised medicine scope offered by other models, being more suited to drug development testing (Olubajo *et al.*, 2020).

1.4.4. Microfluidics

Microfluidics has become an increasing research area of interest in several cancers, including GBM, over the past several years. The premise of microfluidics is to maintain a micro-biopsy of tissue with a microfluidics chip, which maintains a constant flow of medium, with a Reynold's number of less than 100 (Ziółkowska, 2011), preventing the tissue from dying rapidly over the course of several days or weeks (Bolivar *et al.*, 2011). The fluid represents the interstitial flow which tissues are constantly exposed to in the body, through blood, lymph and interstitial fluid and is able to constantly remove cellular waste from the tissue and provide cells with fresh nutrients, as would occur within the body (Ziółkowska, 2011). The microfluidics system recapitulates the TME and can be scaled up for drug testing, making the model a potentially high-throughput operation (Gomez-Oliva *et al.*, 2020). Maintaining and treating individual patients' tissues over an extended period of time and monitoring tumour response aims to determine potential patient-personalised treatments. There are several microfluidics devices being used for research and the type of chip is entirely dependent on the type of tissue in use and the types of experiments that are being performed on the tissue (Sylvester, 2013, Dawson *et al.*, 2016, Astolfi *et al.*, 2016). Some microfluidics models aim to mimic the BBB, which can comprise of cocultures of astrocytes, pericytes and endothelial cells (Cho *et al.*, 2017); or enable the study of the tumour necrotic core and the behaviour of the tumour in response to blood vessel obstruction (Ayuso *et al.*, 2017). Others, including the microfluidics system utilised in this communication, mimic the TME and provide real-time insights into tumour adaptation (Barry *et al.*, 2023, Samuel *et al.*, 2021) in a shorter period of time than afforded by the murine models (Olubajo *et al.*, 2020).

1.5. Post-translational modifications

Post-translational modifications (PTM), such as phosphorylation, hydroxylation, ubiquitylation, SUMOylation, acetylation and methylation, allow the rapid, fine-tuned control of proteins involved in many cellular processes and can all be dysregulated in cancer (Pienkowski *et al.*, 2023).Figure 1.1.7*,* Figure 1.1.8 and the proceeding information give a brief outline of some of the PTMs and examples of which are found to be involved in the development, progression and treatment of GBM.

1.5.1. Phosphorylation

Phosphorylation is involved in the regulation of around 30% of proteins and helps to modulate signalling in a variety of pathways, including RTKs, CDKs and metabolism pathways. Protein kinases catalyse the addition of a phosphate group to the hydroxyl or amine group of an amino acid, triggering a conformational shift and change in protein function. Phosphorylation can then be reversed by protein phosphatases, which remove the phosphate group upon reception of a negative feedback stimulus (Bhullar *et al.*, 2018). Protein kinases and phosphorylases work in tandem to augment protein activity, such as activation of tumour suppressor, p53, through phosphorylation (Singh *et al.*, 2017). Phosphorylation has been linked to the development and progression of glioma, *via* several pathways. Casein kinase (CK)1α and glycogen synthase kinase-3β (GSK3β) prime and phosphorylate histone demethylase 1A (KDM1A) serine-683, inducing its deubiquitylation and tumourigenesis through demethylation of H3K4 and transcriptional activation of cancer stem cell renewal and tumorigenic factors, such as cyclin dependent kinase N1A (CDKN1A) (Zhou *et al.*, 2016). Inhibition of GSK3β phosphorylation by ERK and mTOR targeting, consequently allows microtubule-associated protein 1B (MAP1B) phosphorylation and resensitises GBM cells to chemotherapy (Laks *et al.*, 2018). Phosphorylation of YTH N6-methyladenosine RNA binding protein 2 (YTHDF2) serine-39 and threonine-381, in the EGFR/SRC/ERK pathway, reduces liver X receptor α (LXRα) by m^6A-mediated mRNA decay, thereby increasing intracellular cholesterol required for GBM cell growth, again contributing to glioma development (Fang *et al.*, 2021, Bovenga *et al.*, 2015). Inhibition of tyrosine-56 phosphorylation in thyroid receptor interacting protein-13 (TRIP13) was also found to attenuate EGFR/EGFRvIII signalling and GBM growth in glioma spheroids and mice xenografts (Hu *et al.*, 2020a). Phosphorylation of proteins and its dysfunction occurs frequently in the cell cycle and therefore is an attractive target to treat rapidly dividing GBM cells. Fasudil is a cytoskeletal regulatory protein rho-kinase 2 (ROCK2) inhibitor that has been shown to inhibit cell proliferation and migration in TMZ-resistant GBM cells, speculatively through abrogation of the ROCK2/moesin/β-catenin/adenosine triphosphate (ATP)-binding cassette G2 (ABCG2) phosphorylation cascade, which may be important for drug efflux in the BBB (Zhang *et al.*, 2018a). It has also been suggested that therapeutic induction of phosphorylation of oligodendrocyte transcription factor 2 (OLIG2)

may inhibit migration of GBM, *via* attenuation of TGFβ2 expression, which otherwise promotes invasive mesenchymal properties of GBM cells (Singh *et al.*, 2016, Pi *et al.*, 2022).

1.5.2. Hydroxylation

Hydroxylation involves the addition of a hydroxyl (-OH) group, usually onto a carbon atom of an alkyl side chain, or aromatic ring of an amino acid, by hydroxylase enzymes. This allows proteins to form hydrogen bonds with various other molecules. One of the most important examples of hydroxylation in GBM is that of HIF1α by prolyl hydroxylase (PHD) (Domenech *et al.*, 2021). Under normoxic, oxygen-rich conditions, PHD hydroxylates two proline residues in the oxygen-dependent degradation domains (ODDD) of HIF1α, leading to degradation targeted by E3 ubiquitin-ligase Von Hippel-Lindau (VHL) (Kamura *et al.*, 2000). Under oxygen-deprived, hypoxic conditions, stable HIF1α translocates to the nucleus, dimerises with HIF1β and induces transcription of genes involved in angiogenesis and cell invasion. This attempts to increase blood and oxygen flow, which is required for cellular survival, and which is highly modulated in the tumour, due to the hypoxic core (Semenza, 2004, Domenech *et al.*, 2021). Factor-inhibiting HIF (FIH) asparagine hydroxylation of HIF1 also blocks its binding to transcriptional activating factors, again exemplifying hydroxylation as an important modulator of hypoxic response in GBM (Monteiro *et al.*, 2017) and the potential for therapeutic targeting of hydroxylases (Sturla *et al.*, 2016). PHD inhibitor, Roxadustat, amplifies the HIF pathway in GBM cells, encouraging iron-dependent cell death (ferroptosis), thereby tackling invasive mesenchymal GBM cells, which have higher levels of free iron (Su *et al.*, 2023).

1.5.3. Ubiquitylation

Ubiquitination is a very versatile PTM and generally targets proteins for enzymatic destruction by the proteasome complex (Humphreys *et al.*, 2021, Maksoud, 2021). The ubiquitin enzymatic cascade begins with an E1-activating enzyme binding ATP and magnesium ions (Mg^{2+}) and loading several small ubiquitin molecules, which are then transferred to a cognate E2 ubiquitin conjugating enzyme. The ubiquitins are finally transferred to E3 ubiquitin ligases, before being attached to substrate lysine residues of target proteins (Scholz *et al.*, 2020). Dependent upon the location and extent of ubiquitination, this PTM can induce several downstream functions. Polyubiquitylation of target proteins occurs *via* linkage of ubiquitin molecules to their own

lysine residues, or N-terminal methionine and ligation to a protein targets it for proteasomal degradation (Chau *et al.*, 1989). Monoubiquitylation of K63 has also been linked with autophagy (Pickart, 1997), whereas polyubiquitination of the lysine residue leads to trans-aconitate decarboxylase (TAD1) phosphorylation of inhibitor of NFκB (IκB) kinase (IκK), K48 polyubiquitination, degradation of IκK and subsequent transcriptional activation of NFκB genes (Wang *et al.*, 2001), involved in the DDR (Gallo *et al.*, 2017). The constitutive photomorphogenesis 9 (COP9) signalosome complex subunit (CSN6) is overexpressed in GBM, and it is postulated that it may destabilise EGFR by interfering with E3 ligase carboxyl terminus heat shock chaperone (Hsc)70-interacting protein (CHIP), promoting autoubiquitination of CHIP and dysregulation of EGFR signalling (Zhou *et al.*, 2003); as well as E3 ubiquitin ligase tripartite motif containing 11 (TRIM11), which modulates EGFR-driven GBM cell stemness (Di *et al.*, 2013). Mothers against decapentaplegic homolog 7 (Smad7) is an inhibitory protein of TGFβ signalling, which has been shown to contribute to aggressive GBM mesenchymal cell states (Bruna *et al.*, 2007), and is also a docking site for E3 ubiquitin ligase ubiquitin carboxyl-terminal hydrolase 15 (USP15), which prevents polyubiquitination of TGFβR and USP15 knockdown has been shown to decrease tumourigenesis in GBM (Eichhorn *et al.*, 2012). E3 ubiquitin ligase homologous to the E6-AP carboxyl terminus (Hect3) has also been associated with K63-liked polyubiquitination of USP7 and downstream HIF1α activation, leading to glioma to mesenchymal transition (GMT) (Wu *et al.*, 2016b). Overexpression of E3 ubiquitin ligase MDM2 is also linked to p53 ubiquitination and targeted degradation by the proteasome, thereby attenuating its tumour suppressor function and promoting unchecked cell proliferation (Iyappan *et al.*, 2010).

1.5.4. SUMOylation

SUMOylation is a dynamic PTMs and involves the addition of a small ubiquitin-like modifier (SUMO) to target proteins, many of which are involved in the cell cycle and DDR. Much like the ubiquitination cascade, there is a SUMOylation cascade whereby the E1 SUMO-activating enzyme 1 and 2 (SAE1, SAE2) heterodimer activates mature SUMO proteins, leading to translocation of SUMO to the E2 SUMO-specific conjugating enzyme (Ubc9), joining with the target protein and completing the transfer *via* SUMO E3 ligases, such as inhibitor of activated STAT (PIAS) and Ras-related nuclear protein (Ran) binding protein 3 (RanBP3), both of which have extensive functionalities (Fox *et al.*, 2019, Gu *et al.*, 2023a, Gu *et al.*, 2023b). CDKs are

known SUMOylation targets and the PTM has been shown to be increased in the presence of DNA damage, targeting proteins for destruction and dysregulation promotes pathological cell cycle progression. SUMOylation of CDK6 in GBM means that the protein is not targeted for degradation after G1 arrest, by ubiquitylation, as it normally might be, and the cell cycle is driven through G1-S transition (Bellail *et al.*, 2014). Topotecan is a topoisomerase inhibitor with a secondary function in inhibiting SUMOylation and has been shown to reduce cell cycle progression, as well as augmenting cellular metabolism *via* inhibition of CDK6 and HIF1α (Bernstock *et al.*, 2017), which it stabilises, driving angiogenesis and GMT (Xu *et al.*, 2015). Global upregulation of SUMOylation-related machinery is upregulated in GBM (Yang *et al.*, 2013), for example, SAE1 overexpression was found to increase SUMOylation of Akt, alongside phosphorylation, thereby inducing both *in vivo* and *in vitro* glioma cell growth (Yang *et al.*, 2019). Radiotherapy resistance has also been attributed to SUMOylation, whereby radiation induces PIAS1 interaction with stress-inducible phosphoprotein 1 (STI1), causing nuclear accumulation and GBM radioresistance (Soares *et al.*, 2013).

1.5.5. Acetylation

Proteins and histones are acetylated by lysine (KAT) and histone acetylases (HAT) and deacetylated by deacetylases (KDAC/HDAC)(McCornack *et al.*, 2023). Acetylation of H3K9 by HATs allows transcription to occur through neutralisation of the lysine by the acetyl group and the dissociation of the DNA from the histone, opening up the chromatin and allowing transcription complex access (Jones *et al.*, 2019). Akin to other PTMs, this process can be dysregulated in GBM to aid, or hinder development and progression of the tumour. Inhibition of HDAC1 leads to hyperacetylation of NFκB subunit p65, which prevents interaction with KAT2B/3B, instead promoting interaction with tumour suppressor inhibitor of growth family member 4 (ING4) and resensitisation of GBM cells to TMZ-induced cell death (Li *et al.*, 2016, Dali-Youcef *et al.*, 2015). P53 acetylation is mediated by KAT cyclic adenosine monophosphate (cAMP)-response element binding protein (CREB) binding protein (CBP)/p300 and general control non-depressible 5 (GCN5)/P300/CBP-associated factor (PCAF), which then allow downstream transcription of p21, mediating cellular apoptosis under G1 arrest (Barlev *et al.*, 2001). In GBM, overexpression of EP300-interacting inhibitor of differentiation 3 (EID3) prevents the acetylation of p53, thereby allowing the cell cycle to continue on, unchecked (Diao *et al.*, 2020). KAT6A acetylates H3K23, recruiting nuclear

receptor binding protein TRIM24, activating PI3K catalytic subunit alpha (PIK3CA) transcription and allowing PI3K/AKT-mediated proliferation of GBM cells. Conversely, when PIK3CA is overexpressed, or KAT6A is inhibited by pan-PI3K inhibitor LY294002, the growth-promoting effects of KAT6A are silenced (Lv *et al.*, 2017). Yan *et al.* (2023) performed a whole transcriptome analysis of GBM patients from the TCGA and gene ontology (GEO) databases in order to identify histone acetylation gene-based biomarkers within the GBM TME. The results indicated that histone acetylation enrichment is positively correlated with immune cells, known to be involved in tumour immunity, such as B cells and myeloid dendritic cells, reinforcing the important role of acetylation in tumour treatment response.

Acetylation is diametrically opposed by methylation, in terms of histone PTMs, with this fine balance of crosstalk being dysregulated in GBM (Azab, 2023, McCornack *et al.*, 2023). Ye *et al.* (2024) observed H3K9 acetylation may increase recruitment of the SP1 transcription factor to the MGMT transcription factor binding site, leading to an increase in MGMT expression in MGMT unmethylated promoter GBM. In post-treatment, recurrent samples, it was also determined that there was an increase in H3K9 acetylation, specificity protein 1 (SP1) and MGMT, compared to their matched primary, treatment-naïve samples.

1.5.6. Methylation

Protein methylation is the transfer of a methyl (CH_3) group, onto the cationic guanidino group (N^+H) of an arginine, or lysine residue. This facilitates a switch to a more hydrophobic residue, by removing the hydrogen bond donor (Bedford and Richard, 2005) and dispersing the cationic charge towards the methyl group. Methylation then alters arginine, or lysine interactions with nucleic acids and other proteins, with the bulkier residue preferring to form aromatic clusters (Beaver and Waters, 2016, Tripsianes *et al.*, 2011) with residues such as phenylalanine and tryptophan, such as those within Tudor domains, in the case of arginine methylation(Chen *et al.*, 2011, Cote and Richard, 2005, Guccione and Richard, 2019) (Figure 1.1.7). Whilst both types of histone methylation facilitate the fine-tuned control of gene expression, non-histone methylation is also involved in the control of various other cellular processes, such as transcription, translation, RNA binding, chaperone and membrane proteins (Wei, 2019). Lysine methylation is performed by a family of eight methyltransferases which mono-, di- and tri-methylate lysine side chains and is a dynamic and transient process (Jones *et al.*, 2019). An

example of lysine methylation in GBM is through tonicity-responsive enhancer binding protein (NFAT). EGFR activation, which has been described previously to be a dysregulated pathway in GBM (section 1.2.1.4) phosphorylates serine-21 of EZH2 and subsequent methylation of K668 of NFAT5. This hinders lysosomal degradation of NFAT5, promoted by E3 ligase TNF receptor associated factor (TRAF6) and resultant MGMT upregulation, which is a poor prognostic biomarker in GBM, due to its ability to repair alkylating adducts introduced by TMZ (section 1.3.1) (Li et al., 2023a).

Arginine methylation is generally considered to be more a more stable and ubiquitous mark, performed by PRMTs, which mono-, or di-methylate arginine side chains. Arginine residues (pKa 13.8) have an aliphatic side chain consisting of three carbon atoms and ending with a positively-charged (Fitch *et al.*, 2015) guanidino group (Figure 1.1.7), allowing π-stacking interactions with other aromatic residues (Gallivan and Dougherty, 1999). Proteins involved in the methylation process form approximately 1% of the functional genome, allowing regulation of cellular processes, including gene transcription (Katz *et al.*, 2003). PRMTs are responsible for the deposition of both activating (histone 4 arginine 3 asymmetric dimethylation (aDMA) (H4R3me2a), histone 4 arginine 3 symmetric dimethylation (sDMA) (H3R2me2s), H3R17me2a, H3R26me2a) and repressive (H3R2me2a, H3R8me2a, H3R8me2s, H4R3me2s) histone marks (Blanc and Richard, 2017), as well as non-histone targets, including 53BP1 (Boisvert *et al.*, 2005a, Boisvert *et al.*, 2005b) and Sm proteins (Owens *et al.*, 2020). Methylation patterns have been shown to play an important role in GBM.

1.6. Protein arginine methyltransferases (PRMTs) in GBM

PRMTs methylate arginine residues of proteins involved in the DNA damage response, alternative splicing and gene regulation; therefore, PRMT upregulation found in various cancers facilitates tumourigenesis (Wang *et al.*, 2019b, Jarrold and Davies, 2019). There are nine PRMTs, which can be subdivided into three types: I, II and III. All PRMTs are able to perform monomethylation (mMA) of one guanidino group of an arginine residue. Type I PRMTs perform aDMA of a guanidino group and include PRMT1, 2, 3, 4 (also known as coactivator-associated arginine methyltransferase 1 (CARM1)), 6 and 8. Type II PRMTs include PRMT5 and 9 and cause sDMA. PRMT7 is the only enzyme classed as Type III, as it can only perform mMA (Jarrold and Davies, 2019).

PRMTs facilitate the addition of a methyl group from S-adenosyl-L-methionine (SAM/ AdoMet) to the arginine guanidino group, forming arginine methylation and S-adenosyl-L-homocysteine (SAH/ AdoHcy) (Figure 1.1.7). PRMTs are ubiquitously expressed in both the cytoplasm and the nucleus, as well as at tissue level, with the exception of PRMT8, which is associated with the plasma membrane and is exclusively located within the CNS (Lee *et al.*, 2005) and PRMT6, which is largely nucleic (Veland *et al.*, 2017).

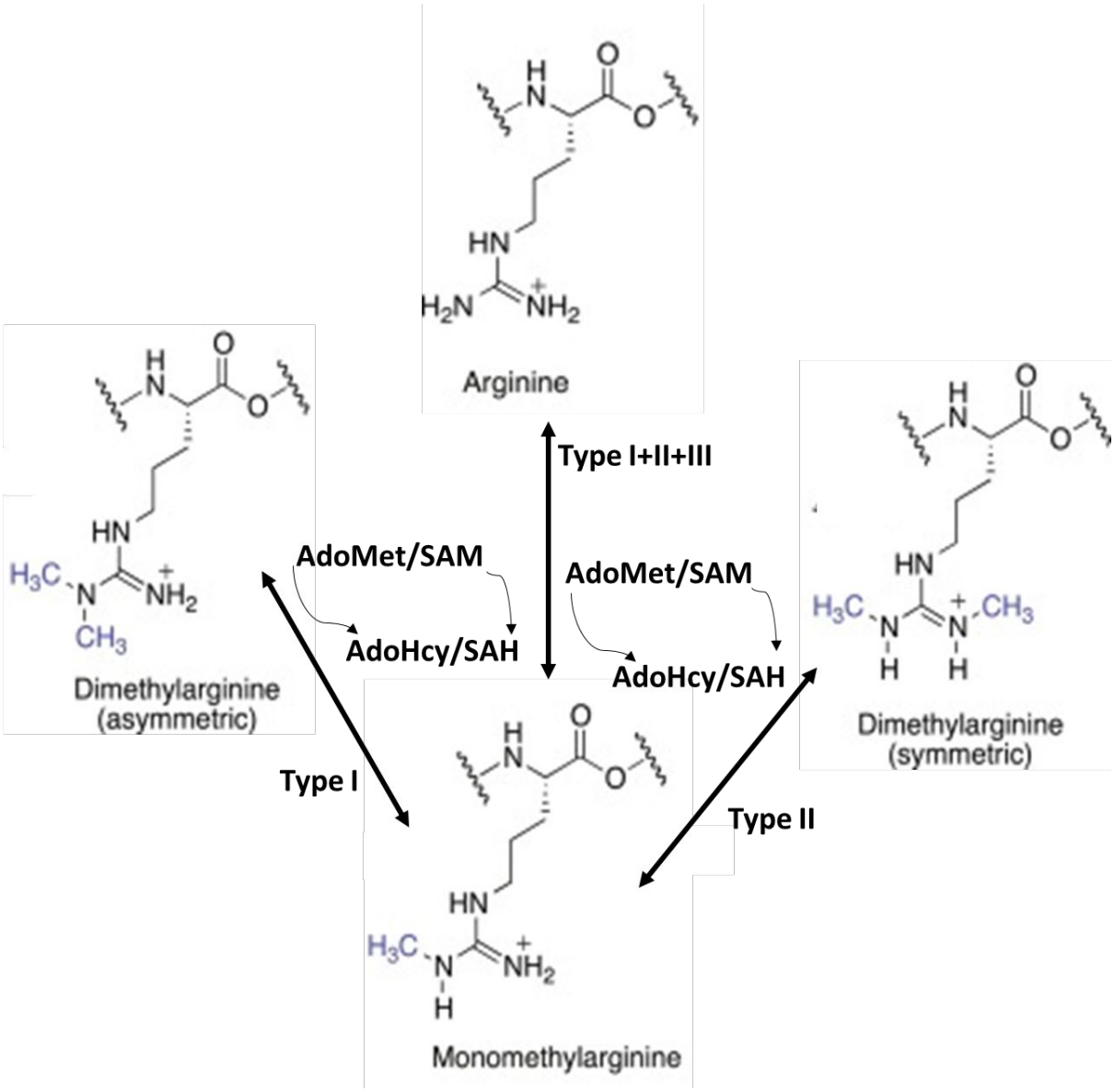

Figure 1.1.7.: Arginine Methylation by PRMTs

All protein arginine methyltransferases (PRMTs) monomethylate (mMA) arginine residue guanidino groups. PRMTs bind S-adenosyl-L-methionine (SAM/AdoMet), which donates the methyl group to the substrate residue, forming a methylated arginine and S-adenosyl-L-homocysteine (SAH/AdoHcy) still bound to PRMTs.

Most PRMTs have a conserved catalytic N-terminal Rossman fold, which is comprised of six signature motifs. The AdoMet binding pocket consists of VLD/VGXGXG, V/I-X-G/A-X-D/E, E/K/CDII and LK/XXGXXXP which form the core of the binding site, form hydrogen bonds with AdoMet and form two β-sheets to stabilise the interaction, respectively. The EE loop

(SEXMGXXLXXEXM) is responsible for holding the arginine substrate and the THW loop, near to the active site, stabilises the N-terminal α-helix, and is required for substrate binding. The α-helices within the Rossman fold domain then bind the AdoMet substrate and the arginine residue to facilitate methyl transfer. At the C-terminal there is a 7 strand β-barrel, for substrate recognition and binding. The dimerization arm is an α-helix, which extends into the Rossman fold, from the β-barrel (Zheng *et al.*, 2023). Individual PRMTs have unique protein interaction domains at the N-terminus (Schapira and Ferreira de Freitas, 2014, Tewary *et al.*, 2019). PRMTs are regulated through a myriad of processes, including: splice variants, post-translational modifications, miRNAs and other protein-protein interactions (Samuel *et al.*, 2021) (Figure 1.1.8).

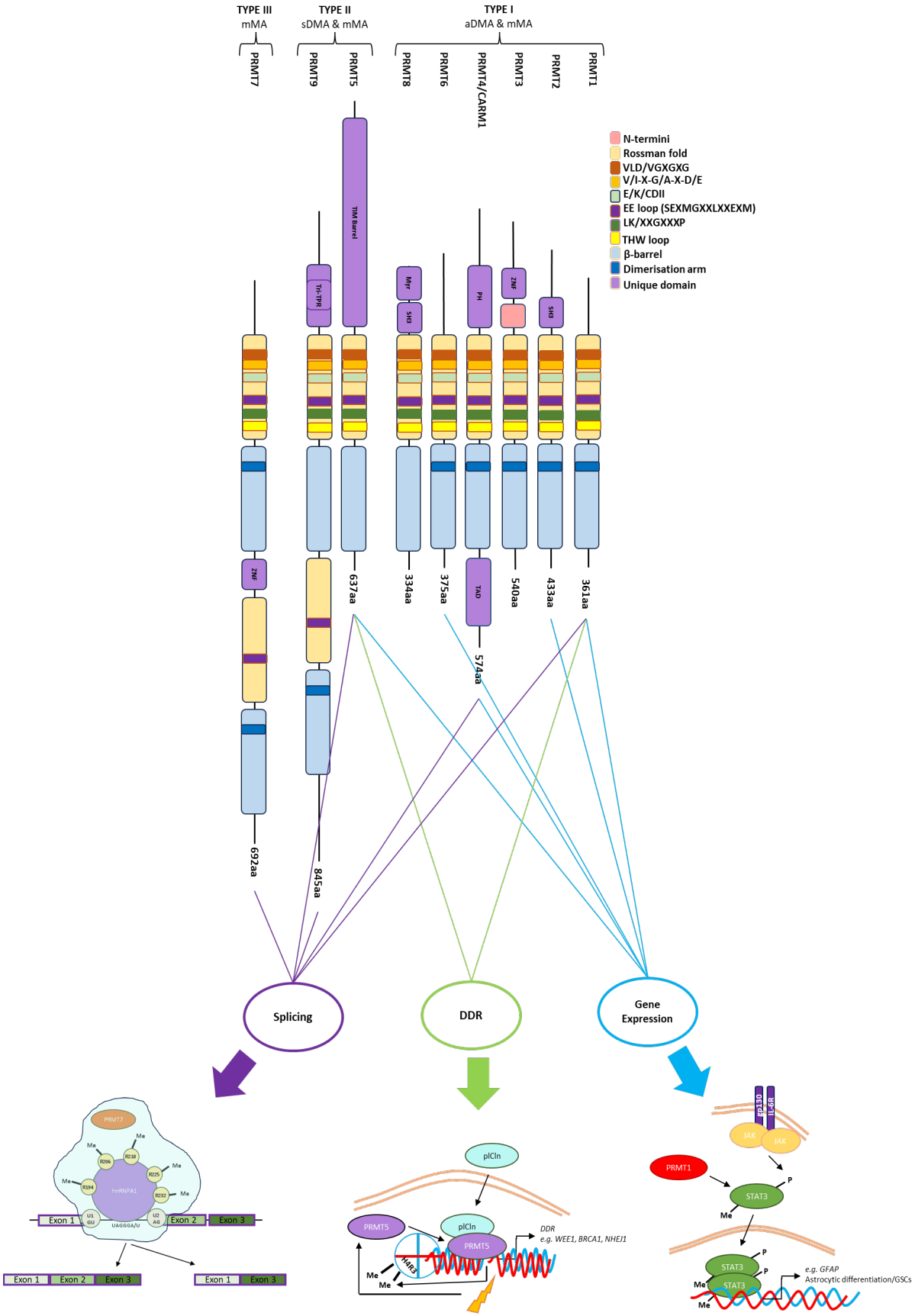

Figure 1.1.8.: Schematic of PRMT structure and examples of function.

*Type I protein arginine methyltransferases (PRMTs) (PRMT1, PRMT2, PRMT3, PRMT4, PRMT6 and PRMT8) perform asymmetric dimethylation (aDMA) and monomethylation (mMA) of arginine. Type II PRMTs (PRMT5 and PRMT9) perform symmetric dimethylation (sDMA) and mMA. Type III PRMTs (PRMT7) perform mMA only. Domains highlighted in key: Src homology 3 (SH3); zinc finger (ZNF); plekstrin homology (PH); myristylation (Myr); triosephosphate isomerase (TIM) and tetratricopeptide (Tri-TPR) . PRMT7 methylates (me) arginine (R)194, 206, 218, 225 and 232 of human nuclear ribosomal nucleoprotein A1 (hnRNPA1) in the spliceosome to produce alternatively spliced isoforms. DNA damage repair (DDR) and gene expression. DNA damage recruits the ion chloride nucleotide-sensitive protein (pICln) and PRMT5 methylosome to the DNA double strand breaks. PRMT5 deposits an sDMA mark on R3 of histone 4 (H4R3) which allows transcription of DDR genes, such as WEE1, breast cancer gene 1 (BRCA1) and non-homologous end-joining 1 (NHEJ1). Activation of gp130 receptors, such as interleukin-6 receptor (*IL6*R) causes Janus kinase (JAK) phosphorylation of signal transducer and activator of transcription (STAT) and PRMT1-mediated methylation. STAT dimerization and translocation to the nucleus occurs, inducing transcription of genes associated with astrocytic lineage differentiation of glial stem cells (GSCs), including glial fibrillary acidic protein (GFAP). Figure adapted from (Wu et al., 2023, Owens et al., 2020, Bryant et al., 2021).*

1.6.1. Type I PRMTs

Type I PRMTs facilitate aDMA, which transfers two methyl groups onto the same nitrogen atom of the guanidino group. Type I PRMTs contains 3 active site α-helices, which are stabilised upon AdoHcy binding. Substrate arginine is also surrounded by two methionine residues within the PRMT active site, which sterically inhibit conformational change of the substrate in the active site after addition of the first methyl group, thereby ensuring aDMA and not sDMA (Cheng *et al.* 2005). The dimerization arm of type I PRMTs allows for the formation of a doughnut-shaped homodimer (Zheng *et al.*, 2023). Overexpression of type I PRMTs has been shown to lead to alterations in gene expression and oncogenesis, as well as proliferation and invasiveness of solid and hematopoietic cancers, including GBM, through aDMA of histone and non-histone substrates (Hwang *et al.*, 2021, Fedoriw *et al.*, 2019, Cheung *et al.*, 2007). Inhibition of aDMA though type I PRMT inhibitors may therefore lead to a decrease in tumour cell proliferation (El-Khoueiry *et al.*, 2023).

1.6.1.1. *PRMT1*

PRMT1 is a predominantly nuclear 361 amino acid (aa) protein and the first PRMT to be classified (Lin *et al.*, 1996) and is responsible for the vast majority of aDMA. PRMT1 causes H4R3me2a, leading to transcriptional co-activation of genes associated with cell cycle progression, DDR and epigenetic regulation (Bedford and Clarke, 2009, Auclair and Richard, 2013). Knockdown of PRMT1 has been shown to interrupt cell cycle progression in mouse xenograft models and induce apoptosis (Wang *et al.*, 2012) by inducing chromosomal instability, DNA damage and increased sensitivity to chemotherapeutic agents (Yu *et al.*, 2009). Other known substrates of PRMT1 include DSB recognition protein meiotic recombination 11 (MRE11) and DNA binding protein 53BP1, through which aDMA limits their association with sites of DNA damage (Boisvert *et al.*, 2005a, Boisvert *et al.*, 2005b). MRE11 associates with DSB ends and recruits and activates ATM serine/threonine kinase which initiates the phosphorylation cascade leading to activation of tumour suppressors such as p53, which instigates cell cycle arrest (Lee and Paull, 2005). Knockout of PRMT1 in mouse models also indicated that the protein plays a role in glial cell lineage determination through methylation of STAT3 within the JAK/STAT pathway (section 1.2.1.4), leading to transcription of genes associated with astrocytic identity, including GFAP (Honda *et al.*, 2017, Takizawa *et al.*, 2001, Liang *et al.*, 2018). Knockdown also results in the loss of oligodendrocyte maturation and axon myelination, which then leads to reactive astrogliosis, whereby there is an increase in astrocytes due to the CNS damage (Hashimoto *et al.*, 2021).

PRMT1 has seven isoforms which contribute to a variety of methylation activity, dependent upon their N-terminal sequence and residues M48 and M115, some of which also have the ability to perform sDMA. PRMT1v2 is an isoform of PRMT1, which is localised to the cytoplasm, due to the presence of a constitutive nuclear export sequence (NES) (Goulet *et al.*, 2007) and has been linked to breast cancer cell aggression by reducing cell-cell adhesion (Baldwin *et al.*, 2012). MiRNA-503 can also regulate PRMT1 by binding the 3'-untranscribed regions (3'UTR) of PRMT1, sequestering it and inhibiting the EMT in hepatocellular carcinoma (Li *et al.*, 2015). Phosphorylation of PRMT1 by CK1α1 regulates PRMT1 binding to chromatin and downstream cell self-renewal pathways (Bao *et al.*, 2017b) and the PRMT can also be ubiquitinated by E3 ligase E4B (Bhuripanyo *et al.*, 2018), targeting it for

proteasomal degradation. Methylated proteins which are degraded by the proteasome leave behind metabolites NG,NG-dimethyl-L-arginine, NG,N'G-dimethyl-L-arginine and NG-monomethyl-L-arginine as products of aDMA, sDMA and mMA, respectively (Tsikas *et al.*, 2018). Dimethylarginine dimethylaminohydrolase (DDAH) hydrolyses mMA and aDMA into mono- and di-methylamine and citrulline before excretion, whilst sDMA remains intact (Said *et al.*, 2019). Alternatively, alanine:glycoxylate aminotransferase 2 (AGXT2) transaminates aDMA and sDMA into a/symmetric α-keto-dimethylguanidinovaleric acid (Jarzebska *et al.*, 2019).

1.6.1.2. *PRMT2*

PRMT2 is a 433aa primarily nuclear protein, although it is found at low levels in the cytoplasm and contains an N-terminal Src homology domain (SH3) domain. PRMT2 has weak enzymatic activity but has been shown to associate with other proteins and PRMTs to elicit various responses, including promotion of apoptosis. PRMT2 has been shown to interact with Rb, leading to a delay in cell cycle progression from G1/S (Yoshimoto *et al.*, 2006). PRMT2 has been shown to promote inhibition of IκB-α complex nuclear export and reduction in NFκB binding to DNA, and therefore in the transcription of genes associated with inflammation and immunity, again inducing apoptosis (Ganesh *et al.*, 2006). PRMT2 has also been associated with several splicing factors, including those associated with apoptotic protein B cell lymphoma X (BCL-X) (Vhuiyan *et al.*, 2017). The unique SH3 domain recognises proline-rich motifs within splicing factors such as PRMT1 substrate Src associated in mitosis of 68 kDa (SAM68). Heteromeric binding of PRMT1 and PRMT2 increases the enzymatic activity of PRMT1 (Pak *et al.*, 2011), leading to promotion of the small, pro-apoptotic BCL-X, *via* SAM68 (Paronetto *et al.*, 2007). This phenomenon is more prevalent in cells with increased levels of inflammatory marker TNFα, potentially encouraged by the induction of NFκB, indicating that PRMT2 promotes apoptosis, *via* alternative splicing, under inflammatory conditions (Vhuiyan *et al.*, 2017). Zhang *et al. (2024a)* recently confirmed this finding, identifying that association of PRMT2 and MAPK substrate chromosome 15 open reading frame 39 (C15orf39) causes a downregulation of NFκB signalling, leading to a reduction in IL6 and TNFα inflammatory markers and allowing regulation of microglia-mediated inflammation, which is involved in a multitude of glia-associated diseases. The SH3 domain of PRMT2 also associates with actin nucleator protein cordon-bleu (Cobl) and R1226me2 and

R1234me2 of Cobl allows its binding to actin and induces dendritic arborisation and dendritogenesis, required for neuronal signalling, proliferation (Hou *et al.*, 2015, Hou *et al.*, 2018) and T-cell mediated immunity (Hervas-Stubbs *et al.*, 2011).

Dong *et al.* (2018) identified PRMT2 as a pro-tumourigenic factor, which is increased in GBM and correlates with poorer prognosis. Knockdown of PRMT2 consistently reduced cell growth across various GBM cell lines, as well as GSC sphere formation and decrease in stem-cell-associated genes, sex determining region (SRY)-related high mobility group (HMG)-box transcription factor 2 (SOX2) and octamer-binding transcription factor 4 (OCT4) and tumour formation in mouse xenografts. There are also recorded interactions with oestrogen receptor α (Shen *et al.*, 2018) and androgen receptors (Meyer *et al.*, 2007), which increase transcriptional activity, leading to proliferation and cell cycle progression (Cura and Cavarelli, 2021). Additionally, cell-cycle-associated genes such as CDK4 and CDK6 and oncogenic signalling pathways, such as JAK/STAT are also significantly downregulated upon PRMT2 depletion. Chromatin immunoprecipitation (ChIP) analysis of promoter and enhancer regions of genes such as *CDK6* indicated that loss of PRMT2 caused loss of repressive histone mark H3R8me32a which results in activation and maintenance of oncogenic transcription, leading to tumour growth (Dong *et al.*, 2018). PRMT2 is alternatively spliced into four isoforms, found in breast cancer cells, each of which have varying levels of methyltransferase activity and localisation due to truncation within the third domain of the protein and the THW loop (Zhong *et al.*, 2012).

1.6.1.3. *PRMT3*

Cytoplasmic PRMT3 is a 531aa protein and contains a zinc finger (Znf) binding domain, which tethers it to its substrates (Tang *et al.*, 1998). Differential expression analysis found that type I PRMT3 expression is highly enriched in GBM and is correlated with poorer survival rate. PRMT3 has been associated with ribosomes, through methylation of 40S ribosomal protein S2, although the biological importance of this is yet to be determined (Swiercz *et al.*, 2007). Other PRMT3 substrates include p53 and voltage-gated sodium channel $Na_v1.5$ (Beltran-Alvarez *et al.*, 2013). Although the former interaction has not yet been characterised, it is mediated by tumour suppressor proteins VHL30 and ARF (Lai *et al.*, 2011). The latter are upregulated in many cancers and are the targets of therapeutic research in glioma (Griffin *et al.*, 2020).

Knockdown and pharmacological inhibition of PRMT3 has been shown to attenuate G2/M phase proliferation and migration in GSCs as well as tumour growth in mouse xenografts. This coincides with an increase in apoptosis, detected *via* western blotting and immunostaining for cleaved PARP and caspase-3 and wound healing assays, which found reduced wound closure in the absence of PRMT3. This effect could be reversed upon overexpression of PRMT3 in GSC lines, determining that the observed effect was specific to PRMT3 presence or absence. This has been found to be due to the promotion of glycolysis by the presence of PRMT3, which encourages GSC growth *via* HIF1α (Liao *et al.*, 2022). HIF1α expression is significantly upregulated with overexpression of PRMT3, and co-immunoprecipitation indicated that the proteins form a complex under hypoxic conditions. PRMT3 inhibits polyubiquitination of HIF1α, which would otherwise lead to its degradation (Tarade and Ohh, 2018), and allows glycolytic gene expression.

1.6.1.4. *PRMT4/CARM1*

PRMT4 is a 608aa nuclear protein with a unique plekstrin homology (PH) domain, which aids in forming large protein complexes (Chen *et al.*, 1999, Lemmon, 2007). PRMT4 prefers methylation of proline rich motifs (Shishkova *et al.*, 2017). PRMT4, or CARM1, is a type I PRMT which is recruited to transcription sites by p300/CBP-mediated acetylation of H3K18 and H3K23 and is associated with switch/sucrose non-fermentable (SWI/SNF) chromatin remodelling proteins (Xu *et al.*, 2004). CARM1 then causes H3R17me2a and H3R26me2a, which in turn methylate and recruit SRC1-3, resulting in transcriptional activation (Bedford and Clarke, 2009). Affected genes include stem-cell genes, such as *Nanog, Sox2* and *Oct4,* which form part of a regulatory network for the determination of astrocytic cell lineage, impeding differentiation, through miR10a, miR92a, miR575 and CARM1 methylation (Selvi *et al.*, 2015 {Wu, 2009 #776, Cho *et al.*, 2011). It has also been shown to methylate and regulate RNA-binding proteins, such as splicing factor CA150. This aids CA150 in tethering transcriptional machinery to the spliceosome and regulating transcription elongation by repressing RNA polymerase II (RNAPII) (Goldstrohm *et al.*, 2001, Sims *et al.*, 2011).

Through transfection of CARM1 mutants, alongside a minigene, which can be alternatively spliced to include or exclude exons, into cells, CARM1 has been found to cause alternative splicing by exon skipping (Cheng, 2006). Inhibition of CARM1 in CD8 T cells resulted in increased tumour cell killing *in vitro,* depicting CARM1 as a negative regulator of tumour-targeting T cells. CARM1 inhibition in melanoma and breast cancer mouse models displayed reduced tumour growth and reduction in CD8 T cells restored tumour growth, indicating that CARM1 plays a role in the TME-mediated therapeutic resistance of tumours (Kumar *et al.*, 2021), which is known to be important in GBM (Sharma *et al.*, 2023).

CARM1 is regulated by several pathways. WD repeat domain 5 (WDR5), which is overexpressed in GBM, has been shown to promote binding of myelocytomatosis oncogene (Myc) transcription factor to the CARM1 promoter, thereby inducing its expression, leading to tumourigenesis and proliferation of GBM cells (Wang *et al.*, 2020a). MiRNAs, such as miR-181c, are also significantly increased in CARM1 overexpressing cells and post-transcriptionally regulate CARM1 through direct repression of its 3'UTR (Xu *et al.*, 2013). PRMT4 can be phosphorylated to regulate activity, including at S572 BY P38MAPK, which prevents nuclear translocation and subsequent myogenesis (Chang *et al.*, 2018). PRMT4 also has the ability to auto-methylate R550, which allows regulation of transcriptional coactivator and splice protein interaction (Kuhn *et al.*, 2011). Regulation can also be achieved through alternative splicing of CARM1 into two known isoforms, of which PRMT4Δ15 eliminates the automethylation ability, but maintains catalytic activity (Wang *et al.*, 2013a).

1.6.1.5. *PRMT6*

PRMT6 is a 375aa nuclear protein (Lander *et al.*, 2001) and is primarily responsible for the H3R2me2a mark, which prevents trimethylation of the H3K4 residue and the H3R17me2a mark, alongside PRMT4 (Cheng *et al.*, 2020). The arginine residue sterically blocks lysine methyltransferase mixed lineage leukaemia (MLL) complex subunit WRD5 binding (Guccione *et al.*, 2007). It is therefore associated with transcriptional repression of tumour suppression genes, including Myc targets, reducing senescence and increased proliferation (Kleinschmidt *et al.*, 2012). *Homeobox protein A (HOXA)* genes, which affect neuronal differentiation, have also been shown to be affected by PRMT6 and elements of the Polycomb repressive complexes (PRC), which recognise histone methylation marks and lead to transcriptional repression (Stein

et al., 2016). The H3R2me2a mark produced by PRMT6 has also been associated with the maintenance of cell division cycle 20 (CDC20) transcription, which leads to the ubiquitination and subsequent degradation of CDKN1B (p27) and stalling of G0/G1 phase (Wang *et al.*, 2023a). PTEN is known to be activated upon R159me by PRMT6, leading to inhibition of the PI3K/AKT signalling pathway, thereby acting in a tumour suppressive manner (Feng *et al.*, 2019). PRMT6 is also known to be involved in anti-retroviral pathways through methylation and inhibition of human immunodeficiency virus-1 (HIV1)-associated proteins, such as Tat (Boulanger *et al.*, 2005) and as an androgen receptor (AR) coactivator (Scaramuzzino *et al.*, 2015).

Phosphorylation and subsequent deubiquitylation of PRMT6 by CK2α also promote PRMT6-mediated R214 methylation of regulator of chromatin condensation 1 (RCC1) (Huang *et al.*, 2021). RCC1 is a guanine nucleotide exchange factor (GEF) for RAN-GTPase, which is methylated by PRMT6 and targeted to the chromatin, where it is required for mitotic spindle assembly (Clarke and Zhang, 2008). Overexpression of PRMT6 in mouse xenograft models rescued tumour sphere growth cause by PRMT6 depletion, thereby suggesting n oncogenic role of PRMT6 in GSC proliferation (Huang *et al.*, 2021). PRMT6 can be regulated *via* other PRMTs, such as PRMT1, which methylates R106 and increases enzymatic activity (Cao *et al.*, 2023) and is also capable of automethylation at R35, whereby it increases its stability, leading to an increase in activity (Singhroy *et al.*, 2013).

1.6.1.6. *PRMT8*

PRMT8 is the smallest PRMT protein with 394aa and is uniquely localised to the plasma membranes of the brain through its N-terminal myristylation site (Sayegh *et al.*, 2007). It is also the only known PRMT to function dually as a phospholipase (Kim *et al.*, 2015). Its phospholipase activity converts phosphatidylcholine into choline, which is then converted to acetylcholine and used in neurotransmission for neural plasticity, as well as promoting dendritic arborisation (Park *et al.*, 2019b). Much like some other PRMTs, expression of PRMT8 has been found to be linked to pluripotency associated transcription factors, such as *SOX2, OCT4* and *Nanog*, which are responsible for neural progenitor cell differentiation (Solari *et al.*, 2016). Whole genome sequencing (WGS) of GBM not only indicates that PRMT8 is generally depleted, but that SNPs in the PRMT8 promoter could be linked to familial

gliomagenesis (Liu *et al.*, 2012). When this PRMT8 depletion is recapitulated in mouse embryonic stem cells, these markers of gliomagenesis are increased (Simandi *et al.*, 2015).

Methylation of Ras GTPase accelerating protein (GAP) SH3 domain-binding protein 1 (G3BP1) by PRMT8 modulates production of stress granules, brought about by oxidative stress (Lo *et al.*, 2020). The fork head-associated (FHA) domain of antigen Kiel 67 (Ki-67) (NIFK) is a methylation substrate of PRMT8 which is required for large subunit ribosomal RNA maturation (Lee *et al.*, 2005). Co-expression of voltage-gated sodium channel, $Na_v1.2$ and PRMT8, as well as increased $Na_v1.2$ methylation in mouse seizure models, causes a large increase in the current passing through the channel, which is required for neuronal signalling (Baek *et al.*, 2014). As mentioned previously, voltage-gated sodium channels are currently of therapeutic interest in GBM. PRMT8 expression is also regulated by nuclear retinoid receptor-mediated transcription and in later stages of cellular development, through dimerisation with PRMT1, becomes a coactivator of retinoid receptor signalling (Simandi *et al.*, 2015). PRMT8 has been found to have interactions with several splicing-related transcriptional cofactors, such as fused in sarcoma (FUS) and Ewing sarcoma (EWS) members of the ten-eleven translocation (TET) family (Pahlich *et al.*, 2008) and inhibition of PRMT8 was found to reduce FUS accumulation in amyotrophic lateral sclerosis (ALS) cell models (Scaramuzzino *et al.*, 2013). PRMT8 can also automethylated at its N-terminal, resulting in prevention of AdoMet from entering the catalytic site and prevention of further methylation activity (Sayegh *et al.*, 2007).

1.6.2. Type II PRMTs

Type II PRMTs perform sDMA, whereby one methyl group each is placed on adjacent nitrogen atoms of the same arginine guanidino group (Figure 1.1.7). Type II PRMTs contains 2 active site α-helices and there is a resulting motif change in the α-helices, from YFXXY in Type I, which forms hydrogen bonds within the EE loop to hold substrate arginine, to PLXXN in Type II, which aids in AdoMet recognition. Substrate arginine is also surrounded by phenylalanine and serine residues and mutational studies by Sun *et al. (2011)* found that PHE379 was critical for ensuring sDMA, but that sDMA and aDMA shared similar catalytic activities.

1.6.2.1. *PRMT5*

PRMT5 is a 637aa protein found in the nucleus, cytoplasm and Golgi apparatus and contains a triosephosphate isomerase (TIM) barrel which is required for oligomerisation into tetramers, resulting in a shorter dimerization arm in the β-barrel and for binding of co-protein methylosome protein 50 (MEP50), which is required for efficient catalytic activity (Antonysamy *et al.*, 2012). PRMT5 recognises GAR motifs in its substrates, resulting in substrate specificity, distinct from its PRMT9 type II counterpart (Hadjikyriacou *et al.*, 2015).

PRMT5 has been shown to promote tumourigenesis through alternative splicing and inhibition has been shown to lead to cell cycle defects, resulting in apoptosis (Braun *et al.*, 2017, Sachamitr *et al.*, 2021). PRMT5-mediated H3R8me2s and H4R3me2s marks are associated with global transcriptional repression of downstream genes, whereas H3R2me2s is linked to impediment to corepressor binding (Migliori, 2012) (Saha *et al.*, 2016). sDMA of H4R3 by PRMT5 is associated with undifferentiated neural stem cells (Chittka *et al.*, 2012) and has also been indicated in the regulation of glial cell differentiation (Favia *et al.*, 2019). Knockdown of PRMT5 causes an increase in inhibitor of differentiation/DNA binding 2 and 4 (Id2 and Id4) levels, associated with hypomethylation of promoter CpG islands and decrease in differentiation promoter Sox10. Methylation of these CpG islands is normally performed through PRMT5-mediated H4R3me2s, recruiting DNA methyltransferase 3S (DNMT3A), leading to Id2 and Id4 inhibition. Together, these findings suggest that PRMT5 is involved in the self-renewal of glioma cells, cell-cycle progression and therefore, tumourigenesis (Huang *et al.*, 2011, Bezzi *et al.*, 2013).

PRMT5 is known to deposit the R1810me2s mark on subunit RNA polymerase II subunit A (POLR2A), at the C terminal of RNAPII. This then recruits the Tudor domain of the survival motor neuron (SMN) protein and this complex, alongside helicase senataxin, resolves DNA/RNA R-loops and allows termination and dissociation of RNAPII from the template(Zhao *et al.*, 2016). PRMT5 has been shown to interact with Sm proteins *via* methylosome component and assembly chaperone, ion chloride nucleotide-sensitive protein (pICln), whereby pICln forms a ring complex with Sm proteins (Owens *et al.*, 2020). These are then methylated by the PRMT5/pICln methylosome complex and phosphorylation of pICln allows the transfer of Sm proteins to the SMN complex, leading to the formation of small

nuclear ribonuclear proteins (snRNPs) required for RNA splicing (Pesiridis *et al.*, 2009). The pICln-PRMT5 interaction, potentially independently of MEP50, has also been associated with becoming an epigenetic activator and direct regulator of DSB repair genes (Schmitz *et al.*, 2021). PRMT5 is also known to interact with Myc and plays a role in *MYC* target gene silencing, which is overcome by oncogenic variations of Myc in GBM, thereby leading to tumourigenesis (Mongiardi *et al.*, 2015).

Induction of DNA damage increases expression of both proteins, leading to upregulation of DDR and G2 arrest genes, such as radiation sensitive protein 51 (*RAD51)* and *WEE1*, respectively. It is thought that PRMT5 directly targets serine/threonine checkpoint kinase WEE1, allowing G2 arrest and subsequent DSB repair by RAD51 and other proteins (Owens *et al.*, 2020). Indirectly, PRMT5 depletion has been shown to induce p53-mediated apoptosis in response to DNA damage. Upon DNA damage, stress-responsive activator of p300 (STRAP) is phosphorylated by ATM and forms an association with p53 cofactor junction-mediating and regulatory protein (JMY) and p300, which then recruits PRMT5 to the p53 protein. PRMT5 methylates p53, affecting oligomerisation and altering p53 promoter binding activity. Lower levels of PRMT5 influencing apoptotic peptidase activating factor 1 (*APAF1)* transcription and therefore apoptosis and higher levels contributing to *p21* transcription and G1 arrest upon the induction of DNA damage (Jansson *et al.*, 2008). PDGFRα and EGFR are targets of PRMT5 methylation. sDMA of E3 ligase casitas B-lineage lymphoma (Cbl) prevents its targeting of PDGFRα for proteolysis, thereby maintaining its proliferative activity (Calabretta *et al.*, 2018). Dephosphorylation and inhibition of RAS pathway proteins is mediated by a complex of autophosphorylated EGFR in conjunction with protein-tyrosine phosphatase Src homology region 2 domain-containing phosphatase-1 (SHP1), initiated by PRMT5 methylation of EGFR R1175 (Hsu *et al.*, 2011). Inhibition of PRMT5 has also led to resensitisation of GBM neurospheres and *in vivo* GBM mouse models to MEK inhibitor trametinib, through the reduction of trametinib-induced EGFR/AKT activity. It has been suggested that inhibition of PRMT5 may be used in conjunction with existing chemotherapies in order to eliminate tumour escape pathways (Banasavadi-Siddegowda *et al.*, 2018).

Small Nucleolar RNA host gene 16 (SNHG16) is a lncRNA which is upregulated in GBM tissues and has been found to absorb PRMT5 regulator miR-4518, resulting in increased

viability of GBM cells and a reduction in apoptosis (Pal *et al.*, 2007, Zhang *et al.*, 2017a). Upon SNHG16 depletion, anti-apoptotic Bcl-2, phosphorylated AKT and PRMT5 levels were reduced, whereas pro-apoptotic Bax and miR-4518 were upregulated, suggesting that SNHG16 regulates apoptosis and PI3K/AKT signalling *via* sequestration of miR4518, leading to release of PRMT5 *(Lu et al., 2018)*. PRMT5 is regulated by phosphorylation, whereby addition of a phosphate group at residues T132, T139 and T144 are required for PRMT5 activation. Phosphorylation at Y304 and Y307, downregulate PRMT5 activity, by interrupting protein-protein interactions with its coactivator MEP50 (Liu *et al.*, 2011). IL1β induces PKC phosphorylation of PRMT5 at S15, which allows NFκB activation (Hartley *et al.*, 2020). PRMT5 is also regulated by glutathionylation, which is the reversible addition of a glutathione group to a cysteine residue of proteins experiencing oxidative stress, which reduces PRMT5 catalytic activity by disrupting MEP50 interaction (Yi *et al.*, 2020).

1.6.2.2. *PRMT9*

PRMT9 is the largest PRMT protein and the least well characterised, with 845aa, an N-terminal tetratricopeptide (Tri-TPR) domain and two catalytic domains (Tewary *et al.*, 2019, Hadjikyriacou *et al.*, 2015). It is described as having functions in splicing, through sDMA of spliceosome-associated protein 145 (SAP145) at R508, generating a binding site for SMN protein and thereby encouraging U2snRNP maturation (Yang *et al.*, 2015). Shen *et al. (2024)* have also found PRMT9 to methylate splicing factor 3B subunit 2 (SF3B2), therefore being involved in alternative splicing dysregulation, leading to abnormal synapse development and impaired memory and learning in knockout mouse models. PRMT9 can be regulated by miR-543 (Pal *et al.*, 2007, Zhang *et al.*, 2017a) and has been found to target the 3'UTR region of PRMT9 mRNA, inhibiting its translation. Knockdown of miR-543 results in PRMT9 increase and G1/S arrest and overexpression increase glycolysis and, in PDX mouse models, promotes tumorigenesis. Reduction of PRMT9 stabilises HIF1α in osteosarcoma cells, leading to an increase in cellular proliferation (Zhang *et al.*, 2017a), suggesting that PRMT9 may act as a tumour suppressor (Ju *et al.*, 2015). Ju *et al. (2015)* suggests that this may be due to the F-box domain of PRMT9, which allows the PRMT to act as an E3 ubiquitin ligase, targeting HIF1α mRNA for proteasomal degradation. Dong *et al. (2024)* found that PRMT9 ablation in acute myeloid leukaemia (AML) leads to a reduction in methylation of DDR and translation effectors and suppression of cancer stem cell maintenance, as well as playing a role in cancer immune

evasion. Knockdown of PRMT9 is significantly affected methylation of poly adenylate (polyA) binding protein cytoplasmic 1 (PABPC1) and 5'-3' exoribonuclease 2 (XRN2), which reduces the efficacy of translation (Qi *et al.*, 2022) and triggers the DDR. This triggers IFN pathways through activation of cyclic guanosine monophosphate (GMP)-AMP synthase (cGAS), which then alters T cell populations and affects immune memory, effectively resensitising aberrant cells to host immunity (Dong *et al.*, 2024).

1.6.3. Type III PRMTs

Type III PRMTs can only perform mMA and thus far, PRMT7 is the sole enzyme in this group. In PRMT7, the N-terminal α-helix sequence changes to VSLIE and is arranged such that the AdoMet binding pocket is more exposed. Substrate arginine is also surrounded by methionine and alanine residues, which ensure a small binding pocket which does not allow for the addition of a second methyl group (Wang *et al.*, 2014).

1.6.3.1. *PRMT7*

PRMT7 is a 692aa protein which consists of two tandem repeat PRMT modules, each with a Rossman fold, and β-barrel with a dimerization arm. The two double E loops are required for preferential methylation of RXR substrate sequences (Feng *et al.*, 2013). The two modules are linked by a zinc finger motif, which locks the C-terminal PRMT module in an inactive conformation when bound to SAH (Halabelian and Barsyte-Lovejoy, 2021). The C-terminal PRMT module, however, does not contain several of the motifs required for SAM/AdoMet binding, thereby it is generally accepted that it is catalytically inactive. PRMT7 functions as a monomer, with the tandem repeated domains forming a pseudodimer (Cura *et al.*, 2014).

PRMT7 is involved with transcriptional, DDR and splicing regulation and although some studies have shown that PRMT7 mutations were present in a small sample of patients with brain tumours, implying that there may be some indications of PRMT7 involvement in neuropathogenesis (Birnbaum *et al.*, 2019), no established role in GBM development or progression have been discovered (Bryant *et al.*, 2021). The type III PRMT has, however, been implicated in the EMT in breast cancer metastasis through modulation of the H4R3me2s mark. Automethylation of PRMT7 R531 causes PRMT7-HDAC3 recruitment to the E-cadherin

promoter by yin-yang 1 (YY1), thereby maintaining the repressive histone mark, reducing E-cadherin expression, leading to cell migration and invasion (Geng *et al.*, 2017).

Methylation of an RXR motif in eukaryotic initiation factor 2α (eIF2α) by PRMT7 is important in the cellular stress response. eIF2α is phosphorylated at ser-51 upon induction of cellular stress and this is made possible due to PRMT7-mediated methylation of the protein at R54 (Haghandish *et al.*, 2019). Heat shock protein 70 (HSP70) is another known methylation target of PRMT7, with R249me also being important for stress granule formation (Szewczyk *et al.*, 2020a, Szewczyk *et al.*, 2020b). This response has been associated with neurodegeneration through initiation of protein aggregation and growth arrest and DNA damage-inducible protein 34 (GADD34) transcription (Bond *et al.*, 2020). PRMT7 is also known to be involved in the DDR by epigenetic methylation of H2R3 and H4R3, which represses expression of DNA polymerase subunit POLD1 and other genes involved in DNA repair (Karkhanis *et al.*, 2012). Loss of PRMT7 has also been shown to inhibit MLL4 recruitment to chromatin and subsequent methylation of H3K4, thereby losing self-renewal capability of neural stem cells and forcing entry into the MLL4-driven differentiation program (Dhar *et al.*, 2012). Additionally, PRMT7 has been shown to methylate splicing factor hnRNPA1 at several sites and depletion of the PRMT lead to several thousand alternative splicing events (Li *et al.*, 2021b).

1.6.4. PRMT Inhibition

There are several PRMT inhibitors which have been proposed for use in a variety of cancers and are currently in clinical trials. PRMT inhibitors can target the AdoMet/SAM binding pocket, or the substrate binding pocket, competitively, or non-competitively. A more recent development in PRMT inhibition is the use of proteolysis-targeting chimera (PROTACs), which targets proteins for ubiquitylation by E3 ubiquitin ligases and subsequent degradation by the proteasome. The use of this technology opens up the possibility of overcoming chemotherapeutic resistance to small molecule inhibitors and provides flexibility to the specific proteins the therapies could target (Sun et al., 2019, Li et al., 2022a).

1.6.4.1. *Type I PRMT Inhibitors*

Type I PRMT inhibitors have proven difficult to synthesise and translate into effective inhibitors in preclinical studies (Hwang *et al.*, 2021), which is what makes it imperative to repurpose the drugs that have shown effectivity in other cancers and diseases. AMI-1 was the first type I PRMT inhibitor, discovered by Cheng *et al.* (2004), spurring the development of other PRMT inhibitors, such as Furamidine (Yan *et al.*, 2014) and Allantodapsone (Spannhoff *et al.*, 2007), which were found to have high PRMT1 specificity and being entered into pre-clinical trials (Smith *et al.*, 2018). Inhibitors such as these have been used in combination with immunotherapies, such as anti-PD-L1 antibodies, which upregulated CD8 T-cell infiltration into pancreatic tumour cells and increased apoptosis (Zhang *et al.*, 2020). SGC707 is an AdoMet non-competitive inhibitor and an allosteric inhibitor of PRMT3 which is being used as a template for further SAM-binding non-competitive inhibitors (Kaniskan *et al.*, 2015). EZM2302 and TP064 are PRMT4/CARM1 inhibitors with higher potency than their earlier counterpart SGC2085 (Ferreira de Freitas *et al.*, 2016, Sack *et al.*, 2011, Smith *et al.*, 2018). Inhibitors with increased selectivity, such as compound 49, were also developed from previous, weaker iterations of drugs (Guo *et al.*, 2019). PRMT6 inhibitor EPZ020411 was shown to increase in vivo survival in conjunction with ionising radiation, by inducing differentiation of GSCs and cell cycle arrest (Banasavadi-Siddegowda *et al.*, 2018). MS023 was developed by Eram *et al.* (2016), from 6′-methyleneamine sinefungin (GMS) (Wu *et al.*, 2016a), which led to the development of MS049, a PRMT4/PRMT6 dual inhibitor (Shen *et al.*, 2016).

1.6.4.1.1. MS023

MS023 is a cell-active, non-competitive, potent inhibitor, selective of type I PRMTs, which binds to the substrate binding site of its target. It has been reported to decrease levels of histone arginine asymmetric dimethylation, whilst also increasing monomethylation and symmetric dimethylation (Eram *et al.*, 2016). MS023 was designed (Figure 1.1.9) by Eram *et al.* (2016), based upon previous PRMT-specific inhibitor discoveries of: EPZ020411, targeting PRMT6 (Mitchell *et al.*, 2015) and campomelic dysplasia 1 (CMPD-1), targeting PRMT4 (Sack *et al.*, 2011). MS023 consists of an arginine mimetic ethylenediamine side chain, as well as a *para*-isopropoxy and terminal amino group for type I PRMT inhibitory properties, two basic amino groups for increased potency and a pyrrole ring (Figure 1.1.9). MS023 was found to potently inhibit PRMT1 (50% inhibitory concentration (IC_{50}) = 30 ± 9 nM), PRMT3 (IC_{50} = 119 ± 14

nM), PRMT4 (IC_{50} = 83 ± 10 nM), PRMT6 (IC_{50} = 4 ± 0.5 nM) and PRMT8 (IC_{50} = 5 ± 0.1 nM), but not any type II or III PRMTs, or lysine demethylases.

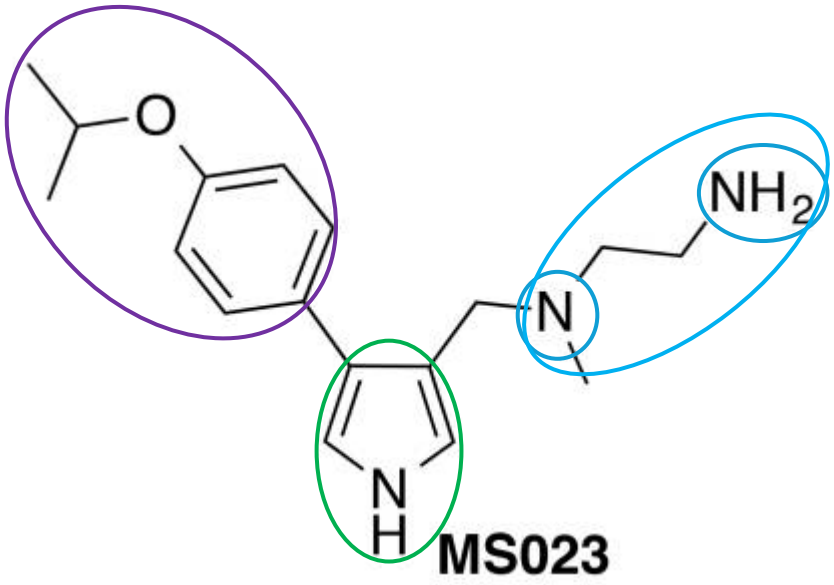

Figure 1.1.9.: MS023 Chemical Structure

Ethylenediamine side chain shown in blue. Para-isoproproxy group shown in purple circle. Amino groups shown in yellow circles. Pyrrole ring shown in green circle. Taken from Eram et al. 2016.

Pharmacological inhibition of PRMTs by MS023 in cells resulted in a decrease of basal H4R3me2a levels, a histone mark attributed to PRMT1 (Strahl *et al.*, 2001), as well as global Rme2a levels, similar to PRMT1 knockdown (Eram *et al.*, 2016). Levels were not affected by treatment with the negative control, MS094, which contained several variations of the MS023 structure. Cell growth studies on eight cell lines indicated a decrease in cell growth, after several days, at concentration above 1μM(Eram *et al.*, 2016). Previous studies have indicated that inhibition of type I PRMTs contributed to decreased proliferation and increased cellular senescence (Elakoum *et al.*, 2014).

1.6.4.2. *GSK3368715*

GSK5568715 is a general type I PRMT inhibitor (Figure 1.1.10). Its effects involve inhibiting arginine methylation of hnRNPs, thereby altering exon usage and RNA splicing (Fedoriw *et al.*, 2019). It was developed, alongside GSK3368712, from Epizyme's protein methyltransferase biased compound collection, as a PRMT1 inhibitor.

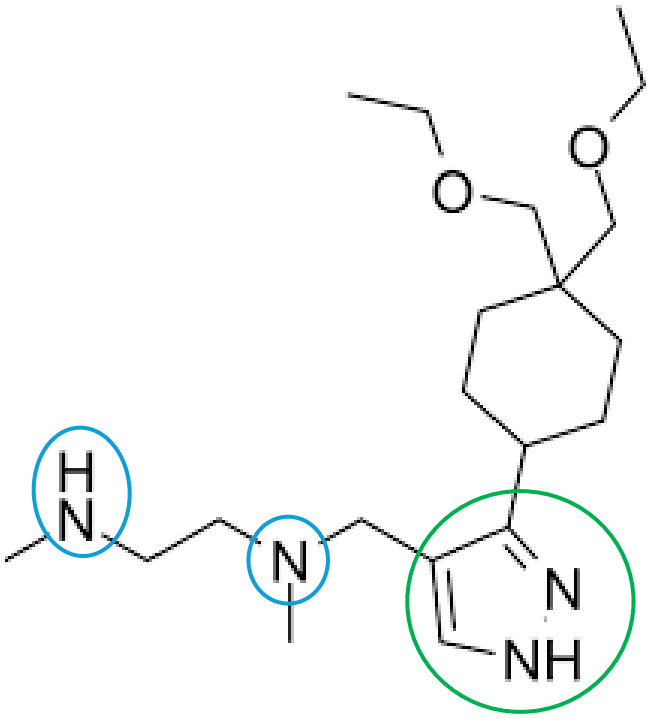

Figure 1.1.10. GSK3368715 chemical structure

Schematic of GSK3368715, taken from Fedoriw et al. 2019. Amino groups shown in yellow circles. Pyrazole ring shown in green circle.

GSK3368715 is a reversible, but potent, non-competitive type I PRMT inhibitor. GSK3368715 displays IC_{50} values of 3.1nM (PRMT1), 48nM (PRMT3), 1148nM (PRMT4), 5.7nM (PRMT6) and 1.8nM (PRMT8) and displays time-dependent inhibition. Proliferation assays across 12 tumour types, represented by 249 cell lines indicated greater than 50% growth reduction over most cell lines. Mouse models of Toledo pancreatic cancer cell line tumour growth were treated with 75 mg/kg GSK3368715 and found tumour regression, along with 78% and 97% tumour regression in BxPC3 xenografts at 150 mg/kg and 300 mg/kg dosages (Fedoriw *et al.*, 2019).

Previous, published studies in my host lab (Samuel *et al.*, 2018) and in other research groups (Dhar *et al.*, 2013, Fedoriw *et al.*, 2019) have indicated that inhibition of type I PRMTs through GSK3368715 causes global reduction in aDMA and an accumulation of sDMA and mMA. This unidirectional crosstalk in not recapitulated in reverse. Inhibition of type II PRMTs I *via* drugs such as GSK591 does not cause an accumulation of aDMA but does decrease global sDMA (Samuel *et al.*, 2018). Most solid tumour cell lines tested with the drug display cytostatic responses, whilst some cytotoxic response can be seen in other cancers, associated with methyladenosine phosphorylase (MTAP) deficiency. MTAP loss is common in cancers due to its proximity to tumour suppressor CDKN2A, which is commonly deleted (El-Khoueiry *et al.*, 2023). This causes an increase in 2-methyladenosine (MTA) in cells, which in-turn causes inhibition of PRMT5, a type II inhibitor which has confirmed links to tumourigenesis. This could potentially increase sensitivity of tumours to type I PRMT inhibition and this hypothesis has been further strengthened through studies into the synergistic effects of concurrent type I and II PRMT inhibition in mice (Fedoriw *et al.*, 2019). Pathway analysis of cell lines treated with GSK3368715 showed enrichment in mRNA processing and splicing, including through the Myc program, with downstream target pathways including cell cycle and mitosis (Favia *et al.*, 2019). Association of type I PRMT inhibition with splicing factor proline and glutamine-rich (SFPQ) and FUS members of the hnRNP family are factors indicating that the method of GSK3368715 action is through aberrant exon skipping an alternative splicing (Fedoriw *et al.*, 2019).

GSK3368715 was entered into a phase 1 clinical trial (NCT03666988) to determine preliminary efficacy, safety and pharmacokinetics of the drug in advanced stage solid tumours in adults. Part 1 of the clinical trial was halted after thromboembolic events (TEE) in 25% of patients with 200 mg oral dose. The trial was resumed at 100 mg oral dose, where the best response achieved was stable disease in 29% of patients, but limited target engagement within the solid tumours was seen, leading to premature termination of the study. It was, however, noted in the study that only one of the thirty-one patients was treated for more than 6 months, resembling a relatively short time period (El-Khoueiry *et al.*, 2023).

1.6.4.3. *Type II and III PRMT Inhibitors*

Several type II PRMT5 inhibitors have been entered into clinical trials and have displayed more encouraging outcomes, potentially due to the large range of targets under PRMT5 influence. Binding of drugs which target the substrate binding site, including EPZ015666 (Chan-Penebre *et al.*, 2015) and GSL3326595, of which the latter was entered into clinical trials, is enhanced by binding of AdoMet. As mentioned previously, MTA competes with SAM binding and therefore, LLY-283 and JNJ-64619178 were developed to mimic AdoMet binding, the latter of which is currently entered into phase I clinical (Hwang *et al.*, 2021). LLY-283 was also shown to have good BBB penetrance, which improved *in vivo* survival (Sachamitr *et al.*, 2021). PRMT5 inhibitors PRT811 (NCT04089449) and GSK3326595 (NCT02783300, NCT03614728) have been in clinical trials against cohorts of patients with GBM. Within the same realm, the use of drugs to bring about the stabilisation of MTA, or the prevention of the PRMT5:MEP50 interaction has also been explored. MS4322 is the first PRMT5-targeted PROTAC and it bridges substrate binding site drug EPZ015666 with E3 ligase VHL, which then targets PRMT5 for proteasomal destruction (Shen *et al.*, 2020, Hwang *et al.*, 2020). The first type III inhibitor, DS-437, showed specificity against PRMT5 and PRMT7 (Smil *et al.*, 2015) and more recently, the more potent and PRMT7-specific SGC3027 has been found to inhibit HSP70 R469 methylation, augmenting cellular stress response (Szewczyk *et al.*, 2020a).

The recent research into the role of PRMTs in GBM tumourigenesis, particularly PRMT5 and PRMT1, and the use of inhibitors in haematological cancers, has led to the interest in the use of PRMT inhibitors as potential GBM therapies (Bryant *et al.*, 2021). Research by Fedoriw *et al. (2019)* found synergy between PRMT5 and type I PRMT inhibitor GSK3368715, which became some of the basis for this study. Further research into BBB penetrating technologies, or modulation of small molecule inhibitors to increase penetration of the BBB are required to increase efficacy of these drugs. In addition, investigation into the impact of these drugs on the TME is required to further characterise their efficacy (McCornack *et al.*, 2023) and model development is imperative to elucidate this mechanism.

1.6.5. FUS

1.6.5.1. *Structure and Function*

FUS, also known as translocated in liposarcoma (TLS), is a 70 kDa RNA/DNA binding protein (Figure 1.1.11), hnRNP P2, belonging to the FUS/TLS, EWS, TATA-box binding protein associated factor 15 (TAF15) (FET) family (Neumann *et al.*, 2009a, Neumann *et al.*, 2009b, Neumann *et al.*, 2006). It is normally located in the nucleus, where it is involved in the DNA damage response, transcriptional and translational regulation, splicing and many other cellular processes involved in genome stability and protein biosynthesis.

FUS is a 526 aa multidomain protein with an N-terminal transcriptional activation domain, multiple nucleic acid binding domains and a C-terminal nuclear localisation signal (NLS) domain. The intrinsically disordered, prion-like N-terminal transactivation domain (Patel *et al.*, 2015) consists of an SYGQ-rich sequence (Figure 1.1.11), which has been shown to be important for concentration-dependent liquid-liquid phase transition and liquid-to-solid phase transition in stress granules. The C-terminal domain is comprised of a three repeat RGG/RG-rich domain (RGG3), followed by a proline-tyrosine (PY) domain, forming the RGG3-PY NLS (Dormann *et al.*, 2010). This domain interacts with nuclear import receptor Transportin (TNPO1)/Karyopherin- β2 (Kapβ2) (Lee, 2006) to translocate into the nucleoplasm.

FUS has DNA homologous pairing activity and binds to single strand DNA breaks and promotes its annealing to complementary single stranded DNA and D-loop formation (Baechtold *et al.*, 1999). FUS also interacts with the transcriptional pre-initiation complex, including RNAPII and transcription factor II D (TFIID), gene specific transcription factors such as NFκB, binds to TCCCCGT in the promoter region of target genes, FET proteins interact with intronic elements near to the splice site and recruit hnRNPs and the spliceosome, through both of these interactions couple splicing and transcription, shuttles between nucleus and cytoplasm and could play a role in mRNA export, in neurons, FUS is involved in the transport of specific mRNAs, such as encoding actin-stabilising protein novel Kelch family gene (Nd1-L) into dendritic ends and affect cell spreading in fibroblasts (Dormann *et al.*, 2012).

FUS has been shown to reduce proliferator factors, such as cyclin D1 and Cdk6, whilst increasing anti-proliferation factors and proliferative inhibitory factors such as CDK and p27 – thus increasing the rate of apoptosis in prostate cancer cells. Immunohistochemistry (IHC)

analysis identified that there was an inverse correlation between FUS and the degree of prostate cancer, indicating that higher FUS levels increase survival (Ghanbarpanah *et al.*, 2018).

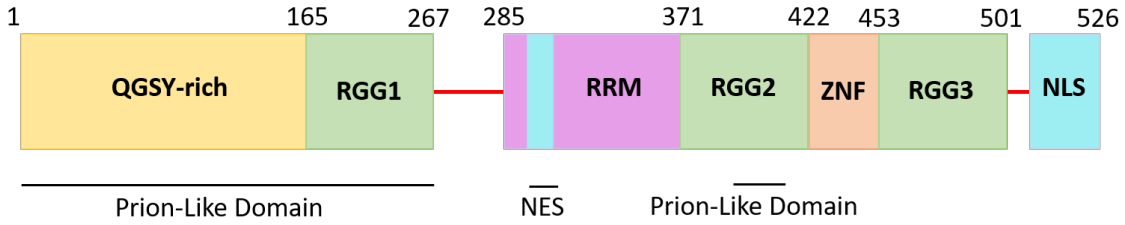

Figure 1.1.11.: Structure of FUS.

FUS is a multi-domain protein, with a prion-like N-terminal domain, consisting of a QSGY-rich sequence and RGG sequence motif. It has a central nuclear export sequence (NES), preceding the RRM domain and a second prion-like domain, which sits within the second RGG-rich sequence. Finally, the C-terminal contains a zinc-finger motif (ZNF) and a third RGG-rich sequence and ends with a nuclear localisation signal (NLS).

1.6.5.1.1. Liquid-to-liquid phase transition

Molliex *et al.* (2015) and Patel *et al.* (2015) have shown that, at particular concentrations, FUS forms protein droplets in a reversible liquid phase separation. This underpins the role of FUS in the formation of ribonucleoprotein granules and other transient membrane free organelles (Weber and Brangwynne, 2012), driven by cation-π interactions between tyrosines in the intrinsically disordered low-complexity domains and arginines in the highly-structured C-termini (whose methylation tunes these interactions (Qamar *et al.*, 2018)). These membrane-free organelles organize the transport of RNA and proteins within subcellular niches, such as components of neuronal cells. FUS knockdown abolishes serine-139 phosphorylation of H2A histone family member X (γH2AX) formation in response to double strand breaks (Wang *et al.*, 2013b). Phase separation at laser-induced DSB sites transiently and reversibly reorganizes the intracellular space by separating prion-like domain containing proteins from the soluble intracellular space, *via* increasing poly-ADP ribose (PAR) levels at DSB sites (nucleic acid-mimicking biopolymer nucleates intracellular phase separation), potentially allowing space for DNA damage sensor proteins.

1.6.5.1.2. Liquid-to-solid phase transition

At critical condition, this then becomes an irreversible liquid-to-solid phase transition in stress granules to fibrous aggregates *in vitro* and FUS is exported from the nucleus and clusters in the cytoplasm of neuronal and glial cells (Burke *et al.*, 2015). This process has been demonstrated to occur in motor neuron disease (MND) patients due to N-terminal NLS truncation (Dormann *et al.*, 2010); frontotemporal dementia (FTD) patients and in the *post-mortem* brain. Loss of nuclear import would mean loss of nuclear functions, such as splicing, gene expression regulation and miRNA biosynthesis, or gain of function, such as initiation of aggregation within stress granules (Ratti and Buratti, 2016, Hofweber *et al.*, 2018).

1.6.5.1.3. Neuropathy

Normally, FUS is located within the nucleus of neuronal and glial cells, however in *post-mortem* brains and patients with ALS/MND, or FTD it is located within cytoplasmic aggregates (Mackenzie *et al.*, 2010). In MND patients, FUS mutations which involve the truncation of the C-terminal NLS contribute to defective nuclear import and rapid MND onset and pathogenesis (Dormann *et al.*, 2010). Loss of nuclear import would mean loss of nuclear functions, such as splicing, gene expression regulation and miRNA biosynthesis, or gain of function, such as initiation of aggregation within stress granules (Ratti and Buratti, 2016, Hofweber *et al.*, 2018). FUS null mice have been shown to have hypersensitivity to irradiation-induced chromosomal damage, as well as issues with homologous recombination and in mice with FUS overexpression causes motor neuron deficits and premature death (Ratti and Buratti, 2016).

1.6.5.1.4. Arginine methylation and FUS

The RGG3 domain of FUS is modified extensively with aDMA groups, by PRMT1 and PRMT8 (Type 1). In FTD-FUS patients FUS deposits are un- or mono-methylated(Dormann *et al.*, 2012, Suarez-Calvet *et al.*, 2016). RGG2-ZnF-RGG3 domain is the most likely RNA binding domain with a preference for GU-rich motifs(Bentmann *et al.*, 2012, Iko *et al.*, 2004, Lerga *et al.*, 2001). FUS mutations in *de novo* and recessive inheritance most frequently occur in the C-terminal domain. R521C within the RGG domain is most frequently seen (Ratti and Buratti, 2016). Hofweber *et al.* (2018) showed that TNPO1 interacts with the arginines of the RGG3-PY domain and acts as a chaperone, preventing the aggregation of FUS. Post-

translational arginine methylation of the RGG domains of the C-termini contribute to the regulation of this phase separation. Inhibition of arginine methylation also directly promotes FUS aggregation, implying that the PTM is essential for correct nuclear import. Arginine hypomethylation leads to the formation of stable antiparallel intermolecular β-sheet-rich hydrogels (Patel *et al.*, 2015), formed by residues 39-95 of the low-complexity domains (Murray *et al.*, 2017) which disrupt RNP function and protein synthesis (Qamar *et al.*, 2018). Arginine methylation regulates TNPO1 chaperone and FUS binding and nuclear import and is defective in MND and FTD patients (Dormann *et al.*, 2012). Both PRMT1 and PRMT8 have been linked to FUS in neurological diseases, such as ALS (Dong *et al.*, 2021). Mutated FUS is a major component in the inclusion bodies, found within motor neurons of ALS patients and this has been found alongside PRMT1 and PRMT8 in patient-derived cells. Inhibition of both PRMT1 and PRMT8 have been shown to reduce FUS-positive ALS cells *in vitro,* although the opposite effect was seen *ex vivo* in *Drosophila* FUS-positive ALS models (Scaramuzzino *et al.*, 2013).

Sf9 cells, grown in the presence of adenosine-2,3-dialdehyde (AdOx), a general PRMT inhibitor, indicated a large reduction in aDMA FUS (Qamar *et al.*, 2018). The use of isobaric tags for relative and absolute quantitation (iTRAQ) and spectral counting mass spectrometry were used to identify which arginines were differentially methylated between untreated and AdOx-treated cells. In the presence of AdOx, several arginines (216, 259, 407, 473 and 476) were converted from dimethylated status to mono- or unmethylated status, indicating that PRMT inhibitors do have a profound effect on FUS methylation status. Arginines 394 and 481 remained predominantly dimethylated. Alanine mutation screens, whereby the arginines whose methylation status was funded to be robustly changed in the iTRAQ experiments, caused disruption of the π-cation interactions and abrogated FUS phase separation (Qamar *et al.*, 2018).

LncRNA a disintegrin and metalloproteinase with thrombospondin type 1 motif 9 antisense RNA 2 (ADAMTS9-AS2) has been shown to promote TMZ resistance in GBM by directly interacting with RNA recognition motif (RRM) and Znf_RanBP2 domains of FUS and decreasing interaction between FUS and MDM2, inhibiting ubiquitination of K38 and subsequent downregulation of FUS by the E3 ligase. LncRNA knockdown results in FUS

destabilization through K38 ubiquitination and reduces progression and metastasis in TMZ-resistant cells (Yan *et al.*, 2019). It could be hypothesied that the induction of FUS *via* sDMA, through aDMA inhibition results in the upregulation of the FUS/MDM2 ubiquitination axis, thereby elucidating a cause of TMZ resistance. TMZ resistance could be due to the upregulation of FUS, through sDMA and other mechanisms.

1.6.6. Apoptosis Pathway

Apoptosis, or programmed cell death, is an essential part of cellular homeostasis and is often manipulated and dysregulated in cancer. Cellular apoptosis can occur due to a selection of external and internal stimuli, including radiation, alkylating agents and issues with DNA replication. Cells undergoing apoptosis are typically shrunken, have a damaged cell membrane, condensed chromatin and DNA cleavage (Saraste and Pulkki, 2000). Cell contents are then packaged into membrane bound apoptotic bodies, which are cleared from tissues by macrophages. Both the extrinsic and intrinsic pathways lead to the activation of cysteine aspartase, or caspase proteins, which bring about final programmed cell death (Lossi, 2022). Caspases are required for the selective proteolysis of key proteins which perpetuate the pathways of apoptosis. There are 3 subtypes of caspases, including: inflammatory, initiator and effector caspases which exist as zymogens before being processed by other caspases, to induce an active proteolytic cascade, culminating in apoptosis. The caspases have a myriad of targets which ensure the dedication of a cell to apoptosis (Shi, 2004) (Figure 1.1.12).

The intrinsic pathway is triggered by detrimental changes within the cell microenvironment, such as DNA damage and hypoxia. It is characterised by the release of cytochrome C, second mitochondria-derived activator of caspase (Smac)/ direct inhibitor of apoptosis-binding protein with low pi (Diablo) from the mitochondrial intermembrane space and into the cytosol, triggering the formation of an apoptosome. Stress sensor p53 is phosphorylated by ATM and checkpoint factor 2 (Chk2) and MDM2-mediated ubiquitination of p53 is inhibited. p53 is targeted to the Bcl-2 gene family promoter region and activates transcription of pro-apoptotic genes and represses transcription of anti-apoptotic genes (Ren *et al.*, 2010). p53 is also responsible for upregulating p53-upregulated modulator of apoptosis (PUMA), PTEN and APAF1 which contribute to increase in mitochondria-damaging reactive oxygen species (ROS) and the apoptotic response (Lahav, 2008). The damaged mitochondria then release Smac,

Diablo and Omi/high temperature requirement protein 2 (HTRA2), which prevent activation of inhibitor of apoptosis proteins (IAPs), allowing cleavage and activation of caspase 3 (Cagnol *et al.*, 2011). Caspase 3 cleaves inhibitor of caspase-activated DNase (ICAD), releasing CAD, allowing oligomerisation, DNA fragmentation and chromatin condensation (Figure 1.1.12).

The extrinsic pathway is induced by perturbations in the extracellular microenvironment, which can follow either a receptor activation pathway, or cytotoxic stress pathway. Receptor-mediated pathways are activated by death receptors of the tumour necrosis factor receptor (TNFR) family and contain a death domain (Muntane, 2011). These include death receptor (DR)4/DR5, Fas and TNFR1. As an example, Fas ligand binding to Fas causes receptor oligomerisation and Fas-associated death domain (FADD) cofactor death effector domain (DED) binding. FADD recruits procaspase 8, which oligomerises and self-cleaves, from which then proceeds the caspase pathways, whereby caspases 3 and 7 are activated (Schneider and Tschopp, 2000). Caspase 8 cleaves Bcl2 interacting protein (BID), which triggers cytochrome C release from mitochondria. Cytochrome C then binds to APAF1 and procaspase 9, which is then also activated, which in turn activates procaspase 3. Alternatively, caspase 8 directly cleaves procaspase 3. Activation of TNFR1 causes dynamic activation of apoptosis. When associated with TNFR1 associated death domain (TRADD), recruits TNF receptor associated factor-2 (TRAF2), cellular inhibitor of apoptosis-1 (CIAP1), receptor-interacting protein-1 (RIP1) kinase and subsequently IκK, which activates NFκB and cell survival. Upon sufficient recruitment of NFκB, Fas-associated death domain protein-like interleukin-1α-converting enzyme-like inhibitory protein (FLIP) inhibits caspase 8. Dissociation of TRADD from TNFR1 leads to recruitment of FADD and initiator caspase 8 when NFκB recruitment is insufficient. Growth factors and their associated receptors activate PI3K and Akt, which modulates pro-apoptotic Bcl2-antagonist of cell death (BAD) (Shirley *et al.*, 2011, Shi, 2004, Valdes-Rives *et al.*, 2017) (Figure 1.1.12).

Cellular stress, such as from cytotoxic radiation or drugs, also induces apoptosis. Mitochondrial membrane permeabilisation (MitoMP) may occur through association of voltage dependent anion channel (VDAC), adenine nucleotide transporter (ANT), peripheral-type benzodiazepine receptor (PBR) and cyclophilin D, along with BAX, Bcl2 antagonist killer 1 (BAK1), BIM, or BclXL, to form and regulate opening and closing of the permeability transition pore complex

(PTPC) (Ren *et al.*, 2010). Alternatively, or additionally, BAX and BID may translocate to the nucleus and oligomerise, forming pores. The former is released from microtubules and the latter is activated through cleavage by caspase 8 *via* DR signalling (Flores-Romero *et al.*, 2020, Oropesa-Avila *et al.*, 2013, Kantari and Walczak, 2011).

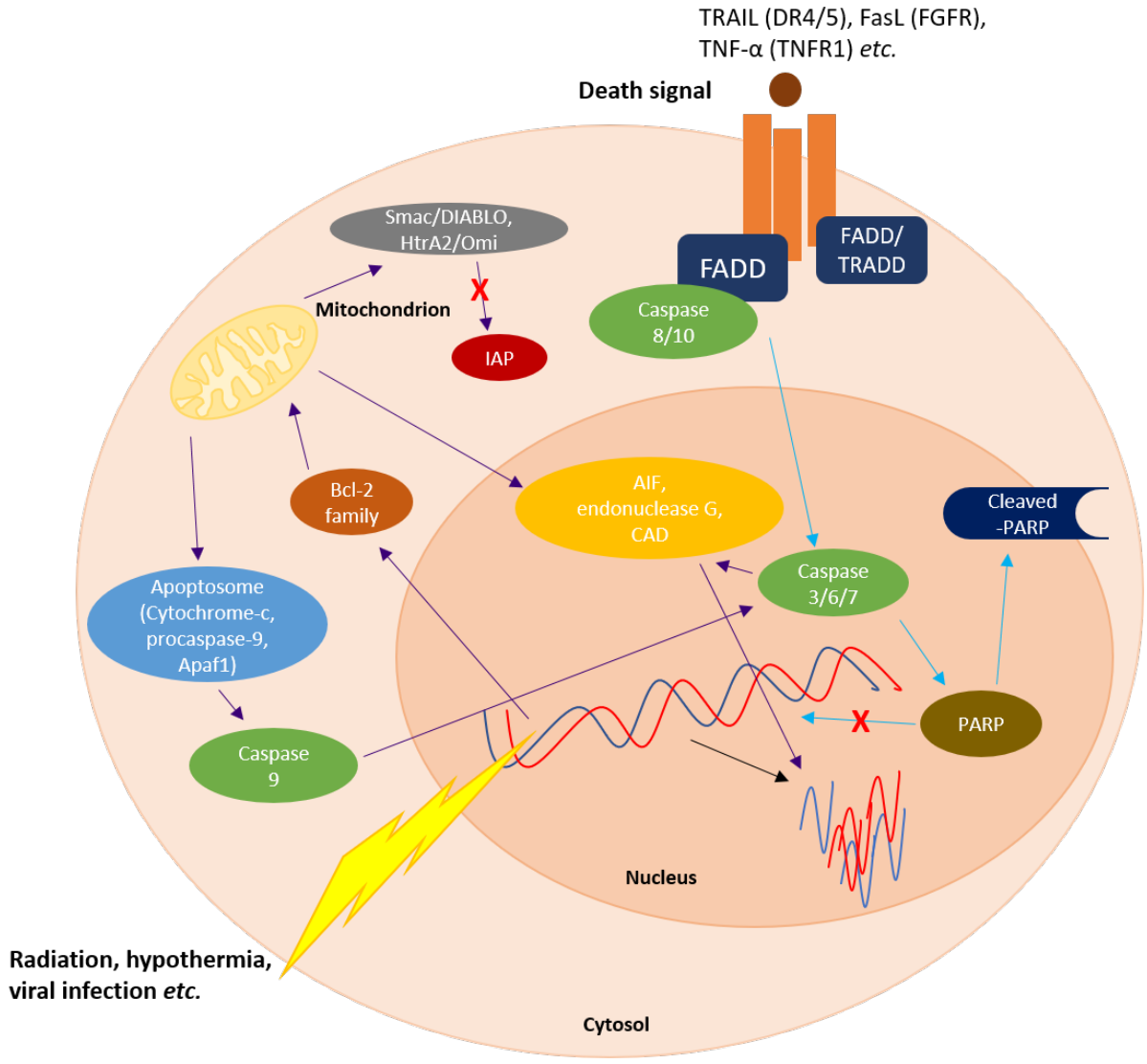

Figure 1.1.12.: Schematic of the apoptosis pathway

TNF related apoptosis inducing ligand (TRAIL); Death receptor 4/5 (DR4/5); apoptosis antigen (Fas); Fas ligand (FasL); fibroblast growth factor receptor (FGFR); tumour necrosis factor-α (TNF-α); tumour necrosis factor receptor 1 (TNFR1); Fas associated death domain (FADD); TNFR1 associated death domain (TRADD); apoptosis inducing factor (AIF); caspase

activated DNase (CAD); poly-ADP ribose polymerase (PARP); apoptosis associated factor 1 (APAF1); apoptotic B-cell lymphoma 2 (Bcl-2); inhibitor of apoptosis protein (IAP); second mitochondria-derived activator of caspase (Smac); high temperature requirement protein A2 (HTRA2).

1.6.6.1. *Cleaved-PARP as a marker of cell death*

PAR polymerase 1 (PARP1) is a double zinc finger DNA-break binding protein, which catalyses DNA repair *via* the BER pathway. The N-terminal DNA binding domain binds at the site of a DNA break. The C-terminal catalytic domain then catalyses the transfer of PAR from the nicotinamide adenine dinucleotide (NAD+) substrate to protein acceptors within the chromatin, which then recruits other repair proteins, such as MRE11 and topoisomerase-1, to the DNA break site (Chaitanya *et al.*, 2010). Cleavage of PARP into 89kDa and 24kDa fragments by caspases 3 and 7, ensures cellular breakdown and irreversibility of apoptosis, through prevention of DNA repair (Gobeil *et al.*, 2001).

1.6.6.2. *Annexin V as a marker of cell death*

Annexin A5/V is thought to compete for phosphatidylserine binding sites with prothrombin and to inhibit phospholipase A1 by shielding and blocking negatively charged phospholipids, from entering into blood coagulation reactions. Normally, phosphatidylserine residues reside on the cytosolic side of the plasma membrane (Crowley *et al.*, 2016). Expression of Annexin V indicates that phosphatidylserine residues are being expressed on the cell surface (Banfalvi, 2017), which is a feature of apoptosis and other forms of cell death (Kari *et al.*, 2022).

HYPOTHESIS AND AIMS

Hypothesis:

Type I PRMT inhibitor GSK3368715 causes apoptosis of GBM tissue maintained in a novel perfusion system *ex vivo.*

Aims:

- **Determine the ability of GSK3368715 to cause apoptosis** using GBM patient biopsies in a novel perfusion device.
- **Assess/evaluate transcriptomic changes** upon treatment of GBM with GSK3368715 *ex vivo*, with the ultimate goal of identifying novel drivers of GBM formation and indicators of lethality, synergising with personalised patient care and precision medicine
- **Investigate the differences between healthy brain tissue and GBM, in response to GSK3368715,** *ex vivo,* at the molecular level.

CHAPTER 2: GENERAL METHODS AND MATERIALS

2.1. Immortalised cell lines

U-87 MG cells (ATCC® HTB-14™) (Allen *et al.*, 2016) were obtained from colleagues at the University of Hull. U-87 MG cells were thawed for one minute in a 37 ºC bead bath, from liquid nitrogen storage, at passage 20. Warmed Dulbecco's Modified Eagles Medium (DMEM) (Table 2.1) was added dropwise to the cells, up to 5 ml, to prevent osmotic lysis, transferred to a 15 ml centrifuge tube and cells pelleted in a centrifuge at 300xg, for 5 minutes, to remove dimethyl sulfoxide (DMSO). The supernatant was removed, and cells were resuspended in 5 ml DMEM, transferred to a filtered T25 flask (Sigma) and incubated at 37°C with 5% carbon dioxide (CO_2). After ~7 days, DMEM was removed and the cells washed with warmed phosphate buffered saline (PBS), prepared by dissolving 1 tablet in 200 ml deionised water (diH_2O) and autoclaving in a Duran bottle) (Sigma). The adherent cells were dislodged from the bottom of the flask with warmed 2 ml 1x 0.25% Trypsin- Ethylenediaminetetraacetic acid (EDTA) solution (Sigma), which was then neutralised with 10 ml DMEM upon cell suspension and transferred to a 15 ml centrifuge tube. Cells were centrifuged at 300xg, for 5 minutes, the supernatant discarded, and cells resuspended 1:10 in an appropriate volume of DMEM, to be transferred into a larger filtered T175 flask (Sigma). Medium was discarded and replaced every 2-3 days and cells passaged every 4-5 days, once ~75% confluency was reached. To freeze down cells for storage, media was removed from 75% confluent T75 flasks, adherent cells dislodged using trypsinisation and cells pelleted using centrifugation, as described previously. The pellet was resuspended in 3 ml of medium with 10% DMSO, before transferring into 1 ml cryovials and freezing in an isopropanol bath overnight at -80°C and long-term storage in liquid nitrogen.

Table 2.1.: Constituents of immortalised cell line medium

Reagent	**Final Concentration**	**Manufacturer**	**Catalogue no.**
Dulbecco's Modified Eagle's Medium (DMEM) (1x) (4500 mg/L glucose, L-glutamine, and sodium bicarbonate, sterile-filtered)	1x	Sigma Aldrich	D5796

FCS	10% (v/v)	Sigma-Aldrich	F7524
Sodium pyruvate (100mM)	1mM/1% (v/v)	Gibco	11360070
Antimycotic/antibiotic cocktail (100x) (10,000 units penicillin, 10 mg streptomycin and 25 μg amphotericin B per mL, 0.1 μm filtered)	1x/1% (v/v)	Sigma Aldrich	A5955

2.2. MTS Assay

The 3-(4,5-dimethylthiazol-2-yl)-5-(3-carboxymethoxyphenyl)-2-(4-sulfophenyl)-2H-tetrazolium (MTS) assay is a colorimetric assay which quantitatively determines the level of proliferation of cells, to investigate the action of anti-tumour drugs on cell lines (Primon *et al.*, 2013). Due to the novelty of PRMT inhibitor GSK3368715, MTS assays were employed to ascertain changes to U87-MG cell line proliferation through treatment with the drug and in combination with other PRMT inhibitors. This was performed both in 2D and in 3D cultures.

2.2.1. 2D Cells

Cells were plated onto 96-well plates (Corning) at a density of 20,000 cells/well and allowed to incubate at 37 ºC for 24 hours before treatment was applied. Cultured cells are incubated with 10% (v/v) MTS reagent (Abcam), for 30 minutes at 37 ºC, 5% CO_2. Outer wells were filled with PBS (grey) to prevent sample media evaporation and to maintain inner plate temperature.

2.2.2. Spheroids

Cells were plated into 96-well round-bottom plates (Corning), containing 100ul 1% sterile agarose (Sigma) at a density of 20,000 cells/well. Spheroids were allowed to form for 72 hours at 37 ºC, 5% CO_2. Media was then changed, taking care not to disturb the spheroid, or the underlying agarose and treatments added. The MTS reagent was added to the spheroids for 3 hours at 37 ºC, 5% CO_2. Spheroids are exposed to the reagent for a longer time period due to the reduced volume: surface area ratio.

2.2.3. Reading absorbance

Plates are then placed onto a shaker for 2 minutes to diffuse the colour. An equal amount of solution from each well was then transferred to the corresponding well of a clean, flat-bottomed 96-well plate, taking care not to transfer cells. Absorbance is then read at 490 nm, using the BioTek™ ELx800™ absorbance microplate reader, correcting for 680 nm. Media-only absorbance values were subtracted from the treated well absorbance values and all values normalised to the DMSO control and multiplied by 100 to attain percentage cell viability.

2.3. Nuclear and Cytoplasmic extraction

U87-MG cells were seeded at a density of $1x10^6$ into 150mm cell culture plates (Corning) and allowed to adhere for 24 hours, at 37 ºC, 5% CO_2 before treatment with PRMT inhibitors. Cells were treated with: 1 µM GSK3368715; 1 µM Furamidine; 1 µM GSK3368715 + 1 µM Furamidine; 1 µM GSK3368715 + 1 µM GSK591; 1 µM GSK3368715 + 1 µM Furamidine + 1 µM GSK591 and a DMSO negative control. After 48 hours, the media was aspirated, and cells were washed twice with PBS. Cells were then harvested using PBS containing phosphatase and protease inhibitors by scraping and aspirating into a 15 ml falcon tube. Cells were then pelleted at 500xg, 5 minutes, PBS aspirated and stored at -80 ºC.

Cells were thawed on ice and 100 µl transferred to 1.5 ml microcentrifuge tubes, pelleted at 500xg for 3 minutes and the supernatant discarded. Using the NE-PER™ Nuclear and Cytoplasmic Extraction kit (ThermoFisher Scientific) and following the manufacturer's instructions, 100 µl per 10 µg packed-cell volume of ice-cold CERI was added to the cells, agitated *via* vortex for 15 seconds and incubated on ice for 10 minutes. Ice-cold CERII was then added at 11:200 with CERI and vortexed for 5 seconds before incubation on ice. After 1 minute, the samples were vortexed again and centrifuged at ~17,000xg, 5 minutes. The cytoplasmic supernatant was transferred to a clean, pre-chilled microcentrifuge tube and stored at -20 ºC before use. NER was added to the remaining pellet at 100: 11 CERII and samples kept on ice and agitated for 15 seconds, every 10 minutes, for 40 minutes. Samples were centrifuged at 17,000xg for 10 minutes and the nuclear supernatant transferred to a clean, pre-

chilled microcentrifuge tube and stored at -20 ºC for immediate use. The remaining chromatin fraction pellet was also stored at -20 ºC. Long-term storage of the extracts was at -80 ºC.

2.4. LI-COR Odyssey Clx

U87-MG cells were seeded at a density of $1x10^6$ in 6-well plates (Corning) and treated with a combination of PRMT inhibitors, including 1 µM GSK3368715; 1 µM Furamidine; 1 µM GSK3368715 + 1 µM Furamidine; 1 µM GSK3368715 + 1 µM GSK591; 1 µM GSK3368715 + 1 µM Furamidine + 1 µM GSK591 and a DMSO negative control. They were then harvested using radioimmunoprecipitation assay (RIPA) buffer and protein concentration determined using Bicinchoninic acid (BCA) assay analysis as described previously. Samples then underwent sodium dodecyl sulphate – poly-acrylamide gel electrophoresis (SDS-PAGE) and western analysis, however, were transferred onto a polyvinylidene difluoride (PVDF) membrane, which has a higher protein binding capacity, and a low background, making it more sensitive and giving a cleaner signal: noise ratio. PVDF membranes were activated for 10 seconds in 100% methanol and then allowed to soak in transfer buffer before use. Membranes were blotted with FUS, sDMA and a-tubulin proteins (Table 2.2) overnight, rolling at 4 ºC and then incubated with a cocktail of IRDye® secondary antibodies (Table 2.3) for 2 hours, rolling at room temperature.

Table 2.2.: Primary and secondary (Horseradish Peroxidase (HRP)-conjugated) antibodies used for western blotting.

Antibody against	**HRP conjugated?**	**Species Raised**	**Manufacturer**	**Catalogue no.**
FUS/TLS	No	Mouse	Protein Tech	60160-1-1g
FUS/TLS	No	Rabbit	Abcam	Ab70381
α-tubulin	No	Mouse	Protein Tech	66031-1-1g
sDMA	No	Rabbit	Cell Signalling	13222S
aDMA	No	Rabbit	Cell Signalling	13522S
Dimethyl arginine	No	Mouse	Abcam	Ab412

Mouse	Yes	Rabbit	Dako	P0161
Rabbit	Yes	Goat	Dako	P0448

Table 2.3.: IRDye® Secondary antibodies used for LI-COR Odyssey Clx

Antibody against	**IRDye® wavelength**	**Species Raised**	**Catalogue no.**
Mouse	800CW	Goat	926-32210
Rabbit	680RD	Goat	926-68071

2.5. A novel perfusion device

Organ-on-chip technology has been developed over the past several years as a tool of precision and personal medicine, to mimic the *in vivo* settings of various tissues, with the aim of predicting patient outcome in a relatively real-time setting. There are several tumour-on-chip models which have been used to model of a variety of disease conditions and tissue systems (Riley *et al.*, 2021, Rodriguez *et al.*, 2020), including brain tissue (Cho et al., 2021a, Olubajo et al., 2020). Tissues are micro-dissected from patient biopsies and, sustaining their structure and microenvironment, are maintained *ex vivo,* allowing continuous supply of nutrient medium and removal of waste from tissues. It has been documented that the microenvironment is extremely important in the propagation and success of cancer and there are many studies, including in GBM, which target the microenvironment as a potential therapy (Liu *et al.*, 2022). This choice of *ex vivo* perfusion devices reduces the requirement for speciality fabrication equipment, thereby overcoming common barriers of expertise and cost that prevent the widespread implementation of additional, valuable research models.

Custom-designed chips () were made in-house, by Alex Iles, from four individual laser-cut (LS6840, HPC Laser, UK) polymethyl methacrylate (PmMA) pieces (Barry *et al.*, 2023), bonded together with chloroform, making up one 30 mm chamber (Akhil *et al.*, 2016). The central piece contains a semipermeable barrier, with 37 × 100 μm holes, to allow media to flow

through, whilst retaining the tissue in the 4 mm diameter internal chamber. The chip chamber is flanked by 1/32" Tygon 66 silicon inlet and outlet tubes (Coleparmer), connected by female/male Luer connects (Ibidi) (and Figure 2.2).

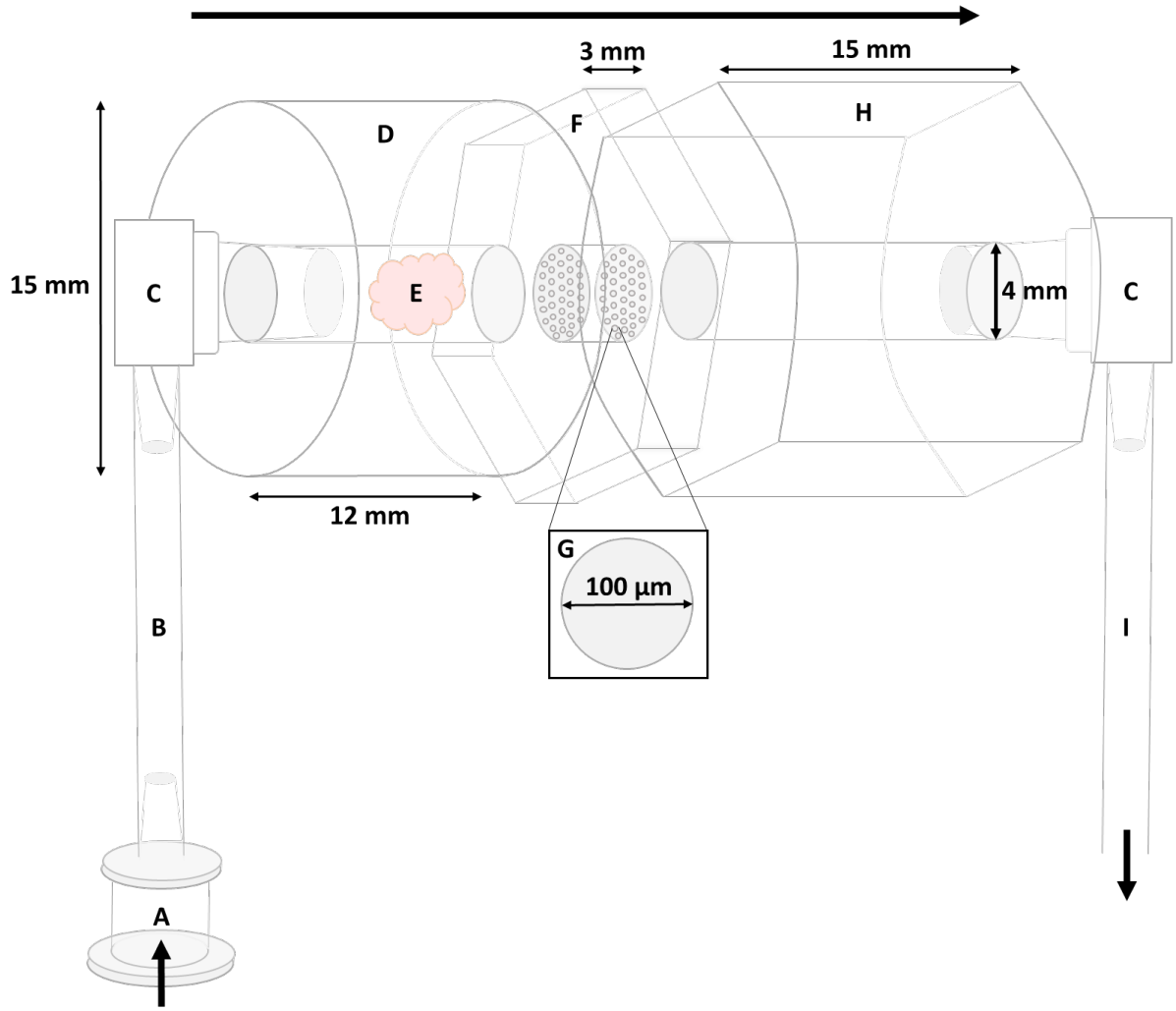

Figure 2.1.: Diagram of the GBM-on-chip chamber.

The chip is assembled from three polymethylmethacrylate (PmMA) components, fused together using chloroform. A) female Luer connector to attached to syringe-filter; B) 1/32" Tygon silicon inlet tube; C) male Luer connectors, inserted into inlet and outlet chambers; D) 12 mm x 15 mm inlet chamber, housing the tissue within 4 mm diameter internal chamber; E) micro-dissected tissue (~ 3 mm diameter); F) 3 mm x 15 mm central frit, permeability barrier, allowing media to flow through without losing the tissue; G) 100 µm diameter pore within the permeability barrier; H) 15 mm x 15 mm outlet chamber; I) 1/32" Tygon silicon outlet tube.

A few drops of chloroform are pipetted onto the surface of each piece to dissolve the PmMA, taking care to not allow chloroform to enter the frit in the permeability barrier, when fusing it to the outlet section and to the chip chamber, as to not block the flow of media. The pieces are then pressed together for several seconds, to allow the chloroform to evaporate and the pieces to fuse together.

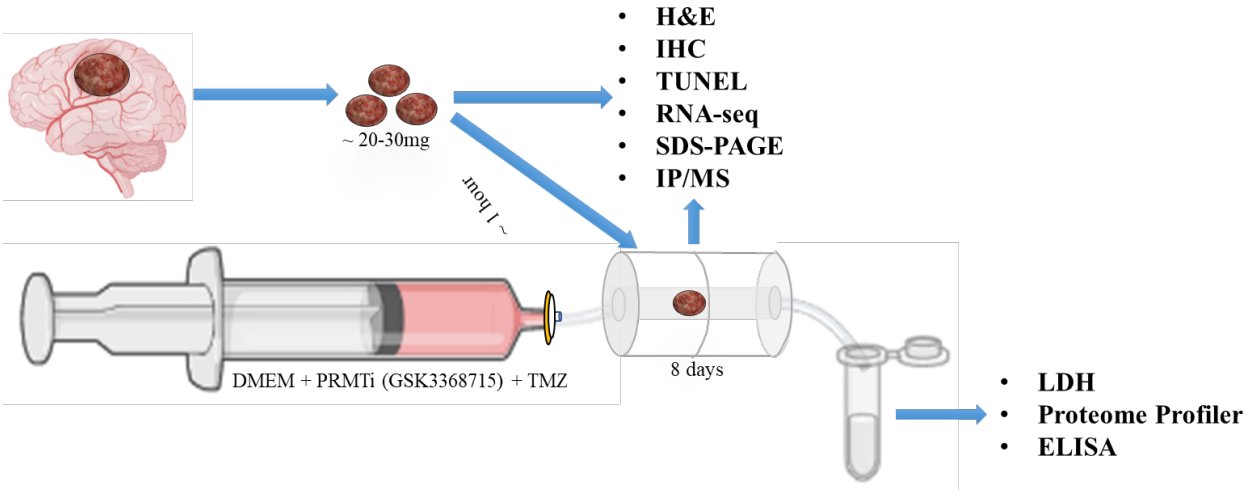

Figure 2.2: Novel perfusion device schematic and workflow.

Brain tumour samples are received from Hull Royal Infirmary and micro-dissected into 20-30mg sections. They are then inserted into a PmMA chamber, pre-filled with medium, which is fed by a filtered syringe at a rate of 3µl/minute through inlet and outlet tubes. Effluent is collected from the outlet tube every 24 hours. This can be used lactate dehydrogenase (LDH) assay, proteome profiler and enzyme-linked immunosorbent assays (ELISA). Pre-perfused and post-perfused tissue can then be fresh-frozen or formalin-fixed paraffin embedded for haematoxylin and eosin (H&E) staining, immunohistochemistry (IHC), terminal deoxynucleotidyl transferase biotin- 2′-Deoxyuridine, 5′-Triphosphate (dUTP) nick end labelling (TUNEL); snap frozen in liquid nitrogen for RNA-sequencing; or lysed in 1% Triton X-100 (+PBS) for sodium dodecyl sulphate – poly-acrylamide gel electrophoresis (SDS-PAGE)) and immunoprecipitation (IP) and/or mass spectrometry (MS) preparation.

2.6. Ethical Patient Participation

This project received ethical approval from the Integrated Research Application System (IRAS) Ethics Committee of the Faculty of Health Sciences at the University of Hull and the National Institute for Health and Care Research (NIHR), with the chief investigator being Professor John Greenman at the University of Hull and the NHS contact being Mr Shailendra Achawal (IRAS project code: 131630, Local Research Ethics Committee (LREC) ethics code: 13/YH/0238). Brain tumour tissue, which was not needed for histopathological analysis and suspected to be GBM, was donated between 2020 and 2023 from Hull Royal Infirmary (HRI), Hull University Teaching Hospitals NHS Trust. Informed, written consent was obtained from patients with suspected primary or recurrent GBM, by Mr Amr Moursi, Neurosurgery Registrar at HRI and M.D. student at the University of Hull. Brain tumours were diagnosed via neuroimaging and patients may or may not have undergone prior treatment with radiotherapy and TMZ. Patients were given 8 mg anti-inflammatory corticosteroid DEX twice per day for 48 hours, upon initial diagnosis, which was reduced to 2-4 mg, twice per day, until the day of surgery. Dose increased to 8 mg immediately post-surgery for 48 hours and again reduced to 2 mg. Pathology results were not known upon initial chip setup. In total 36 brain tumour samples have been collected since the start of this project.

2.7. Fluidics System Setup

In a class II biological hood, High glucose DMEM (Table 2.1) was treated with the appropriate drugs (Table 2.4), in 50 ml falcon tubes. Sterile, single-use syringes (BD Biosciences) were used to draw up >20 ml medium. The air bubble was then pushed out of the syringe, before it was connected to the 33 μm filter (Starlabs). The filter was then connected to the inlet tube and medium pushed all the way through the perfusion device, ensuring the absence of air pockets. These were then stored in an egg incubator at 37°C for up to 4 hours, until use. After micro-biopsies were added to the chambers, the syringes were then loaded onto a Harvard Apparatus PHD-ULTRA syringe pump, set to allow the medium to flow through the perfusion systems at a rate of 3 μl/min. The foot of the syringe depressor in slotted into the back of the apparatus, whilst the wings of the syringe are made flush with the front of the apparatus, to prevent the syringe sliding, rather than depressing. The bar across the top was also screwed down, to clamp the syringes in place. Ten devices were routinely set up in parallel to enable dynamic throughput. Calculated Reynold No. was 0.5×10^{-2} with shear stress calculated at $4.9 \times 10{-}5$

dyne per cm^2 (Equation 2.1 and Equation 2.2). The media flows over the tissue in the perfusion device chamber and exits via the outlet tube into a 15 ml falcon tube, which is collected every 24 hours and stored at 4°C short term and -80°C long-term. The entire microfluidics system sits within a custom-built Perspex temperature-controlled insulated box, set to 37°C and monitored with a digital thermometer (Figure 2.3), to mimic optimal *in vivo* temperatures. Alternatively, the chip chamber, along with the effluent tubes, may sit inside an egg incubator (Amazon, UK) set to 37°C and monitored with a spirit-filled thermometer, whilst the syringes may sit in the syringe pump outside of the incubator.

Table 2.4.: Treatments infused in DMEM

Treatment	**Type**	**Manufacturer**	**Catalogue No.**
Dimethyl sulfoxide	Control/vesicle	Sigma Aldrich	D8418
GSK3368715 dihydrochloride (25mg)	Type I PRMT Inhibitor	Cambridge Bioscience Ltd	HY-128717A
Furamidine dihydrochloride (25mg) /DB75	Type I PRMT Inhibitor	Tocris Bioscience	5202
GSK591 dihydrochloride (10mg)	Type II PRMT Inhibitor	Tocris Bioscience	5777
Temozolomide (TMZ)	Alkylating agent	Sigma-Aldrich	T2577

Equation 2.1.: Calculation of the velocity (u):

Relation between fluid velocity and the flow rate: $Q = A.u$

Q = flow rate (m^3s^{-1}) = 2 $\mu l min^{-1}$ = 3.33 10^{-11} m^3s^{-1}

A = Area (m^2) = $\pi (d/2)^2$ = 1.25 x 10^{-5} m^2

$Q = A.u \rightarrow u = Q / A$ = 2.6 x 10^{-6} ms^{-1}

Equation 2.2.: Calculation of Reynold number (Re):

$Re = \rho.u.d/\mu$ (non-dimensional, Freund *et al.*, (2012)) where:

ρ = Density of the medium (kgm^{-3}) = 1007 kgm^{-3} (Poon, 2022)

u = Velocity of the liquid in the channel (ms^{-1}) = 2.6 x 10^{-6} ms^{-1} (Equation 2.1)

d = Diameter of the microchannel of the chip (m) = 4 mm = 4 x 10^{-3} m

μ = Dynamic viscosity (Nsm^{-2}) = 9.4 x 10-4 Nsm^{-2} (Fröhlich *et al.*, 2013)

Re = 0.5 x 10^{-2}

Figure 2.3: Perfusion system setup.

Up to 10 syringes can be loaded onto the Harvard Apparatus Ultra PHD pump system. The back of the syringes slot into the pump and the hydraulic arms are adjusted so that the syringe wings sit against the front of the syringe rest. The syringes are clamped down to ensure they do not move, and the backs also pushed into place to ensure no sliding. Outlets are placed into collection tubes The entire pump is situated inside an insulated Perspex box, which is maintained at 37°C through a heated mat and monitored via digital thermometer. Access to the box is through a Perspex door covering two access point in the front of the box. Inset: Brain tumour tissue in the chamber section of the fluidic device.

2.8. Preparation of tissues

Chips had first been sterilised with 70% ethanol. Brain tumour tissue samples were transported in 10 ml DMEM (Table 2.1), in an insulated box. The box was always collected directly from

theatre by myself, or Amr Moursi and the journey from HRI to the lab took 25-45 minutes. Upon receipt, brain tissue biopsies were turned out onto a 20 mm petri dish (Corning) in an Air Stream Esco class II hood. Initial samples weighed between 35 mg to 3 g. Taking care to avoid areas of cauterised tissue, visible necrosis and blood vessels, tissue was manually micro-dissected, with the guidance of Amr Moursi, into 20-30 mg (± 10%) samples, using single use, sterile Swann–Morton curved blade no. 2 scalpels and forceps. Samples were generally spherical, around 3 mm in diameter (for an approximate volume of 14 mm^3). Micro-biopsies were then weighed using a microbalance and biopsies trimmed, using the scalpel, until they reached the standardised weight. 'Pre-perfused' tissue samples were immediately fresh-frozen, or formalin-fixed and paraffin-embedded.

The remaining samples were randomly allocated to the pre-filled PmMA chambers within an hour of receipt and within two hours of resection (Figure 2.2 and inset Figure 2.3). This was done by removing the inlet tube, whilst keeping the outlet tube pointing upwards, to prevent media leakage. The micro-biopsy was carefully inserted into the chamber using forceps and any air pockets replaced manually with medium, before the inlet tube was replaced, tightly, to ensure no leakage. The syringe-perfusion chambers were then inserted into the custom-made box (Figure 2.3). Over the next few hours, the chip system was monitored to ensure no leaks and connections tightened, should these appear. Tissue was maintained in the system for between 8 and 12 days, experiment dependent. After 4 days, the syringes and perfusion devices were removed from the system, in order to replace the medium in the syringes. These new syringes of treated medium were prepared at the time of the first syringes and stored at 4°C until use. The new syringes were brought up to 37°C in an incubator, prior to installation. In an Air Stream Esco class II hood, the inlet tube was again removed, with the outlet tube pointing upwards to prevent leakage. The old and empty syringe and filter were removed from the other end of the inlet tube and the new syringe and filter attached. The new media was flushed through the inlet tube to remove the old media and any air pockets in the chamber manually refilled, before reattaching the inlet tubing. This process took ~ 20 minutes and the replenished perfusion devices were immediately put back onto the Harvard Apparatus PHD-ULTRA syringe pump, in the heated box and the pump restarted for the remaining time. If tissues were being perfused for 12 days, there was a second syringe change at day 8. The media in the syringes were made fresh, prior to the syringe change, to ensure drug activity was maintained in the media.

At the end of the time in the perfusion system, the syringes are removed from the apparatus and, in an Air Stream Esco class II hood, the inlet tube removed and tissues extracted from the chamber using forceps, taking care not to damage the tissue. Processing of the tissue is dependent upon downstream analysis and is described in the following sections.

2.9. SDS-PAGE and Western Analysis

SDS-PAGE and western analysis was performed on both 2D U-87 MG cells and tissues.

2.9.1. Lysate preparation of 2D cells

U-87 MG cells were trypsinised, spun down and resuspended in medium. Cell count was measured using a haemocytometer and cells diluted accordingly, in order that they could be seeded at a density of $1x10^6$ in 6-well plates (Corning), with a maximum of 2 ml medium and allowed to adhere for twenty-four hours at 37 ºC, 5% CO_2. Cells were then treated with a combination of PRMT inhibitors (Table 2.4) for forty-eight hours, at 37 ºC, 5% CO_2. The media was then aspirated, and wells were washed twice with 1 ml warmed PBS, before harvesting into a 1.5 ml microcentrifuge tube, with 1% NP40 + 1% Triton X-100 in PBS plus protease inhibitor cocktail (Pierce Protease Inhibitor Tablets (ThermoFisher)) and a cell scraper. Tubes were incubated rotating at 4˚C for 1 hour, then at centrifuged at 16,200xg for 20 min at 4˚C. The supernatant was transferred to a pre-chilled 1.5ml microcentrifuge tube and stored at -20˚C, whilst the cell debris pellet was discarded.

2.9.2. Tissue lysate preparation

Protein lysates were produced from GBM biopsies both pre-perfusion and post perfusion, after extraction from the chamber. Tissues were homogenised manually in 200 µL 1% Triton X-100 in PBS plus protease inhibitor cocktail (Pierce Protease Inhibitor Tablets (ThermoFisher)) using a plastic Dounce homogeniser. Crude lysates were incubated on a rotating wheel for 1 hour at 4 °C and centrifuged at 13 000×g for 15 minutes at 4 °C. The aqueous layer was

siphoned off as the protein lysate, taking care not to disturb the nucleic acid and cell debris pellet. Tissue lysates were stored at -20 °C until use.

2.9.3. BCA Assays

BCA assays (Pierce), or Smith assays were performed on all cell harvests which would undergo SDS-PAGE and western analysis, to determine the quantity of protein to load. The BCA assay is a biochemical assay which determines protein concentration in a sample, compared to a standard curve of known protein concentrations (Table 2.5). Cupric ions (Cu^{2+}) are reduced to cuprous ions (Cu^{+}) by the sample protein peptide bonds, which then captured by two BCA molecules, forming a BCA-Cu^{+} complex (Figure 2.4) and producing a violet colour, which emits light at a wavelength of 562 nm and the intensity of which is directly proportional to protein concentration (Chen *et al.*, 2012).

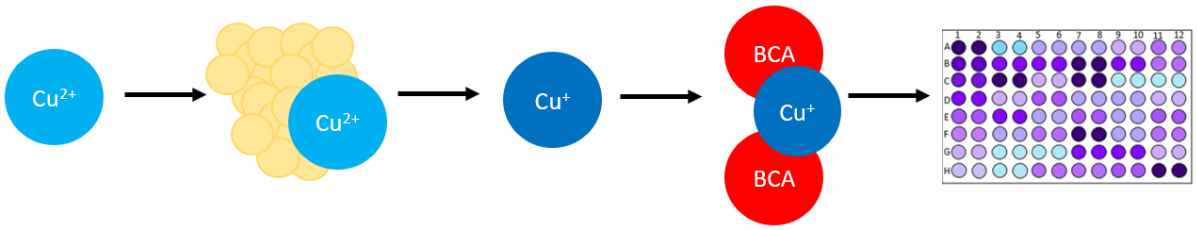

Figure 2.4: Chemistry of the BCA Assay.

Cu^{2+} ions are chelated by the sample protein and are reduced to Cu^{+} ions by the peptide bonds. Bicinchoninic acid (BCA) then interacts with the Cu^{+} ions, releasing light at 562 nm. The more reduced copper cations, the more intense the violet colour of the assay and the higher the protein concentration.

Table 2.5.: Standard concentrations of BSA for BCA assay

Standard	Volume of diluent (µl)	Volume and source of BSA (µl)	Final BSA concentration (µg/ml)
A	0	100, stock	2000
B	32.5	112.5, stock	1500
C	97.5	97.5, stock	1000

D	52.5	52.5, B	750
E	97.5	97.5, C	500
F	97.5	97.5, E	250
G	97.5	97.5, F	125
H	120	30, G	25
I	120	0	0

The diluent used to make up the bovine serum albumin (BSA) was the harvesting reagent, PBS + 1% Triton-X100.

The working reagents A and B are combined at a ratio of 50:1, according to manufacturer's instructions and 200 µl of this added to 25 µl sample to be tested, per well of a 96-well, flat-bottomed plate. The plate is incubated for 30 minutes at 37 ºC, 5% CO_2, before absorbance is measured using the BioTek™ ELx800™ absorbance microplate reader, at 595 nm. This is within the range of detection for BCA assay, which absorbs light at a maximum of 562 nm and allows for limitations of the equipment. Diluent-only control absorbance values are subtracted from the sample absorbance values and these are then normalised to the I standard which does not contain any protein. From this, protein concentration per µl of sample can be calculated.

2.9.4. SDS-PAGE

Samples were aliquoted into 10 µg fractions in microcentrifuge tubes according to BCA assay analysis and the appropriate volume of 4x Laemmli loading buffer (Table 2.6) added to each sample, according to the lowest concentration of protein lysate. Volumes were made up to the total using PBS. Samples were then boiled at 100 ºC, on a hot block, for 10 minutes, to denature the proteins, before loading onto a 12% polyacrylamide gel (Table 2.7Table 2.7), in electrophoresis running buffer (Table 2.6) alongside a pre-stained ladder of known recombinant protein sizes (Spectra Multicolour Broad Range Protein Ladder (ThermoFisher

Scientific, USA)) and subject to electrophoresis at 120 V for 90 minutes, using the Mini-PROTEAN Tetra Cell (Bio-Rad).

Table 2.6.: List of reagents and compositions required for SDS-PAGE and western blotting.

Reagent	**Reagent Ingredients (final concentrations)**
SDS-Sample buffer (4x Laemmli loading buffer)	320 nM Tris-hydrochloric acid (HCl), pH6.8, 8% SDS, 40% glycerol, 10% β-mercaptoethanol (β-ME), 0.04% bromophenol blue, ddH_2O
Running buffer	25 mM Tris, 190 mM glycine, 1.8 mM SDS, ddH_2O
Transfer buffer	20 mM Tris, 150 mM glycine, 3.5 mM SDS, 10% methanol, ddH_2O
TBS	150 mM sodium chloride (NaCl), 200 mM Tris-HCl pH7.6, ddH_2O
TTBS	150 mM NaCl, 200 mM Tris-HCl pH7.6, 0.1% Tween-20, ddH_2O

Table 2.7: Reagents required for two 12% 1.5 mm polyacrylamide gels for use in western blotting.

Reagent	**Running Gel (12%)**	**Stacking Gel (5%)**
Acrylamide (40%)	4.3 ml (12%)	500 µl (5%)
ddH2O	6.8 ml (16.5% v/v)	3.1 ml (32.7% v/v)
1.5 M Tris-HCl, pH 8.5	3.75 ml	/
0.5 M Tris-HCl, pH 6.8	/	1.25 ml
SDS (10%)	150 µl	50 µl
N, N, N', N'-Tetramethylethan-1,2diamine (TEMED)	23 µl (0.002% v/v)	10 µl (0.0012% v/v)
Ammonium persulphate (APS) (10%)	69 µl (0.1%)	30 µl (0.2%)

Total	**15.092 ml**	**4.94 ml**

After electrophoresis, the protein gel was removed from between the glass plates and placed onto Whatmann™ paper (GE Healthcare Life Sciences), soaked in transfer buffer (Table 2.6), with nitro-cellulose membrane (enhanced chemiluminescence (ECL) Hybond), also soaked in transfer buffer, placed on top. The bubbles were then smoothed out. This was sandwiched between another layer of soaked Whatmann™ paper and wire sponges, encased in a cassette. Transfer was performed in transfer buffer at 30 V, for 16 hours, before blocking in 5% milk (Marvel)/Tris-buffered saline (TBS) (w/v) solution for one hour at room temperature. Membranes were washed twice in TBS with 1% Tween-20 (TTBS) (Table 2.6) for 5 minutes, rocking, before incubation at 4 ^{o}C for 16 hours in 10 ml 1% milk (w/v) diluents containing 1:1000 antibody dilutions (Table 2.6). Membranes were washed twice in TTBS for 10 minutes, rocking at room temperature, before incubation with an appropriate horseradish peroxidase (HRP)-conjugated secondary antibody (Table 2.2) at a dilution of 1:2000.

Membranes were washed twice for 10 minutes in TTBS and once for 10 minutes in TBS. Clarity™ ECL Western substrate (Bio-Rad) was added to the membranes for 1 minute, before exposure using a ChemiDoc™ Imaging system (Bio-Rad). Densitometry analysis was performed in ImageJ (1997) and relative expression of target proteins determined through Equation 2.3. All values were then normalised to the negative control.

Equation 2.3.: Protein expression index:

$$\frac{\text{Peak Area (Intensity) of protein of interest}}{\text{Peak Area (Intensity) of loading control protein}}$$

2.9.5. Fresh-frozen tissue

Micro-biopsies were immediately acclimatised in Optimal Cutting Temperature compound (OCT) (TissueTek®), in tissue cryomoulds (TissueTek®) for 10 minutes. Cryomoulds containing the tissue were then submerged in in an aluminium can, which was one-quarter

filled with methylbutane (Honeywell) and had been pre-chilled in liquid nitrogen, for approximately 10 minutes, until a frost formed around the inside perimeter of the aluminium container. Taking care not to allow the methylbutane to cover the OCT-coated tissue, the cryomould was inserted into the chilled methylbutane until ~1 mm OCT remained unfrozen. These frozen blocks were then wrapped in aluminium foil and stored at -80°C. This ensured more even and quicker freezing than the formaldehyde fixing method, but also helped to prevent cell damage and artefacts caused by snap freezing directly in liquid nitrogen.

2.9.6. Formalin-fixed paraffin-embedded (FFPE) tissue

Alternatively, micro-biopsies were fixed for ~16 hours in 4% formaldehyde (ThermoFisher) and then stored in 70% ethanol, at 4°C. To prepare for paraffin embedding, tissues were dehydrated in increasing concentrations of ethanol (90% 30 minutes, 90% 15 minutes, 95% 30 minutes, 95% 15 minutes, 100% 30 minutes, 100% 15 minutes) before being incubated in Histoclear clearing agent (Histochoice®), twice, for 30 minutes. They were then submerged in liquid paraffin wax at 62°C for one hour and this step was repeated for 30 minutes before embedding. Embedding was performed using the Leica Biosystems embedding station, using paraffin wax, heated to ~62°C. Tissue was placed into the metal tray mould, wax poured into the tray and the embedding cassette placed on the top, ensuring no tissue floated through the cassette at it was pushed down to create the wax seal. Tissue cassettes were placed onto a cold plate set to -5°C to allow the wax to set, before being removed from the metal mould trays. FFPE tissues were stored at room temperature until sectioning.

2.10. Lactate Dehydrogenase Assay

Lactate dehydrogenase (LDH) is a cytosolic enzyme present in many different cell types and is a well-established and reliable indicator of cellular toxicity. Damage of the plasma membrane results in a release of LDH into the surrounding cell culture medium. This extracellular LDH can be quantified by a coupled enzymatic reaction in which LDH catalyses the conversion of lactate to pyruvate via NAD+ reduction to NADH. Diaphorase then uses NADH to reduce a tetrazolium salt (INT) to a red formazan product that can be measured at 490 nm (Figure 2.5). The level of formazan formation is directly proportional to the amount of LDH released into the medium (Vanderlinde, 1985).

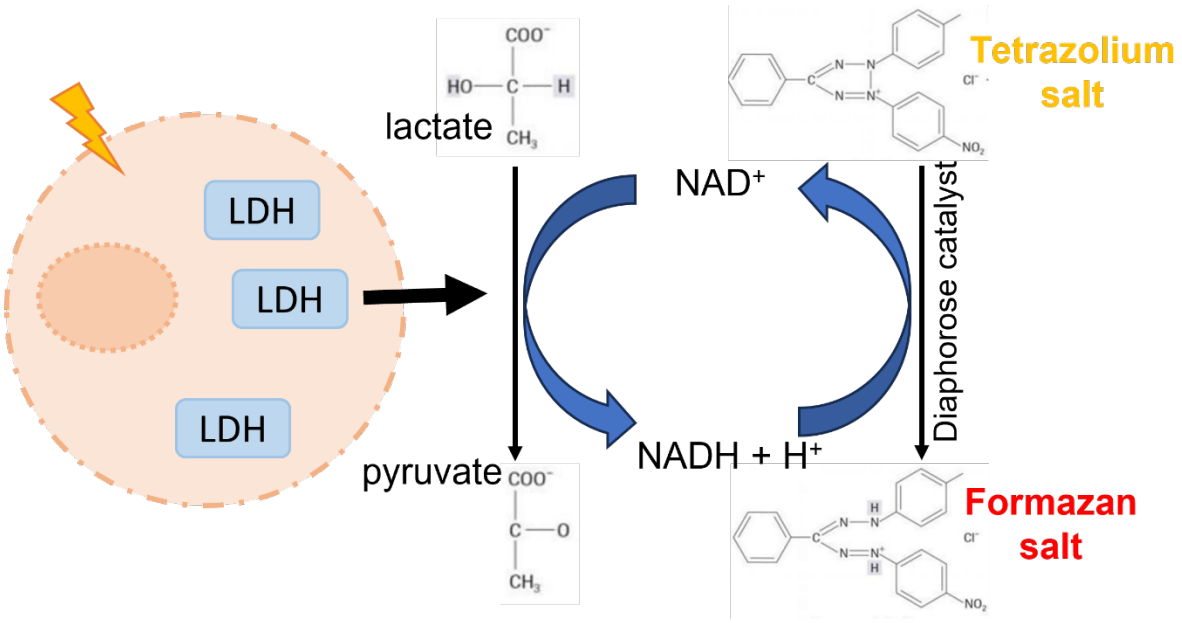

Figure 2.5.: Lactate dehydrogenase assay reaction schematic.

Cell stress causes disruption to the cell membrane, releasing LDH into the surrounding medium. LDH catalyses the conversion of lactate into pyruvate, through conversion of NAD^+ to NADH + H^+. In turn, this causes the catalysis of tetrazolium salt (yellow) into formazan salt (red) by diaphorase, in the catalyst-dye solution, through the loss of H^+ from NADH.

LDH assays were performed on the effluents collected for each 24-hour period and stored at 4 °C. Assays were performed on the last day of effluent collection, using the Cytotoxicity Detection KitPLUS (Roche), according to the manufacturer's instructions. Effluents (50 µl) were analysed in duplicate in a 96-well plate (Corning), with an equal volume of catalyst-dye solution (1:45). Two wells in each plate also contained medium-only, which had not been passed through the fluidics system. After 30 minutes at 37 °C in the absence of light, 1 M HCl (25 µl) was added to stop the reaction. Absorbance was recorded at 495 nm, correcting at 690 nm, using the BioTek™ ELx800™ absorbance microplate reader with Gen5 software 1.08. The medium-only absorbance was subtracted from effluent sample absorbance and the average absorbance for each sample was calculated and normalised per mg of starting tissue weight.

2.11. Immunohistochemistry

2.11.1. Slide Preparation

Twin frost 76mm x 26mm x 1mm microscope slides (VWR) for use in IHC were coated with poly-L-lysine (Sigma). These slides were first soaked in 1 M HCl with 1:100 70% ethanol and incubated in a drying oven, at 30 ºC for ~16 hours. This was to remove any residue on the slides and increase porosity of the glass slides. Slides were then cleaned with 70% ethanol before soaking for 5 minutes in poly-L-lysine, diluted 1:10 with ddH_2O. The slides were allowed to dry for several hours before use. The poly-L-lysine coats the slides with a positively charged residue, which increases the electrostatic interaction with the cell surface membranes of the tissue, thereby promoting tissue adhesion to the glass slide.

2.11.2. Sample preparation and sectioning

Pre- and post-perfusion tissue samples were extracted from the perfusion device chamber using forceps, taking care not to perforate, or tear the tissue.

2.11.2.1. *Fresh frozen micro-biopsies*

Samples between D1 and D28 were fresh frozen. Samples frozen in OCT were sliced to a thickness of 8 µm using a cryostat (Leica Microsystems, Germany) and displayed on the poly-L-Lysine coated microscope slides. They were then stored at -20°C until use. Samples required fixing prior to staining and this was performed in 100% methanol, for 10 minutes, which had been pre-chilled at -20 ºC.

2.11.2.2. *FFPE micro-biopsies*

Samples from D29 onwards were formalin-fixed and paraffin embedded. FFPE samples were sliced to a thickness of 5 µm using the microtome (Leica Biosystems, Germany). Samples were sliced into ribbons using the automatic setting and placed into a water bath at 50°C. Wax-embedded tissue ribbons were then scooped onto poly-L-lysine coated slides, placed in the water. The wax was left to melt onto the slides, on a hot plate at >62°C for 5 minutes and then

racked to allow water to run off the slides and dried overnight at room temperature. Slides were stored at room temperature until use.

FFPE samples were first heated above 62 °C on a hot block and then were incubated in Histoclear (Histochoice®), twice for 30 minutes. Tissues were then rehydrated in decreasing concentrations of ethanol (100%, 90%, 70%, 40%) for 5 minutes each and then in diH_2O for 5 minutes. Slides were racked and covered with citric acid antigen retrieval buffer (2BScientific), diluted 1:100 with diH_2O. The buffer-coated slides were heated on high power in an 800 W microwave until the buffer just started to boil. The microwave power was then reduced to low to maintain buffer temperatures of just below boiling to ensure optimal antigen retrieval, whilst reducing the risk of lifting tissue from the slides due to the boiling action. Hot buffer was then replaced with cold diH_2O under a steady stream before the IHC process could begin.

2.11.3. Antibody incubation and staining

All sample slides were incubated for 15 minutes, in 3% hydrogen peroxide (H_2O_2) in 100% methanol to block endogenous peroxidase activity. Slides were then placed in TBS, before loading onto sequenza racks. Slides were washed 3 times with TBS, by filling up the reservoir at the top of the holder using a 20 ml syringe. The Vectastain Elite kit (Vector Laboratories) protocol was then followed to complete the IHC. Slides were incubated with 100 µl normal horse serum (1 drop (50 µl) normal horse serum in 5 ml TBS), for 15 minutes, to block non-specific binding. 3 drops of Avidin solution, followed by 3 drops of Biotin solution were then added to each slide, for 20 minutes each and separated by 3 TBS washes, to further block non-specific binding. Slides were then incubated with primary antibody, diluted in accordance with the manufacturer's instructions with TBS, for ~16 h, 4 ºC.

Slides were washed 3 times with TBS and then incubated with secondary antibody (2 drops biotinylated secondary antibody and 2 drops normal horse serum in 5 ml TBS, with all 5 ml distributed equally between slides) for 30 minutes. After 3 more washes in TBS, the slides were racked in ddH_2O and one tablet each of 3,3-Diaminobenzidine (DAB) and H_2O_2 dissolved in ddH_2O. Slides were dried carefully, avoiding the samples and the DAB solution applied to each sample for 5 minutes, before rinsing with ddH_2O. Samples were then counterstained for 15

seconds with Harris haematoxylin and again rinsed with ddH_2O. Samples were then dehydrated in increasing grades of ethanol (70%, 90%, 100%) for 1 minute each, before being sequentially submerged in Histoclear I and II, each for 1 minute. Slides were allowed to dry completely before mounting glass coverslips (VWR) using Histomount (National Diagnostics) and drying overnight, at room temperature.

Table 2.8: Primary antibodies used in IHC

Antibody against	**Species raised**	**Species Against**	**Manufacturer**	**Catalogue no.**
Cleaved-PARP (Asp214) (D6E10)	Rabbit	Human	Cell Signalling	5625S
Annexin V	Mouse	Human, Zebrafish	Nordic MUbio	MUB0106P
Annexin V	Rabbit	Human, Mouse, Rat	Thermofisher	PA5-78784

2.12. TUNEL ASSAYS

Terminal deoxynucleotidyl transferase 2′-Deoxyuridine, 5′-Triphosphate **(**dUTP) nick end labelling (TUNEL) assays are a method for distinguishing cells that have undergone apoptosis through detecting excessive DNA fragmentation. The terminal deoxynucleotidyl (TdT) enzyme preferentially attaches fluorochrome fluorescein to 3'-hydroxyl termini of DNA double strand breaks caused by apoptosis and not from necrosis, cytostatic drugs or irradiation (Ferreira and Afreen, 2017) and visualisation using a fluorescence microscope allows quantification of apoptosis in individual cells. TUNEL assays were performed on GBM tissue using the *in-situ* cell death detection kit, Fluorescein (Merck) according to the manufacturer's instructions.

2.12.1. in situ CELL DEATH DETECTION

Samples from SD0032 onwards required fixing prior to TUNEL assay which was performed in fixing solution (4% paraformaldehyde (PFA), PBS, pH 7.4) for 20 minutes, at room temperature. If storing at this stage, slides were dehydrated in ethanol (70%, 90%, 100%) and stored at -20ºC. Cells were then permeabilised using permeabilization solution (0.1% Triton-X100, 0.1% sodium citrate) for 2 minutes, on ice and then the slides flooded twice with PBS for 5 minutes, to wash. The positive control was incubated for 10 minutes, at room temperature, with DNaseI recombinant enzyme (30 U/ml, 50 mM Tris-HCl pH 7.5, 1 mg/ml BSA) to induce DNA damage, prior to labelling. The positive control was then washed twice with PBS, for 5 minutes. Two negative controls were incubated with 50ul label solution each and the remaining label solution (450ul) added to the TdT enzyme (50ul) and aliquoted between each of the other slides (~50ul), including the positive control. Slides were then incubated for 1 hour, at 37ºC, in a humidified, dark box. Slides were washed three times with PBS, for 5 minutes before drying around the samples and mounting coverslips with Vectashield 4′,6-diamidino-2-phenylindole (DAPI). The samples were stored at 4 ºC.

2.12.1.1. *Fluorescence Microscopy*

TUNEL assay slides were visualised within 24 hours using the Zeiss confocal microscope, at x10 and x40 magnification with DAPI and green fluorescent protein (GFP) light filters, using the Zen software.

2.12.1.2. *Quantification of TUNEL using CellProfiler*

TUNEL samples were quantified using the CellProfiler program, using the pipeline displayed in Figure 2.6. A percentage of cells undergoing apoptosis in each image was calculated by dividing the number of green, fluorescent cells by the total number of green and blue fluorescent cells and multiplying by 100. The average percentage of cells undergoing apoptosis for each sample was then calculated.

Figure 2.6: Cell Profiler Pipeline for TUNEL assay cell counting.

Overall pipeline - Settings are altered and run through in 'Test Mode' to determine the most ideal conditions for image processing the full pipeline for image processing is split into 12 modules. The eye icon, when 'switched on' will show the results of each step of the pipeline; B) NamesAndTypes; C) ColorToGray - converts all objects with highest green pixel density to grey; D) ColorToGray – converts all objects with high blue pixel density to grey; E) IdentifyPrimaryObjects – identifies DAPI-stained objects (blue channel); F) IdentifyPrimaryObjects – identifies enzyme labelled objects (green channel); G)RelateObjects – identifies colocalization of blue and green stains; H) FilterObjects – changes blue/green relationship into binary e.g. if there is blue=1, if there is no blue=0; I) MeasureObjectIntenstiy – measures green stain intensity within each nuclei object; J) OverlayOutlines – outlines objects of interest in corresponding colours; K) DisplayDataOnImage – intensity threshold for green stain; L) ClassifyObjects; M) CalclateMath – calculates percentage positive green and apoptotic cells overlapping (coexpressed with) DAPI-stained live cells and N) ExportToSpreadsheet.

2.12.2. Microscopy

Images were taken of the DAB-stained IHC slides at x40 magnification using the Olympus IX71 inverted fluorescence microscope, on the brightfield setting, phase 2 and using CellSens software 1.18.

2.12.3. Quantification of cleaved PARP IHC using CellProfiler

Images were then fed into a Cell Profiler 4.1.3. pipeline (Figures 2.7 to 2.13), which was designed and developed by myself to distinguish DAB-stained positive cells from haematoxylin counter-stained negative cells and to provide the cell count output. The average positive cell index per treatment was calculated using:

Equation 2.4: Calculation of cleaved PARP expression index

$$\frac{\text{DAB} - \text{stained cells (positive)}}{\text{Haematoxylin} - \text{stained cells (negative)} \; + \; \text{DAB} - \text{stained cells}}$$

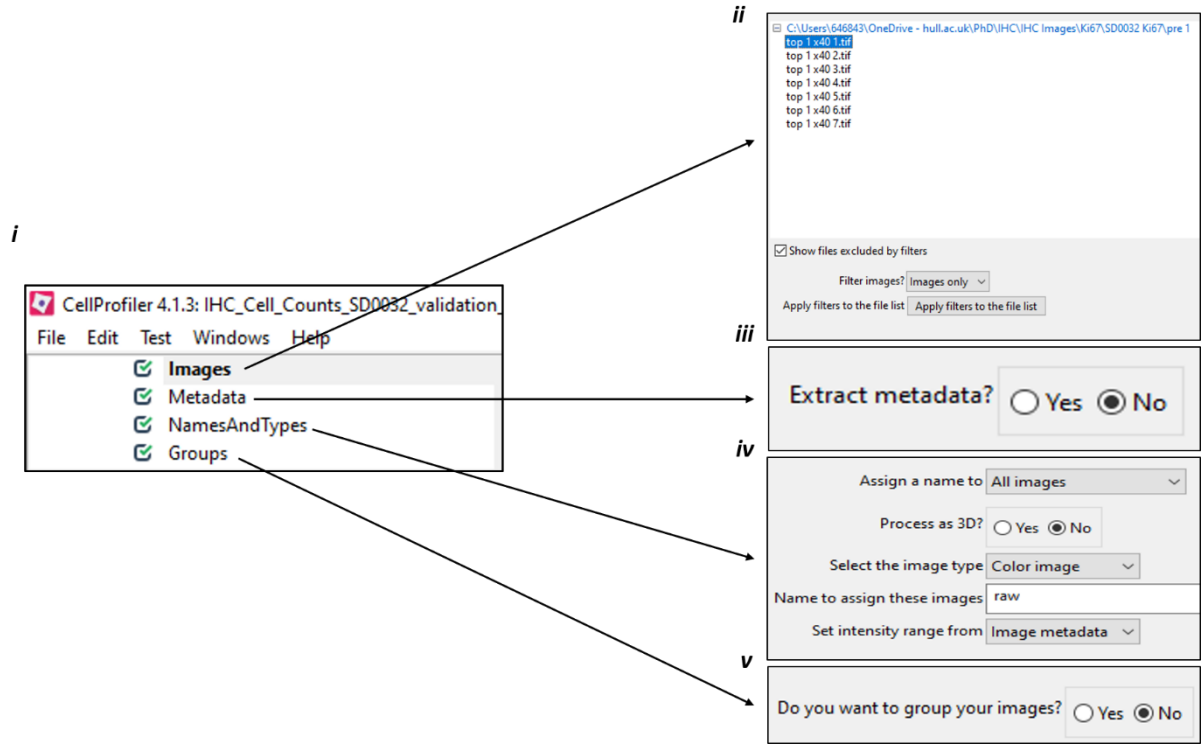

Figure 2.7: CellProfiler Data Input

(i) *Initial setup menu.* ***ii)*** *A list of images was compiled into the 'Images' tab.* ***iii)*** *Image metadata was not required and 'No' was selected in the 'Metadata' tab.* ***iv)*** *Images were*

labelled 'raw' to distinguish the original image from the processed image, in the 'NamesandTypes' tab. ***v)*** *Images were not grouped in the 'Groups' tab as different groups of images, such as from different slides, or samples, were processed separately.*

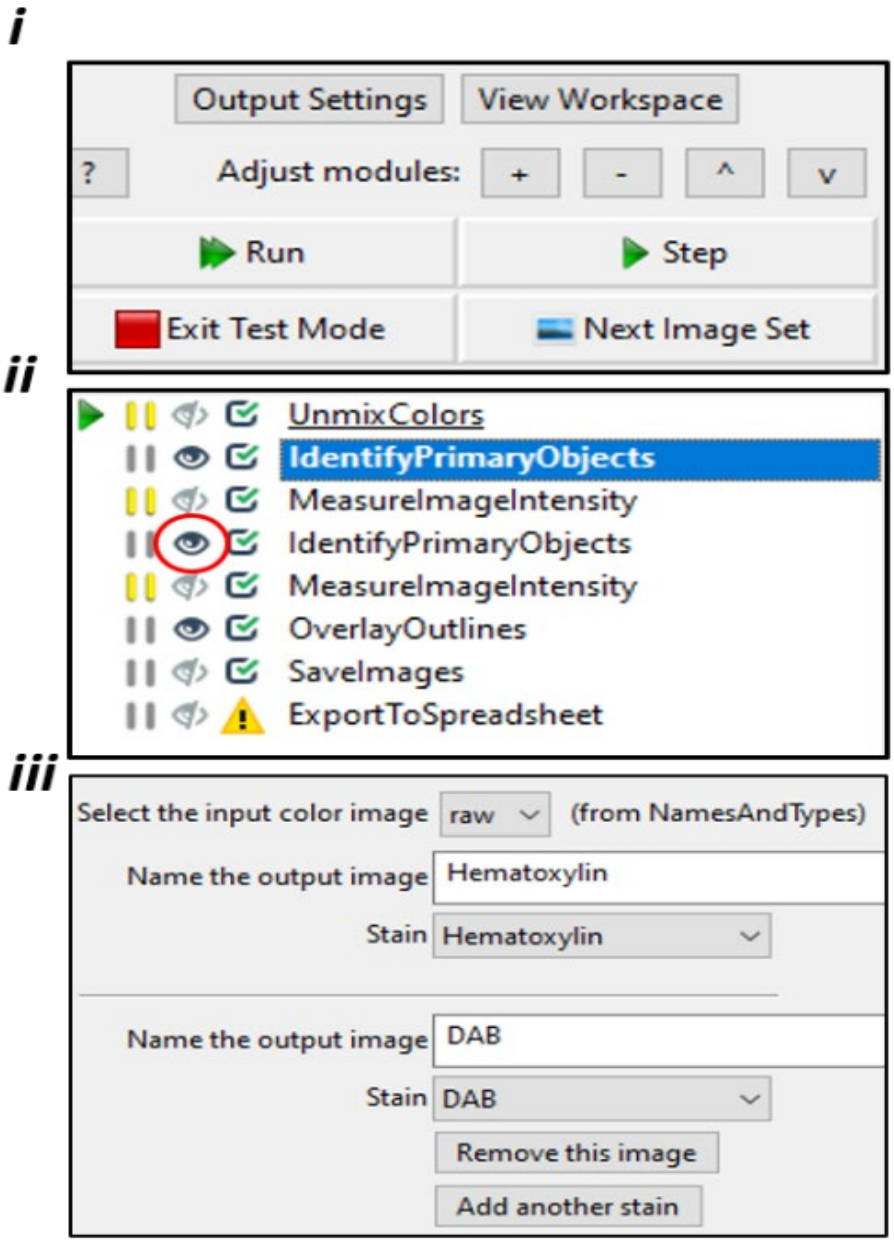

Figure 2.8: CellProfiler Pipeline Schematic **– UnmixColors module.**

i) Settings are altered and run through in 'Test Mode' to determine the most ideal conditions for image processing. ii) The full pipeline for image processing is split into 8 modules. The eye icon (shown in the red circle), when 'switched on' will show the results of each step of the pipeline. Modules can be run through stepwise in 'Test Mode'. The following images depict

the settings for each modules of the pipeline. iii) UnmixColors – transforms images into greyscales, to distinguish colours in cells due to pixel intensity.

i

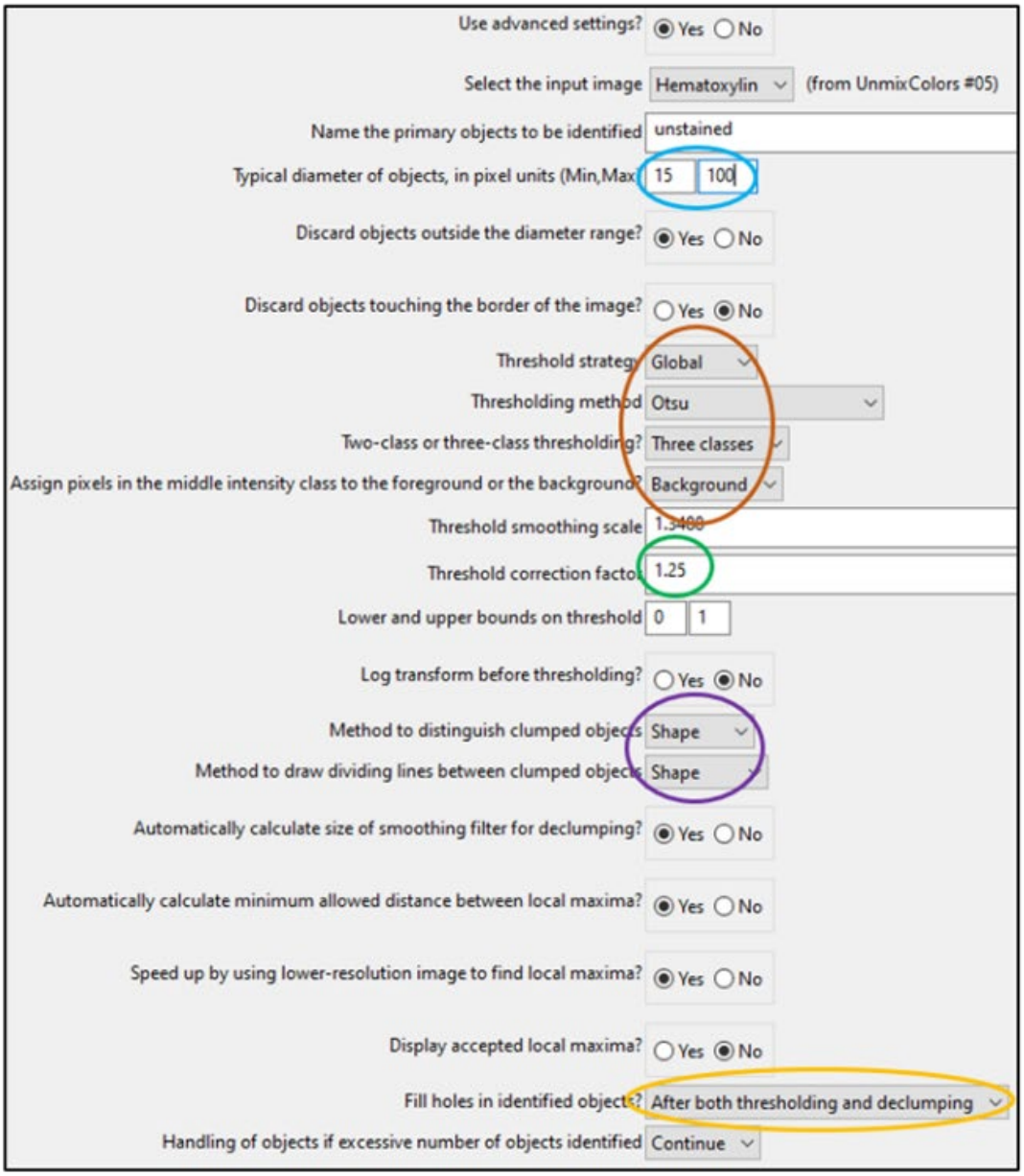
Use advanced settings? Yes No
Select the input image Hematoxylin (from UnmixColors #05)
Name the primary objects to be identified unstained
Typical diameter of objects, in pixel units (Min,Max) 15 100
Discard objects outside the diameter range? Yes No
Discard objects touching the border of the image? Yes No
Threshold strategy Global
Thresholding method Otsu
Two-class or three-class thresholding? Three classes
Assign pixels in the middle intensity class to the foreground or the background? Background
Threshold smoothing scale 1.3488
Threshold correction factor 1.25
Lower and upper bounds on threshold 0 1
Log transform before thresholding? Yes No
Method to distinguish clumped objects Shape
Method to draw dividing lines between clumped objects Shape
Automatically calculate size of smoothing filter for declumping? Yes No
Automatically calculate minimum allowed distance between local maxima? Yes No
Speed up by using lower-resolution image to find local maxima? Yes No
Display accepted local maxima? Yes No
Fill holes in identified objects? After both thresholding and declumping
Handling of objects if excessive number of objects identified Continue

ii

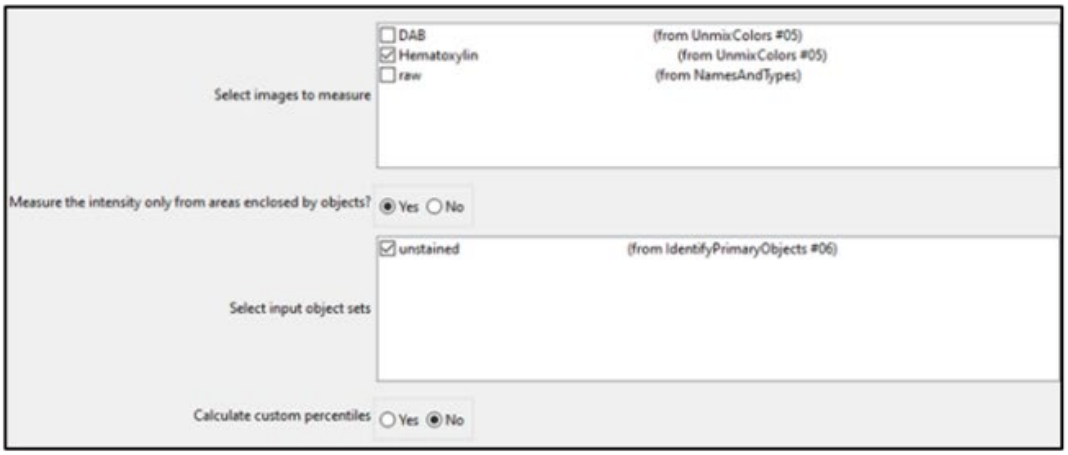
Select images to measure
DAB (from UnmixColors #05)
Hematoxylin (from UnmixColors #05)
raw (from NamesAndTypes)
Measure the intensity only from areas enclosed by objects? Yes No
Select input object sets
unstained (from IdentifyPrimaryObjects #06)
Calculate custom percentiles Yes No

Figure 2.9.: CellProfiler Pipeline Schematic – i) IdentifyPrimaryObjects and ii) MeasureImageIntensity modules

Identifies the haematoxylin counter-stained cells in the image. Cell diameter was always set between 15 uM and 100 uM (blue circle) and any cells that lay outside of this range were discarded, but those touching the border of the image were retained in the final count. Objects (cells) were distinguished from the background using the Global Otsu method (orange circle). This splits pixel intensity into 3 categories (low, medium and high), with low and mid-intensity pixels being classed as background and not cells. High intensity pixels were determined to be the nucleus of cells. High intensity pixels were distinguished from neighbouring pixels using shape (purple circle), which decides that only smooth, more rounded objects can be cells. The threshold correction factor (green circle) changed for each batch of images to account for differences in the intensity of the staining between slides, tissue quality etc. Local maxima were determined automatically as the centre of a cell, which would have the highest pixel density. Gaps between the cells were finally filled after these thresholding and declumping steps (yellow circle) for the best results in haematoxylin-stained cells. This module was supported by MeasureImageIntensity (ii).

i

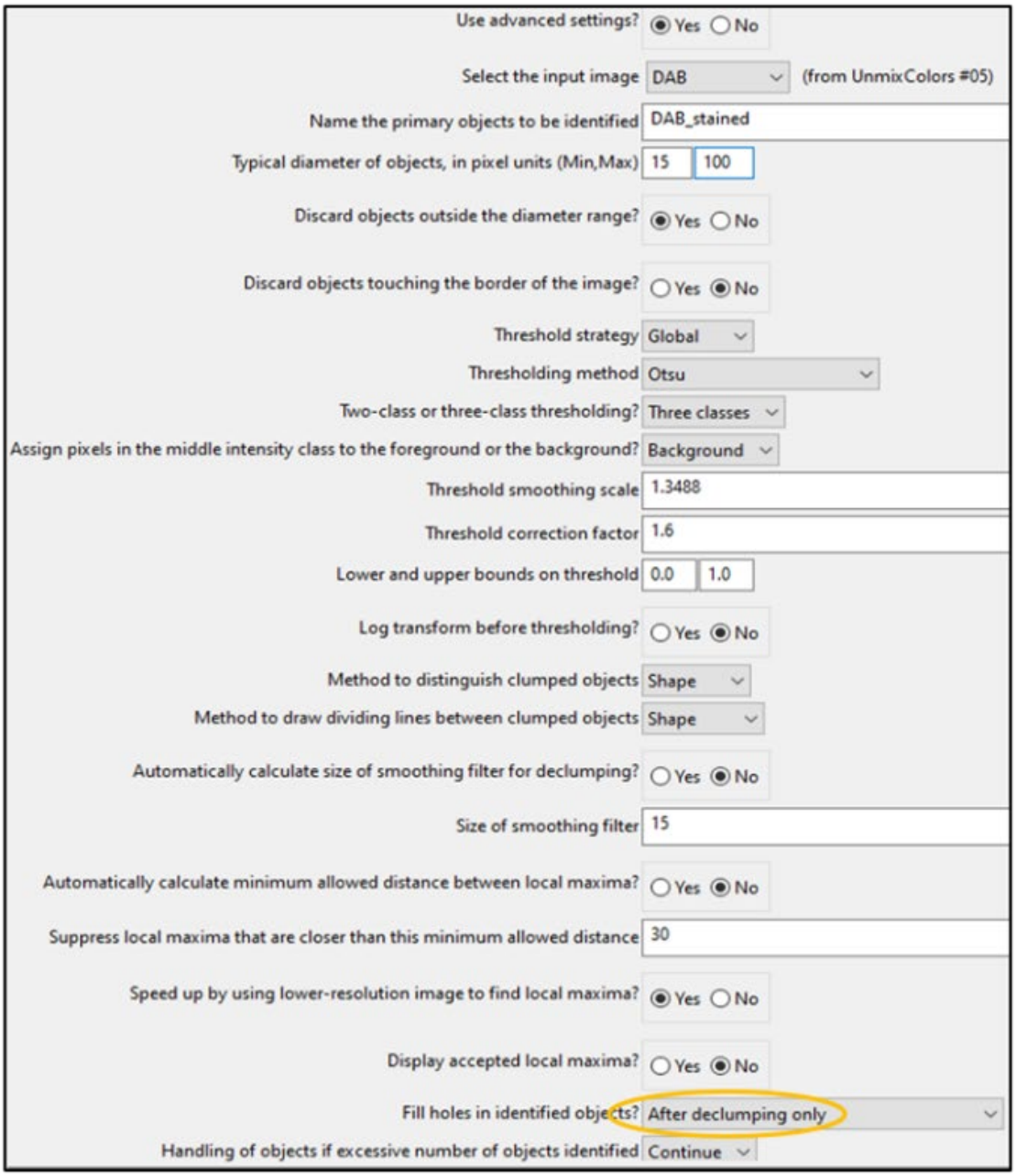
Use advanced settings? Yes No
Select the input image DAB (from UnmixColors #05)
Name the primary objects to be identified DAB_stained
Typical diameter of objects, in pixel units (Min,Max) 15 100
Discard objects outside the diameter range? Yes No
Discard objects touching the border of the image? Yes No
Threshold strategy Global
Thresholding method Otsu
Two-class or three-class thresholding? Three classes
Assign pixels in the middle intensity class to the foreground or the background? Background
Threshold smoothing scale 1.3488
Threshold correction factor 1.6
Lower and upper bounds on threshold 0.0 1.0
Log transform before thresholding? Yes No
Method to distinguish clumped objects Shape
Method to draw dividing lines between clumped objects Shape
Automatically calculate size of smoothing filter for declumping? Yes No
Size of smoothing filter 15
Automatically calculate minimum allowed distance between local maxima? Yes No
Suppress local maxima that are closer than this minimum allowed distance 30
Speed up by using lower-resolution image to find local maxima? Yes No
Display accepted local maxima? Yes No
Fill holes in identified objects? After declumping only
Handling of objects if excessive number of objects identified Continue

ii

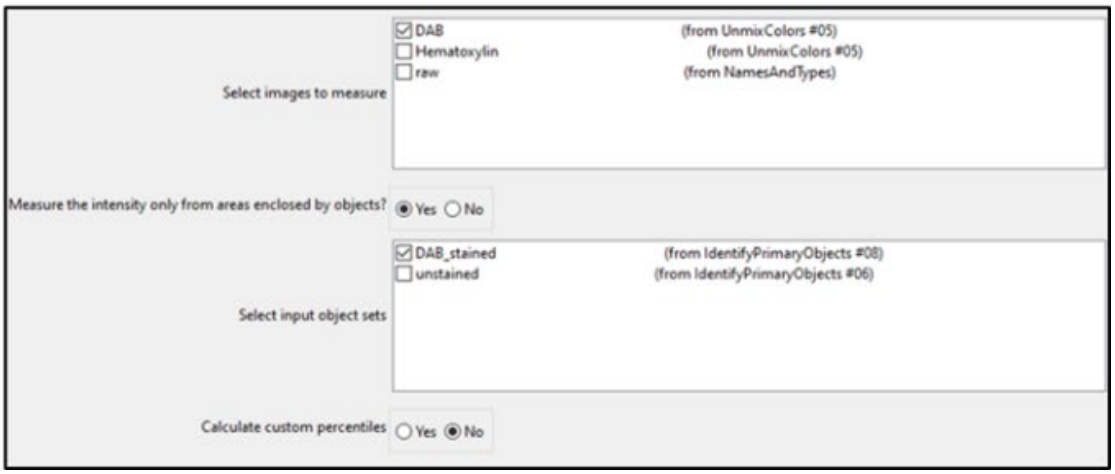
Select images to measure
DAB (from UnmixColors #05)
Hematoxylin (from UnmixColors #05)
raw (from NamesAndTypes)
Measure the intensity only from areas enclosed by objects? Yes No
Select input object sets
DAB_stained (from IdentifyPrimaryObjects #08)
unstained (from IdentifyPrimaryObjects #06)
Calculate custom percentiles Yes No

Figure 2.10.: CellProfiler Pipeline Schematic –i) IdentifyPrimaryObjects and ii) MeasureImageIntensity modules

The same parameters were used to distinguish the DAB-stained cells. Threshold correction factor was changed and the gaps between objects were filled after declumping only. This module was supported by another MeasureImageIntensity module (ii).

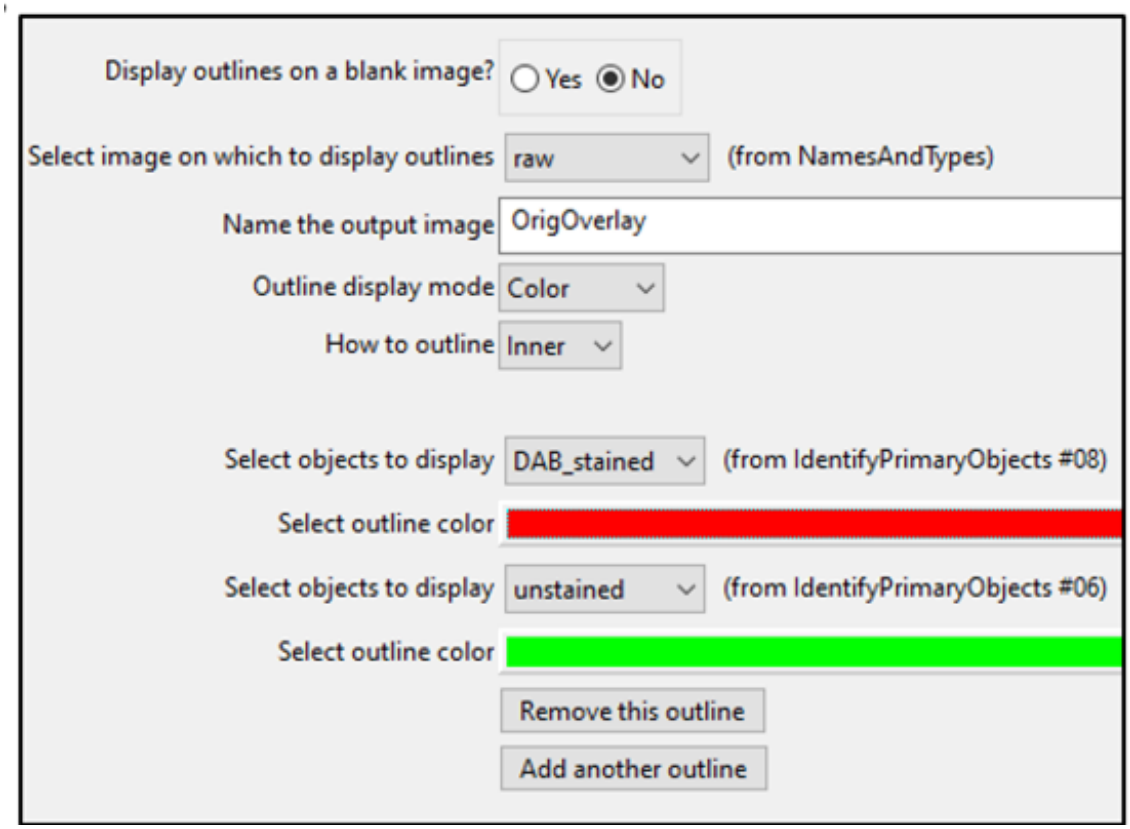

Figure 2.11.: CellProfiler Pipeline Schematic – OverlayOutlines module

The software outlines the DAB-stained cells in red and the haematoxylin-stained cells in green for easier distinction.

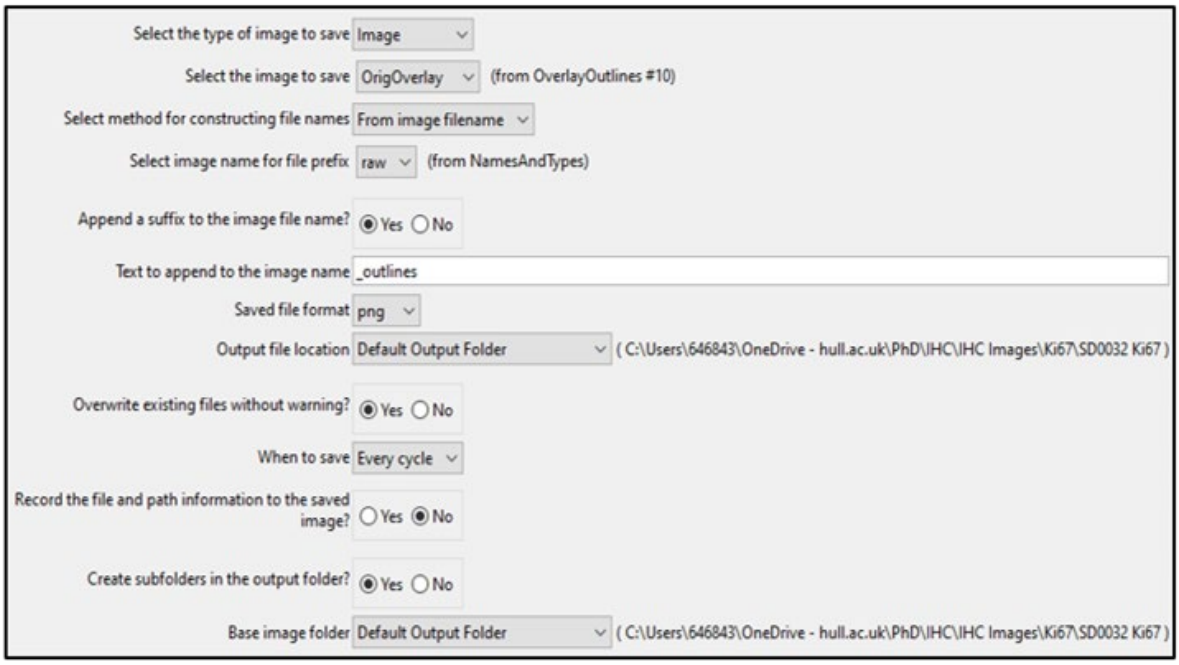

Figure 2.12.: CellProfiler Pipeline Schematic –SaveImages module

Images are then saved to a designated location, outlines in Output Settings ***(i)*** *and the outlines images given a name.*

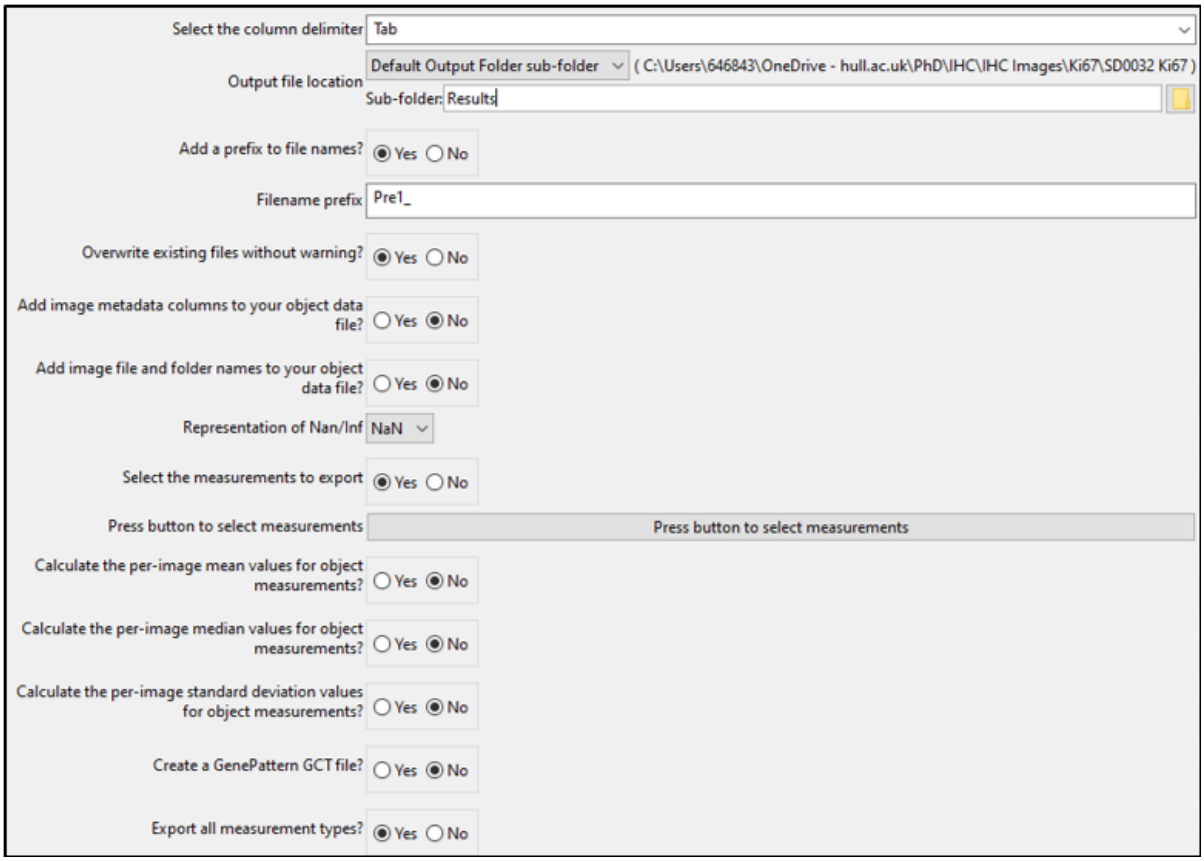

Figure 2.13.: CellProfiler Pipeline Schematic –ExportToSpreadsheet module

T*he final count data (DAB-stained vs haematoxylin-stained, is then put into an Excel document.*

The use of this automated cell counting pipeline was validated using the D37 sample (Appendix 1), which had been blotted with 1:200 Ki67 antibody (mouse, M7240, Dako). It was determined that the threshold value for each set of images should be altered for each tissue slice, to obtain the most accurate index value for the automated counts.

2.12.4. Quantification of Annexin V IHC using CellProfiler

Annexin V is presented on the outside membranes of apoptotic cells and therefore a different approach was required when identifying positive staining through CellProfiler, however, using the same modules (Figure 2.7 to Figure 2.13). Initially, the image was processed in the same way, through the UnmixColors module to change the image to greyscale and the IdentifyPrimaryObjects module, to identify haematoxylin-stained nuclei. IdentifySecondaryObjects was utilised to identify the whole section of tissue in the field of

view and this was quality-controlled against the identification of nuclei and from the raw image. The second IdentifyPrimaryObjects module highlighted the DAB-stained sections of tissue from the tissue sections. Due to the extensive nature of the staining and the lack of cytoplasmic marker, the threshold was altered to detect the most intense staining. The MeasureImageOccupied module then measured the number of pixels occupied by the entire tissue section and the DAB-stained sections. The remaining three modules were the same as for cleaved PARP measurement. Annexin V index was calculated using the equation:

Equation 2.5: Calculation of Annexin V expression index

$$\frac{Area\ occupied\ by\ DAB\ stained\ tissue}{Total\ area\ occupied\ by\ tissue}$$

2.13. Haematoxylin and Eosin Staining

Haematoxylin and eosin (H&E) staining was performed for pre- and post-chip slides to determine whether regions of necrosis were dependent upon whether the samples had undergone microfluidic perfusion for 8 days, or if the regions of necrosis were routine present in GBM samples, before they went onto the perfusion device.

Tissues were sliced and mounted onto poly-L-lysine coated slides and stored, as described previously. Slides were allowed to defrost to room temperature for 10 minutes, prior to H&E staining. Tissues were fixed with 4% PFA for 10 minutes at room temperature and endogenous peroxidase blocked with 3% H_2O_2 with 100% methanol for 20 minutes. Slides were dipped in a Coplin jar of haematoxylin for 3 minutes and then rinsed for 6 minutes under running tap water. Tissues were partially dehydrated in 20%, 40%, 70% and 90% ethanol for one minute each, before dipping in a Coplin jar of eosin for 1 minute. Tissue was then fully dehydrated in 90% ethanol for 30 seconds and 100% ethanol for 1 minute before dipping in Histoclear for 3 minutes, drying and mounting coverslips with Histochoice® mounting solution. Microscope images were taken using the Olympus microscope and images sent to Dr Ian Scott, a Consultant Neuropathologist at The Walton Centre NHS Foundation Trust, Liverpool, for analysis.

2.14. Immunoprecipitation of FUS

2.14.1. 2D cell lines

U87-MG cells were seeded at a density of $5x10^6$ in 150mm plates (Corning) and allowed to adhere and grow for seventy-two hours. They were then washed twice with 5 ml PBS and harvested with 5 ml 1% Triton-X100 (sigma) in PBS (Fisher Bioreagents) with complete, EDTA-free protease inhibitors (Roche), using a cell scraper. Cell lysates were incubated on a spinning wheel, at 4ºC, for 1 hour. Samples were pelleted at ~17,000xg, 4ºC for 5 minutes and the supernatant transferred to clean microcentrifuge tubes. The remaining pellet was stored at -80ºC.

A sample of the lysate was stored at -20ºC, as the input sample, which should contain an abundance of the protein of interest. The anti-FUS antibody, raised in mice, was added to the remaining lysate, including a lysis buffer only control, at 1:1000 and incubated on a spinning wheel, at 4ºC, for 3 hours. Protein A beads were aliquoted into microcentrifuge tubes, on a magnetic rack, at 40 µl per 500 µl lysate and ethanol aspirated, leaving 20 µl protein A beads. The beads were washed 3 times with lysis solution before adding the lysate-antibody mix. This was then put back on the spinning wheel, overnight, at 4ºC.

The lysates and beads were put back onto the magnetic rack and the supernatant aspirated into a clean microcentrifuge tube as the flow through, which should not contain the protein of interest. The protein of interest is then eluted from the beads using 50 µl 5x Laemmli loading buffer, at room temperature for 10 minutes – agitating the beads with a pipette every 2 minutes. The samples are put back on the magnetic rack and the loading buffer, containing the protein of interest, is aspirated into a clean microcentrifuge tube and the beads discarded.

The appropriate volume of loading buffer is then added to the input and flow through samples, including the lysis buffer-only controls and boiled for 10 minutes at 100ºC before SDS-PAGE and western analysis. Membranes are blotted with an anti-FUS antibody, raised in rabbits

(Table 2.2) to prevent any crosstalk using an antibody raised in the same species and the appropriate secondary antibody.

2.14.2. Tissue

2.14.2.1. *Lysate preparation*

Tissues were removed from storage at -80°C, placed on ice and washed with chilled 1x PBS (Sigma*)* to remove residual media. Two biopsies from each treatment condition, from 3 patients, were pooled together to form two homogenous lysates: one control and one treated with 1uM GSK3368715. Biopsies were put into a pre-chilled mortar with enough liquid nitrogen to cover them and them macerated with a pestle until they resembled a fine powder. Tissues were lysed using the Ultra Turrax T25 homogeniser for 30 seconds in 500ul of 1X PBS, with 1% Triton-X100 and 1mM cOmplete EDTA-free protease inhibitor (Roche). The homogeniser tip was rinsed with a further 500ul lysis buffer, into the tube, which was incubated on ice for two minutes before another 30 seconds of homogenisation. They were then incubated on ice for 30 minutes, vortexing occasionally. The sample tubes were centrifuged at 10,000xg for 20 minutes, at 4°C to pellet cell debris. Supernatant was transferred to a clean microcentrifuge tube and protein concentration determined by BCA assay. Samples were stored at -80°C until use.

2.14.2.2. *Immunoprecipitation*

Lysates were pre-cleared by adding 50ul protein A bead (Merck) slurry per 0.5mg total protein to the lysates and incubated on a rotary mixer for 30 minutes, at 4°C. Beads were then separated from the lysate via centrifugation at 1000rpm for 3 minutes at 4°C and the supernatant transferred to another tube. Primary anti-FUS antibody (mouse IgG_1) (Cell Signalling) concentration was titrated between the recommended 0.5 and 4ug per 500ul lysate. A negative control was set up using an IgG with some of the remaining pre-cleared cell lysate. This was then incubated overnight, at 4°C on a rotary wheel, before addition of the protein A beads used for clearing and a further 4 hours of incubation at 4°C on a rotary wheel. The IP mixture was centrifuged at 1000rpm for 30 seconds, at 4°C to precipitate the beads and the supernatant

transferred to another tube. The beads were washed 4 times with 1x 0.2% TBST (Table 2.6) with 1x cOmplete EDTA-free protease inhibitor (Roche) and then centrifuged at 1000rpm for 30 seconds and the supernatant discarded. Bound protein was eluted from the beads using 50ul 4x SDS sample buffer and heated for 5 minutes at 95°C, then centrifuged at 10,000 xg for 3 minutes. Western blotting was performed on 10% of the total volume of the eluent, using PVDF membrane, to check validity of IP.

2.14.2.3. *Gel Electrophoresis*

The remaining 90% of the total IP lysate volume underwent gel electrophoresis on an 10% gel. The gel was then removed from the electrophoresis tank and separated from the glass plates and put into a tray with 50ml GelCode Coomassie blue stain (Sigma). The gel was incubated in the stain for 1 hour, rocking, at room temperature. The Coomassie stain was then replaced with ddH_2O to wash overnight, rocking, at room temperature to expose the 70kDa FUS band.

2.14.2.4. *Digestion Theory*

The Uniprot website was used to identify the location of arginine sites of interest within the FUS protein. The FUS protein sequence was inputted into Expasy and PhosphositePlus to determine the best digestion enzyme which would retain the arginine sites upon cleavage. It was determined that chymotrypsin would be the best enzyme for the FUS protein, as it would conserve the majority of the arginine sites of interest.

2.15. RNA Sequencing

2.15.1. RNA Extraction – RNeasy kits (Qiagen)

Four patient tumours were micro-dissected into 12 ~20mg pieces. Three of the biopsies were immediately snap-frozen in 1.5 ml microcentrifuge tubes in liquid nitrogen, upon sample receipt and stored at -80ºC; three biopsies were treated in the perfusion device with the DMSO control; three biopsies were treated on the perfusion device with 1uM GSK3368715 and the remaining three were left in static culture, in a 15ml falcon tube of 10ml DMEM, within the incubator. After 8-days, the samples were extracted from the chamber using forceps and put into 1.5ml microcentrifuge tubes and snap frozen in liquid nitrogen and stored at -80ºC. RNA

for RNA-sequencing was initially extracted using the Qiagen RNeasy kit, following the manufacturer's instructions. Individual samples were lysed using 350 ul lysis buffer, with added β-ME, using a dounce homogeniser and then using a p200 pipette. The first lysate was then added to the column and spun down, followed by the second lysate of the same treatment *etc.* When the wash buffers were added, the filter column was rotated along the horizontal axis to ensure all remaining lysate was washed into the RNA filter. RNA content and purity was then measured using the Nanodrop2000 and stored at -20 ºC until use.

2.15.2. RNA Extraction – TRIzol

A second method of RNA extraction was employed for a second set of samples, after the previous samples failed the initial quality control (QC) check due to potential genomic contamination, unqualified RNA integrity number (RIN) and low RNA yields. Five patient GBM samples were sectioned into 12 pieces: four were immediately snap-frozen in 1.5ml microcentrifuge tubes in liquid nitrogen, upon sample receipt and stored at -80ºC; four biopsies were treated on-chip with the DMSO control; four biopsies were treated on-chip with 1uM GSK3368715. This was to increase RNA yield.

TRIzol™ (ThermoFisher Scientific) was added to the pooled tissue biopsies at 10% total volume and tissues were lysed using the Ultra Turrax T25 homogeniser (Cole-Parmer®) for one minute. This was then incubated at room temperature for 5 minutes. Chloroform was added 1:5 to TRIzol™ and tubes inverted gently for 15 seconds until a cloudy precipitate formed and then incubated for 3 minutes on ice. Samples were centrifuged for 15 minutes at 12,000 xg, at 4°C. The upper, colourless, aqueous phase was carefully transferred to a clean microcentrifuge tube and isopropanol added 1:2 to TRIzol™ and the tube again inverted. Samples were then incubated overnight at -80°C before centrifuging for 10 minutes, a12,000 xg, at 4°C. Supernatant was removed as much as possible, without disturbing the RNA pellet. RNA was washed twice in 75% ethanol at 1:1 with TRIzol™ and the samples vortexed briefly before centrifuging for 5 minutes, at 7500 xg, at 4°C. The supernatant was discarded and the RNA pellet air dried on a 37°C heat block for 5 minutes. RNA was then dissolved in RNase-free water by pipetting and incubation on a 55°C heat block for 10 minutes. RNA content and purity was then measured using the Nanodrop2000. RNA was stored at -80°C before packaging samples in dry ice for transport to Novogene for RNA-sequencing.

2.15.3. RNA-sequencing

RNA samples from and were sent to Novogene for RNA-sequencing (Figure 2.14). The initial QC report reported that 12 of the first 16 samples failed QC due to genomic contamination and unqualified RIN. Samples which passed QC and were taken forward with library preparation were D27-30. These samples were checked for RNA purity, with a A260/280 ratio between 1.8-2.0 and concentration >5ng/µl.

To purify and enrich mRNA in the samples, total RNA is fragmented and ribosomal RNA (rRNA) and other non-coding RNAs are removed from total RNA using polyT oligonucleotide-containing magnetic beads, which attract the polyadenylated mRNA tails. mRNA is converted to complementary DNA (cDNA) *via* reverse transcriptase and adapters were ligated for PCR amplification. One the libraries were constructed, Illumina Novaseq 6000 performed paired end reads, whereby each cDNA strand was read forwards and in reverse. Quality and accuracy of reads was checked using base calling and subsequent bioinformatics analysis was performed on these clean reads.

Clean reads were filtered through data QC analysis, which sequenced the error base rate and GC content of reads. Reads where the error base rate was >1% were eliminated from analysis (Petrackova *et al.* 2019). Reads are then aligned to the human reference genome version 38 (hg38). Alterations within the tumour genetic sequences were then quantified and translated into meaningful transcriptomic information *via* annotation through various online genetic databases.

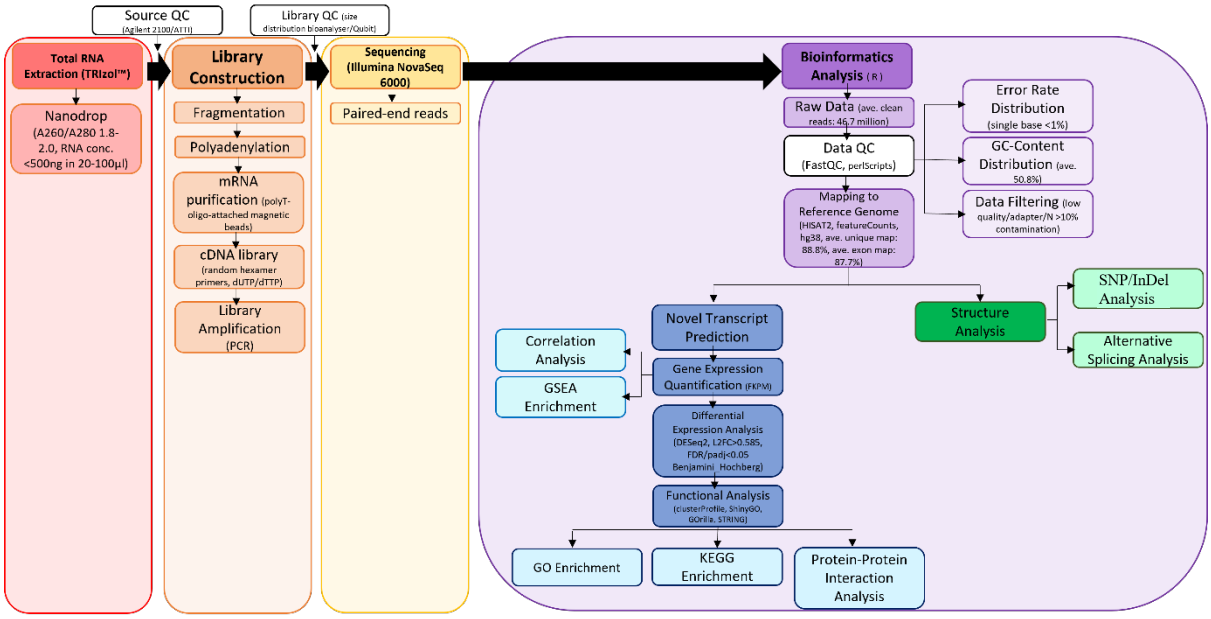

Figure 2.14.: Workflow for RNA-sequencing by Novogene®.

RNA was extracted using TRIzol™ and quantified using the Nanodrop2000, ensuring RNA concentration was <500ng in 20-100ul and A260/A280 was between 1.8-2.0. RNA samples were shipped to Novogene on dry ice, where they underwent source quality control (QC) using Agilent 2100/ATTI. Samples that passed QC were taken forward for library construction, where RNA is fragmented and polyadenylated for mRNA purification using poly thymidine (polyT)-oligo-attached magnetic beads. The cDNA library is created using random hexamer primers and dUTP/deoxythymidine triphosphate (dTTP) residues. Library QC is performed using a size distribution bioanalyser/Qubit. Paired end read RNA-sequencing then takes place using Illumina NovaSeq6000. Novogene then performed bioinformatics analysis using R. Raw data underwent data QC using FastQC and perlScripts packages. RNA fragments are then mapped to the human reference genome (hg38) genome using hierarchical indexing for spliced alignment of transcripts (HISAT2) and featureCounts packages. Novel transcript prediction was calculated alongside single nucleotide polymorphism (SNP) and insertion-deletion (InDel) analysis and alternative splicing analysis. Gene expression was quantified from the mapped clean reads, leading to correlation analysis and gene set enrichment analysis (GSEA) enrichment. Differential gene expression analysis was determined using the DESeq2 package, using a log2FoldChange (Log2FC) cutoff of 0.585 in either direction and adjusted p values (padj), using Benjamini-Hochberg correction, of <0.05 were deemed to be significant. Functional analysis was performed using the clusterProfile package and filtered through the

ShinyGO, GOrilla and STRING databases, for gene ontology (GO) enrichment, KEGG enrichment and protein-protein interaction analysis.

2.16. MaxQuant and Viper

A metadata search, using the Proteomics Identification Database European Molecular Biology Laboratory-European Bioinformatics Institute (EMBL-EBI) (PRIDE) and using the search term 'Glioblastoma' was utilised to identify mass spectrometry datasets of treated and untreated GBM tissues and cell lines. This data would then be run through MaxQuant, a quantitative proteomics software, to identify any proteins of interest which are routinely methylated (mMA, sDMA, or aDMA), in the presence or absence of various treatments. Due to the large quantity and size of files within several datasets, the Viper high performance computing cluster at the University of Hull was employed to allow the processing of greater quantities of data, simultaneously.

2.17. Statistical Analysis

All statistical analysis was performed using R 4.1.2., or R 4.3.1. using RStudio 2023.06.0+421 "Mountain Hydrangea" Release. Specific statistical methods are described in individual result figure legends. Exploratory data analysis for data which contained two or more groups was undertaken using Shapiro-Wilk normality {González-Estrada, 2019 #952} and Levene's homogeneity of variance testing (Nordstokke, 2010). Should the values for these tests be greater than 0.05, the parametricity, or homogeneity assumption of the variance is met and the data is treated as parametric and of equal variance, respectively. In this case, a Student's t test (Kim, 2015), or ANOVA (Cuevas, 2004) is chosen to test the data, depending on whether there are two, or more groups. In the case of ANOVA testing, one-way ANOVA was performed to compare the means of two groups of one independent variable. Two-way ANOVA was used to understand the interaction between two different independent variables, split over factors, on a dependent variable. Bonferroni correction was used to adjust for multiple comparisons, to account for type 1 errors, which produce false positives. Bonferroni corrections can be used for small numbers of comparisons, as reported in this study and compensate for significance value inflation (Cuevas, 2004). If the data do not meet these assumptions, a log10 data transformation was performed to satisfy the normality and variance assumptions for Student's t test or

ANOVA. Data was transformed back for presentation (Curran-Everett, 2018). If the data transform did not satisfy the normality assumptions, the original data was used and a Mann-Whitney U (MacFarland, 2016), or Kruskal-Wallis (Ostertagova, 2014) test was chosen.

2.18. Clinical Data

Table 2.9.: Clinical Data of all patient samples used

Patient	Sex	Age	Primary vs Recurrent	Location	IDH	1p/19Q	MGMT	EGFR	TERT	ATRX	Necrosis	BRAF	CDKN2A	TP53	PTEN	Surgery-Death (days)	Surgery-EODC (days)
D1	M	79	Metastatic adenocarcinoma	left frontal												193	
D2	M	46	Recurrent	right parietal	-	-		+			-			+		199	
D3	M	67	Primary	left parietal	-	+			-							833	
D4	M	58	Primary	left parito-occipital	-	-	+		+		-					16	
D5	F	70	Primary	left temporal	-	-	+		-		-					490	
D6	F	57	Primary	left frontal	-	-	+	-	-						-		795
D7	M	56	Primary	right temporal	-	-	-	+	-	+	-		+		+	572	
D8a	M	65	Primary	left temporal	-	-	=		-	++						683	
D9	M	75	Primary	left parietal	-	-	+			+						120	
D10	M	67	Recurrent	tempo-partietal	-	-	-		-	++						76	
D11	F	50	Primary	right parieto-temporal	-	-	-	+	-	++	-						704
D12	M	71	Primary	right frontal	-	-	-		-	++						133	
D13	M	54	Meningioma I	right occipito-parietal						-							670
D14	M	72	Recurrent	right parieto-occipital	-	-	-		-	+						234	
D15	F	51	Meningioma I	right temporal													562
D16	M	63	Primary	right parietal	-		-		-							195	
D17	M	69	Primary	right frontal	-		-		-							318	
D18	F	63	Oligodendroglioma III	left frontal	+	+	+	+	-		-	-		+		459	
D19	M	67	Oligodendroglioma II	parietal	-		-		-							443	
D20	F	74	Primary	right tempo-parietal	-		-		=							385	
D21	F	73	Primary	right occipital	-		+		-							44	
D22	F	44	Recurrent	right parietal	+	-	-	-	-		-	+				411	
D23	F	58	NSCCL metastases	right fronto-parietal													432
D24	M	67	Primary	right occipital	-	-	+		-		-	+					439
D25	F	63	Primary	left parietal	-	+	-		-		-			-		44	
D26	M	70	Primary	left frontal	-		-		-		-					41	
D27	M	56	Primary	left frontal	-		-		-	++	-					46	
D28	M	51	Recurrent	right parietal	-		-		-		-					326	
D29	M	58	Primary	left temporal	-		+		-		-						289
D30	M	58	Primary	right temporal	-		-		-								286
D31	M	76	Primary	right frontal	-		+		-								263
D8b	M	67	Recurrent	left temporal	-				-	++						263	
D32	M	45	Primary	left parieto-occipital	-		-	+	-		-	+					198
D33	F	55	Primary	right occipital	-		-	+	-		-	+					158
D34	M	69	Primary	right fronto-parietal	-		-	+	-		-						85
D35	M	63	Primary	right temporal	-		+		-							63	
D36	M	69	Primary	right temporal	-		-							-			80
D37	M	74	Primary	Right frontal	-		-		-							245	

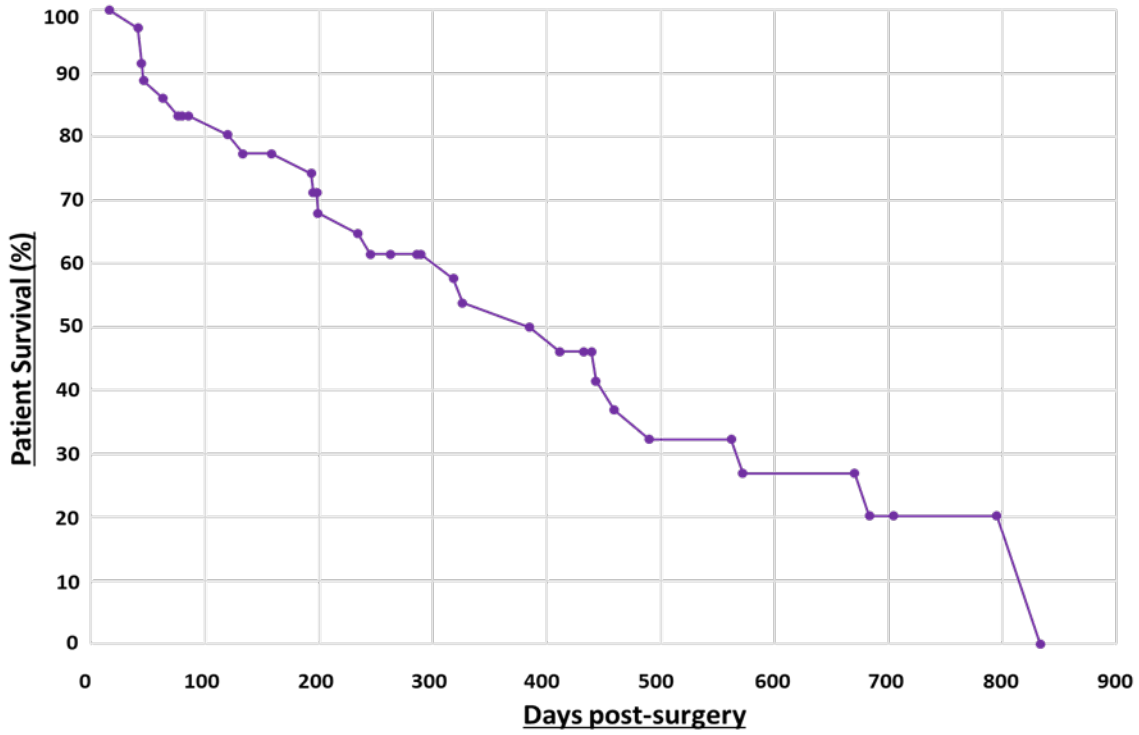

Figure 2.15.: Survival curve of 37 patients involved in this study.
Survival was defined as the number of days between the first surgery and either the death of the patient, or the end of data collection (27/08/2023).

Of the 37 patients involved in this study, 13 patients remained alive by the end of data collection. Twenty-six of the total number of patients had confirmed primary GBM and five had confirmed recurrence, with one of these being patient D8, from whom we received both biopsies. Two patients had grade I meningioma, two had grade II/III oligodendroglioma and two patients had distal metastatic disease (Figure 2.15).

CHAPTER 3: INVESTIGATING THE EFFECTS OF PRMT INHIBITION ON GBM TISSUE CELL DEATH IN A MICROFLUIDICS SYSTEM

Results in the chapter have been published in Lab on a chip.

Barry, A., Samuel, S.F., Hosni, I., Moursi, A., Feugere, L., Sennett, C., Deepak, S., Achawal, S., Rajaraman, C., Iles, A., Valero, K.C.W., Scott, I.S., Green, V., Stead, L.F., Greenman, J., Wade, M.A, and Beltran-Alvarez, P. (2023). Investigating the effects of arginine methylation inhibitors on micro-dissected brain tumour biopsies maintained in a miniaturised perfusion system. *Lab on a Chip*, 23(11), pp.2664-2682. DOI: 10.1039/D3LC00204G.

3.1. Introduction

In this chapter, I will explore the use of PRMT inhibitors in 2D and 3D cells lines, as well as in GBM tissue using the techniques outlined in the previous chapter. Previous work in this lab has ascertained that other type I PRMT inhibitors such as Furamidine, lead to a reduction in cell viability in 2D and 3D GBM cell line models (Samuel *et al.*, 2018). Simultaneously, I will be assessing the fortitude of the novel perfusion system as a model of GBM and its practicality in evaluating the efficacy of drugs used to target GBM.

3.1.1. GBM treatment through inhibition of arginine methylation

Post translational modifications, including arginine methylation, have repeatedly been shown to be involved in the development and progression of GBM. As described previously, changes to arginine methylation can be responsible for activation and repression of gene transcription and alteration of protein behaviour, which may be responsible for the progression of GBM. PRMTs are responsible for arginine methylation of proteins involved in the DDR and splicing pathways, which will be supported in the subsequent chapters. In the Samuel *et al.* (2018) paper, the work profiled overall PRMT expression in U87-MG cell lines and found all PRMTs to be present, including isoforms, except CARM1. In alternative studies, CARM1 has been found to be expressed in GBM, correlated with expression of genes associated with pluripotency, such as OCT4 and SOX2 (Rios *et al.*, 2022). As mentioned previously, most PRMTs have been linked to, and their expression is increased in, GBM and, therefore,

augmentation of PRMT function may be a therapeutic target for GBM (Bryant *et al.*, 2021, Samuel *et al.*, 2021, Samuel *et al.*, 2018). Indeed, there are several investigations into the use of PRMT inhibitors in GBM, such as abrogation of IFNγ-induced de-differentiation markers *via* inhibition of PRMT1 (Ghildiyal and Sen, 2017); inhibition of Myc-driven oncogene expression through PRMT5 inhibition (Mongiardi *et al.*, 2015) and others (Banasavadi-Siddegowda *et al.*, 2017).

3.1.2. Cytokines and Chemokines in GBM

Cytokines and chemokines are essential aspects of the immune system and are involved in the migration of immune cells to sites of stress within the body and for their function once they arrive at the injury site (Ramesh *et al.*, 2013). Cytokines and chemokines are associated with inflammation, development, and progression of many diseases, including cancer. In GBM, cytokine-chemokine ligand 12 (CXCL12)/receptor 4 (CXCR4) have been linked to GBM progression and inhibition of the receptor indicated reduced tumour growth (Savarin-Vuaillat and Ransohoff, 2007). As mentioned previously, the tumour microenvironment is essential for the development and progression of GBM. The immunosuppressive mechanisms which inform immune modulation and contribute to the dissolution of anti-tumour responses and immunosuppressive cytokine and chemokine secretion is paramount to this (Yeo *et al.*, 2021). In a study by Morawin and Zembron-Lacny (2023), GBM patients were found to have 1.5-2-fold higher expression of pro-inflammatory cytokines IL1β, IL6 and IL8 and reduced expression of TNFα and HMGB1. The researchers suggested that these GBM-specific molecular signatures of cytokines may therefore be reliable prognostic indicators of GBM progression.

3.1.3. Aims and Objectives

The overarching aims of this chapter were to explore the effect of the PRMT inhibitor GSK3368715 on cell viability in 2D and 3D U87-MG models, before moving onto investigating the apoptotic effects of the PRMT inhibitor in GBM *ex vivo.*

- Assess whether GBM can be maintained in the novel perfusion device for 8-12 days.

- Determine whether GSK3368715 causes cell death in GBM tissue in the perfusion device.
- Understand the synergy between GSK3368715, other PRMT inhibitors and TMZ.
- Identify some of the patient clinical factors which may be associated with variation in GSK3368715 treatment response, such as patient age, sex and biomarkers.

3.2. Materials and Methods

The methodologies and statistical analysis producing the majority of the results in this chapter were undertaken by myself and have been outlined in the previous chapter. The procedures described in this materials and methods section were performed, for the most part, by M.D. student Amr Moursi, towards the completion of his M.D. project, for which I was involved in the grant and in his laboratory supervision. The statistical analysis for these methods were carried out largely by Lauric Feugere.

3.2.1. Human XL Cytokine Array Detection

Proteome profiling was performed using the Human XL Cytokine Array Detection kits (Roche) and was utilised to assay 105 cytokines which may be present in the effluents of GBM-on-chip samples, taken at several time points, over the course of sample time on-chip. Effluents were stored, long-term, at -80 ºC and defrosted on ice prior to use. Membranes, pre-loaded with the array of anti-cytokine antibodies, were blocked for one hour, before incubating overnight, rocking at 4 ºC with diluted effluent, according to the manufacturer's instructions. The effluents used were from two chips treated with either DMSO, or 1uM GSK3368715 and 10uM TMZ and at 48 hours, 96 hours, and 192 hours. Membranes were then washed three times, for 10 minutes with wash buffer, rocking at room temperature and incubated with the antibody detection cocktail for one hour, rocking at room temperature. After a further three washes, membranes were incubated for 30 minutes, rocking at room temperature, with streptavidin-HRP. Membranes were washed for a final time and Clarity™ ECL Western substrate (Bio-Rad) was added to the membranes for 1 minute, before exposure using a ChemiDoc™ Imaging system (Bio-Rad) (Figure 3.1). Densitometry was analysed using R&D-approved software and statistics performed by Lauric Feugere using R4.3.0.

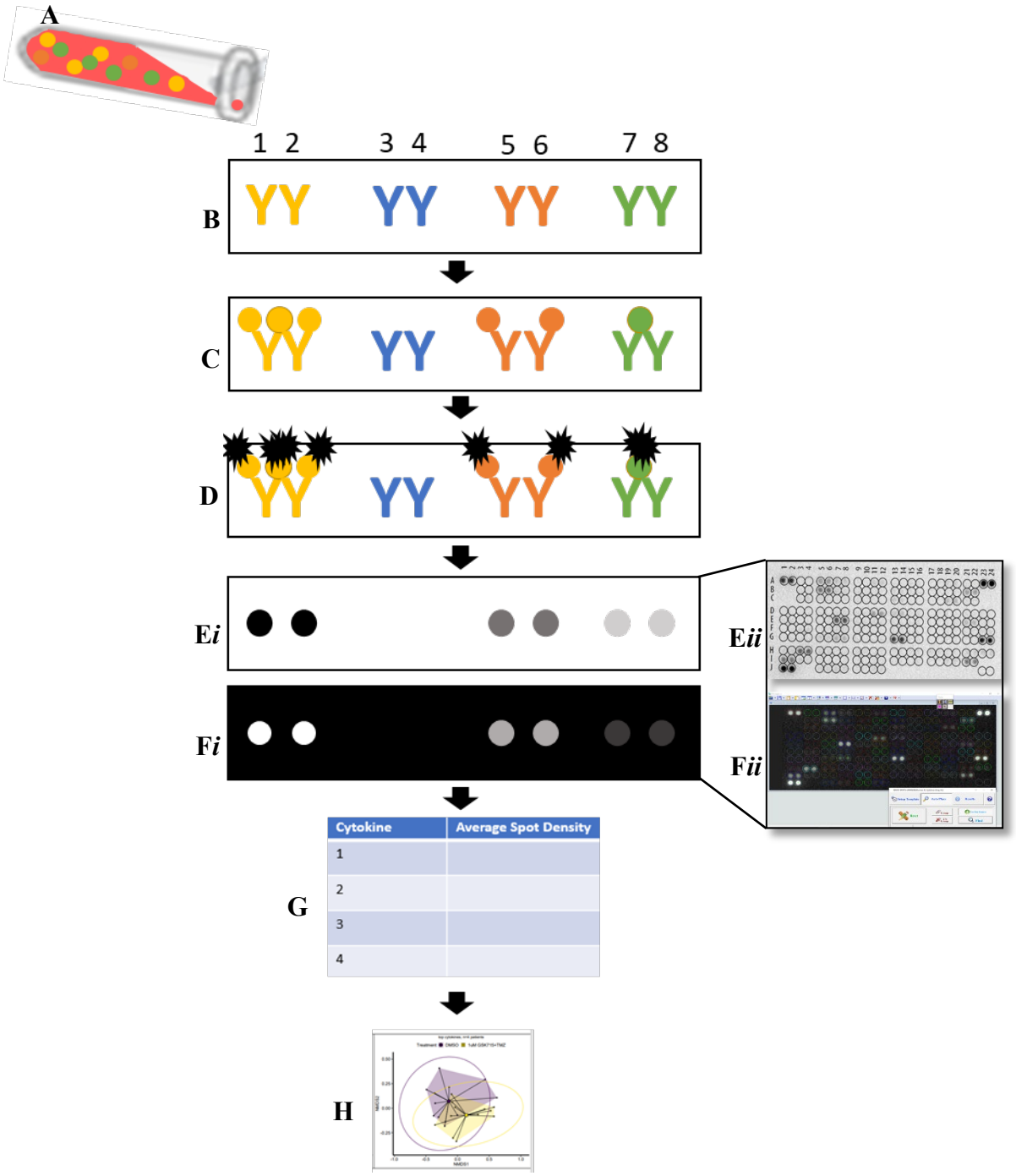

Figure 3.1.: Workflow of Human XL Cytokine Detection Kit

A) *Effluent at 24, 48, or 192 hours, treated with DMSO control or 1uM GSK3368715+ 10uM TMZ;* ***B)*** *Effluent is poured onto membrane containing pairs of primary antibody dots against 105 different cytokines;* ***C)*** *Cytokines, if present in the effluent, bind to the specific, corresponding antibodies present at each location;* ***D)*** *Secondary HRP-conjugated antibody is added to the membrane and binds the primary antibody in proportion to the amount of protein*

bound; ***Ei)*** *the Chemidoc® is used to visualise HRP;* ***Eii)*** *Chemidoc® image of a membrane indicating several bound cytokines;* ***Fi)*** *use of R&D-approved software to calculate spot density, proportional to amount of cytokine bound to membrane;* ***Fii)*** *true image of reversed colour to highlight absorbance density in R&D-approved software;* ***G)*** *an automatic table of density is created by the software, where average spot density of the paired dots can be calculated and values normalised to the positive controls;* ***H)*** *data is filtered to remove negligible absorbance values and statistical significance calculated by Lauric Feugere. Images taken by Amr Moursi.*

3.2.2. ELISA

ELISAs (R&D) were performed for several cytokines, which appeared changed in the proteome profiler array results and required more in-depth exploration. These included: angiopoietin 2, MMP9, serine protease inhibitor clade E member 1 (serpin E1), C3L1, IL6, IL8 and VEGF. Samples included effluents from time points 24-, 48-, 192- and 288-hours, which had been used for the proteome profiler arrays. Capture antibody was diluted in coating buffer, according to the manufacturer's instructions and used to coat 96-well plates (Corning), which were left overnight at 4°C. The coating solution was aspirated, and plates washed with wash buffer. All wash steps included washing plates five times using an automatic plate washer and tapping excess liquid onto absorbent paper. Plates were then blocked with blocking buffer, for one hour, at room temperature and the liquid then aspirated. Kit-provided standards and effluent samples were prepared in blocking buffer and incubated for one hour at room temperature with continuous gentle shaking ~500 rpm. Plates were then washed again and detection antibody, diluted in blocking buffer, added for 2 hours at room temperature, with continuous gentle shaking. Plates were washed before adding 1:5000 Streptavidin-HRP in blocking buffer and incubating at room temperature for one hour, gently shaking. After the final wash, TMB substrate solution was added, for 30 minutes at room temperature, to develop colour and then stop solution added to each well. Absorbance was measured at 450nm immediately using the BioTek™ ELx800™ absorbance microplate reader with Gen5 software 1.08. Statistical analysis was performed by Lauric Feugere using R 4.3.0.

3.3. Results

3.3.1. GSK3368715 maintains cell viability in U87-MG cells

Prior to any experiments involving the novel GSK338715 PRMT inhibitor in GBM tissue, on the perfusion device, its viability was tested in U87-MG cells. This was done using the MTS cell viability assay on both 2D and 3D U87-MG cell cultures. U87-MG cells were cultured in 2D, in 96-well plates and allowed to culture for up to 72 hours, before the MTS assay was performed.

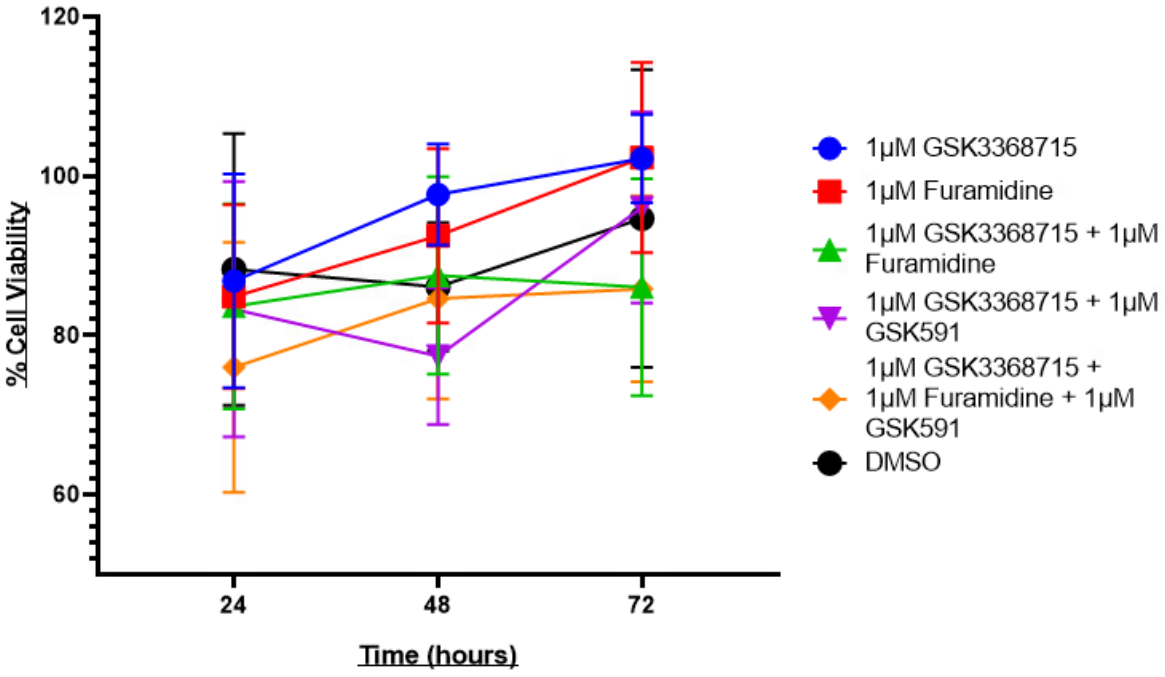

Figure 3.2: Percentage cell viability ± SEM of U87-MG cells in 2D culture.

U87-MG cells were cultured in 96-well plates and treated with: 1 μM GSK3368715 (blue circle), 1 μM Furamidine (red square), 1 μM GSK3368715 + 1 μM Furamidine (green up triangle), 1 μM GSK3368715 + 1 μM GSK591 (purple down triangle), 1 μM GSK3368715 + 1 μM Furamidine + 1 μM GSK591 (orange diamond), DMSO negative control (black circle), in triplicate, for 24, 48 and 72 hours before undergoing MTS assay (n=5) to determine % cell viability. Statistical analysis was performed using two-way ANOVA with Bonferroni testing, using Graphpad Prism 8.0.

Despite there being a slight upwards trend in cell viability of all U87-MG cells with time (Figure 3.2), using 1 µM of all of the treatments did not significantly affect cell viability in comparison with the DMSO control, at any time point. The variability in cell viability between the treatment groups was not statistically significant.

Spheroids were cultured in round-bottomed ultra-low adherence 96-well plates, containing 1% agarose, and allowed to form for 72 hours before the treatments were applied. Media was then changed before treatment, taking care not to disturb the spheroids. Treatment was applied to the 3D cultures for longer periods of time than 2D cultures due to the increased volume to surface area ratio of the spheroids, meaning that the treatment would take longer to penetrate to the internal cells. Media was changed again after 72-hours, and fresh treatment added.

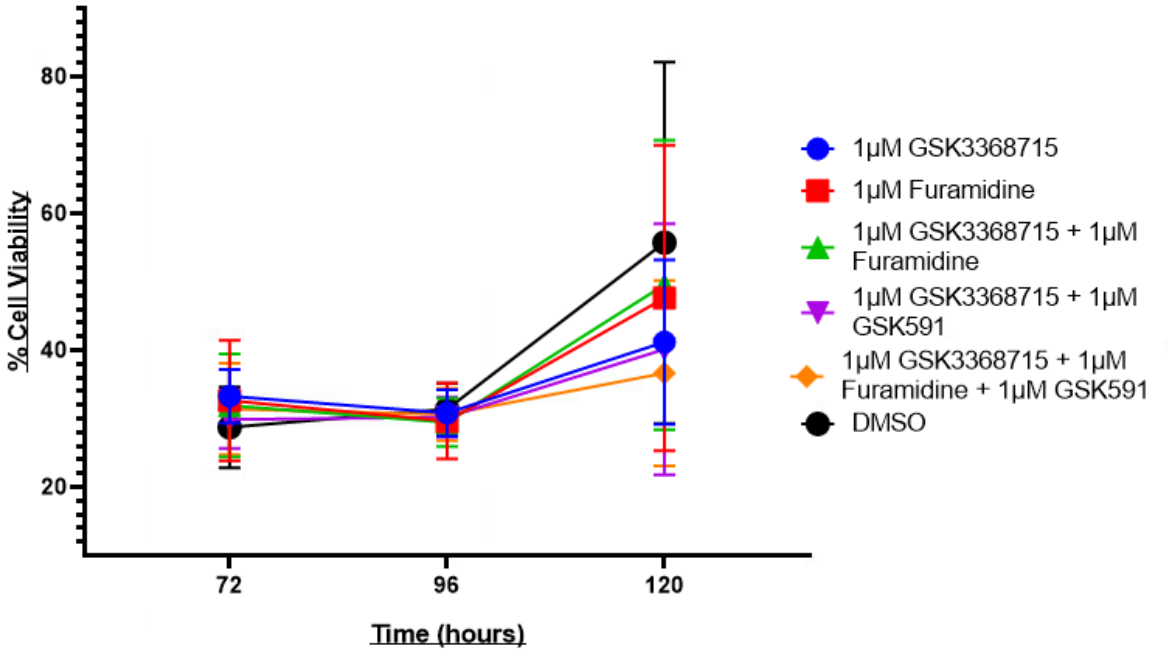

Figure 3.3: Percentage cell viability ± SEM of U87-MG cells in 3D culture.

U87-MG spheroids were cultured in 96-well plates and treated with: 1 µM GSK3368715 (blue circle), 1 µM Furamidine (red square), 1 µM GSK3368715 + 1 µM Furamidine (green up triangle), 1 µM GSK3368715 + 1 µM GSK591 (purple down triangle), 1 µM GSK3368715 + 1 µM Furamidine + 1 µM GSK591 (orange diamond), DMSO negative control (black circle), in triplicate, for 72, 96 and 120 hours before undergoing MTS assay (n=4) to determine % cell

viability. Statistical analysis was performed using two-way ANOVA with Bonferroni testing, using Graphpad Prism 8.0.

All treatment groups appeared to show the same trend in cell viability, with levels decreasing slightly at 96-hours, but increasing again at 120-hours (Figure 3.3). The similarity between the treatment groups could be to do with penetrance of the drug into the core of the spheroids, or penetrance of the MTS assay reagent. Similarly, to the 2D-cultured cells, no significance was found in cell viability with time, in the same group, nor between each of the treatment groups, in comparison with the DMSO control. This could suggest that the drugs should be applied over a more continuous period of time.

3.3.2. GSK3368715 causes aDMA-sDMA crosstalk in U87-MG cells

Despite the non-significant changes to cell viability found in the initial experiments, previous data had indicated that 1 μM GSK3368715 was sufficient to bring about a protein-level response in 2D and 3D cells, as well as tissue (Barry *et al.*, 2023, Samuel *et al.*, 2018). In accordance with the literature, this concentration was taken forward for subsequent experiments. U87-MG cells were treated in 2D cultures with varying concentrations of the novel Type I PRMT inhibitor GSK3368715, or the previous Type I inhibitor MS023 for forty-eight hours, as a positive control. Samples underwent western blot analysis whereby membranes were blotted with antibodies against aDMA and sDMA and densitometry data normalised to a β-actin loading control and compared to a DMSO negative control.

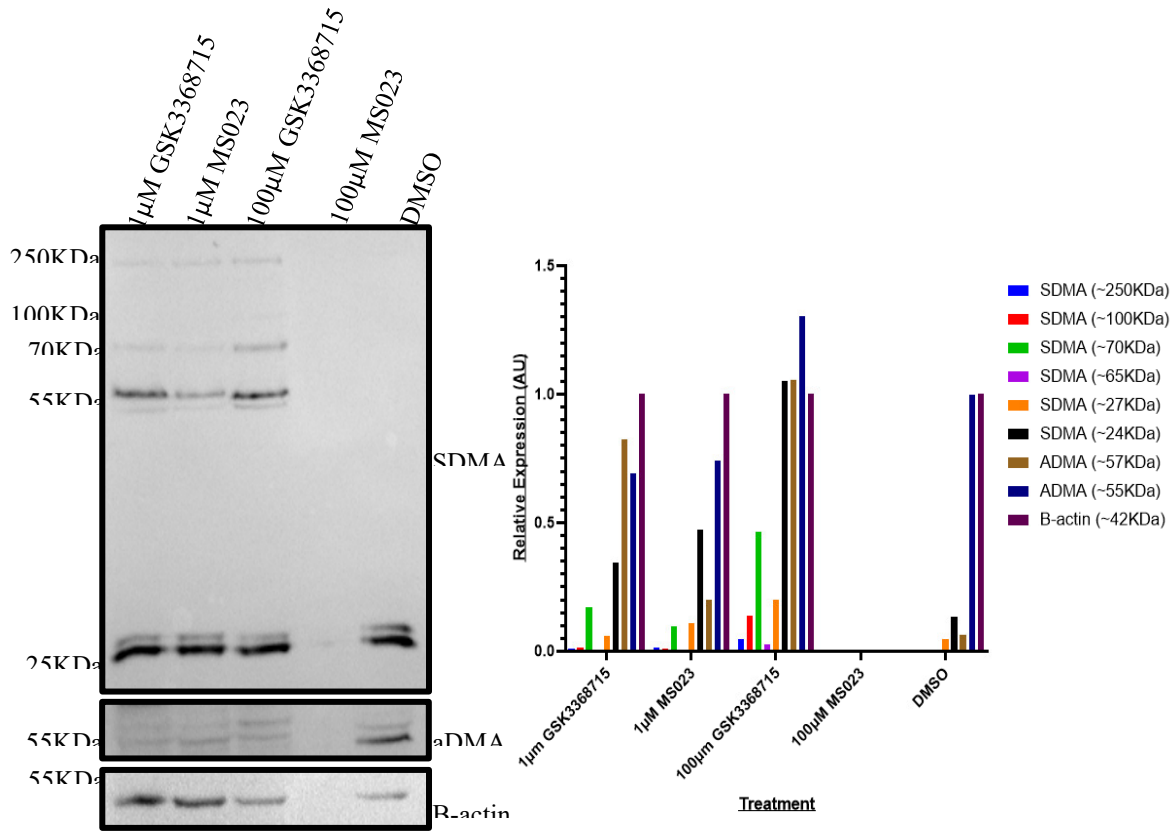

Figure 3.4: GSK3368715 induces aDMA-sDMA crosstalk in U87-MG cells.

A) U87-MG cells were treated with 1 µM and 100 µM Type I PRMT inhibitors MS023 and GSK3368715 and incubated with antibodies against aDMA (~50 kDa) and sDMA (~70 kDa, ~55kDa + ~25 kDa), along with B-actin loading control (~42 kDa) (n=1). B) Densitometry analysis was performed using ImageJ.

Upon aDMA inhibition with Type I PRMT inhibitors (100 kDa), sDMA of proteins increases (~55kDa) which is shown in Figure 3.4. This confirms the results from previous work in this lab, which described this unidirectional crosstalk between aDMA and sDMA (Samuel et al., 2018). There is also another band that appears at 70kDa upon Type I PRMT inhibition, when sDMA is blotted for. This appears to be stronger when using the novel inhibitor, than when using MS023, indicating that the novel inhibitor is potentially a better model and more potent than its previous counterpart. There is no significant increase in crosstalk levels between cells treated with 1 µM *vs* 100 µM GSK3368715, therefore in accordance with these findings and

the dosage used in clinical trials, it was decided that the lower dose should be taken forward into the GBM perfusion work.

3.3.3. GBM can be maintained in the novel perfusion device for 8 days

To address the first two objectives of this section of the project, LDH assays were performed to understand changes in cellular stress over the course of 8 to 12 days in the perfusion chip. Histology for apoptotic markers cleaved PARP and Annexin V, as well as for histological markers, were also utilised to determine whether the perfusion device maintained the tissues in a viable state and so pre- and post-perfused tissues were compared.

3.3.3.1. *Low cellular stress in GBM tissues up to 12 days*

Samples D3-D7, D8a, D9-D12, D14, D31 were used for 8-day LDH analysis. LDH is released from cells upon cellular stress, LDH assays are colorimetric assays which measure absorbance in the region of 495 nm. Absorbance is then directly proportional to LDH released into the effluent every 24 hours from GBM tissues, whilst on-chip, which is directly proportional to GBM-tissue cellular stress. The aim of performing LDH assays was to determine how stressed GBM tissues were in the microfluidics device in real-time and therefore if, after 8-days, the microfluidics system was a viable device upon which to maintain GBM tissue alive for 8 days. Effluents, collected every 24 hours from both DMSO control and drug-treated chips, were plated in duplicate onto 96-well plates and mixed with a dye-catalyst solution, before incubation at 37°C for 30 minutes for the colour to develop. Absorbance was then read at 490 nm, with a wavelength correction of 690 nm, to account for wavelength artefacts, such as scratches to the plate. Duplicate absorbance values were averaged and the negative, media-only, control subtracted.

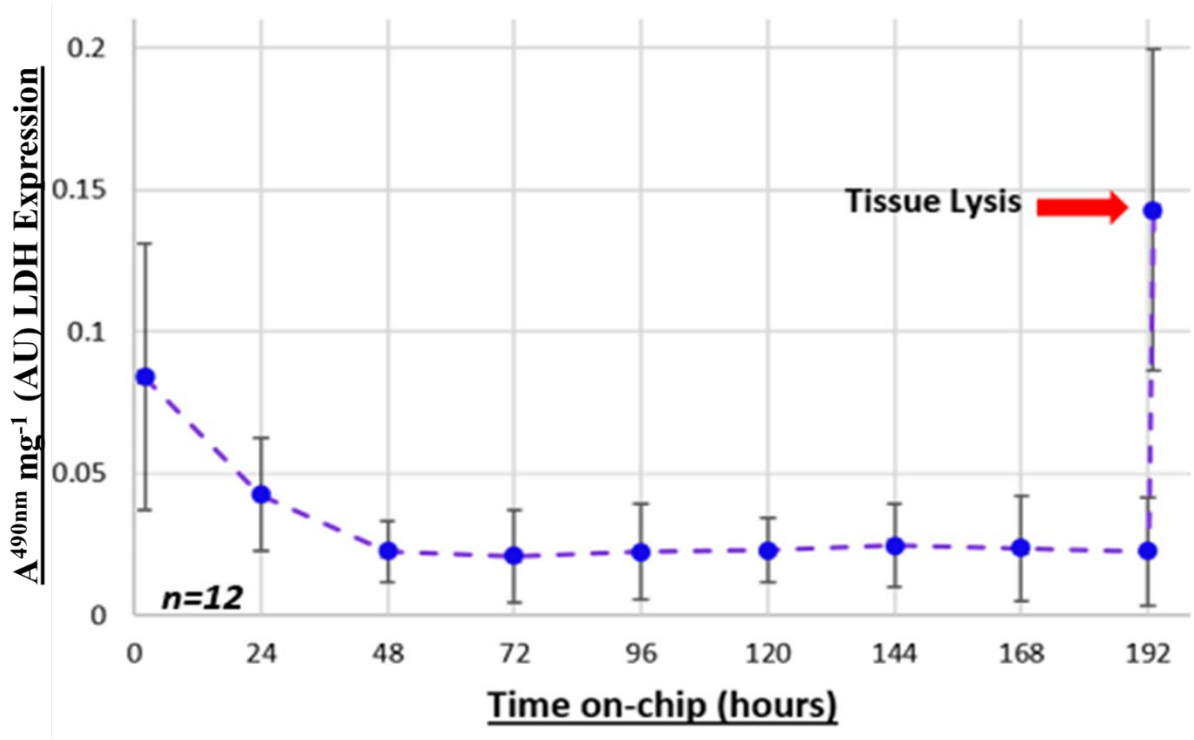

Figure 3.5.: Lactate dehydrogenase expression of GBM (n=12) over 8 days, with post-perfusion tissue lysis (n=3).

Lactate dehydrogenase (LDH) activity was measured in the effluent, collected every 24 hours over 8 days, via *absorbance at 490 nm (A^{490nm}) (*n *= 12, D3-D7, D8a, D9-D12, D14, D31, see Table 4.1). LDH activity decreased to 0.023 AU (absorbance units)/mg ± 0.011 at 48 hours and fluctuated minimally (*F *= 1.11, df = 7,* p *= 0.37) between 0.021–0.025 AU mg^{-1} for the remaining 6 days, these fluctuations correlated with syringe refilling with medium at day 4. One-way ANOVA performed using R 4.2.0 after data transformation. After 8 days, tissues were lysed to assess remaining LDH within the biopsies (*n *= 10), leading to a peak reading at 0.143 AU mg^{-1} ± 0.06 (indicated by red arrow) (*t *= -6.64, df = 97,* p *= 1.80 × 10^{-9}, compared to baseline expression). Two sample T test performed using R4.2.0. Error bars indicate standard deviation.*

Statistical analysis showed that there were no significant differences in LDH expression over time. LDH expression and therefore absorbance started off high, which is expected due to the stress put upon the tissue from being removed from the brain, transported and micro-dissected and therefore not connected to a blood, or nutrient supply for approximately 2 hours. This then decreased over the first 48 hours on-chip to a relatively low absorbance value, indicating that

LDH release from the tissue slowed and cellular stress decreased whilst it is receiving nutrients from the media (Figure 3.5). The baseline value was calculated as the mean LDH expression over 24- to 192-hours, as no significant fluctuation in LDH release was found between the time points. There was a small peak in absorbance at 120 hours, consistent with the syringe change after 96 hours, whereby the microfluidics pump must be stopped for approximately 15 minutes, but this quickly returned to the baseline recorded prior. At the end of the 8 days, tissue was lysed to release any retained LDH, which was a significant amount compared to baseline expression.

Another aim of the project was to extend the time of the tissue in the perfusion device to 12 days. LDH assays were performed for four GBM samples, which were incubated in the perfusion device for 12 days and lysis performed on two samples of post-perfused tissue, as previous. Samples D21, D24, D35 and D36 were used for 12-day LDH analysis.

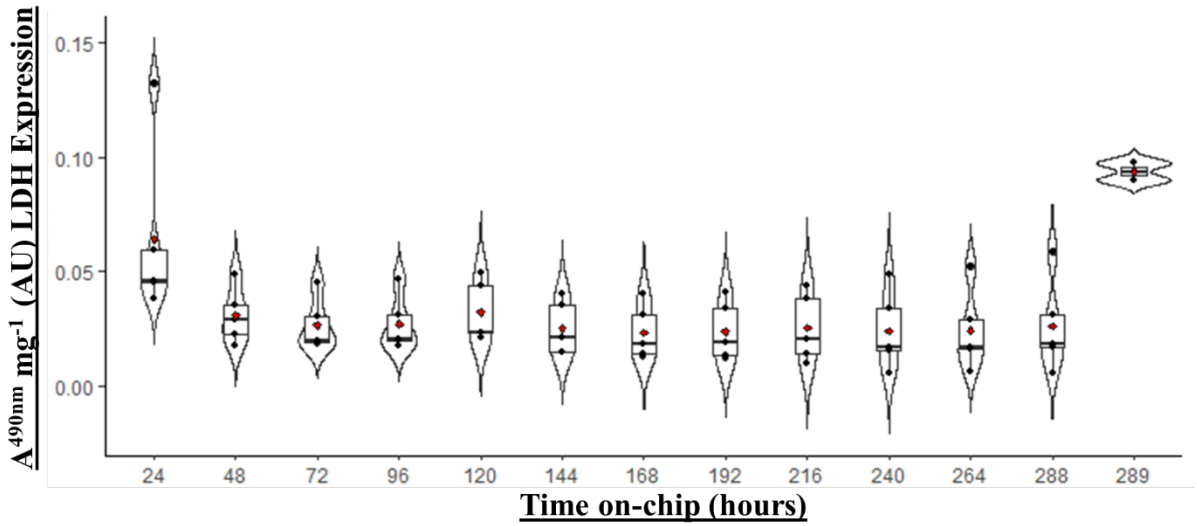

Figure 3.6.: Lactate Dehydrogenase expression in GBM tissue (n=4), over 12 days, with post-perfusion tissue lysis (n=2).

Lactate dehydrogenase (LDH) activity was measured in the effluent, collected every 24 hours over 12 days, via absorbance at 490 nm (A^{490nm}) (n = 4, D24, D31, D35, D36, see Table x). LDH activity decreased to 0.031 AU (absorbance units)/mg ± 0.012 at 48 hours and fluctuated ($F = 1.38$, $df = 11$, $p = 0.22$) between 0.023–0.032 AU mg^{-1} for the remaining 10 days, these

fluctuations correlated with syringe refilling with medium at days 4 and 8. One-way ANOVA performed using R 4.2.0 after data transformation. After 12 days, tissues were lysed to assess remaining LDH within the biopsies (n = 2), leading to a peak reading at 0.094 AU mg^{-1} *± 0.005 (indicated by red arrow) (t = -7.08, df =55 , p =2.81 ×* 10^{-9}*, compared to baseline expression). Two sample T test performed using R4.2.0. Error bars indicate standard deviation.*

The 12-day LDH assay displayed a similar output to the 8-day LDH assay, with no significant changes in expression between consecutive time points. There was a slight upward flection at 120-hours and 216-hours, consistent with syringe changes just after the previous time points (Figure 3.6). Coupled with the tissue lysis releasing retained LDH after 12 days, compared to baseline expression, this again indicated that the tissues were not stressed in the perfusion device.

3.3.3.2. *Evidence of mitosis after 8- and 12-days of perfusion*

To ascertain whether the novel perfusion device caused any structural abnormalities and to ensure that the tissue was initially viable and remained so, H&E staining was performed. H&E staining was undertaken on both fresh-frozen tissues (8-day perfusion) and FFPE tissues (12-day perfusion). Paired GBM patient samples, pre- 8- and 12-days post-perfusion were stained with haematoxylin and eosin and a sample set of images sent to neuropathologist Dr. Ian Scott. The images were analysed for mitotic figures, which can be seen in the images, inset (Figure 3.7).

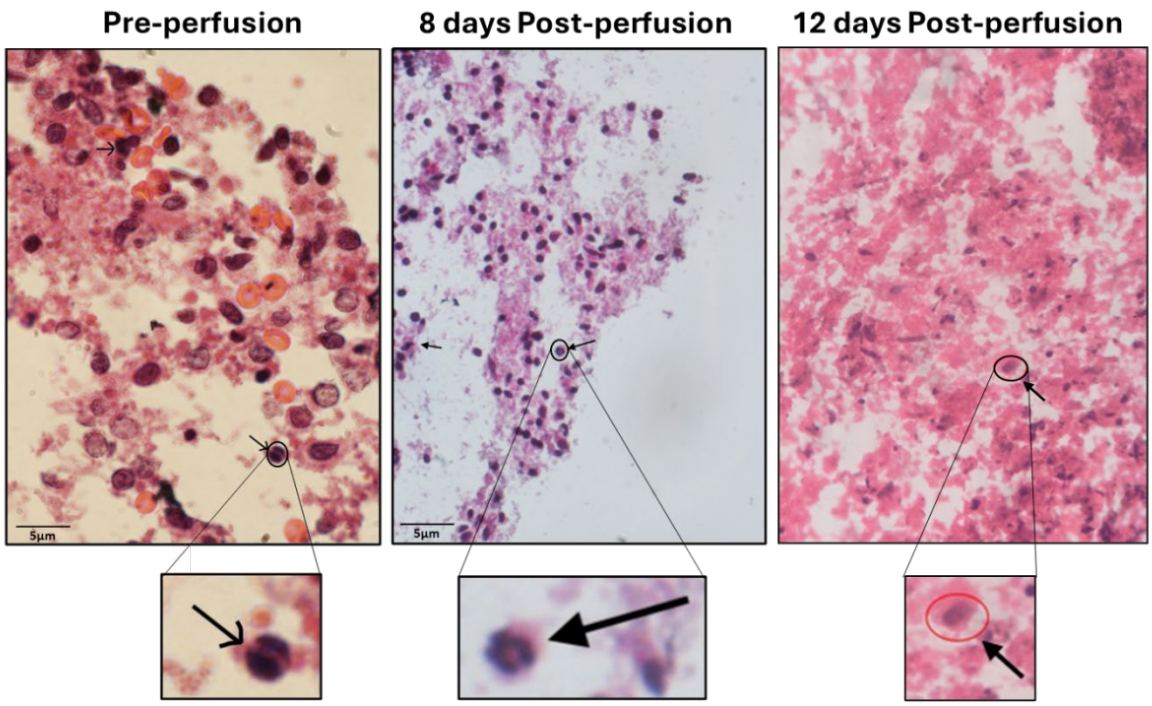

Figure 3.7.: Representative H&E staining of GBM tissue pre-, 8 days and 12 days post-perfusion [inset: mitotic figures].

Haematoxylin (purple) stains nuclear aspects of cells and eosin staining highlights cytosolic cellular fractions. Arrows on both images highlight mitotic figures, with inset showing magnified images. Images at x40 magnification were taken on an Olympus IX71 inverted fluorescence microscope using CellSens software 1.18 and assessed together with neuropathologist Dr. Ian Scott.

These mitotic figures indicate that there are dividing cells, both pre- and post-perfusion. This shows that at least some of the GBM tissue was viable upon receipt from the hospital and maintained viability after 8 days of perfusion. Indicating that GBM tissue remained “alive” and in a mitotic state post-perfusion. In all of the inset images, the arrangement of the chromosomal material on the mitotic spindle appeared uneven, with there being a higher proportion of chromatin in one half of the pre-perfused nucleus and the 8- and 12-day post-perfused nucleus displaying chromatin which remained attached at one end of the metaphase plate. The presence of atypical mitotic figures as it suggested that the cell division is in the tumour and not in background, normal, "contaminant" tissue (Figure 3.7) (Appendix 2 and Appendix 3).

3.3.3.3. *Validation of the CellProfiler pipeline*

The cleaved PARP Cell Profiler pipeline was used to quantify IHC staining and was validated using a cohort of images taken from sample D37, stained for nuclear proliferative marker Ki67. The images of the probed IHC tissues were take using the Olympus IX71 inverted fluorescence microscope using CellSens software 1.18 and loaded into CellProfiler. The pipeline was validated using three technical replicates (slides) each from pre-perfused tissue and 10 post-perfused tissues (A-J). The parameters were changed in test mode for each set of images until the most accurate test image was obtained (Figure 3.8).

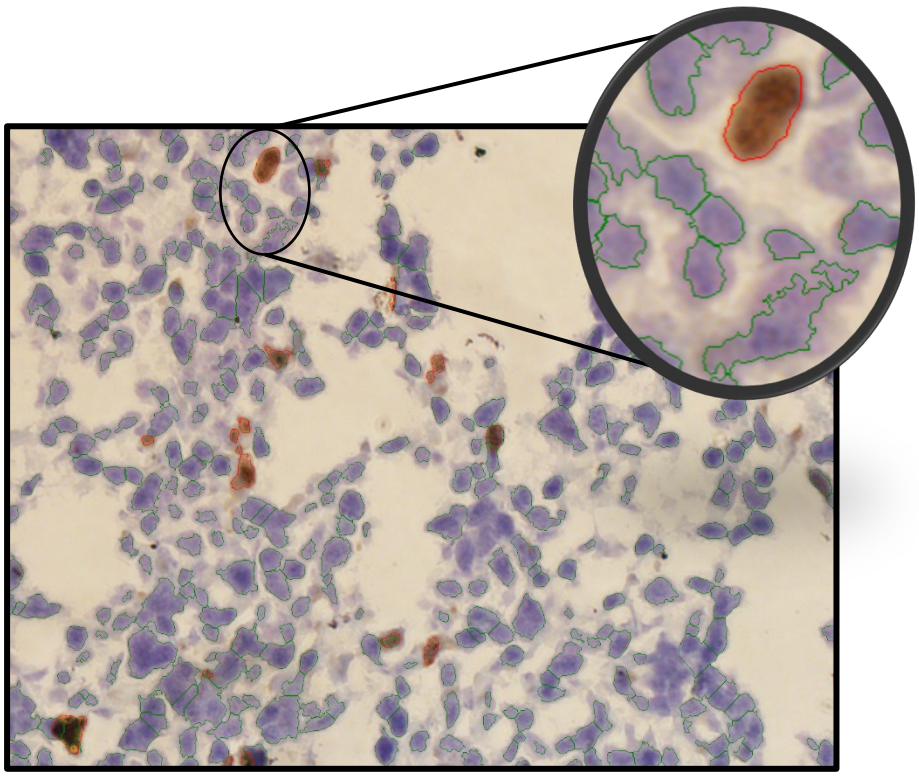

Figure 3.8.: CellProfiler output image [inset: magnified section]

In the representative images, haematoxylin stains cell nuclei blue, whilst 2'2'-diaminobenzidine (DAB) stains cleaved PARP *expressing cells brown. Images at x40 magnification were taken on an Olympus IX71 inverted fluorescence microscope using CellSens software 1.18. Green outlines highlight blue haematoxylin-stained cells, which do not appear to be expressing the protein for which is being probed. Red outlines highlight brown DAB-stained cells, which do appear to be expressing the protein of interest.*

The pipeline was then run on one set of images, with all images in a set from one slide. The same images were then manually counted with the aid of ImageJ. A Ki67 index was obtained, which was a ratio between positively stained, Ki67 expressing cells and total number of cells (Appendix 1). This was repeated for all 33 image sets. The Ki67 index for each image set was then compiled and the confidence intervals for the two sets of data compared (Figure 3.9).

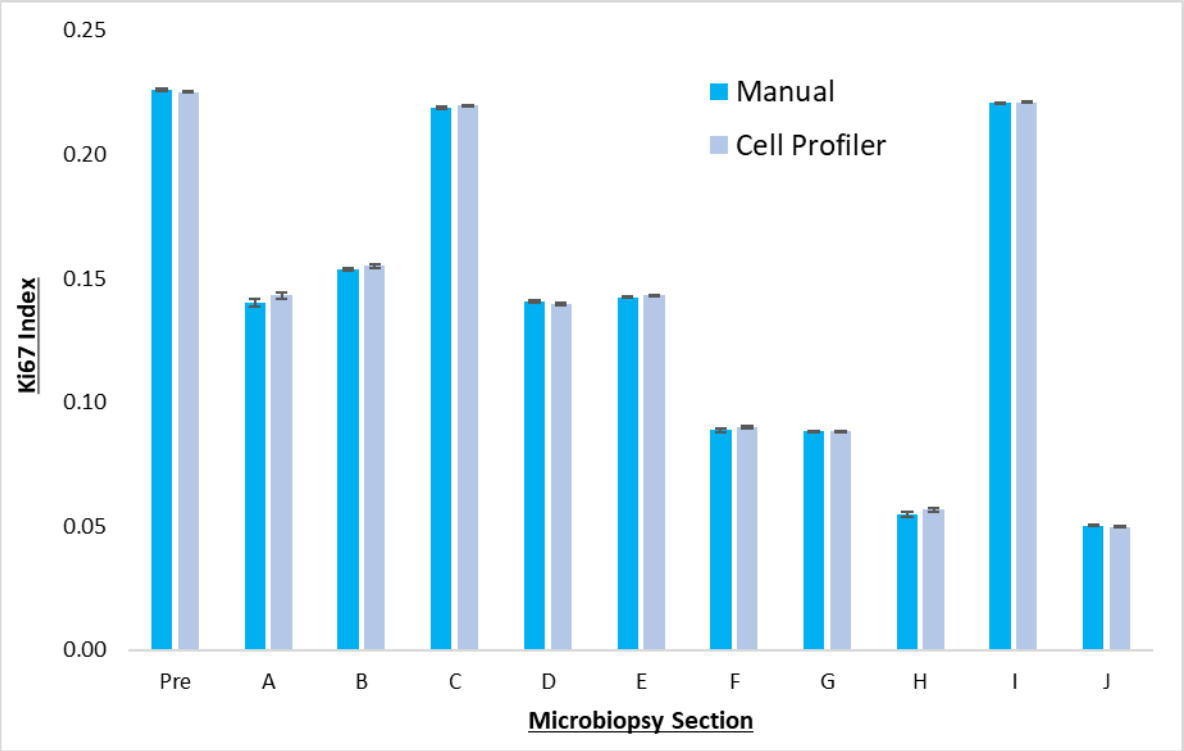

Figure 3.9.: Cell Profiler Validation Sample D37.

Using patient biopsy sample D37, IHC was performed with proliferative marker Ki67. A Ki67 expression index was created from both Cell Profiler cell counts and manual cell counts. Error bars indicate standard deviation between Ki67 index in Cell Profiler counts vs Manual counts.

After running the images through CellProfiler, outliers were identified and manually counted, for input into the final dataset. This is a practise that was carried forward throughout analysis of subsequent images. Alternatively, outliers were rerun through CellProfiler with different parameters to obtain a more accurate cell count for the minority of images, which may be affected due to image, or tissue quality. This resulted in error which fell within the 95% confidence intervals.

3.3.3.4. *No significant change in apoptosis 8-12 days post-perfusion*

To ensure that any changes in apoptosis were down to the drugs being used and not due to the microfluidics method itself, cleaved PARP expression was compared pre-, 8- (Figure 3.10) (Appendix 4) and 12-days post-chip (Figure 3.11) (Appendix 6). The samples used for this analysis were D3-D7, D8a, D9-D12, D14, D21, D24, D31 and D35. Histology and proteome profiling methods were utilised to understand whether GBM tissues could be maintained in the fluidics system for up to 12 days.

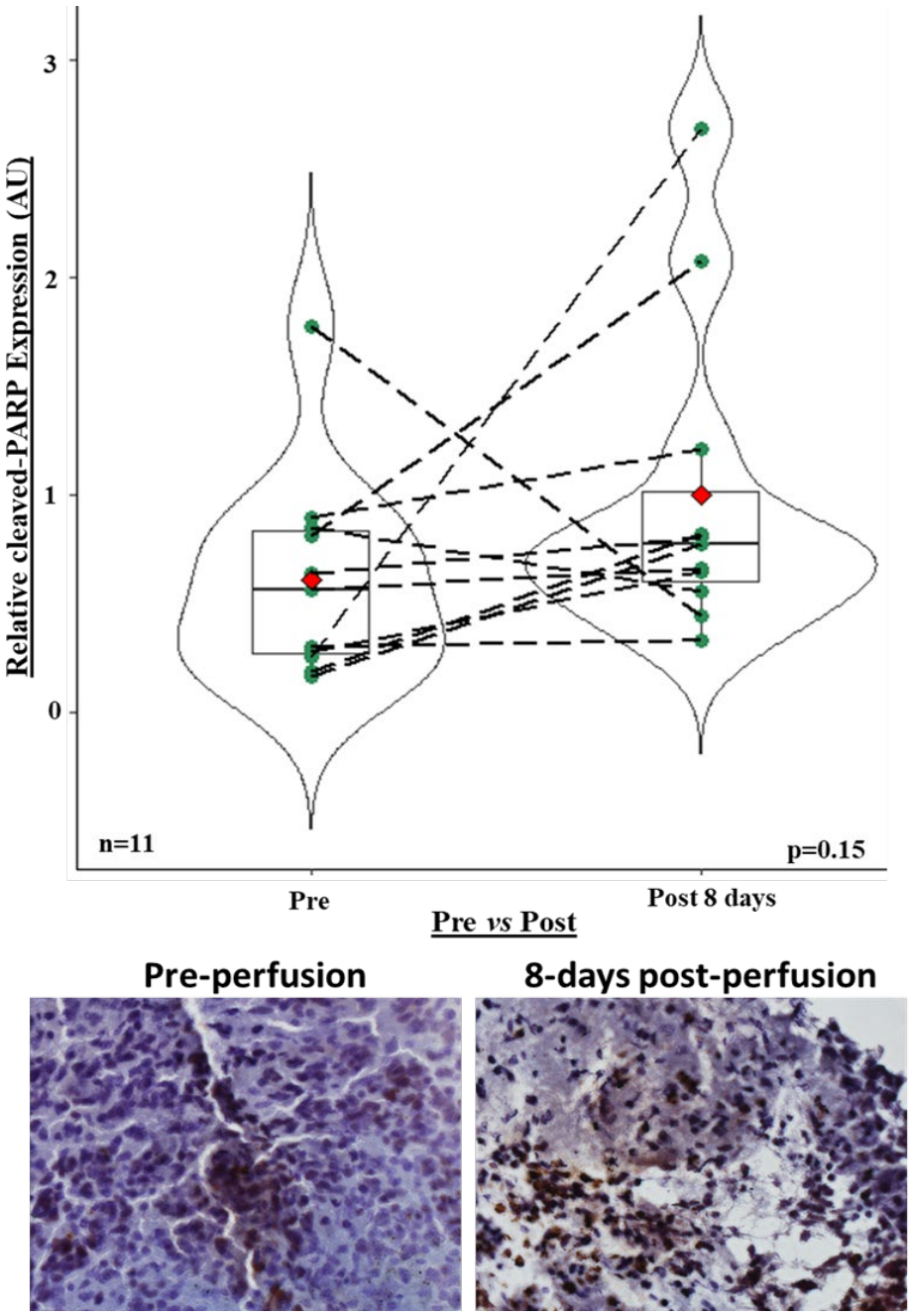

Figure 3.10.: Immunohistochemistry of* cleaved PARP *expression in GBM in pre- 8-day (n=11) representative images.

Samples used for this analysis were D3-D7, D8a, D9-D12, D14. Immunohistochemistry of GBM tissue pre- and 8-day post-perfusion with the apoptotic marker, cleaved PARP, normalised to post-perfusion values. Analysis was performed using R 4.1.2. with paired Mann-Whitney U test (w = 38, p = 0.151). Mean cleaved PARP *expression pre-perfusion was 0.61 ± 0.47 and 8-days post-perfusion was 1 ± 0.73. Dashed lines indicate paired patient samples. In the representative images, haematoxylin stains cell nuclei blue, whilst 2'2'-diaminobenzidine*

(DAB) stains cleaved PARP *expressing cells brown. Images at x40 magnification were taken on an Olympus IX71 inverted fluorescence microscope using CellSens software 1.18.*

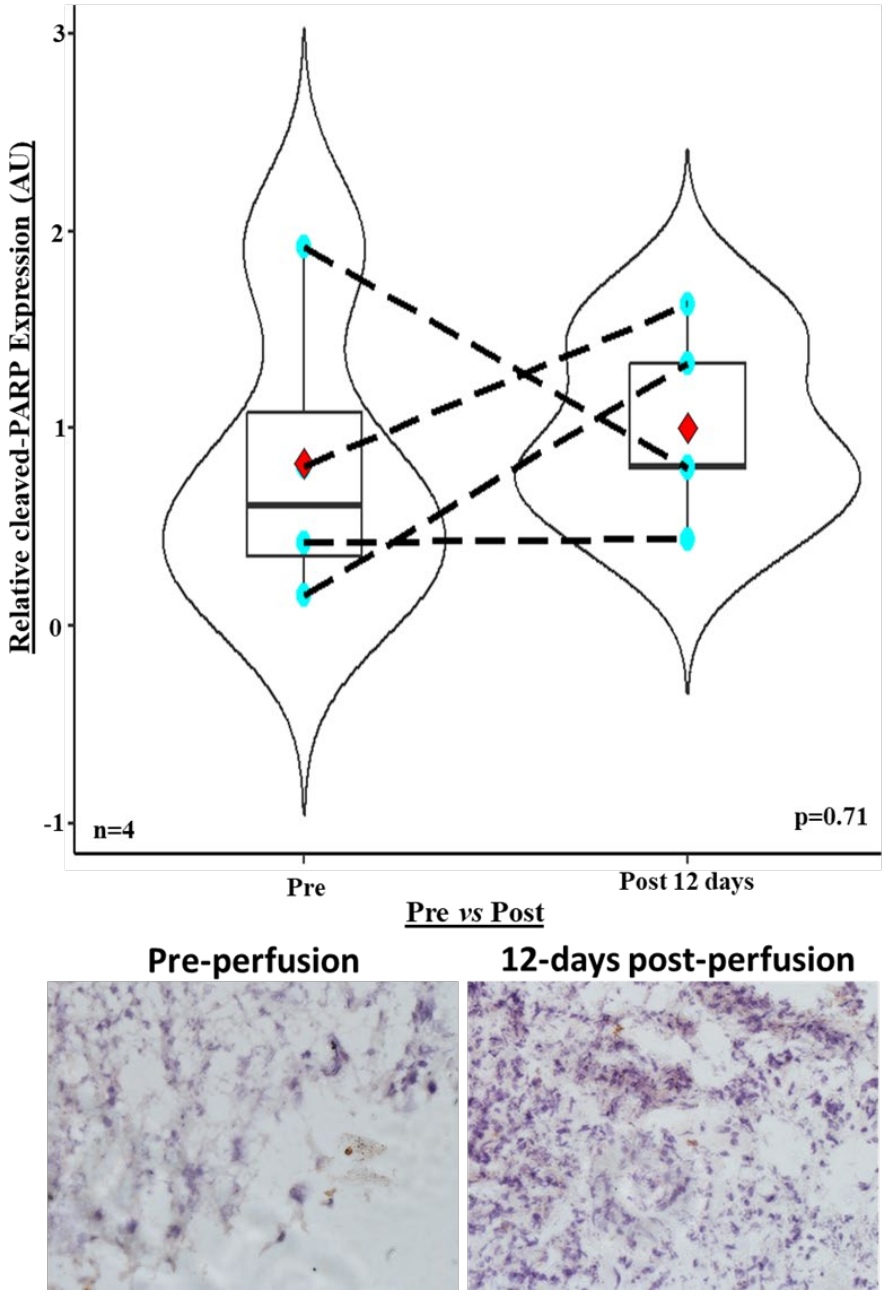

Figure 3.11.: ***Immunohistochemistry of* cleaved PARP *expression in GBM in pre-* and *12-day (n=4) post-perfused control (DMSO) tissue, with representative images.***

Samples used for this analysis were D21, D24, D31 and D35. Immunohistochemistry of GBM tissue pre- and post-perfusion with the apoptotic marker, cleaved PARP, normalised to post-perfusion values. Analysis was performed in R 4.1.2., using the paired Student's t test (t = -

0.40, df = 4.75, p-value = 0.71). Mean cleaved PARP *expression (red diamonds) pre-perfusion was 0.82 ± 0.78 and 12-days post-perfusion was 1 ± 0.48. In the representative images, haematoxylin stains cell nuclei blue, whilst 2'2'-diaminobenzidine (DAB) stains* cleaved PARP *expressing cells brown. Images at x40 magnification were taken on an Olympus IX71 inverted fluorescence microscope using CellSens software 1.18.*

No statistically significant increase in cleaved PARP expression was found between pre-perfused and post-perfused 8-, (Figure 3.10) or 12-day GBM control tissue (Figure 3.11). To corroborate this finding, TUNEL assays were attempted to determine cell viability in the tissue slides. TdT enzyme attaches fluorochrome fluorescein to 3'-hydroxyl termini of apoptotic DNA double strand breaks, allowing them to fluoresce green under the microscope and allow *in situ* cell death detection (Figure 3.12). Cell Profiler was used to automate counting of positive cells stained with fluorescein *vs* total cells stained with DAPI and a percentage cell viability calculated (Figure 3.12). TUNEL assays were performed for n=1 for sample D14 as optimisation. Images were taken of one slice of tissue per chip cell viability of each image calculated using Cell Profiler. Each image's viability data was then compiled with images from the same chip and any duplicate chips measured and into a tissue viability percentage per treatment.

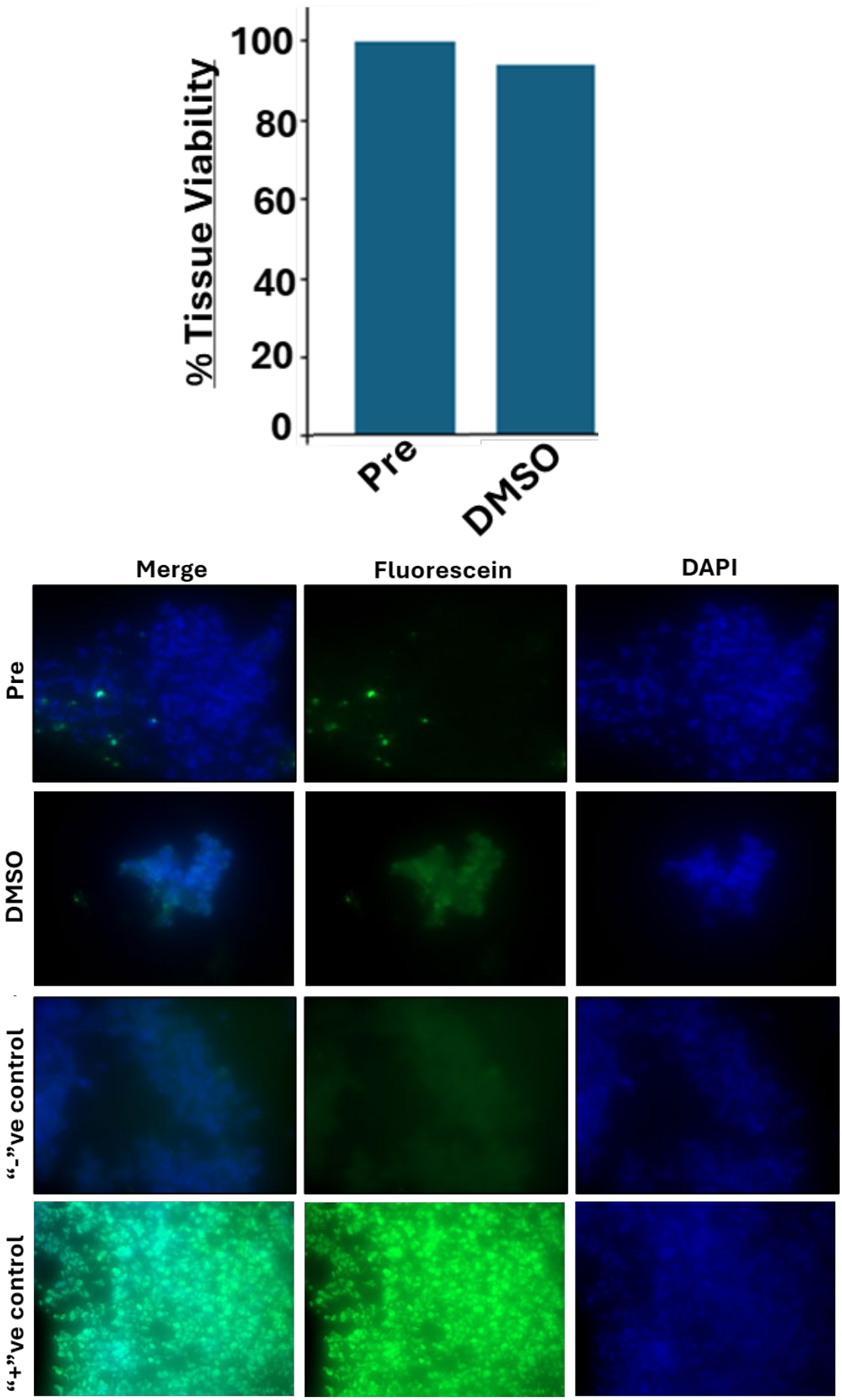
% Tissue Viability
100
80
60
40
20
0
Pre
DMSO
Merge
Fluorescein
DAPI
Pre
DMSO
"-"ve control
"+"ve control

Figure 3.12.: Percentage tissue viability of TUNEL assay images of D14 (n=1) pre-, vs 8-days post-perfusion, with representative images

TUNEL assay of GBM tissues from sample D14, pre-perfusion (99.9%) and 8-day post-perfused DMSO control (93.6%). Percentage tissue viability calculated through ratio of positive fluorescein labelled cells vs total number of DAPI stained cells."-" ve control was pre-perfused tissue treated with diluent only. "+" ve control was pre-perfused tissue which had been treated with DNAse. Images at x40 magnification were taken on an ***Olympus IX71 inverted fluorescence microscope*** *using CellSens software 1.18.*

Percentage cell viability determined from n=1 of sample D14 did show a small drop in cell viability between pre- and post-perfusion, consistent with the cleaved PARP expression data (Figure 3.10). It did not, however, decrease as much as anticipated and the pre-perfused tissue would not be expected to have remained entirely viable. This would be due to the tissue stress, mentioned previously, which would mean that some of the tissue at least would die between transport from the hospital to the lab, as well as the biological aspects of the tumour in itself, whereby it would be expected to have areas of cell death. The negative and positive controls worked well for the first TUNEL assay of this sample (Figure 3.12). No data analysis was performed on this data due to there being only one technical, or biological repeat available. More data would be required to ascertain whether this data is supportive of cleaved PARP expression pre- *vs* post-perfusion.

Annexin V was a second apoptotic marker that was employed to determine the level of cell death in GBM pre- *vs* post-perfused tissue. Immunohistochemistry was performed on the same pre- and 8-day post-perfused tissue samples as cleaved PARP, with the exception of D14 (Figure 3.13) (Appendix 5). The annexin V data indicated the same result as the cleaved PARP data, with a paired t-test showing no significant changes in apoptosis with time in the perfusion device (Figure 3.10).

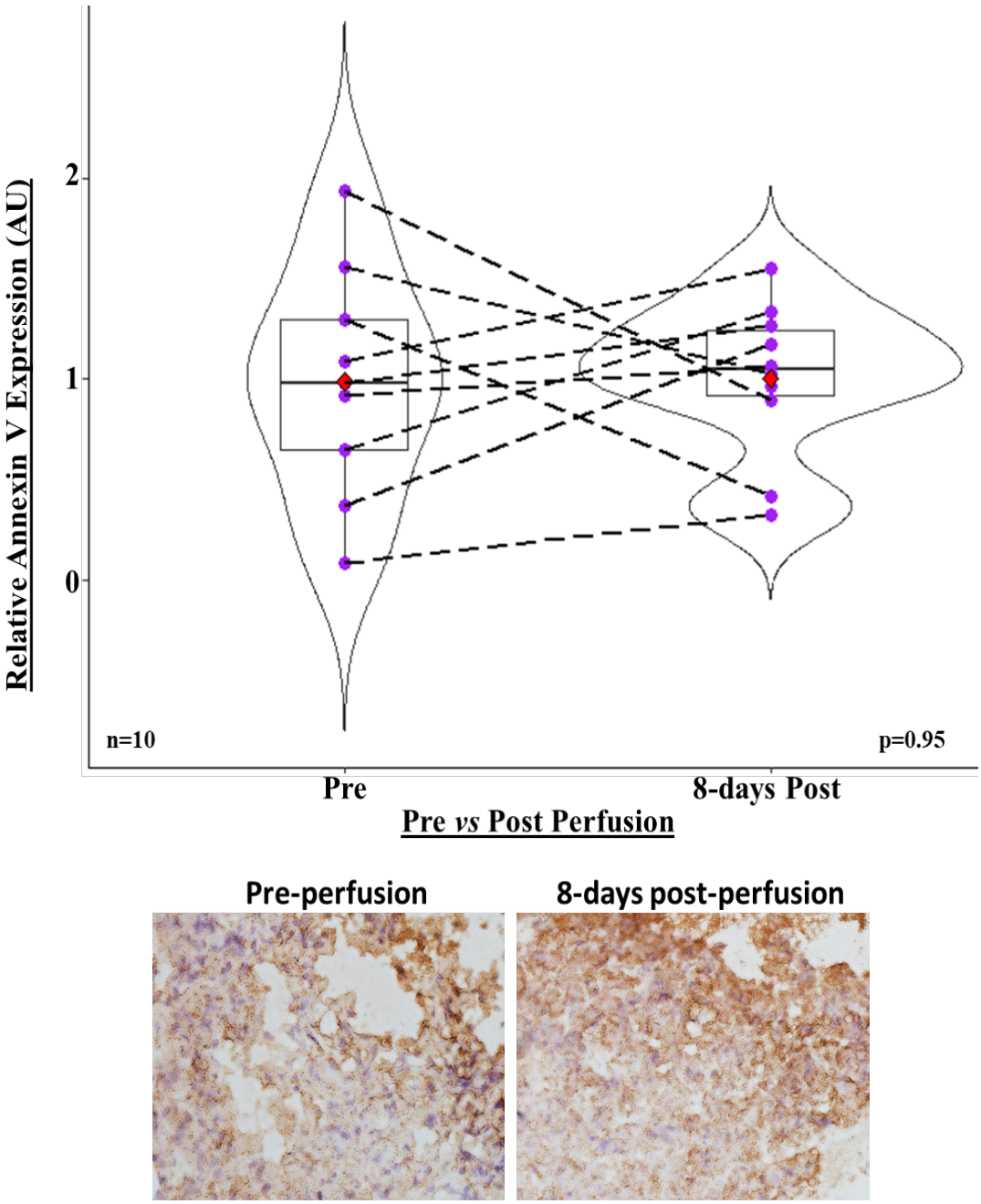

Figure 3.13.: Immunohistochemistry of Annexin V expression in GBM in pre- and 8-day (n=10) post-perfused control (DMSO) tissue, with representative images.

Samples used for this analysis were D3-D7, D8a and D9-D12. Immunohistochemistry of GBM tissue pre- and post-perfusion with the apoptotic marker, Annexin V, normalised to post-perfusion values. Analysis was performed in R 4.1.2., using the paired t.test function for comparison of medians (t = -0.064, df = 13.76, p = 0.95). Mean annexin V expression (red diamonds) pre-perfusion was 0.99 ± 0.58 and 8-day post-perfused control was 1 ± 0.39. Dashed lines indicate paired patient samples. In the representative images, haematoxylin

stains cell nuclei blue, whilst 2'2'-diaminobenzidine (DAB) stains cleaved PARP *expressing cells brown. Images at x40 magnification were taken on an Olympus IX71 inverted fluorescence microscope using CellSens software 1.18.*

3.3.3.5. *Effluent cytokine levels remain stable over 8 days of perfusion*

Patient samples used for cytokine analysis were: D7, D9-12, D14, D20-21, D24, D29-31. Proteome profiler kits (Roche) were used to determine the expression profiles of 105 cytokines and chemokines, released into the effluent of the microfluidics chips, from the GBM micro-biopsy tissue. Cytokine released in the effluent from DMSO control-treated GBM chips of the initial six samples, which was published in Barry *et al.*. (2023), was monitored over three time points of 48 hours, 96-hours, and 192-hours (Figure 3.14).

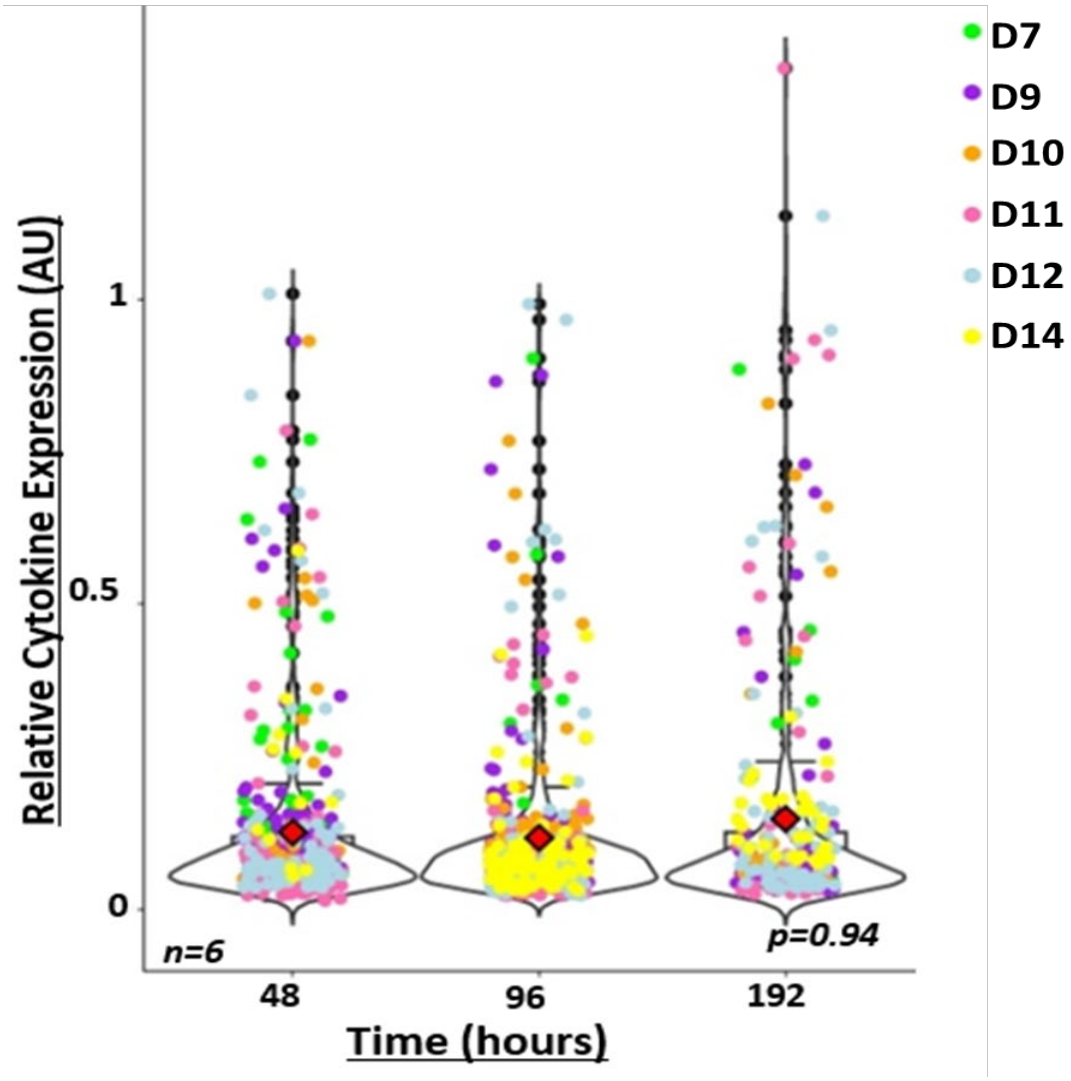

Figure 3.14.: Cytokine expression in effluent from GBM micro-biopsies treated with DMSO at 48-, 96- and 192-hours post-perfusion (n=6).

Cytokine expression in combined duplicate effluents of control samples D7, D9- D12 and D14 (n = 6) after 48, 96 and 192 hours in the perfusion device in arbitrary units (AU). Individual points represent each cytokine. Colours represent individual patient samples. Kruskal-Wallis test performed in R 4.1.2 (X2 = 0.13, df = 2, p-value = 0.94). *Published in Barryet al. (2023).*

Over all six samples and three time points used for this analysis, 63 of 105 cytokines, on average, were consistently detected and quantified in the DMSO-control effluents. No statistically significant changes in cytokine secretion profiles over time were found and this therefore supports the previous data that GBM tissues were maintained in a viable condition in the perfusion device (Figure 3.14). Exploratory analysis of the 12-day cytokine release data was also performed and analysed separately (Figure 3.15).

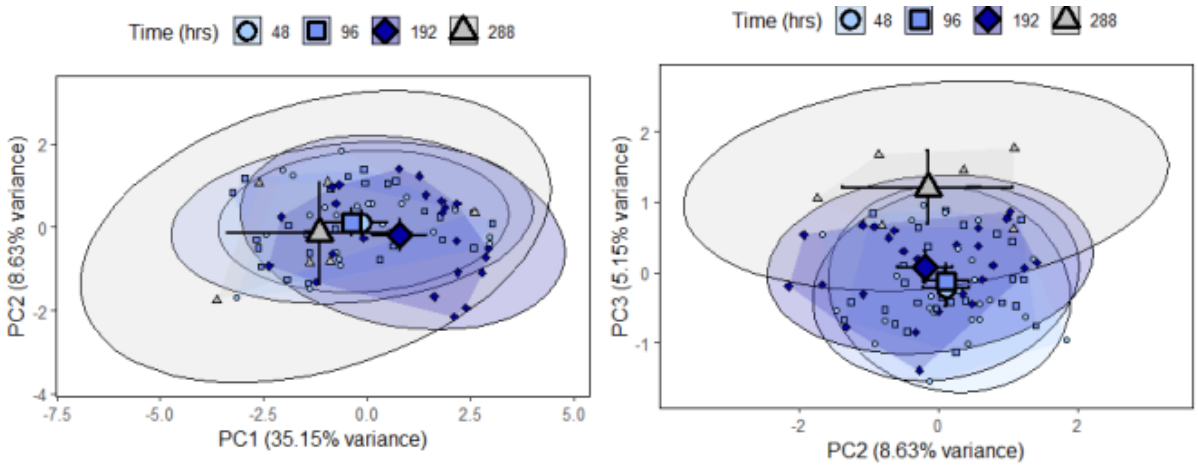

Figure 3.15.: PCA of covariate effects on all cytokines in PC2 and PC3 planes

Central shape indicates centroids with 95% confidence intervals with shaded polygons displaying maximum dispersion. Scattered shapes indicate individual data points.

This found that the cytokine profile at the 288-hour time point varied significantly from the previous time points, suggesting that cytokine profile is maintained up to 96 hours (48h *vs* 288h, F=2.26, df=1, p=0.030; 96h *vs* 288h, F=2.21, df=1, p=0.042), changes at 192 hours (192h

vs 288h, F=3.62, df=1, p=0.0049) and changes further which could not be explained by the dispersion of the data, at 288 hours (F=0.50, p=0.69).

The most abundant and frequently expressed cytokines over all samples and across all time points were IL8, Serpin E1, Osteopontin, C3L1, VEGF, MMP-9, macrophage migration inhibitory factor (MIF), monocyte chemoattractant protein-1 (MCP1), insulin-like growth factor binding protein-2 (IGFBP-2) and extracellular matrix metalloproteinase inducer (EMMPRIN).

3.3.4. GSK3368715 causes apoptosis in GBM *ex vivo*

To determine whether GSK3368715 causes apoptosis in GBM patient samples in the fluidics system, media was treated with either 1μM GSK3368715, or DMSO-control. Following the microfluidics protocol, syringes containing fresh media and PRMT inhibitor were changed after 96 hours. At least two chips per sample, per treatment were treated with either DMSO or GSK3368715 to account for intra-tumour heterogeneity and for technical replicates. GBM tissue was then removed from the chip after 8-days and fresh frozen in OCT, indirectly *via* methylbutane, pre-chilled in liquid nitrogen. Tissue was sliced into 8 μm thick sections using a cryostat onto poly-L-lysine-coated slides and stained using an antibody against cleaved PARP using IHC. An index value of positive, cleaved PARP expressing cells and total cells was collated for each image and this value divided by the average DMSO-control index for each of the eleven patients to give a delta value which showed cleaved PARP expression index, relative to the post-chip control (Figure 3.16). The 12-day post-perfused samples and pre-chip counterparts were FFPE (Figure 3.17).

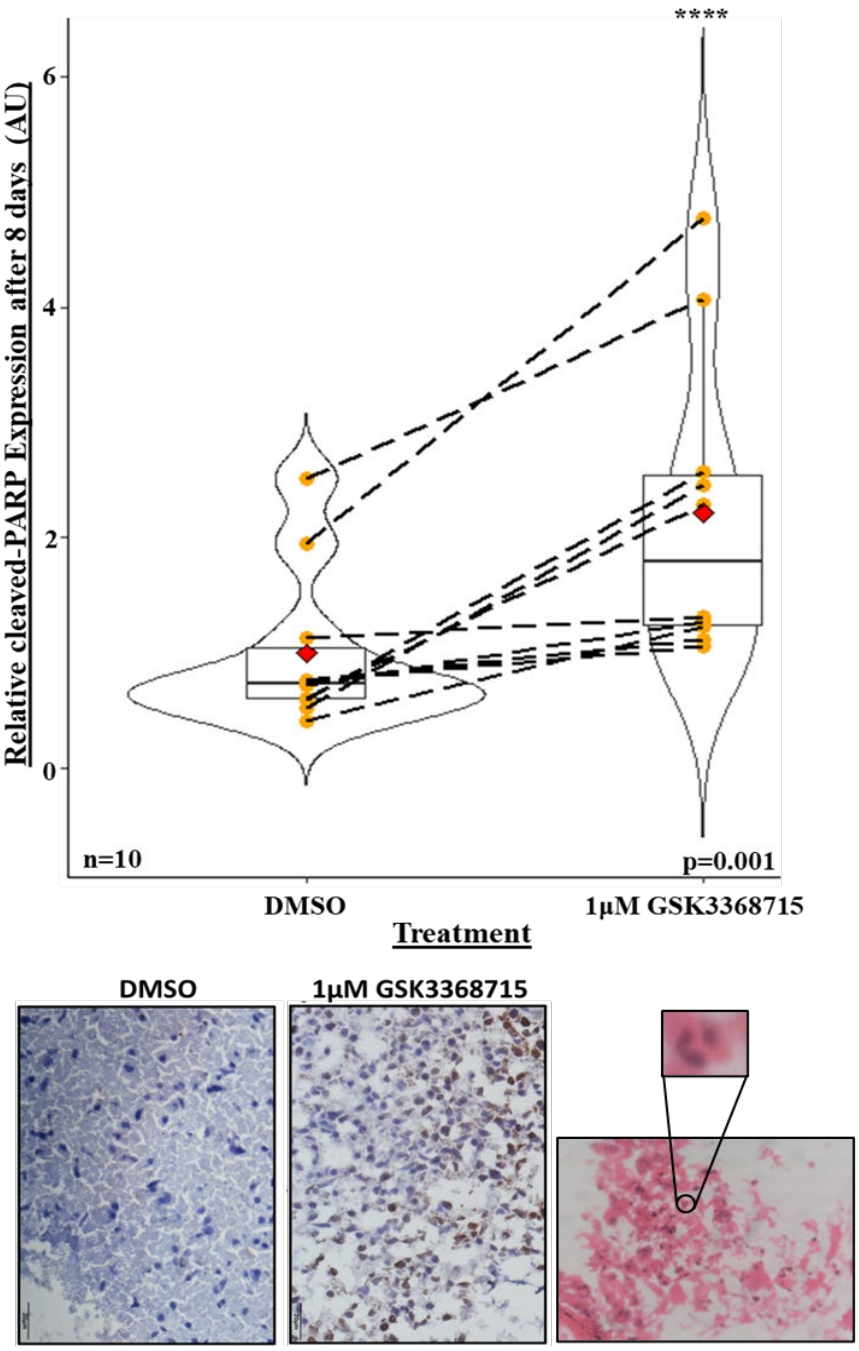

Figure 3.16.: Analysis of cleaved PARP IHC in GBM treated with 1 µM GSK3368715, vs DMSO control at 8-days post-perfusion (n=10), with representative images [inset: apoptotic bodies].

Immunohistochemistry of GBM tissue pre- and post-perfusion with the apoptotic marker, cleaved PARP, normalised to post-perfusion values. Analysis was performed using R 4.1.2., using the paired Student's t test ($t = -4.52$, $df = 9$, $p = 0.001$). Mean cleaved PARP *expression (red diamonds) of the DMSO control was 1 ± 0.61; 8-day treatment with 1µM GSK3368715*

was 2.17 ± 1.10. Dashed lines indicate paired patient samples. In the representative images, haematoxylin stains cell nuclei blue, whilst 2'2'-diaminobenzidine (DAB) stains cleaved PARP *expressing cells brown. There is a noticeable increase in DAB-positive,* cleaved PARP *expressing cells in the GSK3368715-treated cells. H&E staining shows 8-day post-perfused 1μM-GSK3368715-treated tissue, with the inset highlighting apoptotic bodies. Images at x40 magnification were taken on an Olympus IX71 inverted fluorescence microscope using CellSens software 1.18.*

Immunohistochemistry of cleaved PARP in 8-day post-perfused tissue treated with the 1μM GSK3368715 indicated an overall significant increase in cleaved PARP expression and therefore apoptosis, over the DMSO control (Figure 3.16) (Appendix 4). The 8-day post-perfused tissue increased 2.17-fold over the DMSO control. This 8-day perfusion tissue was published in *Lab on a chip* in 2023 (Barry *et al.* 2023). The representative images also depict paired samples of the tissue which were stained for cleaved PARP, post-perfusion (Figure 3.16). The 8-day PRMT inhibitor-treated tissue appears to have much more brown positive staining, and therefore cleaved PARP positive, staining than the DMSO control. The H&E image of 8-day post-perfused 1μM GSK3368715 also highlight a region of pyknosis and karyorrhexis in the tissue, whereby DNA can be seen to have condensed into apoptotic bodies (Figure 3.16), supporting this data.

As with the pre-perfused *vs* 8-day post-perfused DMSO control, IHC with annexin V was utilised to confirm the findings of the cleaved PARP data in 8-day perfused tissue samples. The same samples were used as for the cleaved PARP expression analysis, with the exception of D14 (Figure 3.17) (Appendix 5).

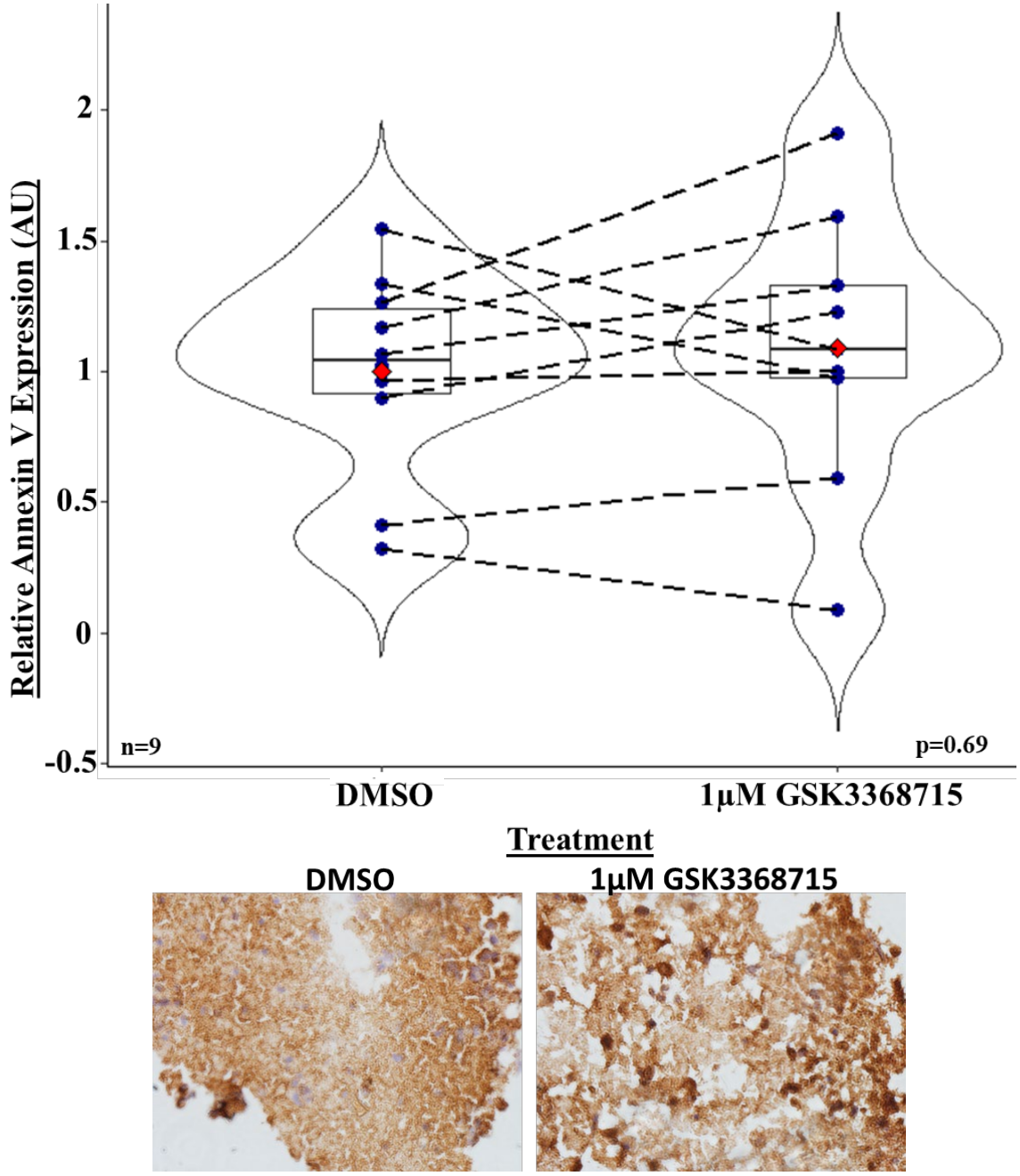

Figure 3.17.: Immunohistochemistry of Annexin V expression in GBM in 8-day post-perfused control (DMSO) tissue and paired 1µM GSK3368715-treated tissue (n=9) with representative images.

Immunohistochemistry of GBM tissue treated with the DMSO control and 1µM GSK3368715 with the apoptotic marker, Annexin V, normalised to post-perfusion values. Analysis was performed using R 4.1.2., using the paired t.test function for comparison of medians (t = -0.41,

df = 14.42, p = 0.69). Mean annexin V expression (red diamonds) pre-perfusion was 1 ± 0.39 and 8-day post-perfused control was 1.09 ± 0.53. Dashed lines indicate paired patient samples. In the representative images, haematoxylin stains cell nuclei blue, whilst 2'2'-diaminobenzidine (DAB) stains cleaved PARP *expressing cells brown. Images at x40 magnification were taken on an Olympus IX71 inverted fluorescence microscope using CellSens software 1.18.*

No significant changes in annexin V expression were seen between the DMSO control and the GSK3368715-treated tissues, as well as very little mean increase in annexin V overall. Although six of the nine samples did show a marginal increase in apoptosis in the treated tissues, there was only a 9% increase in the mean. Annexin V was a difficult antibody from which to quantify staining, which could be reflected in the data shown (Figure 3.17).

TUNEL assays were also performed for n=1 on the 8-day post-perfused DMSO control and *1μM GSK3368715*-treated tissues of D14 (Figures 3.18). Percentage cell viability was calculated as mentioned previously. No data analysis was performed on this data due to there being only one technical, or biological repeat available.

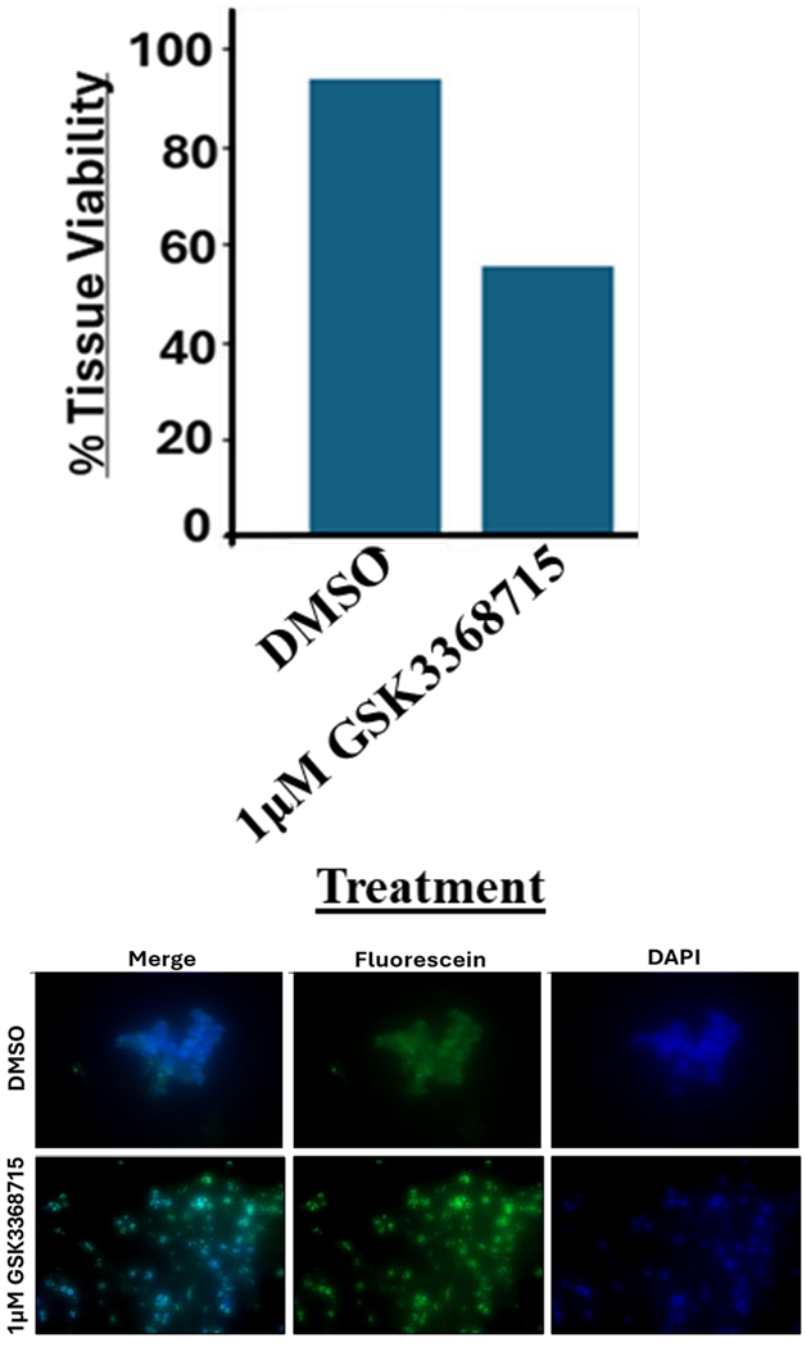

Figure 3.18.: Percentage tissue viability of TUNEL assay images of D14 (n=1) 8-days post-perfusion, DMSO-control and 10µM TMZ and 1µM GSK3368715 + 10µM TMZ-treated, with representative images

TUNEL assay of GBM tissues from sample D14, 8-day post-perfused DMSO control (93.6%) and treated with 10μM TMZ (63.0%) and 1μM GSK3368715 + 10μM TMZ (69.7%). Percentage tissue viability calculated through ratio of positive fluorescein labelled cells vs *total number of DAPI stained cells. Images at x40 magnification were taken on an Olympus IX71 inverted fluorescence microscope using CellSens software 1.18.*

Percentage cell viability determined from n=1 of sample D14 indicated a possible drop in cell viability in GSK3368715-treated tissues (Figure 3.18) and the negative and positive controls worked well for the first TUNEL assay of this sample (Figure 3.12). More data would be required to ascertain whether this data is supportive of cleaved PARP expression and increased apoptosis in GSK3368715-treated GBM tissue, although the preliminary data is potentially positive. Subsequent samples were not able to produce clear images due to technical issues and the assay then began to produce inconsistent results. Several techniques were tried to rectify the issue, including trying with fresh *vs* FFPE tissue, making fresh reagents, and trying different positive controls, such as UV exposure. TUNEL assays therefore remained as preliminary data and alternative avenues of data support were explored.

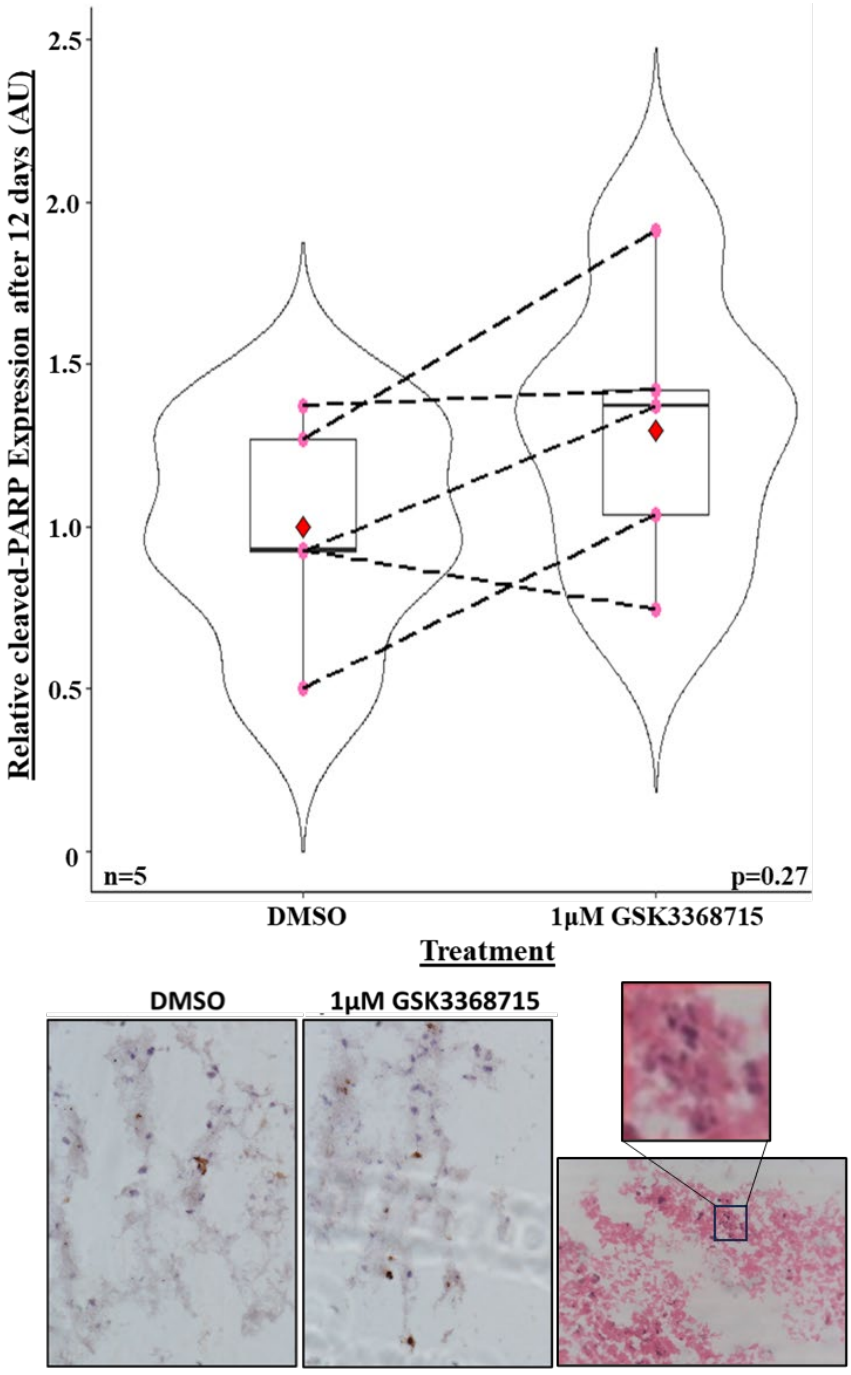

Figure 3.19.: Analysis of IHC in GBM treated with 1 µM GSK3368715, vs DMSO control at 12-days post-perfusion (n=5), with representative images [inset: apoptotic bodies].

Immunohistochemistry of GBM tissue pre- and post-perfusion with the apoptotic marker, cleaved PARP, normalised to post-perfusion values. Analysis was performed using R 4.1.2., using the paired Student's t test for comparison of medians (t = -1.19, df = 7.56, p-value = 0.27). Mean cleaved PARP *expression (red diamonds) of the DMSO control was 1 ± 0.48 and*

12-day treatment with 1μM GSK3368715 was 1.10 ± 0.41. Dashed lines indicate paired patient samples. In the representative images, haematoxylin stains cell nuclei blue, whilst 2'2'-diaminobenzidine (DAB) stains cleaved PARP *expressing cells brown. Images at x40 magnification were taken on an Olympus IX71 inverted fluorescence microscope using CellSens software 1.18.*

Immunohistochemistry of cleaved PARP in 12-day post-perfused tissue treated with the 1μM GSK3368715 indicated no significant increase in cleaved PARP expression and therefore apoptosis, over the DMSO control (Figure 3.19) (Appendix 6). This could potentially be down to the lack of samples, or the quality of the tissue. The representative images support this and show no increase in DAB staining (Figure 3.19).

3.3.5. GSK3368715 shows no synergy with other PRMT inhibitors, or TMZ

Several chips were set up with 1μM GSK3368715 in combination with other drugs, including: 1μM type I PRMT inhibitor Furamidine, 1μM type II PRMT inhibitor GSK591, both PRMT inhibitors, or 10 μM TMZ. It is imperative that any potential novel therapies are tested in conjunction with TMZ, as the current gold standard therapy, and not just as a benchmark to measure drug success. It is likely that any therapy will be utilised alongside TMZ, or as a second line treatment. This is to ensure that novel therapies do not have any detrimental effects on the therapeutic effect of TMZ and *vice versa* which may cause harm to the patient during clinical trials and eventual treatment. During the 8-12 days in the perfusion device, effluent was collected from each chip and a LDH assay performed (Figure 3.20).

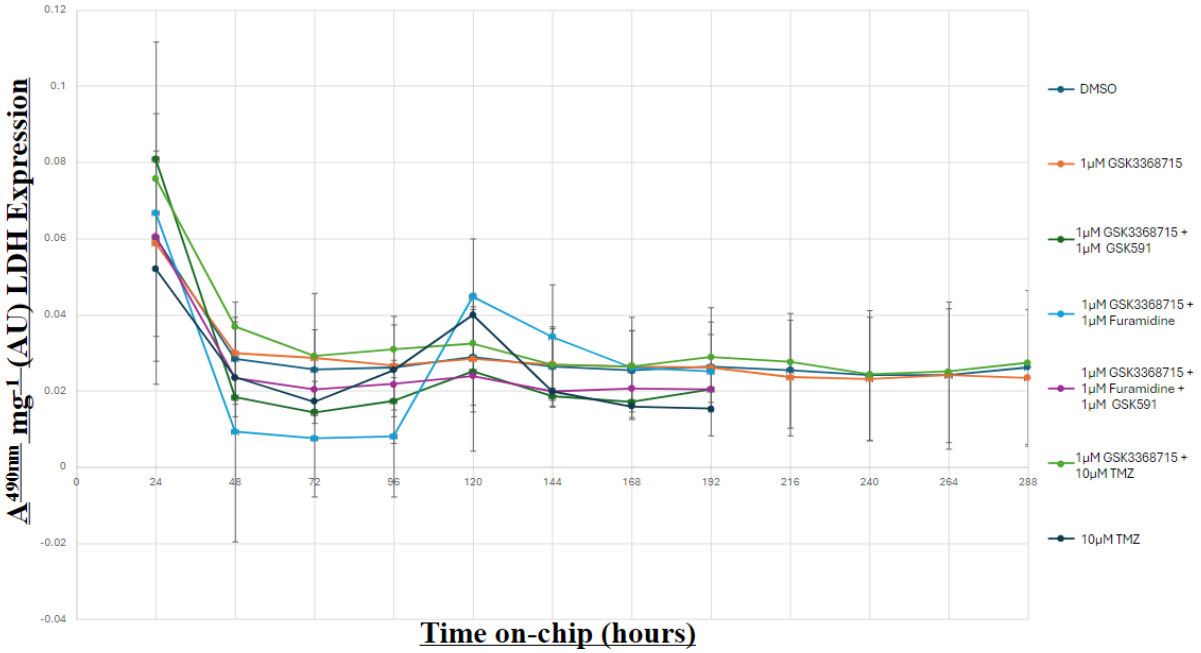

Figure 3.20.: Lactate dehydrogenase (LDH) assays of GBM tissue effluent treated with 1µM GSK3368715 in combination with 1µM type I PRMT inhibitor Furamidine, 1µM type II inhibitor GSK591 and 10µM temozolomide (TMZ), as well as 10µM TMZ alone.

Lactate dehydrogenase (LDH) activity was measured in the effluent, collected every 24 hours over 8 (n=2, D3 and D37) and 12 days (n=5, D21, D24, D31, D35 and D36), ***via*** *absorbance at 490 nm ($\mathbf{A}^{490nm}$) D3, D37, see Table 4.1) for all treatments. Fluctuations correlated with syringe refilling with medium at day 4. GLM was performed using R 4.2.0 which indicated no significant changes in LDH expression between treatments at individual timepoints. Error bars indicate standard deviation.*

As expected, all biopsies begin to release high levels of LDH, between 0.052±0.001 and 0.064±0.023, in the first 48 hours of being paced into the perfusion device, seen previously (Figure 3.5 and Figure 3.6). This then decreases to between 0.029±0.015 and 0.007±0.00 at 72 hours, with fluctuations in most of the chips, corresponding with the medium change at day 4, which then generally returns back to baseline for the remainder of the time on chip. Treatment with 1µM GSK3368715 + 1µM Furamidine, however, appears to increase at 120 hours to 0.033±0.016, with the syringe change and then decreases to around 0.026±0.00 after 168 hours, which is a higher level than the initial baseline of 0.0008±0.00 at 96 hours (Figure 3.20). This could indicate that the combination of these drugs is inducing cellular stress and therefore the tissues are releasing LDH.

After 8 days on-chip, the treated tissues were removed and fresh frozen in OCT, before being sliced using a cryostat and stained immunohistochemically stained for cleaved PARP, to determine levels of apoptosis between the post-chip DMSO control and GSK3368715-treated GBM. Cells in each image, taken over a large number of images which aimed to capture the broader spectrum of cleaved PARP expression over the entire geography of the GBM tissue, were counted and a cleaved PARP index determined, which was then divided by the average post-chip control data across several GBM patient samples (Figure 3.21).

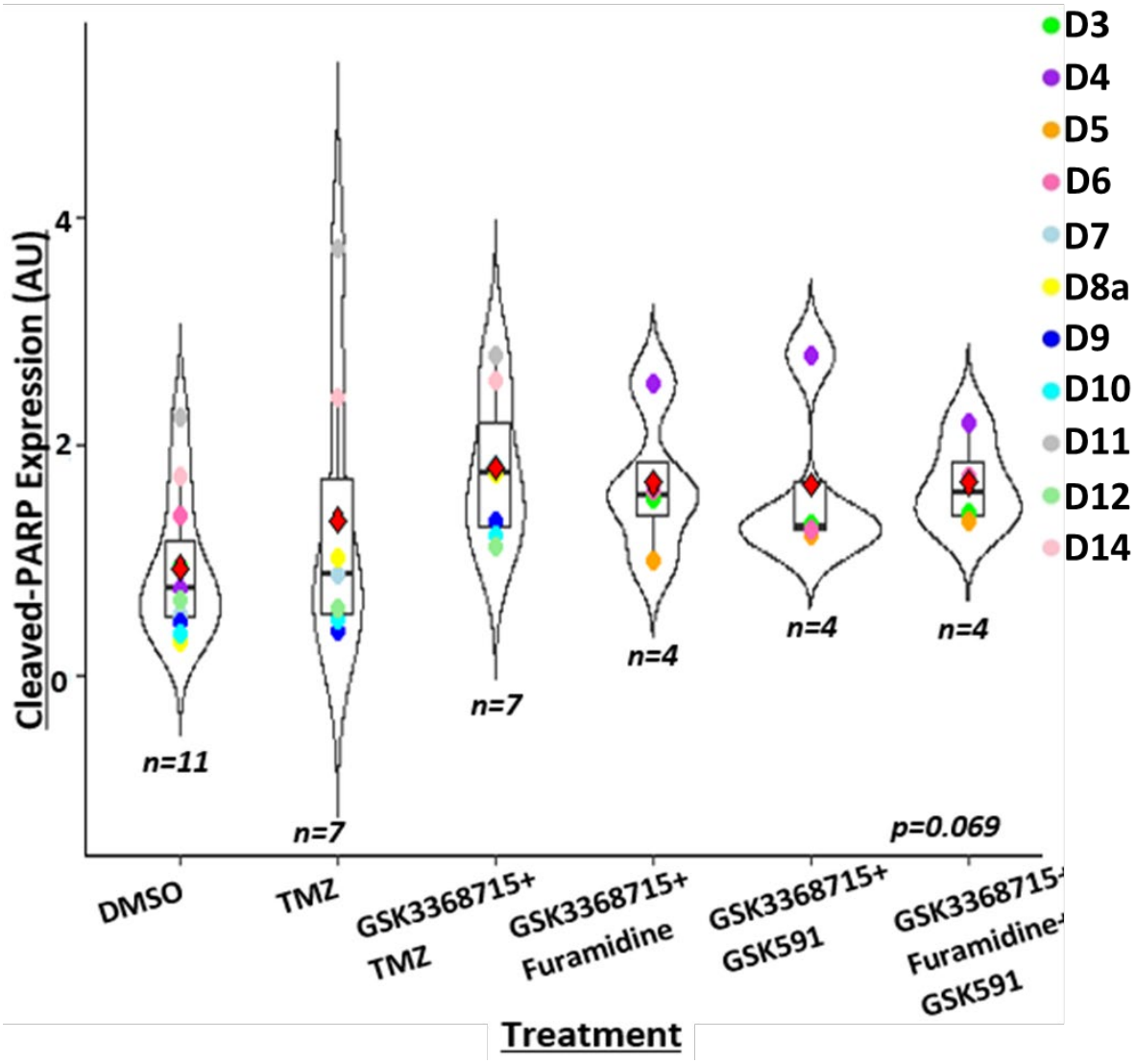
D3
D4
D5
D6
D7
D8a
D9
D10
D11
D12
D14
Cleaved-PARP Expression (AU)
4
2
0
n=11
n=7
n=7
n=4
n=4
n=4
p=0.069
DMSO
TMZ
GSK3368715+ TMZ
GSK3368715+ Furamidine
GSK3368715+ GSK591
GSK3368715+ Furamidine+ GSK591
Treatment

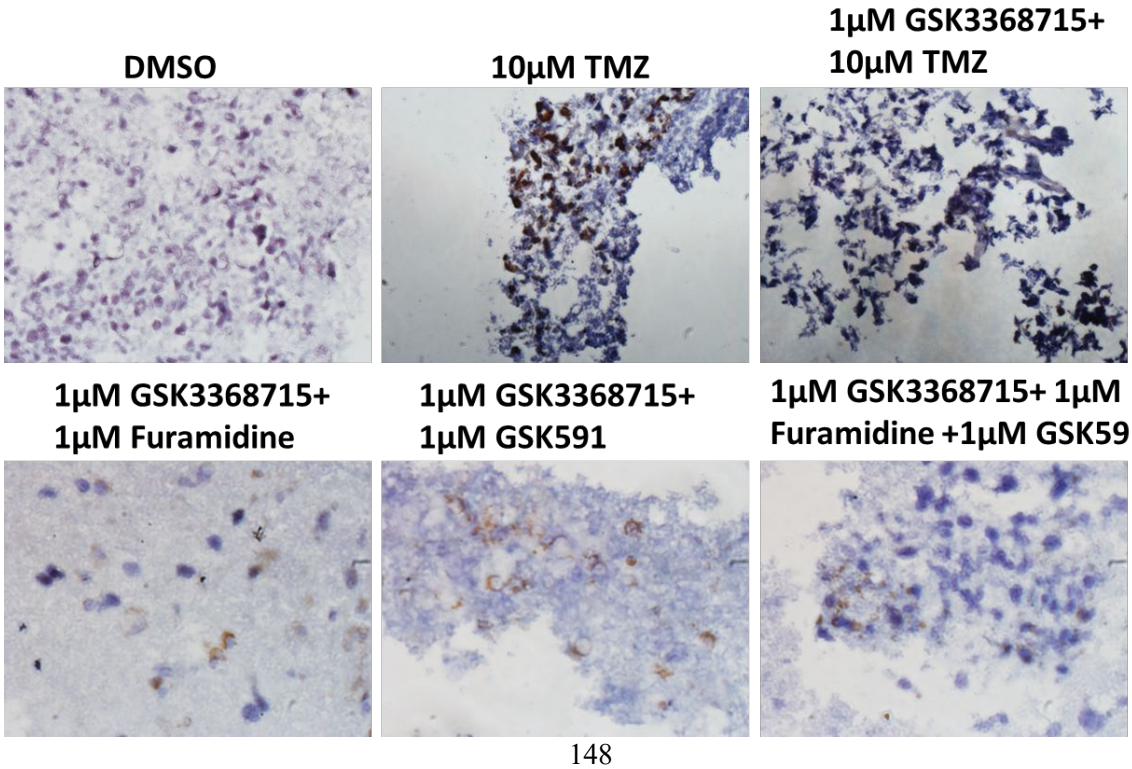
DMSO
10μM TMZ
1μM GSK3368715+ 10μM TMZ
1μM GSK3368715+ 1μM Furamidine
1μM GSK3368715+ 1μM GSK591
1μM GSK3368715+ 1μM Furamidine +1μM GSK591

Figure 3.21.: Immunohistochemistry analysis of cleaved PARP in GBM tissues treated with 1µM GSK3368715 in combination with 1µM type I PRMT inhibitor Furamidine, 1µM type II inhibitor GSK591 and 10µM temozolomide (TMZ), as well as 10µM TMZ alone, with representative images.

Immunohistochemistry of GBM tissue 8-days post-perfusion treated with the DMSO control (1 ± 0.61), 10µM TMZ (1.60 ±1.58), 1µM GSK3368715 + 1µM TMZ (2.09 ±0.82), 1µM GSK3368715 + 1µM Furamidine (1.67 ±0.64), 1µM GSK3368715 + 1µM GSK591 (1.65±0.77) and 1µM GSK3368715 + 1µM Furamidine + 1µM GSK591 (1.68±0.38) with the apoptotic marker, cleaved PARP*, normalised to post-perfusion DMSO values. Analysis was performed using R 4.1.2., using Kruskal-Wallis test (X^2 = -0.41, df = 14,42, p = 0.69). Mean* cleaved PARP *expression (red diamonds) shown in brackets. Dashed lines indicate paired patient samples. In the representative images, haematoxylin stains cell nuclei blue, whilst 2'2'-diaminobenzidine (DAB) stains* cleaved PARP *expressing cells brown. Images at x40 magnification were taken on an Olympus IX71 inverted fluorescence microscope using CellSens software 1.18.*

Despite the statistical threshold of $p<0.05$ not being met when investigating the synergy between GSK3368715, TMZ and other PRMT inhibitors Furamidine and GSK591, it is tempting to suggest that there was an apparent increase in apoptosis in treated samples. GSK3368715 appears to increase cell death when in combination with TMZ, as well as other PRMT inhibitors (Figure 3.21). Overall, despite the visual increase in cleaved PARP expression from the DMSO control, there appeared to be no significant increase in apoptosis.

TUNEL assays were also performed for n=1 on the 8-day post-perfused DMSO control and *10µM TMZ* and *1µM GSK3368715 + 10µM TMZ*-treated tissues of D14 (Figures 3.22). Percentage cell viability was calculated as mentioned previously and indicated some decrease in cell viability.

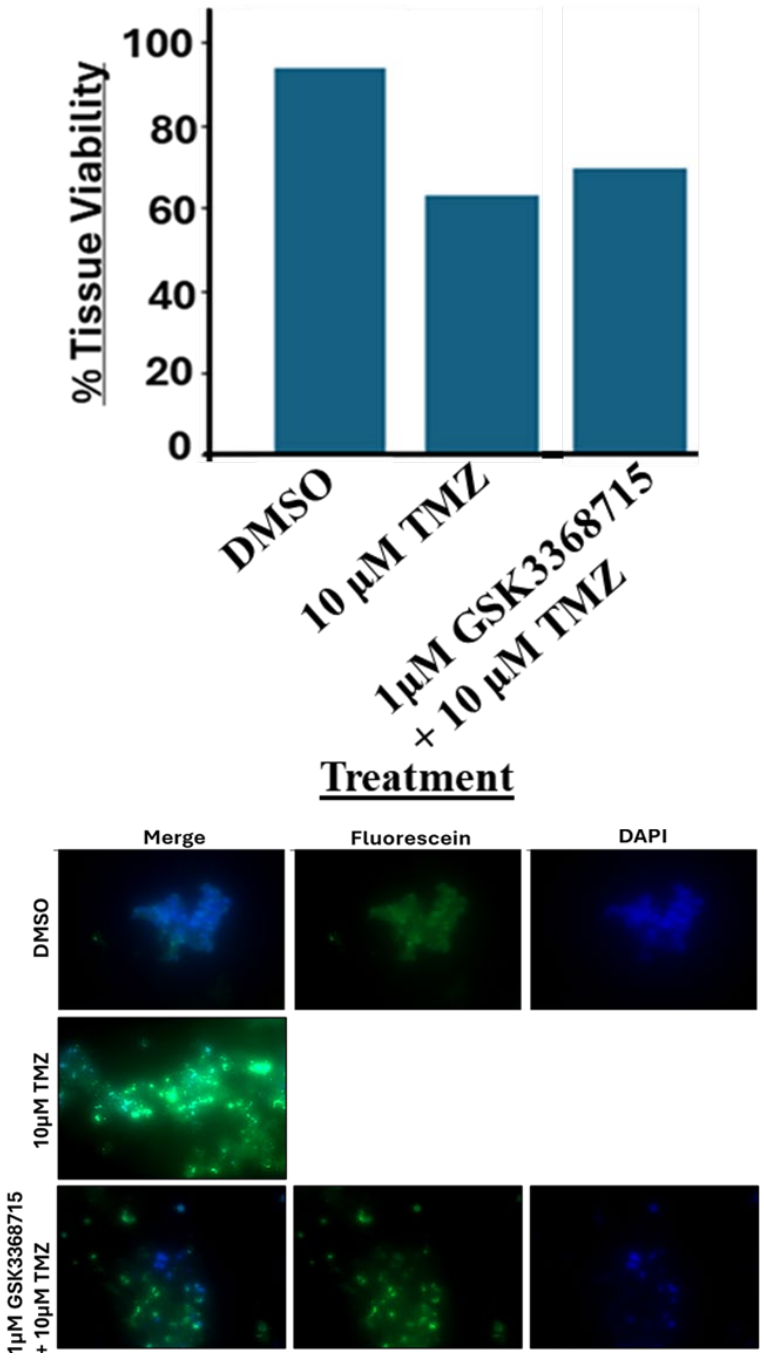

Figure 3.22.: Percentage tissue viability of TUNEL assay images of D14 (n=1) 8-days post-perfusion, DMSO-control and 10µM TMZ and 1µM GSK3368715 + 10µM TMZ-treated, with representative images

TUNEL assay of GBM tissues from sample D14, 8-day post-perfused DMSO control (93.6%) and treated with 10µM TMZ (63.0%) and 1µM GSK3368715 + 10µM TMZ (69.7%). Percentage tissue viability calculated through ratio of positive fluorescein labelled cells vs

total number of DAPI stained cells. Images at x40 magnification were taken on an Olympus IX71 inverted fluorescence microscope using CellSens software 1.18.

No data analysis was performed on this data due to there being only one technical, or biological repeat available. Due to the lack of significant changes in LDH expression (Figure 3.20), cleaved PARP (Figure 3.21) expression and limited TUNEL assay data (Figure 3.22), no synergy between GSK3368715 and any combination of PRMT inhibitors, or TMZ.

An observation made throughout the process of IHC for cleaved PARP and annexin V was the clustering of apoptotic cells throughout pre-perfused and post-perfused DMSO control tissue (Figure 3.23). Although the was also some clustered apoptotic cells in treated tissue, these cells appeared to be more dispersed throughout the tissue.

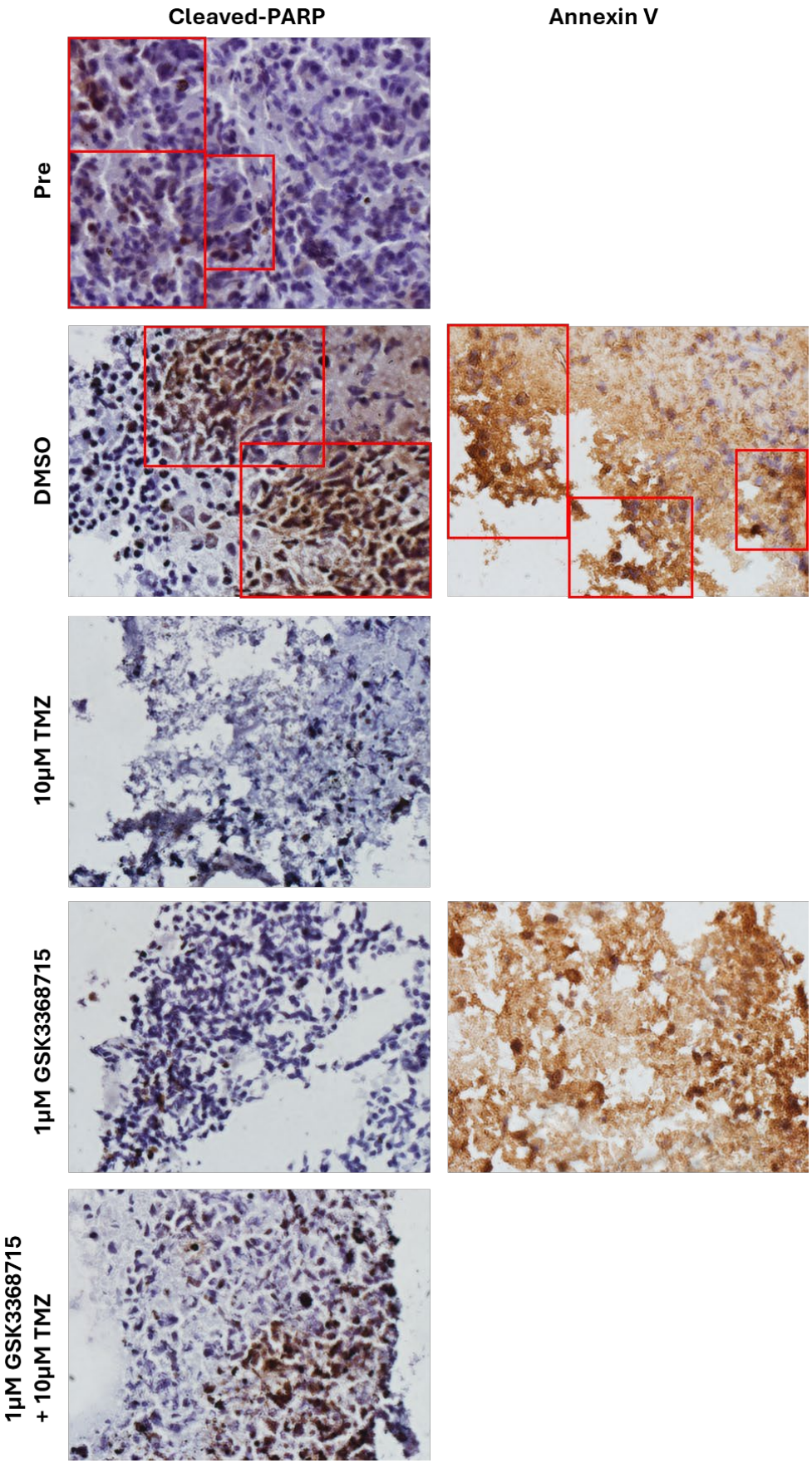
Cleaved-PARP
Annexin V
Pre
DMSO
10μM TMZ
1μM GSK3368715
1μM GSK3368715
+ 10μM TMZ

Figure 3.23.: Representative images showing clustering of apoptotic markers in GBM

Images of sample D14 indicating clustering of cleaved PARP *and annexin V apoptotic markers (indicated by red squares) in pre- and post-perfused DMSO control tissue. 10μM TMZ, 1μM GSK3368715 and 1μM GSK3368715 + 10μM TMZ-treated tissues show more dispersal of apoptosis. Haematoxylin stains cell nuclei blue, whilst 2'2'-diaminobenzidine (DAB) stains* cleaved PARP *expressing cells brown. Images at x40 magnification were taken on an Olympus IX71 inverted fluorescence microscope using CellSens software 1.18.*

3.3.6. Clinical Impact of GSK3368715 treatment on GBM on chip

Eighteen patient biopsies were utilised in this chapter for various experiments, of which 5 survived until the end of data collection. Of the eighteen patients, fifteen had confirmed primary GBM and four had recurrence (including patient D8, from whom we received both biopsies), with IDH wildtype. GBM occurred on the right side of the brain in eleven patients and the left in 6. GBM also appeared across four main lobes of the brain: one sixth of patients had GBM in the parietal lobe, 22.2% frontal, one third temporal and one ninth in each the occipital, parieto-occipital and parieto-temporal lobes. Twelve patients were tested and found negative for 1p/19q codeletion; nine tested positive for MGMT promoter methylation, 8 were negative and 1 was equivocal. All patients that were tested for EGFR amplification, ATRX and BRAF mutation were found to be wildtype. Four out of seven tested patients had TERT promoter mutation and 44.4% of patients were noted to have necrosis within the GBM tissue. CDKN2A mutation appeared in two thirds of tested patients, TP53 mutation in the one patient tested and PTEN mutation in one of the two patients tested (Table 3.1).

Table 3.1.: Clinical Data

Patient	Sex	Age	Primary vs Recurrent	Location	IDH	1p/19Q	MGMT	EGFR	TERT	ATRX	Necrosis	BRAF	CDKN2A	TP53	PTEN	Surgery-Death (days)
D2	M	46	Recurrent	right parietal	-	-	-		+			-		+		199
D3	M	67	Primary	left parietal	-		+			-						833
D4	M	58	Primary	left parieto-occipital	-	-	+		+	-		-				16
D5	F	70	Primary	left temporal	-	-	+		-	-		-				490
D6	F	57	Primary	left frontal	-	-	+	-	-	-		-	-		-	Alive
D7	M	56	Primary	right temporal	-	-	-		+	-	+		+		+	572
D8a	M	65	Primary	left temporal	-	-	=			-	++					683
D9	M	75	Primary	left parietal	-	-	+				+					120
D10	M	67	Recurrent	parieto-temporal	-	-	-			-	++					76
D11	F	50	Primary	right parieto-temporal			-		+	-	++	-				Alive
D12	M	71	Primary	right frontal	-	-	-			-	++					133
D14	M	72	Recurrent	right parieto-occipital	-	-	-			-	+					234
D21	F	73	Primary	right occipital	-		+			-						44
D24	M	67	Primary	right occipital	-	-	+		-	-		-	+			Alive
D31	M	76	Primary	right frontal	-		+			-						Alive
D8b	M	67	Recurrent	left temporal	-						++					263
D35	M	63	Primary	right temporal	-		+			-						63
D36	M	69	Primary	right temporal	-		-							-		Alive
D37	M	74	Primary	right frontal	-		-			-						245

General linear modelling of this data was undertaken to understand whether any interactions between the clinical aspects of the data affected the variation on both LDH release and apoptotic marker expression data. The variables explored were: treatment, time on chip, sex, age, primary *vs* recurrent, tumour location, MGMT promoter methylation status, TERT mutation and CDKN2A and PTEN prevalence. In the case of LDH analysis, treatment2 was added, as a component of treatment and time. CDKN2A and PTEN were incorporated within the same covariate as their presence coincided with one another in the patient samples tested. GLMs without interactions were fitted to identify the best model, using the 'glmulti' package in R. Akaike criterion (AICc) weighting was assessed to determine which variables were the most important contributing factors to variation in LDH release, cleaved PARP and Annexin V expression.

Through a search of models which may explain the variation in LDH, the top twelve were within 2 AICc of the top model of -1596.668, which accounted for 6.03% of the variation. The most frequently occurring model-averaged importance of terms included treatment2, location and time. The final model therefore included these three terms. The coefficients suggested that significant differences were identified in the following components of the treatment2 covariate: DMSO at 48h (coeff. est. ±SE: -0.031±0.012, t=-2.57, p=0.012*), 72h (coeff. est. ±SE: -0.024± 0.0094 t=-2.568 p=0.011), 192h (coeff. est. ±SE: 0.028± 0.012 t=2.32 p=0.021), 216h (coeff. est. ±SE: 0.035± 0.015 t=2.32 p=0.021*), 240h (coeff. est. ±SE: 0.044±0.018 t=2.414 p=0.017), 264h (coeff. est. ±SE: 0.054± 0.021 t=2.53 p=0.012), 288h (coeff. est. ±SE:

0.066±0.024 t=2.70 p=0.0077); 1μM GSK33687125 at 72h (coeff. est. ±SE: -0.029± 0.012 t=-2.43 p=0.016 *), 96h (coeff. est. ±SE: -0.021 ± 0.0094 t=-2.25 p=0.026 *), 240h (coeff. est.±SE: 0.023±0.011 t=2.18 p=0.031 *), 264h (coeff. est.±SE: 0.029±0.012 t=2.36 p=0.019*) and 288h (coeff. est. ±SE: 0.032±0.013 t=2.40 p=0.017 *); 1μM GSK33687125 + 1μM GSK591 at 24h (coeff. est. ±SE: 0.034± 0.017 t=2.08 p=0.039 *), 120h (coeff. est. ±SE: -0.041 ± 0.019 t=2.14 p=0.034 *), 144h (coeff. est.±SE: 0.054±0.022 t=2.48 p=0.014 *), 168h (coeff. est.±SE: 0.051±0.022 t=2.28 p=0.026*) and 192h (coeff. est. ±SE: 0.053±0.024 t=2.25 p=0.026 *); 1μM GSK33687125 + 1μM Furamidine at 24h (coeff. est.±SE: 0.072±0.025 t=2.82 p=0.0053**), 48h (coeff. est.±SE: 0.062± 0.025 t=2.44 p=0.016 *) and 96h (coeff. est.±SE: -0.037± 0.016 t=-2.24 p=0.026 *); 1μM GSK33687125 + 1μM Furamidine + 1μM GSK591 at 24h (coeff. est.±SE:-0.032±0.011 t=-2.92 p=0.0039 **); 1μM GSK3368712 + 10μM TMZ (coeff. est.±SE:-0.022±0.0097 t=-2.22 p=0.027*) (coeff. est.±SE:0.028±0.012 t=2.33 p=0.021 *) (coeff. est.±SE:0.037±0.015 t=2.47 p=0.014*) (coeff. est.±SE:.042±0.018 t=2.43 p=0.016*) (coeff. est.±SE:0.055±0.021 t=2.58 p=0.011*) (coeff. est.±SE:0.067±0.024 t=2.74 p=0.0067 **) and 10μM TMZ at 120h (coeff. est.±SE:0.022±0.0096 t=2.25 p=0.025*). The location covariate also indicated coefficient significance in the right occipital lobe (coeff. est.±SE:0.022±0.0035 t=6.26 p=2.47x10^{-9}***), indicating an increase in LDH above the mean. The significant intercept coefficient (coeff. est. ±SE: 0.075±0.017, t=4.30, p=2.76x10^{-5}*) indicates that there features of the tissue that cannot be explained by this model.

Finally, the estimated marginal means were calculated, using the *emmeans()* package. This was performed as a post-hoc analysis of the GLM, with Tukey pairwise correction, to understand further the relationships between each of the levels, within the variables (Figures 3.24, Figure 3.25 and Figure 3.26). Upon further exploration of the LDH expression data, no significant differences were found between treatment at paired timepoints. Time was only shown to be significant between 24 hours and all other time points: 48h (emmeans±SE: 3.41x10^{-2}±0.0043 df=254, t=7.96, p=<.0001*), 72h (emmeans±SE: 3.81x10^{-2}±8.44, df=254, t=8.45, p=<.0001*), 96h (emmeans±SE: 3.71x10^{-2}±0.0045, df=254, t=8.22, p=<.0001*), 120h (emmeans±SE: -3.26e-02±0.00428 df=254, t=-7.614 p=<.0001*), 144h (emmeans±SE: -3.70x10^{-2}±0.0043 df=254, t=-8.65 p=<.0001*), 168h (emmeans±SE: -3.82x10^{-2}±0.0043 df=254, t=-8.92, p=<.0001*), 192h (emmeans±SE: 3.76x10^{-2}± df=254, t= -8.79, p=<.0001*), 216h (emmeans±SE: -3.75x10^{-2}±0.0051 df=254, t= -739, p=<.0001*), 240h (emmeans±SE: 3.91x10^{-2}±0.0051 df=254, t=7.72, p=<.0001*), 264h (emmeans±SE: 3.85x10^{-2}±0.0051

df=254, t=7.60, p=<.0001*) and 288h (emmeans±SE: $3.73x10^{-2}$±0.0051 df=254, t=7.37, p=<.0001*). This supports the explanation that LDH expression is increased upon first entry of the tissue into the chip and from then it decreases to insignificant levels throughout the remainder of the time in the perfusion device.

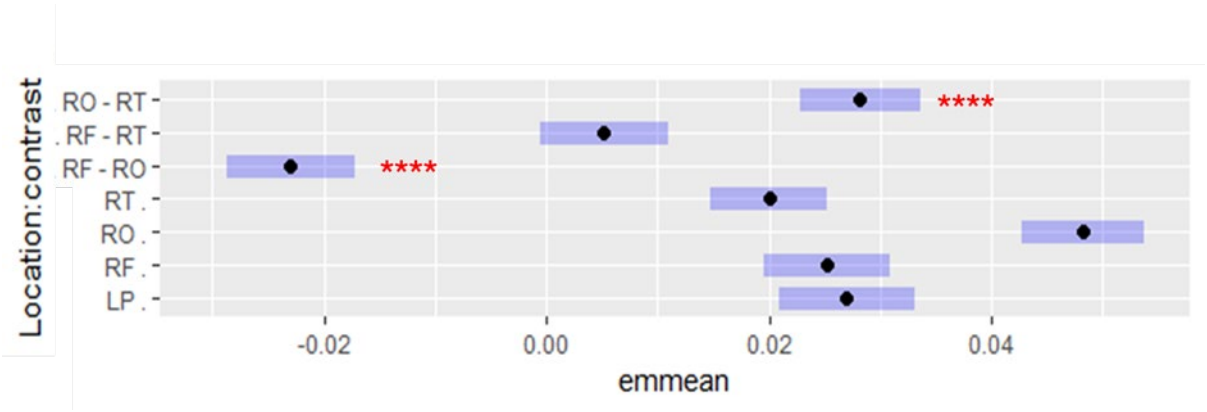

Figure 3.24.: Emmeans comparisons of LDH release in 8-day and 12-day GBM, with tumour location.

Six patient GBM samples, 8- and 12-days post-perfusion found in 4 different locations within the brain had emmeans compared, according to location of the tumour in the brain. Left Parietal (LP) (0.027±0.0021); right frontal (RF) (0.025±0.0020); right occipital (RO) (0.048±0.0019); right temporal (RT) (0.020±0.0018). Averaged over treatment2 levels. Emmeans indicated by black dots. Blue bars indicate standard error (SE). Statistical analysis was performed using ANOVA in R 4.3.1.

Further exploration of the location covariate emmeans showed significant positive shifts in the contrast means of the right occipital (RO) lobe and right temporal (RT) lobes (emmeans±SE: 0.028±0.0019 df=195, t=14.76, p=<.0001*), suggesting that more LDH is released in tissues taken from the RO, than the RT. The right frontal (RF) and RO lobes also show a significant emmeans contrast shift (emmeans±SE: -0.023±0.0020 df=195, t=-11.31, p=<.0001*), whereby RO has a higher LDH release over time, indicating more cellular stress in these tissues. Overall, RO tissues show the most cellular stress over time.

In an exhaustive search of the models to explain cleaved PARP expression variation, six models were within 2 AICc from the top model, with the top model displaying an AICc of 115.79 and explaining ~19% of the variation, with contributions from treatment and location in the first

model and age, time, primary *vs* recurrent and CDKN2A_PTEN exploratory variables in subsequent models. Plotting the most frequently occurring model-averaged importance of terms indicated that treatment and location appeared far more frequently than any of the other covariates in the top models and therefore, these were taken forward in the final GLM.

The coefficient for the intercept showed significant positive regression (coeff. est. ±SE: 0.85±0.29, t=2.98, p=0.0051*). This may indicate that there are factors contributing to variation in apoptotic marker expression, which are not fully explained by the location of the tumour, or the treatment applied to the GBM biopsies in the perfusion device. These underlying components could be individual patients' genetics and epigenetics, particularly those which were not histologically explored and recorded in clinical records. There is significant positive regression of apoptotic marker expression in GBM tissues in the treatment predictor variable: 1µM GSK3368715 (coeff. est.: 1.01±0.19, t=5.29, p=5.42x10^{-6}****); 1µM GSK3368715 + 1µM GSK591 (coeff. est.: 0.76±0.32, t=2.35, p=0.024*); 1µM GSK3368715 + 1µM GSK591 + 1µM Furamidine (coeff. est.: 0.78±0.32, t=2.42, p=0.020); 1µM GSK3368715 + 1µM Furamidine (coeff. est.: 0.78±0.32, t=2.42, p=0.021); 1µM GSK3368715 + 10µM TMZ (coeff. est.: 0.82±0.26, t=3.10, p=0.0036). There is also positive significant regression in the location covariate, including: left parieto-occipital (coeff. est.: 0.69±0.33, t=2.09, p=0.043*); right parieto-occipital (coeff. est.: 1.67±0.39, t=4.32, p=0.00012***) and right parieto-temporal (coeff. est.: 2.08±0.39, t=5.39, p=3.92x10^{-6}).

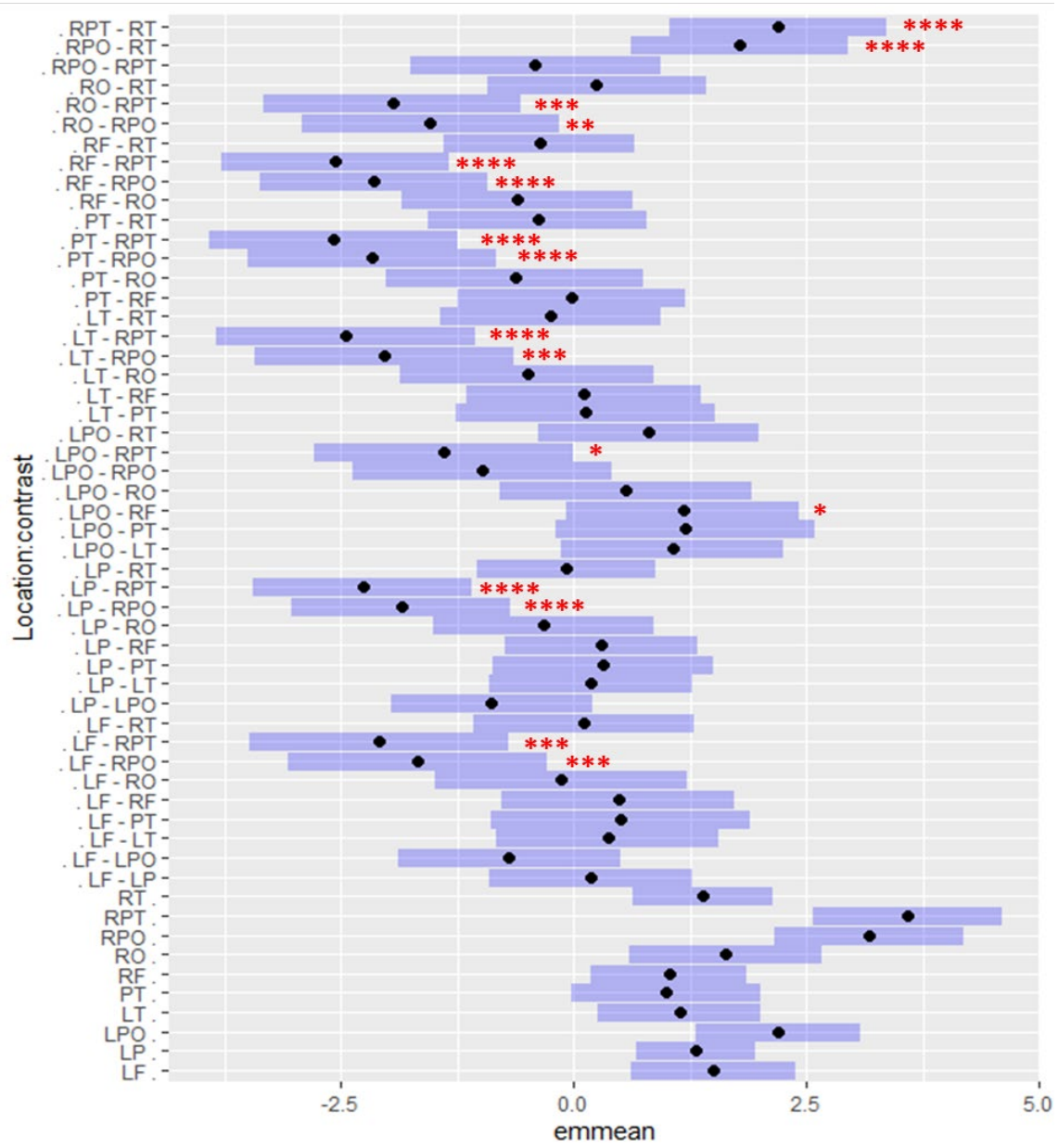

Figure 3.25.: Emmeans comparisons of cleaved PARP expression in 8-day and 12-day GBM, with tumour location.

Fifteen patient GBM samples, 8- and 12-days post-perfusion found in 10 different locations within the brain had emmeans compared, according to location of the tumour in the brain (RT= right temporal (1.38±0.21), RPT- right parieto-temporal (3.58±0.28), RPO= right parieto-occipital (3.17±0.28), RO= right occipital (1.63±0.29), RF=right frontal (1.02±0.24), PT=parietal temporal (1.00±0.28), LT= left temporal (1.13±0.24), LPO= left parieto-occipital (2.19±0.24), LP = left parietal (1.31±0.18), LF= left frontal (1.50±0.24)). Averaged over treatment levels: DMSO control, 1 μM GSK3368715, 10 μM TMZ, 1 μM GSK3368715 + 10

*μM TMZ, 1 μM GSK3368715 + 1 μM Furamidine and 1 μM GSK3368715 + 1 μM Furamidine 1 μM GSK591. Emmeans indicated by black dots. Blue bars indicate standard error (SE). Significant positive correlations in LDH release were found between # RPT and RT (coeff. est.: 2.19±0.33, t=6.736, df=38, p<.0001****); RPO and RT (coeff. est.: 1.78±0.33, t=5.472, df=38, p=0.0001****); RO and RPT (coeff. est.: -1.95±0.38, t=-5.07, df=38, p=0.0004***); RO and RPO (coeff. est.: -1.54±0.38, t=-3.34, df=38, p=0.0095**); RF and RPT (coeff. est.: -2.56±0.34, t=-7.50, df=38, p<0.0001****); RF and RPO (coeff. est.: -2.15±0.34, t=-6.30, df=38, p<0.0001****); PT and RPT (coeff. est.: -2.5789±0.37 t=-6.94 df=38, p<.0001****); PT and RPO (coeff. est.: -2.1676±0.37 t=-5.83 df=38, p<.0001****); LT and RPT (coeff. est.: -2.44±0.39, t=-6.33, df=38, p<.0001****); LT and RPO (coeff. est.: -2.03±0.39, t=-5.27, df=38, p=0.0002***); LPO and RPT (coeff. est.: -1.3854±0.39 t=-3.59 df=38, p=0.0280*); LPO and RF (coeff. est.: 1.1712±0.35 t=3.36 df=38, p=0.0499*); LP and RPT (coeff. est.: -2.2638±0.33 t=-6.91 df=38, p<.0001****); LP and RPO (coeff. est.: -1.8525±0.33 t=-5.65 df=38, p=0.0001****); LF and RPT (coeff. est.: -2.0799±0.39 t=-5.39 df=38, p=0.0002***) and LF and RPO (coeff. est.: -1.6685±0.39 t=-4.32 df=38, p=0.0038***). Statistical analysis was performed using ANOVA in R 4.3.1.*

Interestingly, there appeared to be a larger positive shift in the emmeans of cleaved PARP expression in GBM which is resected from border areas of the brain, between two lobes, for example parieto-occipital (PO) and parieto-temporal (PT) (Figure 3.23). When compared directly with individual lobes from which tumours are resected, GBM which spans multiple lobes, for example between the right parieto-temporal (RPT) and RT, there was a large and significant positive emmeans shift, indicating higher cleaved PARP expression in GBM tissues which were taken from multiple lobes. In particular, there are significant shifts in cleaved PARP expression between left frontal (LF), LP, left parieto-occipital (LPO), left temporal (LT), PT, RF, RO and RT, and RPT and right parieto-occipital (RPO), with the latter two displaying higher cleaved PARP expression. There did not appear to be any significant correlation between tumours resected from the right or left side of the brain.

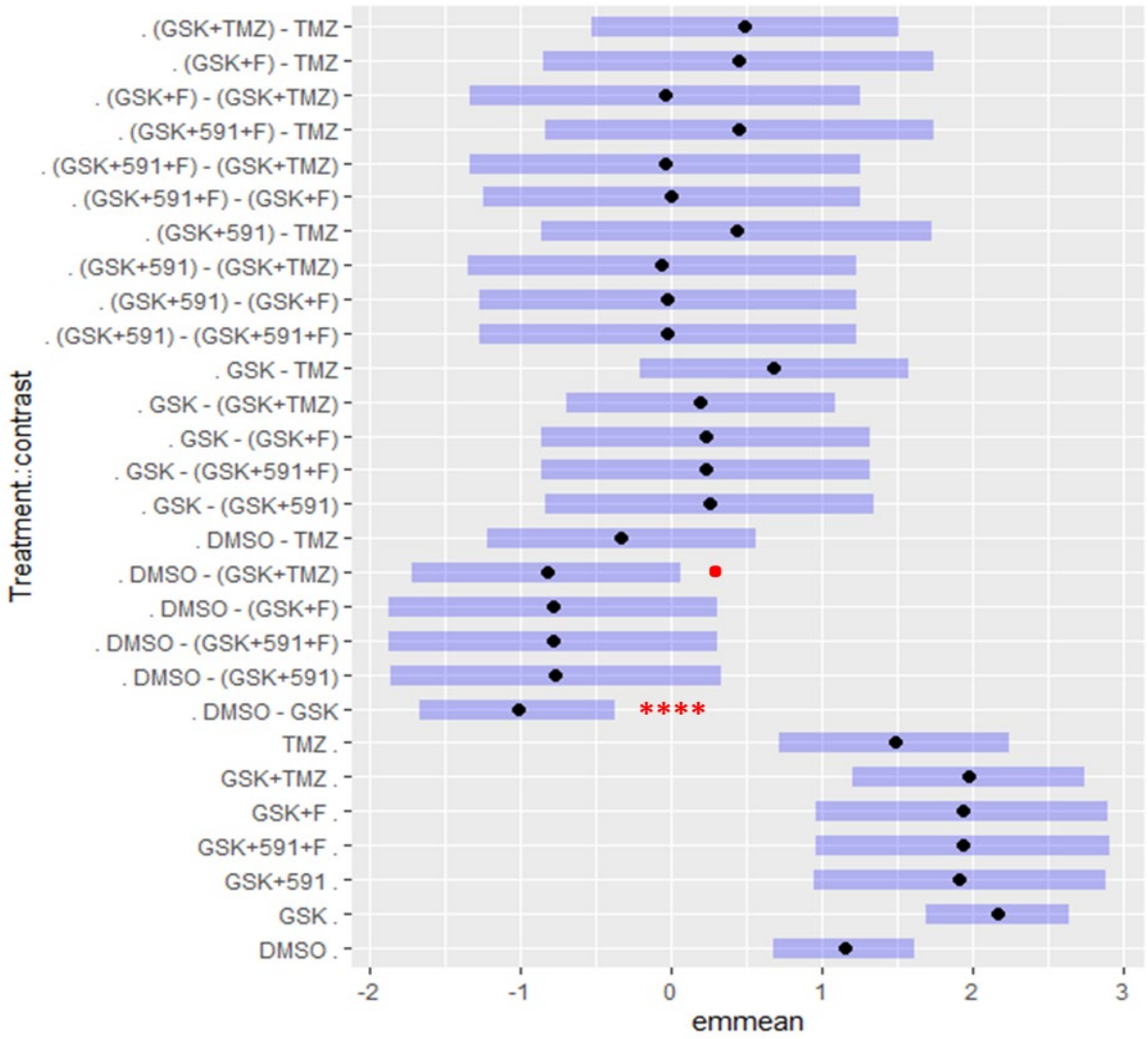

Figure 3.26.: Emmeans comparisons of cleaved PARP in 8-day and 12-day GBM, with treatment.

*Fifteen patient GBM samples, 8- and 12-days post-perfusion found in 10 different locations within the brain had emmeans compared, according to treatment: DMSO control (1.15±0.14), 1 μM GSK3368715 (2.16±0.14), 10 μM TMZ (1.48±0.23), 1 μM GSK3368715 + 10 μM TMZ (1.97±0.23), 1 μM GSK3368715 + 1 μM Furamidine (1.93±0.29), 1 μM GSK3368715 + 1 μM Furamidine + 1 μM GSK591(1.93±0.29) and 1 μM GSK3368715 + 1 μM GSK591 (1.91±0.29). Emmeans indicated by black dots. Blue bars indicate standard error (SE). Significant negative correlations in apoptotic cleaved PARP expression were found between the DMSO control and GSK3368715 (coeff. est.: -1.01±0.19 t=-5.29 df=38, p=0.0001***) and borderline statistical significance between DMSO and GSK33687815 + TMZ (coeff. est.: -0.82±0.27 t=-3.10 df=38, p=0.051.). Statistical analysis was performed using ANOVA in R 4.3.1.*

Significant negative correlations between the DMSO control and GSK3368715 support the data shown in Figure 3.16, whereby GSK3368715 causes apoptosis in 8-day perfused GBM. The negative correlation indicates the shift in emmeans from GSK3368715-treated GBM cleaved PARP expression to the DMSO control. Interestingly, the correlation between the DMSO control and combination treatment of GSK3368715 and TMZ also showed a borderline p-value, whereby there is elevated cleaved PARP expression in combination treated GBM in the perfusion device. The remaining treatment combinations also showed increased apoptosis, compared to the DMSO control ((Figure 3.24), which is consistent with the results shown previously.

Upon performance of GLM for apoptotic marker annexin V data, of the clinical features tested, there did not appear to be any influence of these covariates on the apoptosis of GBM in the perfusion device. The top three models were within 2 AICc, of which the top model did not include any covariates and had an AICc of 27.38 and explained ~15% of the variance. The subsequent two models included primary *vs* recurrence and MGMT promoter methylation status as potential exploratory covariates. Plotting of these covariates did not indicate that they should be included within the model and so the final model was run with no covariates. The intercept coefficient was 1.04±0.10 (t=10.07, $p=7.98x10^{-9}$****), which again highlighted potential factors which were not available to be explored in this data, which may further explain the variance of annexin V expression in this data.

3.3.7. Primary vs Recurrent – D8 case study

One of the initial aims of the study was to determine changes in treatment response to GSK3368715 between primary diagnosis and recurrence. Whilst previous data indicated no significant differences in the effect of GSK3368715 on primary *vs* recurrent tumours; using paired samples would highlight any patient-specific changes and capture the more personalised approach, integral to this study model. Due to the time limitations of this study and the relative rarity of recurrent surgeries, I received only one paired primary and recurrent sample, which were received 420 days apart. It was therefore decided to outline a small case study based on these samples.

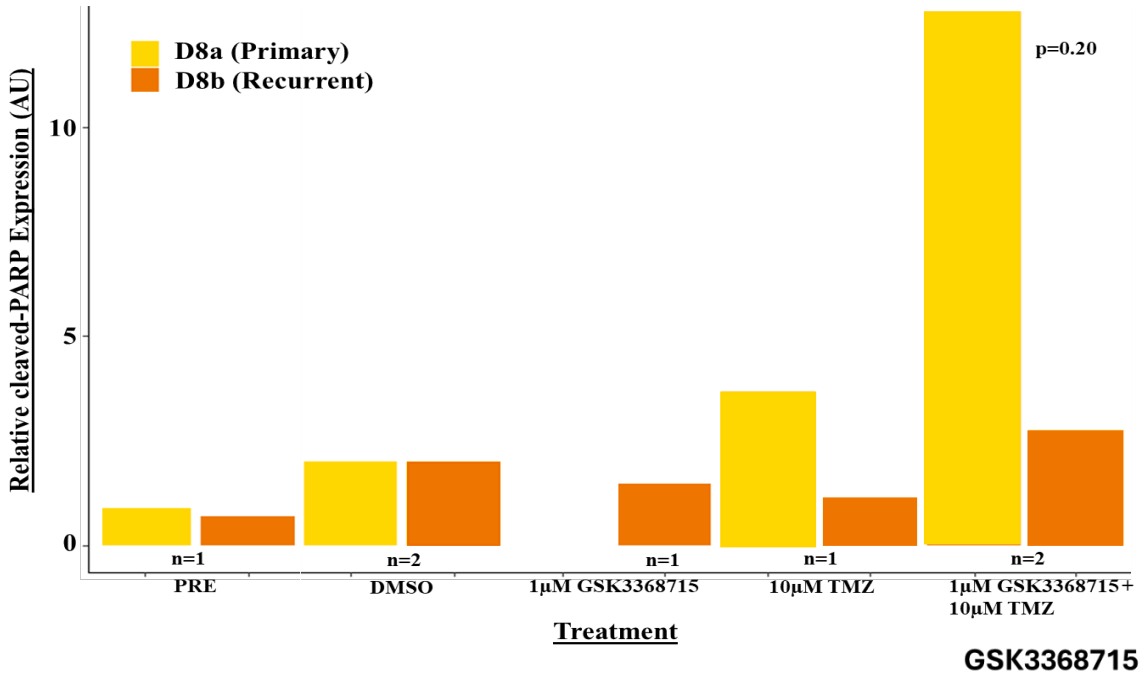
D8a (Primary)
D8b (Recurrent)
p=0.20
Relative cleaved-PARP Expression (AU)
10
5
0
n=1
n=2
n=1
n=1
n=2
PRE
DMSO
1μM GSK3368715
10μM TMZ
1μM GSK3368715+
10μM TMZ
Treatment

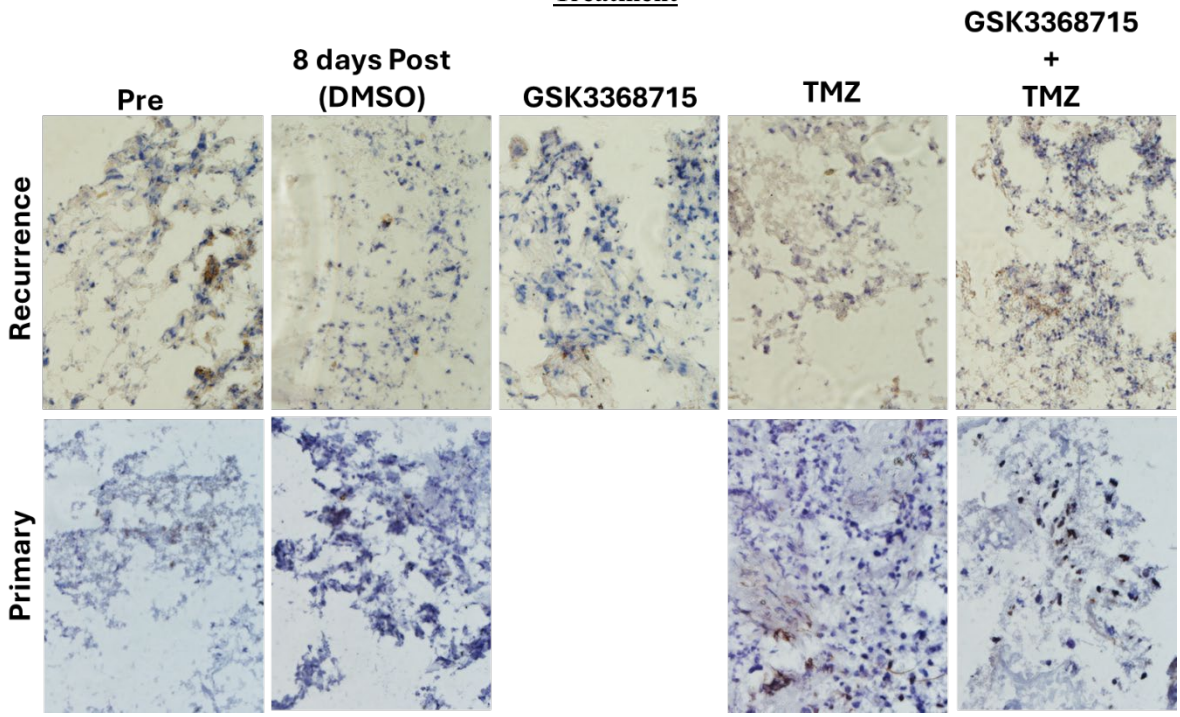
Pre
8 days Post
(DMSO)
GSK3368715
TMZ
GSK3368715
+
TMZ
Recurrence
Primary

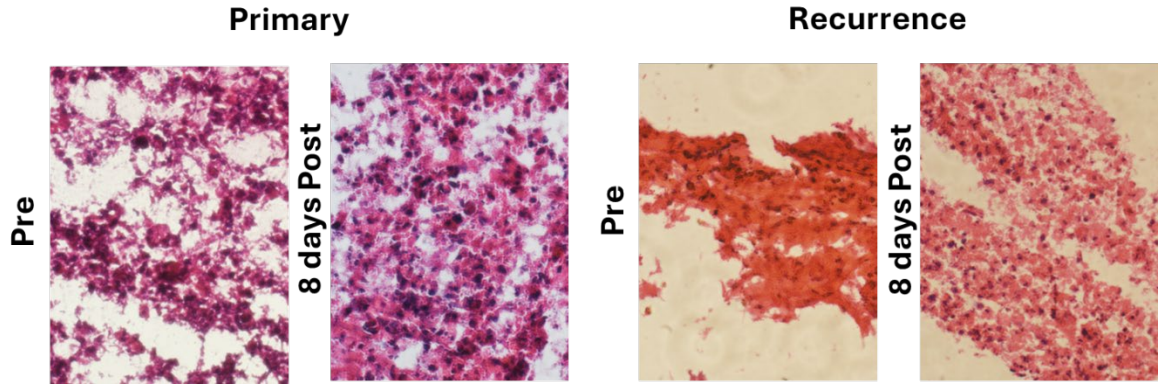
Primary
Recurrence
Pre
8 days Post
Pre
8 days Post

Figure 3.27.: Immunohistochemistry of* cleaved PARP *expression in) D8a (primary tumour) and D8b (recurrent tumour) in 8-day post-perfused control (DMSO) and paired 1μM GSK3368715, 10 μM TMZ and combination-treated tissue, with representative images.

Immunohistochemistry of GBM tissue treated with the DMSO control and 1μM GSK3368715, 10 μM TMZ and combination, with the apoptotic marker, cleaved PARP, normalised to post-perfusion DMSO control values. Analysis was performed using R 4.1.2., using the paired Kruskal.test function (X^2= 10.98, df = 8, p = 0.20). Mean cleaved PARP *expression (red diamonds): primary; pre-perfusion 0.9 (n=1), DMSO control 1 ± 0.15 (n=2), 10μM TMZ 3.68 (n=1), 1μM GSK3368715 + 10μM TMZ 6.38 ± 3.32 (n=2), recurrent; pre-perfusion 1 (n=1), DMSO control 1 ± 0.39 (n=2), 1μM GSK3368715 1.48, 10μM TMZ 1.13 (n=1), 1μM GSK3368715 + 10μM TMZ 1.38 ± 0.023 (n=2). N number refers to the number of chips treated per condition. Dashed lines indicate paired patient samples.*

In the primary sample, the micro-biopsies for both of the GSK3368715-treated chips were too loose and the remaining solid tissue was too small to mount onto slides and then undergo the IHC process. Despite the fact that grouped samples did not show significant changes in apoptosis with treatments other than GSK3368715, over three distinct locations of D8a, TMZ alone indicated an increase in apoptosis over 8 days in the perfusion device and this was elevated in combination with GSK3368715 (Figure 3.25).

3.3.8. Clinical impact of GSK3368715 on cytokine release over time

Through the use of Proteome Profiler ® (Roche), 105 cytokines were analysed in effluents from GBM, treated with 1 μM GSK3368715 + 10 μM TMZ for 8 days, over the DMSO control at 48, 96 and 192 hours, by M.D. student Amr Moursi. Statistical analysis was performed by Lauric Feugere, PhD using R.

Due to the number of variables and covariates within the data, a multivariate analysis was performed. No significant difference in dispersion patterns between different groups was found within the variable of time, treatment, or with their interaction. The sample size of 78, after normalisation and outlier screening, was smaller than the number of cytokines 105 and the data showed multicollinearity between most cytokines. This indicated that any significant

Permutation Analysis of Variance (PERMANOVA) testing showed differences in cytokine profiles, rather than cytokine expression (Figure 3.26). The best fit model was chosen through AICc, using the treatment variable as the main factor of interest. AICc showed that an additive effect of treatment + time + gender + age was the most parsimonious model, with the lowest ΔAICc value (<2) and fewest explanatory variables. The model which incorporated all covariates (gender, age, recurrence, MGMT status and lethality, defined as survival at 6 months post-surgery) could not, however, be excluded from good fit models, due to $p<0.05$ for recurrence and MGMT promoter methylation status. Age was binarised into patients aged >60 years and <60 years. This model indicated that time ($F = 1.91$, $p = 0.0288$), gender ($F = 3.32$, $p = 0.0050$), and age ($F = 4.21$, $p = 0.0021$) had a significant effect on expression of cytokines, across all conditions, whilst no statistically significant effect of treatment ($F = 1.28$, $p = 0.1977$) was found.

The most frequent and abundant cytokines, found consistently throughout the effluents of all 11 patient samples and three timepoints were: C3L1, IL8, osteopontin, chemokine ligand 2 (CCL2), serpin-E1, MMP9 and VEGF. These cytokines consistently make up the known GBM inflammatory microenvironment throughout the literature. Principal component analysis of all covariates was performed to visualise PERMANOVA effects and identify any changes to cytokine levels, dependent upon factors such as time, age, gender, recurrence, MGMT status and lethality (Figure 3.26).

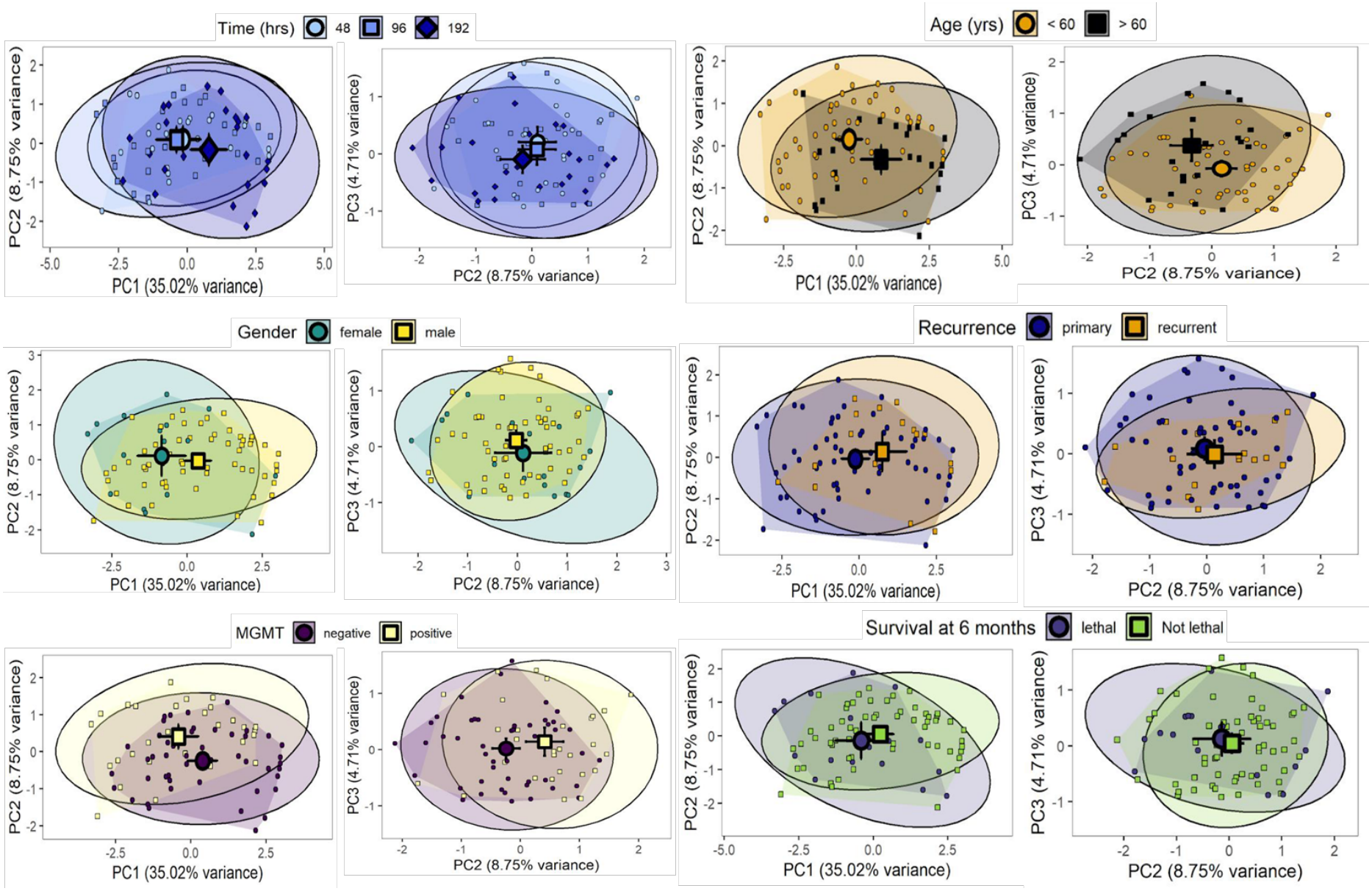
Time (hrs) 48 96 192
PC2 (8.75% variance)
PC1 (35.02% variance)
PC3 (4.71% variance)
PC2 (8.75% variance)
Age (yrs) < 60 > 60
PC2 (8.75% variance)
PC1 (35.02% variance)
PC3 (4.71% variance)
PC2 (8.75% variance)
Gender female male
PC2 (8.75% variance)
PC1 (35.02% variance)
PC3 (4.71% variance)
PC2 (8.75% variance)
Recurrence primary recurrent
PC2 (8.75% variance)
PC1 (35.02% variance)
PC3 (4.71% variance)
PC2 (8.75% variance)
MGMT negative positive
PC2 (8.75% variance)
PC1 (35.02% variance)
PC3 (4.71% variance)
PC2 (8.75% variance)
Survival at 6 months lethal Not lethal
PC2 (8.75% variance)
PC1 (35.02% variance)
PC3 (4.71% variance)
PC2 (8.75% variance)

Figure 3.28.: PCA1, 2 and 3 planes of cytokine data, displaying time and age variables, MGMT status, recurrence, survival at 6 months and gender covariates

Large shapes show the centroids (± 95% confidence intervals). Small shapes show individual data points. Ellipses show the 95% confidence intervals. Polygons show the maximal dispersion between outermost points for each group.

The PCA plots indicate clear separation between PC1 and PC2 axes for the covariates which were identified as being significant predictors of response in the PERMANOVA and less clear separation in those which did not feature in the PERMANOVA, or PC3 axis. PCA data showed some separation in centroid means in time at 48 ($F = 2.09$, $p = 0.0381$) and 96 hours ($F = 3.09$, $p = 0.0117$), compared to 192 hours, along the PC1 axis, with 192 hours showing a positive shift. This suggested that the cytokine profile was maintained up to 96 hours but changed up to and after 192 hours. Data for patients aged >60 years, MGMT negativity, recurrence and male patients also showed a positive PC1 shift, with patients >60 years and those showing MGMT negativity also showing a negative PC2 shift. Male patients and those >60 years indicated a positive PC3 shift.

Univariate analysis was also performed to extrapolate any cytokines of interest, which may change between the treated and control patient samples, whilst accounting for covariates of Age, Gender, and Time (Figure 3.27). Univariate analysis fitted a linear model, comparing the control and treated GBM data with covariate adjustment, identified from AICc model selection, using Limma and then used Partial Least Square Discriminant Analysis (PLS-DA) to mitigate PLS-DA tendency to overfit the data.

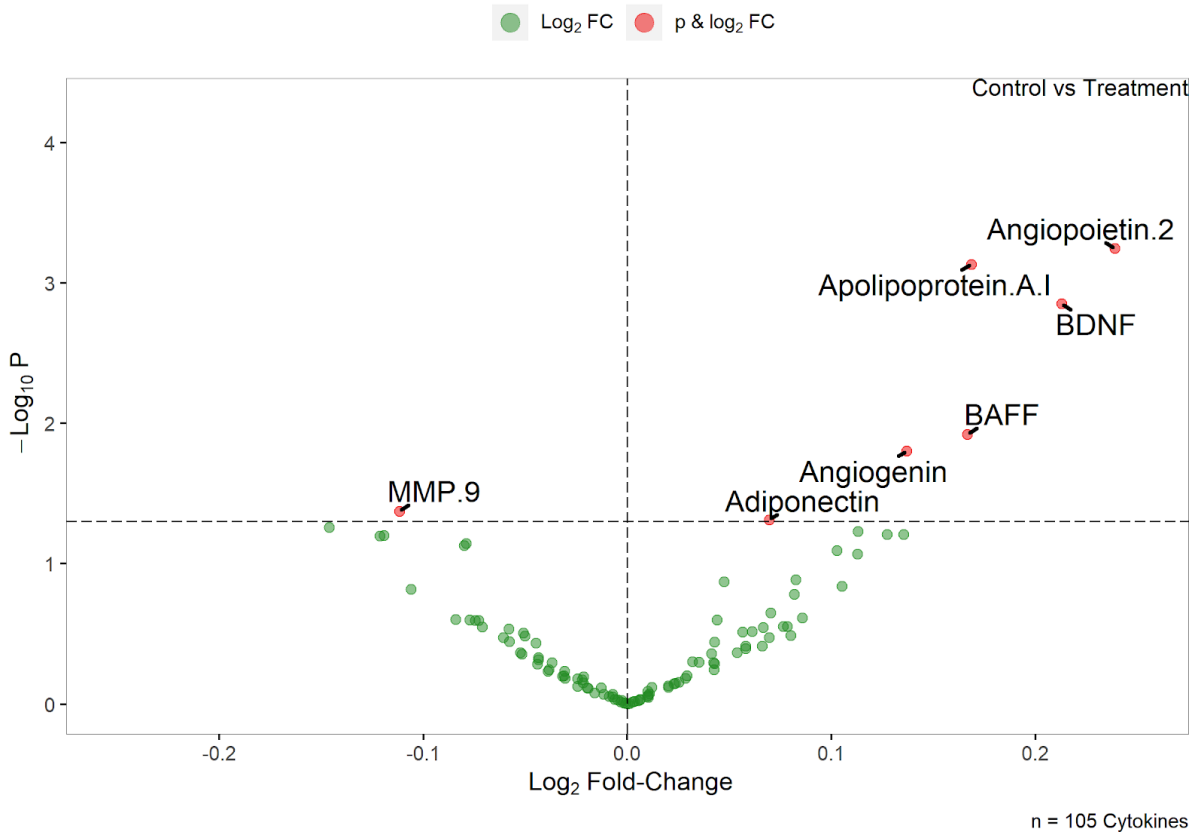

Figure 3.29.: Volcano plot of significant cytokine profile shift due to GSK3368715+TMZ combination treatment after univariate analysis of time, age and gender

Large shapes show the centroids (± 95% confidence intervals). Small shapes show individual data points. Ellipses show the 95% confidence intervals. Polygons show the maximal dispersion between outermost points for each group.

These identified 27 cytokines which discriminated between the treatments, of which 7 were significant after Limma, fitting the linear model accounting for covariates of Time, Age and Gender and which decreased to three cytokines after p-value adjustment form multiple testing (Figure 3.27). These cytokines were Angiopoietin-2, Apolipoprotein-AI and brain-derived neurotrophic factor (BDNF) and displayed a logFC of 0.24 (t=3.58, padj=0.039), 0.17 (t=3.50, padj=0.039) and 0.21 (t=3.30, padj=0.049), respectively. Other significant cytokines, prior to p-value adjustment for multiple testing, included: BAFF (logFC=0.17, t=2.75, p=0.012), Angiogenin (logFC=0.14, t=2.46, p=0.016), and Adiponectin (logFC=0.07, t=2.00, p=0.049),

all of which were upregulated. MMP-9 (logFC=-0.11, t=-2.06, p=0.042) was the only cytokine which appeared to be downregulated with GSK3368715 and TMZ combined treatment.

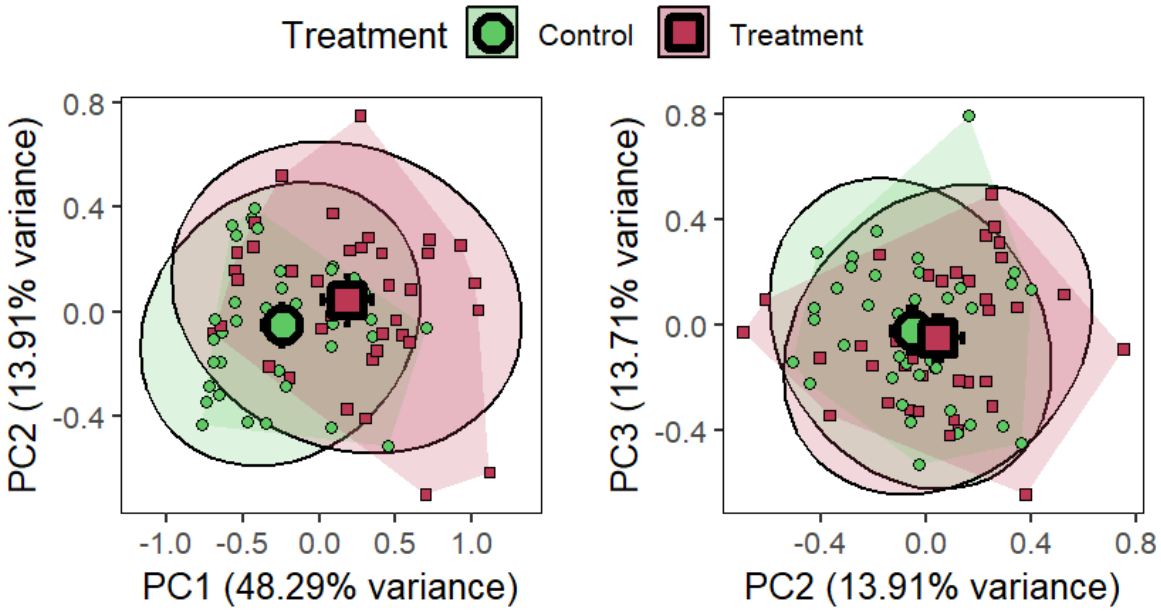

Figure 3.30.: PCA plot of the effects of treatment for all times for cytokines of interest

Large shapes show the centroids (± 95% confidence intervals). Small shapes show individual data points. Ellipses show the 95% confidence intervals. Polygons show the maximal dispersion between outermost points for each group.

Multivariate analysis of this data was based on AICc model selection which found treatment ($F = 8.47$, $p = 0.0002$) and age ($F = 2.96$, $p = 0.0267$) best described the variance in the expression of cytokines of interest, which were most influenced by treatment. The PCA plots (Figure 3.28) indicate clear separation on the PC1 plane, but not between PC2 and PC3 planes.

Using this data to further explore the cytokines most commonly and abundantly released by GBM in the perfusion device and the change in profiles affected by treatment, ELISA was performed. Seven cytokines were chosen to take forward for ELISA, which included: Angiopoietin-2, MMP9, serpin E1, C3L1, IL6, IL8, and VEGF. Model selection indicated that all covariates should be included in the analysis and PERMANOVA suggested that treatment

significantly influenced the expression of the cytokines taken forward for further investigation by ELISA ($F = 4.94$, $p = 0.0048$).

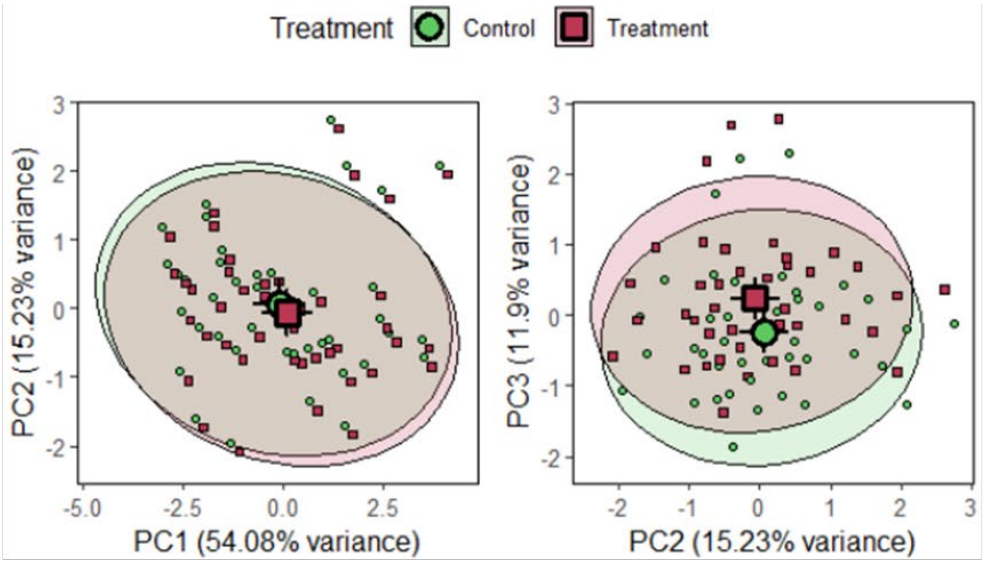
Treatment
Control
Treatment
PC2 (15.23% variance)
PC1 (54.08% variance)
PC3 (11.9% variance)
PC2 (15.23% variance)

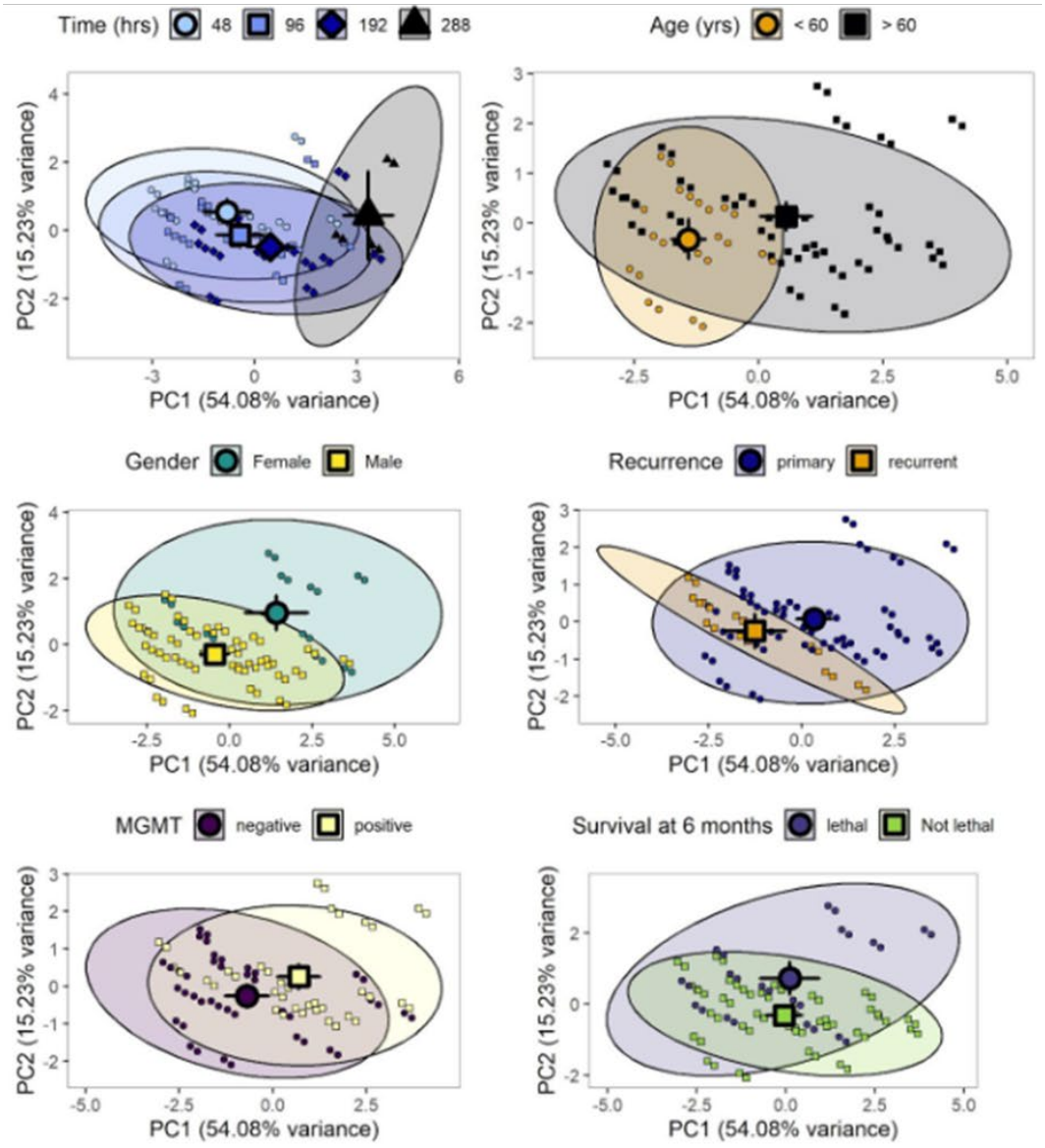
Time (hrs)
48
96
192
288
Age (yrs)
< 60
> 60
PC2 (15.23% variance)
PC1 (54.08% variance)
Gender
Female
Male
Recurrence
primary
recurrent
MGMT
negative
positive
Survival at 6 months
lethal
Not lethal

Figure 3.31.: PCA plot of treatment predictor and all covariates for cytokine expression explored by ELISA

Large shapes show the centroids (± 95% confidence intervals). Small shapes show individual data points. Ellipses show the 95% confidence intervals. Polygons show the maximal dispersion between outermost points for each group.

Clear separation was seen for the PC3 plane of the treatment analysis. Pairwise PERMANOVA analysis of the cytokine expression levels over time indicated a significant reduction: 48h *vs* 96h (F=9.43, df=1, p=0.0004); 48h *vs* 192h (F=24.89, df=1, p=0.0001); 48h *vs* 288h (F=38.26, df=1, p=0.0001); 96h *vs* 192h (F=9.66, df=1, p=0.0001); 96h *vs* 288h (F=29.97, df=1, p=0.0001) and 192h *vs* 288h (F=17.37, df=1, p=0.0001). This data suggests that, in the four 12-day samples, cytokine profiles were maintained up to 48 hours before changing between 96-, 192- and 288-hours. Variation was explained in both the PC1 and PC2 axes, with the greatest cytokine profile variation seen after 288-hours in the PC1 axis, explaining most of the variation in this variable. The covariates of age, gender, recurrence and MGMT also show the greatest dispersal in the PC1 axis, with all but recurrence also showing clear separation on the PC2 axis (Figure 3.29).

Univariate analysis of ELISA data confirmed that the same cytokines which appeared to be most abundant and change with treatment in proteome profiler analysis were also abundant and changed with treatment upon ELISA, with this positive correlation providing cross-method validation.

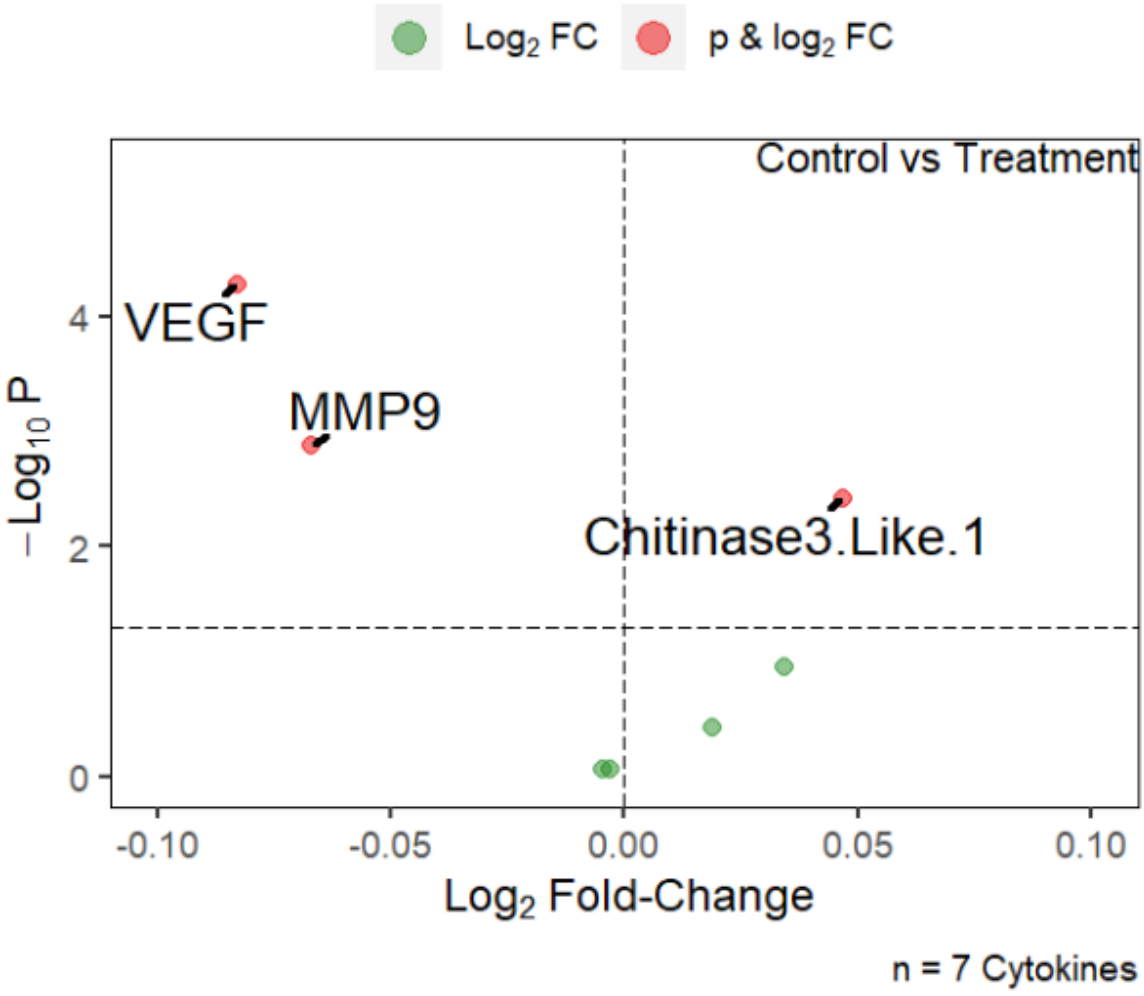

Figure 3.32.: Volcano plot of significant cytokine expression changes in ELISA due to GSK3368715+TMZ combination treatment after univariate analysis, adjusted for all covariates

Vascular endothelial growth factor (VEGF) (logFC=-0.08, t=-4.25, padj=0.0004); matrix metalloproteinase 9 (MMP9) (logFC=-0.07, t=-43.32, padj=0.0046); Chitinase 3 like 1 (logFC=0.05, t=-2.97, padj=0.0088).

Accounting for all covariates and utilising multiple methods of comparison, such as student's t tests and *Limma*, ELISA results also indicated that MMP9 and VEGF secretion significantly decreased upon combination treatment, relative to the control, whilst C3L1 increased (Figure 3.30).

3.4. Discussion

This chapter has investigated the effects of GSK3368715 on cell viability *in vitro* in 2D and 3D cell culture, as well as in *ex vivo* GBM tissue, assessing the expediency of the novel perfusion device in doing so. The data have found that GBM tissue can be maintained in the perfusion device for up to 12 days, 1 μM GSK3368715 is sufficient to cause aDMA-sDMA crosstalk in GBM tissue, supported by Samuel *et al.* (2021) and the PRMT inhibitor can cause significant increase in apoptosis after 8 days in the perfusion device.

Initial cell viability data in this chapter indicated that, although there was an upward trend in proliferation in 2D and 3D U87-MG cultures, there was no significant change in cell viability with treatment. These preliminary assays were performed in U87-MG cells, which are now widely accepted to be highly divergent from their original source and not very reflective of true GBM geno- and phenotypes (Poorna et al., 2021, Arthurs et al., 2020). Despite this, previous work in this lab (Samuel *et al.* 2018), has shown that PRMT inhibitors can reduce cell viability in 2D and 3D and have been shown to induce various other effects on both cell lines and tissue. aDMA inhibition with Type I PRMT inhibitors also causes the appearance of proteins with sDMA. This confirms the results from previous work in this lab (Samuel et al., 2018)(Barry *et al.* 2023), which described this unidirectional crosstalk between aDMA and sDMA as a potential mechanism for chemotherapeutic resistance in GBM. There is also another band that appears at 70 kDa upon Type I PRMT inhibition, when sDMA is blotted for. This is proposed to be a protein of interest which undergoes methylation switching as a result of type I PRMT inhibition (Barry *et al.* 2023). Due to the cell type used in the viability assays, the aDMA-sDMA switch and the evidence from previous data, it was decided that 1μM GSK3368715 could be taken forward for further investigation in tissue *ex vivo.*

One of the main objectives set out in the project grant was to extend the time that GBM was able to be maintained on the device from 8- to 12 days. The reasoning behind this was to potentiate a prolonged exposure of the GBM tissue to treatment, for a more realistic, real-time view *ex vivo,* of how a tumour may behave *in vivo.* Whilst there are several models of GBM, including mouse models, which comprise the microenvironment, immune capabilities and general tumourigenesis (Sharma *et al.*, 2023, Majc *et al.*, 2021), there are few which recapitulate the unique aspect of GBM and the influence of an individual's genetic and

epigenetic makeup on the physiology of their tumour and its treatment (Xie *et al.*, 2023). The microfluidics chip aims to anticipate treatment responses in tumours and allow more personalised treatment of an individual, based upon the performance of the tumour in the perfusion device (Liu *et al.*, 2022, Maghsoudi, 2021).

The use of LDH assays was to determine cellular stress of the tissues in the perfusion device, with the concept being that stressed cells would release LDH into the effluent (Vanderlinde, 1985). These results may not accurately predict cellular stress of the tissues, as there was no apparent effect of treatment on the release of LDH and the results do not mirror the those captured through IHC. LDH levels released throughout the time course of the perfusion device were very low and at the sensitivity limits of the kit being used. Other studies into microfluidics devices have utilised alternative cellular stress assays, alongside LDH assays, such bromodeoxyuridine (BrdU), or propidium iodide (PI) uptake, which validated that tissue remained alive on the chip (Riley *et al.*, 2019). The CytoTox-Glo assay has also been used to evaluate cellular toxicity through protease levels in microfluidics effluents, finding similar levels of protease across several time points on-chip (Collins *et al.*, 2021). An improvement to these assays would be to use a positive control, which would have to remain on the perfusion device and be treated with DNase, or UV, which would induce cellular stress (Pronin *et al.*, 2017). The high starting point of cellular stress corresponds with removal of the tissue from the original environment and transport to the lab, prior to be putting on chip. The subsequent decrease to a low, steady level suggests that the amount of LDH released is proportional to the levels of cellular stress. As there were fluctuations in the LDH release, consistent with syringe changes and time off-chip, it was determined throughout the experiments that the assays were a good indicator of relative cellular stress.

These experiments were also performed in addition to H&E, IHC for apoptotic markers and cytokine assays in this study for robustness. These were also supported by previous work in this lab, such as IHC for proliferative markers, which have been published (Samuel *et al.* 2021)(Barry *et al.* 2022). Histological analyses also suggested that there were some areas of the GBM tissue, pre-perfusion, which contained necrotic and inviable cells. In this case, the chips do not revitalise the tissue, but will incubate the dead tissue for the duration of time in the perfusion device. This results in some pockets of the micro-biopsies being inviable which

reduces the overall metabolic activity which can be quantified. This invariably creates disparities between chips treated with the same drug, or between the slides of tissue slices that are being probed for markers. This can be somewhat negated through an increase in number of technical repeats performed, such as increasing the number of chips treated with the same drug, or the number of slides being probed. Without time constraints on a project such as this, there is scalable potential of the microfluidics device and downstream investigations. Some of the main issues with this would be the availability of tissue material to put into the chips, both in the initial biopsy received and the number of micro-biopsies that can be attained from it and in the small size of the micro-biopsies, making the amount of data obtainable from one chip relatively finite.

Chips were also loaded with tissue micro-biopsies at random, therefore ensuring that no favour was given to particular treatments as to which drug was treating which micro-biopsy. In the current situation in Hull, we receive tissue directly from the operating theatre, often before histology has reported back to the surgeons and therefore, although guided visualisation and practitioner expertise tries to ensure what we get is active tumour, it is not formally confirmed what it is that it being put in the chip. It is not until up to several weeks later that molecular biomarkers confirm whether the tissue is GBM and at that point, we remain unaware of the exact cellular makeup of the samples we are given. Another suggestion for improving this further would be the establishment of a tissue bank, which would encourage the collaboration between the lab, surgeons and neuropathologists, who would ensure the tissue received and put on chip was from the infiltrating edge and active tumour, rather than the necrotic core, or surrounding areas of normal brain, which are inevitably taken during resection.

During the course of this project, the storage of tissues was changed from indirect freezing in methylbutane to FFPE. Initially, fresh freezing the tissue was due to the obtainment of a Ki67 antibody, which was more effective in IHC on fresh frozen tissue, rather than FFPE. This practise therefore carried on throughout the samples which were used for 8-days on-chip, in order that the biological replicates were comparable. Upon reception of the 12-day samples, it was decided to change the tissue processing to FFPE, as the antibodies being used for IHC were compatible with the more widely used processing method and would potentially ensure cleaner images. The 12-day samples would not be directly compared to the 8-day samples, as

they were not paired, therefore maintaining consistency. Histological analysis of GBM tissue samples, both pre- and post-perfusion control indicated that mitotic figures could be seen in the tissue and therefore tissue remained viable whilst on-chip. The data is supported by the similar levels of both cleaved PARP and annexin V expression, as well as the preliminary TUNEL cell viability data. Further exploration of the tissue viability through TUNEL assays would increase the robustness of this data, ensuring specificity to apoptosis detection, rather than cell death by other means, including necrosis (Kyrylkova *et al.* 2012). This ensures that any treatments applied to the tissues could be metabolised by the cells and therefore could potentially produce a quantifiable output.

The initial cytokine analysis of the DMSO-control effluents, over 8-days, included six samples and found no statistically significant change in cytokine profiles over time. The most abundant cytokines were most often associated with invasion and immunosuppression and the majority have been found to be significantly expressed in GBM (Morawin and Zembron-Lacny 2023). EMMPRIN has been found to be increased in the extracellular vesicles originating from GBM, when exposed to ionising radiation. This in turn causes an upregulation of the MAPK/JNK pathway, which stimulates the release of MMPs, therefore aiding in the GMT (Colangelo and Azzam, 2020). MMP-9 is also packaged into extracellular vesicles, which can cross the BBB. MMP9 is also correlated with glioma grade and aggression and potentially plays a role in the GMT through degrading the extracellular matrix, allowing GBM invasion (Dobra *et al.*, 2023, Xue *et al.*, 2017).

Serpin E1 has been identified as a driver of GBM cell dispersion, allowing infiltration of GBM cells into the surrounding brain tissue (Seker *et al.*, 2019). Increase in VEGF and IL6 was also associated with an increase in serpinE1 (Chen et al., 2022b) and also likely play major roles in the invasiveness of GBM, promoting angiogenesis (Weathers and de Groot, 2015) and migration (West *et al.*, 2018). VEGF involvement in GBM was discussed previously and several VEGF inhibitors have been trialled in GBM, to prevent the porosity and genesis of blood vessels, thereby limiting GBM invasion (Keunen *et al.*, 2011) (Eatmann *et al.* 2023). IL6 is involved in the induction of programmed death-ligand 1 (PD-L1), *via* STAT3 signalling, leading to T cell apoptosis and immunosuppression (Lamano *et al.*, 2019).

IL8, MIF and MCP1 are also involved in the immune response of GBM to therapy. IL8 expression leads to GBM cell proliferation (Sharma *et al.*, 2018), and inhibition leads to increased tumour cell killing by immune checkpoint blockade, using anti-PDL1 therapies. This is through the innate-like features exhibited by IL8-expressing CD4+ T cells, which cluster at tumour sites and are responsible for therapeutic immunity (Liu *et al.*, 2023). Otvos *et al.* (2016) identified an immunosuppressive pathway, whereby immature myeloid progenitor myeloid-derived suppressor cells (MDSCs) are activated by MIF, secreted from CSCs. Inflammatory mediator MIF exerts its macrophage and B cell proliferative function through the MAPK pathway and inhibits T cell activation and polarises macrophages to an anti-inflammatory phenotype, leading to an overturn of anti-cancer immune responses, such as downregulation of NFκB signalling and allowing tumour progression (Matejuk *et al.*, 2024, Alban *et al.*, 2018, Alban *et al.*, 2023). MCP1, or CCL2 is induced through inflammatory stimuli, such as IL6 and attracts immunosuppressive cell populations, such as Tregs and MDSCs, leading to GBM progression (Yeo *et al.*, 2021, Deng *et al.*, 2023). Osteopontin is a glycoprotein and is associated with hypoxia and maintenance of stemness and migration in GSCs. Osteopontin expression is increased in recurrent tumours, consistent with tumour progression through association with integrin receptors (Ellert-Miklaszewska *et al.*, 2020, Polat *et al.*, 2022).

IGFBP2 is associated with short-term survival of patients and is linked with tumour aggression and proliferative modulation. It has been proposed as an oncogenic master regulator of the dysregulated gene network associated with the GMT, through integrin β1, immunosuppression and short-term survival in GBM patients (Kalya *et al.*, 2021, Cai *et al.*, 2018). Hsieh *et al.* (2010) found IGFBP2 to be present in GSC populations and was responsible for their self-renewal and clonogenicity, therefore contributing to GBM resistance to genotoxic stress. IGFBP2 has been shown to be downregulated in long-term survival patients, categorised at patients who survive beyond 36 months from diagnosis (Han *et al.*, 2014, Franceschi *et al.*, 2015, Cai *et al.*, 2018). C3L1 has also been associated with macrophage polarisation, leading to immune suppression (Chen *et al.*, 2021) activation of the NFκB pathway and positively correlates with PD-L1 (Zhao et al., 2022b). C3L1 is known to induce differentiation of oligodendrocyte precursor cells (OPCs) into mature oligodendrocytes, playing a role in astrocytic migration and proliferation (Singh *et al.*, 2011, Stead, 2022).

The low numbers of cytokine expression from tissues could indicate that the tissue is dying in the perfusion device. This is, however, dispelled by the histology data, which shows clear changes in expression of apoptotic markers, as well as mitotic figures. Tissue viability is also supported by previous work in this lab, whereby proliferative markers are also detected in post-perfused tissue (Samuel *et al.* 2021, Barry *et al.* 2023). The types of cytokines released and their involvement in inflammation and GBM progression are consistent with the literature, as described. This indicates that the perfusion system potentially maintained the same cytokine profiles, post-chip, as seen in patients. It is interesting that no significant changes were seen between primary and recurrent tumours in the control samples, however, seeing as only two of the six analysed were recurrent samples, a greater number would be required to further understand whether the cytokine profiles seen between primary and recurrent tumours of patients is reflected on the perfusion system.

In the fifteen patient micro-biopsies undergoing perfusion with GSK3368715 alone, there was a significant increase in apoptosis, using the cleaved PARP marker (Barry *et al.*, 2023); an upward trend in apoptosis in tissue treated with GSK3368715 in combination with TMZ, or other PRMT inhibitors and a decrease in the cell viability of D14. It therefore appears that GSK3368715 did have a detrimental effect on the viability of GBM tissue in the perfusion device. The sample group for which histology was performed to detect apoptotic markers, was made up of 45.5% MGMT promoter methylation positive, 45.5% MGMT promoter methylation negative and 9% equivocal, or borderline methylated MGMT promoter. This could explain why no significant increase in apoptosis was identified in the initial analysis with TMZ alone and in combination with GSK3368715. TMZ is purported to work best on MGMT promoter methylation positive tumours, due to the suppression of the MGMT DDR enzyme and subsequent disrepair of alkyl adducts, leading to cell death (Shaw *et al.*, 2024) (Kitange *et al.*, 2009).

The 12-day tissue sections were all MGMT promoter methylation positive with the exception of D36, which did not show MGMT promoter methylation. With extended resources, treating these tissues with TMZ may have been a good positive control for apoptosis, to compare with the 1 μM GSK3368715-treated tissue, as MGMT-positive tumours do tend to respond better to TMZ and it would therefore be expected to see more apoptosis in these samples, as opposed to

MGMT negative. One of the key aims of studies such as these is to identify drugs which target the more chemotherapeutic-resistant MGMT-negative tumours, which do have the capability of DNA adduct repair and therefore, these data may indicate that the PRMT inhibitor is unsuitable for MGMT-positive tumours. The lack of significance seen after 12-days in the perfusion device is more likely down to the low number of biological repeats and more samples would be required to fully understand effect of PRMT inhibition on the tissue in general. G*Power 3.1.9.7 software was employed to calculate the number of samples which may be required to produce a power, or confidence level of 0.95 in these data, based upon the effect size (0.22) calculated using the means ± SE of both control and treated sample groups for the existing analysis. This suggested that the total sample size required to produce a significant value would be 225. Due to the large sample number and the shift in cytokine profiles in the PCA, this supports the idea that the tissue may be slowing down in metabolic activity because of the time spent on chip and therefore not processing the drug in the same way as the 8-day perfused tissue. Further optimisation of the extension of time for which the GBM tissue can be perfused would be required, which could include changing the medium for NBA, which may be more supportive for primary tissue maintenance (Sahu *et al.* 2019) or changing flow rates.

The clustering of apoptotic markers cleaved PARP and somewhat of annexin V observed through IHC staining of GBM tissues is something that could also be explored more thoroughly through clustering analysis. Small clusters of cells, or single cells is a common feature of apoptosis (Elmore, 2007) and therefore, the larger swathes of apoptosis could be due to areas of the tissue pre-perfusion, which degrade during transportation and prior to processing. Cleavage of PARP prevents cells undergoing apoptosis and therefore is a specific marker of apoptosis (Herceg and Wang, 1999). The same precise clustering is not seen in Annexin V-stained cells, as the permeability of the membrane brought about by both apoptosis and necrosis allow annexin V to bind (Crowley *et al.*, 2016). This may explain why there appears to be excessive binding of annexin V in some tissues and is the reason more apoptosis-specific assays, such as TUNEL, were performed. Comparisons between pre- and post-perfused, and control and treated tissues with annexin V staining remain consistent in terms of quantifying cell death and relevant when comparing to the healthy control tissue. Qualitatively, there appeared to be more clustering of apoptotic cells in various pockets of tissue in the pre-perfused and post-perfused DMSO control tissue, whereas the treated tissue appeared to have more dispersed apoptotic cells. In the post-perfused control, this could potentially be due to the

effects of the perfusion device, with some areas of the micro-biopsies not receiving perfusion as much as other areas, therefore starving them of nutrients from the medium. These pockets could also be due to clonal heterogeneity of the tissue, with some sections of the tissue being less adapted to the environment and therefore clonal selection meaning that these sections die more quickly. With all of the treatments seeming to have more widespread apoptosis, this could indicate that the treatments are perfusing into the micro-biopsies and causing more thorough cell killing (Elmore, 2007). With more time, it would be interesting to try and quantify this phenomenon and potentially understand whether different treatments cause more or less dispersal of the apoptotic cells.

The symptoms of patients are highly dependent upon the location in which the GBM is formed and has also been linked to the prognosis of patients. This could be due to a variety of factors, including the capacity for bulk resection due to tumour accessibility and tolerability of radiotherapy in particularly sensitive areas of the brain (Yuile *et al.*, 2006). Patients with central tumours, in the basal ganglia and corpus collosum, tended to have a prognosis of less than 6 months (McKinnon *et al.*, 2021, Fyllingen *et al.*, 2021). Most of the patients in this study had left-, or right-sided tumours, which manifested in various lobes of the brain, such as the parietal, frontal, temporal and occipital lobes, or on the borders of multiple lobes. Lethality, defined as patient survival of less than six months, was not deemed to be a strong indicator of apoptosis due to treatment in this study. Patients with left-sided tumours have also been shown to have poorer prognosis in general, than those with right-sided tumours (Fyllingen *et al.*, 2021). Interestingly, because the emmeans calculation for location of the tumour is averaged over the levels of treatment, this could mean that treatment is affecting the right-sided GBM tumours more and driving cleaved PARP expression. The RPT and RPO are generally more sensitive areas of the brain, responsible for sensory functions (Yuile *et al.* 2006). Tumours which span the geography of multiple lobes of the brain could be more susceptible to cell death through the application of drugs because tumours may be more heterogenous in both cell type, structure, and function and therefore more unstable. RPT and RPO, however, are only represented by one patient each and therefore, more data would be required to understand whether this is a robust trend.

There did not appear to be any significant influence of primary *vs* recurrence on the outcome of treatment in the perfusion device. It might be expected that primary tumours would respond better to treatment, being treatment-naïve and therefore have not yet developed chemotherapy-associated resistance (Yalamarty *et al.*, 2023, Dymova *et al.*, 2021). Recurrent tumours, therefore, may not respond so dramatically to the treatment, particularly TMZ, due to chemotherapy-driven heterogenous clonal expansion of GBM, post-treatment. The samples used for detection of apoptotic markers were a mix of primary and recurrent samples, as well as having various biomolecular profiles (

Table 3.1). This sample group, particularly those in the recurrent group, is too small to identify any solid links between GSK3368715 treatment and primary *vs* recurrent tumours. Additionally, the relative rarity of recurrent GBM surgeries meant that only one paired sample could be sourced for interrogation of the effect of GSK3368715 on primary and recurrent GBM, on the same patient. The main perfusion model used in this study focuses on creating a more personalised screening process for drugs, which can then be translated into the clinic and therefore longitudinal analysis would improve our understanding of, not only the drugs used, but also the validity of the model itself, by comparing like with like. With a greater number of samples, deeper longitudinal investigation into the changes in arginine methylation and PRMTs, as well as the effects of GSK3368715 on these factors, could be explored.

Upon exploration of the seven most frequent and abundant cytokines across control *vs* 1µM GSK3368715 + 10µM TMZ, all time points and covariates, all covariates were found to contribute somewhat to variation of expression of these cytokines, in response to treatment over time. Large shifts across the PCA1 axis at 192- and 288-hours shows that the cytokine profile changes at both of these time points, which could be due to the tissue dying, or could be due to prolonged effect of the treatment. Cytokine profiles are all dependent on the

covariates of patient age, gender, and time on chip. Cytokine profiles do indicate a shift in variation in older patients (>60 years), MGMT negative patients, recurrence and in males in the PC1 and, or PC2 planes, from their binary counterparts. This shift could indicate a poorer prognosis for patients, and this is also reflected by the negative PC1 and PC2 variation shift in patient survival. It is well documented that these biological features are associated with poorer survival (Wang *et al.*, 2022) and therefore, the presence of these cytokines is correlated with GBM aggression. Older patients and males also show a shift in the PC3 plane, suggesting that this variation in the data is explained by these covariates the least.

In univariate analysis of this data, twenty-seven cytokines were found to change with treatment, with the covariates of age, gender, and time on chip accounting for their variation. Three of the twenty-seven cytokines whose profiles appeared to be the most changed, taking into account treatment, time, age and gender, were significantly altered after p-value adjustment. These included Angiopoietin-2, Apolipoprotein-AI and BDNF, which have all been found to play a role in tumour progression. Angiopoietin-2 is a driver of angiogenesis, which it proceeds through binding of RTK tyrosine kinase with immunoglobin and EGF homology domains (TIE2), alongside VEGF, leading to vascular remodelling and permeabilisation (Kiss, 2019). Angiopoietin 2 blockage, alongside VEGF and PD-1 blockade has been shown to reprogram aberrant cells to quasi-antigen-promoting cells, which allow infiltration of cytotoxic T cells, restoring immune-mediated killing of GBM (Amoozgar, 2022). Apolipoprotein-AI is a structural component of high-density lipoprotein (HDL) and is known to be a fat-reducing biomarker, involved in cholesterol metabolism (Mangaraj *et al.*, 2016). In GBM, there is an accumulation of cholesterol, brought about by the constitutive activation of RTK signalling pathways (Dong *et al.*, 2014). Uptake of cholesterol is an important requirement for GBM cell survival (Villa *et al.*, 2016) and Yamamoto *et al.* (Yamamoto et al., 2018a, Yamamoto et al., 2018b) described that TMZ-resistant cells have lower accumulation of cholesterol and increasing cholesterol in non-resistant cells decreased cell viability through evocation of death receptor 5 signalling, leading to apoptosis. Decrease of apolipoprotein AI may therefore prevent the sequestration of cholesterol in GBM cells, leading to an increase in drug sensitivity and apoptosis. BDNF promotes proliferation in astrocytes (Nakajima *et al.*, 2002), and this has been suggested to be through its role in the adaptive plasticity of synaptic connectivity. BDNF allows the trafficking of neurotransmitters to glioma cell membranes, where they depolarise the membrane, allowing the passage of action potentials, leading to an increase in signalling

for proliferation (Taylor *et al.*, 2023). Decrease of BDNF may therefore lead to reduced proliferative signalling.

More in-depth analysis of these cytokines of interest were then performed, using Angiopoietin-2, MMP9, serpin E1, C3L1, IL6, IL8, and VEGF. These cytokines, as described, had been found to be abundant, or significantly changed with treatment in the proteome profiling arrays. Although IL6 did not fit these criteria, it was available in the lab and has been shown to be involved in GBM, as previously described. Clear separation in the PC3 plane indicates that the variables of treatment and age go some way to explaining the variation in cytokine expression over all time points, between control and 1μM GSK3368715 + 10 μM TMZ-treated samples and therefore treatment in having an effect on the variance of cytokine expression. When the covariates are explored further, similarly to the proteome profiler data, the ELISA data indicated that the later timepoints show a significant shift in cytokine expression, although this time it is from 48 hours. This could indicate that the treatment is having an earlier effect on the cytokine expression. Additionally, and interestingly, characteristics usually associated with poorer prognosis, such as male (Carrano *et al.*, 2021) and older patients (Rabin *et al.*, 2024) show variation dispersal in the opposite direction to the dispersal seen with the lethality covariate, in the PC2 axis. This may indicate that treatment is potentiating a cytokine expression response associated with more positive outcomes in patients. This is not seen in the PC1 axis, whereby negative prognostic indicators of recurrence, male gender and MGMT negativity show a negative shift, alongside younger patients (Carrano *et al.* 2021), which tend to have better survival. Causes of variation in the other axes could be due to older patient tissue generally being more susceptible to cell death and therefore changing cytokine expression through reduction in viable cells. Older patients generally have more comorbidities and compromised immune competency than younger patients, which affects treatment outcomes and survival (Rabin *et al.* 2024). Increased survival in female patients is hypothesised to be due to the protective effect of oestradiol, which had been shown to reduce tumour cell viability (Honikl *et al.*, 2020). Additionally, gender-discriminatory DNA methylation of genes such as KDM6A has been shown to contribute to differential gene expression regulation between males and females, through sex-based transcriptional factors, such as oestrogen receptor-α (ERα) (Carrano *et al.* 2021(Honikl *et al.*, 2020). This is not, however, recapitulated in histology data, whereby a link between patient age, gender and other covariates and apoptotic marker expression may be expected.

ELISA results indicated that VEGF and MMP9 cytokine secretion was significantly reduced upon treatment with GSK3368715 and TMZ, whereas C3L1 was increased. VEGF signalling was described previously and is known to be dysregulated in GBM, leading to vascular permeabilisation, angiogenesis and GBM expansion (Keunen *et al.* 2011) (Chi, 2009)(Ahir, 2020)(Yue, 2015). MMP9, as described previously in this discussion, is responsible for the breakdown of the extracellular matrix and subsequent motility of GBM cells, leading to migration and invasion into surrounding tissue and thereby contributing to metastasis and expansion (Dobra *et al.* 2023)(Xue *et al.* 2017). Decrease of these markers with GSK3368715 and TMZ treatment is C3L1 has been found to be a marker of proneural to mesenchymal transition, found in some recurrent GBM cells, post-treatment, indicating a more quiescent state of the recurrent tumour (Stead 2022). C3L1 is a marker of the mesenchymal GBM cellular state phenotype (Wang *et al.* 2022) and this shift is indicative of the plasticity of GBM cells (Neftel *et al.*, 2019). The statistically significant increase in C1L3 with treatment indicates that there may be some immunosuppressive benefit of GSK3368715 and TMZ concurrent treatment in GBM. Elevated C1L3 could mean that the treatment is the driving a more differentiated mesenchymal phenotype of GBM cells, leading to resensitisation of GBM to treatment, thereby increasing levels of programmed cell death, seen in the IHC.

The increase in cell viability seen in the 2D and 3D cell cultures, despite not being statistically significant, could indicate that GSK3368715 and other PRMT inhibitors cause a switch to a more proliferative phenotype, as supported by the increase in C3L1, which is therefore more sensitive to cell killing, but requires a prolonged duration of treatment before viability begins to decrease. Viability assays in patient-derived cells would be more appropriate, considering the vast interrogation that has occurred on the U87-MG cell line and the recommendation that it is no longer a suitable GBM cell line model. The results seen in *ex vivo* tissue samples, however, are much more reflective of how patients may clinically benefit from GSK3368715.

3.5. Conclusion

The results presented in this chapter highlight the complexity and heterogeneity of GBM and compounds the importance of utilising multiple experimental techniques to confirm drug

effects. Whilst cytokine and LDH data appears to suggest limited effect of PRMT inhibition on GBM, in terms of increasing cytokine levels and cellular stress; histological data has shown significant changes in apoptosis in GSK3368715-treated GBM tissue in the perfusion device after 8 days. Whilst the histological data also shows no synergy with other PRMT inhibitors, or TMZ; importantly, it shows no detrimental effect either. Shifts in cytokine profiles, including the decrease of cytokines associated with GBM aggression and the increase in cytokines associated with the mesenchymal phenotype also provide some indication that GSK3368715 may trigger a plasticity change of GBM cell phenotype to a more sensitive one, promoting cell death. This is imperative when trialling new drugs for translational use, as during clinical trials, these drugs must efficaciously and/or additively function in conjunction with TMZ. In order to understand further this increase in GBM cell death instigated by GSK3368715, the following chapter investigates potential underlying mechanisms of GSK3368715 function.

CHAPTER 4: DETERMINING A MECHANISM OF ACTION FOR GSK3368715-INDUCED APOPTOSIS IN EX VIVO GBM

4.1. Introduction

In the previous chapter, it was discussed that GSK3368715 leads to apoptosis in GBM after 8 days in the *ex vivo* perfusion system. It was also discussed that there was no synergy with other PRMT inhibitors, such as Furamidine, or GSK591, or the current gold standard chemotherapy agent TMZ. The next step was to identify the mechanisms underlying this increase in apoptosis, in response to PRMT inhibition. The work in this chapter attempted to describe the transcriptomic impact of PRMT inhibition, *via* GSK3368715, and to determine transcriptomic pathway changes, which may help to understand the impact of PRMT inhibition in GBM tissues *ex vivo* and any alternative proteins of interest (POIs). In previous work performed in this lab and published by Sabrina Samuel (Samuel *et al.*, 2018), it was found that type I PRMT inhibition causes unidirectional crosstalk, leading to a decrease in aDMA and an increase in sDMA. Preliminary investigations into this crosstalk, using mass spectrometry, indicated FUS as a POI, which could potentially drive this crosstalk. One of the aims of this chapter was to delve further into the validation of FUS as a potential driver of arginine methylation crosstalk, methylation of FUS itself and to ascertain whether FUS could be a potential therapeutic target in GBM, which may lead to understanding more about chemotherapeutic resistance.

4.1.1. Clinical exploration of arginine methylation inhibitors

Several clinical trials have been commissioned into the efficacy of PRMT inhibitors against a variety of solid and haematological cancers, following promising results *in vitro* and in *in vivo* animal models. These have also included GSK3368715, which was entered into a phase I clinical trial (NCT03666988); however, was terminated early in 2023, due to a high incidence of TEEs in patients taking 200 mg, orally (El-Khoueiry *et al.*, 2023). Interestingly, in work undertaken at the University of Hull and published by Marsden *et al.* (2021), GSK3368715 was found to cause alterations in platelet aggregation behaviour, which directly supports the findings of the clinical trial. Concentration of GSK3368715 used for these studies was based upon preclinical and toxicity studies in mice and dogs, which suggested that a safe dose range

should be between 75 mg/kg and 300 mg/kg, according to the Neuenschwander Continual Reassessment Method dose-escalation design (Neuenschwander *et al.*, 2008). The dosage used for these toxicity studies falls within this remit, at the lower end of the clinical trial dosage of 50 mg/kg.

4.1.2. PRMT Inhibition and Alternative Splicing

Type I PRMT inhibition by GSK3368715 has been documented to cause alternative splicing in several cell lines. Cell lines which exhibited the greatest inhibitory response to the drug appeared to have the highest number of alternative splicing events (Fedoriw *et al.*, 2019). This may result in splicing infidelity, due to the change in methylation of known exon usage regulators (Wall and Lewis, 2017). This effect was only amplified when type I PRMT inhibitors are used in combination with PRMT5 inhibitors, indicating synergy (Fedoriw *et al.*, 2019, Fong *et al.*, 2019).

4.1.3. FUS and GBM

FUS is an hnRNP P2 and normally located within the nucleus. It is involved in the DNA damage response, transcription and splicing (Neumann et al., 2009a, Neumann et al., 2006). One function of FUS is to perform phase separation within the nucleus, potentially to allow DNA damage sensor protein access to the DNA (Wang et al., 2013b), driven by methylation (Qamar *et al.*, 2018). Aberrant FUS function, may lead to nuclear export of FUS into the cytoplasm, hypothesised to be through cleavage by caspases (Dormann et al., 2009, Tsai et al., 2022). It then aggregates and causes dysregulation of nuclear events, such as splicing and gene expression regulation (Ratti and Buratti, 2016, Hofweber *et al.*, 2018), potentially due to the subsequent inability to bind associated proteins, such as RNAPII (Tsai et al., 2022). FUS has been shown to reduce proliferator factors, such as cyclin D1 and CDK6, whilst increasing anti-proliferation factors and proliferative inhibitory factors such as CDK and p27 – thus increasing the rate of apoptosis in prostate cancer cells. IHC analysis identified that there was an inverse correlation between FUS and the degree of prostate cancer, indicating that higher FUS levels increase survival (Gahnbarpanah *et al.* 2018). FUS is extensively methylated by type I PRMTs (Suarez-Calvet *et al.*, 2016), which allows interaction with anti-aggregation molecules, such as TNPO1 (Hofweber *et al.*, 2018), maintaining proper nuclear regulation.

4.1.4. Aims and Objectives

Previous studies in this lab by Samuel *et al.* (2018), as well as elsewhere (Huang *et al.*, 2023) have determined that inhibition of aDMA *via* type I PRMTs leads to unidirectional crosstalk, whereby sDMA of proteins increases. In SDS-PAGE and MS work performed by Dr. Sabrina Samuel and published in Lab on a Chip by Barry *et al.* (2023), a specific 70 kDa protein, which is postulated to be FUS, displayed dose-dependent increase in sDMA and reduced aDMA when U-87 MG cells were treated with type I PRMT inhibitors MS023 and GSK3368715. The hypothesis for this chapter is that GSK3368715 causes transcriptomic changes to GBM in the novel perfusion device. The objectives of this chapter are to:

- Explore changes in the transcriptome of GBM *ex vivo*, in terms of not only differential gene expression but also alternative splicing, with GSK3368715 treatment
- Expand on previous findings that FUS may be a target of arginine methylation switching in GBM *ex vivo*

4.2. METHODS AND MATERIALS

4.2.1. Sample Processing for RNA-sequencing

Patient samples used for RNA-sequencing were: D16-17, D19-20, D22, D25-30, D32-33. Pre-perfusion, 8-day static and 8-day post-perfusion DMSO control and GSK3368715-treated samples, prior to D27 were homogenised using a pestle and RNA extracted using the RNeasy kit. Static samples were micro-dissected and put into DMSO-treated medium in a falcon tube and stored in the same incubator as the chips. Pre-perfusion and 8-day post-perfusion DMSO control and GSK3368715-treated samples, D27 and later, were homogenised using the Turrax Homogeniser and RNA extracted using TRIzol®. RNA quantity and quality was checked using the Nanodrop2000, before samples were sent to Novogene for RNA quality control and subsequent RNA-sequencing.

4.2.2. U-87 MG lysate preparation

U-87 MG cells for nuclear and cytoplasmic extraction were seeded in 150 mm plates (Corning) for 24 hours before being treated with: 1 μM GSK3368715, 1 μM Furamidine, 1 μM GSK3368715 + 1 μM Furamidine, 1 μM GSK3368715 + 1 μM GSK591, 1 μM GSK3368715 + 1 μM Furamidine + 1 μM GSK591 and a DMSO negative control, for 48 hours and cells for immunoprecipitation treated for 72 hours. Cells were harvested using 1% Triton-X100 (Sigma) in PBS (Fisher Bioreagents) containing phosphatase and EDTA-free protease inhibitors (Roche) and stored at -80 ºC. Nuclear and Cytoplasmic extraction was performed on the resulting lysates using the NE-PER™ Nuclear and Cytoplasmic Extraction kit (ThermoFisher Scientific), following the manufacturer's instructions. Immunoprecipitation was performed on corresponding lysates using protein A bead extraction and antibodies against FUS.

4.2.3. Tissue lysate preparation

Patient samples used for lysates were: D7, D8a-12, D14. Pre- and post-perfused tissue were homogenised using a pestle and lysed using Triton X-100 in PBS (1% v/v) for one hour, rotating at 4°C. Patient samples used for FUS IP were: D16-17, D19-21, D24-26, D29-31. Tissue samples for pre- and post-perfused DMSO control and GSK3368715-treated were lysed as previous. Clinical data shown in *Table 4.1*. All clinical data up to date as of 27/08/23.

Table 4.1.: Clinical data for patient samples used in this chapter. Where + indicates mutation or presence of associated biomarker (MGMT promoter methylation) and – indicates wildtype status or absence (no MGMT promoter methylation). Gaps show no information available.

Patient	Sex	Age	Primary vs Recurrent	Location	IDH	1p/19Q	MGMT	EGFR	TERT	ATRX	Necrosis	BRAF	CDKN2A	TP53	PTEN	Surgery-Death (days)	Surgery-27/08/23 (days)
D7	M	56	Primary	right temporal	-	-	-	+	-	+		+		+		572	
D8a	M	65	Primary	left temporal	-	-	=			-	++					683	
D9	M	75	Primary	left parietal	-	-	+			-	+					120	
D10	M	67	Recurrent	tempo-partietal	-	-	-			-	++					76	
D11	F	50	Primary	right parieto-temporal	-	-	-		+	-	++	-				Alive	704
D12	M	71	Primary	right frontal	-	-	-			-	++					133	
D14	M	72	Recurrent	right parieto-occipital	-	-	-			-	+					234	
D16	M	63	Primary	right parietal	-		-			-						195	
D17	M	69	Primary	right frontal	-		-			-						318	
D19	M	67	Oligodendroglioma II	parietal	-		-			-						443	
D20	F	74	Primary	right tempo-parietal	-		-			=						385	
D21	F	73	Primary	right occipital	-		+			-						44	
D22	F	44	Recurrent	right parietal	+	-	-	-		-		-	+			411	
D24	M	67	Primary	right occipital	-	-	+			-		-	+			Alive	439
D25	F	63	Primary	left parietal	-	+	-	+	-	-		-		-		44	
D26	M	70	Primary	left frontal	-		-	+	-			-				41	
D27	M	56	Primary	left frontal	-		-	+	-	++		-				46	
D28	M	51	Recurrent	right parietal	-		-	+	-			-				326	
D29	M	58	Primary	left temporal	-		+	+	-			-				Alive	289
D30	M	58	Primary	right temporal	-		-		-							Alive	286
D31	M	76	Primary	right frontal	-		+		-							Alive	263
D32	M	45	Primary	left parieto-occipital	-		-	+	-			-	+			Alive	198
D33	F	55	Primary	right occipital	-		-	+	-			-	+			Alive	158

4.3. RESULTS

4.3.1. GSK3368715 causes differential gene expression associated with reduced cell function

The first aim of this section was to identify any transcriptional changes to GBM tissue *ex vivo,* through treatment of the tissue with PRMT inhibitor GSK3368715. RNA-sequencing and subsequent analysis was performed by Novogene® Illumina Novseq 6000, at a read depth of 34-60 million per sample. RNA-sequencing aimed to identify any transcriptomic changes in patient GBM samples, with treatment of 1 μM GSK3368715. Three micro-biopsies of tissue (across three perfusion devices) per treatment (DMSO control and 1 μM GSK3368715) were pooled and RNA extracted, to account for intra-tumour heterogeneity and to give a broader picture of transcriptomic changes occurring throughout the tumour. Four patient samples (D27-D30), paired post-perfusion DMSO control vs 1 μM GSK3368715, were analysed, after successfully passing QC. All of these patients were male and within a similar age range (51-58), with ¾ having primary tumours and ¼ being MGMT positive. There was equal distribution of right and left sided tumours, with two patients displaying temporal lobe tumours, one patient with GBM in the parietal lobe and the other patient with a frontal lobe tumour. At least ¾ patients showed TERT positivity and BRAF negativity and at least ¼ showed extensive necrosis within the bulk of the tumour. ¾ patients survived beyond the 6-month lethality window. Expression profiles of all genes were compiled into patient-specific volcano plots (Figure 4.1).

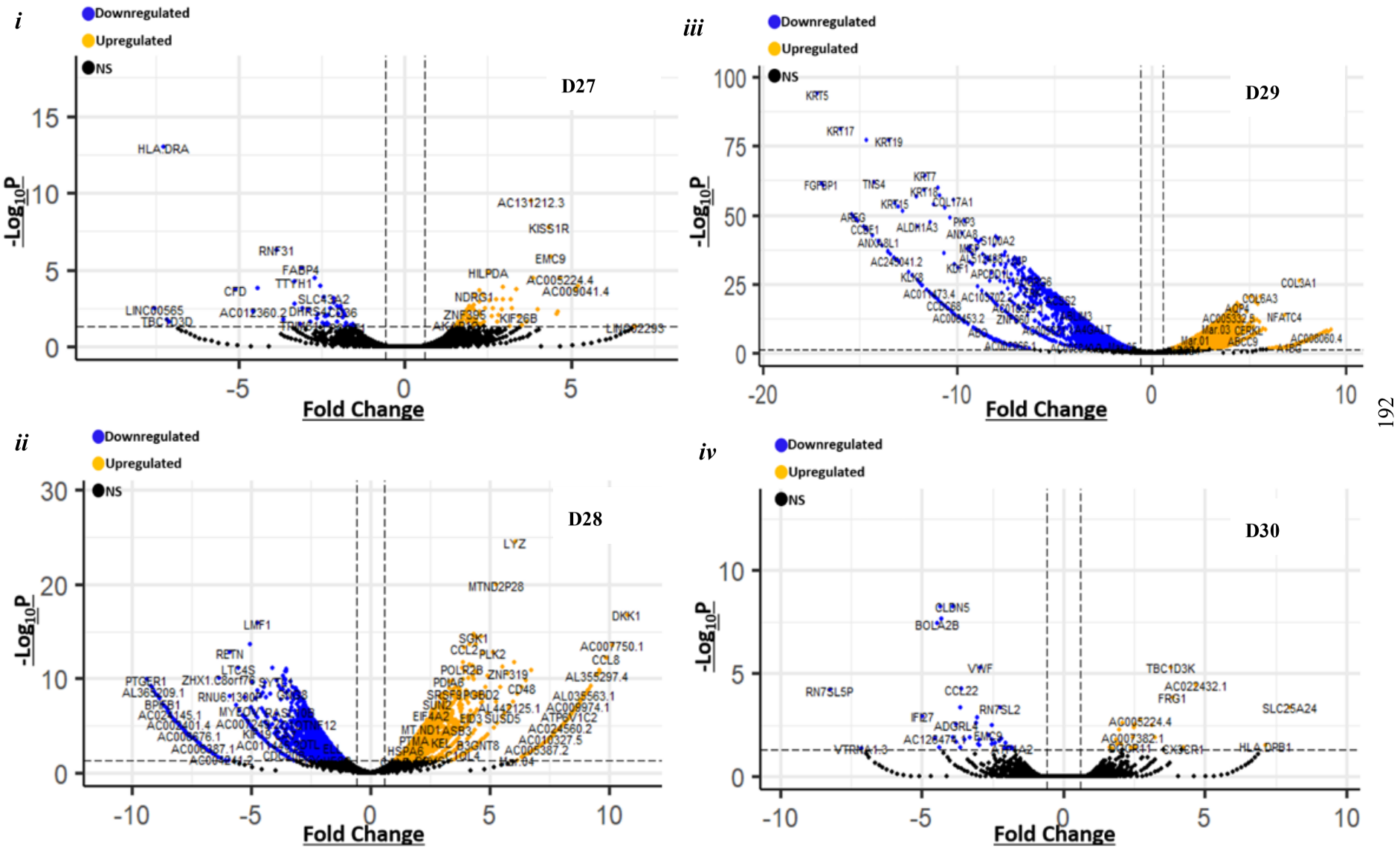
i
Downregulated
Upregulated
NS
D27
-Log10P
Fold Change
HLA-DRA
RNF31
FABP4
TTYH1
CFD
SLC43A2
LINC00565
TBC1D3D
AC012360.2
DHRS4-CCDC86
AC131212.3
KISS1R
EMC9
HILPDA
AC005224.4
AC009041.4
NDRG1
ZNF395
KIF26B
LINC02295
ii
Downregulated
Upregulated
NS
D28
-Log10P
Fold Change
LYZ
MTND2P28
DKK1
LMF1
RETN
LTC4S
PTGER1
ZHX1-C8orf76
AL365209.1
RNU6-1360P
BPGB1
AC024145.1
AC002401.4
AC000676.1
AC006387.1
SGK1
CCL2
PLK2
AC007750.1
CCL8
POLR2B
ZNF319
AL355297.4
PDIA6
CD48
AL035563.1
SRSF3
PGBD2
AL442125.1
AC008974.1
SUN2
EIF4A2
EID3
SUSD5
ATP6V1C2
MT-ND1
ASB3
AC024560.2
PTMA
KEL
B3GNT8
AC010327.5
HSPA6
AC005387.2
iii
Downregulated
Upregulated
NS
D29
-Log10P
Fold Change
KRT5
KRT17
KRT19
FGFBP1
TNS4
KRT7
KRT15
COL17A1
ALDH1A3
PKP3
ANXA8
ANXA8L1
AC243041.2
KDF1
AC011473.4
AC006453.2
COL3A1
COL6A3
AQP4
AC005332.5
NFATC4
Mar.03
CERKL
Mar.01
ABCC9
AC006060.4
iv
Downregulated
Upregulated
NS
D30
-Log10P
Fold Change
CLDN5
BOLA2B
VWF
TBC1D3K
AC022432.1
FRG1
SLC25A24
RN7SL5P
CCL22
RN7SL2
IFI27
ADGRL4
AC005224.4
AC007382.1
AC126475.1
EMC9
HLA-A
VTRNA1-3
CX3CR1
HLA-DRB1

Figure 4.1.: Volcano plots for patients i) D27, ii) D28, iii) D29 and iv) D30 indicating differentially expressed genes in 1 µm GSK3368715-treated cells vs DMSO control.

Vertical dashed lines indicate log2 fold change (log2FC) <0.585 (FC 1.5) and the horizontal dashed line indicates adjusted p-value (padj) >0.05. Blue marks display downregulated genes and yellow marks display upregulated genes. Black marks indicate genes which fall below the log2FC and padj thresholds. Say that you produced this using R

Differential expression analysis discovered thousands of genes which had been significantly ($p<0.05$) differentially expressed (FC >1.5, or <-1.5) upon treatment of *ex vivo* GBM with 1 µM GSK3368715. Abundantly more genes were differentially expressed in patients D28 and D29, as opposed to D27 and D30. Whilst this could potentially be due to D27 and D30 patient GBMs having heterogenous areas of little activity, this was mitigated for by pooling 3 biopsies of the same patient tumour, before extracting RNA. Patients were all also within a similar age range (51-58), likely excluding age as a potential cause of differences between RNA-sequencing outcomes. Patient D27 biopsy displayed high levels of necrosis, which could explain the reduced numbers of DEGs in this sample, although it would then be expected to see a much lower number of reads in this sample. This high level of necrosis is displayed in the swathes of pink, eosin-stained tissue in Figure 4.2 nuclei that are not intact. The most significantly downregulated gene in patient D27 was *histocompatibility complex, class II, DR alpha* (*HLA-DRA*), and GO analysis (ShinyGO(Ge *et al.*, 2020)) indicated significant enrichment in inflammatory response (Appendix 7). The most significantly upregulated genes were long non-coding RNA (lncRNA) *AC131212.3*, *kisspeptin-1 receptor* (*KISS1R*) and *endoplasmic reticulum membrane protein complex subunit-9* (*EMC9*), with significant enrichment in hypoxic response and negative regulation of necrotic cell death (Appendix 7).

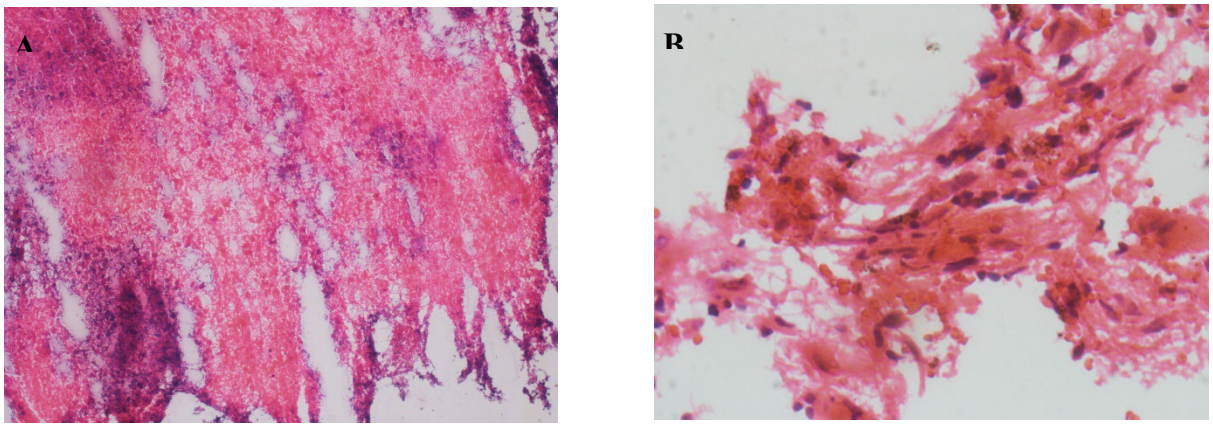

Figure 4.2.: Haematoxylin and Eosin – stained tissue from GBM patients A) D27 x10 magnification and B) D30 x40 magnification.

D28 displayed a relatively even spread of differentially up and down regulated genes (Figure 4.1). GO analysis, performed by GOrilla (Eden *et al.*, 2007, Eden *et al.*, 2009), found that upregulated genes showed enrichment in pathways associated with ion transport and the electron transport chain and downregulated genes showed enrichment in mitochondrial membrane organisation (Appendix 7). Also noteworthy is that over 50% of the genes which were significantly differentially expressed were novel genes, with no assigned Ensembl or Uniprot ID. This could suggest that there are more pathways enriched in both up- and downregulated genes that cannot yet be assessed through RNA-sequencing and bioinformatic analysis. The most significantly upregulated genes were *lysozyme* (*LYZ*), *dickkopf WNT signalling pathway inhibitor-1* (*DKK1*) and *mitochondrially encoded NADH:ubiquinone oxidoreductase core subunit 2 pseudogene 28* (*MTND2P28*). Downregulated genes included *lipase maturation factor-1* (*LMF1*).

Patient D29, interestingly, also appears to show more downregulated genes than upregulated genes, as well as when compared to any of the other patient biopsies (Figure 4.1). This could be due to the molecular features of this sample (Table 4.1), with MGMT promoter methylation causing downregulation of genes associated with mitosis and proliferation when the biopsy is treated with the PRMT inhibitor *(*Appendix 7*).* Downregulated genes with the lowest false discovery rate (FDR) values were keratin encoding genes: *KRT5, KRT17* and *KRT19*. Upregulated genes in D29 also indicate that synapse and signalling pathways, including neuron

development, are more active post-treatment (Appendix 7) (Eden *et al.*, 2007, Eden *et al.*, 2009). The most significantly upregulated genes in patient D29 were *collagen III alpha subunit 1* (*COL3A1*) and *collagen IV alpha subunit 3* (*COL6A3*).

Patient D30 had significantly downregulated genes, such as claudin-1 (*CLDN5*) and bola-like protein-2B (*BOLA2B*) and GO analysis (ShinyGO(Ge *et al.*, 2020)) indicated enrichment in angiogenesis and cell migration. Significantly upregulated genes included TBC1 domain family member 3K (*TBC1D3K*), lncRNA AC005224.4 and facioscapulohumeral muscular dystrophy (*FSHD*) region gene 1 (*FRG1*) and indicated more modest enrichment in leukocyte activity (Appendix 7).

Overall GO analysis (Eden *et al.*, 2007, Eden *et al.*, 2009, Ge *et al.*, 2020) was performed to identify any enrichment in biological processes, cellular components, molecular function and Kyoto Encyclopaedia of Genes and Genomes (KEGG) pathways, which may elucidate a way in which GBM may phenotypically behave due to changes in gene expression. Due to the limited number and heterogeneity of the patients, as seen in *Table 4.1* I decided to expand the search criteria and look for GO enrichments in downregulated genes which were common to two or more of the GBM samples to identify any common pathways affected by PRMT inhibition (Figure 4.3) Large and highly significant enrichment was found in GO terms associated with the ribosome and translation (Figure 4.3 and Appendix 7).

Biological Process

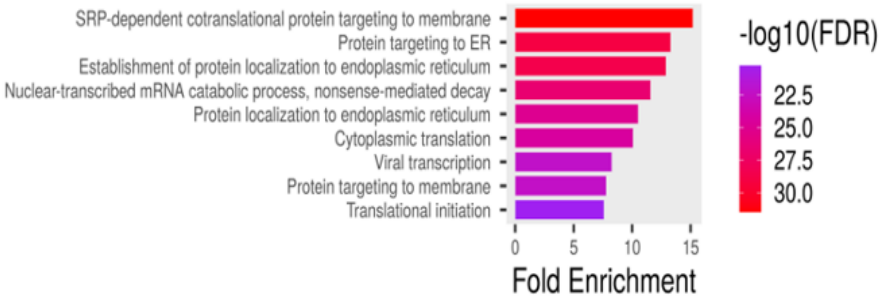

Cellular Component

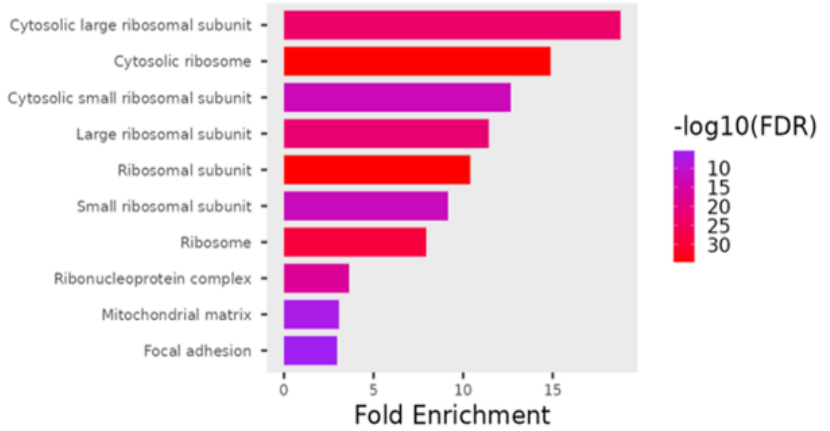

KEGG

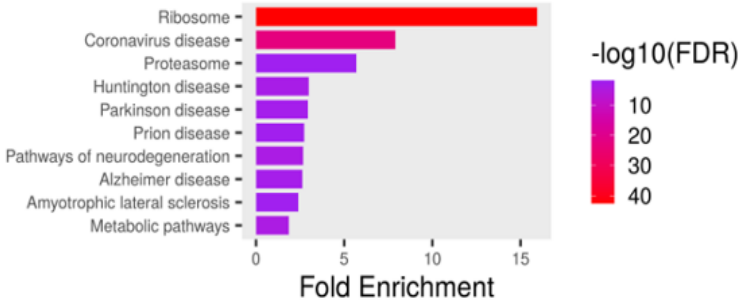

Molecular Function

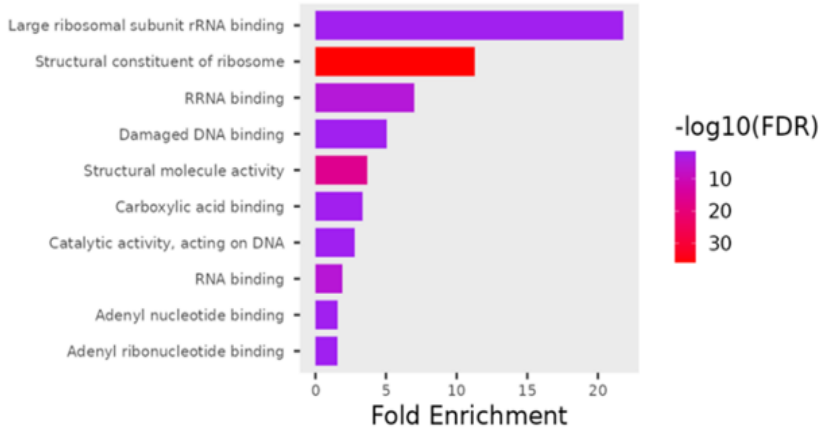

Figure 4.3.: Gene ontology enrichment in pathways associated with downregulated DEGs, in GBM ex vivo, after 1 µm GSK3368715 treatment.

GO analysis (Ge et al., 2020) of significantly ($p<0.05$) downregulated differentially expressed genes (DEGs) (fold change <-0.585), common to 2 or more patients, in RNA-seq analysis of 4 patients (D27-D30) GBM samples, 8-days post-perfusion and treated with 1 µM GSK3368715 vs DMSO control. Full GO analysis can be found in Supplementary Table 4.1.

Similarly, GO enrichment in the upregulated genes of two or more samples were compiled to find enrichment in biological processes, molecular function, cellular component and KEGG pathways (Figure 4.3). Modest enrichment was found in GO terms associated with transcription, cell-cell communication, adhesion, migration and cell surface (Figure 4.3 and Appendix 7).

Biological Process

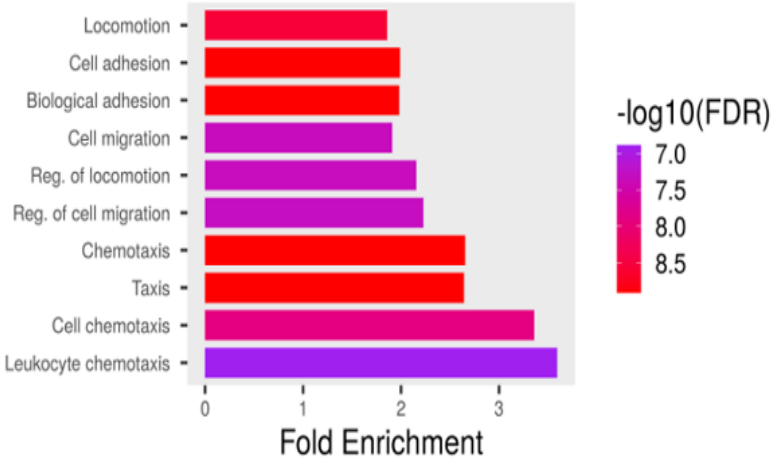

Cellular Component

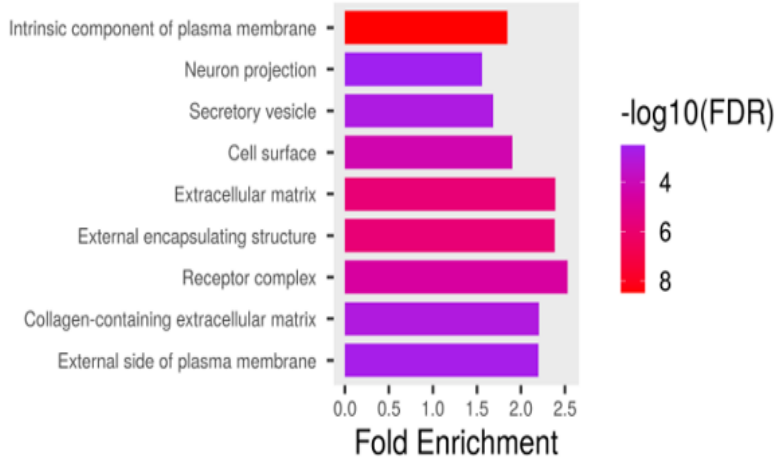

Molecular Function

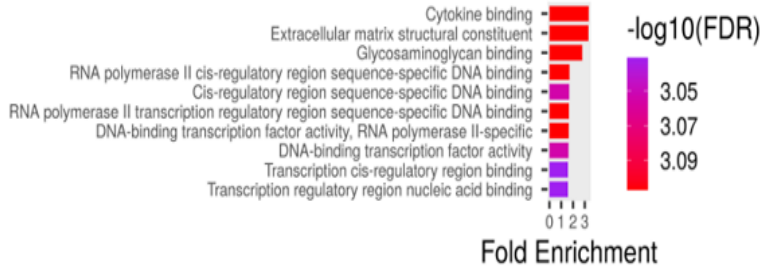

KEGG

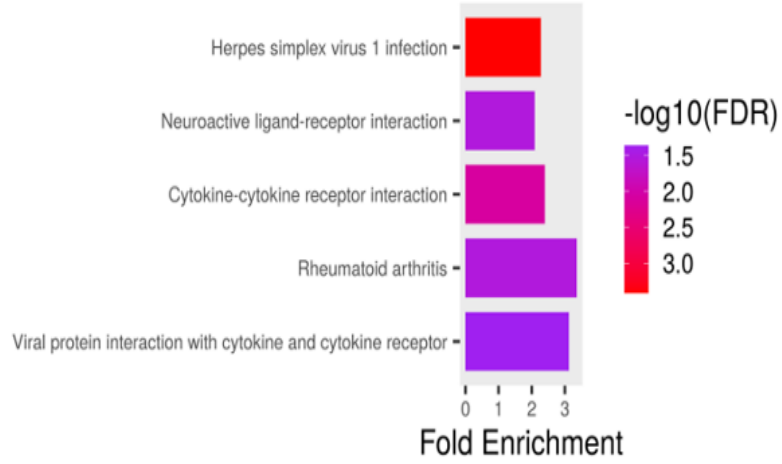

Figure 4.4.: Gene ontology enrichment in pathways associated with upregulated DEGs in GBM ex vivo, after 1 µm GSK3368715 treatment.

GO analysis (ShinyGO (Ge SX, Jung D & Yao R, Bioinformatics 36:2628-2629, 2020; ***http://bioinformatics.sdstate.edu/go/****) of significantly (p<0.05) upregulated differentially expressed genes (fold change >0.585), common to 2 or more patients, in RNA-seq analysis of 4 patients (D27-D30) GBM samples, 8-days post-perfusion and treated with 1 µm GSK3368715 vs DMSO control. Full GO analysis can be found in Appendix 7.*

4.3.2. Stratification of GBM patients into GSK3368715 responders and non-responders

Due to the molecular differences between the samples and the differences in the types and numbers of DEGs, principal component analysis (PCA) of the DEGs was employed to determine any distinct shifts in behaviour of the individual samples, between control and treatment. Figure 4.5 displays the variability between samples and differential responses to PRMT inhibition.

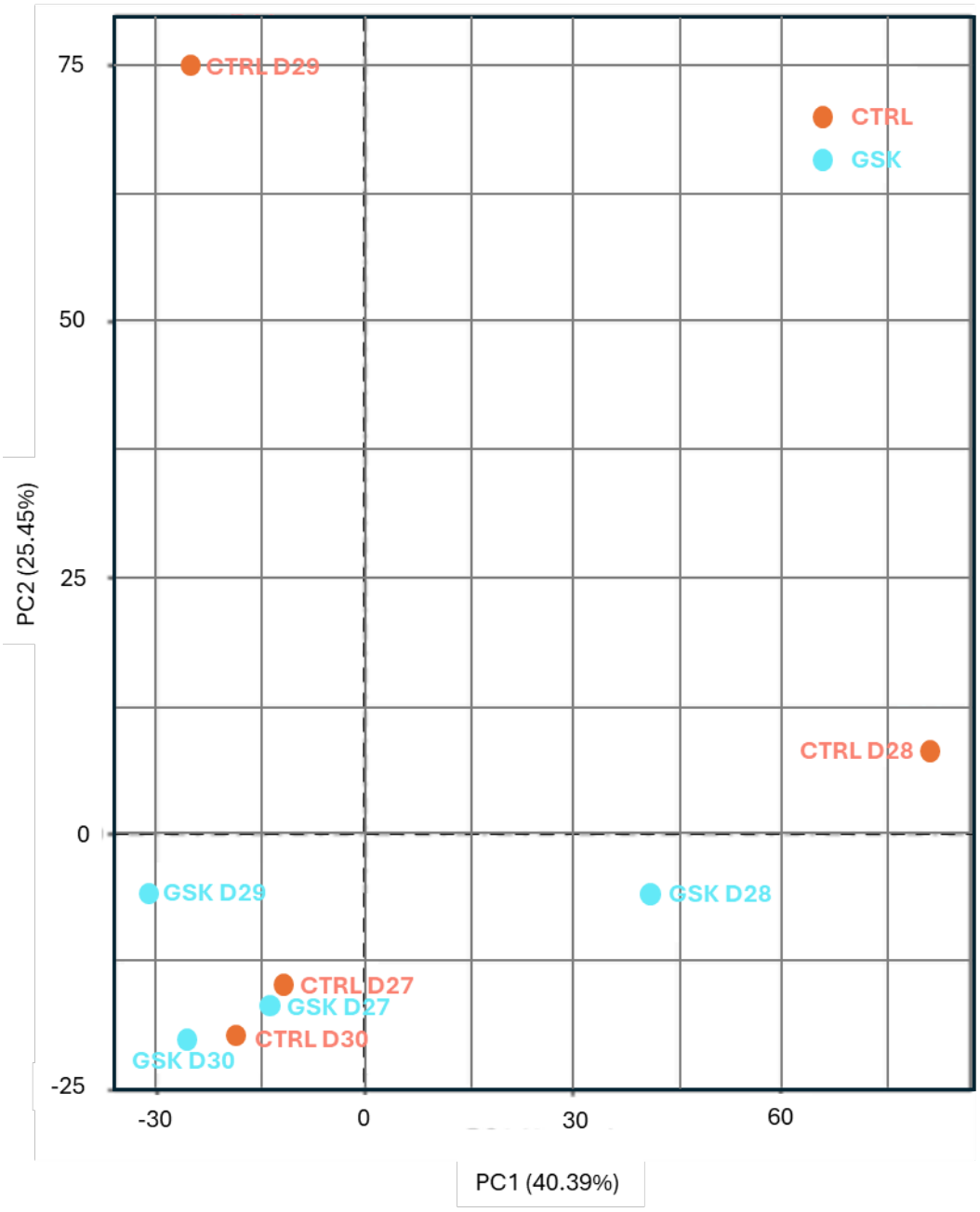

Figure 4.5.: Principal component analysis of GBM (n=4) perfused for 8 days with either 1 µM GSK3368715, or DMSO control.

Red dots indicate DMSO control GBM samples and blue dots indicate 1 µM GSK3368715 treated GBM patient samples.

The PCA plot (Figure 4.5) shows four distinct groups of DEGs associated with each patient and their treatment condition. In the top left of the PCA, there are DEGs associated with patient

sample D28 treated with the DMSO control, indicating a large principal component 1 (PC1) shift of the paired GSK3368715-treated patient sample. Patient sample D29 also has a large principal component 2 (PC2) shift between the DMSO control-treated tissue on the far right and the GSK3368715-treated sample, which is again clustered with all of the other samples: D27 and D30 control and treated and D28 and D29 treated, in the bottom left.

The clinical data shown in *Table 4.1* shows that patient sample D28 was a recurrent tumour, which could explain the PC1 shift. Patient sample D29 was shown to be MGMT positive after neurohistopathological analysis performed by Hull Royal Infirmary. This is reflected in Figure 4.1 which indicates far more DEGs in patients D28 and D29, than in D27 and D30. Treatment appears to cause far more transcriptomic changes in D28 and D29. This could be due to intra-tumour heterogeneity, with sections of the tumour being necrotic, therefore reducing the number of cells which are active; although, this was mitigated for by pooling several pieces of the tumour. The increased number of transcriptomic changes is more likely down to inter-tumour heterogeneity and the variety of molecular features seen between patients.

Whilst recurrence is known to be more clinically aggressive and an indicator of poor prognosis, MGMT positivity is generally a positive prognostic indicator, with median patient survival increasing with incidence of MGMT positivity (Szylberg *et al.* 2022). The fact that the variation between the patients is visualised in two different planes gives credence to the idea that recurrence and MGMT positivity are clinical targets of interest and that there are transcriptomic changes occurring from primary tumours and in MGMT negative tumours. The reduction of variation in patients D28 and D29, specifically with GSK3368715, suggests that type I PRMT inhibition may be having some sort of effect in reducing the variation seen in GBM tumours with these clinical features. In the case of the recurrent tumour, this appears to be reducing aggressive clinical features down to the same level as the less aggressive phenotypes, or more inactive tissues. The same is also true for the GBM tumour expressing MGMT positivity. Treatment shifts the transcriptome of the tumour towards a similar phenotype as the less active tissues, whilst maintaining a higher number of downregulated genes, which are different from those associated with the recurrent tumour. This could indicate different pathways by which the PRMT inhibitor treatment is working in different tissue types. Further investigation would be needed to corroborate why this might occur, but it may be due

to a methylation switch, which is triggered by the type I PRMT inhibitor, which would therefore reduce the "protective" effects of MGMT promoter methylation but target the aspects of the primary tumour which have shifted the variation in gene expression to a less active phenotype.

It would be tempting to stratify these patients into "responders" and non-responders" to GSK3368715, although, this is only n=4 and there is only n=1 of these particular phenotypes (recurrence vs MGMT positive). More patient samples would need to be analysed to give weight to this evidence.

4.3.3. GSK3368715 causes alternative splicing events associated with cell death pathways

RNA-seq analysis also identified significantly alternative spliced genes, associated with 1 µM GSK3368715 treatment, in GBM *ex vivo.* Alternative splicing was described as including: 3' splice site, 5' splice site, multiple exon splicing, intron retention and exon skipping.

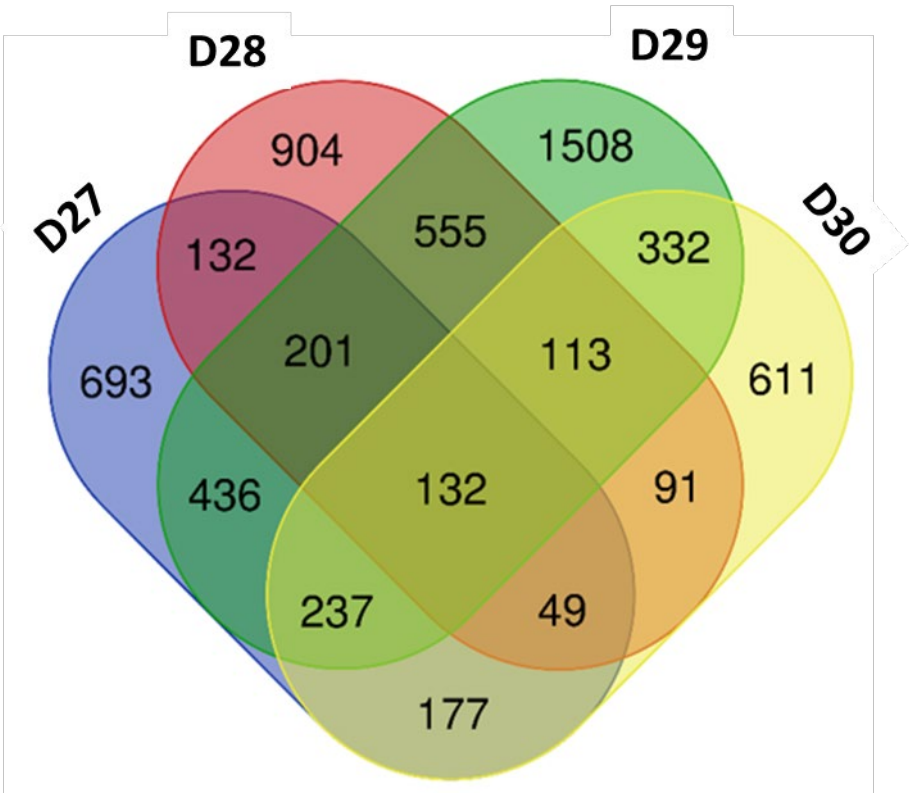

Figure 4.6.: Hundreds of alternatively spliced genes triggered by 1 μM GSK3368715 treatment. *Analysis of all five alternative splicing event pathways identified 2455 genes undergoing differential alternative splicing. Hundreds of differential splicing events occurred in D28 and D29 patient biopsies, as supported by the DEG data; however, in contrast to previous data, a considerable number of alternative splicing events were also occurring in D27 and D30 patient biopsies.*

Out of the 2455 genes undergoing differential alternative splicing with 1 μM GSK3368715 treatment, 132 events were conserved between all four patient samples. GO enrichment was found in annotated keywords related to alternative splicing (KW-0025, 92 of the 132 proteins in our data set *vs.* a total of 10,179 in the human genome, FDR $3.92e^{-06}$) (Figure 4.6 and Appendix 8). For consistency with the DEG data and to account for the small sample size, GO analysis was performed on alternatively spliced genes which were conserved in two or more patient GBM biopsies.

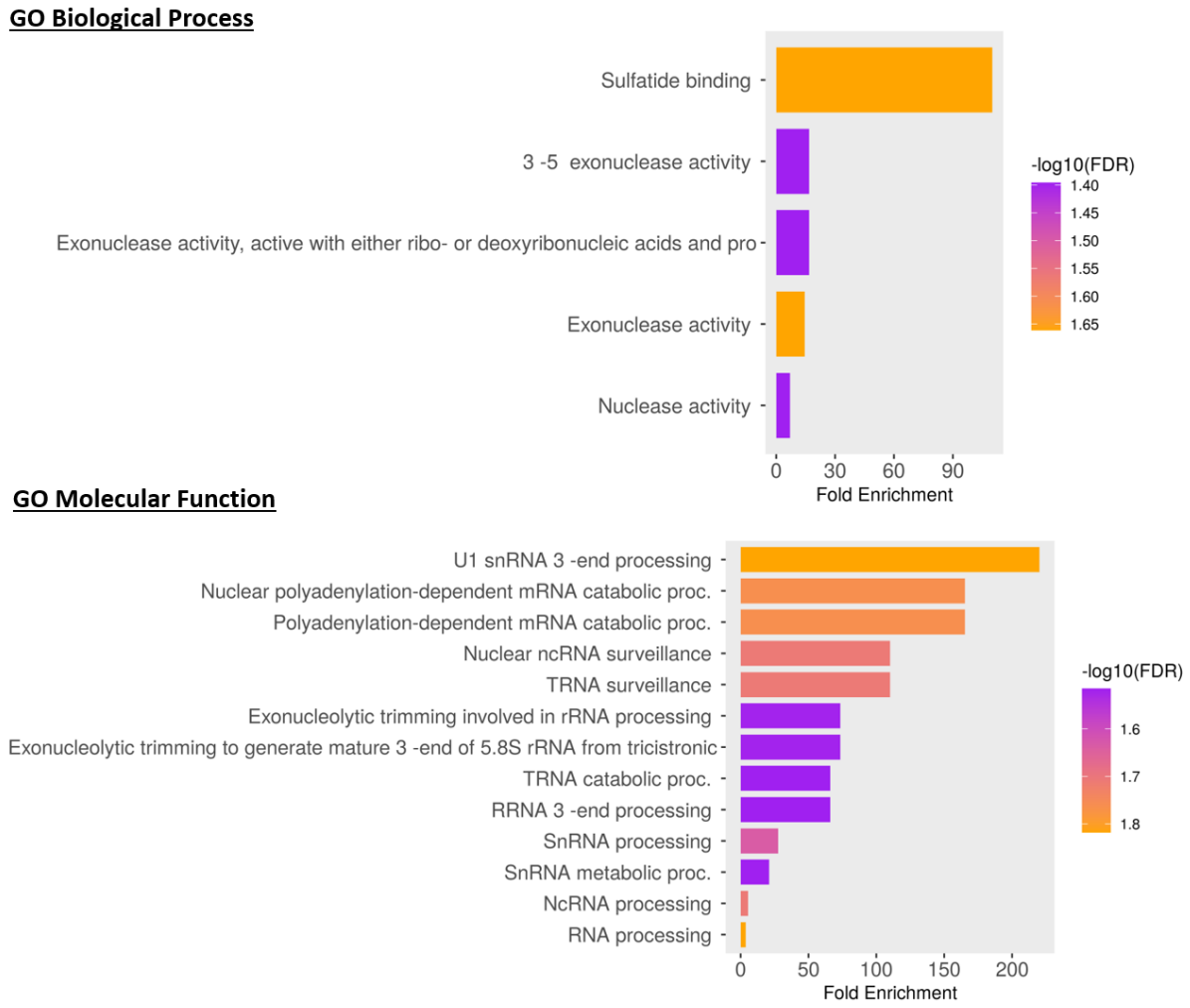

Figure 4.7.: GO Terms associated with alternative splicing events in GBM ex vivo after 1 µM GSK3368715 treatment.

GO analysis (Ge et al., 2020) of significantly ($p<0.05$) alternatively spliced genes, common to 2 or more patients, in RNA-seq analysis of 4 patients (D27-D30) GBM samples, 8-days post-perfusion and treated with 1 µm GSK3368715 vs DMSO control. Full GO analysis can be found in Supplementary Table 4.2.

The broader GO analysis of conserved alternative splicing events in two or more samples revealed enrichment in terms related to DNA damage, RNA processing and cell death (Figure 4.7 and Appendix 8). Taken together, our results provide a mechanism to explain how GSK3368715 causes apoptosis of GBM biopsies that is, through modifying RNA processing, gene splicing and protein translation, which are well-known regulators of apoptosis in GBM.

Alternatively spliced genes, found in two or more patients, were then correlated with proteins which showed arginine methylation switches after GSK3368712 treatment, as published by Fedoriw *et al.* (2019) (Appendix 9). Five cell lines, Toledo and OCI-Ly1 (B-cell lymphoma) and HupT4, Panc 08.13 and Panc 03.18 (Pancreatic Adenocarcinoma) were treated with GSK3368712 (structurally similar to GSK3368715) and mMA, aDMA and sDMA markers identified using affinity enrichment proteomics, using mass spectrometry to identify modified proteins (Fedoriw *et al.*, 2019). This identified 91 genes which had previously been observed to have methylation changes, after treatment of cell lines with GSK3368712, across all five cell lines. These 91 genes make up a subset which could be used for further analysis into arginine methylation switching with PRMT inhibitors and their ability to drive therapeutic resistance. Protein methylation shows redundancy, whereby several methylation types may be attributed to one protein, and these can be further broken down into 84 proteins which switch to mMA, 22 switching to sDMA and 24 to aDMA (Appendix 9).

Biological Process

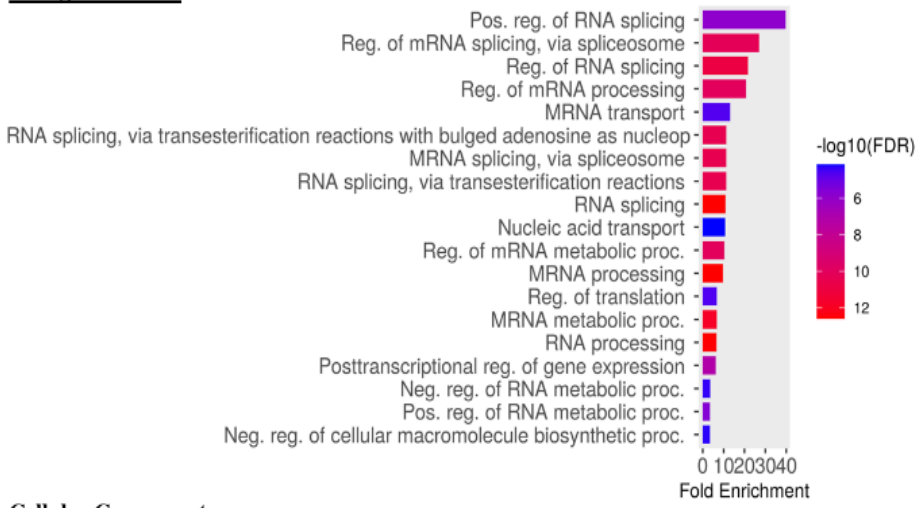

Molecular Function

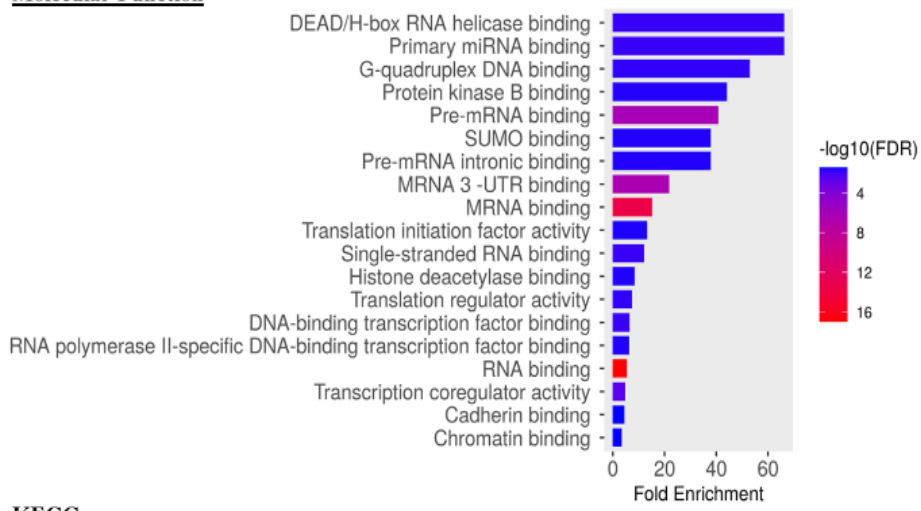

Cellular Component

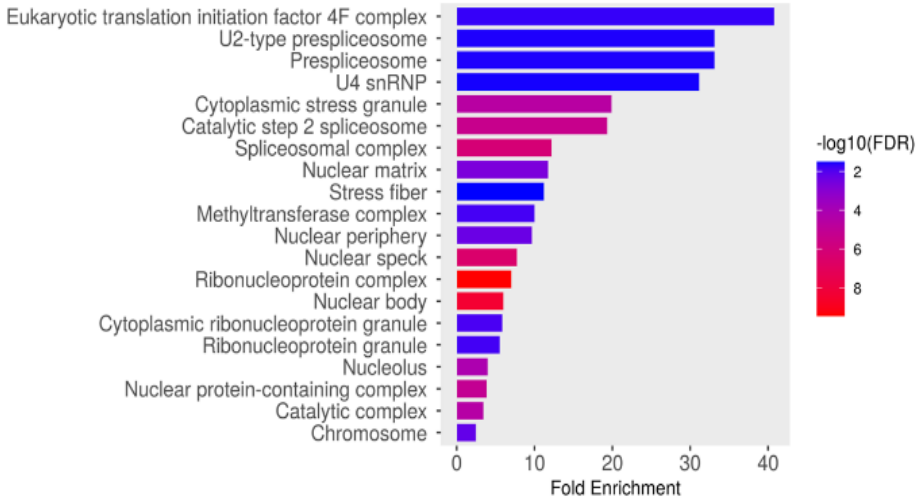

KEGG

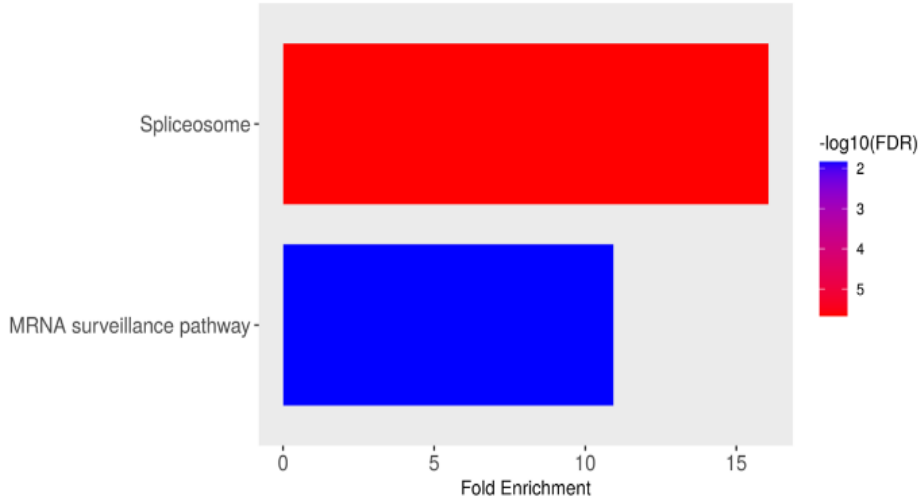

Figure 4.8.: GO Terms associated with alternative splicing events in GBM ex vivo, common to 2+ patients, after 1 μM GSK3368715 treatment vs proteins displaying arginine methylation.

GO analysis (Ge et al., 2020) of significantly ($p<0.05$) alternatively spliced genes, common to 2 or more patients, in RNA-seq analysis of 4 patients (D27-D30) GBM samples, 8-days post-perfusion and treated with 1 μm GSK3368715 vs DMSO control vs proteins, expressed in Toledo and OCI-Ly1 (B-cell lymphoma) and HupT4, Panc 08.13 and Panc 03.18 (Pancreatic Adenocarcinoma) cell lines, displaying arginine methylation switching to mMA, aDMA, or sDMA, after treatment with GSK3368712. Full GO analysis can be found in Supplementary Table 4.3.

Similarly to the GO findings for all alternatively spliced genes, in two or more patients, GO analysis showed that the proteins which displayed alternative arginine methylation after GSK3368712 treatment were largely involved in RNA splicing and mRNA processing (Figure 4.8 and Appendix 9).

AS genes found in two or more patients were also correlated with known FUS targets, as published by Nakaya *et al. (2013)* (Appendix 9). Of the 2455 genes alternatively spliced, 136 were known FUS gene splicing targets, more than expected by chance ($\chi^2 = 7.16$, $p = 0.007$) (Nakaya *et al.*, 2013). These 136 genes were inputted into Search Tool for the Retrieval of Interacting Genes/Proteins (STRING), alongside FUS, to determine any known interactions between these genes and FUS, found within the literature. This determined 54 genes with known interactions between each other and/or FUS and these are shown in Figure 4.9. GO analysis was performed on these genes and this showed that these targets were involved with alternative splicing (Appendix 9).

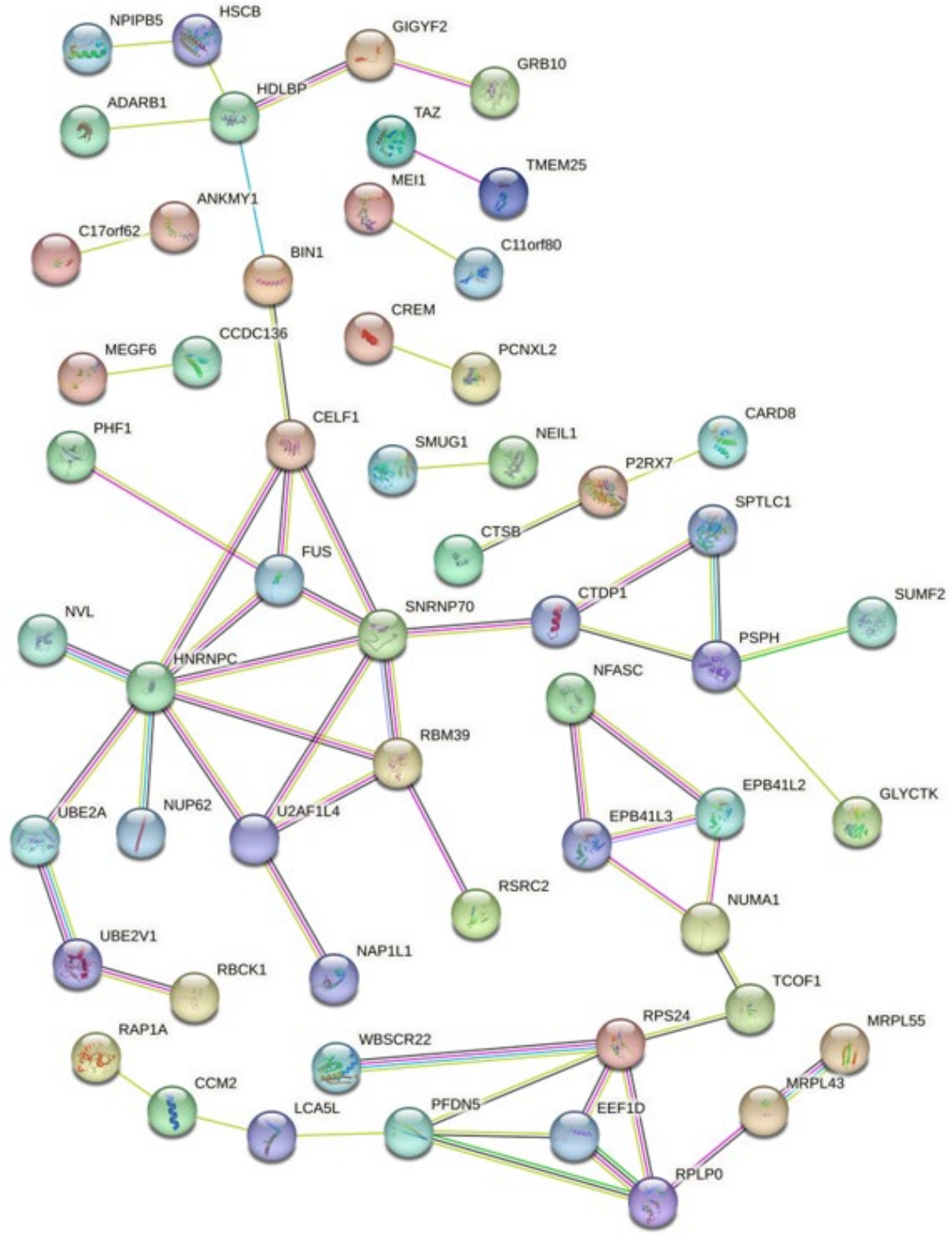

Figure 4.9.: STRING network between genes found to be significantly differentially alternatively spliced in 4 patient GBM samples and FUS. Out of 132 genes and FUS, only those displaying connections are shown.

4.3.4. FUS is a potential driver mechanism of methylation switching

In order to determine the potential underlying mechanism causing the transcriptomic changes outlined previously, I decided to utilise techniques to identify changes in the status, or levels of arginine methylation of the POI FUS, to understand its function, particularly in AS.

Western blotting and LI-COR, conducted previously by Dr. Sabrina Samuel in this lab, identified a 70 kDa protein with a sDMA mark, appearing to increase after type I PRMT inhibition by MS023. This was validated, again using western blotting, using the GSK3368715 Type I PRMT inhibitor. GSK3368715 displayed a much stronger sDMA mark, associated with the 70 kDa protein, than the same concentration of MS023, confirming that GSK3368715 is a more potent type I PRMT inhibitor than its previous counterpart MS023 and would be useful for validation of the 70 kDa protein, suspected to be FUS. FUS is primarily a nuclear protein but has been shown to migrate to the cytoplasm in other neurodegenerative disorders (Hofweber *et al.*, 2018). It was decided to see whether this was also the case in U87-MG, GBM model cells and to determine in which state FUS appears upon PRMT inhibition and in which cellular compartment it mostly localises. Nuclear and cytoplasmic extraction of proteins was performed on U-87 MG cells, treated with combinations of GSK3368715, Furamidine and type II PRMT inhibitor, GSK591, in comparison with the DMSO control, for 48 hours. Protein fractions were then run by gel electrophoresis and membranes probed for FUS. A cardiac total protein lysate was used as a positive control.

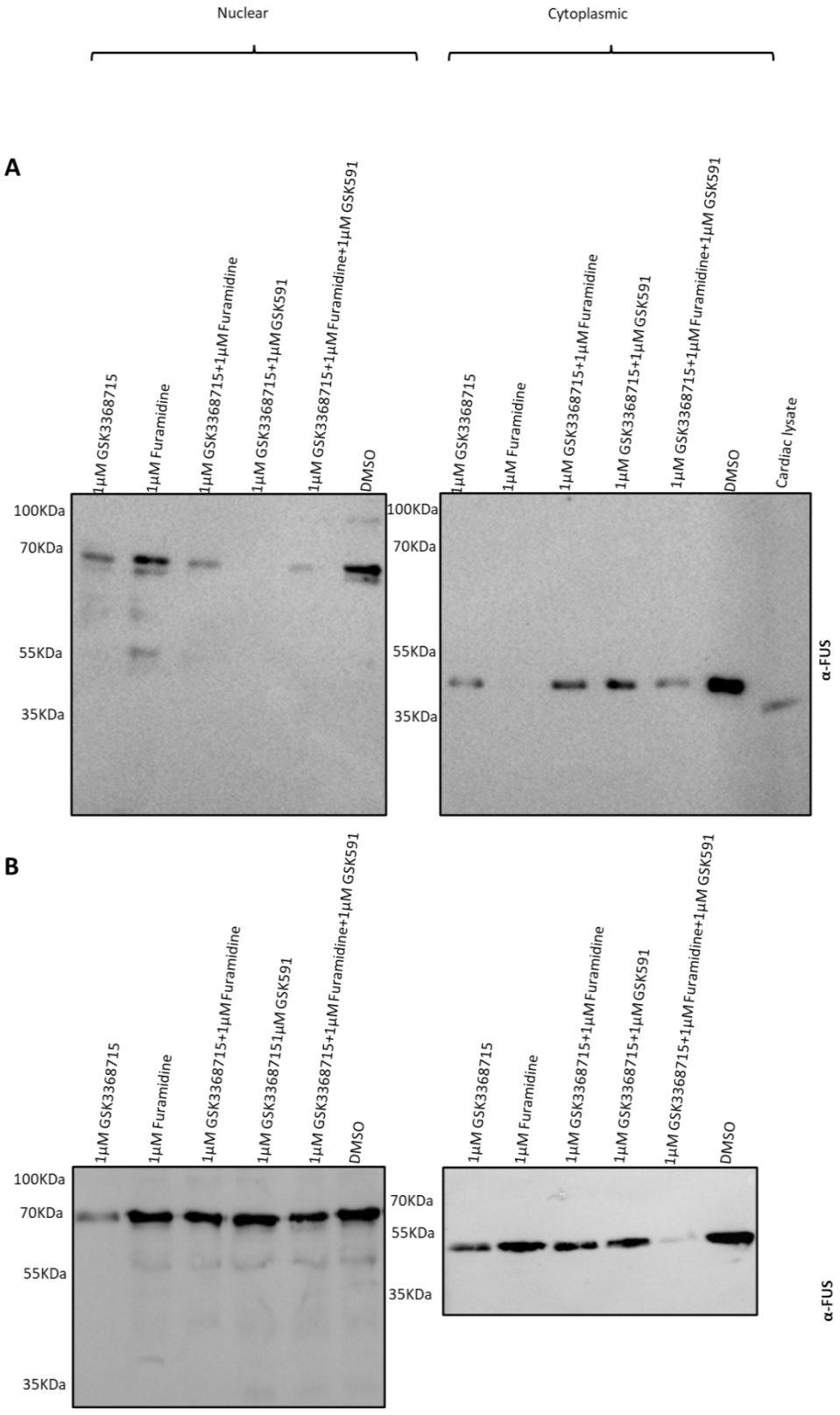

Figure 4.10.: Nuclear/cytoplasmic extraction of U-87 MG cells, treated with PRMT inhibitor combinations and blotted with anti-FUS antibody.

*Bands at ~70 kDa in the nuclear portion and ~50 kDa in the cytoplasmic portion show presence of FUS in **A)** n=1 and **B)** n=2.*

Due to the lack of loading control, it was not possible to determine any increases in the presence of FUS in either the nucleus or the cytoplasm; although, equal amounts of protein were loaded, according to BCA assays. Generally, all treatments retained fairly similar levels of FUS expression, when compared to the DMSO control (Figure 4.10A and Figure 4.10B). It is, however, interesting to notice the disparity in molecular weight of FUS. In the nucleus, FUS appeared at ~70 kDa (expected theoretical molecular weight is 75 kDa), whereas this weight decreased to ~50 kDa in the cytoplasm. This could be due to PTMs present on the FUS protein, including arginine methylation. FUS requires arginine methylation in order to shuttle from the nucleus, into the cytoplasm, therefore explaining the increase in molecular weight, by around 15 Da (molecular weight of CH_3). In the nuclear fraction, there are also several other bands of various molecular weights, potentially accounting for other PTMs, binding proteins, or splice variants.

4.3.5. Immunoprecipitation of FUS from U87-MG cells

To further investigate FUS as a potential POI and therapeutic target in GBM, I decided that FUS should be isolated from both control and GSK3368715-treated cells and tissue, with the intention to submit the isolate for mass spectrometry. This would determine any PTMs, including arginine methylation, which may occur in cells and tissues after treatment with PRMT inhibitors. U87-MG cells were treated with 1 μM GSK3368715 for forty-eight hours before harvesting FUS was immunoprecipitated with a FUS antibody raised in either mouse, or rabbit (Figure 4.11). SDS-PAGE of the samples were then blotted with either rabbit, or mouse anti-FUS antibody, respectively, to prevent species cross reactivity.

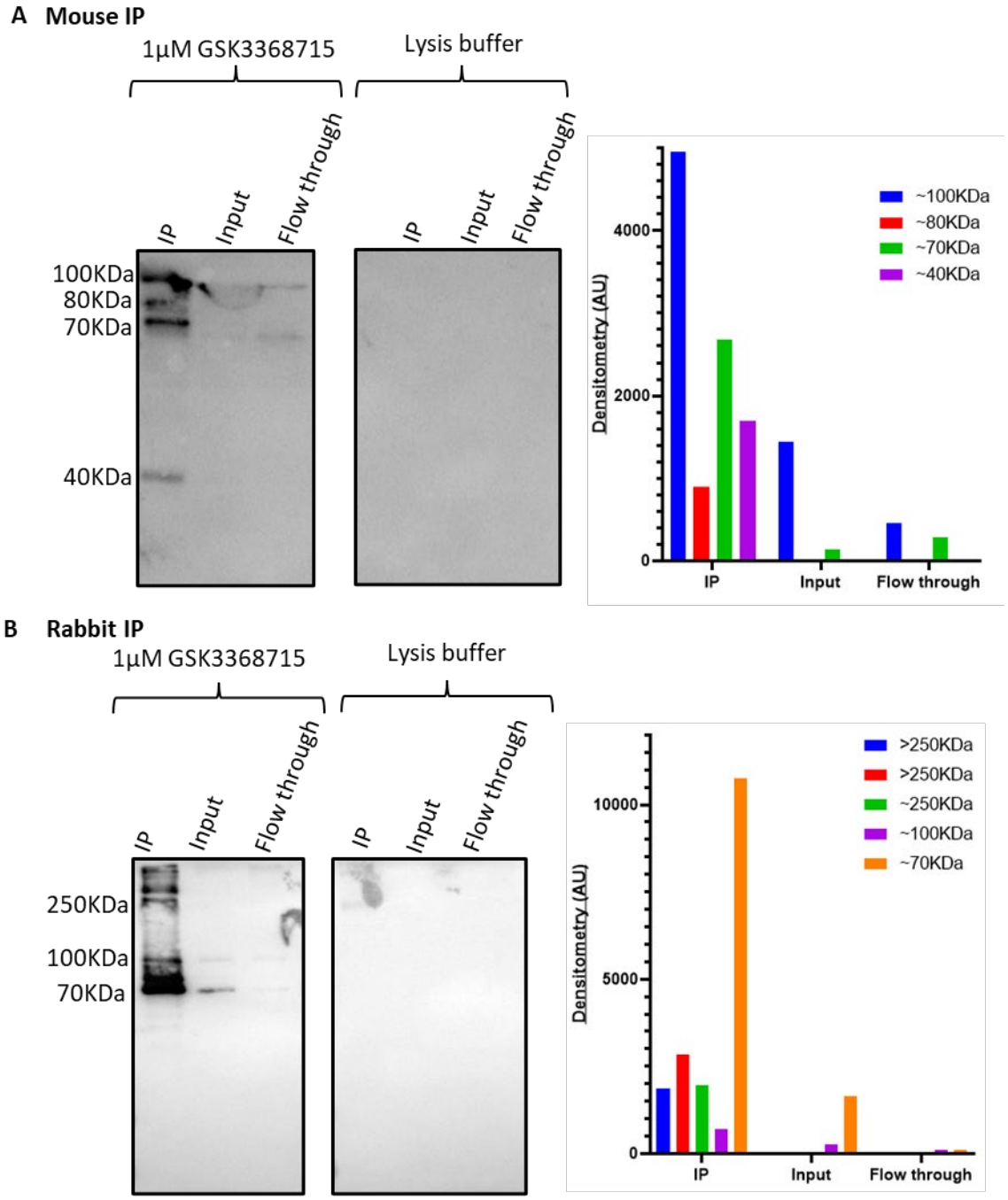

Figure 4.11.: Immunoprecipitation and densitometry of FUS in U87-MG cells treated with GSK3368715.

Immunoprecipitates were run in lane 1, inputs in lane 2 and flow through in lane 3. ***A)*** *IP was performed using a FUS antibody raised in mice and the membrane incubated with an anti-FUS antibody raised in rabbits for western analysis (n=1).* ***B)*** *IP was performed using a FUS antibody raised in rabbits and the membrane was incubated with a FUS antibody raised is mice for western analysis (n=1). Bands at ~70 kDa are the expected size of the FUS protein.*

Lysis buffer only controls underwent the same immunoprecipitation process to behave as IgG controls.

The western blot indicates I was able to immunoprecipitate FUS from U87-MG cells treated with GSK3368715, for forty-eight hours. In both Figure 4.11A and Figure 4.11B a 70 kDa band could be seen in all three lanes, with the strongest densitometry being in the IP lane. It was unexpected to see this 70 kDa band in the flow-through, however, this may be due to inefficient elution, due to a high volume of elution buffer used during IP with the mouse antibody (Figure 4.11A). The volume of elution buffer was reduced when the rabbit antibody was used and the densitometry of the band is smaller, but still present (Figure 4.11B). It is expected that the FUS POI would be seen in the input sample. The heavy chain and light chain of the FUS antibody would be expected to be seen at ~50 kDa and ~25 kDa, respectively and although there are multiple bands in the IP lanes for both of the antibodies, these do not exactly correlate to expected band sizes. Lanes which contain lysis buffer only went under the same immunoprecipitation process and represent IgG controls.

A similar protocol was attempted using GBM tissues, both pre-perfusion and post-perfusion, treated with both the DMSO control and GSK3368715. Tissue was lysed using 1% Triton-X100 in PBS, with protease inhibitors, using the Turrax homogeniser. The lysate was then rotated on a wheel, at 4°C for 1 hour, before centrifuging at 15,000xg for 15 minutes and transferring the aqueous protein layer into a clean microcentrifuge tube. BCA analysis was performed on the lysates, to ensure a good quantity of protein was attained and IP performed. Immunoprecipitation of FUS was unsuccessful and, with more time, further investigations into the method would be required. The amount of protein extracted from the tissues was appropriately high, according to the antibody manufacturer's recommendations and various titrations of antibody were used to pull down the protein. For this reason, this aspect of the project could not be completed and future work in this area may concentrate on successfully immunoprecipitating FUS from U-87 MG cells and GBM tissue, to identify any changes with type I PRMT inhibition and further investigate arginine methylation status of FUS in GBM.

4.4. DISCUSSION

Due to the small sample size, RNA-sequencing data was analysed in various different ways in order to better understand the variety of biological conditions, covered by the four patient samples. As all of the patients were male, of a similar age and all samples were treated the same in the fluidics system, any disparity in behaviour between samples after treatment with GSK3368715 would most likely be down to their genetic biomarkers.

Enrichment in upregulated DEGs were associated with hypoxia in D27, alongside genes such as *AC131212.3, KISS1R* and *EMC9. AC131212.3* function is not yet known. *KISS1R* has been shown to have a role in signalling in cancer metastasis (Li et al., 2022b) and is known to be expressed in GBM (Kim *et al.*, 2020). *KISS1R* silencing with siRNAs found a reduction in *KISS1*-induced GBM cell invasion (Kim *et al.*, 2020), suggesting that *KISS1R* is involved in the invasion and metastatic capabilities of GBM. The *KISS1* endogenous ligand of *KISS1R* is known to be epigenetically regulated in other cancers (Motti and Meccariello, 2019), which may also be true for the receptor. This may explain the change in receptor expression with PRMT inhibitor treatment, causing its activation. Hypoxia could be a symptom of the fluidics system itself, whereby the individual pieces of tissue were starved of oxygen throughout the 8 days. This was, however, mitigated for, by pooling the tissues and this upregulation is relative to the DMSO control, which would also have been starved of oxygen in this case. Hypoxia is also characteristic of GBM itself, with extracellular matrix (ECM) remodelling occurring within the tumour, leading to a reduction in diffusion of oxygen (Mohiuddin and Wakimoto, 2021) and the tumours therefore preferring to use glycolysis. *ECM9* is a soluble component of the endoplasmic reticulum (ER), which is generally responsible for protein biosynthesis, but the particular function of *EMC9* is not yet understood. In cancer, the EMC is responsible for proteostasis through gamma-aminobutyric acid ($GABA_A$) receptors (Whittsette *et al.*, 2022). ER stress has been related to gliomagenesis and GBM (Obacz *et al.*, 2017) causing cellular adaptation and therefore therapeutic resistance and invasiveness through upregulation of proteins involved in the EMT (Markouli *et al.*, 2020).

HLA-DRA is shown in patient D27 to be downregulated in biopsies treated with GSK3368715; alongside biological processes associated with inflammation (Fan *et al.*, 2017). HLA-DRA has been recently associated with a low-grade glioma diagnosis and poor prognosis (Chen et

al., 2022a). This aligns with the idea that inflammation plays a large role in the development and maintenance of GBM. That it is downregulated could indicate that PRMT inhibition reduces inflammation within the tumour microenvironment, thereby resulting in a less favourable environment for tumour growth.

GSK3368715 causes apoptosis of GBM biopsies through modifying RNA processing, gene splicing and protein translation, which are well-known regulators of apoptosis in GBM (Sachamitr *et al.*, 2021). The fact that there appears to be no significant shifts in variation between the control and treated samples, however, does indicate that there are other factors which are driving the transcriptomic changes, such as hypoxia and necrosis as discussed, or due to other unexplored factors, attributed to biomolecular markers which have not be accounted for.

Hoffman and Lambert (2014), and others (Bortner and Cidlowski, 2014) have outlined the importance of ion channels in treatment resistant cancers and in apoptosis. Hoffman and Lambert suggest that one mechanism of treatment resistance is through evasion of drug-induced apoptosis, via modulation of ion transporters. Interestingly, in patient sample D28, ion transport and electron transport chain pathways are upregulated. Due to the PC1 shift in recurrent D28, post-treatment, to the potentially less aggressive primary and treatment-naïve phenotype of D30, it could be argued that the PRMT inhibitor treatment drives molecular changes towards a reduced transcriptomic output, leading to cell death. A potential mechanism for this could be the upregulation of pro-apoptotic ion channels, as seen in the GO analysis, thereby overcoming any treatment resistance of the recurrent tumour. To investigate this further, the specific genes associated with this increase in ion transport pathways should be explored as a subset and individually. Upregulation of the electron transport chain also indicates a change in mitochondrial respiration and generation of ROS. This could be associated with a protective mechanism, by which ROS are increased to trigger GBM cell death – however, this mechanism is often dysregulated in cancers, whereby increasing ROS leads to sustenance of the cancer phenotype, which requires higher energy consumption for increased proliferation (Raimondi *et al.*, 2020).

The most significantly upregulated genes in D28 were *LYZ, DKK1* and *MTND2P28. LYZ* has been found to be part of gene signatures involved in macrophage infiltration in GBM tissues (Pombo Antunes *et al.*, 2021) and are therefore involved in the inflammatory tumour microenvironment. The *DKK1* promoter has been shown to be methylated in GBM (Kafka *et al.*, 2021), whilst methylation of histone tails are another mechanism by which *DKK1* expression may be repressed (Aguilera *et al.*, 2006). *DKK1* has been reported to have a pro-apoptotic function in gliomas (Guo *et al.*, 2014), potentially through epigenetic silencing of negative Wnt signalling regulators. PRMT inhibition therefore could be promoting to production of *DKK1* through the inhibition of aDMA, by inhibiting repressive histone marks, and causing negative regulation of Wnt signalling, leading to more pro-apoptotic phenotype. This would have to be validated with more samples and histology. *MTND2P28* is a lncRNA which has also been associated with the adaptive immune system and the inflammatory tumour microenvironment (Rothzerg *et al.*, 2022).

In contrast, mitochondrial membrane organisation pathways are downregulated, which is linked to the most significantly downregulated gene in D28, *LMF1*. *LMF1* has been identified as a potential risk gene for brain neoplasms, including having high expression in GBM and is found in a locus associated with other known biomarkers of GBM, which are involved in alternative splicing and malignancy. *LMF1* is also localised to the ER and is responsible for the maturation of specific proteins, regulation of ER stress and thereby being involved in the UPR (Lin *et al.*, 2022), resulting in apoptotic evasion (Oakes, 2020). The ER relies on mitochondria to function and therefore the downregulation of mitochondrial membrane organisation would affect the functioning of the ER. Reorganisation of the mitochondrial membrane leads to alterations of energy metabolism, such as a breakdown of oxidative phosphorylation, leading to cell death (Rupprecht *et al.*, 2022), or there may be a switch to glycolysis, which is an oncogenic marker (Greene *et al.*, 2022). Downregulation of the *LMF1* gene could therefore indicate a reduced response to ER stress, causing a bypass of the tumour's ability to avoid cell death by overcoming the UPR. Further research would have to be completed, possibly *via* bioinformatic analysis, to determine whether this could be due to arginine methylation switching, causing alternative epigenetic repression, or potentially by alternative splicing.

GO analysis identified enrichment in cellular and developmental processes, which could be due to change in the structural integrity of the cells. This is supported by the most significantly upregulated genes in D29, *COL3A1* and *COL3A6*. Collagen is responsible for several activities in brain tumours, including cell adhesion, ECM and signal transduction network activation for tumour progression (Snedeker and Gautieri, 2014, Raglow and Thomas, 2015). *COL3A1* has been identified as a potential biomarker for GBM, whereby GEO identified that *COL3A1* expression was positively correlated with glioma grade and related to poor survival (Gao *et al.*, 2016). Gao *et al.* (2018) showed that knockdown of *COL3A1* resulted in inhibition of glioma cell proliferation and migration. *COL6A3* expression is a subunit of collagen VI and has also been noted at low levels in GBM stem-like cells (Fiscon *et al.*, 2018, Wang and Pan, 2020). Methyl-sensitive cut counting analysis (MSCC) showed decreases in *COL6A3* CpG methylation sites, highlighting the importance of the aberrant methylation and subsequent alternative splicing in *COL6A3* expression and tumour progression in GBM. *COL6A3* downregulation in GBM stem-like cells, thought to allow tumour adaptivity due to their similarity to undifferentiated cells, is highly correlated with activation of genes related to neural development and differentiation, such as *OLIG2* and *SOX2*. Induction of *OLIG2* and *SOX2* has been shown to reprogram differentiated cells into GBM stem-like cells, thereby resulting in tumour promotion (Fiscon *et al.*, 2018). Inhibition of *COL6A3* could lead to loss of collagen structures, leading to a breakdown in signalling and causing neoplastic progression and invasion. Activation of *COL6A3* could inhibit tumour progression by restoring balance and repressing neural dedifferentiation genes. Generally, in solid tumours, over expression of ECM components leads to a more rigid tumour environment, make drug delivery and therefore efficacy, much reduced. Increases in collagen proteins can also cause immune trapping, exacerbating the inflammatory environment and reducing immune surveillance and can also prevent movement of oxygen and nutrients, causing hypoxia-related chemo- and radiotherapeutic resistance (Mohiuddin and Wakimoto, 2021). In patient D29, upregulation of *COL6A3* could represent a dedifferentiation of GBM stem-like cells, associated with alternative splicing of COL6A3, brought about by alternative methylation pathways as a result of GSK3368715 type I PRMT inhibition and thereby leading to a reduction in the invasion phenotype. The conflict between the different functions of the most significantly up and downregulated genes, in patient D29, does align with the discussion on the PC2 shifts, seen in *Figure 4.5.*

The extracellular matrix environment is essential for tumour development and maintenance and therefore, it is expected that the most affected proteins are involved in ECM regulation (Gao *et al.*, 2016). GO analysis supports the importance of the ECM in GBM (Mohiuddin and Wakimoto, 2021), with keratinisation being downregulated, in addition to mitosis (*Supplementary Table 4.1*). *KRT5, KRT17* and *KRT19* have all been identified as being involved in proliferation, migration and invasion in several cancers, including prostate (Du *et al.*, 2019), pancreatic (Li *et al.*, 2020) and glioblastoma (Gupta *et al.*, 2013, Zhang *et al.*, 2022). These genes are the most significantly downregulated in GSK3368715-treated D29 biopsies. The first zebrafish models of gliomagenesis were created, using Kirsten rat sarcoma virus $(KRAS)^{G12V}$ overexpression, *via* the *KRT5* neural promoter (Ju *et al.*, 2014, Reimunde *et al.*, 2021). *KRT5* activation in prostate cancer stem cells has been shown to inhibit the Wnt signalling pathway, leading to a reduction in tumour growth in mouse models (Du *et al.*, 2019), hence being a tumour promoter. *KRT17* has been shown to be upregulated in pancreatic cancer and has been associated with worse overall survival (Li *et al.*, 2020). Knockdown of *KRT17 via* siRNA attenuated cell viability functions, including mTOR pathway phosphorylation and in proliferation and invasion assays, in cell line models (Li *et al.*, 2020). *KRT17* has also been associated with release of inflammatory cytokines and knockout was found to resensitise cervical cancer cells to cisplatin (Escobar-Hoyos *et al.*, 2015) and induce apoptosis in several other cancers (Ujiie *et al.*, 2020). *KRT19* knockdown has been shown to increase proliferation of breast cancer cells and promote drug-resistance, *via* expression modulation of cancer stem-like cell biomarkers and overexpression led to cancer property attenuation (Saha *et al.*, 2018). Alternatively, *KRT19* has been shown to interact with miRNAs, such as miR200, to promote lung adenocarcinoma metastasis (Cheng *et al.*, 2013). Hou *et al.* (2019) developed several computational models, based on TCGA datasets, which identified *KRT19* as part of a set of 14 genes which created a potential prognostic signature for GBM. The fact that this gene is seen to decrease with GSK3368715 treatment correlates with this finding, as well as the PC2 shift seen in Figure 4.5.

D30, despite displaying few significant DEGs, did see enrichment in *TBC1D3K, AC005224.4* and *FRG1* in upregulated genes, which was accompanied by an increase in GO terms associated with leukocyte adhesion and rolling. There is little literature associated with *TBC1D3K* and none that can be found on *TBC1D3K* and GBM. The *TBC1D3* family, however, has been indicated in renal clear cell carcinoma, associated with tumour-infiltrating lymphocytes and

increased expression of particular family members is a mark of poor prognosis (Wang *et al.*, 2021). Further investigation would be required to determine the specific function of *TBC1D3K* in GBM and how significant the increase in expression is, with PRMT inhibition. *AC005224.4* knockdown has been found, in ovarian cancer, to reduce tumorigenesis *in vivo* and has been confirmed as an oncogene in ovarian cancer (Xiong *et al.*, 2023). *FRG1* in a GBM cell line, treated with GnRH agonists, was shown to be downregulated, whilst the cells displayed an overall reduction in proliferation (Tripathi *et al.*, 2022). *FRG1* was also found to have high levels of mutation in GBM, along with *TP53* (Li et al., 2021c). This may indicate that *FRG1* is linked to cancer cell proliferation and therefore upregulation may be an indicator of GBM progression. This is in direct contrast to a series of studies, which found that *FRG1* depletion leads to angiogenesis in various cancers (Mukherjee *et al.*, 2023), which matches to the results found in D30.

There was also an enrichment in downregulation of angiogenic pathways, with the top downregulated genes being *CLDN5* and *BOLA2B*. Downregulation of angiogenesis is a positive indicator that GBM is not progressing and is in line with PRMT inhibition taking effect on D30, supported by the increase in *FRG1*. *CLDN5* is associated with tight junctions and downregulation has been found in GBM samples (Karnati *et al.*, 2014). *CLDN5* could promote the invasiveness of GBM by weakening tight junctions, thereby could be a prognostic indicator of GBM progression. *CLDN5* downregulation is also associated with pro-inflammatory phenotypes (Yang *et al.*, 2021), aligning with upregulated enrichment in leukocyte function. Alternatively, *BOLA2B* has been found to be upregulated in several cancers, associated with poor prognosis and negatively correlated with immune infiltration (Liang *et al.*, 2023). The downregulation of *BOLA2B* here could be an indicator of improved prognosis, along with the downregulation of angiogenesis, which is often associated with highly vascularised GBM (Ahir *et al.*, 2020).

Due to the limited number of samples, it was then decided to combine DEGs conserved in two or more patients, to identify any common pathways enriched for in any up- or downregulated DEGs and those undergoing alternative splicing. This indicated decreased protein synthesis capacity and alternative splicing after treatment, consistent with the observation of apoptosis in histology. Dysregulation of protein synthesis and RNA catabolic process as a hallmark in

cancer, suggesting that a downregulation in dysregulated protein synthesis may be an indication of reduced cancer progression. Overall, with the modest enrichment in cell-cell communication and transcription, as well as the myriad of individual genes seen in individual patients, this could indicate the heterogeneity within and between the samples. In general, most of the GBM cells are undergoing changes to their microenvironment, such as the ECM, resulting in decreased capability for protein synthesis, decrease in angiogenesis, reduced Wnt signalling associated with several of the individual genes and subsequent prevention of cancer stem-cell differentiation. There is also evidence to suggest that some of the samples are undergoing apoptosis, potentially associated with upregulation of pre-apoptotic ion channels and ER stress. Overwhelmingly, of the alternatively spliced genes associated with PRMT inhibition, they are, themselves, involved in alternative splicing and more broadly in DNA damage and cell death. There are, however, subsections of cells which are simultaneously being positively selected for in the perfusion device. These are the cells which thrive under hypoxic, inflammatory conditions and are undergoing transcription, adhesion and migration. These are all characteristics associated with the aggressiveness and invasiveness of GBM. It would therefore be necessary to isolate the genes within this subset, to further target them, as it is these populations which give rise to chemotherapeutic resistance in GBM. Several of the genes described are known to undergo epigenetic regulation, which could explain their altered expression with treatment. The PRMT inhibitor could be causing a reduction in mitosis and proliferation in the MGMT positive tissue, but also be taking advantage of neuronal and synaptic plasticity to bypass this, creating new pathways to overcome the pro-apoptotic effects of the drug. The similarities between the processes that are simultaneously up- and down-regulated through GSK3368715 application may also highlight the importance of intra-tumour heterogeneity, displayed within and between the three micro-biopsies pooled for each experimental condition (each donor). It could be that changes to arginine methylation, *via* PRMT inhibition, lead to alternative splicing of several downstream genes, including those involved in alternative exon usage themselves (Fedoriw *et al.*, 2019), such as FUS (Wall and Lewis, 2017), leading to a cascade of DEGs and giving rise to a multitude of downstream effects, described in this chapter.

FUS is known to be involved in numerous neurological conditions, including MND and dementia. Shuttling of FUS between the nucleus and the cytoplasm has been shown to be affected by arginine methylation (Tradewell et al., 2012). In this data, FUS appeared at a higher

weight in the nucleus than in the cytoplasm, suggesting that FUS in the nucleus is methylated. This might therefore suggest that, with arginine methylation inhibition, FUS is no longer efficiently imported into the nucleus and therefore remains in the cytoplasm. TNPO can no longer interact with the methylated arginines and aggregation of FUS is more likely to occur, forming plaques. Through this, FUS may cause more perpetual solid to liquid phase transition in the nucleus, allowing easier access for transcription factors, which then drive gene expression for apoptosis and cell death. Due to the lack of repeats for this data and the fact that no change in FUS expression could be verified with PRMT inhibition, this explanation is speculative.

Type I PRMT inhibition may also encourage alternative modulation of splicing in tumours with high splicing dependency (El-Khoueiry *et al.*, 2023). This is strengthened by the alternative splicing evidence described in this chapter, whereby significantly alternative spliced genes in two or more patients displayed high levels of enrichment in splicing and mRNA processing. This was also reflected in the comparison with alternatively methylated arginines on proteins, after GSK3368715 treatment, in the Fedoriw paper. There was a link between alternatively spliced genes in two or more GBM patient biopsies and proteins which displayed alternative arginine methylation marks, after GSK3368712 treatment. Whilst this might be expected, in that mRNA processing does involve arginine methylation and changes to arginine methylation would be expected due to the nature of the PRMT inhibitors, it highlights splicing as a potential mechanism by which this alternative methylation occurs, potentially as a means to bypass inhibition of the type I PRMTs. The vast majority of these alternatively methylated arginines are also mMA and this can be coupled with the increase in apoptosis seen with GSK3368715 treatment, in GBM biopsies *ex vivo.* It could be postulated that the absence of the second methyl group triggers alternative splicing RNAs thereby leading to augmented, or ineffective function, triggering cellular apoptosis. The lack of the methyl group itself may also render the protein ineffective, for example in attaining tertiary and quaternary structures, or binding to targets. A theme which runs throughout the literature into ECM proteins (Mohiuddin and Wakimoto, 2021), including keratins and collagens, is that individual genes and proteins are very different and sometimes alternate effects on tumour promotion, dependent upon the type of cancer.

Bioinformatics-related research, linked to this project, was started in 2020 as a Covid-19 mitigation strategy, due to the lack of patient samples coming into the lab. This work involved using proteomics software Maxquant, through the University of Hull's high performance computing cluster, Viper, to identify proteins in GBM with changes to arginine methylation, as a result of GSK3368715 treatment. Should this line of inquiry be investigated in the future, it may further strengthen the idea that arginine methylation switching is a driver of chemotherapeutic resistance in GBM and validate the use of PRMTs as therapeutic targets in GBM. This could also elucidate a biomolecular signature in GBM for use in the clinic for diagnosis of GBM and for determining whether a patient may or may not respond to a certain type of treatment and as a less invasive prognostic indicator.

4.5. CONCLUSION

Many of the most significant DEGs displayed in all patients were related to the tumour microenvironment; 1) structurally, leading to signalling changes; 2) related to inflammation and 3) in general, suggesting reduced capacity for protein synthesis. Many of the inflammatory and structural genes in these results indicate that PRMT inhibition is having a role in reducing inflammation and breaking down cell signalling within the tumour, brought about by alterations to structural integrity, . Moreover, alternative splicing has been identified as a potential mechanism by which downstream processes leads to DNA damage and cell death. More samples would increase the number of biological features able to be explored in the data, which may contribute to variation, it may be prudent to identify further DEGs and alternative splicing signatures, through which subsets of genes can be taken forward for further analysis. There has also been some evidence that epigenetic regulation, *via* aDMA inhibition through type I PRMT inhibitor, GSK3368715 could be regulating this alternative splicing. The results also suggest that FUS could be a potential arginine methylation target, for which the function is augmented to trigger a cascade of proteins involved in alternative splicing, leading to a reduced lethality phenotype. These results suggest that FUS is linked to and involved in the process of apoptosis, induced by PRMT inhibition in GBM tissue *ex vivo, via* alternative splicing pathways.

CHAPTER 5: MOUSE AND FISH BRAINS AS HEALTHY CONTROLS ON-CHIP

5.1. Introduction

The previous chapters have described the effect of GSK3368715 on GBM tissue in the fluidics system. Both the IHC data and the transcriptomic data suggested that PRMT inhibition causes apoptosis in the GBM tissue, potentially through aberrations in alternative splicing. This is work that has also been published (Barry *et al.*, 2023). The next logical step was to determine the effect of GSK3368715 on healthy tissue, in order to ascertain any off-target effects, or adverse reactions.

5.1.1. Mouse and cichlid as healthy brain tissue models

Due to the ethical implications of using healthy human brain tissue in microfluidics systems, as well as the lack of availability of such tissue, wild-type mouse and fish brains were considered to be an appropriate alternative. Both mice and fish were readily available on-site and it was feasible to utilise the experience of colleagues who were trained animal handlers and already euthanising the animals for ongoing projects. Mice are already very well-established models for *in vivo* studies into the brain, including GBM xenografts (Haddad *et al.*, 2021). Although the use of cichlids in GBM research has not been well-documented, there is research demonstrating the effect of PRMTs and arginine methylation in zebrafish (Pliakopanou *et al.*, 2023), as well as the use of cichlids in medical research (Schartl, 2014). Although less common models of human disease than zebrafish counterparts, the Cichlidae family have become more prevalent in studies into craniofacial developmental research (Schartl, 2014). This is due to the family being very species rich, with a great deal of physiological changes associated with their variety of ecological niches.

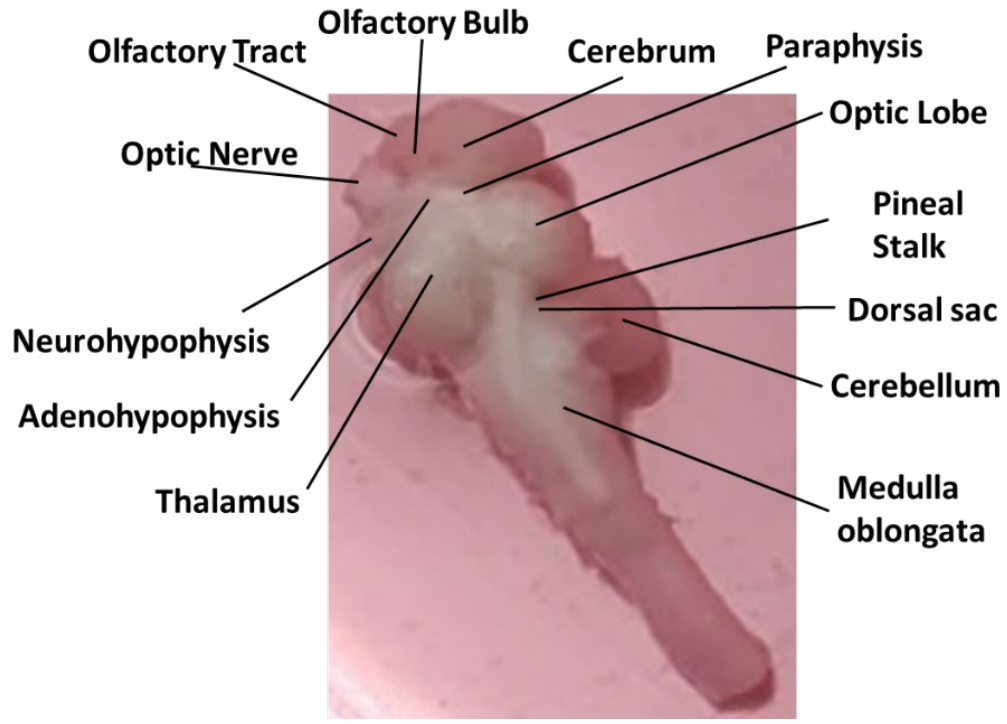

Figure 5.1.: Labelled diagram of a cichlid brain, showing the main anatomical features.

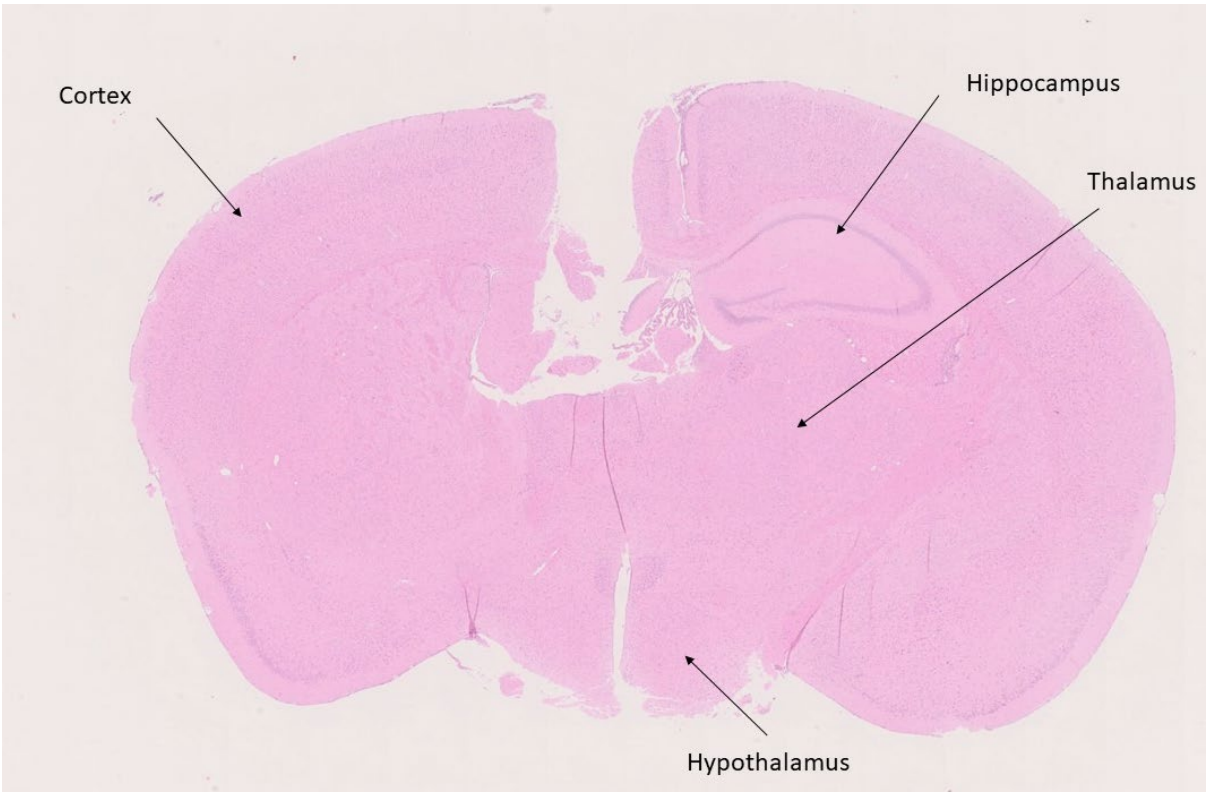

Figure 5.2.: Labelled coronal section diagram of mouse brain showing the main anatomical features.

Due to the small size of the brains, the entirety of the cichlid brain was utilised, with the exception of the medulla oblongata (Figure 5.1). The cortex of the mouse brain (Figure 5.2) was identified as the equivalent to the frontal and temporal lobes of the human brain, in which the vast majority of GBMs arise.

5.1.2. Ki67 as a proliferative marker

Previous chapters have utilised apoptotic markers cleaved PARP and Annexin V to demonstrate increases in apoptosis in GBM, on the novel perfusion device, in the presence of GSK3368715. Validation work of the GBM-on-chip system was performed by Dr Sabrina Samuel and Srihari Deepak and utilised proliferative marker, Ki67. Ki67 was used to determine the impact of the fluidics environment on the GBM tissue sample, by comparing expression pre-perfusion and post-perfusion, at various time points. This would ensure that any differences in proliferation seen with treatment was entirely down to the treatment and not due to the fluidics system itself. As part of the validation process of mouse and cichlid brain tissue in the perfusion device, Ki67 was again employed to determine the proliferative capacity of tissues pre-perfusion vs post-perfusion, as well as with gold standard TMZ treatment and experimental GSK3368715 treatment. Some of this Ki67 validation work was performed by Ricky Akinkuolie in the course of his MSc degree.

Ki67 is present in cells in all phases of the cell cycle, except during resting and G0 (quiescence). Ki67 is expressed via Rb1 and E2F-mediated transcription in G1 phase, through phosphorylation of Rb by CDK4 and CDK6 in complex with cyclin D. Ki67 expression is increased further upon hyperphosphorylation of Rb by CDK2, in complex with Cyclin E and A, during G1/S phase transition, respectively (Scott *et al.*, 2005). Accumulated Ki67 is phosphorylated by CDK1, complexed with cyclin A and B, to push the cell through G2/M transition and into mitosis. There is a sharp decline in Ki67 expression during the metaphase/anaphase transition of mitosis (Figure 5.3) (Menon *et al.*, 2019, Uxa *et al.*, 2021).

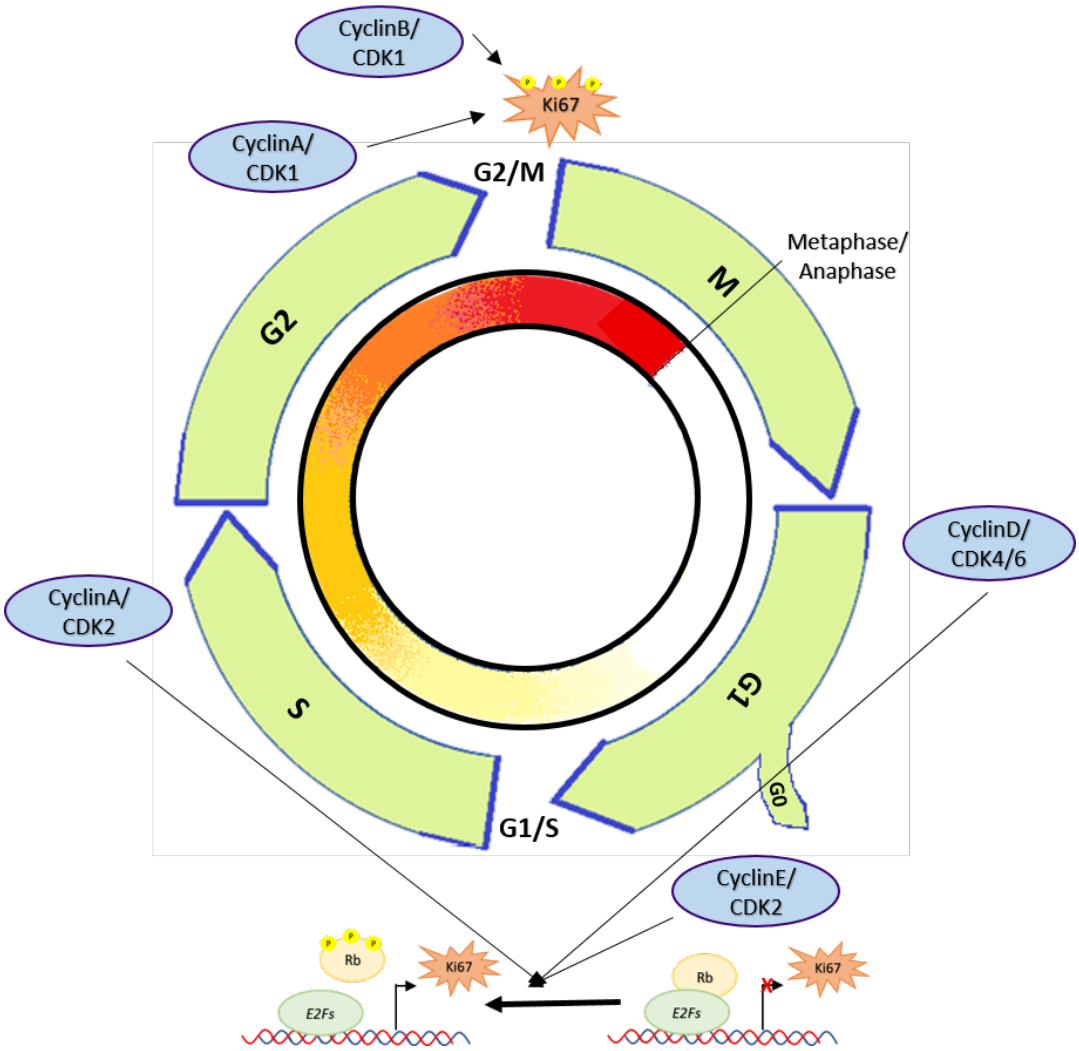

Figure 5.3.: Ki67 Accumulation Throughout the Cell Cycle.

Relative expression of Ki67 throughout the cell cycle is indicated by the inner circle, whereby red shows high concentration and white shows low concentration. Retinoblastoma protein (Rb); E2 promoter binding factor (E2F); phosphorylation (P); cyclin-dependent kinase (CDK).

5.1.3. Aims and Objectives

In the previous chapters, I have described the findings that GSK3368715 kills GBM cells. Due to the ubiquitous nature of arginine methylation, by PRMTs, throughout most tissues; determining whether GSK3368715 also kills healthy brain tissue is imperative. The acquisition of healthy human brain tissue, as well as other healthy human organs was significantly compounded by ethics and by the potential risk of another Covid-19 lockdown.

I decided therefore, to use mouse brain tissues, as a well-established model of human brain tissue, as well as fish brain and gill tissues (the latter as a control), from an ongoing proof-of-concept study into the maintenance of fish tissues in the fluidics device, to establish a platform for environmental studies. In the literature, I was unable to find any other studies which utilised mouse, or cichlid brains in a microfluidics device and therefore, this is a novel study, with optimisation involved.

The aims of this chapter were to:

- Ascertain whether mouse and cichlid tissues can be maintained in viable conditions in the perfusion system, thereby providing a good fluidics model for healthy human brain tissue. This will be assessed using cell stress assays, such as LDH release and proliferation assays, such as Ki67 expression through IHC.
- Understand the apoptotic effects of GSK3368715 on healthy tissues, to further investigate PRMT inhibition as a viable therapeutic tool against GBM.

5.2. Methods

5.2.1. Mouse brain tissue preparation

Twelve mice, M1-M12 (Table 5.1), were used for this study. Mice were kept in appropriate conditions, according to the Animals (Scientific Procedures) Act, 1986 and with ethical approval from the Animal Welfare and Ethical Review Body. Mice were kept in monitored air-filtered cages in groups of 2-5 separated by sex, at 22°C and 60% humidity. Mouse subjects were evenly split between male and female and mice age was between 60 and 128-days, where 6 days is equivalent to 1 year old. All mice were c57/bI6 wildtype mice and were sacrificed through cervical dislocation. Mice were not genetically modified, nor had they undergone any treatment prior to this study. Mice were euthanised by Dr Chris Sennett, or the in-house animal technician team, *via* cervical dislocation. The whole brain was then transported by myself from the on-site animal house to the lab in 10 ml Neurobasal A (NBA) medium (Gibco, Thermofisher Scientific UK, 10888-022) (Table 5.2). I then micro-dissected mouse brains into 25 mg (± 10%) samples, taking care to use sections in the cerebral cortex of the mouse brain (Figure 5.2), equivalent to the frontal, temporal and parietal lobes in which GBM is normally found within humans. Similarly to the GBM samples, mouse brain tissue was then randomly placed into chip-chambers, pre-filled with NBA medium and drugs and connected syringes loaded onto the Harvard Apparatus PHD ULTRA syringe pump system and set at a flow rate of 3 ul/min (section 2.2).

Table 5.1.: Mouse Subjects

Subject ID	Age (days)	Equivalent human Age (Years)	Sex
M1	128	21	F
M2	87	14	M
M3	87	14	F
M4	127	21	M
M5	127	21	M

M6	125	20	M
M7	96	16	F
M8	96	16	F
M9	96	16	F
M10	106	17	M
M11	106	17	F
M12	60	10	M

Table 5.2.: Supplements added to Neurobasal A medium for mouse and cichlid brain microfluidics

Reagent	**Final Concentration**	**Manufacturer**	**Catalogue no.**
FCS	1% (v/v)	Merck, Sigma	F7524
B-27	2% (v/v)	Invitrogen™, Thermofisher Scientific	A35828-01
L-Glutamine (200mM)	2mM/1% (v/v)	Gibco™, Thermofisher Scientific	A2916801
Antibiotic Antimycotic Solution (100×), Stabilized	1% (v/v)	Merck	A5955

5.2.2. Cichlid brain tissue preparation

Five cichlids, F1-F5, were used for this study (Table 5.3). Cichlids were kept in accordance with the Animals (Scientific Procedures) Act, 1986 and with ethical approval from the Animal Welfare and Ethical Review Body. Cichlids were not genetically modified, nor had they undergone any treatment prior to this study. Cichlid subjects were 80% male and of the species *Astalatilapia caliptera.* The only female was of the species *Nyassachromis microcephalus.*

Cichlids were euthanised by Dr Domino Joyce *via* anaesthetic and spinal cord severance in the context of a valid Home Office Animal Licence. The whole brain was then transported from the on-site animal house to the lab in 10 ml NBA medium (Table 5.2). Cichlid brains were micro-dissected into 41 mg (± 30%) samples, modified as optimisation occurred, taking care to use sections in the cerebrum of the fish brain (Figure 5.), equivalent to the frontal, temporal and parietal lobes in which GBM is commonly found within humans. These brain tissue sections were excess tissue from a proof-of-concept study being performed by Karen Lister, which aimed to ascertain whether cichlid brain and gill tissue could be maintained on the microfluidics system. Gill tissue was micro-dissected into ~3mm sections to fit into the chip chamber. Similarly, to the GBM samples, cichlid brain tissue was then randomly placed into chip-chambers, pre-filled with NBA medium and drugs and connected syringes loaded onto the Harvard Apparatus PHD ULTRA syringe pump system and set at a flow rate of 3 µl/min.

Table 5.3.: Fish Subjects

Subject ID	**Species**	**Sex**
F1	*Nyassachromis microcephalus*	F
F2	*Astalatilapia caliptera*	M
F3	*Astalatilapia caliptera*	M
F4	*Astalatilapia caliptera*	M
F5	*Astalatilapia caliptera*	M

5.2.3. Immunohistochemistry

Pre- and post-transfusion mouse and cichlid samples were FFPE, sliced and mounted onto poly-L-lysine-coated slides, as described previously. IHC was performed on the samples using cleaved PARP at 1:100 and Annexin V at 1:100, according to the manufacturer's instructions (*Table 2.8*) and using the same process described previously.

Table 5.4: Primary antibodies used in IHC

Antibody against	Species raised	Species Against	Manufacturer	Catalogue no.
Cleaved-PARP (Asp214) (D6E10)	Rabbit	Human	Cell Signalling	5625S
Cleaved-PARP (Asp214) (D6X6X)	Rabbit	Mouse, Rat	Cell Signaling	94885
Annexin V	Mouse	Human, Zebrafish	Nordic MUbio	MUB0106P
Annexin V	Rabbit	Human, Mouse, Rat	Thermofisher	PA5-78784

5.3. Results

5.3.1. Mouse and cichlid brains can be maintained in the novel perfusion device

Mouse brains were put onto the perfusion system within 1.5 hours, or less, of euthanasia, which is comparable to the GBM samples. Cervical dislocation was deemed to be the most appropriate method of euthanasia as the effects of Ketamine/xylazine on neurological function may affect analysis of the brain and there were some concerns over hypoxia if carbon dioxide (CO_2) euthanasia was used. Cichlids were euthanised in the standard way of introducing anaesthetic in the aquatic environment, before decollation.

LDH analysis was performed on effluents from both mouse and fish brain tissue incubations, as described previously, primarily to determine the effect of the perfusion system on cellular stress over the course of 2 to 8-days, tissue dependent (

Figure 5.4).

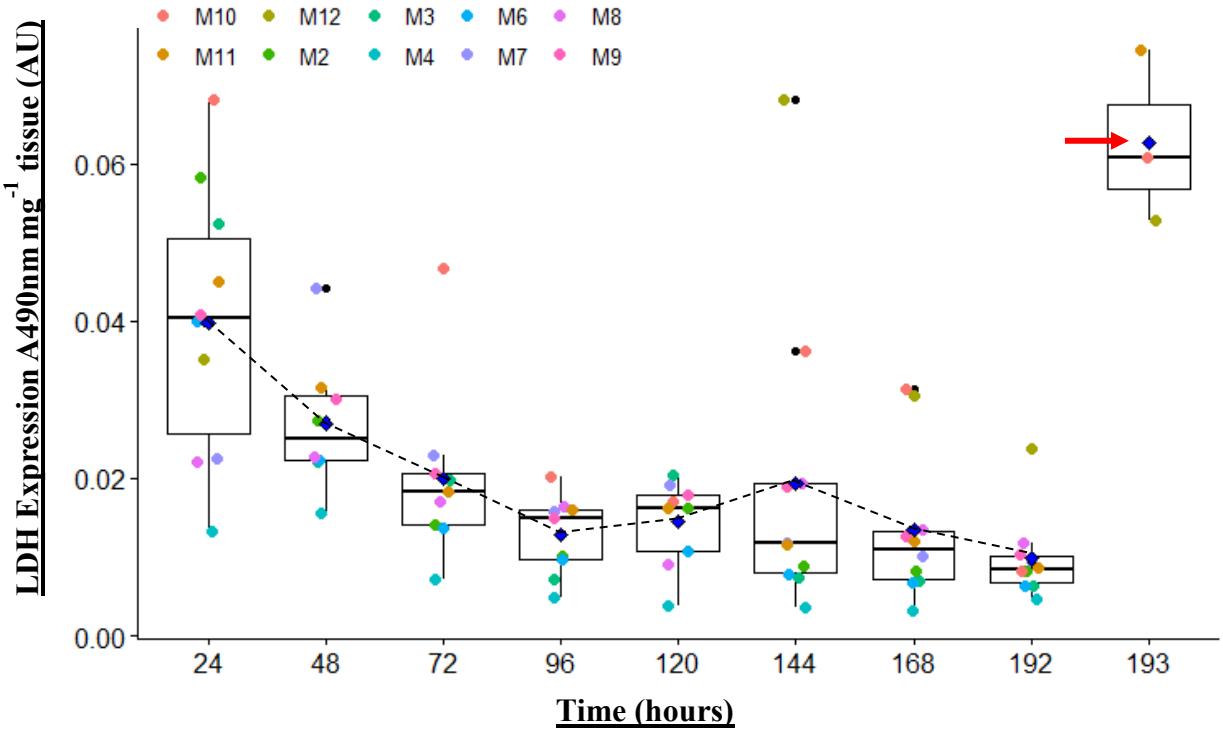

Figure 5.4.: Lactate Dehydrogenase (LDH) (Arbitrary Units (AU)) release from mouse brain tissues (n=11) over 8-days in a novel perfusion device, including post-perfusion tissue lysis (n=3).

*Absorbance of light at wavelength 490 nm (A490 nm^{-1}) directly corresponds to LDH release from mouse brain tissues (mg^{-1}) in the novel perfusion device, into effluents collected every 24 hours, for 8-days. Individual data points indicate biological replicates. Mean LDH expression levels indicated by blue diamonds: day 1, 0.04±0.017 AU mg^{-1}; day 2, 0.027±0.009 AU mg^{-1}; day 3, 0.02±0.011 AU mg^{-1}; day 4, 0.013±0.005 AU mg^{-1}; day 5, 0.014±0.005 AU mg^{-1}; day 6, 0.019±0.019 AU mg^{-1}; day 7, 0.014±0.01 AU mg^{-1}; day 8, 0.01±0.005 AU mg^{-1}. Non-parametricity was identified by Shapiro-Wilk test and rectified by the log10() function in R 4.3.1 and one-way ANOVA performed (F=6.55, df=7, p=6.7e-06****). Significance found between LDH released between 24 hours and 96 hours (p=0.0015**), 120 hours (p=0.006**), 144 hours (p=0.0069**), 168 hours (p=0.00036***) and 192 hours (0.000017****), 48-168 hours (p=0.04*), 48-192 (p=0.004**). No significance found over 6-day period 72-192 hours (0.015±0.011 AU mg^{-1}) through one-way ANOVA (F=1.45, df=5, p=0.22). Significance found*

between LDH stored in 8-day post-perfused tissue lysate (0.063±0.011 AU mg^{-1}) (red arrow) and average LDH released between 72-192 hours in paired Student's t test (t = 3326.1, df = 59, p-value < 2.2e-16). Normality assumptions satisfied after log10() transformation. Boxplot shows median and 25th and 75th quartiles, whiskers show low and high percentiles. Statistical analysis was performed using ANOVA in R 4.3.1.

The data in

Figure 5.4 displays LDH release from mouse brain tissues perfused with DMSO-treated media, as the vehicular control. Absorbance and therefore LDH release and cellular stress, expressed from mouse brain tissue throughout 8-days on chip begins high. This is expected as the mouse brain has been removed from its natural environment and cells are stressed and this is reflected in the significant statistical differences in expression between the 24 hour and 48-hour timepoints, with subsequent timepoints. This stress, however, decreases to a non-significant, low level after 72 hours and only slightly fluctuates from this point. There is a slight increase after 96 hours, peaking at 144 hours and this is most likely due to the media change on day four of the perfusion. This is reflected in other LDH analyses of different tissues. Expression decreases down to a baseline again for the remaining time on the perfusion device after syringe change. After 8-days, the tissues were removed, and protein lysis performed to release any remaining LDH from the cells and thus determine the ratio of released LDH to retained LDH. Due to there only being significant LDH release at 24 and 48 hours, average LDH release across the remaining time points was compared to the lysis value. This indicated a significant amount of LDH remained within the tissue. This shows that not all of the LDH within the tissue was released during incubation and therefore the tissues were able to be maintained on the perfusion system with relatively little biological stress. Similarly to the mouse tissue effluent, the effluent from the cichlid brain tissue, over the course of 6 days, was analysed for LDH expression (Figure 5.5).

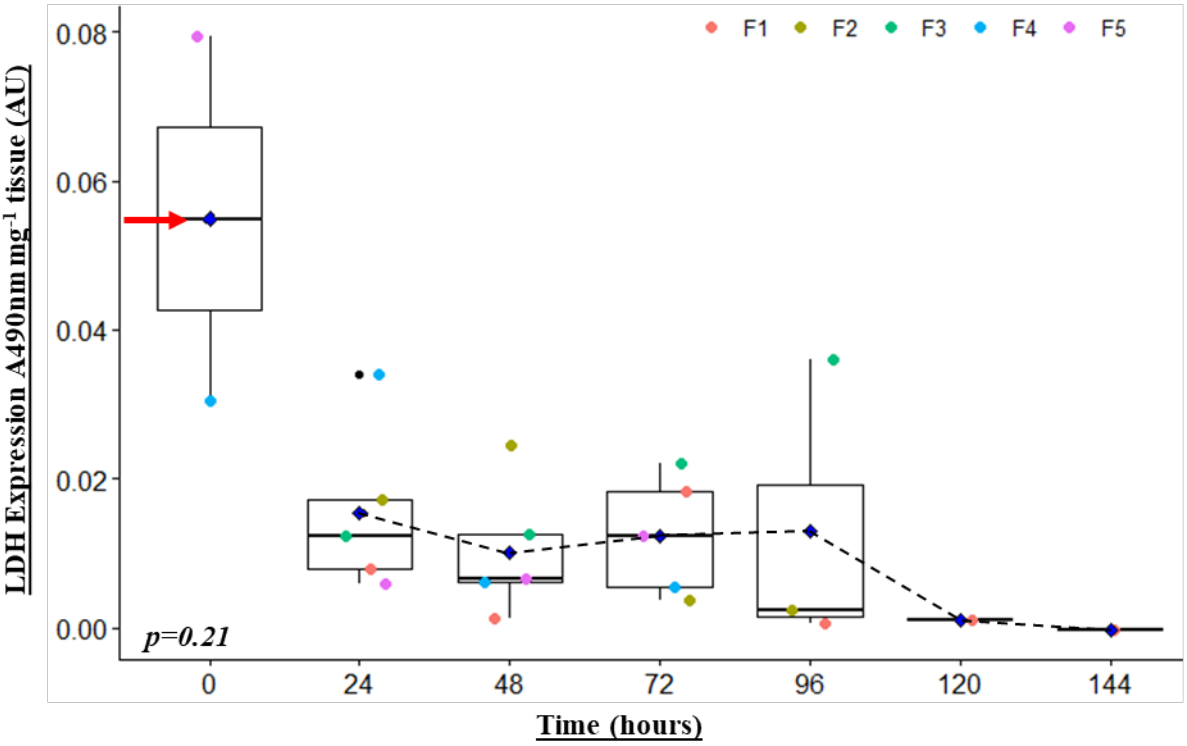

Figure 5.5.: Lactate Dehydrogenase (LDH) (Arbitrary Units (AU)) release from cichlid brain tissues (n=5) over 6 days in a novel perfusion device, including pre-perfusion tissue lysis (n=2).

*Absorbance of light at wavelength 490 nm (A490 nm^{-1}) directly corresponds to LDH release from cichlid brain tissues (mg^{-1}) in the novel perfusion device, into effluents collected every 24 hours, for 6 days. Individual data points indicate biological replicates. Mean LDH expression levels indicated by blue diamonds: day 1, 0.016±0.011 AU mg^{-1}; day 2, 0.01±0.009 AU mg^{-1}; day 3, 0.012±0.008 AU mg^{-1}; day 4, 0.013±0.02 AU mg^{-1}; day 5, 0.001±0 AU mg^{-1}; day 6, 0±0 AU mg^{-1}. Non-parametricity was identified by Shapiro-Wilk test and rectified by the sqrt() function in R 4.3.1 and one-way ANOVA performed (F=1.73, df=1, p=0.21). No significance found between LDH release at any time point over 6 days. Significance found between LDH stored in pre-perfused tissue lysate (0.055±0.034 AU mg^{-1}) (red arrow, 0 hours) and average LDH released over 6 days (0.012±0.011 AU mg^{-1}), in paired Student's t test (t = 13.9, df = 20, p-value = 9.46e-12****). Normality assumptions satisfied after log10() transformation. Boxplot shows median and 25th and 75th quartiles, whiskers show low and high percentiles. Statistical analysis was performed using ANOVA in R 4.3.1.*

As found in both human GBM and healthy mouse tissues, cichlid brain tissue initially releases more LDH, indicating higher levels of cellular stress (Figure 5.5). This does not, however, seem to decrease drastically over the first four days in the perfusion device, but is maintained. LDH release then decreases after days 5 and 6. It is worth noting that the day 5 and 6 data are collated from just one fish and therefore one biological repeat. The earlier days show data from 5 different fish and therefore forms a more accurate representation of cellular stress. No significant change in LDH was found at any time point, over the 6 days that the cichlid brain tissue was on the perfusion device, indicating that the tissue can be maintained, at least up to four days, as LDH is still being produced. Two pre-perfusion cichlid brain tissue samples were also lysed, which indicated a much higher starting level of LDH within the fish brains. The amount of LDH in the pre-perfused tissue was significantly higher than the amount released over the 6 days, from the perfused tissues. This indicates that cichlid brain tissue can be maintained on the perfusion device and therefore may be a good model for healthy brain tissue, on which to determine off-target effects of GSK3368715 treatment.

Following analysis of the LDH data, the histology of the tissue was assessed by neuropathologist, Dr Ian Scott. This was to ensure that the tissue entering the perfusion devices was of appropriate quality, that it was alive and proliferating and whether this changed post-proliferation. H&E staining was performed on several sections of each of the tissues, both pre- and post-perfusion, to determine this and examples are shown in Figure 5.6, Figure 5.7, Appendix 10 and Appendix 11.

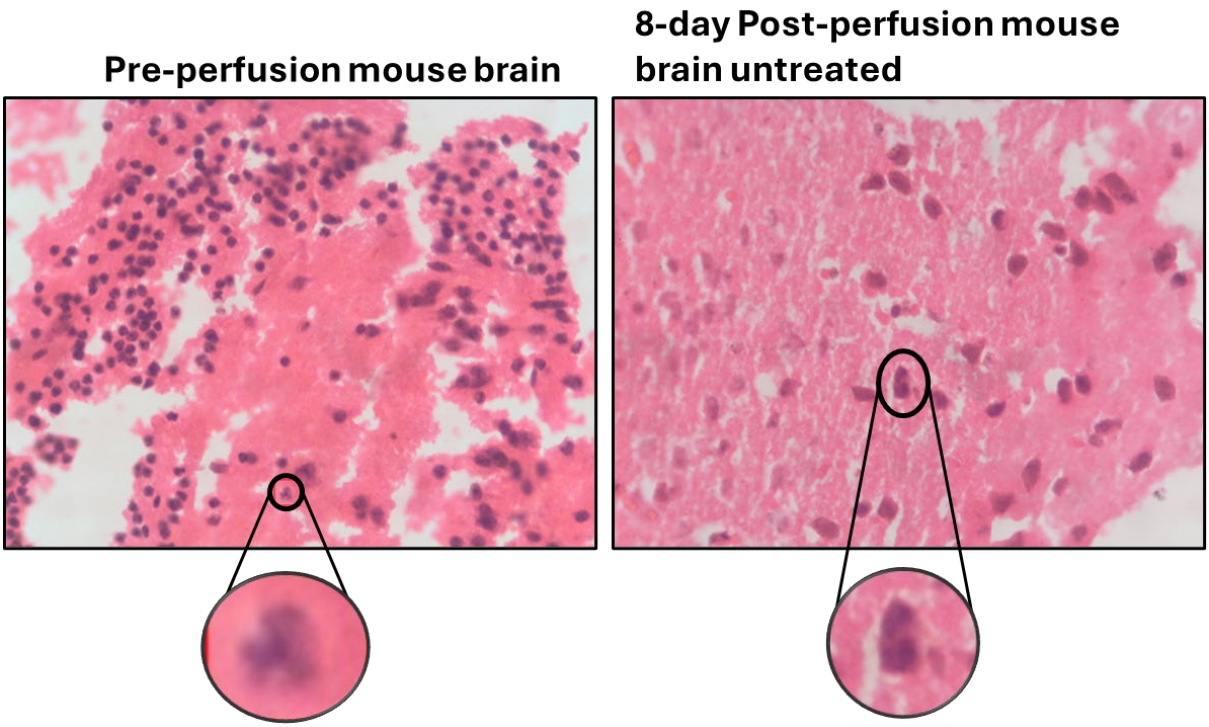

Figure 5.6.: H&E staining of pre- and DMSO-control post-perfused mouse brain tissue [inset: mitosis].

Mouse brains were maintained for 8-days in the perfusion device, treated with DMSO and remained viable throughout, indicated by haematoxylin-stained nuclei of equal and even shape. Both pre- and post-perfused tissues showed signs of mitosis, shown inset. Images captured using DinoCapture 2.0 on an inverted microscope and assessed by Dr. Ian Scott.

H&E staining indicated that the mouse brain tissue remained alive for eight days in the perfusion device, with examples of mitoses shown inset, making it a viable healthy control for screening the PRMT inhibitors. In the pre-perfused image, the example of mitosis shown is an atypical, but normal starburst mitosis (Donovan *et al.*, 2021).

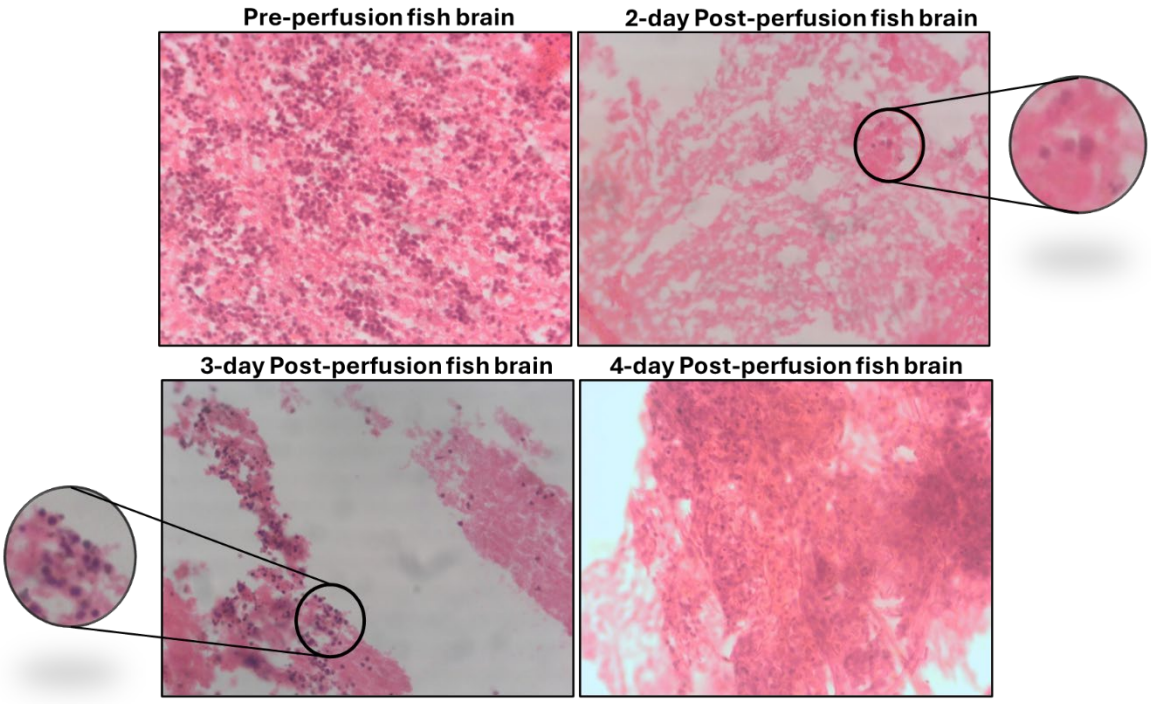

Figure 5.7.: H&E staining of pre- and 2, 3 and 4-day post-perfused cichlid brain tissue [inset: viable cells].

Cichlid brains were maintained for up to 4-days in the perfusion device with no treatments and remained viable throughout, indicated by swathes of haematoxylin-stained nuclei of equal and even shape. Images captured using DinoCapture 2.0 on an inverted microscope and assessed by Dr. Ian Scott.

H&E staining indicated that the cichlid brain tissue remained alive for the four days for which it was left in the perfusion device. The image of the tissue after 2-days perfusion reinforces the importance of getting the tissue onto the chip very quickly, due to autolysis of fish tissue. The tissue is mostly non-viable, although there are some small clusters of viable cells, shown inset. At 3-day post-perfusion, there are areas of viability and areas on dead tissue, which highlights the heterogeneity of normal tissue.

To quantify the survival of the tissue through the process of the perfusion device, IHC was performed for several biomarkers. The obtainment and analysis of the raw IHC data was based upon a system where the sensitivity would have, ideally, been higher. Several controls were utilised to ensure that the data collected was of optimum quality. Alongside the negative,

secondary antibody-only control, there were a series of positive controls. Several antibodies, which were recommended for FFPE-specific IHC in mouse tissue, such as Ki67 cleaved PARP and Annexin V were utilised to check that the tissue quality and processing were adequate and that cells were able to uptake other antibodies. The Ki67 antibody was used to determine whether healthy brain tissue cells were proliferating as would be expected from a healthy tissue. Frozen mouse tissue sections were also used in conjunction with the mouse-specific cleaved PARP antibody, to confirm tissue quality and processing efficacy. Human FFPE tissue with the corresponding human-specific cleaved PARP antibody, was used to ensure that FFPE processing did not disrupt antibody, DAB, or haematoxylin dye ability from entering the cell, thereby preventing accurate cell counting. Finally, human tissue which had been fresh frozen was also utilised, as this had shown strong staining in previous GBM IHC and therefore was a good positive control to confirm the efficacy of the staining technique.

To ensure that data between the GBM and mouse samples were comparable, it was necessary to determine the level of programmed cell death occurring in the mouse brain samples. Cleaved PARP was again used to identify the levels of apoptosis occurring within the tissue. To validate that the mouse brain tissue was suitable for incubation in the perfusion device, IHC was performed on pre-perfused and post-perfused, DMSO-treated tissue. Images were taken of the IHC tissue, and a cleaved PARP positivity index collated (Figure 5.8). The average indices were made relative to the post-perfusion control. A paired t-test for parametric, homoscedastic data was performed to determine any significant changes between cleaved PARP expression pre-perfusion and post-perfusion. IHC of healthy mouse brain tissues indicated no significant changes in cleaved PARP expression between pre- and post-perfusion tissue samples (Figure 5.8).

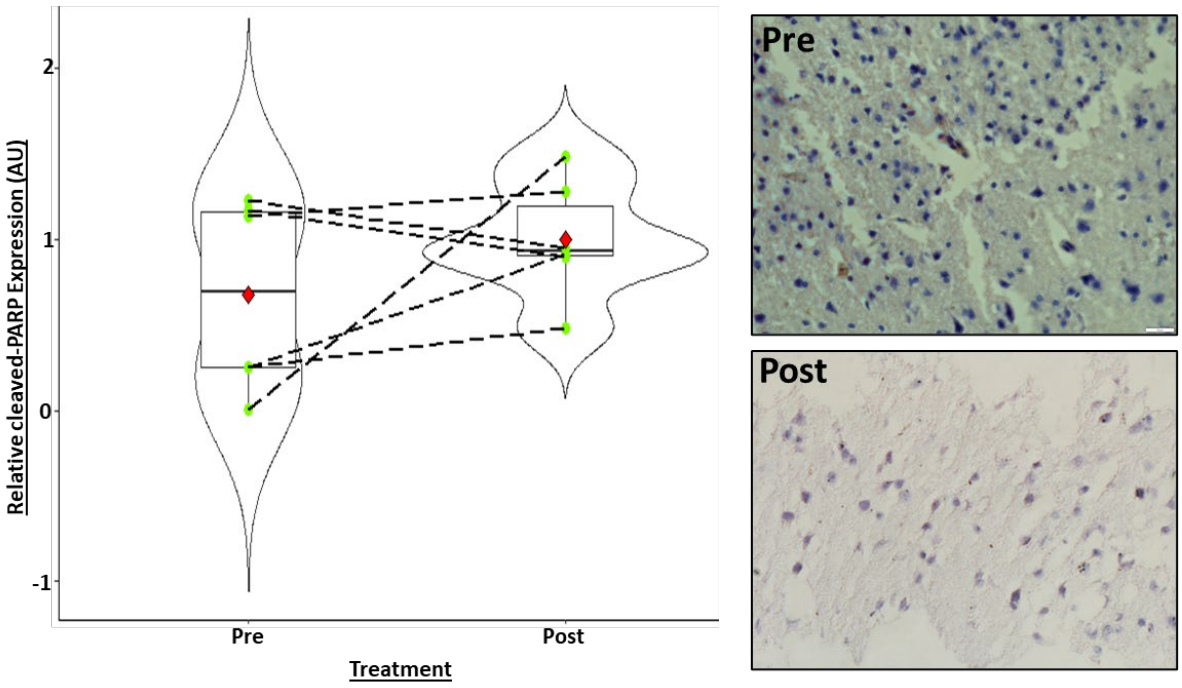

Figure 5.8.: Relative cleaved PARP expression (Arbitrary Units (AU)) in mouse brain tissue, pre- and 8-day post-perfusion, with representative images.

IHC of mouse brain tissue, pre- (0.89±0.495 AU) and 8-days post-perfusion (0.98±0.16 AU) (n=6), using apoptotic marker cleaved PARP, indicated no significant changed in apoptosis whilst in the perfusion device, using Welch's paired t-test (t = 0.020, df = 2, p = 0.99). Dashed lines show cleaved PARP expression between treatments, within the same sample. Green points indicate individual mouse samples. Red diamonds indicate mean cleaved PARP expression, relative to the post-perfusion sample. Images taken using an ***Olympus IX71 inverted fluorescence microscope, on the brightfield setting, phase 2 and using CellSens software 1.18 at x40 magnification.*** *Statistical analysis was performed using ANOVA in R 4.3.1.*

Annexin V antibody was used to cross validate the apoptosis results gained from the cleaved PARP antibody. An Annexin V positivity index was collated from the images and the averages made relative to the post-perfusion control (Figure 5.9) (Appendix 13). A paired t-test for parametric, homoscedastic data was performed to determine any significant changes between Annexin V expression pre-perfusion and post-perfusion.

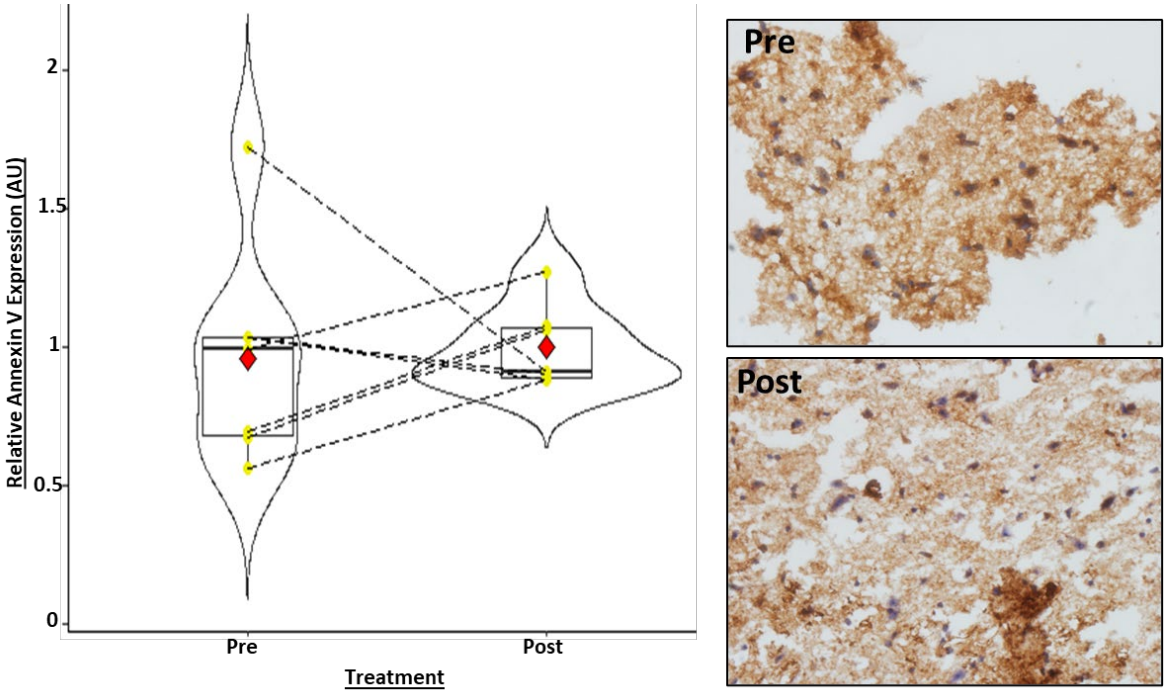

Figure 5.9.: Relative Annexin V expression (Arbitrary Units (AU)) in mouse brain tissue, pre- and 8-day post-perfusion, with representative images.

IHC of mouse brain tissue, pre- (0.96±0.39 AU) and 8-days post-perfusion (1.00±0.15 AU) (n=7), using apoptotic marker Annexin V, indicated no significant change in apoptosis whilst in the perfusion device, in a Welch's paired t test (t = -0.23, df = 6, p = 0.82). Dashed lines show cleaved PARP expression between treatments, within the same sample. Yellow points indicate individual mouse samples. Red diamonds indicate mean Annexin V expression, relative to the post-perfusion sample. Images taken using an ***Olympus IX71 inverted fluorescence microscope, on the brightfield setting, phase 2 and using CellSens software 1.18 at x40 magnification.*** *Statistical analysis was performed using ANOVA in R 4.3.1.*

The IHC results of Annexin V expression (Figure 5.9) confirmed that there was no significant change in apoptosis between pre-perfused and 8-days post-perfused tissue (Appendix 14). This confirms that the tissue can be maintained on chip and that the perfusion system does not cause significant apoptosis to the tissue.

Annexin V was also used to determine the capacity of cichlid brain tissues to be maintained on the device. This was initial data to ascertain whether the cichlid brain tissue would be a suitable model for further downstream analysis into PRMT inhibitors. IHC with Annexin V was

performed on five cichlid brain tissue samples pre-perfusion and post-perfusion, after 2, 3, or 4-days, dependent upon the fish sample. IHC was performed to n=2 for most samples. The Annexin V positivity index was found for each image, as previous and an average of all of the images taken (Figure 5.10)(Appendix 12). This was then made relative to the pre-perfusion control (as there were multiple, untreated post-perfusion controls, unlike previous samples) and Kruskal-Wallis analysis performed for non-parametric data, with no corrections for heteroscedasticity.

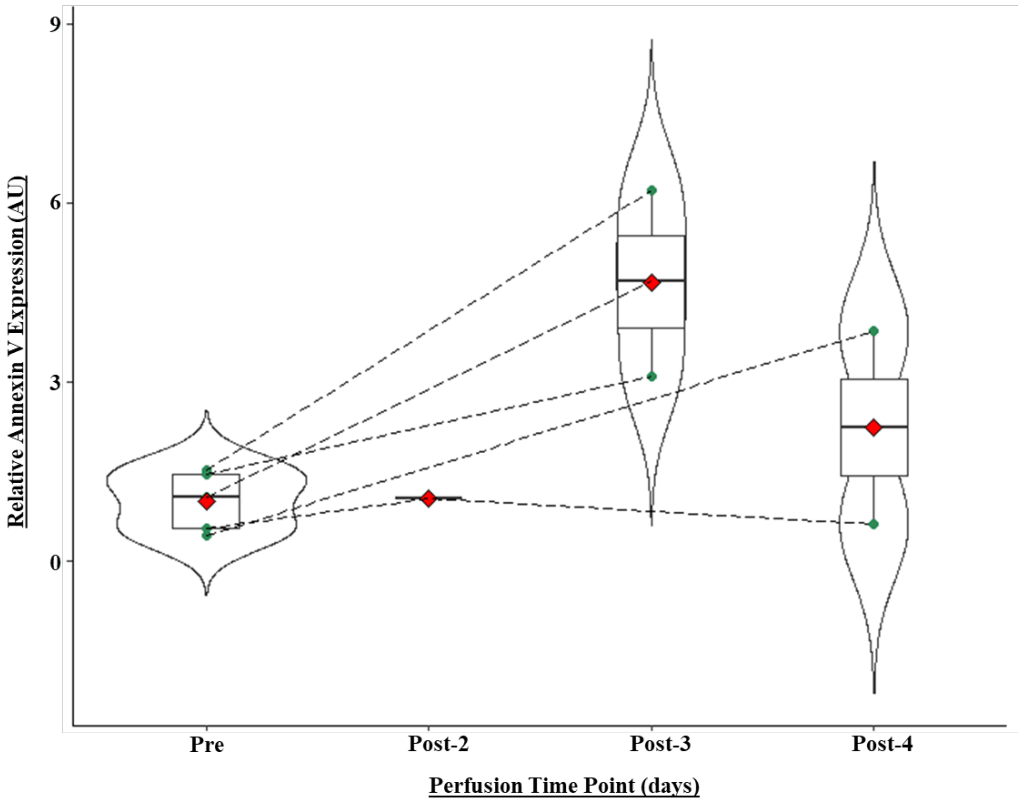

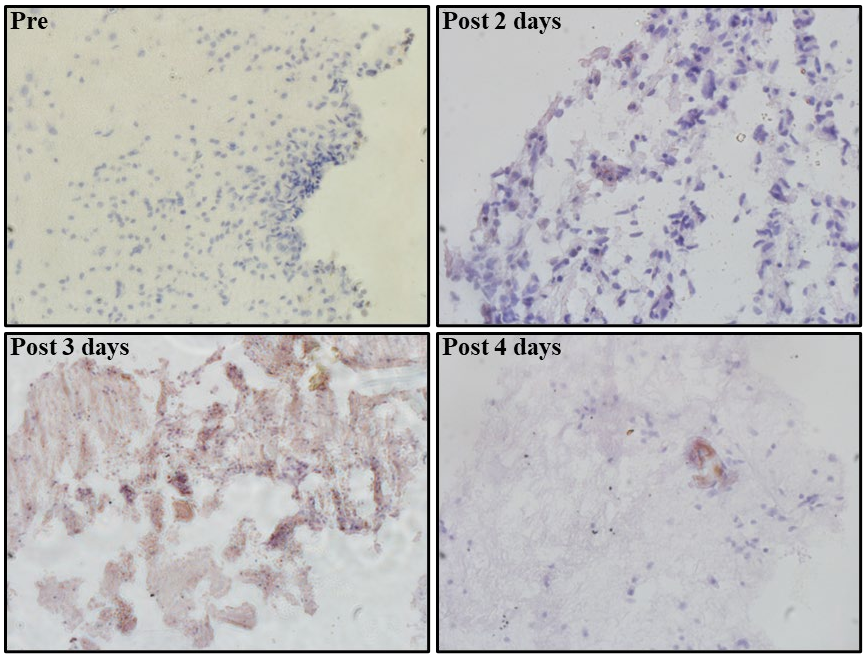

Figure 5.10.:Relative Annexin V expression (Arbitrary Units (AU)) in cichlid brain tissue, pre- and 2, 3- and 4-day post-perfusion, with representative images.

IHC of cichlid brain tissue, pre- (1.00±0.51 AU) (n=5), 2-days (1.05) (n=1), 3-days (4.67±1.56 AU) (n=3) and 4-days post-perfusion (2.23±2.29 AU) (n=2), using apoptotic marker Annexin V, indicated no significant changes in apoptosis whilst in the perfusion device, using a Kruskal-

Wallis test (X^2=5.50, df = 3, p = 0.14). Dashed lines show cleaved PARP expression between treatments, within the same sample. Green points indicate individual mouse samples. Red diamonds indicate mean Annexin V expression, relative to the pre-perfusion sample. Images taken using an ***Olympus IX71 inverted fluorescence microscope, on the brightfield setting, phase 2 and using CellSens software 1.18 at x40 magnification.*** *Statistical analysis was performed using ANOVA in R 4.3.1.*

As found with both the human and mouse tissues, cichlid brain tissue was maintained in the perfusion device in apparently viable conditions, albeit for a much shorter period of time. It was found that extending beyond 3 days in the system caused the brain tissue to disaggregate and become less solid and therefore more difficult to handle. It was determined to maintain the fish brains for no more than 3 days in the perfusion system for later samples. In Figure 5.10, although there is no significant increase in Annexin V expression and therefore apoptosis of the fish brain tissue, there does appear to be a strong upwards deflection in Annexin V expression, post-3 days. Although this rectifies at 4-days post-perfusion, this could support the visual and technical findings described. This is also reflected in the representative images (Figure 5.10 and Appendix 12).

5.3.2. Cichlid gills cannot be maintained in the novel perfusion device

Due to the ubiquitous nature of PRMTs, cichlid gills were utilised as a control to determine off-target effects of the GSK3368715 drug on other organs. Prior to treating the gills with drugs, this optimisation study used gills perfused with only NBA medium and no additional drugs, to determine whether the gills could be successfully maintained in the perfusion device. As with the mouse and cichlid brain tissues, the gill sections were maintained in the perfusion device for up to 8-days and then underwent H&E staining. This was to determine any histological features which would confirm whether the tissue remained alive whilst in the device and if so, the optimal time at which the gills should be removed from the device. Time points of 2-days, 4-days and 7-days were chosen (Figure 5.11). This was to be able to track any potential degradation over time, whilst maintaining some continuity with the time that GBM samples spent on the perfusion device, for comparability. This work was performed in partnership with Karen Lister, in a laboratory research technician capacity.

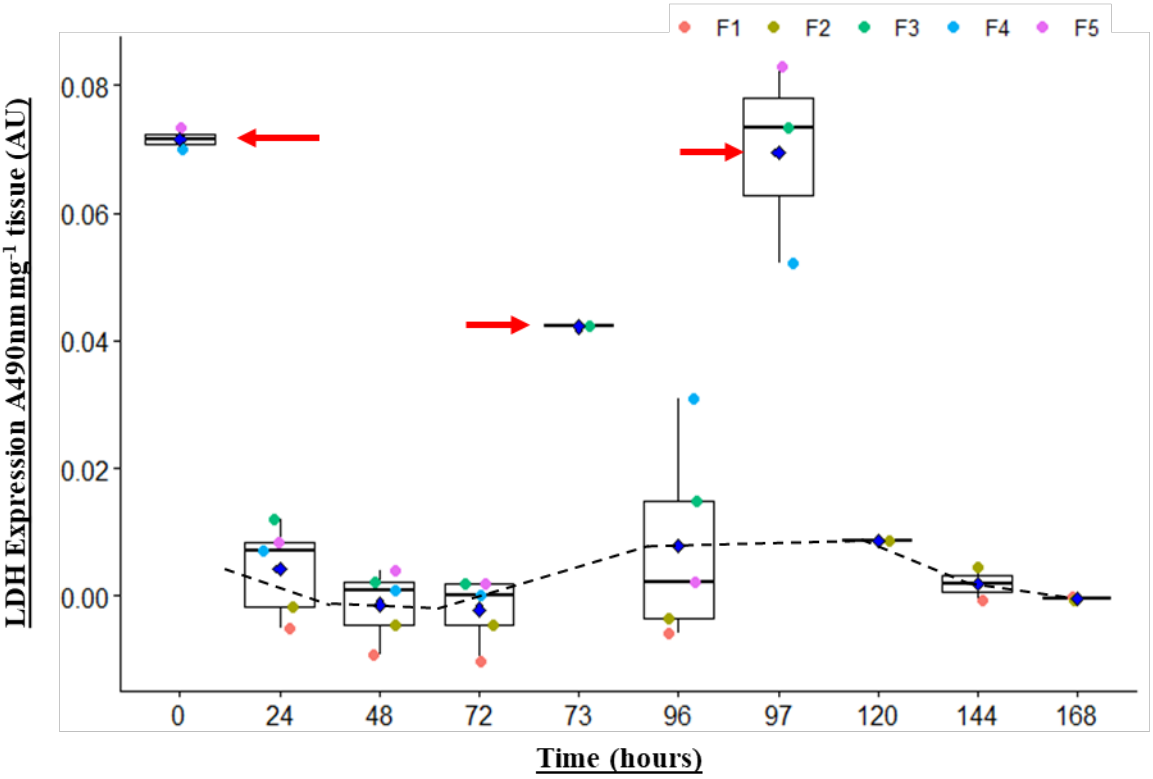

Figure 5.11.:Lactate Dehydrogenase (LDH) (Arbitrary Units (AU)) release from cichlid gill tissues (n=5) over 7-days in a novel perfusion device, including pre- (n=2) and post-perfusion tissue lysis at 3 days (n=1) and 4-days (n=3).

*Absorbance of light at wavelength 490 nm (A490 nm^{-1}) directly corresponds to LDH release from cichlid gill tissues (mg^{-1}) in the novel perfusion device, into effluents collected every 24 hours, for 7-days. Individual data points indicate biological replicates. Mean LDH expression levels indicated by blue diamonds: day 1, 0.004±0.007 AU mg^{-1}; day 2, -0.001±0.005 AU mg^{-1}; day 3, -0.002±0.005 AU mg^{-1}; day 4, 0.008±0.015 AU mg^{-1}; day 5, 0.009±0 AU mg^{-1}; day 6, 0.002±0.004 AU mg^{-1}; day 7, 0±0 AU mg^{-1}. Non-parametricity was identified by Shapiro-Wilk test and in R 4.3.1 and Kruskal-Wallis test performed (X^2= 4.02, df = 6, p-value= 0.68). No significance was found between LDH release at any time point over 6 days. Significance was found between LDH stored in pre-perfused tissue lysate (0.072±0.002 AU mg^{-1}) (red arrow, 0 hours) and average LDH released over 6 days (0.002±0.009 AU mg^{-1}), in paired Student's t test (t = 10.4, df = 15, p-value = 3.27e-08****). Significance found between LDH stored in 3-day post-perfused tissue lysate (0.042 AU mg^{-1}) (red arrow, 73 hours) and average LDH released over 6 days (0.002±0.009 AU mg^{-1}), in paired Student's t test (t = 25.5, df = 14, p-value = 3.95e-13****). Significance was found between LDH stored in 4-day post-perfused*

*tissue lysate (0.069±0.016 AU mg^{-1}) (red arrow, 97 hours) and average LDH released over 6 days (0.002±0.009 AU mg^{-1}), in paired Student's t test (t = 22.9, df = 16, p-value = 1.19e-13****). Normality assumptions satisfied after log10() or sqrt() transformation. Boxplot shows median and 25th and 75th quartiles, whiskers show low and high percentiles. Statistical analysis was performed using ANOVA in R 4.3.1.*

LDH release from the gills began much lower than anticipated but was consistent with the LDH release results from the brain. The LDH release decreased slightly over 72 hours, before increasing again to a peak between 96 and 120 hours and then slightly reduced. Whilst there generally was a small increase in cellular stress in the cichlid and mouse brains and the GBM tissue in previous chapters, it did tend to settle back down to a baseline after around 24 hours, which it did not appear to do with the gills. Stored LDH in the tissues also remained high, which might suggest that the tissues were, largely, not stressed in the microfluidics device, although this too was variable throughout the 7-days in the perfusion device, as seen at time points 0, 73 and 97 hours (Figure 5.11). More lysates from multiple fish gills would require testing for stored LDH to draw any significant conclusions from this data.

H&E staining examples of these tissues are displayed in Figure 5.12.

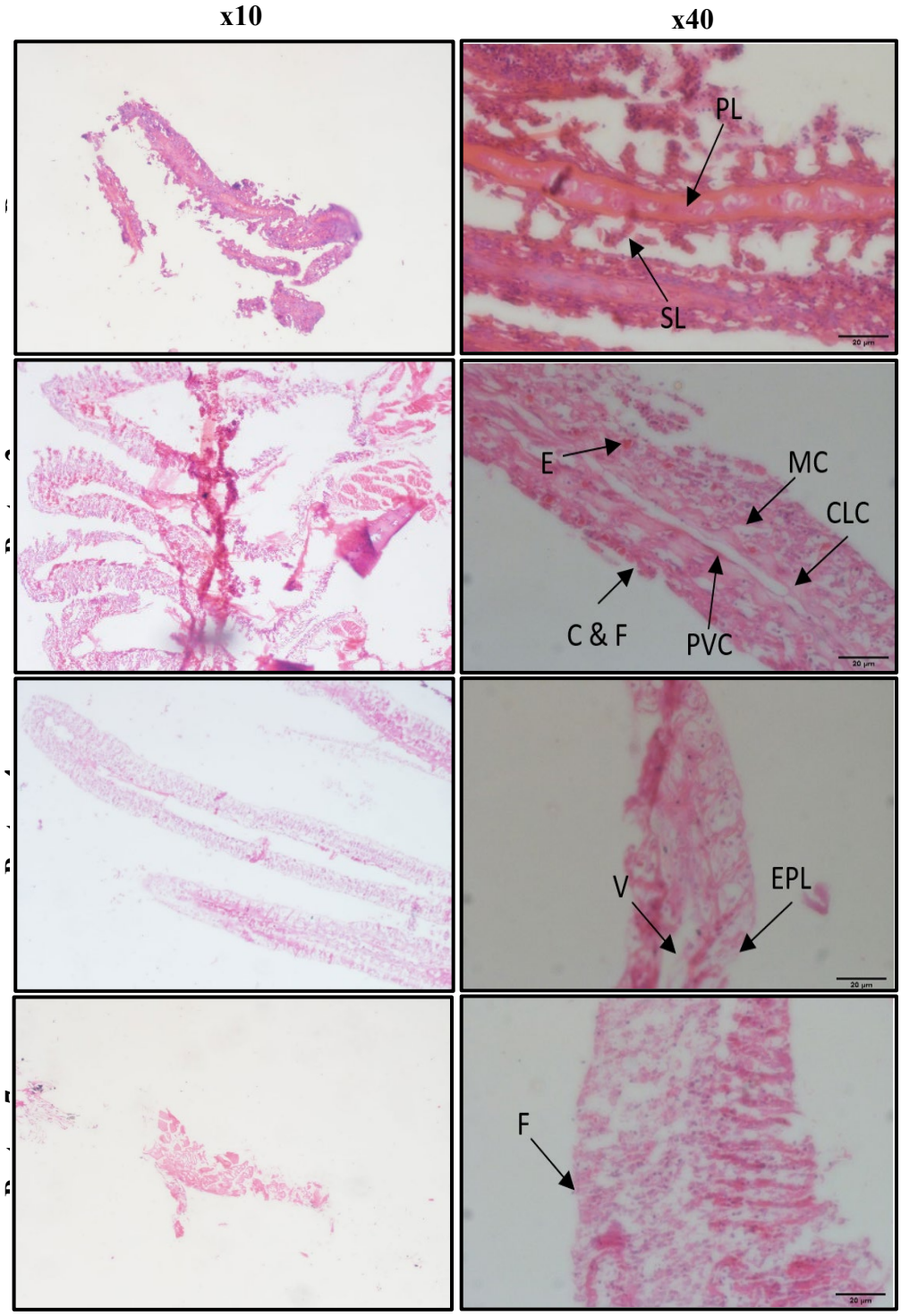

Figure 5.12.:Representative H&E images of cichlid gills.

Images taken using an Olympus IX71 inverted fluorescence microscope, on the brightfield setting, phase 2 and using CellSens software 1.18 at x10 and x40 magnification. PL- primary lamellae; SL- secondary lamellae. C&F some secondary lamellae clubbing and fusion; MC- mucous cell; PVC- pavement cell; E- erythrocytes CLC- chloride cell; V- vacuole; EPL-

epithelium lifting. H&E performed, and images taken and labelled in conjunction with Karen Lister.

Cichlid brain and gill histology were assessed by speciality histologist, Jorge del Pozo and in collaboration with Kim Thompson, at the University of Edinburgh. Cichlid gills were determined to be inviable prior to being put in the perfusion device. This can be seen by the large pink, eosin-stained areas and breakdown of structure, including clubbing and fusion of secondary lamellae and epithelium lifting, particularly post-perfusion (Figure 5.12).

5.3.3. GSK3368715 does not cause apoptosis in healthy mouse and fish brain tissue, or propagate cell proliferation

The work in the previous chapters indicated that GSK3368715 causes apoptosis to occur in *ex vivo* patient GBM samples and influences changes in the transcriptome and alternative splicing. These changes resulted in reduction of protein synthesis capacity, as well as increases in pathways associated with apoptosis. Increases in apoptosis were also indicated by increased expression in apoptotic marker cleaved PARP in IHC analysis. Similar techniques were performed on healthy mouse and fish brain tissues, to assess the effect of GSK3368715, including: stress assays, using LDH release into effluents; IHC for mouse-specific cleaved PARP and mouse- and fish-specific Annexin V to ensure reproducibility.

LDH analysis was performed on all mouse brain effluents from chips in the perfusion device, for GSK3368715, TMZ and combination treatments, over the 8-days. Each time point for treatments was compared to the same time point in the DMSO control and to other treatments, at the same time point. Figure 5.13 shows LDH release from eleven mouse brain tissues over 8-days, for all treatments.

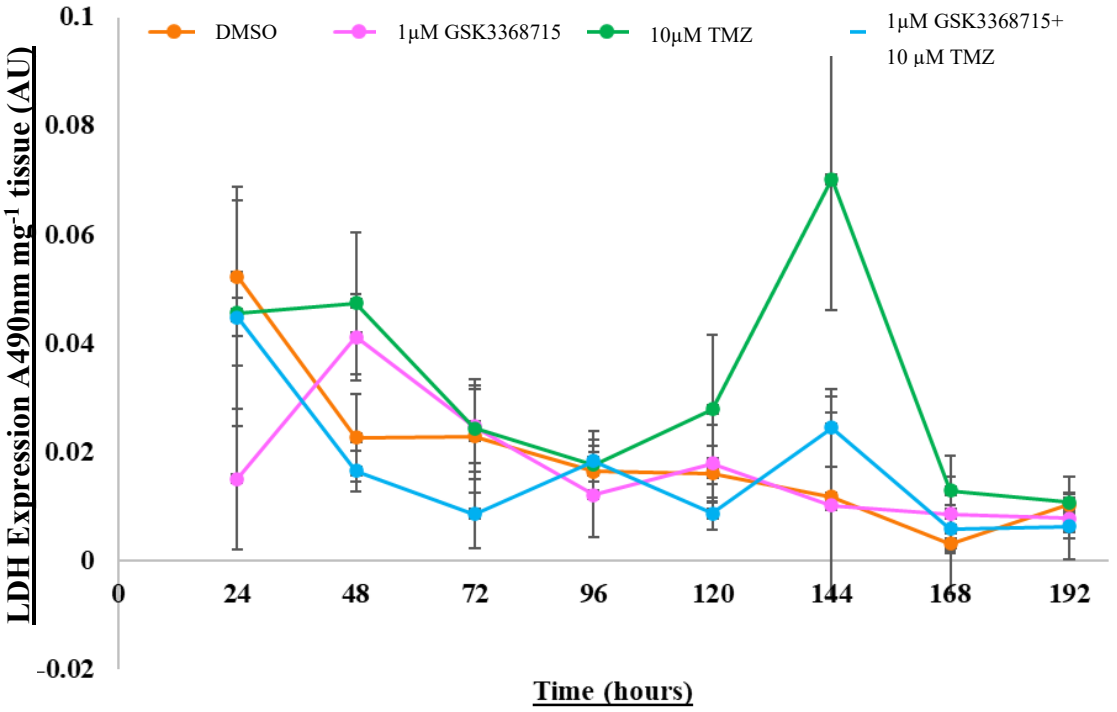

Figure 5.13.: Average lactate dehydrogenase (LDH) (Arbitrary Units (AU)) release from mouse brain tissues (n=11), with 1 µM GSK3368715 and 10 µM TMZ treatment, over 8-days in a novel perfusion device.

Absorbance of light at wavelength 490 nm (A490 nm) directly corresponds to LDH release per milligram of mouse brain tissues (mg^{-1}) in the novel perfusion device, into effluents collected every 24 hours, for 8-days. DMSO control (orange), 10 µM TMZ (green) and Combo treatment (1 µM GSK3368715 and 10 µM TMZ) (blue) begin with highest LDH expression, between 0.04-0.06 $AUmg^{-1}$ tissue, before reducing and fluctuating at a lower level for the remainder of time in the perfusion system. 10 µM TMZ shows a peak at 144 hours of around 0.07 $AUmg^{-1,}$ before decreasing again. 1 µM GSK3368715 (pink) increases slightly after 48 hours, before reducing again and remaining low. Statistical analysis was performed using GLM in R 4.3.1.

Generally, all treatments begin with high levels of LDH release into the effluent, from the mouse brain tissues, which then decreases over time and remains low for the remaining time on-chip. There are some anomalies, including the amount of LDH in the effluent of GSK3368715-treated mouse brains after 24 hours, which is lower than the rest and then increases after 48 hours, before following the general pattern of the DMSO and combination-

treated tissues. The TMZ-treated tissues generally showed an overall downward trend in LDH release, with the exception of a large peak after 144 hours. This could potentially be because of a blockage in one of the chips, which reduced the amount of media available to the brain tissue, thereby increasing cellular stress. There is a large standard error shown in Figure 5.13 at this time point and treatment, which supports this theory.

GLM was performed to identify factors which significantly effect LDH expression in mice. The variables explored were: treatment, treatment with the time component (Treatment2), age and sex. Time as a unique factor was excluded from this analysis, due to the findings with the control LDH sample, which indicated no significant changes in LDH release, over time. GLMs with and without interactions were fitted to identify the best model, using the 'glmulti' package in R. Akaike criterion (AICc) weighting was assessed to determine which variables were the most important contributing factors to variation in LDH. In an exhaustive search of the non-interacting model, the top two models indicated AICc of -1334.220 and -1332.770 and shared 99.99% of the variation, with contributions from all exploratory variables. A second exhaustive model was run with interactions for all variables, which indicated the top, linked twenty-four models with an AICc score of -1337.058, contributing to only 54.4% of the variation. The non-interacting model, including all variables, was chosen as the final model.

The coefficient for the intercept showed significant positive regression (coeff. est. ±SE: $2.02x10^{-2}±5.22x10^{-3}$, t=3.88, $p=1.48x10^{-4}$). This may indicate underlying components of the individual mouse sample genetics and epigenetics, which were not tested, which contribute to variation in LDH release, which outlines that there are factors contributing to variation which are not fully explained by the model. There is significant negative regression of LDH release within mice at 125 days of age (coeff. est.: $-1.12x10^{-2}±3.33x10^{-3}$, t=-3.36, $p=9.49x10^{-4}$), 127-days (coeff. est.: $-1.99x10^{-2}±3.33x10^{-3}$, t=-5.97, $p=1.27x10^{-8}$) and 87-days (coeff. est.: $-5.70x10^{-3}±2.39x10^{-3}$, t=-2.38, $p=1.83x10^{-2}$). There is a positive significant regression in the Treatment2 variable, including: Combo at 24 hours (coeff. est.: $2.71x10^{-2}±7.09x10^{-3}$, t=3.81, $p=1.87x10^{-4}$); DMSO at 24 hours (coeff. est.: $2.59x10^{-2}±4.62x10^{-3}$, t=5.61, $p=7.47x10^{-8}$) and 48 hours (coeff. est.: $1.52x10^{-2}±4.88x10^{-3}$, t=3.12, $p=2.14x10^{-3}$); GSK3368715 at 24 hours (coeff. est.: $2.73x10^{-2}±4.49x10^{-3}$, t=6.09, $p=6.51x10^{-9}$) and 48 hours (coeff. est.: $1.29x10^{-2}±4.85x10^{-3}$, t=2.87, $p=4.57x10^{-3}$) and TMZ at 24 hours (coeff. est.: $3.98x10^{-2}±7.09x10^{-3}$,

t=5.61, p=7.41x10^{-8}) (Figure 5.14). The positive regression at time points of 24 and 48 hours are expected and consistent with the findings of the control-only data. This is because the brain tissue has been taken out of its original environment and is therefore more stressed, producing more LDH.

Finally, the estimated marginal means were calculated, using the *emmeans()* package. This was performed as a post-hoc analysis of the GLM, with Tukey pairwise correction, to understand further the relationships between each of the levels, within the variables. The emmeans contrasts were calculated between treatments, both with and without the element of time and also age and sex (Figure 5.14).

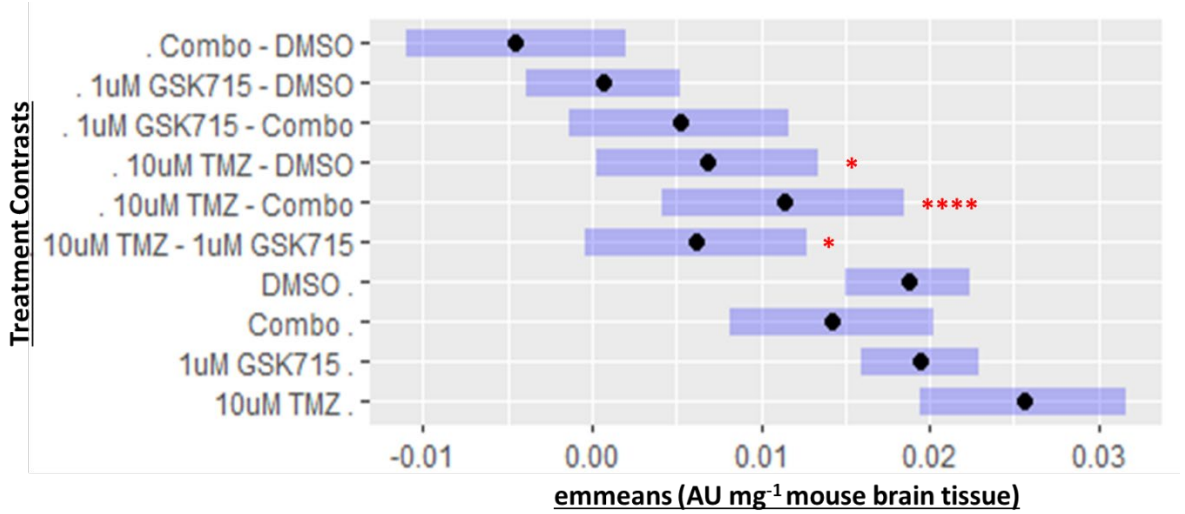

Figure 5.14.: Emmeans comparisons of LDH expression (AU mg^{-1} mouse brain tissue) in healthy mouse brains between Treatment.

Eleven healthy mouse brains treated with: DMSO control, 1 µM GSK3368715, 10 µM TMZ and 1 µM GSK3368715 + 10 µM TMZ, for 8-days in the novel perfusion system had emmeans compared. Emmeans indicated by black dots. Blue bars indicate standard error (SE). Significant positive correlations in LDH release were found between the DMSO control and TMZ (coeff. est.: 6.83x10^{-3}±2.32x10^{-3}, t=2.94, df=180, p=0.019), TMZ and the combination treatment (coeff. est.: 1.13x1^{-2}±2.32x10^{-3}, t=4.48, df=180, p=0.0001****) and TMZ and GSK3368715 (coeff. est.: 6.15x10^{-3}±2.32x10^{-3}, t=2.65, df=180, p=0.043*). Statistical analysis was performed using ANOVA in R 4.3.1.*

There is a positive correlation between the DMSO control and TMZ, suggesting an increase in cellular stress with TMZ treatment. There is also a positive correlation between the TMZ treatment and combination, indicating that the addition of GSK3368715 to the healthy tissue results in a reduction in cell stress. Positive correlation between TMZ and GSK3368715 also suggests that TMZ produces higher cellular stress than GSK3368715. Treatment with the time element (Treatment2) only showed significant negative correlation between the DMSO control at 24 hour and 192-hour timepoints (coeff. est.: $-2.99\text{x}10^{-2}\pm4.48\text{x}10^{-3}$, t=-4.67, df=180, $p=2.34\text{x}10^{-3}$*) (Figure 5.15). The negative correlation between the 24-hour time point and later time point is reflective of the control LDH release data. This indicates a reduction in LDH release over time, which is expected.

In the exploration of the emmeans of age (Figure 5.15), there was an interesting split between the older and younger mice, in terms of how tissue responded to stress, resulting in LDH release.

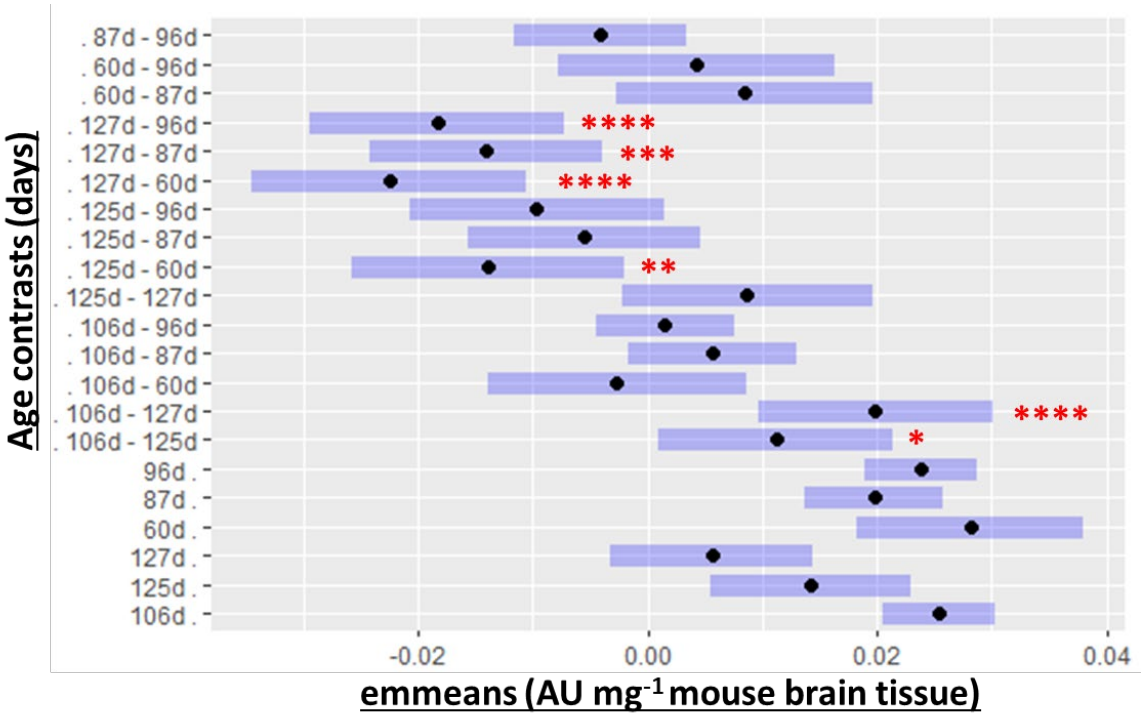

Figure 5.15.: Emmeans comparisons of LDH expression (AU mg^{-1} mouse brain tissue) in healthy mouse brains with age.

Eleven mice of various ages (60 days, 87-days, 96 days, 106 days, 125 days and 127-days) had emmeans compared. Emmeans indicated by black dots. Blue bars indicate standard error (SE). There is a significant positive correlation between 106 days and 125 days ($1.12x10^{-2}\pm3.33x10^{-3}$, df=180, t=3.36, $p=1.2x10^{-2}$) and 127-days (coeff. est.: $1.99x10^{-2}\pm3.33x10^{-3}$, df=180, t=5.97, $p=<1.00x10^{-4}$****). There is also significant negative correlation between 125 days and 60 days ($-1.39x10^{-2}\pm3.39x10^{-3}$, df=180, t=-3.60, $p=5.40x10^{-3}$**) 127-days and 60 days (coeff. est.: $-2.26x10^{-2}\pm3.86x10^{-3}$, t=-5.87, df=180, $p=<1.00x10^{-4}$****), 87-days (coeff. est.: $-1.42x10^{-2}\pm3.30x10^{-3}$, t=-4.29, df=180, $p=4.00x10^{-4}$***) and 96 days (coeff. est.: $-1.83x10^{-2}\pm3.61x10^{-3}$, t=-5.08, df=180, $p=<1.00x10^{-4}$****). Statistical analysis was performed using ANOVA in R 4.3.1.*

This data shows that tissue from older mice have lower LDH emmeans than younger mice, indicating that they may be less stressed in the perfusion device, generally. The lack of interaction models suggests that there is no significant interaction between treatment and age and therefore there are no differences between how younger mice and older mice react to the various treatments, in terms of LDH expression (Figure 5.15).

The final variable to be investigated was the effect of sex of the mice on mean LDH expression, over the 8-days of perfusion, across any treatment (Figure 5.16). Sex did not show any differences in emmeans comparisons of LDH expression, between male and female mice, in any treatment or time point. This suggests that there is no significant difference in cellular stress, between male or female mice (Figure 5.16).

Figure 5.16.: Emmeans comparisons of LDH expression (AU mg^{-1} mouse brain tissue) in healthy mouse brains with sex.

Eleven mice, both male and female, had emmeans of LDH expression, across any time point and treatment, compared. Emmeans indicated by black dots. Blue bars indicate standard error (SE). No significance found in mean LDH expression between male and female mice. Statistical analysis was performed using ANOVA in R 4.3.1.

IHC analysis of Ki67 expression in healthy mouse brain samples, for this project, was performed by Ricky Akinkuolie, for the completion of his MSc degree, under supervision from myself (Figure 5.17). The rationale for the use of Ki67 was two-fold. Firstly, to solidify findings that the mouse brain tissue could be maintained within the perfusion device, by comparing pre-perfused and 8-day post-perfused, DMSO-treated control tissue. Secondly, Ki67 would be used as an inverse measure, to ascertain whether GSK3368715 and TMZ may cause significant decreases in healthy tissue proliferation, indicating potential cell death and whether the drugs were responsible for any increases in healthy brain tissue proliferation, which may in itself be a negative consequence of the use of the PRMT inhibitor.

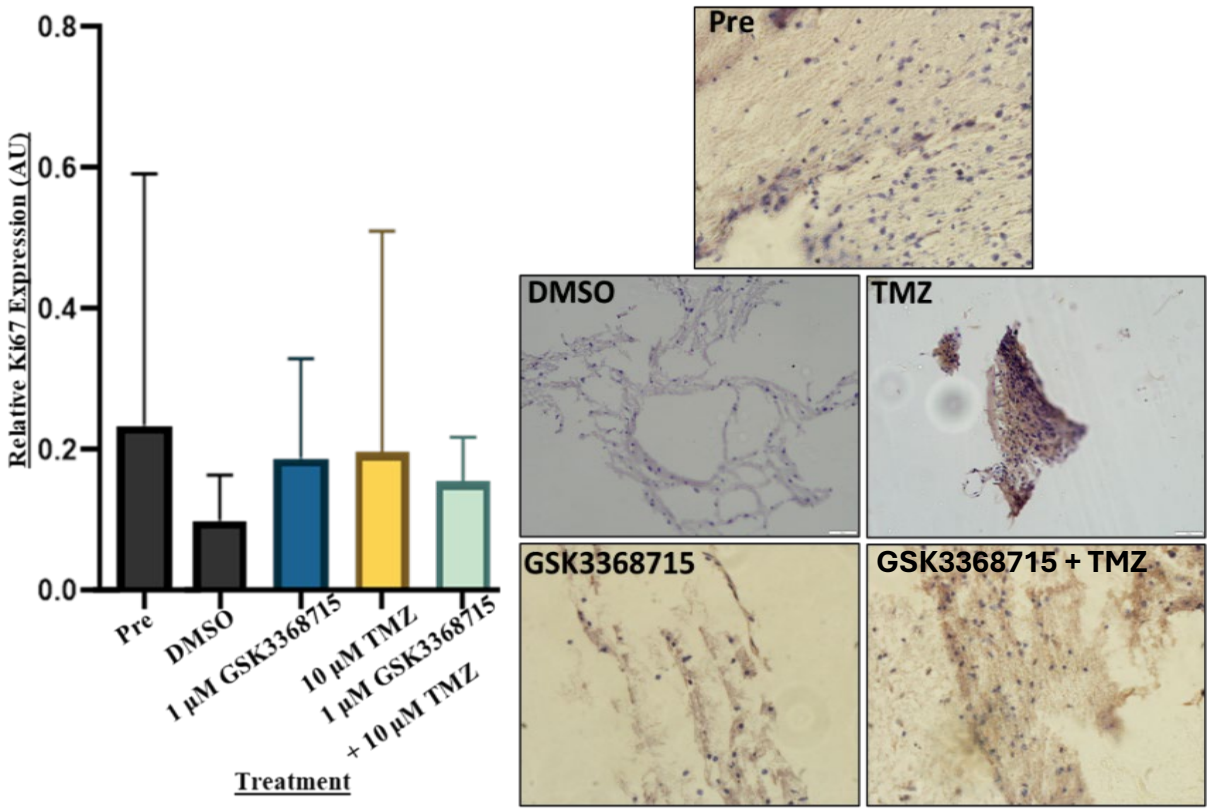

Figure 5.17.: Relative Ki67 expression (Arbitrary Units (AU)) in mouse brain tissue (n=1), pre-perfusion and post-perfusion, treated with 1 μM GSK3368715, 10 μM TMZ and a combination, compared to the DMSO control, with representative images.

Ki67 for all treatments were quantified using cell profiler 4.1.3 and data represents Ki67-labelled nuclei, normalised to the DMSO control average, with standard error. Analysis of Ki67 expression in pre-perfusion and all treatments vs DMSO control post-perfusion was performed using Graph-pad prism 9.41 v. Shapiro-Wilk test denoted non-parametric data. Kruskal-Wallis test was used to calculate the p-value = 0.6194. Data is representative of sample M9 with n=3 technical repeats per treatment. Images taken using an Olympus IX71 inverted fluorescence microscope, on the brightfield setting, phase 2 and using CellSens software 1.18 at x40 magnification. Graph and statistics performed by Ricky Akinkuolie, MSc.

No significant changes to proliferative marker, Ki67, were identified within the 6 healthy mouse brains screened. The maintenance of proliferation between pre-perfusion and post-perfusion samples indicate that healthy mouse brains can be sustained in the perfusion system and therefore, any significant changes are likely to be due to treatment of the tissue. Interestingly, there is also no significant change in Ki67 expression with treatment, suggesting that neither the GSK3368715 type I PRMT inhibitor, nor current gold standard TMZ decrease proliferation in healthy brain tissue cells (Figure 5.17).

To further investigate whether GSK3368715 had any significant apoptotic effect on healthy mouse brain tissue, IHC using apoptotic markers cleaved PARP and Annexin V was performed. This IHC was performed using tissue treated with 1 μM GSK3368715, 10 μM TMZ and a combination of those drugs, in comparison with the DMSO vesicle control (Figure 5.18). Up to seven mice were used, with tissues from three distinct areas of the frontal and temporal lobes making up the technical repeats.

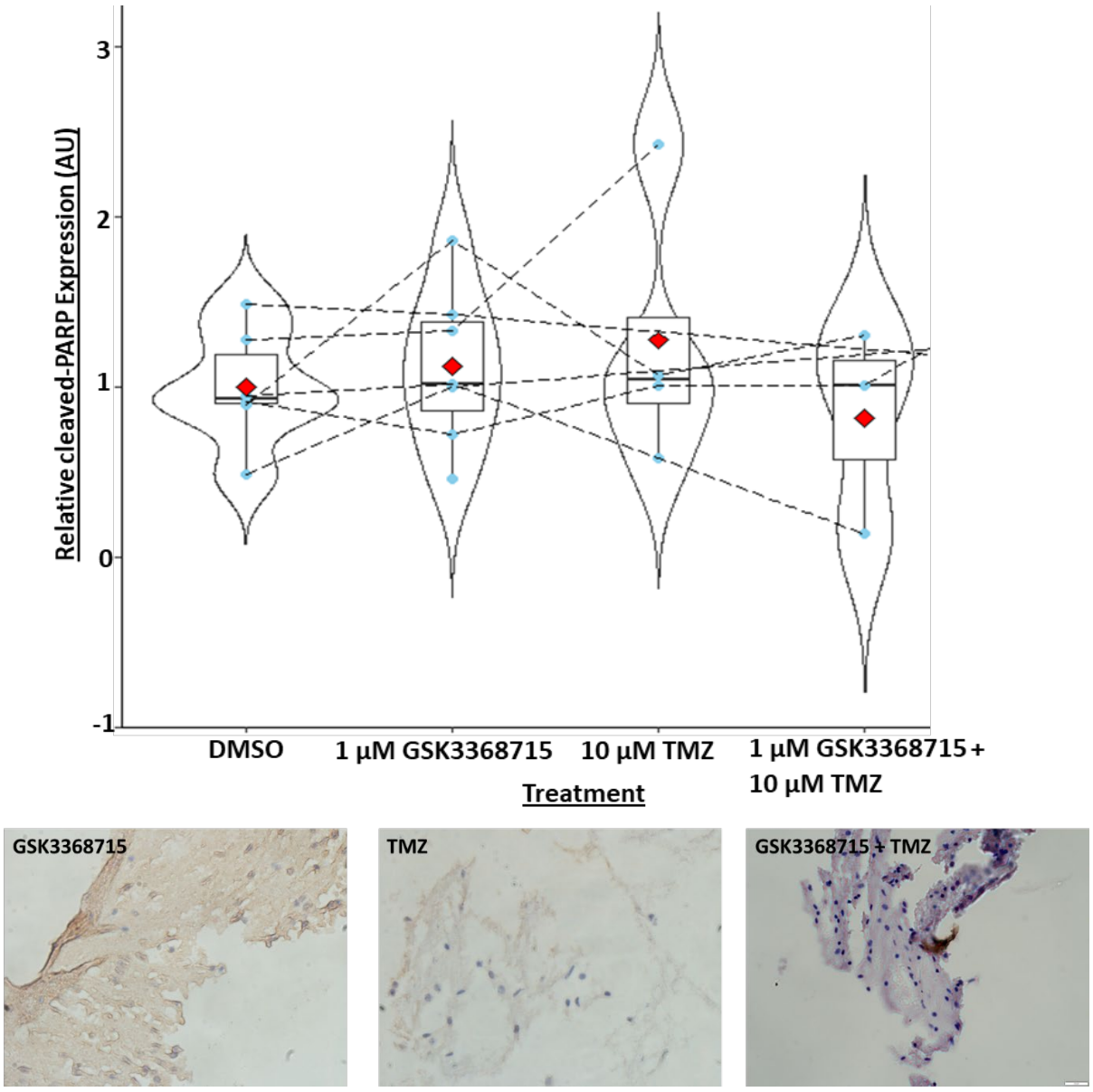

Figure 5.18.: Relative cleaved PARP expression (Arbitrary Units (AU)) in mouse brain tissue, between DMSO control, 1 µM GSK3368715, 10 µM TMZ and combinations treatments, 8-days post-perfusion, with representative images.

IHC of mouse brain tissue treated with DMSO control (1.00±0.35 AU) (n=6), 1 µM GSK3368715 (1.12±0.47 AU) (n=7), 10 µM TMZ (1.27±0.0.80 AU) (n=4) and combination (0.82±0.61 AU) (n=3) using apoptotic marker cleaved PARP*, indicated no significant changed in apoptosis whilst in the perfusion device (F=0.47, df=3, p=0.71). In a paired Welch's t test between the DMSO control and 1 µM GSK3368715, no significant change in* cleaved PARP *expression was found (t=-1.20, df=5, p=0.28). Dashed lines show* cleaved PARP *expression between treatments, within the same sample. Red diamonds indicate mean* cleaved PARP

expression, relative to the post-perfusion sample. Statistical analysis was performed using ANOVA in R 4.3.1. Images taken using an Olympus IX71 inverted fluorescence microscope, on the brightfield setting, phase 2 and using CellSens software 1.18 at x40 magnification.

Cleaved-PARP expression was found to increase 12% in healthy mouse brain tissues, in the presence of GSK3368715, over 8-days in the perfusion device. This increase was found not to be significant. Treatment with TMZ also appeared to increase cleaved PARP expression by 27% and the combination of GSK3368715 and TMZ decreased cleaved PARP expression by 0.18 AU. The biological repeats for both TMZ and the combination treatments were lower than that of DMSO and GSK3368715, due to the GBM data indicating no synergy between other treatments and GSK3368715 and so more data was collected for GSK3368715-treated healthy tissues (Figure 5.18)(Appendix 13). Upon further investigation into the variation between the samples, a GLM was used which indicated that the exploratory values of treatment, age and sex were not responsible for any variation. There was, however, significant variation found in the coefficients (Estimate =1.11±0.10, t=10.75, p=3.18e-10 ***) between the samples, which cannot be accounted for by the three variables measured.

In order to corroborate this data, apoptotic expression was also assessed using IHC with Annexin V (Figure 5.19).

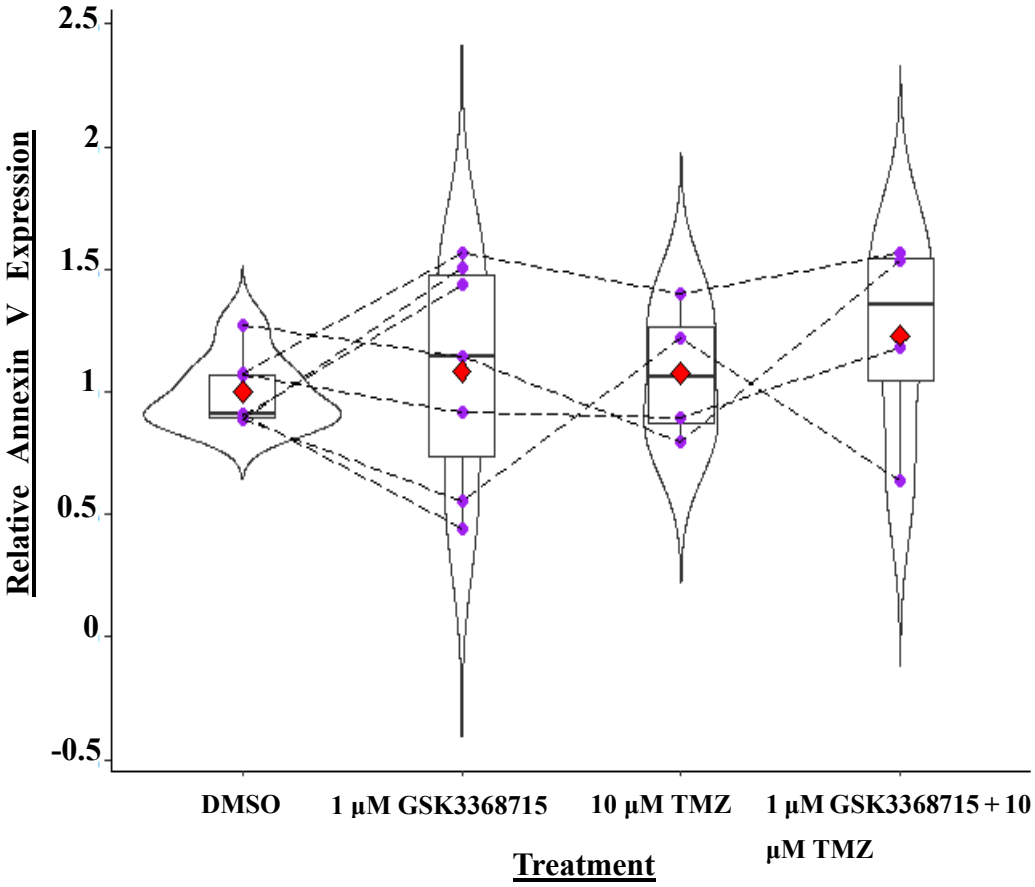
Relative Annexin V Expression
2.5
2
1.5
1
0.5
0
-0.5
DMSO
1 µM GSK3368715
10 µM TMZ
1 µM GSK3368715 + 10 µM TMZ
Treatment

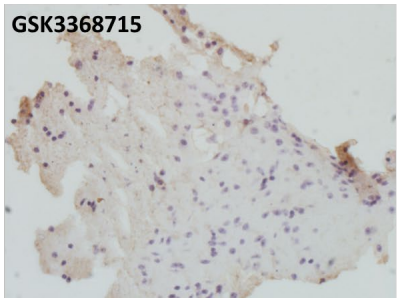
GSK3368715

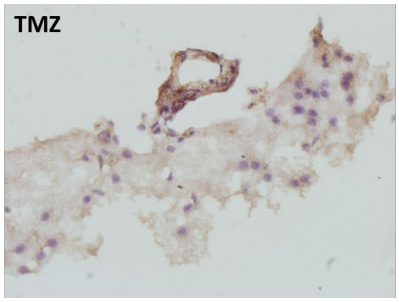
TMZ

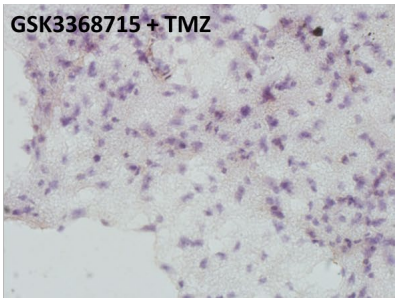
GSK3368715 + TMZ

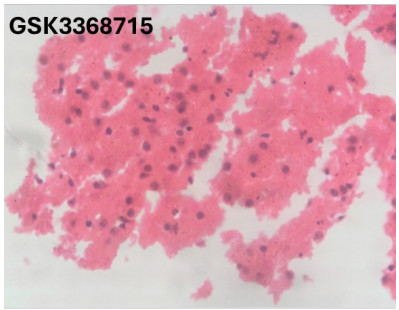
GSK3368715

Figure 5.19.: Relative Annexin V expression (Arbitrary Units (AU)) in mouse brain tissue, between DMSO control, 1 μM GSK3368715 and 10 μM TMZ, 8-days post-perfusion and H&E of GSK3368715-treated tissue, with representative images.

IHC of mouse brain tissue treated with DMSO control (1.00±0.15 AU) (n=7), 1 μM GSK3368715 (1.08±0.46 AU) (n=7), 10 μM TMZ (1.08±0.28 AU) (n=4) and 1 μM GSK3368715 + 10 μM TMZ (1.23±0.43 AU) (n=4), using apoptotic marker Annexin V, indicated no significant changed in apoptosis whilst in the perfusion device, through one-way ANOVA (F = 0.37, df = 3, p = 0.78). In a paired Welch's t test between the DMSO control and 1 μM GSK3368715, no significant change in Annexin V expression was found (t=-0.47, df=6, p=0.65). Dashed lines show cleaved PARP *expression between treatments, within the same sample. Red diamonds indicate mean Annexin V expression, relative to the post-perfusion sample. Statistical analysis was performed using ANOVA in R 4.3.1. H&E image of GSK3368715-treated tissue shows viable cells. Images taken using an Olympus IX71 inverted fluorescence microscope, on the brightfield setting, phase 2 and using CellSens software 1.18 at x40 magnification.*

Both GSK3368715 and TMZ showed a small, 8% increase in apoptosis, whilst the combination treatment increased annexin V expression by 23% (Figure 5.19)(Appendix 14). Despite this, no significant changes were found in Annexin V expression with any treatment, after 8-days in the perfusion device, in comparison with the DMSO control This Annexin V expression data corroborates the result found when analysing cleaved PARP expression. This indicates that GSK3368715, at this concentration, along with TMZ, do not cause significant increases in cellular apoptosis in healthy mouse brain tissues. Upon further investigation into the variation between the samples, a GLM was used which indicated that the exploratory values of treatment, age and sex were not responsible for any variation. There was, however, significant variation found in the coefficients (coeff. est. =1.08±0.071, t=15.21, p=8.23e-13 ***) between the samples, which cannot be accounted for by the three variables measured. H&E images also indicate that cells are viable after treatment with GSK3368715, with even and equal, haematoxylin-stained nuclei. This significance is also supported by the cleaved PARP expression data, indicating that there is another factor at play when it comes to the slight variation in apoptosis between the treatments.

5.4. Discussion

The results in this chapter have shown that cichlid and mouse brain tissues remain viable throughout the 4- and 8-days on-chip, respectively, through cellular stress assays, and histological examination. The data have indicated that mouse and fish brain tissues are good contenders as models of healthy brain tissue, which can be utilised in the microfluidics device.

Although there are other labs who have been known to use tissue from patients undergoing surgery for epilepsy, as well as from cadavers, it was deemed inappropriate in this instance. The main reason for using mouse brains was the ethical implications and time involved processing such an application. Another was supply of healthy brain tissue, which would be low, due to the frequency of these sorts of operations at Hull Royal Infirmary, as well as access to and cooperation with mortuary staff to receive brain tissue immediately after the death of a medical organ donor. Mouse brain tissue was suggested due to the availability of mice on-site, along with the expertise of Dr Christopher Sennett and others in euthanising and dissecting the mice. Despite these obvious drawbacks and limitations in comparing mouse with human tissue, mouse models are used extensively for GBM research, as well as in the wider research community and are well-established and valid for *in vivo* and *ex vivo* research. Mice have specifically been used in studies involving arginine methylation (Sauter *et al.*, 2022) and other mouse tissues, including intervertebral discs (Dai *et al.*, 2019), neuronal monolayers (Habibey *et al.*, 2022) and brain organoids with extracellular matrix (Cho et al., 2021a, Li et al., 2023b), have been used in the microfluidics system. This is the first study, to my knowledge, where an entire section of mouse brain has been placed into a perfusion system. It was decided that mouse and fish brains would require a change in medium from the GBM tissue. The GBM tissue is much more robust than healthy brain tissue and is mostly made up of astrocytes and viability assays showed that the tissue performed well in DMEM. Healthy brain tissue would be more suited to NBA medium with B-27 and L-glutamine supplements, which supports not only astrocytic cells, but neuronal cells and other glial cell types, found in the healthy brain. A lower percentage of FCS was also used, in line with guidance on primary cell line culturing (Sahu *et al.*, 2019) and antibiotic/antimycotic solution remained to eliminate infection risk, as the microfluidics system was not contained within a class II biological hood.

The obtainment of cichlid brains and gills was in conjunction with a proof-of-concept experiment, that I was also employed to assist with, in determining the efficacy of the *ex vivo* model in maintaining cichlid tissues, in order that it may be a useful model for the release of microplastics and other pollutants into aquatic ecosystems (Barboza *et al.*, 2020, Bhuyan, 2022). Using spare tissues, which were not being used for this purpose, it was decided to use the fish gills (Cadiz and Jonz, 2020) as a comparator to the fish brains to determine whether GSK3368715 may have any off-target effects on other organs. As described in previous chapters, phase I clinical trials of GSK3368715 were prematurely halted due to an increased number of TEEs in patients receiving the drug (El-Khoueiry *et al.*, 2023). This suggests that there is a link between the dosing of the drug and the respiratory and cardiovascular systems. The gills of the fish in this study are somewhat representative of the respiratory system and therefore a relevant organ to investigate potential off target effects . Other research groups at the university of Hull are investigating the use of multiple chips in series, which could also be useful for further investigations into the off-target effects of drugs, in determining how the drugs pass through the various organs in the body and what effect they may have.

Initially, I needed to determine whether the mouse and cichlid brains could be maintained in the perfusion device for several days, to ensure that any changes to the tissue during the experiment would be as a result of treatment and not from the perfusion device itself. The validation tests carried out were the same as those carried out with the GBM tissue, described in chapter 3, to maintain consistency and comparability. Analysis of LDH release from the mouse tissues, treated only with the DMSO control and cichlid gill and brain tissues with no additional treatment, indicated no significant changes in overall LDH release, across all timepoints. For mice, the lack of significance occurred once the tissues had 72 hours to settle to basal LDH levels. In cichlid gills, although the LDH levels decrease in the first 72 hours, the cellular stress levels increase again after 96 hours and do not settle back down completely. LDH, as described in previous chapters, is an enzyme involved in aerobic and anaerobic glycolysis and is a hypoxic marker of oxidative stress. Anaerobic glycolysis, or the Warburg Effect, is a common hallmark of cancer and hypoxia, utilising LDH to increase the rate of glycolysis *via* conversion of pyruvate to lactate, using NADH reduction, in the absence of oxygen (Valvona *et al.*, 2016, Jovanovic *et al.*, 2010). LDH can therefore be used to measure oxidative stress of the tissues in the fluidics system. It should not, however, be the primary investigative procedure into oxidative stress and overall tissue health. This is because levels of

LDH can vary due to mechanical tissue damage, bacterial infection and various drugs applied to the tissue, either through patient ingestion, or experimental design (Kaja *et al.*, 2017). To overcome these issues where possible, all LDH values were made relative to the DMSO control of individual patients, with several micro-biopsies averaged and all micro-biopsies had been prepared in the same way.

This data was observed in conjunction with H&E data, which was analysed by experienced neuropathologists for signs of tissue damage and stress. Cichlid tissues were assessed by an aquatic pathology specialist at the University of Edinburgh. Unfortunately, throughout the course of these parallel studies, it was determined that the cichlid gills were not suitable for maintenance in the perfusion device and therefore could not be taken forward for studies involving GSK3368715. This is due to the extent of autolysis that cichlid tissues undergo when removed from a homeostatic environment, with gills being more severely affected than other organs (Furnesvik *et al.*, 2022). Additional optimisation studies would have to be performed in order to maintain the gills in the perfusion device. In contrast to this, the cichlid brains were slightly better maintained in the device. Speculatively, this may be due to the fact that cichlid gills continually filter water to glean nutrients to pass onto other organs of the body and are therefore respond to changes in the external environment more quickly than an internal organ, such as the brain (Furnesvik *et al.*, 2022). Due to this being an optimisation study, many of the fish that were received were cichlids that were being removed from the aquarium anyway, due to suffering from conditions, such as ‘dropsy’, or ‘bloat’. There were examples of gills that were visibly infected, or damaged, potentially by the bloat. The fish gills were therefore not taken forward for further analysis. Mouse and fish brain H&E were assessed by neuropathologist Dr Ian Scott, who also assessed the GBM histology data. This resulted in the identification of mitotic figures and viable cells both pre- and post-perfusion, in both mouse and fish brains, suggesting that they do make good potential models for healthy brain tissue within the fluidics device.

Previous validations of the GBM-on-chip system, by Dr Sabrina Samuel and Srihari Deepak, included performing IHC for proliferative marker Ki67. It is expected that Ki67 levels would decrease from pre-perfused tissue to post-perfused tissue, however, tissues should still retain some proliferative capacity throughout the time under perfusion (Barry *et al.*, 2023). Ricky

Akinkuolie, in contribution to his MSc project, performed IHC on mouse brain tissue for Ki67. The non-significant decrease in proliferative capacity of the post-perfused tissue, reflected Ki67 expression results in GBM tissues (Barry *et al.*, 2023). Due to the lack of fish-specific cleaved PARP antibodies for IHC, an Annexin V antibody was chosen to investigate apoptotic markers in the cichlid brain tissues. Annexin V antibodies were also available for human and mouse tissues and the second marker was therefore also used to validate cleaved PARP expression data and therefore apoptosis in mouse brain tissue. Annexin V is commonly used as an apoptotic marker, as it is a Ca^{2+} binding protein, binding to phosphatidylserine residues, exposed on apoptotic cells (Pellicciari *et al.*, 1997). IHC for both cleaved PARP and Annexin V in mouse and fish brain tissues indicated no significant increases in apoptotic markers between pre- and post-perfused tissue, consistent with LDH, H&E and Ki67 expression results in healthy mouse brain tissue and with previous results in the GBM tissues. This completed the validation of the tissues in the perfusion device, affirming that these tissues remain viable for up to 8-days. The mouse brain tissues were taken forward for analysis, whilst the cichlid brain tissues would be recommended for analysis in further studies. More cichlid brain samples would be required to draw any significant conclusions from this data and to establish cichlid brains as an appropriate model for use in the perfusion device.

LDH analysis of GBM in the *ex vivo* device did not indicate any significant changes in cellular stress between treatments, but it was imperative that the same analysis was performed for healthy tissue. In the healthy mouse brain tissue, there was no overall LDH significance between 48-hours and 192-hours, however the resulting GLM between all time points and treatments indicated that the positive correlation between the DMSO control and TMZ suggest an increase in cellular stress with TMZ treatment. This is expected as TMZ is an alkylating chemotherapy agent, which causes DNA damage in order to cause cellular stress, inhibition of the cell cycle and cell death (Stupp *et al.*, 2009). The positive correlation between the TMZ treatment and combination indicates than the addition of GSK3368715 to the healthy tissue results in a reduction in cell stress. This could be to do with PRMT inhibition causing an impact on the effect of the alkylating agent in healthy cells and reducing cellular stress. It is, however, interesting to note that there is a positive correlation between TMZ and GSK3368715, which suggests that TMZ produces higher cellular stress than GSK3368715, which is also supported by the previous statement. Treatment with the time element (Treatment2) only showed significant negative correlation between the DMSO control at 24 hour and 192-hour timepoints.

The high LDH release to begin with is proportionate to higher cellular stress, as the tissue is removed from its natural environment and settles into the perfusion device. This indicates a reduction in LDH release over time, which is expected. Interestingly, older mice indicated lower emmeans for LDH release than younger mice. Previous studies have indicated that there is a higher level of lactate and LDH within the brain tissue of older and premature ageing mice than their less aged counterparts (Ross *et al.*, 2010, Datta and Chakrabarti, 2018). It therefore stands to reason that it might be expected that older tissue would harbour more biological stress than younger tissue (Polsky *et al.*, 2022), but the opposite is reflected in these results. A potential explanation for this could be that the inherent biological stress in the older mouse tissues means that the stress experienced within the perfusion device is much smaller in comparison. There was also no significant difference in cellular stress between sexes, although this is a small sample group and there were not equal numbers of male *vs* female mice. The significance of the intercept in the coefficient analysis of the LDH data indicates that unknown variables are also at work and the importance of this cannot be understated. This reflects not only how heterogenous GBM is, but how complex healthy brains are and qualifies the need for further understanding of an individual's genetics and epigenetics, their influence over their cancer and personalised medicine.

IHC for apoptotic markers was performed on mouse brain tissues which had undergone treatment with GSK3368715, TMZ and a combination of the drugs, over the course of up to 8-days in the novel perfusion device. TMZ is an alkylating agent and as such, it does not show discrete selectivity between healthy cells and cancerous cells, other than that it targets more rapidly replicating DNA, such as in GBM tumour cells (Ortiz *et al.*, 2021). For this reason, it was expected that there would be some cell death in the tissues that had only been treated with TMZ. Additionally, it was expected that there may be a decrease in proliferation markers for the same reason. Despite the fact that TMZ did not indicate any significant changes in expression of apoptosis markers in the GBM tissue, for comparison, healthy mouse brain tissues were still treated with TMZ, in combination with GSK3368715. This was also to ensure that there were no unwanted synergistic effects of GSK3368715 with TMZ in healthy tissues, which were not observed in the GBM tissue alone. Cleaved-PARP was initially chosen to determine any apoptotic effects of GSK3368715 in the GBM tissues and was also therefore used to interrogate the use of GSK3368715 in the mouse tissue. In previous chapters, GSK3368715 was used on GBM tissue in the *ex vivo* model was described to cause a 2-fold

increase in apoptosis. This was not recapitulated in combination with the current gold standard TMZ, although there was an upward trend. In healthy brain tissue, TMZ is not expected to have a significant impact due to the lack of rapid proliferation of healthy brain cells (Gotz and Huttner, 2005). Across both the cleaved PARP and Annexin V markers, there was no significant change in apoptosis in the mouse brain tissues, with any treatment. This is supported by the GLM findings, which showed that any significance in apoptotic marker release was not due to any of the measurable data available, but again of unknown variables, such as the individuals genetics, epigenetics and potential slight variations in environment.

5.5. Conclusion

The lack of apoptotic response to the PRMT inhibitors in the healthy tissues is a good indicator that the drugs may not cause significant effects in healthy human brain tissue. Translationally, this suggests that the drug has some selectivity for tumour cells. Further studies, however, would be required to determine off-target effects. Previous clinical trials into the drug have described TEEs which prevented the completion of the clinical trials over ethical safety concerns to patients. The TEEs, however, are indicative of systematic effects that GSK3368715 is having on the overall function of the body. Further investigations into cichlid gills may be a suitable model for these types of studies, as well as mouse, or indeed, human lung tissue.

CHAPTER 6: DISCUSSION

6.1. Overview

GBM is the most common primary malignancy in the CNS and the most devastating, with a median survival of 18 months post-diagnosis. Several experimental therapy methods are currently undergoing investigation in primary research and in clinical trials, including PRMT inhibitors. PRMTs have been implicated in numerous diseases, including neurological disorders and GBM. Arginine methylation is an extremely ubiquitous PTM and therefore it is imperative to understand the impact of inhibiting these PRMT enzymes on both the tumour and the surrounding healthy tissue. GSK3368715 showed aDMA-sDMA crosstalk in U87-MG cells, at the same concentration as MS023, which has previously been found to cause this crosstalk in GBM tissue lysates. TMZ has been shown to increase cleaved PARP expression in GBM cells (Ciechomska, 2018) and cleaved PARP has also been known to be increased in neuroblastoma cells after inhibition of PRMT1 (Hua *et al.*, 2020), highlighting cleaved PARP as an ideal marker of interest. My study has shown that patient GBM tissue was maintained in a viable state for up to twelve days in the microfluidics device and that PRMT inhibition with GSK3368715, a type I PRMT inhibitor used in clinical trials, caused cell death in the GBM tissue, but not in the healthy mouse controls, maintained on the microfluidics system. My study also identified that PRMT inhibition could cause changes in alternative splicing, which may present a mechanism for how GSK3368715 works to cause cell death in GBM. The function and influence of the TME in GBM has also become the focus of several studies and due to the involvement of PRMTs in immune cells, splicing and signalling pathways, exploring the implications of PRMT inhibition on the TME is also an important factor to consider.

6.2. Tissue viability in the microfluidics system

U87-MG cells are widely renowned to be poor representations of GBM, due to the lack of heterogeneity and divergence from the original patient tumour from which they came (Allen *et al.*, 2016). To improve the initial viability assays, the utilisation of multiple cell lines, such as A172 (Kiseleva *et al.*, 2016), or M059K (Anderson and Allalunis-Turner, 2000) would provide a deeper understanding of how drugs affect specific cell types. Using patient-derived cell lines would also potentially give a more representative view of the breadth of genetic and epigenetic

features associated with GBM (Kim *et al.*, 2023). The use of more complex 3D models, such as tumouroids, may also provide more accurate visualisation of how the heterogeneous cells interact and metabolise the drugs being tested (Wang et al., 2023b). Increasing tumour volume through the propagation of these tumouroids from patient-derived cells would improve the scalability of the microfluidics system, although this may result in the loss of intra-tumour heterogeneity which is present when working directly with patient micro-biopsies. The vast majority of work in this thesis, however, is performed on *ex vivo* patient tissues, which represent an ideal model for studying inter- and intra-patient heterogeneity, as well as the TME. Mice are well-established models of human disease and have been used specifically for arginine methylation (Sauter *et al.*, 2022) and in microfluidics platforms (Habibey *et al.*, 2022). Improvements in the comparison of GBM and healthy tissue would be made through the use of human tissue, such as that resected from patients with severe epilepsy; however, this may come with its own risks of having misleading biomarkers associated with epilepsy.

The microfluidics system is a model which was designed to encompass a variety of *in vivo* aspects, which other models lack. This includes the use of patient tissue for a personalised medicine approach; interstitial flow, attempting to replicate the delivery of nutrients and drugs and removal of waste products within the body and the maintenance of tissue metabolic activity (Ziółkowska, 2011). The use of patient, or mouse and fish tissue, incorporates the multicellular and heterogeneic characteristic of the intra- and inter-tissue microenvironment, which varies between subjects and has a large bearing on their ability to combat GBMs growing in the environment and respond to therapeutics. This can include dual chamber chips, which create a semi-permeable membrane to allow cellular invasion across the barrier, representing the EMT, as well as fluidics chip chains, which incorporate several different tissues in a system, in order to assess metastasis, or effects of drugs on various organs of the body (Sylvester, 2013, Dawson *et al.*, 2016, Astolfi *et al.*, 2016).

This model, as all models do, does have limitations. GBM tissues, as well as healthy mouse brain tissues can be maintained for up to 8 days and fish brain tissues for up to 4 days. Optimisation of the fluidics system would be required to allow viable tissue extension up to 12 days to allow for more clinically relevant prolonged drug exposure. Cellular stress, through low LDH release and the presence of mitotic figures in pre- and post-perfused tissue do indicate that, if the tissues are viable when they are entered into the chip chamber, they remain viable

post-perfusion. The data shown in this study, however, does reiterate the fact that this is not a chip which will revitalise tissues. The slight, although non-significant increase in expression of apoptotic markers, as well as the reduced numbers of and changed cytokine profiles of GBM and proliferative capacity of healthy tissues, may indicate the tissue is slowly reducing metabolic activity. This could be tested using other metabolic assays, such as ELISA, or flow cytometry for mitochondrial function markers such as cytochrome c oxidase subunit 1 (COX1) (Sighel *et al.*, 2021), or voltage-dependent anion channel 1 (VDAC1) (Arif *et al.*, 2017). The maintenance of GBM cytokine profiles until 96 hours and the shift beyond this point is supportive of previous data from this lab and others, which found a decrease in proliferative capacity, identified through IHC for Ki67, between 72-, (Olubajo et al., 2020) and 96-hours (Riley et al., 2019) of perfusion. *In vivo* interstitial flow rates are generally accepted to be around $1x10^{-4}$-10 mm $s^{-}1$ (Wagner and Wiig, 2015, Wiig and Swartz, 2012). This change in tissue metabolism in the device may be mitigated by using faster flow rates (>3µl/min) to aid in removing cytokines and other waste products quicker, which may help to prevent cytokine-induced signalling from triggering a metabolism slow down. Alternatively, patient tissues could be undergoing shear stress due to the force of the flow rate, although it might be expected that there would be an indication of increased LDH output if this were the case. Another limitation of the model is that it does not replicate the BBB and therefore, any drugs applied to the fluidics system for screening would need to be confirmed as already being able to cross the BBB. Alternatively, further experimentation must be performed in order to package the drug for effective delivery and would therefore be required to be screened again, to ensure that the packaging does not decrease the efficacy of the drug.

Microfluidics models have also been used to try and tackle the issue of early and minimally invasive diagnosis of GBM. Confirmation of GBM diagnosis is required to be through surgical intervention and due to the location and the diffuse nature of GBM, biopsy and resection is extremely difficult. Liquid biopsies are taken from blood, cerebral spinal fluid or other bodily fluids and contain circulating tumour cells (CTCs) (Zhang et al., 2024b) and membrane-bound extracellular vesicles (EVs) (Chandran, 2024), which reflect the genetics of the GBM cell from whence they came (Dai *et al.* 2024). CTCs and EVs released from GBM in the microfluidics chip could provide useful information on the molecular subtype of GBM, as well as any progression (Lessi *et al.* 2023). Syndecan-1 is an EV marker which discriminates high from low grade glioma, which changes with tumour resection (Chandran *et al.* 2019). This could be

used for monitoring of patients in a more accurate way than MRI and CT scans, which do not distinguish well between true progression and pseudo-progression and in a less invasive way than repeated cranial surgeries. Longitudinal analysis may also identify the development of chemotherapeutic resistance *in vivo.* As mentioned in this study and as trialled in other studies (Barthel *et al.*, 2019, Tanner *et al.*, 2024), longitudinal analysis in GBM so far has been performed through receiving paired primary and recurrent patients samples. This has its place as it is crucial to identify the biomarkers of resistance and progression in the tissue associating it with relevant biomarkers in CTCs and EVs. PRMT inhibition-specific biomarkers, such as hnRNPA1 (Noto *et al.*, 2020) have also been identified in peripheral blood mononuclear cells and cancer cell lines. These biomarkers could be identified using mass spectrometry and GSEA and quantified using qPCR, ELISA, or protein-dependent functional assays. Through the use of the microfluidics system, tissue biomarkers, as well as the contents of EVs and CTCs in effluents, could be investigated and applied in clinic and utilised to understand the efficacy of new drugs (Meggiolaro *et al.*, 2022, Logun *et al.*, 2018).

The medium used in the microfluidics device remained the same as that which was utilised to culture U87-MG cells, however, the use of serum-free medium may help to promote more GSC population proliferation, which would help to further understand the dynamic plasticity of GBM cell types and how they may change with treatment (Joseph *et al.*, 2015). The medium used for the mouse and fish brains was changed in comparison to the GBM tissues. Mouse and fish brains were perfused with NBA medium, supplemented with B27 and L-glutamine, to ensure optimal maintenance of healthy brain cells. The medium was also supplemented with serum (Sahu *et al.*, 2019) and antibiotic/antimycotics, to maintain similarities with the GBM tissue. The use of this medium, along with an increase in flow rate, may help to optimise the system and allow extension of perfusion time up to 12 days, or potentially beyond.

6.3. GSK3368715 is selective for GBM tissue

This research shows that PRMT inhibition with GSK3368715 in GBM tissue in the novel perfusion device can cause apoptosis after 8 days, but this is not mirrored in the healthy mouse tissue control. Whilst this could be down to metabolic differences between species, mice are well established models of human tissue and disease and without the access to healthy human

tissue, this was deemed to be the most viable option. Cichlid brains, but not gills, were also identified as a viable tissue for use in the microfluidics device, with potential for future application. In the most recent outcomes of the clinical trial (NCT03666988) involving GSK3368715 in humans (El-Khoueiry *et al.*, 2023), trials were prematurely terminated due to the number of TEEs, where prevalence was 29% in a small population (12 participants). Despite this being equivocal to the expected occurrence of TEEs in GBM without GSK3368715 treatment (Robins *et al.*, 2006) investigating the effects of GSK3368715 on both healthy tissue and distal organ tissue is vital.

GSK3368715 was tested alone and in combination with multiple PRMT inhibitors, including type I Furamidine and MS023, to identify any cumulative effects of using multiple inhibitors. Type II inhibitor GSK591 was also introduced, with some studies indicating that simultaneous inhibition of type I and type II PRMTs cause a synergistic effect (Fedoriw *et al.* 2019). GSK3368715 alone caused an increase in cleaved PARP in GBM on chip, supported by the reduced capacity for protein synthesis, found through DEGs and hundreds of alternative splicing events. Overall, in both cell viability assays and in GBM histology samples, combination of GSK3368715 and other PRMT inhibitors did not indicate any significant changes in viability, cellular stress, or apoptosis. In combination with other type I PRMT inhibitors, this could be down to the crosstalk with type II inhibitors, which may compensate for the lack of aDMA deposits, by increasing the number of sDMA deposits. It could also be due to drug specificity, with GSK3368715 possessing a much lower IC_{50} (3.1nM) than Furamidine (9.4μM), there may be some level of redundancy in using both type I inhibitors (Yan *et al.*, 2014, Fedoriw *et al.*, 2019). GSK591, however, did not indicate any synergy with GSK3368715 either, although other studies have indicated that GSK591 decreases sDMA in tissues (Samuel *et al.*, 2018) and inhibition of both PRMT types should have a synergistic effect (Nguyen *et al.*, 2023). This does, however, appear to be more effective through an intrinsic mechanism of secondary inhibition, such as MTA accumulation through MTAP loss, which is a common feature of GBM and leads to PRMT5 inhibition (Fedoriw *et al.* 2019). It would be interesting to include alternative type II inhibitors to further explore this synergy.

To further understand whether expression of these molecules is due to serendipitous hypoxia caused by the perfusion device, histology of ELISA for hypoxia and metabolism markers, such as HIF1α, or glucose transporter 1 (GLUT1) across various tissue locations could be performed

(Sadlecki *et al.* 2014). Mitochondrial function tests with fluorescent probes, such as Peroxy-orange, may be used to detect hydrogen peroxide and cellular stress (Javega *et al.* 2023). Changes to protein synthesis through ER stress could be detected using markers of the UPR, such as inositol-requiring protein 1 (IRE1)α phosphorylation, or ER-stress induced activating transcription factor 4 (ATF4) expression, through western blotting, qPCR, or histology (Sicari *et al.* 2020).

Both GBM and mouse brains, however, did indicate a correlation between age and treatment when it came to cytokine expression and LDH release, respectively. Healthy mouse brains indicated that younger subjects appeared to be more susceptible to cellular stress and GBM indicated that younger patient cytokine profiles displayed a variation shift with GSK3368715 + TMZ treatment, in an opposing direction to the 288-hour time point of the time covariate. If tissues are dying as time in the perfusion device increases, this could indicate that the combined treatment is having more of an effect on younger patients, causing a change in cytokine profile. This could be linked to a reduction in aggressive cytokines and an increase in cytokines associated with a shift to a more mesenchymal phenotype and therefore meaning they are more susceptible to treatment. This would support the idea that with older patients tissues, there are fewer viable cells to excrete cytokines and drive the response induced by the treatment. The lack of effect upon inhibition of both type I and type II PRMTs may be indicative of some issues with the microfluidics model, highlighted by the lack of significant apoptotic output with TMZ treatment. It would be anticipated that inhibition of both PRMT types would potentially cause some off-target effects, due to the somewhat redundancy arginine methylation, whereby Type II PRMTs may methylate aDMA targets in the absence of type I PRMTs and with the inhibition of both, this would significantly reduce global methylation. Testing of these drugs in healthy tissues, as well as in other organs, would be imperative to understanding the widespread effects of dual PRMT inhibition. Alternatively, enhancing endogenous methods of PRMT inhibition, such as the loss of MTAP in GBM subsequently hindering sDMA, through treatment with PRMT1 inhibitors may bypass these off-target effects (Fedoriw *et al.*, 2019).

TMZ was also included as both an individual treatment and in combination with GSK3368715. This was because TMZ is the current gold standard of care in GBM (Stupp *et al.*, 2009) and therefore, any new treatments would be required to work better than, or in conjunction with TMZ. GSK3368715 results could therefore be compared to TMZ alone, or any cumulative

effect of the two drugs could be identified, potentially through the resensitisation of GBM cells to DNA damage by TMZ. Despite the fact that no significant cumulative effect could be seen with combined GSK336715 and TMZ treatment in the production of apoptotic markers, there was a general upward trend in the expression of cleaved PARP. Differential gene expression of micro-biopsies treated with GSK3368715 also indicated significant changes in alternative splicing and genes associated with splicing, decrease in inflammation and disruption of cell signalling through changes to cellular structural integrity. Again, this is supported by the analysis of abundantly expressed cytokines in proteome profiler arrays and ELISA. The decrease in genes associated with invasion (MMP9) and angiogenesis (VEGF) suggests that the combined treatment, over time in the chip, may be working to reduce the aggressive properties of the GBM tumours. The increase in C3L1 as a result of treatment could indicate that the cells are shifting to a more mesenchymal phenotype (Neftel *et al.*, 2019, Tanner *et al.*, 2024), thereby resensitising the cells to TMZ treatment and leading to an increase in irreparable DNA damage and an increase in apoptosis. It is interesting that the spread of the data in cleaved PARP expression is so large and the fact that there is an almost 50% split in the number of patient samples tested, which are positive for MGMT promoter methylation, may suggest that the reason for this is that there is a large proportion of patients which have this protective characteristic and respond well to TMZ treatment (Kitange *et al.*, 2009).

The lack of response to TMZ could be due to the slowing down of proliferative capacity in GBM on chip, found in previous work done in this group, due to the reliance of TMZ on the MMR. TMZ requires several rounds of replication before replication fork collapse, cell cycle arrest and subsequent apoptosis (Teraiya *et al.*, 2023). The slowing down of proliferative capacity, coupled with the change in cytokine profiles and lack of significant increase in apoptosis caused by TMZ, both with and without GSK3368715, may explain a somewhat reduced impact of PRMT inhibition on GBM tissues in the perfusion device. Although GBM indicates a slowing of proliferative capacity in the microfluidics system, the same may not be true for the healthy mouse tissue. This could be due to the change in medium used for the mouse tissues, which may be more appropriate for maintaining the tissues and therefore more supportive of proliferative capacity (Sahu *et al.* 2019), indicated by Ki67 expression. It may also be due to the genetic makeup of the mice and whether they have MGMT promoter methylation. It would be interesting to perform histology staining to ascertain this information and to understand why this trend is seen.

Both GBM and healthy tissue groups, however, displayed significant intercept coefficients in GLM, indicating further explanations for variation were at play, which were not included in this study. A challenge faced through statistical analysis of these data was the gaps in molecular profiles, with genetic and epigenetic markers not being consistently reported on after clinical histology (). In these cases, it is difficult to amass a clear picture of how molecular profiles may be affecting the function of these drugs and with PRMT inhibition having such wide-ranging cellular effects, it would be interesting to see whether there are any disparities between patient samples who exhibit particular biomarkers. For example, the effect of PRMTs on EGFR signalling is well documented and EGFR methylation has been investigated (Gomori *et al.*, 2012, Hsu *et al.*, 2011), yet without the clinical information, it is difficult to collate a picture of how patient micro-biopsies, with and without mutations in EGFR, respond to GSK3368715 *in vitro*.

6.4. FUS and arginine methylation as a mechanism for chemotherapeutic resistance

The 70 kDa band which appears in western blotting of GBM lysates was hypothesised to be FUS. Previous work by Dr. Sabrina Samuel (Samuel *et al.* 2018) indicated that FUS was the only protein to be monomethylated when treated with type I PRMT inhibitor, MS023 and this was in line with the induction of crosstalk in GBM tissue (Barry *et al.* 2023). Additionally, analysis of datasets produced by Fedoriw *et al.* (2019) described FUS as being alternatively methylated upon GSK3368715 treatment, leading to splicing defects. It was hypothesised that PRMT inhibition caused alternative splicing as a result of alterations to methylation of factors associated with splicing, such as FUS. Conversely, changes to alternative splicing through PRMT inhibition could be driving the actions of FUS, and/or other proteins, which then impacts downstream factors, such as transcription, exon skipping and immune changes.

To further confirm this theory, western blotting using the LICOR system was attempted, which would make the visualisation and overlapping of protein bands easier to see, due to the use of colours. Unfortunately, this did not produce any usable data and would require further optimisation. Immunoprecipitation of FUS from U87-MG cell lines indicated that FUS could be immunoprecipitated from tissue that had been treated with GSK3368715, but the blot was

not clean and was unable to be excised from the gel. When performed in tissues, an IP of FUS was not achieved to sufficient quality. The aim of this would be to excise the protein from the gel and for it to undergo mass spectrometry, to confirm whether methylation of the protein was increased in these samples. Further optimisation of this would also be required to understand whether FUS methylation plays a role in aDMA-sDMA crosstalk with type I PRMT inhibition.

Thirdly, nuclear-cytoplasmic extraction was performed on U87-MG cells, due to the fact that FUS is known to shuttle between the cytoplasm and the nucleus, dependent upon methylation status. The results indicated that, in the cytoplasm, FUS appeared as a 70 kDa protein and in the nucleus, the weight of FUS was reduced. This is consistent with the literature that depletion of PRMT1 leads to a prevention of proper FUS shuttling to the cytoplasm, due to lack of methylation (Tradewell *et al.*, 2012). In the nuclear portion, there appeared to be a decrease in cytoplasmic shuttling of FUS with treatment of U87-MG cells with GSK3368715, supporting the aforementioned theory. Should the shuttling of FUS cease to occur due to PRMT inhibition in GBM, this could lead to the reduction of proper phase separation (Hofweber *et al.*, 2018, Qamar *et al.*, 2018). As a direct result, this could lead to inappropriate transcription occurring as transcription factors find it more difficult to bind to DNA in the nucleus and therefore leading to apoptosis of the cells. The fact that a significant decrease in apoptosis is not seen in the healthy brain tissue controls suggests that this could be more selective of rapidly proliferating cells, such as those in cancerous tumours. The hundreds of alternative splicing events seen through RNA-sequencing of the GBM and that these alternatively spliced genes have gene ontology terms associated with cell death pathways gives credence to this hypothesis. It would be beneficial to increase the number of patient samples analysed for DEGs and alternative splicing events. This would enable us to gain a better understanding of the functional pathways impacted by GSK3368715 across multiple covariates, such as age and gender and to further explore the heterogeneity between samples. This would be particularly interesting between paired primary and recurrent samples to see if and how these functional pathways not only change with longitudinal analysis but change between geographical regions of the tumour to further characterise the theory of clonal expansion leading to recurrence in GBM (Wang *et al.*, 2016, Ceresa *et al.*, 2023). This was, however, preliminary data within the context of my other work and a full conclusion could not be drawn from this.

Alternative methodologies of exploring the role of FUS and the methylation changes to other proteins in GBM tissue, with GSK3368715, are required. These might include the use of methyl-FUS, or methyl-site targeted antibodies (Dormann *et al.*, 2012)(Khumar *et al.*, 2020). Modified FUS containing either sDMA, aDMA or mMA modifications could be incubated with GBM tissues and isolated using a streptavidin-biotin system, through which any co-bound proteins would also be isolated. This would determine whether changes to the methylation type cause functional changes to the protein, thereby altering the associated proteins. Research by Maron *et al. (2022)* into a lung adenocarcinoma cell line found that Rme2a off FUS was decreased upon PRMT type I inhibition, with Rme2s and Rme1 increased, but with type II inhibition, no changes in methylation status were observed. This could provide a reason as to why no synergistic effect were found with both inhibitors, in this data, should FUS be a potential driver of PRMT type I inhibitor activity. Site directed mutagenesis of target proteins would have a similar effect, whereby methylation status would be augmented and downstream functional assays, such as proliferation and metabolomics could be performed (Liu *et al.*, 2020, Jeong *et al.*, 2020). The measurement of enzymatically active and inactive PRMT kinetics would indicate whether the enzymatic activity of certain PRMTs are required for the aDMA-sDMA crosstalk, or downstream functional consequences (Hevel and Price, 2020, Radzisheuskaya *et al.*, 2019). Some PRMTs, such as PRMT2 have weak enzymatic activity, but can still execute particular functions (Yoshimoto *et al.*, 2006). Mass spectrometry of a plethora of tissues treated with GSK3368715, may help to elucidate any genetic and epigenetic influences of PRMT inhibition on the methylation status of proteins of interest, including FUS. Additionally, more in-depth bioinformatics analysis of GBM methylome datasets would provide a solid foundation for the exploration of other proteins of interest, when identifying the mechanisms and downstream consequences of aDMA-sDMA crosstalk in the tumours of patients living with GBM.

CHAPTER 7: CONCLUSION

Type I PRMT inhibition by GSK3368715 causes apoptosis and drives alternative splicing in GBM tissue in the novel perfusion device. Alternative splicing potentially mediated through changes in FUS methylation, may lead to a more differentiated phenotype and resensitisation of cells to TMZ treatment. GSK3368715 may also reduce expression of factors associated with GBM invasion and TME inflammation. The crosstalk between aDMA and sDMA could not fully be explored in this thesis and further work, as suggested, would be required to elucidate a mechanism for this and any links it and FUS may have to chemotherapeutic resistance. Taken together, the research performed throughout the preparation of this thesis has provided insight into the tumour-specific effects of GSK3368715 and its potential for targeting GBM.

CHAPTER 8: BIBLIOGRAPHY

ABBOTT, N. J., PATABENDIGE, A. A., DOLMAN, D. E., YUSOF, S. R. & BEGLEY, D. J. 2010. Structure and function of the blood-brain barrier. *Neurobiol Dis,* 37**,** 13-25.

AGLIARDI, G., LIUZZI, A. R., HOTBLACK, A., DE FEO, D., NUNEZ, N., STOWE, C. L., FRIEBEL, E., NANNINI, F., RINDLISBACHER, L., ROBERTS, T. A., RAMASAWMY, R., WILLIAMS, I. P., SIOW, B. M., LYTHGOE, M. F., KALBER, T. L., QUEZADA, S. A., PULE, M. A., TUGUES, S., STRAATHOF, K. & BECHER, B. 2021. Intratumoral IL12 delivery empowers CAR-T cell immunotherapy in a pre-clinical model of glioblastoma. *Nat Commun,* 12**,** 444.

AGUILERA, O., FRAGA, M. F., BALLESTAR, E., PAZ, M. F., HERRANZ, M., ESPADA, J., GARCIA, J. M., MUNOZ, A., ESTELLER, M. & GONZALEZ-SANCHO, J. M. 2006. Epigenetic inactivation of the Wnt antagonist DICKKOPF-1 (DKK-1) gene in human colorectal cancer. *Oncogene,* 25**,** 4116-21.

AHIR, B. K., ENGELHARD, H. H. & LAKKA, S. S. 2020. Tumor Development and Angiogenesis in Adult Brain Tumor: Glioblastoma. *Mol Neurobiol,* 57**,** 2461-2478.

AHMADIPOUR, Y., JABBARLI, R., GEMBRUCH, O., PIERSCIANEK, D., DARKWAH OPPONG, M., DAMMANN, P., WREDE, K., OZKAN, N., MULLER, O., SURE, U. & EL HINDY, N. 2019. Impact of Multifocality and Molecular Markers on Survival of Glioblastoma. *World Neurosurg,* 122**,** e461-e466.

AKHIL, A. V., RAJ, D. D. D., RAJ, M. K., BHAT, S. R., AKSHAY, V., BHOWMIK, S., RAMANATHAN, S. & AHMED, S. 2016. Vaporized solvent bonding of polymethyl methacrylate. *Journal of Adhesion Science and Technology,* 30**,** 826-841.

ALBAN, T. J., ALVARADO, A. G., SORENSEN, M. D., BAYIK, D., VOLOVETZ, J., SERBINOWSKI, E., MULKEARNS-HUBERT, E. E., SINYUK, M., HALE, J. S., ONZI, G. R., MCGRAW, M., HUANG, P., GRABOWSKI, M. M., WATHEN, C. A., AHLUWALIA, M. S., RADIVOYEVITCH, T., KORNBLUM, H. I., KRISTENSEN, B. W., VOGELBAUM, M. A. & LATHIA, J. D. 2018. Global immune fingerprinting in glioblastoma patient peripheral blood reveals immune-suppression signatures associated with prognosis. *JCI Insight,* 3.

ALBAN, T. J., GRABOWSKI, M. M., OTVOS, B., BAYIK, D., WANG, W., ZALAVADIA, A., MAKAROV, V., TROIKE, K., MCGRAW, M., RABLJENOVIC, A., LAUKO, A., NEUMANN, C., ROVERSI, G., WAITE, K. A., CIOFFI, G., PATIL, N., TRAN, T. T., MCCORTNEY, K., STEFFENS, A., DIAZ, C. M., BROWN, J. M., EGAN, K. M., HORBINSKI, C. M., BARNHOLTZ-SLOAN, J. S., RAJAPPA, P., VOGELBAUM, M. A., BUCALA, R., CHAN, T. A., AHLUWALIA, M. S. & LATHIA, J. D. 2023. The MIF promoter SNP rs755622 is associated with immune activation in glioblastoma. *JCI Insight,* 8.

ALEXANDER, B. M. & CLOUGHESY, T. F. 2017. Adult Glioblastoma. *J Clin Oncol,* 35**,** 2402-2409.

AL-KHARBOOSH, R., REFAEY, K., LARA-VELAZQUEZ, M., GREWAL, S. S., IMITOLA, J. & QUINONES-HINOJOSA, A. 2020. Inflammatory Mediators in Glioma Microenvironment Play a Dual Role in Gliomagenesis and Mesenchymal Stem Cell Homing: Implication for Cellular Therapy. *Mayo Clin Proc Innov Qual Outcomes,* 4**,** 443-459.

ALLEN, M., BJERKE, M., EDLUND, H., NELANDER, S. & WESTERMARK, B. 2016. Origin of the U87MG glioma cell line: Good news and bad news. *Sci Transl Med,* 8**,** 354re3.

ALTINOZ, M. A., OZPINAR, A. & ELMACI, I. 2019. Reproductive epidemiology of glial tumors may reveal novel treatments: high-dose progestins or progesterone antagonists as endocrino-immune modifiers against glioma. *Neurosurg Rev,* 42**,** 351-369.

AMOOZGAR, Z. R., J.; WANG, N.; ANDERSSON, P.; FERRARO, G.B.; KRISHNAN, S.; LEI, P.; SUBUDHI, S.; KAWAGUCHI, K.; TAY, R.E.; GOMES-SANTOS, I.L.; HUANG, P.; KIM, H.; FUKUMURA, D. AND JAIN, R.K. 2022. Combined blockade of VEGF, Angiopoietin-2, and PD1 reprograms glioblastoma endothelial cells into quasi-antigen-presenting cells. *The Journal for Immunotherapy of Cancer.*

AN, J., FREEMAN, E., STEWART, I. J. & DORE, M. 2024. Association of Traumatic Brain Injury and Glioblastoma Multiforme: A Case Series. *Mil Med,* 189**,** e391-e395.

AN, Z., KNOBBE-THOMSEN, C. B., WAN, X., FAN, Q. W., REIFENBERGER, G. & WEISS, W. A. 2018. EGFR Cooperates with EGFRvIII to Recruit Macrophages in Glioblastoma. *Cancer Res,* 78**,** 6785-6794.

ANDERSON, C. W. & ALLALUNIS-TURNER, M. J. 2000. Human TP53 from the malignant glioma-derived cell lines M059J and M059K has a cancer-associated mutation in exon 8. *Radiat Res,* 154**,** 473-6.

ANGOM, R. S., NAKKA, N. M. R. & BHATTACHARYA, S. 2023. Advances in Glioblastoma Therapy: An Update on Current Approaches. *Brain Sci,* 13.

ANTONYSAMY, S., BONDAY, Z., CAMPBELL, R. M., DOYLE, B., DRUZINA, Z., GHEYI, T., HAN, B., JUNGHEIM, L. N., QIAN, Y., RAUCH, C., RUSSELL, M., SAUDER, J. M., WASSERMAN, S. R., WEICHERT, K., WILLARD, F. S., ZHANG, A. & EMTAGE, S. 2012. Crystal structure of the human PRMT5:MEP50 complex. *Proc Natl Acad Sci U S A,* 109**,** 17960-5.

ARIF, T., KRELIN, Y., NAKDIMON, I., BENHARROCH, D., PAUL, A., DADON-KLEIN, D. & SHOSHAN-BARMATZ, V. 2017. VDAC1 is a molecular target in glioblastoma, with its depletion leading to reprogrammed metabolism and reversed oncogenic properties. *Neuro Oncol,* 19**,** 951-964.

ARITA, H., MATSUSHITA, Y., MACHIDA, R., YAMASAKI, K., HATA, N., OHNO, M., YAMAGUCHI, S., SASAYAMA, T., TANAKA, S., HIGUCHI, F., IUCHI, T., SAITO, K., KANAMORI, M., MATSUDA, K. I., MIYAKE, Y., TAMURA, K., TAMAI, S., NAKAMURA, T., UDA, T., OKITA, Y., FUKAI, J., SAKAMOTO, D., HATTORI, Y., PAREIRA, E. S., HATAE, R., ISHI, Y., MIYAKITA, Y., TANAKA, K., TAKAYANAGI, S., OTANI, R., SAKAIDA, T., KOBAYASHI, K., SAITO, R., KUROZUMI, K., SHOFUDA, T., NONAKA, M., SUZUKI, H., SHIBUYA, M., KOMORI, T., SASAKI, H., MIZOGUCHI, M., KISHIMA, H., NAKADA, M., SONODA, Y., TOMINAGA, T., NAGANE, M., NISHIKAWA, R., KANEMURA, Y., KUCHIBA, A., NARITA, Y. & ICHIMURA, K. 2020. TERT promoter mutation confers favorable prognosis regardless of 1p/19q status in adult diffuse gliomas with IDH1/2 mutations. *Acta Neuropathol Commun,* 8**,** 201.

ARTHURS, A. L., KEATING, D. J., STRINGER, B. W. & CONN, S. J. 2020. The Suitability of Glioblastoma Cell Lines as Models for Primary Glioblastoma Cell Metabolism. *Cancers (Basel),* 12.

ASTOLFI, M., PEANT, B., LATEEF, M. A., ROUSSET, N., KENDALL-DUPONT, J., CARMONA, E., MONET, F., SAAD, F., PROVENCHER, D., MES-MASSON, A. M. & GERVAIS, T. 2016. Micro-dissected tumor tissues on chip: an ex vivo method for drug testing and personalized therapy. *Lab Chip,* 16**,** 312-25.

AUCLAIR, Y. & RICHARD, S. 2013. The role of arginine methylation in the DNA damage response. *DNA Repair (Amst),* 12**,** 459-65.

AYUSO, J. M., MONGE, R., MARTINEZ-GONZALEZ, A., VIRUMBRALES-MUNOZ, M., LLAMAZARES, G. A., BERGANZO, J., HERNANDEZ-LAIN, A., SANTOLARIA, J., DOBLARE, M., HUBERT, C., RICH, J. N., SANCHEZ-GOMEZ, P., PEREZ-GARCIA, V. M., OCHOA, I. & FERNANDEZ, L. J. 2017. Glioblastoma on a microfluidic chip: Generating pseudopalisades and enhancing aggressiveness through blood vessel obstruction events. *Neuro Oncol,* 19**,** 503-513.

AZAB, M. A. 2023. The Potential Role of Histone Modifications in Glioblastoma Therapy: Review Article. *J. Mol. Pathol.,* 4**,** 196-212.

BAECHTOLD, H., KURODA, M., SOK, J., RON, D., LOPEZ, B. S. & AKHMEDOV, A. T. 1999. Human 75-kDa DNA-pairing protein is identical to the pro-oncoprotein TLS/FUS and is able to promote D-loop formation. *J Biol Chem,* 274**,** 34337-42.

BAEK, J. H., RUBINSTEIN, M., SCHEUER, T. & TRIMMER, J. S. 2014. Reciprocal changes in phosphorylation and methylation of mammalian brain sodium channels in response to seizures. *J Biol Chem,* 289**,** 15363-73.

BALDWIN, R. M., MORETTIN, A., PARIS, G., GOULET, I. & COTE, J. 2012. Alternatively spliced protein arginine methyltransferase 1 isoform PRMT1v2 promotes the survival and invasiveness of breast cancer cells. *Cell Cycle,* 11**,** 4597-612.

BANASAVADI-SIDDEGOWDA, Y. K., RUSSELL, L., FRAIR, E., KARKHANIS, V. A., RELATION, T., YOO, J. Y., ZHANG, J., SIF, S., IMITOLA, J., BAIOCCHI, R. & KAUR, B. 2017. PRMT5-PTEN molecular pathway regulates senescence and self-renewal of primary glioblastoma neurosphere cells. *Oncogene,* 36**,** 263-274.

BANASAVADI-SIDDEGOWDA, Y. K., WELKER, A. M., AN, M., YANG, X., ZHOU, W., SHI, G., IMITOLA, J., LI, C., HSU, S., WANG, J., PHELPS, M., ZHANG, J., BEATTIE, C. E., BAIOCCHI, R. & KAUR, B. 2018. PRMT5 as a druggable target for glioblastoma therapy. *Neuro Oncol,* 20**,** 753-763.

BANFALVI, G. 2017. Methods to detect apoptotic cell death. *Apoptosis,* 22**,** 306-323.

BAO, D., CHENG, C., LAN, X., XING, R., CHEN, Z., ZHAO, H., SUN, J., WANG, Y., NIU, C., ZHANG, B. & FANG, S. 2017a. Regulation of p53wt glioma cell proliferation by androgen receptor-mediated inhibition of small VCP/p97-interacting protein expression. *Oncotarget,* 8**,** 23142-23154.

BAO, X., SIPRASHVILI, Z., ZARNEGAR, B. J., SHENOY, R. M., RIOS, E. J., NADY, N., QU, K., MAH, A., WEBSTER, D. E., RUBIN, A. J., WOZNIAK, G. G., TAO, S., WYSOCKA, J. & KHAVARI, P. A. 2017b. CSNK1a1 Regulates PRMT1 to Maintain the Progenitor State in Self-Renewing Somatic Tissue. *Dev Cell,* 43**,** 227-239 e5.

BARBOZA, L. G. A., LOPES, C., OLIVEIRA, P., BESSA, F., OTERO, V., HENRIQUES, B., RAIMUNDO, J., CAETANO, M., VALE, C. & GUILHERMINO, L. 2020. Microplastics in wild fish from North East Atlantic Ocean and its potential for causing neurotoxic effects, lipid oxidative damage, and human health risks associated with ingestion exposure. *Sci Total Environ,* 717**,** 134625.

BARLEV, N. A., LIU, L., CHEHAB, N. H., MANSFIELD, K., HARRIS, K. G., HALAZONETIS, T. D. & BERGER, S. L. 2001. Acetylation of p53 activates transcription through recruitment of coactivators/histone acetyltransferases. *Mol Cell,* 8**,** 1243-54.

BARRY, A., SAMUEL, S. F., HOSNI, I., MOURSI, A., FEUGERE, L., SENNETT, C. J., DEEPAK, S., ACHAWAL, S., RAJARAMAN, C., ILES, A., WOLLENBERG VALERO, K. C., SCOTT, I. S., GREEN, V., STEAD, L. F., GREENMAN, J., WADE, M. A. & BELTRAN-ALVAREZ, P. 2023. Investigating the effects of arginine methylation inhibitors on micro-dissected brain tumour biopsies maintained in a miniaturised perfusion system. *Lab Chip,* 23**,** 2664-2682.

BARTHEL, F. P., JOHNSON, K. C., VARN, F. S., MOSKALIK, A. D., TANNER, G., KOCAKAVUK, E., ANDERSON, K. J., ABIOLA, O., ALDAPE, K., ALFARO, K. D., ALPAR, D., AMIN, S. B., ASHLEY, D. M., BANDOPADHAYAY, P., BARNHOLTZ-SLOAN, J. S., BEROUKHIM, R., BOCK, C., BRASTIANOS, P. K., BRAT, D. J., BRODBELT, A. R., BRUNS, A. F., BULSARA, K. R., CHAKRABARTY, A., CHAKRAVARTI, A., CHUANG, J. H., CLAUS, E. B., COCHRAN, E. J., CONNELLY, J., COSTELLO, J. F., FINOCCHIARO, G., FLETCHER, M. N., FRENCH, P. J., GAN, H. K., GILBERT, M. R., GOULD, P. V., GRIMMER, M. R., IAVARONE, A., ISMAIL, A., JENKINSON, M. D., KHASRAW, M., KIM, H., KOUWENHOVEN, M. C. M., LAVIOLETTE, P. S., LI, M., LICHTER, P., LIGON, K. L., LOWMAN, A. K., MALTA, T. M., MAZOR, T., MCDONALD, K. L., MOLINARO, A. M., NAM, D. H., NAYYAR, N., NG, H. K., NGAN, C. Y., NICLOU, S. P., NIERS, J. M., NOUSHMEHR, H., NOORBAKHSH, J., ORMOND, D. R., PARK, C. K., POISSON, L. M., RABADAN, R., RADLWIMMER, B., RAO, G., REIFENBERGER, G., SA, J. K., SCHUSTER, M., SHAW, B. L., SHORT, S. C., SMITT, P. A. S., SLOAN, A. E., SMITS, M., SUZUKI, H., TABATABAI, G., VAN MEIR, E. G., WATTS, C., WELLER, M., WESSELING, P., WESTERMAN, B. A., WIDHALM, G., WOEHRER, A., YUNG, W. K. A., ZADEH, G., HUSE, J. T., DE GROOT, J. F., STEAD, L. F., VERHAAK, R. G. W. & CONSORTIUM, G. 2019. Longitudinal molecular trajectories of diffuse glioma in adults. *Nature,* 576**,** 112-120.

BATCHELOR, T. T., WON, M., CHAKRAVARTI, A., HADJIPANAYIS, C. G., SHI, W., ASHBY, L. S., STIEBER, V. W., ROBINS, H. I., GRAY, H. J., VOLOSCHIN, A., FIVEASH, J. B., ROBINSON, C. G., CHAMARTHY, U., KWOK, Y., CESCON, T. P., SHARMA, A. K., CHAUDHARY, R., POLLEY, M. Y. & MEHTA, M. P. 2023. NRG/RTOG 0837: Randomized, phase II, double-blind, placebo-controlled trial of chemoradiation with or without cediranib in newly diagnosed glioblastoma. *Neurooncol Adv,* 5**,** vdad116.

BEAVER, J. E. & WATERS, M. L. 2016. Molecular Recognition of Lys and Arg Methylation. *ACS Chem Biol,* 11**,** 643-53.

BEDFORD, M. T. & CLARKE, S. G. 2009. Protein arginine methylation in mammals: who, what, and why. *Mol Cell,* 33**,** 1-13.

BEDFORD, M. T. & RICHARD, S. 2005. Arginine methylation an emerging regulator of protein function. *Mol Cell,* 18**,** 263-72.

BELL, R. J., RUBE, H. T., XAVIER-MAGALHAES, A., COSTA, B. M., MANCINI, A., SONG, J. S. & COSTELLO, J. F. 2016. Understanding TERT Promoter Mutations: A Common Path to Immortality. *Mol Cancer Res,* 14**,** 315-23.

BELLAIL, A. C., OLSON, J. J. & HAO, C. 2014. SUMO1 modification stabilizes CDK6 protein and drives the cell cycle and glioblastoma progression. *Nat Commun,* 5**,** 4234.

BELTRAN-ALVAREZ, P., ESPEJO, A., SCHMAUDER, R., BELTRAN, C., MROWKA, R., LINKE, T., BATLLE, M., PEREZ-VILLA, F., PEREZ, G. J., SCORNIK, F. S., BENNDORF, K., PAGANS, S., ZIMMER, T. & BRUGADA, R. 2013. Protein arginine methyl transferases-3 and -5 increase cell surface expression of cardiac sodium channel. *FEBS Lett,* 587**,** 3159-65.

BENTMANN, E., NEUMANN, M., TAHIROVIC, S., RODDE, R., DORMANN, D. & HAASS, C. 2012. Requirements for stress granule recruitment of fused in sarcoma (FUS) and TAR DNA-binding protein of 43 kDa (TDP-43). *J Biol Chem,* 287**,** 23079-94.

BERNSTOCK, J. D., YE, D., GESSLER, F. A., LEE, Y. J., PERUZZOTTI-JAMETTI, L., BAUMGARTEN, P., JOHNSON, K. R., MARIC, D., YANG, W., KOGEL, D., PLUCHINO, S. & HALLENBECK, J. M. 2017. Topotecan is a potent inhibitor of SUMOylation in glioblastoma multiforme and alters both cellular replication and metabolic programming. *Sci Rep,* 7**,** 7425.

BEZZI, M., TEO, S. X., MULLER, J., MOK, W. C., SAHU, S. K., VARDY, L. A., BONDAY, Z. Q. & GUCCIONE, E. 2013. Regulation of constitutive and alternative splicing by PRMT5 reveals a role for Mdm4 pre-mRNA in sensing defects in the spliceosomal machinery. *Genes Dev,* 27**,** 1903-16.

BHULLAR, K. S., LAGARON, N. O., MCGOWAN, E. M., PARMAR, I., JHA, A., HUBBARD, B. P. & RUPASINGHE, H. P. V. 2018. Kinase-targeted cancer therapies: progress, challenges and future directions. *Mol Cancer,* 17**,** 48.

BHURIPANYO, K., WANG, Y., LIU, X., ZHOU, L., LIU, R., DUONG, D., ZHAO, B., BI, Y., ZHOU, H., CHEN, G., SEYFRIED, N. T., CHAZIN, W. J., KIYOKAWA, H. & YIN, J. 2018. Identifying the substrate proteins of U-box E3s E4B and CHIP by orthogonal ubiquitin transfer. *Sci Adv,* 4**,** e1701393.

BHUYAN, S. 2022. Effects of Microplastics on Fish and in Human Health. *Frontiers Environmental Science,* 10.

BIAN, S., REPIC, M., GUO, Z., KAVIRAYANI, A., BURKARD, T., BAGLEY, J. A., KRAUDITSCH, C. & KNOBLICH, J. A. 2018. Genetically engineered cerebral organoids model brain tumor formation. *Nat Methods,* 15**,** 631-639.

BINABAJ, M. M., BAHRAMI, A., SHAHIDSALES, S., JOODI, M., JOUDI MASHHAD, M., HASSANIAN, S. M., ANVARI, K. & AVAN, A. 2018. The prognostic value of MGMT promoter methylation in glioblastoma: A meta-analysis of clinical trials. *J Cell Physiol,* 233**,** 378-386.

BIRNBAUM, R., YOSHA-ORPAZ, N., YANOOV-SHARAV, M., KIDRON, D., GUR, H., YOSOVICH, K., LERMAN-SAGIE, T., MALINGER, G. & LEV, D. 2019. Prenatal and postnatal presentation of PRMT7 related syndrome: Expanding the phenotypic manifestations. *Am J Med Genet A,* 179**,** 78-84.

BIROCCHI, F., CUSIMANO, M., ROSSARI, F., BERETTA, S., RANCOITA, P. M. V., RANGHETTI, A., COLOMBO, S., COSTA, B., ANGEL, P., SANVITO, F., CALLEA, M., NORATA, R., CHAABANE, L., CANU, T., SPINELLI, A., GENUA, M., OSTUNI, R., MERELLI, I., COLTELLA, N. & NALDINI, L. 2022. Targeted inducible delivery of immunoactivating cytokines reprograms glioblastoma microenvironment and inhibits growth in mouse models. *Sci Transl Med,* 14**,** eabl4106.

BLANC, R. S. & RICHARD, S. 2017. Arginine Methylation: The Coming of Age. *Mol Cell,* 65**,** 8-24.

BOBOLA, M. S., ALNOOR, M., CHEN, J. Y., KOLSTOE, D. D., SILBERGELD, D. L., ROSTOMILY, R. C., BLANK, A., CHAMBERLAIN, M. C. & SILBER, J. R. 2015. O(6)-methylguanine-DNA methyltransferase activity is associated with response to alkylating agent therapy and with MGMT promoter methylation in glioblastoma and anaplastic glioma. *BBA Clin,* 3**,** 1-10.

BOBOLA, M. S., KOLSTOE, D. D., BLANK, A., CHAMBERLAIN, M. C. & SILBER, J. R. 2012. Repair of 3-methyladenine and abasic sites by base excision repair mediates glioblastoma resistance to temozolomide. *Front Oncol,* 2**,** 176.

BOHN, A., BRALEY, A., RODRIGUEZ DE LA VEGA, P., ZEVALLOS, J. C. & BARENGO, N. C. 2018. The association between race and survival in glioblastoma patients in the US: A retrospective cohort study. *PLoS One,* 13**,** e0198581.

BOISVERT, F. M., DERY, U., MASSON, J. Y. & RICHARD, S. 2005a. Arginine methylation of MRE11 by PRMT1 is required for DNA damage checkpoint control. *Genes Dev,* 19**,** 671-6.

BOISVERT, F. M., RHIE, A., RICHARD, S. & DOHERTY, A. J. 2005b. The GAR motif of 53BP1 is arginine methylated by PRMT1 and is necessary for 53BP1 DNA binding activity. *Cell Cycle,* 4**,** 1834-41.

BOLIVAR, J. M., WIESBAUER, J. & NIDETZKY, B. 2011. Biotransformations in microstructured reactors: more than flowing with the stream? *Trends Biotechnol,* 29**,** 333-42.

BOND, S., LOPEZ-LLOREDA, C., GANNON, P. J., AKAY-ESPINOZA, C. & JORDAN-SCIUTTO, K. L. 2020. The Integrated Stress Response and Phosphorylated Eukaryotic Initiation Factor 2alpha in Neurodegeneration. *J Neuropathol Exp Neurol,* 79**,** 123-143.

BOULANGER, M. C., LIANG, C., RUSSELL, R. S., LIN, R., BEDFORD, M. T., WAINBERG, M. A. & RICHARD, S. 2005. Methylation of Tat by PRMT6 regulates human immunodeficiency virus type 1 gene expression. *J Virol,* 79**,** 124-31.

BOVENGA, F., SABBA, C. & MOSCHETTA, A. 2015. Uncoupling nuclear receptor LXR and cholesterol metabolism in cancer. *Cell Metab,* 21**,** 517-26.

BRAMBLE, M. S., ROACH, L., LIPSON, A., VASHIST, N., ESKIN, A., NGUN, T., GOSSCHALK, J. E., KLEIN, S., BARSEGHYAN, H., ARBOLEDA, V. A. & VILAIN, E. 2016. Sex-Specific Effects of Testosterone on the Sexually Dimorphic Transcriptome and Epigenome of Embryonic Neural Stem/Progenitor Cells. *Sci Rep,* 6**,** 36916.

BRAUN, C. J., STANCIU, M., BOUTZ, P. L., PATTERSON, J. C., CALLIGARIS, D., HIGUCHI, F., NEUPANE, R., FENOGLIO, S., CAHILL, D. P., WAKIMOTO, H., AGAR, N. Y. R., YAFFE, M. B., SHARP, P. A., HEMANN, M. T. & LEES, J. A. 2017. Coordinated Splicing of Regulatory Detained Introns within Oncogenic Transcripts Creates an Exploitable Vulnerability in Malignant Glioma. *Cancer Cell,* 32**,** 411-426 e11.

BRENNAN, C. W., VERHAAK, R. G., MCKENNA, A., CAMPOS, B., NOUSHMEHR, H., SALAMA, S. R., ZHENG, S., CHAKRAVARTY, D., SANBORN, J. Z., BERMAN, S. H., BEROUKHIM, R., BERNARD, B., WU, C. J., GENOVESE, G., SHMULEVICH, I., BARNHOLTZ-SLOAN, J., ZOU, L., VEGESNA, R., SHUKLA, S. A., CIRIELLO, G., YUNG, W. K., ZHANG, W., SOUGNEZ, C., MIKKELSEN, T., ALDAPE, K., BIGNER, D. D., VAN MEIR, E. G., PRADOS, M., SLOAN, A., BLACK, K. L., ESCHBACHER, J., FINOCCHIARO, G., FRIEDMAN, W., ANDREWS, D. W., GUHA, A., IACOCCA, M., O'NEILL, B. P., FOLTZ, G., MYERS, J., WEISENBERGER, D. J., PENNY, R., KUCHERLAPATI, R., PEROU, C. M., HAYES, D. N., GIBBS, R., MARRA, M., MILLS, G. B., LANDER, E., SPELLMAN, P., WILSON, R., SANDER, C., WEINSTEIN, J., MEYERSON, M., GABRIEL, S., LAIRD, P. W., HAUSSLER, D., GETZ, G., CHIN, L. & NETWORK, T. R. 2013. The somatic genomic landscape of glioblastoma. *Cell,* 155**,** 462-77.

BROWN, C. E., HIBBARD, J. C., ALIZADEH, D., BLANCHARD, M. S., NATRI, H. M., WANG, D., OSTBERG, J. R., AGUILAR, B., WAGNER, J. R., PAUL, J. A., STARR, R., WONG, R. A., CHEN, W., SHULKIN, N., AFTABIZADEH, M., FILIPPOV, A., CHAUDHRY, A., RESSLER, J. A., KILPATRICK, J., MYERS-MCNAMARA, P., CHEN, M., WANG, L. D., ROCKNE, R. C., GEORGES, J., PORTNOW, J., BARISH, M. E., D'APUZZO, M., BANOVICH, N. E., FORMAN, S. J. & BADIE, B. 2024. Locoregional delivery of IL13Ralpha2-targeting CAR-T cells in recurrent high-grade glioma: a phase 1 trial. *Nat Med,* 30**,** 1001-1012.

BROWN, T. J., BRENNAN, M. C., LI, M., CHURCH, E. W., BRANDMEIR, N. J., RAKSZAWSKI, K. L., PATEL, A. S., RIZK, E. B., SUKI, D., SAWAYA, R. & GLANTZ, M. 2016. Association of the Extent of Resection With Survival in Glioblastoma: A Systematic Review and Meta-analysis. *JAMA Oncol,* 2**,** 1460-1469.

BRUNA, A., DARKEN, R. S., ROJO, F., OCANA, A., PENUELAS, S., ARIAS, A., PARIS, R., TORTOSA, A., MORA, J., BASELGA, J. & SEOANE, J. 2007. High TGFbeta-Smad activity confers poor prognosis in glioma patients and promotes cell proliferation depending on the methylation of the PDGF-B gene. *Cancer Cell,* 11**,** 147-60.

BRYANT, J. P., HEISS, J. & BANASAVADI-SIDDEGOWDA, Y. K. 2021. Arginine Methylation in Brain Tumors: Tumor Biology and Therapeutic Strategies. *Cells,* 10.

BUCZKOWICZ, P., HOEMAN, C., RAKOPOULOS, P., PAJOVIC, S., LETOURNEAU, L., DZAMBA, M., MORRISON, A., LEWIS, P., BOUFFET, E., BARTELS, U., ZUCCARO, J., AGNIHOTRI, S., RYALL, S., BARSZCZYK, M., CHORNENKYY, Y., BOURGEY, M., BOURQUE, G., MONTPETIT, A., CORDERO, F., CASTELO-BRANCO, P., MANGEREL, J., TABORI, U., HO, K. C., HUANG, A., TAYLOR, K. R., MACKAY, A., BENDEL, A. E., NAZARIAN, J., FANGUSARO, J. R., KARAJANNIS, M. A., ZAGZAG, D., FOREMAN, N. K., DONSON, A., HEGERT, J. V., SMITH, A., CHAN, J., LAFAY-COUSIN, L., DUNN, S., HUKIN, J., DUNHAM, C., SCHEINEMANN, K., MICHAUD, J., ZELCER, S., RAMSAY, D., CAIN, J., BRENNAN, C., SOUWEIDANE, M. M., JONES, C., ALLIS, C. D., BRUDNO, M., BECHER, O. & HAWKINS, C. 2014. Genomic analysis of diffuse intrinsic pontine gliomas identifies three molecular subgroups and recurrent activating ACVR1 mutations. *Nat Genet,* 46**,** 451-6.

BURKE, K. A., JANKE, A. M., RHINE, C. L. & FAWZI, N. L. 2015. Residue-by-Residue View of In Vitro FUS Granules that Bind the C-Terminal Domain of RNA Polymerase II. *Mol Cell,* 60**,** 231-41.

CADIZ, L. & JONZ, M. G. 2020. A comparative perspective on lung and gill regeneration. *J Exp Biol,* 223.

CAGNOL, S., MANSOUR, A., VAN OBBERGHEN-SCHILLING, E. & CHAMBARD, J. C. 2011. Raf-1 activation prevents caspase 9 processing downstream of apoptosome formation. *J Signal Transduct,* 2011**,** 834948.

CAI, J., CHEN, Q., CUI, Y., DONG, J., CHEN, M., WU, P. & JIANG, C. 2018. Immune heterogeneity and clinicopathologic characterization of IGFBP2 in 2447 glioma samples. *Oncoimmunology,* 7**,** e1426516.

CALABRETTA, S., VOGEL, G., YU, Z., CHOQUET, K., DARBELLI, L., NICHOLSON, T. B., KLEINMAN, C. L. & RICHARD, S. 2018. Loss of PRMT5 Promotes PDGFRalpha Degradation during Oligodendrocyte Differentiation and Myelination. *Dev Cell,* 46**,** 426-440 e5.

CALVO TARDON, M., ALLARD, M., DUTOIT, V., DIETRICH, P. Y. & WALKER, P. R. 2019. Peptides as cancer vaccines. *Curr Opin Pharmacol,* 47**,** 20-26.

CANCER RESEARCH UK. 2021. Glioma [Online]. Available: https://www.cancerresearchuk.org/about-cancer/brain-tumours/types/glioma-adults [Accessed 06/01/21 2021].

CAO, M. T., FENG, Y. & ZHENG, Y. G. 2023. Protein arginine methyltransferase 6 is a novel substrate of protein arginine methyltransferase 1. *World J Biol Chem,* 14**,** 84-98.

CARDONA, A. F., JARAMILLO-VELASQUEZ, D., RUIZ-PATINO, A., POLO, C., JIMENEZ, E., HAKIM, F., GOMEZ, D., RAMON, J. F., CIFUENTES, H., MEJIA, J. A., SALGUERO, F., ORDONEZ, C., MUNOZ, A., BERMUDEZ, S., USECHE, N., PINEDA, D., RICAURTE, L., ZATARAIN-BARRON, Z. L., RODRIGUEZ, J., AVILA, J., ROJAS, L., JALLER, E., SOTELO, C., GARCIA-ROBLEDO, J. E., SANTOYO, N., ROLFO, C., ROSELL, R. & ARRIETA, O. 2021. Efficacy of osimertinib plus bevacizumab in glioblastoma patients with simultaneous EGFR amplification and EGFRvIII mutation. *J Neurooncol,* 154**,** 353-364.

CARRANO, A., JUAREZ, J. J., INCONTRI, D., IBARRA, A. & GUERRERO CAZARES, H. 2021. Sex-Specific Differences in Glioblastoma. *Cells,* 10.

CENCIARINI, M., VALENTINO, M., BELIA, S., SFORNA, L., ROSA, P., RONCHETTI, S., D'ADAMO, M. C. & PESSIA, M. 2019. Dexamethasone in Glioblastoma Multiforme Therapy: Mechanisms and Controversies. *Front Mol Neurosci,* 12**,** 65.

CERESA, D., ALESSANDRINI, F., LUCCHINI, S., MARUBBI, D., PIAGGIO, F., MENA VERA, J. M., CECCHERINI, I., REVERBERI, D., APPOLLONI, I. & MALATESTA, P. 2023. Early clonal extinction in glioblastoma progression revealed by genetic barcoding. *Cancer Cell,* 41**,** 1466-1479 e9.

CHAI, R., LI, G., LIU, Y., ZHANG, K., ZHAO, Z., WU, F., CHANG, Y., PANG, B., LI, J., LI, Y., JIANG, T. & WANG, Y. 2021. Predictive value of MGMT promoter methylation on the survival of TMZ treated IDH-mutant glioblastoma. *Cancer Biol Med,* 18**,** 272-282.

CHAITANYA, G. V., STEVEN, A. J. & BABU, P. P. 2010. PARP-1 cleavage fragments: signatures of cell-death proteases in neurodegeneration. *Cell Commun Signal,* 8**,** 31.

CHANDRAN, I. V. G., S.; VENKAT, E.H.; KJOLBY, M. AND NEJSUM, P. 2024. Extracellular vesicles in glioblastoma: a challenge and an opportunity. *NPJ Precis Oncol. ,* 8**,** 103.

CHANG, N. C., SINCENNES, M. C., CHEVALIER, F. P., BRUN, C. E., LACARIA, M., SEGALES, J., MUNOZ-CANOVES, P., MING, H. & RUDNICKI, M. A. 2018. The Dystrophin Glycoprotein Complex Regulates the Epigenetic Activation of Muscle Stem Cell Commitment. *Cell Stem Cell,* 22**,** 755-768 e6.

CHAN-PENEBRE, E., KUPLAST, K. G., MAJER, C. R., BORIACK-SJODIN, P. A., WIGLE, T. J., JOHNSTON, L. D., RIOUX, N., MUNCHHOF, M. J., JIN, L., JACQUES, S. L., WEST, K. A., LINGARAJ, T., STICKLAND, K., RIBICH, S. A., RAIMONDI, A., SCOTT, M. P., WATERS, N. J., POLLOCK, R. M., SMITH, J. J., BARBASH, O., PAPPALARDI, M., HO, T. F., NURSE, K., OZA, K. P., GALLAGHER, K. T., KRUGER, R., MOYER, M. P., COPELAND, R. A., CHESWORTH, R. & DUNCAN, K. W. 2015. A selective inhibitor of PRMT5 with in vivo and in vitro potency in MCL models. *Nat Chem Biol,* 11**,** 432-7.

CHAU, V., TOBIAS, J. W., BACHMAIR, A., MARRIOTT, D., ECKER, D. J., GONDA, D. K. & VARSHAVSKY, A. 1989. A multiubiquitin chain is confined to specific lysine in a targeted short-lived protein. *Science,* 243**,** 1576-83.

CHEN, A., JIANG, Y., LI, Z., WU, L., SANTIAGO, U., ZOU, H., CAI, C., SHARMA, V., GUAN, Y., MCCARL, L. H., MA, J., WU, Y. L., MICHEL, J., SHI, Y., KONNIKOVA, L., AMANKULOR, N. M., ZINN, P. O., KOHANBASH, G., AGNIHOTRI, S., LU, S., LU, X., SUN, D., GITTES, G. K., WANG, Q., XIAO, X., YIMLAMAI, D., POLLACK, I. F., CAMACHO, C. J. & HU, B. 2021. Chitinase-3-like 1 protein complexes modulate macrophage-mediated immune suppression in glioblastoma. *J Clin Invest,* 131.

CHEN, C., NOTT, T. J., JIN, J. & PAWSON, T. 2011. Deciphering arginine methylation: Tudor tells the tale. *Nat Rev Mol Cell Biol,* 12**,** 629-42.

CHEN, D., MA, H., HONG, H., KOH, S. S., HUANG, S. M., SCHURTER, B. T., ASWAD, D. W. & STALLCUP, M. R. 1999. Regulation of transcription by a protein methyltransferase. *Science,* 284**,** 2174-7.

CHEN, D., YAO, J., HU, B., KUANG, L., XU, B., LIU, H., DOU, C., WANG, G. & GUO, M. 2022. New biomarker: the gene HLA-DRA associated with low-grade glioma prognosis. *Chin Neurosurg J,* 8**,** 12.

CHEN, L., YU, Z., LEE, Y., WANG, X., ZHAO, B. & JUNG, Y. M. 2012. Quantitative evaluation of proteins with bicinchoninic acid (BCA): resonance Raman and surface-enhanced resonance Raman scattering-based methods. *Analyst,* 137**,** 5834-8.

CHEN, S., LI, Y., ZHU, Y., FEI, J., SONG, L., SUN, G., GUO, L. & LI, X. 2022. SERPINE1 Overexpression Promotes Malignant Progression and Poor Prognosis of Gastric Cancer. *J Oncol,* 2022**,** 2647825.

CHENG, D. C., J.; SHAABAN, S. AND BEDFORD, M.; 2006. The Arginine Methyltransferase CARM1 Regulates the Coupling of Transcription and mRNA Processing. *Molecular Cell,* 25**,** 71-83.

CHENG, D., GAO, G., DI LORENZO, A., JAYNE, S., HOTTIGER, M. O., RICHARD, S. & BEDFORD, M. T. 2020. Genetic evidence for partial redundancy between the arginine methyltransferases CARM1 and PRMT6. *J Biol Chem,* 295**,** 17060-17070.

CHENG, D., YADAV, N., KING, R. W., SWANSON, M. S., WEINSTEIN, E. J. & BEDFORD, M. T. 2004. Small molecule regulators of protein arginine methyltransferases. *J Biol Chem,* 279**,** 23892-9.

CHENG, Q., YI, B., WANG, A. & JIANG, X. 2013. Exploring and exploiting the fundamental role of microRNAs in tumor pathogenesis. *Onco Targets Ther,* 6**,** 1675-84.

CHEUNG, N., CHAN, L. C., THOMPSON, A., CLEARY, M. L. & SO, C. W. 2007. Protein arginine-methyltransferase-dependent oncogenesis. *Nat Cell Biol,* 9**,** 1208-15.

CHI, A. S., SORENSEN, A. G., JAIN, R. K. & BATCHELOR, T. T. 2009. Angiogenesis as a therapeutic target in malignant gliomas. *Oncologist,* 14**,** 621-36.

CHIANG, J., HARRELD, J. H., TINKLE, C. L., MOREIRA, D. C., LI, X., ACHARYA, S., QADDOUMI, I. & ELLISON, D. W. 2019. A single-center study of the clinicopathologic correlates of gliomas with a MYB or MYBL1 alteration. *Acta Neuropathol,* 138**,** 1091-1092.

CHITTKA, A., NITARSKA, J., GRAZINI, U. & RICHARDSON, W. D. 2012. Transcription factor positive regulatory domain 4 (PRDM4) recruits protein arginine methyltransferase 5 (PRMT5) to mediate histone arginine methylation and control neural stem cell proliferation and differentiation. *J Biol Chem,* 287**,** 42995-3006.

CHO, A. N., JIN, Y., AN, Y., KIM, J., CHOI, Y. S., LEE, J. S., KIM, J., CHOI, W. Y., KOO, D. J., YU, W., CHANG, G. E., KIM, D. Y., JO, S. H., KIM, J., KIM, S. Y., KIM, Y. G., KIM, J. Y., CHOI, N., CHEONG, E., KIM, Y. J., JE, H. S., KANG, H. C. & CHO, S. W. 2021. Microfluidic device with brain extracellular matrix promotes structural and functional maturation of human brain organoids. *Nat Commun,* 12**,** 4730.

CHO, C. F., WOLFE, J. M., FADZEN, C. M., CALLIGARIS, D., HORNBURG, K., CHIOCCA, E. A., AGAR, N. Y. R., PENTELUTE, B. L. & LAWLER, S. E. 2017. Blood-brain-barrier spheroids as an in vitro screening platform for brain-penetrating agents. *Nat Commun,* 8**,** 15623.

CHO, J. A., PARK, H., LIM, E. H. & LEE, K. W. 2011. MicroRNA expression profiling in neurogenesis of adipose tissue-derived stem cells. *J Genet,* 90**,** 81-93.

CHO, U., YANG, S. H. & YOO, C. 2021. Estimation of the occurrence rates of IDH1 and IDH2 mutations in gliomas and the reconsideration of IDH-wildtype anaplastic astrocytomas: an institutional experience. *J Int Med Res,* 49**,** 3000605211019258.

CIECHOMSKA, I. A. 2018. The role of autophagy in cancer - characterization of crosstalk between apoptosis and autophagy; autophagy as a new therapeutic strategy in glioblastoma. *Postepy Biochem,* 64**,** 119-128.

CLARKE, P. R. & ZHANG, C. 2008. Spatial and temporal coordination of mitosis by Ran GTPase. *Nat Rev Mol Cell Biol,* 9**,** 464-77.

COCCO, E., SCALTRITI, M. & DRILON, A. 2018. NTRK fusion-positive cancers and TRK inhibitor therapy. *Nat Rev Clin Oncol,* 15**,** 731-747.

COLANGELO, N. W. & AZZAM, E. I. 2020. Extracellular vesicles originating from glioblastoma cells increase metalloproteinase release by astrocytes: the role of CD147 (EMMPRIN) and ionizing radiation. *Cell Commun Signal,* 18**,** 21.

COLLINS, T., PYNE, E., CHRISTENSEN, M., ILES, A., PAMME, N. & PIRES, I. M. 2021. Spheroid-on-chip microfluidic technology for the evaluation of the impact of continuous flow on metastatic potential in cancer models in vitro. *Biomicrofluidics,* 15**,** 044103.

CONTE, B., RICH, B. J., GULTEKIN, S. H., AZZAM, G. & DEL PILAR GUILLERMO PRIETO EIBL, M. 2022. A Case of Glioblastoma, Isocitrate Dehydrogenase Wild Type, With Widely Disseminated Osseous Metastasis. *Cureus,* 14**,** e28803.

CORREA, B. R., DE ARAUJO, P. R., QIAO, M., BURNS, S. C., CHEN, C., SCHLEGEL, R., AGARWAL, S., GALANTE, P. A. & PENALVA, L. O. 2016. Functional genomics analyses of RNA-binding proteins reveal the splicing regulator SNRPB as an oncogenic candidate in glioblastoma. *Genome Biol,* 17**,** 125.

COTE, J. & RICHARD, S. 2005. Tudor domains bind symmetrical dimethylated arginines. *J Biol Chem,* 280**,** 28476-83.

CRIMMINS, E. M., THYAGARAJAN, B., LEVINE, M. E., WEIR, D. R. & FAUL, J. 2021. Associations of Age, Sex, Race/Ethnicity, and Education With 13 Epigenetic Clocks in a Nationally Representative U.S. Sample: The Health and Retirement Study. *J Gerontol A Biol Sci Med Sci,* 76**,** 1117-1123.

CROWLEY, L. C., MARFELL, B. J., SCOTT, A. P. & WATERHOUSE, N. J. 2016. Quantitation of Apoptosis and Necrosis by Annexin V Binding, Propidium Iodide Uptake, and Flow Cytometry. *Cold Spring Harb Protoc,* 2016.

CURA, V. & CAVARELLI, J. 2021. Structure, Activity and Function of the PRMT2 Protein Arginine Methyltransferase. *Life (Basel),* 11.

CURA, V., TROFFER-CHARLIER, N., WURTZ, J. M., BONNEFOND, L. & CAVARELLI, J. 2014. Structural insight into arginine methylation by the mouse protein arginine methyltransferase 7: a zinc finger freezes the mimic of the dimeric state into a single active site. *Acta Crystallogr D Biol Crystallogr,* 70**,** 2401-12.

DAI, J., XING, Y., XIAO, L., LI, J., CAO, R., HE, Y., FANG, H., PERIASAMY, A., OBERHOZLER, J., JIN, L., LANDERS, J. P., WANG, Y. & LI, X. 2019. Microfluidic Disc-on-a-Chip Device for Mouse Intervertebral Disc-Pitching a Next-Generation Research Platform To Study Disc Degeneration. *ACS Biomater Sci Eng,* 5**,** 2041-2051.

DALI-YOUCEF, N., FROELICH, S., MOUSSALLIEH, F. M., CHIBBARO, S., NOEL, G., NAMER, I. J., HEIKKINEN, S. & AUWERX, J. 2015. Gene expression mapping of histone deacetylases and co-factors, and correlation with survival time and 1H-HRMAS metabolomic profile in human gliomas. *Sci Rep,* 5**,** 9087.

D'ANGELO, F., CECCARELLI, M., TALA, GAROFANO, L., ZHANG, J., FRATTINI, V., CARUSO, F. P., LEWIS, G., ALFARO, K. D., BAUCHET, L., BERZERO, G., CACHIA, D., CANGIANO, M., CAPELLE, L., DE GROOT, J., DIMECO, F., DUCRAY, F., FARAH, W., FINOCCHIARO, G., GOUTAGNY, S., KAMIYA-MATSUOKA, C., LAVARINO, C., LOISEAU, H., LORGIS, V., MARRAS, C. E., MCCUTCHEON, I., NAM, D. H., RONCHI, S., SALETTI, V., SEIZEUR, R., SLOPIS, J., SUNOL, M., VANDENBOS, F., VARLET, P., VIDAUD, D., WATTS, C., TABAR, V., REUSS, D. E., KIM, S. K., MEYRONET, D., MOKHTARI, K., SALVADOR, H., BHAT, K. P., EOLI, M., SANSON, M., LASORELLA, A. & IAVARONE, A. 2019. The molecular landscape of glioma in patients with Neurofibromatosis 1. *Nat Med,* 25**,** 176-187.

DANIEL, P., SABRI, S., CHADDAD, A., MEEHAN, B., JEAN-CLAUDE, B., RAK, J. & ABDULKARIM, B. S. 2019. Temozolomide Induced Hypermutation in Glioma: Evolutionary Mechanisms and Therapeutic Opportunities. *Front Oncol,* 9**,** 41.

DATTA, S. & CHAKRABARTI, N. 2018. Age related rise in lactate and its correlation with lactate dehydrogenase (LDH) status in post-mitochondrial fractions isolated from different regions of brain in mice. *Neurochem Int,* 118**,** 23-33.

DAWSON, A., DYER, C., MACFIE, J., DAVIES, J., KARSAI, L., GREENMAN, J. & JACOBSEN, M. 2016. A microfluidic chip based model for the study of full thickness human intestinal tissue using dual flow. *Biomicrofluidics,* 10**,** 064101.

DAY, E. K., SOSALE, N. G., XIAO, A., ZHONG, Q., PUROW, B. & LAZZARA, M. J. 2020. Glioblastoma Cell Resistance to EGFR and MET Inhibition Can Be Overcome via Blockade of FGFR-SPRY2 Bypass Signaling. *Cell Rep,* 30**,** 3383-3396 e7.

DE LA IGLESIA, N., KONOPKA, G., PURAM, S. V., CHAN, J. A., BACHOO, R. M., YOU, M. J., LEVY, D. E., DEPINHO, R. A. & BONNI, A. 2008. Identification of a PTEN-regulated STAT3 brain tumor suppressor pathway. *Genes Dev,* 22**,** 449-62.

DENG, L., REN, J., LI, B., WANG, Y., JIANG, N., WANG, Y. & CUI, H. 2023. Predictive value of CCL2 in the prognosis and immunotherapy response of glioblastoma multiforme. *BMC Genomics,* 24**,** 746.

DESCHENES-SIMARD, X., KOTTAKIS, F., MELOCHE, S. & FERBEYRE, G. 2014. ERKs in cancer: friends or foes? *Cancer Res,* 74**,** 412-9.

DHAR, S. S., LEE, S. H., KAN, P. Y., VOIGT, P., MA, L., SHI, X., REINBERG, D. & LEE, M. G. 2012. Trans-tail regulation of MLL4-catalyzed H3K4 methylation by H4R3 symmetric dimethylation is mediated by a tandem PHD of MLL4. *Genes Dev,* 26**,** 2749-62.

DHAR, S., VEMULAPALLI, V., PATANANAN, A. N., HUANG, G. L., DI LORENZO, A., RICHARD, S., COMB, M. J., GUO, A., CLARKE, S. G. & BEDFORD, M. T. 2013. Loss of the major Type I arginine methyltransferase PRMT1 causes substrate scavenging by other PRMTs. *Sci Rep,* 3**,** 1311.

DI COSTANZO, A., SCARABINO, T., TROJSI, F., GIANNATEMPO, G. M., POPOLIZIO, T., CATAPANO, D., BONAVITA, S., MAGGIALETTI, N., TOSETTI, M., SALVOLINI, U., D'ANGELO, V. A. & TEDESCHI, G. 2006. Multiparametric 3T MR approach to the assessment of cerebral gliomas: tumor extent and malignancy. *Neuroradiology,* 48**,** 622-31.

DI STEFANO, A. L., FUCCI, A., FRATTINI, V., LABUSSIERE, M., MOKHTARI, K., ZOPPOLI, P., MARIE, Y., BRUNO, A., BOISSELIER, B., GIRY, M., SAVATOVSKY, J., TOUAT, M., BELAID, H., KAMOUN, A., IDBAIH, A., HOUILLIER, C., LUO, F. R., SORIA, J. C., TABERNERO, J., EOLI, M., PATERRA, R., YIP, S., PETRECCA, K., CHAN, J. A., FINOCCHIARO, G., LASORELLA, A., SANSON, M. & IAVARONE, A. 2015. Detection, Characterization, and Inhibition of FGFR-TACC Fusions in IDH Wild-type Glioma. *Clin Cancer Res,* 21**,** 3307-17.

DI, K., LINSKEY, M. E. & BOTA, D. A. 2013. TRIM11 is overexpressed in high-grade gliomas and promotes proliferation, invasion, migration and glial tumor growth. *Oncogene,* 32**,** 5038-47.

DIAO, P. Y., LI, S. X., PENG, J., YANG, J. H., PAN, Y. C., XU, X. P., TANG, H., HU, J. X., ZHAO, H. F. & HUANG, G. D. 2020. Overexpression of EP300-interacting inhibitor of differentiation 3 predicts poor prognosis in patients with glioblastoma multiforme. *Int J Clin Exp Pathol,* 13**,** 979-988.

DING, H. N., A.; GUTMANN, D.H.; GUHA, A. AND GURMANN, D. 2000. A review of astrocytoma models. *Neurosurgery Focus,* 8**,** 1-8.

DOBRA, G., GYUKITY-SEBESTYEN, E., BUKVA, M., HARMATI, M., NAGY, V., SZABO, Z., PANKOTAI, T., KLEKNER, A. & BUZAS, K. 2023. MMP-9 as Prognostic Marker for Brain Tumours: A Comparative Study on Serum-Derived Small Extracellular Vesicles. *Cancers (Basel),* 15.

DOMENECH, M., HERNANDEZ, A., PLAJA, A., MARTINEZ-BALIBREA, E. & BALANA, C. 2021. Hypoxia: The Cornerstone of Glioblastoma. *Int J Mol Sci,* 22.

DONG, F., LI, Q., YANG, C., HUO, D., WANG, X., AI, C., KONG, Y., SUN, X., WANG, W., ZHOU, Y., LIU, X., LI, W., GAO, W., LIU, W., KANG, C. & WU, X. 2018. PRMT2 links histone H3R8 asymmetric dimethylation to oncogenic activation and tumorigenesis of glioblastoma. *Nat Commun,* 9**,** 4552.

DONG, F., MO, Z., EID, W., COURTNEY, K. C. & ZHA, X. 2014. Akt inhibition promotes ABCA1-mediated cholesterol efflux to ApoA-I through suppressing mTORC1. *PLoS One,* 9**,** e113789.

DONG, H., HE, X., ZHANG, L., CHEN, W., LIN, Y. C., LIU, S. B., WANG, H., NGUYEN, L. X. T., LI, M., ZHU, Y., ZHAO, D., GHODA, L., SERODY, J., VINCENT, B., LUZNIK, L., GOJO, I., ZEIDNER, J., SU, R., CHEN, J., SHARMA, R., PIRROTTE, P., WU, X., HU, W., HAN, W., SHEN, B., KUO, Y. H., JIN, J., SALHOTRA, A., WANG, J., MARCUCCI, G., LUO, Y. L. & LI, L. 2024. Targeting PRMT9-mediated arginine methylation suppresses cancer stem cell maintenance and elicits cGAS-mediated anticancer immunity. *Nat Cancer,* 5**,** 601-624.

DONG, R., LI, X. & LAI, K. O. 2021. Activity and Function of the PRMT8 Protein Arginine Methyltransferase in Neurons. *Life (Basel),* 11.

DONO, A., RAMESH, A. V., WANG, E., SHAH, M., TANDON, N., BALLESTER, L. Y. & ESQUENAZI, Y. 2021. The role of RB1 alteration and 4q12 amplification in IDH-WT glioblastoma. *Neurooncol Adv,* 3**,** vdab050.

DONOVAN, T. A., MOORE, F. M., BERTRAM, C. A., LUONG, R., BOLFA, P., KLOPFLEISCH, R., TVEDTEN, H., SALAS, E. N., WHITLEY, D. B., AUBREVILLE, M. & MEUTEN, D. J. 2021. Mitotic Figures-Normal, Atypical, and Imposters: A Guide to Identification. *Vet Pathol,* 58**,** 243-257.

DORMANN, D., MADL, T., VALORI, C. F., BENTMANN, E., TAHIROVIC, S., ABOU-AJRAM, C., KREMMER, E., ANSORGE, O., MACKENZIE, I. R., NEUMANN, M. & HAASS, C. 2012. Arginine methylation next to the PY-NLS modulates Transportin binding and nuclear import of FUS. *EMBO J,* 31**,** 4258-75.

DORMANN, D., RODDE, R., EDBAUER, D., BENTMANN, E., FISCHER, I., HRUSCHA, A., THAN, M. E., MACKENZIE, I. R., CAPELL, A., SCHMID, B., NEUMANN, M. & HAASS, C. 2010. ALS-associated fused in sarcoma (FUS) mutations disrupt Transportin-mediated nuclear import. *EMBO J,* 29**,** 2841-57.

DOZ, F., VAN TILBURG, C. M., GEOERGER, B., HOJGAARD, M., ORA, I., BONI, V., CAPRA, M., CHISHOLM, J., CHUNG, H. C., DUBOIS, S. G., GALLEGO-MELCON, S., GERBER, N. U., GOTO, H., GRILLEY-OLSON, J. E., HANSFORD, J. R., HONG, D. S., ITALIANO, A., KANG, H. J., NYSOM, K., THORWARTH, A., STEFANOWICZ, J., TAHARA, M., ZIEGLER, D. S., GAVRILOVIC, I. T., NORENBERG, R., DIMA, L., DE LA CUESTA, E., LAETSCH, T. W., DRILON, A. & PERREAULT, S. 2022. Efficacy and safety of larotrectinib in TRK fusion-positive primary central nervous system tumors. *Neuro Oncol,* 24**,** 997-1007.

DRILON, A., OU, S. I., CHO, B. C., KIM, D. W., LEE, J., LIN, J. J., ZHU, V. W., AHN, M. J., CAMIDGE, D. R., NGUYEN, J., ZHAI, D., DENG, W., HUANG, Z., ROGERS, E., LIU, J., WHITTEN, J., LIM, J. K., STOPATSCHINSKAJA, S., HYMAN, D. M., DOEBELE, R. C., CUI, J. J. & SHAW, A. T. 2018. Repotrectinib (TPX-0005) Is a Next-Generation ROS1/TRK/ALK Inhibitor That Potently Inhibits ROS1/TRK/ALK Solvent- Front Mutations. *Cancer Discov,* 8**,** 1227-1236.

DU, H., WANG, X., DONG, R., HU, D. & XIONG, Y. 2019. miR-601 inhibits proliferation, migration and invasion of prostate cancer stem cells by targeting KRT5 to inactivate the Wnt signaling pathway. *Int J Clin Exp Pathol,* 12**,** 4361-4379.

DYMOVA, M. A., KULIGINA, E. V. & RICHTER, V. A. 2021. Molecular Mechanisms of Drug Resistance in Glioblastoma. *Int J Mol Sci,* 22.

EATMANN, A.I., HAMOUDA, E., HAMOUDA, H., FAROUK, H.K., JOBRAN, A.W., OMAR, A.A., MADEEH, A.K., AL-DARDERY, N.M., ELNOAMANY, S., ABD-ELNASSER, E.G. AND KORAIEM, A.M., 2023. Potential use of thalidomide in glioblastoma treatment: an updated brief overview. *Metabolites*, *13*(4), p.543.

EDEN, C. J., JU, B., MURUGESAN, M., PHOENIX, T. N., NIMMERVOLL, B., TONG, Y., ELLISON, D. W., FINKELSTEIN, D., WRIGHT, K., BOULOS, N., DAPPER, J., THIRUVENKATAM, R., LESSMAN, C. A., TAYLOR, M. R. & GILBERTSON, R. J. 2015. Orthotopic models of pediatric brain tumors in zebrafish. *Oncogene,* 34**,** 1736-42.

EDEN, E., LIPSON, D., YOGEV, S. & YAKHINI, Z. 2007. Discovering motifs in ranked lists of DNA sequences. *PLoS Comput Biol,* 3**,** e39.

EDEN, E., NAVON, R., STEINFELD, I., LIPSON, D. & YAKHINI, Z. 2009. GOrilla: a tool for discovery and visualization of enriched GO terms in ranked gene lists. *BMC Bioinformatics,* 10**,** 48.

EICHHORN, P. J., RODON, L., GONZALEZ-JUNCA, A., DIRAC, A., GILI, M., MARTINEZ-SAEZ, E., AURA, C., BARBA, I., PEG, V., PRAT, A., CUARTAS, I., JIMENEZ, J., GARCIA-DORADO, D., SAHUQUILLO, J., BERNARDS, R., BASELGA, J. & SEOANE, J. 2012. USP15 stabilizes TGF-beta receptor I and promotes oncogenesis through the activation of TGF-beta signaling in glioblastoma. *Nat Med,* 18**,** 429-35.

EL MESKINI, R., IACOVELLI, A. J., KULAGA, A., GUMPRECHT, M., MARTIN, P. L., BARAN, M., HOUSEHOLDER, D. B., VAN DYKE, T. & WEAVER OHLER, Z. 2015. A preclinical orthotopic model for glioblastoma recapitulates key features of human tumors and demonstrates sensitivity to a combination of MEK and PI3K pathway inhibitors. *Dis Model Mech,* 8**,** 45-56.

ELAKOUM, R., GAUCHOTTE, G., OUSSALAH, A., WISSLER, M. P., CLEMENT-DUCHENE, C., VIGNAUD, J. M., GUEANT, J. L. & NAMOUR, F. 2014. CARM1 and PRMT1 are dysregulated in lung cancer without hierarchical features. *Biochimie,* 97**,** 210-8.

EL-KHOUEIRY, A. B., CLARKE, J., NEFF, T., CROSSMAN, T., RATIA, N., RATHI, C., NOTO, P., TARKAR, A., GARRIDO-LAGUNA, I., CALVO, E., RODON, J., TRAN, B., O'DWYER, P. J., CUKER, A. & ABDUL RAZAK, A. R. 2023. Phase 1 study of GSK3368715, a type I PRMT inhibitor, in patients with advanced solid tumors. *Br J Cancer*.

ELLERT-MIKLASZEWSKA, A., POLESZAK, K., PASIERBINSKA, M. & KAMINSKA, B. 2020. Integrin Signaling in Glioma Pathogenesis: From Biology to Therapy. *Int J Mol Sci,* 21.

ELLOR, S. V., PAGANO-YOUNG, T. A. & AVGEROPOULOS, N. G. 2014. Glioblastoma: background, standard treatment paradigms, and supportive care considerations. *J Law Med Ethics,* 42**,** 171-82.

ELMORE, S. 2007. Apoptosis: a review of programmed cell death. *Toxicol Pathol,* 35**,** 495-516.

ENDERLIN, M., KLEINMANN, E. V., STRUYF, S., BURACCHI, C., VECCHI, A., KINSCHERF, R., KIESSLING, F., PASCHEK, S., SOZZANI, S., ROMMELAERE, J., CORNELIS, J. J., VAN DAMME, J. & DINSART, C. 2009. TNF-alpha and the IFN-gamma-inducible protein 10 (IP-10/CXCL-10) delivered by parvoviral vectors act in synergy to induce antitumor effects in mouse glioblastoma. *Cancer Gene Ther,* 16**,** 149-60.

ENGLAND, B., HUANG, T. & KARSY, M. 2013. Current understanding of the role and targeting of tumor suppressor p53 in glioblastoma multiforme. *Tumour Biol,* 34**,** 2063-74.

ERAM, M. S., SHEN, Y., SZEWCZYK, M., WU, H., SENISTERRA, G., LI, F., BUTLER, K. V., KANISKAN, H. U., SPEED, B. A., DELA SENA, C., DONG, A., ZENG, H., SCHAPIRA, M., BROWN, P. J., ARROWSMITH, C. H., BARSYTE-LOVEJOY, D., LIU, J., VEDADI, M. & JIN, J. 2016. A Potent, Selective, and Cell-Active Inhibitor of Human Type I Protein Arginine Methyltransferases. *ACS Chem Biol,* 11**,** 772-781.

ESCOBAR-HOYOS, L. F., SHAH, R., ROA-PENA, L., VANNER, E. A., NAJAFIAN, N., BANACH, A., NIELSEN, E., AL-KHALIL, R., AKALIN, A., TALMAGE, D. & SHROYER, K. R. 2015. Keratin-17 Promotes p27KIP1 Nuclear Export and Degradation and Offers Potential Prognostic Utility. *Cancer Res,* 75**,** 3650-62.

FABIAN, D., GUILLERMO PRIETO EIBL, M. D. P., ALNAHHAS, I., SEBASTIAN, N., GIGLIO, P., PUDUVALLI, V., GONZALEZ, J. & PALMER, J. D. 2019. Treatment of Glioblastoma (GBM) with the Addition of Tumor-Treating Fields (TTF): A Review. *Cancers (Basel),* 11.

FAN, C. H., LIU, W. L., CAO, H., WEN, C., CHEN, L. & JIANG, G. 2013. O6-methylguanine DNA methyltransferase as a promising target for the treatment of temozolomide-resistant gliomas. *Cell Death Dis,* 4**,** e876.

FAN, X., LIANG, J., SHAN, X., QIAO, H. & JIANG, T. 2017. Expression of HLA-DR genes in gliomas: correlation with clinicopathological features and prognosis. *Chinese Neurosurgical Journal,* 3.

FANG, R., CHEN, X., ZHANG, S., SHI, H., YE, Y., SHI, H., ZOU, Z., LI, P., GUO, Q., MA, L., HE, C. & HUANG, S. 2021. EGFR/SRC/ERK-stabilized YTHDF2 promotes cholesterol dysregulation and invasive growth of glioblastoma. *Nat Commun,* 12**,** 177.

FAROOQ, M., KHAN, A. W., KIM, M. S. & CHOI, S. 2021. The Role of Fibroblast Growth Factor (FGF) Signaling in Tissue Repair and Regeneration. *Cells,* 10.

FAVIA, A., SALVATORI, L., NANNI, S., IWAMOTO-STOHL, L. K., VALENTE, S., MAI, A., SCAGNOLI, F., FONTANELLA, R. A., TOTTA, P., NASI, S. & ILLI, B. 2019. The Protein Arginine Methyltransferases 1 and 5 affect Myc properties in glioblastoma stem cells. *Sci Rep,* 9**,** 15925.

FECTEAU, A. H., PENN, I. & HANTO, D. W. 1998. Peritoneal metastasis of intracranial glioblastoma via a ventriculoperitoneal shunt preventing organ retrieval: case report and review of the literature. *Clin Transplant,* 12**,** 348-50.

FEDORIW, A., RAJAPURKAR, S. R., O'BRIEN, S., GERHART, S. V., MITCHELL, L. H., ADAMS, N. D., RIOUX, N., LINGARAJ, T., RIBICH, S. A., PAPPALARDI, M. B., SHAH, N., LARAIO, J., LIU, Y., BUTTICELLO, M., CARPENTER, C. L., CREASY, C., KORENCHUK, S., MCCABE, M. T., MCHUGH, C. F., NAGARAJAN, R., WAGNER, C., ZAPPACOSTA, F., ANNAN, R., CONCHA, N. O., THOMAS, R. A., HART, T. K., SMITH, J. J., COPELAND, R. A., MOYER, M. P., CAMPBELL, J., STICKLAND, K., MILLS, J., JACQUES-O'HAGAN, S., ALLAIN, C., JOHNSTON, D., RAIMONDI, A., PORTER SCOTT, M., WATERS, N., SWINGER, K., BORIACK-SJODIN, A., RIERA, T., SHAPIRO, G., CHESWORTH, R., PRINJHA, R. K., KRUGER, R. G., BARBASH, O. & MOHAmMAD, H. P. 2019. Anti-tumor Activity of the Type I PRMT Inhibitor, GSK3368715, Synergizes with PRMT5 Inhibition through MTAP Loss. *Cancer Cell,* 36**,** 100-114 e25.

FENG, J., DANG, Y., ZHANG, W., ZHAO, X., ZHANG, C., HOU, Z., JIN, Y., MCNUTT, M. A., MARKS, A. R. & YIN, Y. 2019. PTEN arginine methylation by PRMT6 suppresses PI3K-AKT signaling and modulates pre-mRNA splicing. *Proc Natl Acad Sci U S A,* 116**,** 6868-6877.

FENG, Y., MAITY, R., WHITELEGGE, J. P., HADJIKYRIACOU, A., LI, Z., ZURITA-LOPEZ, C., AL-HADID, Q., CLARK, A. T., BEDFORD, M. T., MASSON, J. Y. & CLARKE, S. G. 2013. Mammalian protein arginine methyltransferase 7 (PRMT7) specifically targets RXR sites in lysine- and arginine-rich regions. *J Biol Chem,* 288**,** 37010-25.

FERREIRA DE FREITAS, R., ERAM, M. S., SMIL, D., SZEWCZYK, M. M., KENNEDY, S., BROWN, P. J., SANTHAKUMAR, V., BARSYTE-LOVEJOY, D., ARROWSMITH, C. H., VEDADI, M. & SCHAPIRA, M. 2016. Correction to Discovery of a Potent and Selective Coactivator Associated Arginine Methyltransferase 1 (CARM1) Inhibitor by Virtual Screening. *J Med Chem,* 59**,** 7698.

FISCON, G., CONTE, F. & PACI, P. 2018. SWIM tool application to expression data of glioblastoma stem-like cell lines, corresponding primary tumors and conventional glioma cell lines. *BMC Bioinformatics,* 19**,** 436.

FITCH, C. A., PLATZER, G., OKON, M., GARCIA-MORENO, B. E. & MCINTOSH, L. P. 2015. Arginine: Its pKa value revisited. *Protein Sci,* 24**,** 752-61.

FLORES-ROMERO, H., ROS, U. & GARCIA-SAEZ, A. J. 2020. Pore formation in regulated cell death. *EMBO J,* 39**,** e105753.

FONG, J. Y., PIGNATA, L., GOY, P. A., KAWABATA, K. C., LEE, S. C., KOH, C. M., MUSIANI, D., MASSIGNANI, E., KOTINI, A. G., PENSON, A., WUN, C. M., SHEN, Y., SCHWARZ, M., LOW, D. H., RIALDI, A., KI, M., WOLLMANN, H., MZOUGHI, S., GAY, F., THOMPSON, C., HART, T., BARBASH, O., LUCIANI, G. M., SZEWCZYK, M. M., WOUTERS, B. J., DELWEL, R., PAPAPETROU, E. P., BARSYTE-LOVEJOY, D., ARROWSMITH, C. H., MINDEN, M. D., JIN, J., MELNICK, A., BONALDI, T., ABDEL-WAHAB, O. & GUCCIONE, E. 2019. Therapeutic Targeting of RNA Splicing Catalysis through Inhibition of Protein Arginine Methylation. *Cancer Cell,* 36**,** 194-209 e9.

FOX, B. M., JANSSEN, A., ESTEVEZ-ORDONEZ, D., GESSLER, F., VICARIO, N., CHAGOYA, G., ELSAYED, G., SOTOUDEH, H., STETLER, W., FRIEDMAN, G. K. & BERNSTOCK, J. D. 2019. SUMOylation in Glioblastoma: A Novel Therapeutic Target. *Int J Mol Sci,* 20.

FRANCESCHI, E., TOSONI, A., MINICHILLO, S., DEPENNI, R., PACCAPELO, A., BARTOLINI, S., MICHIARA, M., PAVESI, G., URBINI, B., CRISI, G., CAVALLO, M. A., TOSATTO, L., DAZZI, C., BIASINI, C., PASINI, G., BALESTRINI, D., ZANELLI, F., RAMPONI, V., FIORAVANTI, A., GIOMBELLI, E., DE BIASE, D., BARUZZI, A., BRANDES, A. A. & GROUP, P. S. 2018. The Prognostic Roles of Gender and O6-Methylguanine-DNA Methyltransferase Methylation Status in Glioblastoma Patients: The Female Power. *World Neurosurg,* 112**,** e342-e347.

FRANCESCHI, S., MAZZANTI, C. M., LESSI, F., ARETINI, P., CARBONE, F. G., M, L. A. F., SCATENA, C., ORTENZI, V., VANNOZZI, R., FANELLI, G., PASQUALETTI, F., BEVILACQUA, G., ZAVAGLIA, K. & NACCARATO, A. G. 2015. Investigating molecular alterations to profile short- and long-term recurrence-free survival in patients with primary glioblastoma. *Oncol Lett,* 10**,** 3599-3606.

FREEDMAN, L. P., GIBSON, M. C., ETHIER, S. P., SOULE, H. R., NEVE, R. M. & REID, Y. A. 2015. Reproducibility: changing the policies and culture of cell line authentication. *Nat Methods,* 12**,** 493-7.

FU, M., ZHOU, Z., HUANG, X., CHEN, Z., ZHANG, L., ZHANG, J., HUA, W. & MAO, Y. 2023. Use of Bevacizumab in recurrent glioblastoma: a scoping review and evidence map. *BMC Cancer,* 23**,** 544.

FURNARI, F. B., CLOUGHESY, T. F., CAVENEE, W. K. & MISCHEL, P. S. 2015. Heterogeneity of epidermal growth factor receptor signalling networks in glioblastoma. *Nat Rev Cancer,* 15**,** 302-10.

FURNESVIK, L., ERKINHARJU, T., HANSEN, M., YOUSAF, M. N. & SETERNES, T. 2022. Evaluation of histological post-mortem changes in farmed Atlantic salmon (Salmo salar L.) at different time intervals and storage temperatures. *J Fish Dis,* 45**,** 1571-1580.

FYLLINGEN, E. H., BO, L. E., REINERTSEN, I., JAKOLA, A. S., SAGBERG, L. M., BERNTSEN, E. M., SALVESEN, O. & SOLHEIM, O. 2021. Survival of glioblastoma in relation to tumor location: a statistical tumor atlas of a population-based cohort. *Acta Neurochir (Wien),* 163**,** 1895-1905.

GAILLARD, F. S., R.; MURPHY, A. *ET AL.* 2008. Glioblastoma, IDH-wildtype. *Radiopaedia.org*.

GALLIVAN, J. P. & DOUGHERTY, D. A. 1999. Cation-pi interactions in structural biology. *Proc Natl Acad Sci U S A,* 96**,** 9459-64.

GALLO, L. H., KO, J. & DONOGHUE, D. J. 2017. The importance of regulatory ubiquitination in cancer and metastasis. *Cell Cycle,* 16**,** 634-648.

GANESH, L., YOSHIMOTO, T., MOORTHY, N. C., AKAHATA, W., BOEHM, M., NABEL, E. G. & NABEL, G. J. 2006. Protein methyltransferase 2 inhibits NF-kappaB function and promotes apoptosis. *Mol Cell Biol,* 26**,** 3864-74.

GAO, Y. F., MAO, X. Y., ZHU, T., MAO, C. X., LIU, Z. X., WANG, Z. B., LI, L., LI, X., YIN, J. Y., ZHANG, W., ZHOU, H. H. & LIU, Z. Q. 2016. COL3A1 and SNAP91: novel glioblastoma markers with diagnostic and prognostic value. *Oncotarget,* 7**,** 70494-70503.

GAO, Y. F., ZHU, T., CHEN, J., LIU, L. & OUYANG, R. 2018. Knockdown of collagen alpha-1(III) inhibits glioma cell proliferation and migration and is regulated by miR128-3p. *Oncol Lett,* 16**,** 1917-1923.

GARG, R., BENEDETTI, L. G., ABERA, M. B., WANG, H., ABBA, M. & KAZANIETZ, M. G. 2014. Protein kinase C and cancer: what we know and what we do not. *Oncogene,* 33**,** 5225-37.

GARNIER, D., MEEHAN, B., KISLINGER, T., DANIEL, P., SINHA, A., ABDULKARIM, B., NAKANO, I. & RAK, J. 2018. Divergent evolution of temozolomide resistance in glioblastoma stem cells is reflected in extracellular vesicles and coupled with radiosensitization. *Neuro Oncol,* 20**,** 236-248.

GE, S. X., JUNG, D. & YAO, R. 2020. ShinyGO: a graphical gene-set enrichment tool for animals and plants. *Bioinformatics,* 36**,** 2628-2629.

GENG, P., ZHANG, Y., LIU, X., ZHANG, N., LIU, Y., LIU, X., LIN, C., YAN, X., LI, Z., WANG, G., LI, Y., TAN, J., LIU, D. X., HUANG, B. & LU, J. 2017. Automethylation of protein arginine methyltransferase 7 and its impact on breast cancer progression. *FASEB J,* 31**,** 2287-2300.

GENOUD, V., MARINARI, E., NIKOLAEV, S. I., CASTLE, J. C., BUKUR, V., DIETRICH, P. Y., OKADA, H. & WALKER, P. R. 2018. Responsiveness to anti-PD-1 and anti-CTLA-4 immune checkpoint blockade in SB28 and GL261 mouse glioma models. *Oncoimmunology,* 7**,** e1501137.

GHANBARPANAH, E., KOHANPOUR, M. A., HOSSEINI-BEHESHTI, F., YARI, L. & KESHVARI, M. 2018. Structure and function of FUS gene in prostate cancer. *Bratisl Lek Listy,* 119**,** 660-663.

GHILDIYAL, R. & SEN, E. 2017. Concerted action of histone methyltransferases G9a and PRMT-1 regulates PGC-1alpha-RIG-I axis in IFNgamma treated glioma cells. *Cytokine,* 89**,** 185-193.

GHIMENTI, C., FIANO, V., CHIADO-PIAT, L., CHIO, A., CAVALLA, P. & SCHIFFER, D. 2003. Deregulation of the p14ARF/Mdm2/p53 pathway and G1/S transition in two glioblastoma sets. *J Neurooncol,* 61**,** 95-102.

GHOUZLANI, A., KANDOUSSI, S., TALL, M., REDDY, K. P., RAFII, S. & BADOU, A. 2021. Immune Checkpoint Inhibitors in Human Glioma Microenvironment. *Front Immunol,* 12**,** 679425.

GILBERT, M. R., WANG, M., ALDAPE, K. D., STUPP, R., HEGI, M. E., JAECKLE, K. A., ARMSTRONG, T. S., WEFEL, J. S., WON, M., BLUMENTHAL, D. T., MAHAJAN, A., SCHULTZ, C. J., ERRIDGE, S., BAUMERT, B., HOPKINS, K. I., TZUK-SHINA, T., BROWN, P. D., CHAKRAVARTI, A., CURRAN, W. J., JR. & MEHTA, M. P. 2013. Dose-dense temozolomide for newly diagnosed glioblastoma: a randomized phase III clinical trial. *J Clin Oncol,* 31**,** 4085-91.

GIL-GIL, M. J., MESIA, C., REY, M. & BRUNA, J. 2013. Bevacizumab for the treatment of glioblastoma. *Clin Med Insights Oncol,* 7**,** 123-35.

Glioblastoma Multiforme. *South. Clin. Ist. Euras,* 29**,** 203-205.

GLIOMODEL. 2012. *GlioModel: A Preclinical Modelling Resource for High Grade Glioma* [Online]. [Accessed 21st June 2021].

GOBEIL, S., BOUCHER, C. C., NADEAU, D. & POIRIER, G. G. 2001. Characterization of the necrotic cleavage of poly(ADP-ribose) polymerase (PARP-1): implication of lysosomal proteases. *Cell Death Differ,* 8**,** 588-94.

GOENKA, A., TIEK, D., SONG, X., HUANG, T., HU, B. & CHENG, S. Y. 2021. The Many Facets of Therapy Resistance and Tumor Recurrence in Glioblastoma. *Cells,* 10.

GOFF, S. L., MORGAN, R. A., YANG, J. C., SHERRY, R. M., ROBBINS, P. F., RESTIFO, N. P., FELDMAN, S. A., LU, Y. C., LU, L., ZHENG, Z., XI, L., EPSTEIN, M., MCINTYRE, L. S., MALEKZADEH, P., RAFFELD, M., FINE, H. A. & ROSENBERG, S. A. 2019. Pilot Trial of Adoptive Transfer of Chimeric Antigen Receptor-transduced T Cells Targeting EGFRvIII in Patients With Glioblastoma. *J Immunother,* 42**,** 126-135.

GOLD, S. M., WILLING, A., LEYPOLDT, F., PAUL, F. & FRIESE, M. A. 2019. Sex differences in autoimmune disorders of the central nervous system. *Semin Immunopathol,* 41**,** 177-188.

GOLDSTROHM, A. C., ALBRECHT, T. R., SUNE, C., BEDFORD, M. T. & GARCIA-BLANCO, M. A. 2001. The transcription elongation factor CA150 interacts with RNA polymerase II and the pre-mRNA splicing factor SF1. *Mol Cell Biol,* 21**,** 7617-28.

GOMEZ-OLIVA, R., DOMINGUEZ-GARCIA, S., CARRASCAL, L., ABALOS-MARTINEZ, J., PARDILLO-DIAZ, R., VERASTEGUI, C., CASTRO, C., NUNEZ-ABADES, P. & GERIBALDI-DOLDAN, N. 2020. Evolution of Experimental Models in the Study of Glioblastoma: Toward Finding Efficient Treatments. *Front Oncol,* 10**,** 614295.

GOMORI, E., PAL, J., KOVACS, B. & DOCZI, T. 2012. Concurrent hypermethylation of DNMT1, MGMT and EGFR genes in progression of gliomas. *Diagn Pathol,* 7**,** 8.

GOTZ, M. & HUTTNER, W. B. 2005. The cell biology of neurogenesis. *Nat Rev Mol Cell Biol,* 6**,** 777-88.

GOULET, I., GAUVIN, G., BOISVENUE, S. & COTE, J. 2007. Alternative splicing yields protein arginine methyltransferase 1 isoforms with distinct activity, substrate specificity, and subcellular localization. *J Biol Chem,* 282**,** 33009-21.

GREENE, J., SEGARAN, A. & LORD, S. 2022. Targeting OXPHOS and the electron transport chain in cancer; Molecular and therapeutic implications. *Semin Cancer Biol,* 86**,** 851-859.

GRIFFIN, M., KHAN, R., BASU, S. & SMITH, S. 2020. Ion Channels as Therapeutic Targets in High Grade Gliomas. *Cancers (Basel),* 12.

GU, C., GAO, F., ZHANG, S., KANG, L., ZHANG, W., FENG, X., LIU, J., TIAN, Y., WEI, Q., DU, Y., XING, Y., LIU, Q. & LIU, S. 2023a. Role of SUMOylation of STAT1 in tubular epithelial-mesenchymal transition induced by high glucose. *Mol Med Rep,* 27.

GU, Y., FANG, Y., WU, X., XU, T., HU, T., XU, Y., MA, P., WANG, Q. & SHU, Y. 2023b. The emerging roles of SUMOylation in the tumor microenvironment and therapeutic implications. *Exp Hematol Oncol,* 12**,** 58.

GUCCIONE, E. & RICHARD, S. 2019. Author Correction: The regulation, functions and clinical relevance of arginine methylation. *Nat Rev Mol Cell Biol,* 20**,** 567.

GUCCIONE, E., BASSI, C., CASADIO, F., MARTINATO, F., CESARONI, M., SCHUCHLAUTZ, H., LUSCHER, B. & AMATI, B. 2007. Methylation of histone H3R2 by PRMT6 and H3K4 by an MLL complex are mutually exclusive. *Nature,* 449**,** 933-7.

GUO, C. C., ZHANG, X. L., YANG, B., GENG, J., PENG, B. & ZHENG, J. H. 2014. Decreased expression of Dkk1 and Dkk3 in human clear cell renal cell carcinoma. *Mol Med Rep,* 9**,** 2367-73.

GUO, G., GONG, K., BECKLEY, N., ZHANG, Y., YANG, X., CHKHEIDZE, R., HATANPAA, K. J., GARZON-MUVDI, T., KODURU, P., NAYAB, A., JENKS, J., SATHE, A. A., LIU, Y., XING, C., WU, S. Y., CHIANG, C. M., MUKHERJEE, B., BURMA, S., WOHLFELD, B., PATEL, T., MICKEY, B., ABDULLAH, K., YOUSSEF, M., PAN, E., GERBER, D. E., TIAN, S., SARKARIA, J. N., MCBRAYER, S. K., ZHAO, D. & HABIB, A. A. 2022. EGFR ligand shifts the role of EGFR from oncogene to tumour suppressor in EGFR-amplified glioblastoma by suppressing invasion through BIN3 upregulation. *Nat Cell Biol,* 24**,** 1291-1305.

GUO, Z., ZHANG, Z., YANG, H., CAO, D., XU, X., ZHENG, X., CHEN, D., WANG, Q., LI, Y., LI, J., DU, Z., WANG, X., CHEN, L., DING, J., SHEN, J., GENG, M., HUANG, X. & XIONG, B. 2019. Design and Synthesis of Potent, Selective Inhibitors of Protein Arginine Methyltransferase 4 against Acute Myeloid Leukemia. *J Med Chem,* 62**,** 5414-5433.

GUPTA, M. K., POLISETTY, R. V., RAMAMOORTHY, K., TIWARY, S., KAUR, N., UPPIN, M. S., SHIRAS, A. & SIRDESHMUKH, R. 2013. Secretome analysis of Glioblastoma cell line--HNGC-2. *Mol Biosyst,* 9**,** 1390-400.

HABIBEY, R., ROJO ARIAS, J. E., STRIEBEL, J. & BUSSKAMP, V. 2022. Microfluidics for Neuronal Cell and Circuit Engineering. *Chem Rev,* 122**,** 14842-14880.

HADDAD, A. F., YOUNG, J. S., AMARA, D., BERGER, M. S., RALEIGH, D. R., AGHI, M. K. & BUTOWSKI, N. A. 2021. Mouse models of glioblastoma for the evaluation of novel therapeutic strategies. *Neurooncol Adv,* 3**,** vdab100.

HADJIKYRIACOU, A., YANG, Y., ESPEJO, A., BEDFORD, M. T. & CLARKE, S. G. 2015. Unique Features of Human Protein Arginine Methyltransferase 9 (PRMT9) and Its Substrate RNA Splicing Factor SF3B2. *J Biol Chem,* 290**,** 16723-43.

HAGHANDISH, N., BALDWIN, R. M., MORETTIN, A., DAWIT, H. T., ADHIKARY, H., MASSON, J. Y., MAZROUI, R., TRINKLE-MULCAHY, L. & COTE, J. 2019. PRMT7 methylates eukaryotic translation initiation factor 2alpha and regulates its role in stress granule formation. *Mol Biol Cell,* 30**,** 778-793.

HALABELIAN, L. & BARSYTE-LOVEJOY, D. 2021. Structure and Function of Protein Arginine Methyltransferase PRMT7. *Life (Basel),* 11.

HAN, S., LI, Z., MASTER, L. M., MASTER, Z. W. & WU, A. 2014. Exogenous IGFBP-2 promotes proliferation, invasion, and chemoresistance to temozolomide in glioma cells via the integrin beta1-ERK pathway. *Br J Cancer,* 111**,** 1400-9.

HANAHAN, D. & WEINBERG, R. A. 2000. The hallmarks of cancer. *Cell,* 100**,** 57-70.

HANAHAN, D. & WEINBERG, R. A. 2011. Hallmarks of cancer: the next generation. *Cell,* 144**,** 646-74.

HANNA, C., KURIAN, K. M., WILLIAMS, K., WATTS, C., JACKSON, A., CARRUTHERS, R., STRATHDEE, K., CRUICKSHANK, G., DUNN, L., ERRIDGE, S., GODFREY, L., JEFFERIES, S., MCBAIN, C., SLEIGH, R., MCCORMICK, A., PITTMAN, M., HALFORD, S. & CHALMERS, A. J. 2020. Pharmacokinetics, safety, and tolerability of olaparib and temozolomide for recurrent glioblastoma: results of the phase I OPARATIC trial. *Neuro Oncol,* 22**,** 1840-1850.

HARNED, R. K., BUCK, J. L., OLMSTED, W. W., MOSER, R. P. & ROS, P. R. 1991. Extracolonic manifestations of the familial adenomatous polyposis syndromes. *AJR Am J Roentgenol,* 156**,** 481-5.

HARTLEY, A. V., WANG, B., JIANG, G., WEI, H., SUN, M., PRABHU, L., MARTIN, M., SAFA, A., SUN, S., LIU, Y. & LU, T. 2020. Regulation of a PRMT5/NF-kappaB Axis by Phosphorylation of PRMT5 at Serine 15 in Colorectal Cancer. *Int J Mol Sci,* 21.

HASHEMI, M., ETEMAD, S., REZAEI, S., ZIAOLHAGH, S., RAJABI, R., RAHMANIAN, P., ABDI, S., KOOHPAR, Z. K., RAFIEI, R., RAEI, B., AHMADI, F., SALIMIMOGHADAM, S., AREF, A. R., ZANDIEH, M. A., ENTEZARI, M., TAHERIAZAM, A. & HUSHMANDI, K. 2023. Progress in targeting PTEN/PI3K/Akt axis in glioblastoma therapy: Revisiting molecular interactions. *Biomed Pharmacother,* 158**,** 114204.

HASHIMOTO, M., FUKAMIZU, A., NAKAGAWA, T. & KIZUKA, Y. 2021. Roles of protein arginine methyltransferase 1 (PRMT1) in brain development and disease. *Biochim Biophys Acta Gen Subj,* 1865**,** 129776.

HE, Z., CUI, L., PAULE, M. G. & FERGUSON, S. A. 2015. Estrogen Selectively Mobilizes Neural Stem Cells in the Third Ventricle Stem Cell Niche of Postnatal Day 21 Rats. *Mol Neurobiol,* 52**,** 927-33.

HERCEG, Z. & WANG, Z. Q. 1999. Failure of poly(ADP-ribose) polymerase cleavage by caspases leads to induction of necrosis and enhanced apoptosis. *Mol Cell Biol,* 19**,** 5124-33.

HERRLINGER, U., TZARIDIS, T., MACK, F., STEINBACH, J. P., SCHLEGEL, U., SABEL, M., HAU, P., KORTMANN, R. D., KREX, D., GRAUER, O., GOLDBRUNNER, R., SCHNELL, O., BAHR, O., UHL, M., SEIDEL, C., TABATABAI, G., KOWALSKI, T., RINGEL, F., SCHMIDT-GRAF, F., SUCHORSKA, B., BREHMER, S., WEYERBROCK, A., RENOVANZ, M., BULLINGER, L., GALLDIKS, N., VAJKOCZY, P., MISCH, M., VATTER, H., STUPLICH, M., SCHAFER, N., KEBIR, S., WELLER, J., SCHAUB, C., STUMMER, W., TONN, J. C., SIMON, M., KEIL, V. C., NELLES, M., URBACH, H., COENEN, M., WICK, W., WELLER, M., FIMMERS, R., SCHMID, M., HATTINGEN, E., PIETSCH, T., COCH, C., GLAS, M. & NEUROONCOLOGY WORKING GROUP OF THE GERMAN CANCER, S. 2019. Lomustine-temozolomide combination therapy versus standard temozolomide therapy in patients with newly diagnosed glioblastoma with methylated MGMT promoter (CeTeG/NOA-09): a randomised, open-label, phase 3 trial. *Lancet,* 393**,** 678-688.

HERVAS-STUBBS, S., PEREZ-GRACIA, J. L., ROUZAUT, A., SANMAMED, M. F., LE BON, A. & MELERO, I. 2011. Direct effects of type I interferons on cells of the immune system. *Clin Cancer Res,* 17**,** 2619-27.

HEVEL, J. M. & PRICE, O. M. 2020. Rapid and direct measurement of methyltransferase activity in about 30 min. *Methods,* 175**,** 3-9.

HIDALGO, M., AMANT, F., BIANKIN, A. V., BUDINSKA, E., BYRNE, A. T., CALDAS, C., CLARKE, R. B., DE JONG, S., JONKERS, J., MAELANDSMO, G. M., ROMAN-ROMAN, S., SEOANE, J., TRUSOLINO, L. & VILLANUEVA, A. 2014. Patient-derived xenograft models: an emerging platform for translational cancer research. *Cancer Discov,* 4**,** 998-1013.

HIGA, N., AKAHANE, T., HAMADA, T., YONEZAWA, H., UCHIDA, H., MAKINO, R., WATANABE, S., TAKAJO, T., YOKOYAMA, S., KIRISHIMA, M., MATSUO, K., FUJIO, S., HANAYA, R., TANIMOTO, A. & YOSHIMOTO, K. 2023. Distribution and favorable prognostic implication of genomic EGFR alterations in IDH-wildtype glioblastoma. *Cancer Med,* 12**,** 49-60.

HOFWEBER, M., HUTTEN, S., BOURGEOIS, B., SPREITZER, E., NIEDNER-BOBLENZ, A., SCHIFFERER, M., RUEPP, M. D., SIMONS, M., NIESSING, D., MADL, T. & DORMANN, D. 2018. Phase Separation of FUS Is Suppressed by Its Nuclear Import Receptor and Arginine Methylation. *Cell,* 173**,** 706-719 e13.

HONDA, M., NAKASHIMA, K. & KATADA, S. 2017. PRMT1 regulates astrocytic differentiation of embryonic neural stem/precursor cells. *J Neurochem,* 142**,** 901-907.

HONIKL, L. S., LAMMER, F., GEMPT, J., MEYER, B., SCHLEGEL, J. & DELBRIDGE, C. 2020. High expression of estrogen receptor alpha and aromatase in glial tumor cells is associated with gender-independent survival benefits in glioblastoma patients. *J Neurooncol,* 147**,** 567-575.

HORI, K., MATSUMINE, A., NIIMI, R., MAEDA, M., UCHIDA, K., NAKAMURA, T. & SUDO, A. 2010. Diffuse gliomas in an adolescent with multiple enchondromatosis (Ollier's disease). *Oncol Lett,* 1**,** 595-597.

HOU, W., IZADI, M., NEMITZ, S., HAAG, N., KESSELS, M. M. & QUALMANN, B. 2015. The Actin Nucleator Cobl Is Controlled by Calcium and Calmodulin. *PLoS Biol,* 13**,** e1002233.

HOU, W., NEMITZ, S., SCHOPPER, S., NIELSEN, M. L., KESSELS, M. M. & QUALMANN, B. 2018. Arginine Methylation by PRMT2 Controls the Functions of the Actin Nucleator Cobl. *Dev Cell,* 45**,** 262-275 e8.

HOU, Z., YANG, J., WANG, H., LIU, D. & ZHANG, H. 2019. A Potential Prognostic Gene Signature for Predicting Survival for Glioblastoma Patients. *Biomed Res Int,* 2019**,** 9506461.

HSIEH, D., HSIEH, A., STEA, B. & ELLSWORTH, R. 2010. IGFBP2 promotes glioma tumor stem cell expansion and survival. *Biochem Biophys Res Commun,* 397**,** 367-72.

HSU, J. M., CHEN, C. T., CHOU, C. K., KUO, H. P., LI, L. Y., LIN, C. Y., LEE, H. J., WANG, Y. N., LIU, M., LIAO, H. W., SHI, B., LAI, C. C., BEDFORD, M. T., TSAI, C. H. & HUNG, M. C. 2011. Crosstalk between Arg 1175 methylation and Tyr 1173 phosphorylation negatively modulates EGFR-mediated ERK activation. *Nat Cell Biol,* 13**,** 174-81.

HU, J. L., OMOFOYE, O. A., RUDNICK, J. D., KIM, S., TIGHIOUART, M., PHUPHANICH, S., WANG, H., MAZER, M., GANAWAY, T., CHU, R. M., PATIL, C. G., BLACK, K. L., SHIAO, S. L., WANG, R. & YU, J. S. 2022. A Phase I Study of Autologous Dendritic Cell Vaccine Pulsed with Allogeneic Stem-like Cell Line Lysate in Patients with Newly Diagnosed or Recurrent Glioblastoma. *Clin Cancer Res,* 28**,** 689-696.

HU, L., SHEN, D., LIANG, D., SHI, J., SONG, C., JIANG, K., MENGLIN, R., DU, S., CHENG, W., MA, J., LI, S., BI, X., BARR, M. P., FANG, Z., XU, Q., LI, W., PIAO, H. & MENG, S. 2020a. Thyroid receptor-interacting protein 13 and EGFR form a feedforward loop promoting glioblastoma growth. *Cancer Lett,* 493**,** 156-166.

HU, Z., MI, Y., QIAN, H., GUO, N., YAN, A., ZHANG, Y. & GAO, X. 2020b. A Potential Mechanism of Temozolomide Resistance in Glioma-Ferroptosis. *Front Oncol,* 10**,** 897.

HUA, Z. Y., HANSEN, J. N., HE, M., DAI, S. K., CHOI, Y., FULTON, M. D., LLOYD, S. M., SZEMES, M., SEN, J., DING, H. F., ANGELASTRO, J. M., FEI, X., LI, H. P., WU, C. R., YANG, S. Y., MALIK, K., BAO, X., GEORGE ZHENG, Y., LIU, C. M., SCHOR, N. F., LI, Z. J. & LI, X. G. 2020. PRMT1 promotes neuroblastoma cell survival through ATF5. *Oncogenesis,* 9**,** 50.

HUANG, J., VOGEL, G., YU, Z., ALMAZAN, G. & RICHARD, S. 2011. Type II arginine methyltransferase PRMT5 regulates gene expression of inhibitors of differentiation/DNA binding Id2 and Id4 during glial cell differentiation. *J Biol Chem,* 286**,** 44424-32.

HUANG, Q., LIU, Y., CHENG, Y., JIA, F., PU, C., YAN, Q., CHANG, Z., LIAO, P., MA, D., XU, L., ZHANG, H., LU, Y., LIU, X. & LIU, K. 2023. High-throughput quantitation of serological dimethylarginines by LC/MS/MS: Potential cardiovascular biomarkers for rheumatoid arthritis. *J Pharm Biomed Anal,* 232**,** 115336.

HUANG, T., YANG, Y., SONG, X., WAN, X., WU, B., SASTRY, N., HORBINSKI, C. M., ZENG, C., TIEK, D., GOENKA, A., LIU, F., BRENNAN, C. W., KESSLER, J. A., STUPP, R., NAKANO, I., SULMAN, E. P., NISHIKAWA, R., JAMES, C. D., ZHANG, W., XU, W., HU, B. & CHENG, S. Y. 2021. PRMT6 methylation of RCC1 regulates mitosis, tumorigenicity, and radiation response of glioblastoma stem cells. *Mol Cell*.

HUANG, X., AGRAWAL, I., LI, Z., ZHENG, W., LIN, Q. & GONG, Z. 2016. Transcriptomic Analyses in Zebrafish Cancer Models for Global Gene Expression and Pathway Discovery. *Adv Exp Med Biol,* 916**,** 147-68.

HUBERT, C. G., RIVERA, M., SPANGLER, L. C., WU, Q., MACK, S. C., PRAGER, B. C., COUCE, M., MCLENDON, R. E., SLOAN, A. E. & RICH, J. N. 2016. A Three-Dimensional Organoid Culture System Derived from Human Glioblastomas Recapitulates the Hypoxic Gradients and Cancer Stem Cell Heterogeneity of Tumors Found In Vivo. *Cancer Res,* 76**,** 2465-77.

HUMPHREYS, L. M., SMITH, P., CHEN, Z., FOUAD, S. & D'ANGIOLELLA, V. 2021. The role of E3 ubiquitin ligases in the development and progression of glioblastoma. *Cell Death Differ,* 28**,** 522-537.

HUSZTHY, P. C., DAPHU, I., NICLOU, S. P., STIEBER, D., NIGRO, J. M., SAKARIASSEN, P. O., MILETIC, H., THORSEN, F. & BJERKVIG, R. 2012. In vivo models of primary brain tumors: pitfalls and perspectives. *Neuro Oncol,* 14**,** 979-93.

HWANG, J. W., CHO, Y., BAE, G. U., KIM, S. N. & KIM, Y. K. 2021. Protein arginine methyltransferases: promising targets for cancer therapy. *Exp Mol Med,* 53**,** 788-808.

HWANG, J. W., KIM, S. N., MYUNG, N., SONG, D., HAN, G., BAE, G. U., BEDFORD, M. T. & KIM, Y. K. 2020. PRMT5 promotes DNA repair through methylation of 53BP1 and is regulated by Src-mediated phosphorylation. *Commun Biol,* 3**,** 428.

IKO, Y., KODAMA, T. S., KASAI, N., OYAMA, T., MORITA, E. H., MUTO, T., OKUMURA, M., FUJII, R., TAKUMI, T., TATE, S. & MORIKAWA, K. 2004. Domain architectures and characterization of an RNA-binding protein, TLS. *J Biol Chem,* 279**,** 44834-40.

IYAPPAN, S., WOLLSCHEID, H. P., ROJAS-FERNANDEZ, A., MARQUARDT, A., TANG, H. C., SINGH, R. K. & SCHEFFNER, M. 2010. Turning the RING domain protein MdmX into an active ubiquitin-protein ligase. *J Biol Chem,* 285**,** 33065-33072.

JANJUA, T. I., REWATKAR, P., AHMED-COX, A., SAEED, I., MANSFELD, F. M., KULSHRESHTHA, R., KUMERIA, T., ZIEGLER, D. S., KAVALLARIS, M., MAZZIERI, R. & POPAT, A. 2021. Frontiers in the treatment of glioblastoma: Past, present and emerging. *Adv Drug Deliv Rev,* 171**,** 108-138.

JANSSON, M., DURANT, S. T., CHO, E. C., SHEAHAN, S., EDELMANN, M., KESSLER, B. & LA THANGUE, N. B. 2008. Arginine methylation regulates the p53 response. *Nat Cell Biol,* 10**,** 1431-9.

JARROLD, J. & DAVIES, C. C. 2019. PRMTs and Arginine Methylation: Cancer's Best-Kept Secret? *Trends Mol Med,* 25**,** 993-1009.

JARZEBSKA, N., MANGONI, A. A., MARTENS-LOBENHOFFER, J., BODE-BOGER, S. M. & RODIONOV, R. N. 2019. The Second Life of Methylarginines as Cardiovascular Targets. *Int J Mol Sci,* 20.

JEONG, H. J., LEE, S. J., LEE, H. J., KIM, H. B., ANH VUONG, T., CHO, H., BAE, G. U. & KANG, J. S. 2020. Prmt7 promotes myoblast differentiation via methylation of p38MAPK on arginine residue 70. *Cell Death Differ,* 27**,** 573-586.

JONATHAN, E. C., BERNHARD, E. J. & MCKENNA, W. G. 1999. How does radiation kill cells? *Curr Opin Chem Biol,* 3**,** 77-83.

JONES, D., WILSON, L., THOMAS, H., GAUGHAN, L. & WADE, M. A. 2019. The Histone Demethylase Enzymes KDM3A and KDM4B Co-Operatively Regulate Chromatin Transactions of the Estrogen Receptor in Breast Cancer. *Cancers (Basel),* 11.

JOSEPH, J. V., VAN ROOSMALEN, I. A., BUSSCHERS, E., TOMAR, T., CONROY, S., EGGENS-MEIJER, E., PENARANDA FAJARDO, N., PORE, M. M., BALASUBRAMANYIAN, V., WAGEMAKERS, M., COPRAY, S., DEN DUNNEN, W. F. & KRUYT, F. A. 2015. Serum-Induced Differentiation of Glioblastoma Neurospheres Leads to Enhanced Migration/Invasion Capacity That Is Associated with Increased MMP9. *PLoS One,* 10**,** e0145393.

JOVANOVIC, P., ZORIC, L., STEFANOVIC, I., DZUNIC, B., DJORDJEVIC-JOCIC, J., RADENKOVIC, M. & JOVANOVIC, M. 2010. Lactate dehydrogenase and oxidative stress activity in primary open-angle glaucoma aqueous humour. *Bosn J Basic Med Sci,* 10**,** 83-8.

JOVCEVSKA, I. 2019. Genetic secrets of long-term glioblastoma survivors. *Bosn J Basic Med Sci,* 19**,** 116-124.

JU, B., CHEN, W., SPITSBERGEN, J. M., LU, J., VOGEL, P., PETERS, J. L., WANG, Y. D., ORR, B. A., WU, J., HENSON, H. E., JIA, S., PARUPALLI, C. & TAYLOR, M. R. 2014. Activation of Sonic hedgehog signaling in neural progenitor cells promotes glioma development in the zebrafish optic pathway. *Oncogenesis,* 3**,** e96.

JU, U. I., PARK, J. W., PARK, H. S., KIM, S. J. & CHUN, Y. S. 2015. FBXO11 represses cellular response to hypoxia by destabilizing hypoxia-inducible factor-1alpha mRNA. *Biochem Biophys Res Commun,* 464**,** 1008-1015.

JUNG, C. S., FOERCH, C., SCHANZER, A., HECK, A., PLATE, K. H., SEIFERT, V., STEINMETZ, H., RAABE, A. & SITZER, M. 2007. Serum GFAP is a diagnostic marker for glioblastoma multiforme. *Brain,* 130**,** 3336-41.

KAFKA, A., BUKOVAC, A., BRGLEZ, E., JARMEK, A. M., POLJAK, K., BRLEK, P., ZARKOVIC, K., NJIRIC, N. & PECINA-SLAUS, N. 2021. Methylation Patterns of DKK1, DKK3 and GSK3beta Are Accompanied with Different Expression Levels in Human Astrocytoma. *Cancers (Basel),* 13.

KAINA, B. & CHRISTMANN, M. 2019. DNA repair in personalized brain cancer therapy with temozolomide and nitrosoureas. *DNA Repair (Amst),* 78**,** 128-141.

KAINA, B. 2023. Temozolomide, Procarbazine and Nitrosoureas in the Therapy of Malignant Gliomas: Update of Mechanisms, Drug Resistance and Therapeutic Implications. *J Clin Med,* 12.

KAJA, S., PAYNE, A. J., NAUMCHUK, Y. & KOULEN, P. 2017. Quantification of Lactate Dehydrogenase for Cell Viability Testing Using Cell Lines and Primary Cultured Astrocytes. *Curr Protoc Toxicol,* 72**,** 2 26 1-2 26 10.

KALUEFF, A. V., STEWART, A. M. & GERLAI, R. 2014. Zebrafish as an emerging model for studying complex brain disorders. *Trends Pharmacol Sci,* 35**,** 63-75.

KALYA, M., KEL, A., WLOCHOWITZ, D., WINGENDER, E. & BEISSBARTH, T. 2021. IGFBP2 Is a Potential Master Regulator Driving the Dysregulated Gene Network Responsible for Short Survival in Glioblastoma Multiforme. *Front Genet,* 12**,** 670240.

KAMURA, T., SATO, S., IWAI, K., CZYZYK-KRZESKA, M., CONAWAY, R. C. & CONAWAY, J. W. 2000. Activation of HIF1alpha ubiquitination by a reconstituted von Hippel-Lindau (VHL) tumor suppressor complex. *Proc Natl Acad Sci U S A,* 97**,** 10430-5.

KANDERI, T., MUNAKOMI, S. & GUPTA, V. 2024. Glioblastoma Multiforme. *StatPearls.* Treasure Island (FL).

KANISKAN, H. U., SZEWCZYK, M. M., YU, Z., ERAM, M. S., YANG, X., SCHMIDT, K., LUO, X., DAI, M., HE, F., ZANG, I., LIN, Y., KENNEDY, S., LI, F., DOBROVETSKY, E., DONG, A., SMIL, D., MIN, S. J., LANDON, M., LIN-JONES, J., HUANG, X. P., ROTH, B. L., SCHAPIRA, M., ATADJA, P., BARSYTE-LOVEJOY, D., ARROWSMITH, C. H., BROWN, P. J., ZHAO, K., JIN, J. & VEDADI, M. 2015. A potent, selective and cell-active allosteric inhibitor of protein arginine methyltransferase 3 (PRMT3). *Angew Chem Int Ed Engl,* 54**,** 5166-70.

KANTARI, C. & WALCZAK, H. 2011. Caspase-8 and bid: caught in the act between death receptors and mitochondria. *Biochim Biophys Acta,* 1813**,** 558-63.

KARI, S., SUBRAMANIAN, K., ALTOMONTE, I. A., MURUGESAN, A., YLI-HARJA, O. & KANDHAVELU, M. 2022. Programmed cell death detection methods: a systematic review and a categorical comparison. *Apoptosis,* 27**,** 482-508.

KARKHANIS, V., WANG, L., TAE, S., HU, Y. J., IMBALZANO, A. N. & SIF, S. 2012. Protein arginine methyltransferase 7 regulates cellular response to DNA damage by methylating promoter histones H2A and H4 of the polymerase delta catalytic subunit gene, POLD1. *J Biol Chem,* 287**,** 29801-14.

KARNATI, H. K., PANIGRAHI, M., SHAIK, N. A., GREIG, N. H., BAGADI, S. A., KAMAL, M. A. & KAPALAVAYI, N. 2014. Down regulated expression of Claudin-1 and Claudin-5 and up regulation of beta-catenin: association with human glioma progression. *CNS Neurol Disord Drug Targets,* 13**,** 1413-26.

KATZ, J. E., DLAKIC, M. & CLARKE, S. 2003. Automated identification of putative methyltransferases from genomic open reading frames. *Mol Cell Proteomics,* 2**,** 525-40.

KEUNEN, O., JOHANSSON, M., OUDIN, A., SANZEY, M., RAHIM, S. A., FACK, F., THORSEN, F., TAXT, T., BARTOS, M., JIRIK, R., MILETIC, H., WANG, J., STIEBER, D., STUHR, L., MOEN, I., RYGH, C. B., BJERKVIG, R. & NICLOU, S. P. 2011. Anti-VEGF treatment reduces blood supply and increases tumor cell invasion in glioblastoma. *Proc Natl Acad Sci U S A,* 108**,** 3749-54.

KFOURY, N., SUN, T., YU, K., ROCKWELL, N., TINKUM, K. L., QI, Z., WARRINGTON, N. M., MCDONALD, P., ROY, A., WEIR, S. J., MOHILA, C. A., DENEEN, B. & RUBIN, J. B. 2018. Cooperative p16 and p21 action protects female astrocytes from transformation. *Acta Neuropathol Commun,* 6**,** 12.

KHAN, I., WAQAS, M. & SHAMIM, M. S. 2017. Prognostic significance of IDH 1 mutation in patients with glioblastoma multiforme. *J Pak Med Assoc,* 67**,** 816-817.

KHOR, Z. W. A. L., H. 2017. PP76. DO LEVELS OF MGMT PROMOTER METHYLATION CORRELATE WITH SURVIVAL AND SENSITIVITY TO TEMOLOZOMIDE? THE NHS TAYSIDE EXPERIENCE. *Neuro Oncology,* 19.

KIM, E., KIM, M., WOO, D. H., SHIN, Y., SHIN, J., CHANG, N., OH, Y. T., KIM, H., RHEEY, J., NAKANO, I., LEE, C., JOO, K. M., RICH, J. N., NAM, D. H. & LEE, J. 2013. Phosphorylation of EZH2 activates STAT3 signaling via STAT3 methylation and promotes tumorigenicity of glioblastoma stem-like cells. *Cancer Cell,* 23**,** 839-52.

KIM, J. D., PARK, K. E., ISHIDA, J., KAKO, K., HAMADA, J., KANI, S., TAKEUCHI, M., NAMIKI, K., FUKUI, H., FUKUHARA, S., HIBI, M., KOBAYASHI, M., KANAHO, Y., KASUYA, Y., MOCHIZUKI, N. & FUKAMIZU, A. 2015. PRMT8 as a phospholipase regulates Purkinje cell dendritic arborization and motor coordination. *Sci Adv,* 1**,** e1500615.

KIM, K. M., SHIM, J. K., CHANG, J. H., LEE, J. H., KIM, S. H., CHOI, J., PARK, J., KIM, E. H., KIM, S. H., HUH, Y. M., LEE, S. J., CHEONG, J. H. & KANG, S. G. 2016. Failure of a patient-derived xenograft for brain tumor model prepared by implantation of tissue fragments. *Cancer Cell Int,* 16**,** 43.

KIM, N. W., PIATYSZEK, M. A., PROWSE, K. R., HARLEY, C. B., WEST, M. D., HO, P. L., COVIELLO, G. M., WRIGHT, W. E., WEINRICH, S. L. & SHAY, J. W. 1994. Specific association of human telomerase activity with immortal cells and cancer. *Science,* 266**,** 2011-5.

KIM, S. C., CHO, Y. E., SHIN, Y. K., YU, H. J., CHOWDHURY, T., KIM, S., YI, K. S., CHOI, C. H., CHA, S. H., PARK, C. K. & KU, J. L. 2023. Patient-derived glioblastoma cell lines with conserved genome profiles of the original tissue. *Sci Data,* 10**,** 448.

KIM, S., PARK, S. J., CHOWDHURY, T., HONG, J. I., AHN, J., JEONG, T. Y., YU, H. J., SHIN, Y. K., KU, J. L., PARK, J. B., HUR, J. K., LEE, H., KIM, K. & PARK, C. K. 2022. Subcellular progression of mesenchymal transition identified by two discrete synchronous cell lines derived from the same glioblastoma. *Cell Mol Life Sci,* 79**,** 181.

KIM, T. H., YOON, J. H. & CHO, S. G. 2020. Kisspeptin Promotes Glioblastoma Cell Invasiveness Via the Gq-PLC-PKC Pathway. *Anticancer Res,* 40**,** 213-220.

KIMELBERG, H. K. & NORENBERG, M. D. 1989. Astrocytes. *Sci Am,* 260**,** 66-72, 74, 76.

KISELEVA, L. N., KARTASHEV, A. V., VARTANYAN, N. L., PINEVICH, A. A. & SAMOILOVICH, M. P. 2016. Characteristics of A172 and T98g Cell Lines. *Tsitologiia,* 58**,** 349-55.

KISS, E. A. A. S., P. I. 2019. Anti-angiogenic Targets: Angiopoietin and Angiopoietin-Receptors. . *Tumor Angiogenesis: A Key Target for Cancer Therapy***,** 227-250.

KITAHARA, C. M., LINET, M. S., BRENNER, A. V., WANG, S. S., MELIN, B. S., WANG, Z., INSKIP, P. D., FREEMAN, L. E., BRAGANZA, M. Z., CARREON, T., FEYCHTING, M., GAZIANO, J. M., PETERS, U., PURDUE, M. P., RUDER, A. M., SESSO, H. D., SHU, X. O., WATERS, M. A., WHITE, E., ZHENG, W., HOOVER, R. N., FRAUMENI, J. F., JR., CHATTERJEE, N., YEAGER, M., CHANOCK, S. J., HARTGE, P. & RAJARAMAN, P. 2014. Personal history of diabetes, genetic susceptibility to diabetes, and risk of brain glioma: a pooled analysis of observational studies. *Cancer Epidemiol Biomarkers Prev,* 23**,** 47-54.

KITANGE, G. J., CARLSON, B. L., SCHROEDER, M. A., GROGAN, P. T., LAMONT, J. D., DECKER, P. A., WU, W., JAMES, C. D. & SARKARIA, J. N. 2009. Induction of MGMT expression is associated with temozolomide resistance in glioblastoma xenografts. *Neuro Oncol,* 11**,** 281-91.

KLEINSCHMIDT, M. A., DE GRAAF, P., VAN TEEFFELEN, H. A. & TIMMERS, H. T. 2012. Cell cycle regulation by the PRMT6 arginine methyltransferase through repression of cyclin-dependent kinase inhibitors. *PLoS One,* 7**,** e41446.

KREISL, T. N., SMITH, P., SUL, J., SALGADO, C., IWAMOTO, F. M., SHIH, J. H. & FINE, H. A. 2013. Continuous daily sunitinib for recurrent glioblastoma. *J Neurooncol,* 111**,** 41-8.

KUHN, P., CHUMANOV, R., WANG, Y., GE, Y., BURGESS, R. R. & XU, W. 2011. Automethylation of CARM1 allows coupling of transcription and mRNA splicing. *Nucleic Acids Res,* 39**,** 2717-26.

KUMAR, S., ZENG, Z., BAGATI, A., TAY, R. E., SANZ, L. A., HARTONO, S. R., ITO, Y., ABDERAZZAQ, F., HATCHI, E., JIANG, P., CARTWRIGHT, A. N. R., OLAWOYIN, O., MATHEWSON, N. D., PYRDOL, J. W., LI, M. Z., DOENCH, J. G., BOOKER, M. A., TOLSTORUKOV, M. Y., ELLEDGE, S. J., CHEDIN, F., LIU, X. S. & WUCHERPFENNIG, K. W. 2021. CARM1 Inhibition Enables Immunotherapy of Resistant Tumors by Dual Action on Tumor Cells and T Cells. *Cancer Discov,* 11**,** 2050-2071.

LAHAV, G. 2008. Oscillations by the p53-Mdm2 feedback loop. *Adv Exp Med Biol,* 641**,** 28-38.

LAI, Y., SONG, M., HAKALA, K., WEINTRAUB, S. T. & SHIIO, Y. 2011. Proteomic dissection of the von Hippel-Lindau (VHL) interactome. *J Proteome Res,* 10**,** 5175-82.

LAKS, D. R., OSES-PRIETO, J. A., ALVARADO, A. G., NAKASHIMA, J., CHAND, S., AZZAM, D. B., GHOLKAR, A. A., SPERRY, J., LUDWIG, K., CONDRO, M. C., NAZARIAN, S., CARDENAS, A., SHIH, M. Y. S., DAMOISEAUX, R., FRANCE, B., OROZCO, N., VISNYEI, K., CRISMAN, T. J., GAO, F., TORRES, J. Z., COPPOLA, G., BURLINGAME, A. L. & KORNBLUM, H. I. 2018. A molecular cascade modulates MAP1B and confers resistance to mTOR inhibition in human glioblastoma. *Neuro Oncol,* 20**,** 764-775.

LAMANO, J. B., LAMANO, J. B., LI, Y. D., DIDOMENICO, J. D., CHOY, W., VELICEASA, D., OYON, D. E., FAKURNEJAD, S., AMPIE, L., KESAVABHOTLA, K., KAUR, R., KAUR, G., BIYASHEV, D., UNRUH, D. J., HORBINSKI, C. M., JAMES, C. D., PARSA, A. T. & BLOCH, O. 2019. Glioblastoma-Derived IL6 Induces Immunosuppressive Peripheral Myeloid Cell PD-L1 and Promotes Tumor Growth. *Clin Cancer Res,* 25**,** 3643-3657.

LANDER, E. S., LINTON, L. M., BIRREN, B., NUSBAUM, C., ZODY, M. C., BALDWIN, J., DEVON, K., DEWAR, K., DOYLE, M., FITZHUGH, W., FUNKE, R., GAGE, D., HARRIS, K., HEAFORD, A., HOWLAND, J., KANN, L., LEHOCZKY, J., LEVINE, R., MCEWAN, P., MCKERNAN, K., MELDRIM, J., MESIROV, J. P., MIRANDA, C., MORRIS, W., NAYLOR, J., RAYMOND, C., ROSETTI, M., SANTOS, R., SHERIDAN, A., SOUGNEZ, C., STANGE-THOMANN, Y., STOJANOVIC, N., SUBRAMANIAN, A., WYMAN, D., ROGERS, J., SULSTON, J., AINSCOUGH, R., BECK, S., BENTLEY, D., BURTON, J., CLEE, C., CARTER, N., COULSON, A., DEaDMAN, R., DELOUKAS, P., DUNHAM, A., DUNHAM, I., DURBIN, R., FRENCH, L., GRAFHAM, D., GREGORY, S., HUBBARD, T., HUMPHRAY, S., HUNT, A., JONES, M., LLOYD, C., MCMURRAY, A., MATTHEWS, L., MERCER, S., MILNE, S., MULLIKIN, J. C., MUNGALL, A., PLUMB, R., ROSS, M., SHOWNKEEN, R., SIMS, S., WATERSTON, R. H., WILSON, R. K., HILLIER, L. W., MCPHERSON, J. D., MARRA, M. A., MARDIS, E. R., FULTON, L. A., CHINWALLA, A. T., PEPIN, K. H., GISH, W. R., CHISSOE, S. L., WENDL, M. C., DELEHAUNTY, K. D., MINER, T. L., DELEHAUNTY, A., KRAMER, J. B., COOK, L. L., FULTON, R. S., JOHNSON, D. L., MINX, P. J., CLIFTON, S. W., HAWKINS, T., BRANSCOMB, E., PREDKI, P., RICHARDSON, P., WENNING, S., SLEZAK, T., DOGGETT, N., CHENG, J. F., OLSEN, A., LUCAS, S., ELKIN, C., UBERBACHER, E., FRAZIER, M., *et al.* 2001. Initial sequencing and analysis of the human genome. *Nature,* 409**,** 860-921.

LANE, R., CILIBRASI, C., CHEN, J., SHAH, K., MESSUTI, E., MAZARAKIS, N. K., STEBBING, J., CRITCHLEY, G., SONG, E., SIMON, T. & GIAMAS, G. 2022. PDGF-R inhibition induces glioblastoma cell differentiation via DUSP1/p38(MAPK) signalling. *Oncogene,* 41**,** 2749-2763.

LARIONOVA, T. D., BASTOLA, S., AKSININA, T. E., ANUFRIEVA, K. S., WANG, J., SHENDER, V. O., ANDREEV, D. E., KOVALENKO, T. F., ARAPIDI, G. P., SHNAIDER, P. V., KAZAKOVA, A. N., LATYSHEV, Y. A., TATARSKIY, V. V., SHTIL, A. A., MOREAU, P., GIRAUD, F., LI, C., WANG, Y., RUBTSOVA, M. P., DONTSOVA, O. A., CONDRO, M., ELLINGSON, B. M., SHAKHPARONOV, M. I., KORNBLUM, H. I., NAKANO, I. & PAVLYUKOV, M. S. 2022. Alternative RNA splicing modulates ribosomal composition and determines the spatial phenotype of glioblastoma cells. *Nat Cell Biol,* 24**,** 1541-1557.

LARIVIERE, M. J., SANTOS, P. M. G., HILL-KAYSER, C. E. & METZ, J. M. 2019. Proton Therapy. *Hematol Oncol Clin North Am,* 33**,** 989-1009.

LASSMAN, A. B., PUGH, S. L., WANG, T. J. C., ALDAPE, K., GAN, H. K., PREUSSER, M., VOGELBAUM, M. A., SULMAN, E. P., WON, M., ZHANG, P., MOAZAMI, G., MACSAI, M. S., GILBERT, M. R., BAIN, E. E., BLOT, V., ANSELL, P. J., SAMANTA, S., KUNDU, M. G., ARMSTRONG, T. S., WEFEL, J. S., SEIDEL, C., DE VOS, F. Y., HSU, S., CARDONA, A. F., LOMBARDI, G., BENTSION, D., PETERSON, R. A., GEDYE, C., BOURG, V., WICK, A., CURRAN, W. J. & MEHTA, M. P. 2023. Depatuxizumab mafodotin in EGFR-amplified newly diagnosed glioblastoma: A phase III randomized clinical trial. *Neuro Oncol,* 25**,** 339-350.

LASSMAN, A. B., SEPULVEDA-SANCHEZ, J. M., CLOUGHESY, T. F., GIL-GIL, M. J., PUDUVALLI, V. K., RAIZER, J. J., DE VOS, F. Y. F., WEN, P. Y., BUTOWSKI, N. A., CLEMENT, P. M. J., GROVES, M. D., BELDA-INIESTA, C., GIGLIO, P., SOIFER, H. S., ROWSEY, S., XU, C., AVOGADRI, F., WEI, G., MORAN, S. & ROTH, P. 2022. Infigratinib in Patients with Recurrent Gliomas and FGFR Alterations: A Multicenter Phase II Study. *Clin Cancer Res,* 28**,** 2270-2277.

LATHIA, J. D., MACK, S. C., MULKEARNS-HUBERT, E. E., VALENTIM, C. L. & RICH, J. N. 2015. Cancer stem cells in glioblastoma. *Genes Dev,* 29**,** 1203-17.

LEE, B. J. C., A.E.; SÜEL, K.E.; LOUIS, T.H.; ZHANG, Z. AND CHOOK, Y.M. 2006. Rules for nuclear localization sequence recognition by karyopherin beta 2. *Cell,* 126**,** 543-558.

LEE, J. H. & PAULL, T. T. 2005. ATM activation by DNA double-strand breaks through the Mre11-Rad50-Nbs1 complex. *Science,* 308**,** 551-4.

LEE, J., SAYEGH, J., DANIEL, J., CLARKE, S. & BEDFORD, M. T. 2005. PRMT8, a new membrane-bound tissue-specific member of the protein arginine methyltransferase family. *J Biol Chem,* 280**,** 32890-6.

LEMMON, M. A. 2007. Pleckstrin homology (PH) domains and phosphoinositides. *Biochem Soc Symp***,** 81-93.

LEMMON, M. A., SCHLESSINGER, J. & FERGUSON, K. M. 2014. The EGFR family: not so prototypical receptor tyrosine kinases. *Cold Spring Harb Perspect Biol,* 6**,** a020768.

LERGA, A., HALLIER, M., DELVA, L., ORVAIN, C., GALLAIS, I., MARIE, J. & MOREAU-GACHELIN, F. 2001. Identification of an RNA binding specificity for the potential splicing factor TLS. *J Biol Chem,* 276**,** 6807-16.

LEROY, B., FOURNIER, J. L., ISHIOKA, C., MONTI, P., INGA, A., FRONZA, G. & SOUSSI, T. 2013. The TP53 website: an integrative resource centre for the TP53 mutation database and TP53 mutant analysis. *Nucleic Acids Res,* 41**,** D962-9.

LEWIS, G. D., RIVERA, A. L., TREMONT-LUKATS, I. W., BALLESTER-FUENTES, L. Y., ZHANG, Y. J. & TEH, B. S. 2017. GBM skin metastasis: a case report and review of the literature. *CNS Oncol,* 6**,** 203-9.

LI, B., LIU, L., LI, X. & WU, L. 2015. miR-503 suppresses metastasis of hepatocellular carcinoma cell by targeting PRMT1. *Biochem Biophys Res Commun,* 464**,** 982-987.

LI, D., NI, X. F., TANG, H., ZHANG, J., ZHENG, C., LIN, J., WANG, C., SUN, L. & CHEN, B. 2020. KRT17 Functions as a Tumor Promoter and Regulates Proliferation, Migration and Invasion in Pancreatic Cancer via mTOR/S6k1 Pathway. *Cancer Manag Res,* 12**,** 2087-2095.

LI, H. Y., SUN, C. R., HE, M., YIN, L. C., DU, H. G. & ZHANG, J. M. 2018. Correlation Between Tumor Location and Clinical Properties of Glioblastomas in Frontal and Temporal Lobes. *World Neurosurg,* 112**,** e407-e414.

LI, H., YAN, R., CHEN, W., DING, X., LIU, J., CHEN, G., ZHAO, Q., TANG, Y., LV, S., LIU, S. & YU, Y. 2021a. Long non coding RNA SLC26A4-AS1 exerts antiangiogenic effects in human glioma by upregulating NPTX1 via NFKB1 transcriptional factor. *FEBS J,* 288**,** 212-228.

LI, W. J., HE, Y. H., YANG, J. J., HU, G. S., LIN, Y. A., RAN, T., PENG, B. L., XIE, B. L., HUANG, M. F., GAO, X., HUANG, H. H., ZHU, H. H., YE, F. & LIU, W. 2021b. Profiling PRMT methylome reveals roles of hnRNPA1 arginine methylation in RNA splicing and cell growth. *Nat Commun,* 12**,** 1946.

LI, X., ZHANG, L., XU, J., LIU, C., ZHANG, X., ABDELMONEIM, A. A., ZHANG, Q., KE, J., ZHANG, Y., WANG, L., YANG, F., LUO, C., JIN, J. & YE, F. 2022. Identification, Synthesis, and Biological Evaluations of Potent Inhibitors Targeting Type I Protein Arginine Methyltransferases. *J Chem Inf Model,* 62**,** 692-702.

LI, Y., GAO, Z., WANG, Y., PANG, B., ZHANG, B., HU, R., WANG, Y., LIU, C., ZHANG, X., YANG, J., MEI, M., WANG, Y., ZHOU, X., LI, M. & REN, Y. 2023. Lysine methylation promotes NFAT5 activation and determines temozolomide efficacy in glioblastoma. *Nat Commun,* 14**,** 4062.

LI, Y., ZENG, P. M., WU, J. & LUO, Z. G. 2023. Advances and Applications of Brain Organoids. *Neurosci Bull,* 39**,** 1703-1716.

LI, Z. Y., LI, Q. Z., CHEN, L., CHEN, B. D., WANG, B., ZHANG, X. J. & LI, W. P. 2016. Histone Deacetylase Inhibitor RGFP109 Overcomes Temozolomide Resistance by Blocking NF-kappaB-Dependent Transcription in Glioblastoma Cell Lines. *Neurochem Res,* 41**,** 3192-3205.

LI, Z., JIN, Y., ZOU, Q., SHI, X., WU, Q., LIN, Z., HE, Q., HUANG, G. & QI, S. 2021. Integrated genomic and transcriptomic analysis suggests KRT18 mutation and MTAP are key genetic alterations related to the prognosis between astrocytoma and glioblastoma. *Ann Transl Med,* 9**,** 713.

LI, Z., LIU, J., INUZUKA, H. & WEI, W. 2022. Functional analysis of the emerging roles for the KISS1/KISS1R signaling pathway in cancer metastasis. *J Genet Genomics,* 49**,** 181-184.

LIANG, J. S., LIN, L. J., LIN, H. C., YANG, M. T., WANG, J. S. & LU, J. F. 2018. An unusual GFAP mutation in a Taiwanese child with infantile Alexander disease. *Pediatr Neonatol,* 59**,** 624-627.

LIANG, M., FEI, Y., WANG, Y., CHEN, W., LIU, Z., XU, D., SHEN, H., ZHOU, H. & TANG, J. 2023. Integrative analysis of the role of BOLA2B in human pan-cancer. *Front Genet,* 14**,** 1077126.

LIAO, Y., LUO, Z., LIN, Y., CHEN, H., CHEN, T., XU, L., ORGUREK, S., BERRY, K., DZIECIATKOWSKA, M., REISZ, J. A., D'ALESSANDRO, A., ZHOU, W. & LU, Q. R. 2022. PRMT3 drives glioblastoma progression by enhancing HIF1A and glycolytic metabolism. *Cell Death Dis,* 13**,** 943.

LIAU, L. M., ASHKAN, K., BREM, S., CAMPIAN, J. L., TRUSHEIM, J. E., IWAMOTO, F. M., TRAN, D. D., ANSSTAS, G., COBBS, C. S., HETH, J. A., SALACZ, M. E., D'ANDRE, S., AIKEN, R. D., MOSHEL, Y. A., NAM, J. Y., PILLAINAYAGAM, C. P., WAGNER, S. A., WALTER, K. A., CHAUDHARY, R., GOLDLUST, S. A., LEE, I. Y., BOTA, D. A., ELINZANO, H., GREWAL, J., LILLEHEI, K., MIKKELSEN, T., WALBERT, T., ABRAM, S., BRENNER, A. J., EWEND, M. G., KHAGI, S., LOVICK, D. S., PORTNOW, J., KIM, L., LOUDON, W. G., MARTINEZ, N. L., THOMPSON, R. C., AVIGAN, D. E., FINK, K. L., GEOFFROY, F. J., GIGLIO, P., GLIGICH, O., KREX, D., LINDHORST, S. M., LUTZKY, J., MEISEL, H. J., NADJI-OHL, M., SANCHIN, L., SLOAN, A., TAYLOR, L. P., WU, J. K., DUNBAR, E. M., ETAME, A. B., KESARI, S., MATHIEU, D., PICCIONI, D. E., BASKIN, D. S., LACROIX, M., MAY, S. A., NEW, P. Z., PLUARD, T. J., TOMS, S. A., TSE, V., PEAK, S., VILLANO, J. L., BATTISTE, J. D., MULHOLLAND, P. J., PEARLMAN, M. L., PETRECCA, K., SCHULDER, M., PRINS, R. M., BOYNTON, A. L. & BOSCH, M. L. 2023. Association of Autologous Tumor Lysate-Loaded Dendritic Cell Vaccination With Extension of Survival Among Patients With Newly Diagnosed and Recurrent Glioblastoma: A Phase 3 Prospective Externally Controlled Cohort Trial. *JAMA Oncol,* 9**,** 112-121.

LIM, M., WELLER, M., IDBAIH, A., STEINBACH, J., FINOCCHIARO, G., RAVAL, R. R., ANSSTAS, G., BAEHRING, J., TAYLOR, J. W., HONNORAT, J., PETRECCA, K., DE VOS, F., WICK, A., SUMRALL, A., SAHEBJAM, S., MELLINGHOFF, I. K., KINOSHITA, M., ROBERTS, M., SLEPETIS, R., WARAD, D., LEUNG, D., LEE, M., REARDON, D. A. & OMURO, A. 2022. Phase III trial of chemoradiotherapy with temozolomide plus nivolumab or placebo for newly diagnosed glioblastoma with methylated MGMT promoter. *Neuro Oncol,* 24**,** 1935-1949.

LIN, J. C., WU, Y. C., YANG, F. C., TSAI, J. T., HUANG, D. Y. & LIU, W. H. 2022. Genome-Wide Association Study Identifies Multiple Susceptibility Loci for Malignant Neoplasms of the Brain in Taiwan. *J Pers Med,* 12.

LIN, W. J., GARY, J. D., YANG, M. C., CLARKE, S. & HERSCHMAN, H. R. 1996. The mammalian immediate-early TIS21 protein and the leukemia-associated BTG1 protein interact with a protein-arginine N-methyltransferase. *J Biol Chem,* 271**,** 15034-44.

LINKOUS, A., BALAMATSIAS, D., SNUDERL, M., EDWARDS, L., MIYAGUCHI, K., MILNER, T., REICH, B., COHEN-GOULD, L., STORASKA, A., NAKAYAMA, Y., SCHENKEIN, E., SINGHANIA, R., CIRIGLIANO, S., MAGDELDIN, T., LIN, Y., NANJANGUD, G., CHADALAVADA, K., PISAPIA, D., LISTON, C. & FINE, H. A. 2019. Modeling Patient-Derived Glioblastoma with Cerebral Organoids. *Cell Rep,* 26**,** 3203-3211 e5.

LIU, C. Z., LIU, X. B., SUN, J., YU, C. Q., YAO, J. C., LIU, Z. & HAO, J. C. 2023. IL8-induced CXCR2 down-regulation in circulating monocytes in hepatocellular carcinoma is partially dependent on MAGL. *BMC Cancer,* 23**,** 626.

LIU, F., ZHAO, X., PERNA, F., WANG, L., KOPPIKAR, P., ABDEL-WAHAB, O., HARR, M. W., LEVINE, R. L., XU, H., TEFFERI, A., DEBLASIO, A., HATLEN, M., MENENDEZ, S. & NIMER, S. D. 2011. JAK2V617F-mediated phosphorylation of PRMT5 downregulates its methyltransferase activity and promotes myeloproliferation. *Cancer Cell,* 19**,** 283-94.

LIU, N., YANG, R., SHI, Y., CHEN, L., LIU, Y., WANG, Z., LIU, S., OUYANG, L., WANG, H., LAI, W., MAO, C., WANG, M., CHENG, Y., LIU, S., WANG, X., ZHOU, H., CAO, Y., XIAO, D. & TAO, Y. 2020. The cross-talk between methylation and phosphorylation in lymphoid-specific helicase drives cancer stem-like properties. *Signal Transduct Target Ther,* 5**,** 197.

LIU, X., CHEN, X., SHI, L., SHAN, Q., CAO, Q., YUE, C., LI, H., LI, S., WANG, J., GAO, S., NIU, M. & YU, R. 2019. The third-generation EGFR inhibitor AZD9291 overcomes primary resistance by continuously blocking ERK signaling in glioblastoma. *J Exp Clin Cancer Res,* 38**,** 219.

LIU, X., SU, Q., ZHANG, X., YANG, W., NING, J., JIA, K., XIN, J., LI, H., YU, L., LIAO, Y. & ZHANG, D. 2022. Recent Advances of Organ-on-a-Chip in Cancer Modeling Research. *Biosensors (Basel),* 12.

LIU, Y., MELIN, B. S., RAJARAMAN, P., WANG, Z., LINET, M., SHETE, S., AMOS, C. I., LAU, C. C., SCHEURER, M. E., TSAVACHIDIS, S., ARMSTRONG, G. N., HOULSTON, R. S., HOSKING, F. J., CLAUS, E. B., BARNHOLTZ-SLOAN, J., LAI, R., IL'YASOVA, D., SCHILDKRAUT, J., SADETZKI, S., JOHANSEN, C., BERNSTEIN, J. L., OLSON, S. H., JENKINS, R. B., LACHANCE, D., VICK, N. A., WRENSCH, M., DAVIS, F., MCCARTHY, B. J., ANDERSSON, U., THOMPSON, P. A., CHANOCK, S., GLIOGENE, C. & BONDY, M. L. 2012. Insight in glioma susceptibility through an analysis of 6p22.3, 12p13.33-12.1, 17q22-23.2 and 18q23 SNP genotypes in familial and non-familial glioma. *Hum Genet,* 131**,** 1507-17.

LO, L. H., DONG, R., LYU, Q. & LAI, K. O. 2020. The Protein Arginine Methyltransferase PRMT8 and Substrate G3BP1 Control Rac1-PAK1 Signaling and Actin Cytoskeleton for Dendritic Spine Maturation. *Cell Rep,* 31**,** 107744.

LOGUN, M., ZHAO, W., MAO, L. & KARUMBAIAH, L. 2018. Microfluidics in Malignant Glioma Research and Precision Medicine. *Adv Biosyst,* 2.

LOMBARDI, G., DE SALVO, G. L., BRANDES, A. A., EOLI, M., RUDA, R., FAEDI, M., LOLLI, I., PACE, A., DANIELE, B., PASQUALETTI, F., RIZZATO, S., BELLU, L., PAMBUKU, A., FARINA, M., MAGNI, G., INDRACCOLO, S., GARDIMAN, M. P., SOFFIETTI, R. & ZAGONEL, V. 2019. Regorafenib compared with lomustine in patients with relapsed glioblastoma (REGOMA): a multicentre, open-label, randomised, controlled, phase 2 trial. *Lancet Oncol,* 20**,** 110-119.

LORY, P., NICOLE, S. & MONTEIL, A. 2020. Neuronal Cav3 channelopathies: recent progress and perspectives. *Pflugers Arch,* 472**,** 831-844.

LOUIS, D. N., PERRY, A., REIFENBERGER, G., VON DEIMLING, A., FIGARELLA-BRANGER, D., CAVENEE, W. K., OHGAKI, H., WIESTLER, O. D., KLEIHUES, P. & ELLISON, D. W. 2016. The 2016 World Health Organization Classification of Tumors of the Central Nervous System: a summary. *Acta Neuropathol,* 131**,** 803-20.

LOUIS, D. N., PERRY, A., WESSELING, P., BRAT, D. J., CREE, I. A., FIGARELLA-BRANGER, D., HAWKINS, C., NG, H. K., PFISTER, S. M., REIFENBERGER, G., SOFFIETTI, R., VON DEIMLING, A. & ELLISON, D. W. 2021. The 2021 WHO Classification of Tumors of the Central Nervous System: a summary. *Neuro Oncol,* 23**,** 1231-1251.

LU, Y. F., CAI, X. L., LI, Z. Z., LV, J., XIANG, Y. A., CHEN, J. J., CHEN, W. J., SUN, W. Y., LIU, X. M. & CHEN, J. B. 2018. LncRNA SNHG16 Functions as an Oncogene by Sponging MiR-4518 and Up-Regulating PRMT5 Expression in Glioma. *Cell Physiol Biochem,* 45**,** 1975-1985.

LV, D., GIMPLE, R. C., ZHONG, C., WU, Q., YANG, K., PRAGER, B. C., GODUGU, B., QIU, Z., ZHAO, L., ZHANG, G., DIXIT, D., LEE, D., SHEN, J. Z., LI, X., XIE, Q., WANG, X., AGNIHOTRI, S. & RICH, J. N. 2022. PDGF signaling inhibits mitophagy in glioblastoma stem cells through N(6)-methyladenosine. *Dev Cell,* 57**,** 1466-1481 e6.

LV, D., JIA, F., HOU, Y., SANG, Y., ALVAREZ, A. A., ZHANG, W., GAO, W. Q., HU, B., CHENG, S. Y., GE, J., LI, Y. & FENG, H. 2017. Histone Acetyltransferase KAT6A Upregulates PI3K/AKT Signaling through TRIM24 Binding. *Cancer Res,* 77**,** 6190-6201.

MACHIDA, Y., NAKAGAWA, M., MATSUNAGA, H., YAMAGUCHI, M., OGAWARA, Y., SHIMA, Y., YAMAGATA, K., KATSUMOTO, T., HATTORI, A., ITOH, M., SEKI, T., NISHIYA, Y., NAKAMURA, K., SUZUKI, K., IMAOKA, T., BABA, D., SUZUKI, M., SAMPETREAN, O., SAYA, H., ICHIMURA, K. & KITABAYASHI, I. 2020. A Potent Blood-Brain Barrier-Permeable Mutant IDH1 Inhibitor Suppresses the Growth of Glioblastoma with IDH1 Mutation in a Patient-Derived Orthotopic Xenograft Model. *Mol Cancer Ther,* 19**,** 375-383.

MACKENZIE, I. R., RADEMAKERS, R. & NEUMANN, M. 2010. TDP-43 and FUS in amyotrophic lateral sclerosis and frontotemporal dementia. *Lancet Neurol,* 9**,** 995-1007.

MAGHSOUDI, S. R., N.; AHMADI, S.; RABIEE, M.; BAGHERZADEH, M. AND KARIMI, M. 2021. Chapter 1 - An overview of microfluidic devices. *In:* KARIMI, M. R. H. A. M. (ed.) *Biomedical Applications of Microfluidic Devices.* Science Direct: Academic Press.

MAJC, B., NOVAK, M., KOPITAR-JERALA, N., JEWETT, A. & BREZNIK, B. 2021. Immunotherapy of Glioblastoma: Current Strategies and Challenges in Tumor Model Development. *Cells,* 10.

MAKSOUD, S. 2021. The Role of the Ubiquitin Proteasome System in Glioma: Analysis Emphasizing the Main Molecular Players and Therapeutic Strategies Identified in Glioblastoma Multiforme. *Mol Neurobiol,* 58**,** 3252-3269.

MANGARAJ, M., NANDA, R. & PANDA, S. 2016. Apolipoprotein A-I: A Molecule of Diverse Function. *Indian J Clin Biochem,* 31**,** 253-9.

MANSOURI, A., HACHEM, L. D., MANSOURI, S., NASSIRI, F., LAPERRIERE, N. J., XIA, D., LINDEMAN, N. I., WEN, P. Y., CHAKRAVARTI, A., MEHTA, M. P., HEGI, M. E., STUPP, R., ALDAPE, K. D. & ZADEH, G. 2019. MGMT promoter methylation status testing to guide therapy for glioblastoma: refining the approach based on emerging evidence and current challenges. *Neuro Oncol,* 21**,** 167-178.

MARJANOVIC, N. D., WEINBERG, R. A. & CHAFFER, C. L. 2013. Cell plasticity and heterogeneity in cancer. *Clin Chem,* 59**,** 168-79.

MARKOULI, M., STREPKOS, D., PAPAVASSILIOU, A. G. & PIPERI, C. 2020. Targeting of endoplasmic reticulum (ER) stress in gliomas. *Pharmacol Res,* 157**,** 104823.

MARON, M. I., CASILL, A. D., GUPTA, V., ROTH, J. S., SIDOLI, S., QUERY, C. C., GAMBLE, M. J. & SHECHTER, D. 2022. Type I and II PRMTs inversely regulate post-transcriptional intron detention through Sm and CHTOP methylation. *Elife,* 11.

MARSDEN, A. J. R., D.R.; BARRY, A.; KHALIL, J.S.; GUINN, B.; KEMP, N.T.; RIVERO, F.; BELTRAN-ALVAREZ, P. 2021. Inhibition of Arginine Methylation Impairs Platelet Function. *ACS Pharmacol. Transl. Sci.,* 4**,** 1567-1577.

MARTINEZ-GARCIA, M., VELASCO, G., PINEDA, E., GIL-GIL, M., ALAMEDA, F., CAPELLADES, J., MARTIN-SOBERON, M. C., LOPEZ-VALERO, I., TOVAR AMBEL, E., FORO, P., TAUS, A., ARUMI, M., HERNANDEZ-LAIN, A. & SEPULVEDA-SANCHEZ, J. M. 2022. Safety and Efficacy of Crizotinib in Combination with Temozolomide and Radiotherapy in Patients with Newly Diagnosed Glioblastoma: Phase Ib GEINO 1402 Trial. *Cancers (Basel),* 14.

MATEJUK, A., BENEDEK, G., BUCALA, R., MATEJUK, S., OFFNER, H. & VANDENBARK, A. A. 2024. MIF contribution to progressive brain diseases. *J Neuroinflammation,* 21**,** 8.

MAWRIN, C., DIETE, S., TREUHEIT, T., KROPF, S., VORWERK, C. K., BOLTZE, C., KIRCHES, E., FIRSCHING, R. & DIETZMANN, K. 2003. Prognostic relevance of MAPK expression in glioblastoma multiforme. *Int J Oncol,* 23**,** 641-8.

MCCORNACK, C., WOODIWISS, T., HARDI, A., YANO, H. & KIM, A. H. 2023. The function of histone methylation and acetylation regulators in GBM pathophysiology. *Front Oncol,* 13**,** 1144184.

MCCRACKEN, D. J., SCHUPPER, A. J., LAKOMKIN, N., MALCOLM, J., PAINTON BRAY, D. & HADJIPANAYIS, C. G. 2022. Turning on the light for brain tumor surgery: A 5-aminolevulinic acid story. *Neuro Oncol,* 24**,** S52-S61.

MCKINNON, C., NANDHABALAN, M., MURRAY, S. A. & PLAHA, P. 2021. Glioblastoma: clinical presentation, diagnosis, and management. *BMJ,* 374**,** n1560.

MEGGIOLARO, A., MOCCIA, V., BRUN, P., PIERNO, M., MISTURA, G., ZAPPULLI, V. & FERRARO, D. 2022. Microfluidic Strategies for Extracellular Vesicle Isolation: Towards Clinical Applications. *Biosensors (Basel),* 13.

MELHEM, J. M., DETSKY, J., LIM-FAT, M. J. & PERRY, J. R. 2022. Updates in IDH-Wildtype Glioblastoma. *Neurotherapeutics,* 19**,** 1705-1723.

MENON, S. S., GURUVAYOORAPPAN, C., SAKTHIVEL, K. M. & RASMI, R. R. 2019. Ki-67 protein as a tumour proliferation marker. *Clin Chim Acta,* 491**,** 39-45.

MEYER, R., WOLF, S. S. & OBENDORF, M. 2007. PRMT2, a member of the protein arginine methyltransferase family, is a coactivator of the androgen receptor. *J Steroid Biochem Mol Biol,* 107**,** 1-14.

MIGLIORI, V. M., J.; PHALKE, S.; LOW, D.; BEZZI, M.; MOK, W.C.; SAHU, S.K.; GUNARATNE, J.; CAPASSO, P.; BASSI, C.; CECATIELLO, V.; DE MARCO, A.; BLACKSTOCK, W.; KUZNETSOV, V.; AMATI, B.; MAPELLI, M. AND GUCCIONE, E. 2012. Symmetric dimethylation of H3R2 is a newly identified histone mark that supports euchromatin maintenance. *Nat Struct Mol Biol,* 19**,** 136-144.

MINNITI, G., LOMBARDI, G. & PAOLINI, S. 2019. Glioblastoma in Elderly Patients: Current Management and Future Perspectives. *Cancers (Basel),* 11.

MIRANDA, A., BLANCO-PRIETO, M., SOUSA, J., PAIS, A. & VITORINO, C. 2017. Breaching barriers in glioblastoma. Part I: Molecular pathways and novel treatment approaches. *Int J Pharm,* 531**,** 372-388.

MITCHELL, L. H., DREW, A. E., RIBICH, S. A., RIOUX, N., SWINGER, K. K., JACQUES, S. L., LINGARAJ, T., BORIACK-SJODIN, P. A., WATERS, N. J., WIGLE, T. J., MORADEI, O., JIN, L., RIERA, T., PORTER-SCOTT, M., MOYER, M. P., SMITH, J. J., CHESWORTH, R. & COPELAND, R. A. 2015. Aryl Pyrazoles as Potent Inhibitors of Arginine Methyltransferases: Identification of the First PRMT6 Tool Compound. *ACS Med Chem Lett,* 6**,** 655-9.

MOHIUDDIN, E. & WAKIMOTO, H. 2021. Extracellular matrix in glioblastoma: opportunities for emerging therapeutic approaches. *Am J Cancer Res,* 11**,** 3742-3754.

MOJAS, N., LOPES, M. & JIRICNY, J. 2007. Mismatch repair-dependent processing of methylation damage gives rise to persistent single-stranded gaps in newly replicated DNA. *Genes Dev,* 21**,** 3342-55.

MOLLIEX, A., TEMIROV, J., LEE, J., COUGHLIN, M., KANAGARAJ, A. P., KIM, H. J., MITTAG, T. & TAYLOR, J. P. 2015. Phase separation by low complexity domains promotes stress granule assembly and drives pathological fibrillization. *Cell,* 163**,** 123-33.

MONGIARDI, M. P., SAVINO, M., BARTOLI, L., BEJI, S., NANNI, S., SCAGNOLI, F., FALCHETTI, M. L., FAVIA, A., FARSETTI, A., LEVI, A., NASI, S. & ILLI, B. 2015. Myc and Omomyc functionally associate with the Protein Arginine Methyltransferase 5 (PRMT5) in glioblastoma cells. *Sci Rep,* 5**,** 15494.

MONTEIRO, A. R., HILL, R., PILKINGTON, G. J. & MADUREIRA, P. A. 2017. The Role of Hypoxia in Glioblastoma Invasion. *Cells,* 6.

MORAWIN, B., TYLUTKA, A., BIELEWICZ, F. & ZEMBRON-LACNY, A. 2023. Diagnostics of inflammaging in relation to sarcopenia. *Front Public Health,* 11**,** 1162385.

MOTTI, M. L. & MECCARIELLO, R. 2019. Minireview: The Epigenetic Modulation of KISS1 in Reproduction and Cancer. *Int J Environ Res Public Health,* 16.

MUKHERJEE, B., BRAHMA, P., MOHAPATRA, T., CHAWLA, S. & DIXIT, M. 2023. Reduced FRG1 expression promotes angiogenesis via activation of the FGF2-mediated ERK/AKT pathway. *FEBS Open Bio,* 13**,** 804-817.

MUNTANE, J. 2011. Harnessing tumor necrosis factor receptors to enhance antitumor activities of drugs. *Chem Res Toxicol,* 24**,** 1610-6.

MURRAY, D. T., KATO, M., LIN, Y., THURBER, K. R., HUNG, I., MCKNIGHT, S. L. & TYCKO, R. 2017. Structure of FUS Protein Fibrils and Its Relevance to Self-Assembly and Phase Separation of Low-Complexity Domains. *Cell,* 171**,** 615-627 e16.

NAKAJIMA, K., TOHYAMA, Y., KOHSAKA, S. & KURIHARA, T. 2002. Ceramide activates microglia to enhance the production/secretion of brain-derived neurotrophic factor (BDNF) without induction of deleterious factors in vitro. *J Neurochem,* 80**,** 697-705.

NAKAYA, T., ALEXIOU, P., MARAGKAKIS, M., CHANG, A. & MOURELATOS, Z. 2013. FUS regulates genes coding for RNA-binding proteins in neurons by binding to their highly conserved introns. *RNA,* 19**,** 498-509.

NASSIRI, F., PATIL, V., YEFET, L. S., SINGH, O., LIU, J., DANG, R. M. A., YAMAGUCHI, T. N., DARAS, M., CLOUGHESY, T. F., COLMAN, H., KUMTHEKAR, P. U., CHEN, C. C., AIKEN, R., GROVES, M. D., ONG, S. S., RAMAKRISHNA, R., VOGELBAUM, M. A., KHAGI, S., KALEY, T., MELEAR, J. M., PEEREBOOM, D. M., RODRIGUEZ, A., YANKELEVICH, M., NAIR, S. G., PUDUVALLI, V. K., ALDAPE, K., GAO, A., LOPEZ-JANEIRO, A., DE ANDREA, C. E., ALONSO, M. M., BOUTROS, P., ROBBINS, J., MASON, W. P., SONABEND, A. M., STUPP, R., FUEYO, J., GOMEZ-MANZANO, C., LANG, F. F. & ZADEH, G. 2023. Oncolytic DNX-2401 virotherapy plus pembrolizumab in recurrent glioblastoma: a phase 1/2 trial. *Nat Med,* 29**,** 1370-1378.

NEFTEL, C., LAFFY, J., FILBIN, M. G., HARA, T., SHORE, M. E., RAHME, G. J., RICHMAN, A. R., SILVERBUSH, D., SHAW, M. L., HEBERT, C. M., DEWITT, J., GRITSCH, S., PEREZ, E. M., GONZALEZ CASTRO, L. N., LAN, X., DRUCK, N., RODMAN, C., DIONNE, D., KAPLAN, A., BERTALAN, M. S., SMALL, J., PELTON, K., BECKER, S., BONAL, D., NGUYEN, Q. D., SERVIS, R. L., FUNG, J. M., MYLVAGANAM, R., MAYR, L., GOJO, J., HABERLER, C., GEYEREGGER, R., CZECH, T., SLAVC, I., NAHED, B. V., CURRY, W. T., CARTER, B. S., WAKIMOTO, H., BRASTIANOS, P. K., BATCHELOR, T. T., STEMMER-RACHAMIMOV, A., MARTINEZ-LAGE, M., FROSCH, M. P., STAMENKOVIC, I., RIGGI, N., RHEINBAY, E., MONJE, M., ROZENBLATT-ROSEN, O., CAHILL, D. P., PATEL, A. P., HUNTER, T., VERMA, I. M., LIGON, K. L., LOUIS, D. N., REGEV, A., BERNSTEIN, B. E., TIROSH, I. & SUVA, M. L. 2019. An Integrative Model of Cellular States, Plasticity, and Genetics for Glioblastoma. *Cell,* 178**,** 835-849 e21.

NEUENSCHWANDER, B., BRANSON, M. & GSPONER, T. 2008. Critical aspects of the Bayesian approach to phase I cancer trials. *Stat Med,* 27**,** 2420-39.

NEUMANN, M., RADEMAKERS, R., ROEBER, S., BAKER, M., KRETZSCHMAR, H. A. & MACKENZIE, I. R. 2009. A new subtype of frontotemporal lobar degeneration with FUS pathology. *Brain,* 132**,** 2922-31.

NEUMANN, M., RADEMAKERS, R., ROEBER, S., BAKER, M., KRETZSCHMAR, H. A. & MACKENZIE, I. R. 2009a. A new subtype of frontotemporal lobar degeneration with FUS pathology. *Brain,* 132**,** 2922-31.

NEUMANN, M., ROEBER, S., KRETZSCHMAR, H. A., RADEMAKERS, R., BAKER, M. & MACKENZIE, I. R. 2009b. Abundant FUS-immunoreactive pathology in neuronal intermediate filament inclusion disease. *Acta Neuropathol,* 118**,** 605-16.

NEUMANN, M., SAMPATHU, D. M., KWONG, L. K., TRUAX, A. C., MICSENYI, M. C., CHOU, T. T., BRUCE, J., SCHUCK, T., GROSSMAN, M., CLARK, C. M., MCCLUSKEY, L. F., MILLER, B. L., MASLIAH, E., MACKENZIE, I. R., FELDMAN, H., FEIDEN, W., KRETZSCHMAR, H. A., TROJANOWSKI, J. Q. & LEE, V. M. 2006. Ubiquitinated TDP-43 in frontotemporal lobar degeneration and amyotrophic lateral sclerosis. *Science,* 314**,** 130-3.

NGUYEN, H. P., LE, A. Q., LIU, E., CESARANO, A., DIMEO, F., PERNA, F., KAPUR, R., WALKER, B. A. & TRAN, N. T. 2023. Protein arginine methyltransferase 1 is a therapeutic vulnerability in multiple myeloma. *Front Immunol,* 14**,** 1239614.

NGUYEN, N., REDFIELD, J., BALLO, M., MICHAEL, M., SORENSON, J., DIBABA, D., WAN, J., RAMOS, G. D. & PANDEY, M. 2021. Identifying the optimal cutoff point for MGMT promoter methylation status in glioblastoma. *CNS Oncol,* 10**,** CNS74.

NOTARANGELO, A., TROMBETTA, D., D'ANGELO, V., PARRELLA, P., PALUMBO, O., STORLAZZI, C. T., IMPERA, L., MUSCARELLA, L. A., LA TORRE, A., AFFUSO, A., FAZIO, V. M., CARELLA, M. & ZELANTE, L. 2014. Establishment and genetic characterization of ANGM-CSS, a novel, immortal cell line derived from a human glioblastoma multiforme. *Int J Oncol,* 44**,** 717-24.

NOTO, P. B., SIKORSKI, T. W., ZAPPACOSTA, F., WAGNER, C. D., MONTES DE OCA, R., SZAPACS, M. E., ANNAN, R. S., LIU, Y., MCHUGH, C. F., MOHAMMAD, H. P., PICCOLI, S. P. & CREASY, C. L. 2020. Identification of hnRNP-A1 as a pharmacodynamic biomarker of type I PRMT inhibition in blood and tumor tissues. *Sci Rep,* 10**,** 22155.

OAKES, S. A. 2020. Endoplasmic Reticulum Stress Signaling in Cancer Cells. *Am J Pathol,* 190**,** 934-946.

OBACZ, J., AVRIL, T., LE RESTE, P. J., URRA, H., QUILLIEN, V., HETZ, C. & CHEVET, E. 2017. Endoplasmic reticulum proteostasis in glioblastoma-From molecular mechanisms to therapeutic perspectives. *Sci Signal,* 10.

OLUBAJO, F., ACHAWAL, S. & GREENMAN, J. 2020. Development of a Microfluidic Culture Paradigm for Ex Vivo Maintenance of Human Glioblastoma Tissue: A New Glioblastoma Model? *Transl Oncol,* 13**,** 1-10.

OLYMPIOS, N., GILARD, V., MARGUET, F., CLATOT, F., DI FIORE, F. & FONTANILLES, M. 2021. TERT Promoter Alterations in Glioblastoma: A Systematic Review. *Cancers (Basel),* 13.

OMURO, A., BRANDES, A. A., CARPENTIER, A. F., IDBAIH, A., REARDON, D. A., CLOUGHESY, T., SUMRALL, A., BAEHRING, J., VAN DEN BENT, M., BAHR, O., LOMBARDI, G., MULHOLLAND, P., TABATABAI, G., LASSEN, U., SEPULVEDA, J. M., KHASRAW, M., VAULEON, E., MURAGAKI, Y., DI GIACOMO, A. M., BUTOWSKI, N., ROTH, P., QIAN, X., FU, A. Z., LIU, Y., POTTER, V., CHALAMANDARIS, A. G., TATSUOKA, K., LIM, M. & WELLER, M. 2023. Radiotherapy combined with nivolumab or temozolomide for newly diagnosed glioblastoma with unmethylated MGMT promoter: An international randomized phase III trial. *Neuro Oncol,* 25**,** 123-134.

OROPESA-AVILA, M., FERNANDEZ-VEGA, A., DE LA MATA, M., MARAVER, J. G., CORDERO, M. D., COTAN, D., DE MIGUEL, M., CALERO, C. P., PAZ, M. V., PAVON, A. D., SANCHEZ, M. A., ZADERENKO, A. P., YBOT-GONZALEZ, P. & SANCHEZ-ALCAZAR, J. A. 2013. Apoptotic microtubules delimit an active caspase free area in the cellular cortex during the execution phase of apoptosis. *Cell Death Dis,* 4**,** e527.

O'ROURKE, D. M., NASRALLAH, M. P., DESAI, A., MELENHORST, J. J., MANSFIELD, K., MORRISSETTE, J. J. D., MARTINEZ-LAGE, M., BREM, S., MALONEY, E., SHEN, A., ISAACS, R., MOHAN, S., PLESA, G., LACEY, S. F., NAVENOT, J. M., ZHENG, Z., LEVINE, B. L., OKADA, H., JUNE, C. H., BROGDON, J. L. & MAUS, M. V. 2017. A single dose of peripherally infused EGFRvIII-directed CAR T cells mediates antigen loss and induces adaptive resistance in patients with recurrent glioblastoma. *Sci Transl Med,* 9.

ORTIZ, R., PERAZZOLI, G., CABEZA, L., JIMENEZ-LUNA, C., LUQUE, R., PRADOS, J. & MELGUIZO, C. 2021. Temozolomide: An Updated Overview of Resistance Mechanisms, Nanotechnology Advances and Clinical Applications. *Curr Neuropharmacol,* 19**,** 513-537.

O'SHEA, J. J., SCHWARTZ, D. M., VILLARINO, A. V., GADINA, M., MCINNES, I. B. & LAURENCE, A. 2015. The JAK-STAT pathway: impact on human disease and therapeutic intervention. *Annu Rev Med,* 66**,** 311-28.

OSSWALD, M., JUNG, E., SAHM, F., SOLECKI, G., VENKATARAMANI, V., BLAES, J., WEIL, S., HORSTMANN, H., WIESTLER, B., SYED, M., HUANG, L., RATLIFF, M., KARIMIAN JAZI, K., KURZ, F. T., SCHMENGER, T., LEMKE, D., GOMMEL, M., PAULI, M., LIAO, Y., HARING, P., PUSCH, S., HERL, V., STEINHAUSER, C., KRUNIC, D., JARAHIAN, M., MILETIC, H., BERGHOFF, A. S., GRIESBECK, O., KALAMAKIS, G., GARASCHUK, O., PREUSSER, M., WEISS, S., LIU, H., HEILAND, S., PLATTEN, M., HUBER, P. E., KUNER, T., VON DEIMLING, A., WICK, W. & WINKLER, F. 2015. Brain tumour cells interconnect to a functional and resistant network. *Nature,* 528**,** 93-8.

OSTROM, Q. T., CIOFFI, G., WAITE, K., KRUCHKO, C. & BARNHOLTZ-SLOAN, J. S. 2021. CBTRUS Statistical Report: Primary Brain and Other Central Nervous System Tumors Diagnosed in the United States in 2014-2018. *Neuro Oncol,* 23**,** iii1-iii105.

OTVOS, B., SILVER, D. J., MULKEARNS-HUBERT, E. E., ALVARADO, A. G., TURAGA, S. M., SORENSEN, M. D., RAYMAN, P., FLAVAHAN, W. A., HALE, J. S., STOLTZ, K., SINYUK, M., WU, Q., JARRAR, A., KIM, S. H., FOX, P. L., NAKANO, I., RICH, J. N., RANSOHOFF, R. M., FINKE, J., KRISTENSEN, B. W., VOGELBAUM, M. A. & LATHIA, J. D. 2016. Cancer Stem Cell-Secreted Macrophage Migration Inhibitory Factor Stimulates Myeloid Derived Suppressor Cell Function and Facilitates Glioblastoma Immune Evasion. *Stem Cells,* 34**,** 2026-39.

OWENS, J. L., BEKETOVA, E., LIU, S., TINSLEY, S. L., ASBERRY, A. M., DENG, X., HUANG, J., LI, C., WAN, J. & HU, C. D. 2020. PRMT5 Cooperates with pICln to Function as a Master Epigenetic Activator of DNA Double-Strand Break Repair Genes. *iScience,* 23**,** 100750.

OZAWA, T., RIESTER, M., CHENG, Y. K., HUSE, J. T., SQUATRITO, M., HELMY, K., CHARLES, N., MICHOR, F. & HOLLAND, E. C. 2014. Most human non-GCIMP glioblastoma subtypes evolve from a common proneural-like precursor glioma. *Cancer Cell,* 26**,** 288-300.

PAHLICH, S., ZAKARYAN, R. P. & GEHRING, H. 2008. Identification of proteins interacting with protein arginine methyltransferase 8: the Ewing sarcoma (EWS) protein binds independent of its methylation state. *Proteins,* 72**,** 1125-37.

PAK, M. L., LAKOWSKI, T. M., THOMAS, D., VHUIYAN, M. I., HUSECKEN, K. & FRANKEL, A. 2011. A protein arginine N-methyltransferase 1 (PRMT1) and 2 heteromeric interaction increases PRMT1 enzymatic activity. *Biochemistry,* 50**,** 8226-40.

PAL, S., BAIOCCHI, R. A., BYRD, J. C., GREVER, M. R., JACOB, S. T. & SIF, S. 2007. Low levels of miR-92b/96 induce PRMT5 translation and H3R8/H4R3 methylation in mantle cell lymphoma. *EMBO J,* 26**,** 3558-69.

PALUCKA, K. & BANCHEREAU, J. 2012. Cancer immunotherapy via dendritic cells. *Nat Rev Cancer,* 12**,** 265-77.

PANDIT, R., CHEN, L. & GOTZ, J. 2020. The blood-brain barrier: Physiology and strategies for drug delivery. *Adv Drug Deliv Rev,* 165-166**,** 1-14.

PAOLILLO, M., COMINCINI, S. & SCHINELLI, S. 2021. In Vitro Glioblastoma Models: A Journey into the Third Dimension. *Cancers (Basel),* 13.

PARK, J., KIM, C. G., SHIM, J. K., KIM, J. H., LEE, H., LEE, J. E., KIM, M. H., HAAM, K., JUNG, I., PARK, S. H., CHANG, J. H., SHIN, E. C. & KANG, S. G. 2019a. Effect of combined anti-PD-1 and temozolomide therapy in glioblastoma. *Oncoimmunology,* 8**,** e1525243.

PARK, S. W., JUN, Y. W., CHOI, H. E., LEE, J. A. & JANG, D. J. 2019b. Deciphering the molecular mechanisms underlying the plasma membrane targeting of PRMT8. *BMB Rep,* 52**,** 601-606.

PARK, Y. W., VOLLMUTH, P., FOLTYN-DUMITRU, M., SAHM, F., AHN, S. S., CHANG, J. H. & KIM, S. H. 2023. The 2021 WHO Classification for Gliomas and Implications on Imaging Diagnosis: Part 1-Key Points of the Fifth Edition and Summary of Imaging Findings on Adult-Type Diffuse Gliomas. *J Magn Reson Imaging,* 58**,** 677-689.

PARONETTO, M. P., ACHSEL, T., MASSIELLO, A., CHALFANT, C. E. & SETTE, C. 2007. The RNA-binding protein Sam68 modulates the alternative splicing of Bcl-x. *J Cell Biol,* 176**,** 929-39.

PATEL, A., LEE, H. O., JAWERTH, L., MAHARANA, S., JAHNEL, M., HEIN, M. Y., STOYNOV, S., MAHAMID, J., SAHA, S., FRANZMANN, T. M., POZNIAKOVSKI, A., POSER, I., MAGHELLI, N., ROYER, L. A., WEIGERT, M., MYERS, E. W., GRILL, S., DRECHSEL, D., HYMAN, A. A. & ALBERTI, S. 2015. A Liquid-to-Solid Phase Transition of the ALS Protein FUS Accelerated by Disease Mutation. *Cell,* 162**,** 1066-77.

PATEL, N. P., LYON, K. A. & HUANG, J. H. 2019. The effect of race on the prognosis of the glioblastoma patient: a brief review. *Neurol Res,* 41**,** 967-971.

PELLICCIARI, C., BOTTONE, M. G. & BIGGIOGERA, M. 1997. Detection of apoptotic cells by annexin V labeling at electron microscopy. *Eur J Histochem,* 41**,** 211-6.

PERRY, J. R., LAPERRIERE, N., O'CALLAGHAN, C. J., BRANDES, A. A., MENTEN, J., PHILLIPS, C., FAY, M., NISHIKAWA, R., CAIRNCROSS, J. G., ROA, W., OSOBA, D., ROSSITER, J. P., SAHGAL, A., HIRTE, H., LAIGLE-DONADEY, F., FRANCESCHI, E., CHINOT, O., GOLFINOPOULOS, V., FARISELLI, L., WICK, A., FEUVRET, L., BACK, M., TILLS, M., WINCH, C., BAUMERT, B. G., WICK, W., DING, K., MASON, W. P. & TRIAL, I. 2017. Short-Course Radiation plus Temozolomide in Elderly Patients with Glioblastoma. *N Engl J Med,* 376**,** 1027-1037.

PERUZZI, P. & CHIOCCA, E. A. 2018. Viruses in cancer therapy - from benchwarmers to quarterbacks. *Nat Rev Clin Oncol,* 15**,** 657-658.

PESIRIDIS, G. S., DIAMOND, E. & VAN DUYNE, G. D. 2009. Role of pICLn in methylation of Sm proteins by PRMT5. *J Biol Chem,* 284**,** 21347-59.

PHILLIPS, H. S., KHARBANDA, S., CHEN, R., FORREST, W. F., SORIANO, R. H., WU, T. D., MISRA, A., NIGRO, J. M., COLMAN, H., SOROCEANU, L., WILLIAMS, P. M., MODRUSAN, Z., FEUERSTEIN, B. G. & ALDAPE, K. 2006. Molecular subclasses of high-grade glioma predict prognosis, delineate a pattern of disease progression, and resemble stages in neurogenesis. *Cancer Cell,* 9**,** 157-73.

PI, Y., FANG, C. L. & SU, Z. Y. 2022. Protein phosphorylation: A potential target in glioma development. *Ibrain,* 8**,** 176-189.

PICKART, C. M. 1997. Targeting of substrates to the 26S proteasome. *FASEB J,* 11**,** 1055-66.

PIENKOWSKI, T., KOWALCZYK, T., CYSEWSKI, D., KRETOWSKI, A. & CIBOROWSKI, M. 2023. Glioma and post-translational modifications: A complex relationship. *Biochim Biophys Acta Rev Cancer,* 1878**,** 189009.

PIERINI, T., NARDELLI, C., LEMA FERNANDEZ, A. G., PIERINI, V., PELLANERA, F., NOFRINI, V., GORELLO, P., MORETTI, M., ARNIANI, S., ROTI, G., GIOVENALI, P., LUPATTELLI, M., METRO, G., MOLICA, C., CASTRIOTO, C., CORINALDESI, R., LAURENTI, M. E., ASCANI, S., MECUCCI, C. & LA STARZA, R. 2020. New somatic TERT promoter variants enhance the Telomerase activity in Glioblastoma. *Acta Neuropathol Commun,* 8**,** 145.

PLIAKOPANOU, A., ANTONOPOULOS, I., DARZENTA, N., SERIFI, I., SIMOS, Y. V., KATSENOS, A. P., BELLOS, S., ALEXIOU, G. A., KYRITSIS, A. P., LEONARDOS, I., VEZYRAKI, P., PESCHOS, D. & TSAMIS, K. I. 2023. Glioblastoma research on zebrafish xenograft models: a systematic review. *Clin Transl Oncol*.

POLAT, B., WOHLLEBEN, G., KOSMALA, R., LISOWSKI, D., MANTEL, F., LEWITZKI, V., LOHR, M., BLUM, R., HERUD, P., FLENTJE, M. & MONORANU, C. M. 2022. Differences in stem cell marker and osteopontin expression in primary and recurrent glioblastoma. *Cancer Cell Int,* 22**,** 87.

POLLARD, S. M., YOSHIKAWA, K., CLARKE, I. D., DANOVI, D., STRICKER, S., RUSSELL, R., BAYANI, J., HEAD, R., LEE, M., BERNSTEIN, M., SQUIRE, J. A., SMITH, A. & DIRKS, P. 2009. Glioma stem cell lines expanded in adherent culture have tumor-specific phenotypes and are suitable for chemical and genetic screens. *Cell Stem Cell,* 4**,** 568-80.

POLSKY, L. R., RENTSCHER, K. E. & CARROLL, J. E. 2022. Stress-induced biological aging: A review and guide for research priorities. *Brain Behav Immun,* 104**,** 97-109.

POMBO ANTUNES, A. R., SCHEYLTJENS, I., LODI, F., MESSIAEN, J., ANTORANZ, A., DUERINCK, J., KANCHEVA, D., MARTENS, L., DE VLAMINCK, K., VAN HOVE, H., KJOLNER HANSEN, S. S., BOSISIO, F. M., VAN DER BORGHT, K., DE VLEESCHOUWER, S., SCIOT, R., BOUWENS, L., VERFAILLIE, M., VANDAMME, N., VANDENBROUCKE, R. E., DE WEVER, O., SAEYS, Y., GUILLIAMS, M., GYSEMANS, C., NEYNS, B., DE SMET, F., LAMBRECHTS, D., VAN GINDERACHTER, J. A. & MOVAHEDI, K. 2021. Single-cell profiling of myeloid cells in glioblastoma across species and disease stage reveals macrophage competition and specialization. *Nat Neurosci,* 24**,** 595-610.

POORNA, M. R., SUDHINDRAN, S., THAMPI, M. V. & MONY, U. 2021. Differentiation of induced pluripotent stem cells to hepatocyte-like cells on cellulose nanofibril substrate. *Colloids Surf B Biointerfaces,* 198**,** 111466.

PRAGER, B. C., BHARGAVA, S., MAHADEV, V., HUBERT, C. G. & RICH, J. N. 2020. Glioblastoma Stem Cells: Driving Resilience through Chaos. *Trends Cancer,* 6**,** 223-235.

PRONIN, S., KOH, C. H. & HUGHES, M. 2017. Effects of Ultraviolet Radiation on Glioma: Systematic Review. *J Cell Biochem,* 118**,** 4063-4071.

PURSHOUSE, K., BULBECK, H. J., ROONEY, A. G., NOBLE, K. E., CARRUTHERS, R. D., THOMPSON, G., HAMERLIK, P., YAP, C., KURIAN, K. M., JEFFERIES, S. J., LOPEZ, J. S., JENKINSON, M. D., HANEMANN, C. O. & STEAD, L. F. 2024. Adult brain tumour research in 2024: Status, challenges and recommendations. *Neuropathol Appl Neurobiol,* 50**,** e12979.

QAMAR, S., WANG, G., RANDLE, S. J., RUGGERI, F. S., VARELA, J. A., LIN, J. Q., PHILLIPS, E. C., MIYASHITA, A., WILLIAMS, D., STROHL, F., MEADOWS, W., FERRY, R., DARDOV, V. J., TARTAGLIA, G. G., FARRER, L. A., KAMINSKI SCHIERLE, G. S., KAMINSKI, C. F., HOLT, C. E., FRASER, P. E., SCHMITT-ULMS, G., KLENERMAN, D., KNOWLES, T., VENDRUSCOLO, M. & ST GEORGE-HYSLOP, P. 2018. FUS Phase Separation Is Modulated by a Molecular Chaperone and Methylation of Arginine Cation-pi Interactions. *Cell,* 173**,** 720-734 e15.

QI, Y., WANG, M. & JIANG, Q. 2022. PABPC1--mRNA stability, protein translation and tumorigenesis. *Front Oncol,* 12**,** 1025291.

RABIN, E. E., HUANG, J., KIM, M., MOZNY, A., LAUING, K. L., PENCO-CAMPILLO, M., ZHAI, L., BOMMI, P., MI, X., POWER, E. A., PRABHU, V. C., ANDERSON, D. E., BARTON, K. P., WALUNAS, T. L., SCHILTZ, G. E., AMIDEI, C., SANCHEZ-GOMEZ, P., THAKKAR, J. P., LUKAS, R. V. & WAINWRIGHT, D. A. 2024. Age-stratified comorbid and pharmacologic analysis of patients with glioblastoma. *Brain Behav Immun Health,* 38**,** 100753.

RADZISHEUSKAYA, A., SHLIAHA, P. V., GRINEV, V., LORENZINI, E., KOVALCHUK, S., SHLYUEVA, D., GORSHKOV, V., HENDRICKSON, R. C., JENSEN, O. N. & HELIN, K. 2019. PRMT5 methylome profiling uncovers a direct link to splicing regulation in acute myeloid leukemia. *Nat Struct Mol Biol,* 26**,** 999-1012.

RAGHAVAN, S., BASKIN, D. S. & SHARPE, M. A. 2020. A "Clickable" Probe for Active MGMT in Glioblastoma Demonstrates Two Discrete Populations of MGMT. *Cancers (Basel),* 12.

RAGLOW, Z. & THOMAS, S. M. 2015. Tumor matrix protein collagen XIalpha1 in cancer. *Cancer Lett,* 357**,** 448-53.

RAIMONDI, V., CICCARESE, F. & CIMINALE, V. 2020. Oncogenic pathways and the electron transport chain: a dangeROS liaison. *Br J Cancer,* 122**,** 168-181.

RAMAKRISHNAN, P. K., SAEED, F., THOMSON, S., CORNS, R., MATHEW, R. K. & SIVAKUMAR, G. 2024. Awake craniotomy for high-grade gliomas - a prospective cohort study in a UK tertiary-centre. *Surgeon,* 22**,** e3-e12.

RAMESH, G., MACLEAN, A. G. & PHILIPP, M. T. 2013. Cytokines and chemokines at the crossroads of neuroinflammation, neurodegeneration, and neuropathic pain. *Mediators Inflamm,* 2013**,** 480739.

RATTI, A. & BURATTI, E. 2016. Physiological functions and pathobiology of TDP-43 and FUS/TLS proteins. *J Neurochem,* 138 Suppl 1**,** 95-111.

REARDON, D. A., BRANDES, A. A., OMURO, A., MULHOLLAND, P., LIM, M., WICK, A., BAEHRING, J., AHLUWALIA, M. S., ROTH, P., BAHR, O., PHUPHANICH, S., SEPULVEDA, J. M., DE SOUZA, P., SAHEBJAM, S., CARLETON, M., TATSUOKA, K., TAITT, C., ZWIRTES, R., SAMPSON, J. & WELLER, M. 2020. Effect of Nivolumab vs Bevacizumab in Patients With Recurrent Glioblastoma: The CheckMate 143 Phase 3 Randomized Clinical Trial. *JAMA Oncol,* 6**,** 1003-1010.

REARDON, D. A., NABORS, L. B., MASON, W. P., PERRY, J. R., SHAPIRO, W., KAVAN, P., MATHIEU, D., PHUPHANICH, S., CSEH, A., FU, Y., CONG, J., WIND, S., EISENSTAT, D. D., GROUP, B. I. T. & THE CANADIAN BRAIN TUMOUR, C. 2015. Phase I/randomized phase II study of afatinib, an irreversible ErbB family blocker, with or without protracted temozolomide in adults with recurrent glioblastoma. *Neuro Oncol,* 17**,** 430-9.

REIMUNDE, P., PENSADO-LOPEZ, A., CARREIRA CRENDE, M., LOMBAO IGLESIAS, V., SANCHEZ, L., TORRECILLA-PARRA, M., RAMIREZ, C. M., ANFRAY, C. & TORRES ANDON, F. 2021. Cellular and Molecular Mechanisms Underlying Glioblastoma and Zebrafish Models for the Discovery of New Treatments. *Cancers (Basel),* 13.

REITHMEIER, T., GRAF, E., PIROTH, T., TRIPPEL, M., PINSKER, M. O. & NIKKHAH, G. 2010. BCNU for recurrent glioblastoma multiforme: efficacy, toxicity and prognostic factors. *BMC Cancer,* 10**,** 30.

RELIER, S., YAZDANI, L., AYAD, O., CHOQUET, A., BOURGAUX, J. F., PRUDHOMME, M., PANNEQUIN, J., MACARI, F. & DAVID, A. 2016. Antibiotics inhibit sphere-forming ability in suspension culture. *Cancer Cell Int,* 16**,** 6.

REN, D., TU, H. C., KIM, H., WANG, G. X., BEAN, G. R., TAKEUCHI, O., JEFFERS, J. R., ZAMBETTI, G. P., HSIEH, J. J. & CHENG, E. H. 2010. BID, BIM, and PUMA are essential for activation of the BAX- and BAK-dependent cell death program. *Science,* 330**,** 1390-3.

RILEY, A., GREEN, V., CHEAH, R., MCKENZIE, G., KARSAI, L., ENGLAND, J. & GREENMAN, J. 2019. A novel microfluidic device capable of maintaining functional thyroid carcinoma specimens ex vivo provides a new drug screening platform. *BMC Cancer,* 19**,** 259.

RILEY, A., JONES, H., ENGLAND, J., KUVSHINOV, D., GREEN, V. & GREENMAN, J. 2021. Identification of soluble tissue-derived biomarkers from human thyroid tissue explants maintained on a microfluidic device. *Oncol Lett,* 22**,** 780.

RIOS, A. F. L., TIRAPELLI, D., CIRINO, M. L. A., RODRIGUES, A. R., RAMOS, E. S. & CARLOTTI, C. G., JR. 2022. Expression of pluripotency-related genes in human glioblastoma. *Neurooncol Adv,* 4**,** vdab163.

RITTIG, S. M., HAENTSCHEL, M., WEIMER, K. J., HEINE, A., MULLER, M. R., BRUGGER, W., HORGER, M. S., MAKSIMOVIC, O., STENZL, A., HOERR, I., RAMMENSEE, H. G., HOLDERRIED, T. A., KANZ, L., PASCOLO, S. & BROSSART, P. 2011. Intradermal vaccinations with RNA coding for TAA generate CD8+ and CD4+ immune responses and induce clinical benefit in vaccinated patients. *Mol Ther,* 19**,** 990-9.

ROBIN, A. M., LEE, I. & KALKANIS, S. N. 2017. Reoperation for Recurrent Glioblastoma Multiforme. *Neurosurg Clin N Am,* 28**,** 407-428.

ROBINS, H. I., WON, M., SEIFERHELD, W. F., SCHULTZ, C. J., CHOUCAIR, A. K., BRACHMAN, D. G., DEMAS, W. F. & MEHTA, M. P. 2006. Phase 2 trial of radiation plus high-dose tamoxifen for glioblastoma multiforme: RTOG protocol BR-0021. *Neuro Oncol,* 8**,** 47-52.

ROBINS, H. I., ZHANG, P., GILBERT, M. R., CHAKRAVARTI, A., DE GROOT, J. F., GRIMM, S. A., WANG, F., LIEBERMAN, F. S., KRAUZE, A., TROTTI, A. M., MOHILE, N., KEE, A. Y., COLMAN, H., CAVALIERE, R., KESARI, S., CHMURA, S. J. & MEHTA, M. 2016. A randomized phase I/II study of ABT-888 in combination with temozolomide in recurrent temozolomide resistant glioblastoma: an NRG oncology RTOG group study. *J Neurooncol,* 126**,** 309-16.

ROCHA PINHEIRO, S. L., LEMOS, F. F. B., MARQUES, H. S., SILVA LUZ, M., DE OLIVEIRA SILVA, L. G., FARIA SOUZA MENDES DOS SANTOS, C., DA COSTA EVANGELISTA, K., CALMON, M. S., SANDE LOUREIRO, M. & FREIRE DE MELO, F. 2023. Immunotherapy in glioblastoma treatment: Current state and future prospects. *World J Clin Oncol,* 14**,** 138-159.

RODRIGUEZ, A. D., HOROWITZ, L. F., CASTRO, K., KENERSON, H., BHATTACHARJEE, N., GANDHE, G., RAMAN, A., MONNAT, R. J., YEUNG, R., ROSTOMILY, R. C. & FOLCH, A. 2020. A microfluidic platform for functional testing of cancer drugs on intact tumor slices. *Lab Chip,* 20**,** 1658-1675.

ROMINIYI, O., AL-TAMIMI, Y. & COLLIS, S. J. 2019. The 'Ins and Outs' of Early Preclinical Models for Brain Tumor Research: Are They Valuable and Have We Been Doing It Wrong? *Cancers (Basel),* 11.

RONG, L., LI, N. & ZHANG, Z. 2022. Emerging therapies for glioblastoma: current state and future directions. *J Exp Clin Cancer Res,* 41**,** 142.

ROSS, J. M., OBERG, J., BRENE, S., COPPOTELLI, G., TERZIOGLU, M., PERNOLD, K., GOINY, M., SITNIKOV, R., KEHR, J., TRIFUNOVIC, A., LARSSON, N. G., HOFFER, B. J. & OLSON, L. 2010. High brain lactate is a hallmark of aging and caused by a shift in the lactate dehydrogenase A/B ratio. *Proc Natl Acad Sci U S A,* 107**,** 20087-92.

ROTHZERG, E., FENG, W., SONG, D., LI, H., WEI, Q., FOX, A., WOOD, D., XU, J. & LIU, Y. 2022. Single-Cell Transcriptome Analysis Reveals Paraspeckles Expression in Osteosarcoma Tissues. *Cancer Inform,* 21**,** 11769351221140101.

RUPPRECHT, A., THEISEN, U., WENDT, F., FRANK, M. & HINZ, B. 2022. The Combination of Delta(9)-Tetrahydrocannabinol and Cannabidiol Suppresses Mitochondrial Respiration of Human Glioblastoma Cells via Downregulation of Specific Respiratory Chain Proteins. *Cancers (Basel),* 14.

RYBIN, M. J., IVAN, M. E., AYAD, N. G. & ZEIER, Z. 2021. Organoid Models of Glioblastoma and Their Role in Drug Discovery. *Front Cell Neurosci,* 15**,** 605255.

RYU, A. H., ECKALBAR, W. L., KREIMER, A., YOSEF, N. & AHITUV, N. 2017. Use antibiotics in cell culture with caution: genome-wide identification of antibiotic-induced changes in gene expression and regulation. *Sci Rep,* 7**,** 7533.

SACHAMITR, P., HO, J. C., CIAMPONI, F. E., BA-ALAWI, W., COUTINHO, F. J., GUILHAMON, P., KUSHIDA, M. M., CAVALLI, F. M. G., LEE, L., RASTEGAR, N., VU, V., SANCHEZ-OSUNA, M., COULOMBE-HUNTINGTON, J., KANSHIN, E., WHETSTONE, H., DURAND, M., THIBAULT, P., HART, K., MANGOS, M., VEYHL, J., CHEN, W., TRAN, N., DUONG, B. C., AMAN, A. M., CHE, X., LAN, X., WHITLEY, O., ZASLAVER, O., BARSYTE-LOVEJOY, D., RICHARDS, L. M., RESTALL, I., CAUDY, A., ROST, H. L., BONDAY, Z. Q., BERNSTEIN, M., DAS, S., CUSIMANO, M. D., SPEARS, J., BADER, G. D., PUGH, T. J., TYERS, M., LUPIEN, M., HAIBE-KAINS, B., ARTEE LUCHMAN, H., WEISS, S., MASSIRER, K. B., PRINOS, P., ARROWSMITH, C. H. & DIRKS, P. B. 2021. PRMT5 inhibition disrupts splicing and stemness in glioblastoma. *Nat Commun,* 12**,** 979.

SACK, J. S., THIEFFINE, S., BANDIERA, T., FASOLINI, M., DUKE, G. J., JAYARAMAN, L., KISH, K. F., KLEI, H. E., PURANDARE, A. V., ROSETTANI, P., TROIANI, S., XIE, D. & BERTRAND, J. A. 2011. Structural basis for CARM1 inhibition by indole and pyrazole inhibitors. *Biochem J,* 436**,** 331-9.

SAHA, K., ADHIKARY, G. & ECKERT, R. L. 2016. MEP50/PRMT5 Reduces Gene Expression by Histone Arginine Methylation and this Is Reversed by PKCdelta/p38delta Signaling. *J Invest Dermatol,* 136**,** 214-224.

SAHA, S. K., KIM, K., YANG, G. M., CHOI, H. Y. & CHO, S. G. 2018. Cytokeratin 19 (KRT19) has a Role in the Reprogramming of Cancer Stem Cell-Like Cells to Less Aggressive and More Drug-Sensitive Cells. *Int J Mol Sci,* 19.

SAHU, M. P., NIKKILA, O., LAGAS, S., KOLEHMAINEN, S. & CASTREN, E. 2019. Culturing primary neurons from rat hippocampus and cortex. *Neuronal Signal,* 3**,** NS20180207.

SAID, M. Y., BOLLENBACH, A., MINOVIC, I., VAN LONDEN, M., FRENAY, A. R., DE BORST, M. H., VAN DEN BERG, E., KAYACELEBI, A. A., TSIKAS, D., VAN GOOR, H., NAVIS, G. & BAKKER, S. J. L. 2019. Plasma aDMA, urinary aDMA excretion, and late mortality in renal transplant recipients. *Amino Acids,* 51**,** 913-927.

SAMUEL, S. F., MARSDEN, A. J., DEEPAK, S., RIVERO, F., GREENMAN, J. & BELTRAN-ALVAREZ, P. 2018. Inhibiting Arginine Methylation as a Tool to Investigate Cross-Talk with Methylation and Acetylation Post-Translational Modifications in a Glioblastoma Cell Line. *Proteomes,* 6.

SANDERS, J., NORDSTROM, H., SHEEHAN, J. & SCHLESINGER, D. 2019. Gamma Knife radiosurgery: Scenarios and support for re-irradiation. *Phys Med,* 68**,** 75-82.

SAREEN, H., MA, Y., BECKER, T. M., ROBERTS, T. L., DE SOUZA, P. & POWTER, B. 2022. Molecular Biomarkers in Glioblastoma: A Systematic Review and Meta-Analysis. *Int J Mol Sci,* 23.

SAUTER, C., SIMONET, J., GUIDEZ, F., DUMETIER, B., PERNON, B., CALLANAN, M., BASTIE, J. N., AUCAGNE, R. & DELVA, L. 2022. Protein Arginine Methyltransferases as Therapeutic Targets in Hematological Malignancies. *Cancers (Basel),* 14.

SAVARIN-VUAILLAT, C. & RANSOHOFF, R. M. 2007. Chemokines and chemokine receptors in neurological disease: raise, retain, or reduce? *Neurotherapeutics,* 4**,** 590-601.

SAXENA, M., VAN DER BURG, S. H., MELIEF, C. J. M. & BHARDWAJ, N. 2021. Therapeutic cancer vaccines. *Nat Rev Cancer,* 21**,** 360-378.

SAYEGH, J., WEBB, K., CHENG, D., BEDFORD, M. T. & CLARKE, S. G. 2007. Regulation of protein arginine methyltransferase 8 (PRMT8) activity by its N-terminal domain. *J Biol Chem,* 282**,** 36444-53.

SCARAMUZZINO, C., CASCI, I., PARODI, S., LIEVENS, P. M. J., POLANCO, M. J., MILIOTO, C., CHIVET, M., MONAGHAN, J., MISHRA, A., BADDERS, N., AGGARWAL, T., GRUNSEICH, C., SAMBATARO, F., BASSO, M., FACKELMAYER, F. O., TAYLOR, J. P., PANDEY, U. B. & PENNUTO, M. 2015. Protein arginine methyltransferase 6 enhances polyglutamine-expanded androgen receptor function and toxicity in spinal and bulbar muscular atrophy. *Neuron,* 85**,** 88-100.

SCARAMUZZINO, C., MONAGHAN, J., MILIOTO, C., LANSON, N. A., JR., MALTARE, A., AGGARWAL, T., CASCI, I., FACKELMAYER, F. O., PENNUTO, M. & PANDEY, U. B. 2013. Protein arginine methyltransferase 1 and 8 interact with FUS to modify its sub-cellular distribution and toxicity in vitro and in vivo. *PLoS One,* 8**,** e61576.

SCHAPIRA, M. & FERREIRA DE FREITAS, R. 2014. Structural biology and chemistry of protein arginine methyltransferases. *Medchemcomm,* 5**,** 1779-1788.

SCHARTL, M. 2014. Beyond the zebrafish: diverse fish species for modeling human disease. *Dis Model Mech,* 7**,** 181-92.

SCHMITZ, K., COX, J., ESSER, L. M., VOSS, M., SANDER, K., LOFFLER, A., HILLEBRAND, F., ERKELENZ, S., SCHAAL, H., KAHNE, T., KLINKER, S., ZHANG, T., NAGEL-STEGER, L., WILLBOLD, D., SEGGEWISS, S., SCHLUTERMANN, D., STORK, B., GRIMMLER, M., WESSELBORG, S. & PETER, C. 2021. An essential role of the autophagy activating kinase ULK1 in snRNP biogenesis. *Nucleic Acids Res,* 49**,** 6437-6455.

SCHNEIDER, P. & TSCHOPP, J. 2000. Apoptosis induced by death receptors. *Pharm Acta Helv,* 74**,** 281-6.

SCHOLZ, N., KURIAN, K. M., SIEBZEHNRUBL, F. A. & LICCHESI, J. D. F. 2020. Targeting the Ubiquitin System in Glioblastoma. *Front Oncol,* 10**,** 574011.

SCOTT, I. S., MORRIS, L. S., RUSHBROOK, S. M., BIRD, K., VOWLER, S. L., BURNET, N. G. & COLEMAN, N. 2005. Immunohistochemical estimation of cell cycle entry and phase distribution in astrocytomas: applications in diagnostic neuropathology. *Neuropathol Appl Neurobiol,* 31**,** 455-66.

SEKER, F., CINGOZ, A., SUR-ERDEM, I., ERGUDER, N., ERKENT, A., UYULUR, F., ESAI SELVAN, M., GUMUS, Z. H., GONEN, M., BAYRAKTAR, H., WAKIMOTO, H. & BAGCI-ONDER, T. 2019. Identification of SERPINE1 as a Regulator of Glioblastoma Cell Dispersal with Transcriptome Profiling. *Cancers (Basel),* 11.

SELVI, B. R., SWAMINATHAN, A., MAHESHWARI, U., NAGABHUSHANA, A., MISHRA, R. K. & KUNDU, T. K. 2015. CARM1 regulates astroglial lineage through transcriptional regulation of Nanog and posttranscriptional regulation by miR92a. *Mol Biol Cell,* 26**,** 316-26.

SEMENZA, G. L. 2004. Hydroxylation of HIF-1: oxygen sensing at the molecular level. *Physiology (Bethesda),* 19**,** 176-82.

SEYSTAHL, K., HENTSCHEL, B., LOEW, S., GRAMATZKI, D., FELSBERG, J., HERRLINGER, U., WESTPHAL, M., SCHACKERT, G., THON, N., TATAGIBA, M., PIETSCH, T., REIFENBERGER, G., LOFFLER, M., WICK, W., WELLER, M. & GERMAN GLIOMA, N. 2020. Bevacizumab versus alkylating chemotherapy in recurrent glioblastoma. *J Cancer Res Clin Oncol,* 146**,** 659-670.

SHARMA, I., SINGH, A., SIRAJ, F. & SAXENA, S. 2018. IL8/CXCR1/2 signalling promotes tumor cell proliferation, invasion and vascular mimicry in glioblastoma. *J Biomed Sci,* 25**,** 62.

SHARMA, P., AAROE, A., LIANG, J. & PUDUVALLI, V. K. 2023. Tumor microenvironment in glioblastoma: Current and emerging concepts. *Neurooncol Adv,* 5**,** vdad009.

SHAW, R., BASU, M., KARMAKAR, S. & GHOSH, M. K. 2024. MGMT in TMZ-based glioma therapy: Multifaceted insights and clinical trial perspectives. *Biochim Biophys Acta Mol Cell Res,* 1871**,** 119673.

SHEN, L., MA, X., WANG, Y., WANG, Z., ZHANG, Y., PHAM, H. Q. H., TAO, X., CUI, Y., WEI, J., LIN, D., ABEYWANADA, T., HARDIKAR, S., HALABELIAN, L., SMITH, N., CHEN, T., BARSYTE-LOVEJOY, D., QIU, S., XING, Y. & YANG, Y. 2024. Loss-of-function mutation in PRMT9 causes abnormal synapse development by dysregulation of RNA alternative splicing. *Nat Commun,* 15**,** 2809.

SHEN, Y., GAO, G., YU, X., KIM, H., WANG, L., XIE, L., SCHWARZ, M., CHEN, X., GUCCIONE, E., LIU, J., BEDFORD, M. T. & JIN, J. 2020. Discovery of First-in-Class Protein Arginine Methyltransferase 5 (PRMT5) Degraders. *J Med Chem,* 63**,** 9977-9989.

SHEN, Y., SZEWCZYK, M. M., ERAM, M. S., SMIL, D., KANISKAN, H. U., DE FREITAS, R. F., SENISTERRA, G., LI, F., SCHAPIRA, M., BROWN, P. J., ARROWSMITH, C. H., BARSYTE-LOVEJOY, D., LIU, J., VEDADI, M. & JIN, J. 2016. Discovery of a Potent, Selective, and Cell-Active Dual Inhibitor of Protein Arginine Methyltransferase 4 and Protein Arginine Methyltransferase 6. *J Med Chem,* 59**,** 9124-9139.

SHEN, Y., ZHONG, J., LIU, J., LIU, K., ZHAO, J., XU, T., ZENG, T., LI, Z., CHEN, Y., DING, W., WEN, G., ZU, X. & CAO, R. 2018. Protein arginine N-methyltransferase 2 reverses tamoxifen resistance in breast cancer cells through suppression of ER-alpha36. *Oncol Rep,* 39**,** 2604-2612.

SHI, Y. 2004. Caspase activation, inhibition, and reactivation: a mechanistic view. *Protein Sci,* 13**,** 1979-87.

SHINAGARE, A. B., GIARDINO, A. A., JAGANNATHAN, J. P., VAN DEN ABBEELE, A. D. & RAMAIYA, N. H. 2011. Hereditary cancer syndromes: a radiologist's perspective. *AJR Am J Roentgenol,* 197**,** W1001-7.

SHIRLEY, S., MORIZOT, A. & MICHEAU, O. 2011. Regulating TRAIL receptor-induced cell death at the membrane : a deadly discussion. *Recent Pat Anticancer Drug Discov,* 6**,** 311-23.

SHISHKOVA, E., ZENG, H., LIU, F., KWIECIEN, N. W., HEBERT, A. S., COON, J. J. & XU, W. 2017. Global mapping of CARM1 substrates defines enzyme specificity and substrate recognition. *Nat Commun,* 8**,** 15571.

SIGHEL, D., NOTARANGELO, M., AIBARA, S., RE, A., RICCI, G., GUIDA, M., SOLDANO, A., ADAMI, V., AMBROSINI, C., BROSO, F., ROSATTI, E. F., LONGHI, S., BUCCARELLI, M., D'ALESSANDRIS, Q. G., GIANNETTI, S., PACIONI, S., RICCI-VITIANI, L., RORBACH, J., PALLINI, R., ROULLAND, S., AMUNTS, A., MANCINI, I., MODELSKA, A. & QUATTRONE, A. 2021. Inhibition of mitochondrial translation suppresses glioblastoma stem cell growth. *Cell Rep,* 35**,** 109024.

SIGISMUND, S., AVANZATO, D. & LANZETTI, L. 2018. Emerging functions of the EGFR in cancer. *Mol Oncol,* 12**,** 3-20.

SILLER, S., LAUSEKER, M., KARSCHNIA, P., NIYAZI, M., EIGENBROD, S., GIESE, A. & TONN, J. C. 2021. The number of methylated CpG sites within the MGMT promoter region linearly correlates with outcome in glioblastoma receiving alkylating agents. *Acta Neuropathol Commun,* 9**,** 35.

SIMANDI, Z., CZIPA, E., HORVATH, A., KOSZEGHY, A., BORDAS, C., POLISKA, S., JUHASZ, I., IMRE, L., SZABO, G., DEZSO, B., BARTA, E., SAUER, S., KAROLYI, K., KOVACS, I., HUTOCZKI, G., BOGNAR, L., KLEKNER, A., SZUCS, P., BALINT, B. L. & NAGY, L. 2015. PRMT1 and PRMT8 regulate retinoic acid-dependent neuronal differentiation with implications to neuropathology. *Stem Cells,* 33**,** 726-41.

SIMS, R. J., 3RD, ROJAS, L. A., BECK, D. B., BONASIO, R., SCHULLER, R., DRURY, W. J., 3RD, EICK, D. & REINBERG, D. 2011. The C-terminal domain of RNA polymerase II is modified by site-specific methylation. *Science,* 332**,** 99-103.

SINGH, S. K., BHARDWAJ, R., WILCZYNSKA, K. M., DUMUR, C. I. & KORDULA, T. 2011. A complex of nuclear factor I-X3 and STAT3 regulates astrocyte and glioma migration through the secreted glycoprotein YKL-40. *J Biol Chem,* 286**,** 39893-903.

SINGH, S. K., FIORELLI, R., KUPP, R., RAJAN, S., SZETO, E., LO CASCIO, C., MAIRE, C. L., SUN, Y., ALBERTA, J. A., ESCHBACHER, J. M., LIGON, K. L., BERENS, M. E., SANAI, N. & MEHTA, S. 2016. Post-translational Modifications of OLIG2 Regulate Glioma Invasion through the TGF-beta Pathway. *Cell Rep,* 16**,** 950-966.

SINGH, V., RAM, M., KUMAR, R., PRASAD, R., ROY, B. K. & SINGH, K. K. 2017. Phosphorylation: Implications in Cancer. *Protein J,* 36**,** 1-6.

SINGHROY, D. N., MESPLEDE, T., SABBAH, A., QUASHIE, P. K., FALGUEYRET, J. P. & WAINBERG, M. A. 2013. Automethylation of protein arginine methyltransferase 6 (PRMT6) regulates its stability and its anti-HIV-1 activity. *Retrovirology,* 10**,** 73.

SMIL, D., ERAM, M. S., LI, F., KENNEDY, S., SZEWCZYK, M. M., BROWN, P. J., BARSYTE-LOVEJOY, D., ARROWSMITH, C. H., VEDADI, M. & SCHAPIRA, M. 2015. Discovery of a Dual PRMT5-PRMT7 Inhibitor. *ACS Med Chem Lett,* 6**,** 408-12.

SMITH, E., ZHOU, W., SHINDIAPINA, P., SIF, S., LI, C. & BAIOCCHI, R. A. 2018. Recent advances in targeting protein arginine methyltransferase enzymes in cancer therapy. *Expert Opin Ther Targets,* 22**,** 527-545.

SNEDEKER, J. G. & GAUTIERI, A. 2014. The role of collagen crosslinks in ageing and diabetes - the good, the bad, and the ugly. *Muscles Ligaments Tendons J,* 4**,** 303-8.

SOARES, I. N., CAETANO, F. A., PINDER, J., RODRIGUES, B. R., BERALDO, F. H., OSTAPCHENKO, V. G., DURETTE, C., PEREIRA, G. S., LOPES, M. H., QUEIROZ-HAZARBASSANOV, N., CUNHA, I. W., SANEMATSU, P. I., SUZUKI, S., BLEGGI-TORRES, L. F., SCHILD-POULTER, C., THIBAULT, P., DELLAIRE, G., MARTINS, V. R., PRADO, V. F. & PRADO, M. A. 2013. Regulation of stress-inducible phosphoprotein 1 nuclear retention by protein inhibitor of activated STAT PIAS1. *Mol Cell Proteomics,* 12**,** 3253-70.

SOLARI, C., ECHEGARAY, C. V., LUZZANI, C., COSENTINO, M. S., WAISMAN, A., PETRONE, M. V., FRANCIA, M., SASSONE, A., CANIZO, J., SEVLEVER, G., BARANAO, L., MIRIUKA, S. & GUBERMAN, A. 2016. Protein arginine Methyltransferase 8 gene is expressed in pluripotent stem cells and its expression is modulated by the transcription factor Sox2. *Biochem Biophys Res Commun,* 473**,** 194-199.

SORENSEN, M. D., DAHLROT, R. H., BOLDT, H. B., HANSEN, S. & KRISTENSEN, B. W. 2018. Tumour-associated microglia/macrophages predict poor prognosis in high-grade gliomas and correlate with an aggressive tumour subtype. *Neuropathol Appl Neurobiol,* 44**,** 185-206.

SPANNHOFF, A., MACHMUR, R., HEINKE, R., TROJER, P., BAUER, I., BROSCH, G., SCHULE, R., HANEFELD, W., SIPPL, W. & JUNG, M. 2007. A novel arginine methyltransferase inhibitor with cellular activity. *Bioorg Med Chem Lett,* 17**,** 4150-3.

STEAD, L. F. 2022. Treating glioblastoma often makes a MES. *Nat Cancer,* 3**,** 1446-1448.

STEIN, C., NOTZOLD, R. R., RIEDL, S., BOUCHARD, C. & BAUER, U. M. 2016. The Arginine Methyltransferase PRMT6 Cooperates with Polycomb Proteins in Regulating HOXA Gene Expression. *PLoS One,* 11**,** e0148892.

STOYANOV, G. S., PETKOVA, L. & DZHENKOV, D. L. 2019. A Practical Approach to the Differential Diagnosis of Intracranial Tumors: Gross, Histology, and Immunoprofile-based Algorithm. *Cureus,* 11**,** e6384.

STOYANOV, G. S., PETKOVA, L., ILIEV, B., ALI, M., TONCHEVA, B., GEORGIEV, R., TONCHEV, T. & ENCHEV, Y. 2023. Extracranial Glioblastoma Metastasis: A Neuropathological Case Report. *Cureus,* 15**,** e35803.

STRAHL, B. D., BRIGGS, S. D., BRAME, C. J., CALDWELL, J. A., KOH, S. S., MA, H., COOK, R. G., SHABANOWITZ, J., HUNT, D. F., STALLCUP, M. R. & ALLIS, C. D. 2001. Methylation of histone H4 at arginine 3 occurs in vivo and is mediated by the nuclear receptor coactivator PRMT1. *Curr Biol,* 11**,** 996-1000.

STUPP, R., HEGI, M. E., MASON, W. P., VAN DEN BENT, M. J., TAPHOORN, M. J., JANZER, R. C., LUDWIN, S. K., ALLGEIER, A., FISHER, B., BELANGER, K., HAU, P., BRANDES, A. A., GIJTENBEEK, J., MAROSI, C., VECHT, C. J., MOKHTARI, K., WESSELING, P., VILLA, S., EISENHAUER, E., GORLIA, T., WELLER, M., LACOMBE, D., CAIRNCROSS, J. G., MIRIMANOFF, R. O., EUROPEAN ORGANISATION FOR, R., TREATMENT OF CANCER BRAIN, T., RADIATION ONCOLOGY, G. & NATIONAL CANCER INSTITUTE OF CANADA CLINICAL TRIALS, G. 2009. Effects of radiotherapy with concomitant and adjuvant temozolomide versus radiotherapy alone on survival in glioblastoma in a randomised phase III study: 5-year analysis of the EORTC-NCIC trial. *Lancet Oncol,* 10**,** 459-66.

STUPP, R., TAILLIBERT, S., KANNER, A., READ, W., STEINBERG, D., LHERMITTE, B., TOMS, S., IDBAIH, A., AHLUWALIA, M. S., FINK, K., DI MECO, F., LIEBERMAN, F., ZHU, J. J., STRAGLIOTTO, G., TRAN, D., BREM, S., HOTTINGER, A., KIRSON, E. D., LAVY-SHAHAF, G., WEINBERG, U., KIM, C. Y., PAEK, S. H., NICHOLAS, G., BRUNA, J., HIRTE, H., WELLER, M., PALTI, Y., HEGI, M. E. & RAM, Z. 2017. Effect of Tumor-Treating Fields Plus Maintenance Temozolomide vs Maintenance Temozolomide Alone on Survival in Patients With Glioblastoma: A Randomized Clinical Trial. *JAMA,* 318**,** 2306-2316.

STURLA, L. M., TONG, M., HEBDA, N., GAO, J., THOMAS, J. M., OLSEN, M. & DE LA MONTE, S. M. 2016. Aspartate-beta-hydroxylase (ASPH): A potential therapeutic target in human malignant gliomas. *Heliyon,* 2**,** e00203.

SU, X., XIE, Y., ZHANG, J., LI, M., ZHANG, Q., JIN, G. & LIU, F. 2023. Correction: HIF-alpha activation by the prolyl hydroxylase inhibitor roxadustat suppresses chemoresistant glioblastoma growth by inducing ferroptosis. *Cell Death Dis,* 14**,** 31.

SUAREZ-CALVET, M., NEUMANN, M., ARZBERGER, T., ABOU-AJRAM, C., FUNK, E., HARTMANN, H., EDBAUER, D., KREMMER, E., GOBL, C., RESCH, M., BOURGEOIS, B., MADL, T., REBER, S., JUTZI, D., RUEPP, M. D., MACKENZIE, I. R., ANSORGE, O., DORMANN, D. & HAASS, C. 2016. Monomethylated and unmethylated FUS exhibit increased binding to Transportin and distinguish FTLD-FUS from ALS-FUS. *Acta Neuropathol,* 131**,** 587-604.

SUN, L., WANG, M., LV, Z., YANG, N., LIU, Y., BAO, S., GONG, W. & XU, R. M. 2011. Structural insights into protein arginine symmetric dimethylation by PRMT5. *Proc Natl Acad Sci U S A,* 108**,** 20538-43.

SUN, Y., WANG, Z., YANG, H., ZHU, X., WU, H., MA, L., XU, F., HONG, W. & WANG, H. 2019. The Development of Tetrazole Derivatives as Protein Arginine Methyltransferase I (PRMT I) Inhibitors. *Int J Mol Sci,* 20.

SWIERCZ, R., CHENG, D., KIM, D. & BEDFORD, M. T. 2007. Ribosomal protein rpS2 is hypomethylated in PRMT3-deficient mice. *J Biol Chem,* 282**,** 16917-23.

SYLVESTER, D. C. H., S.M.; STAFFORD, N.D.; HASWELL, S.J. AND GREENMAN, J. 2013. Development of microfluidic-based analytical methodology for studying the effects of chemotherapy agents on cancer tissue. *Curr Anal Chem,* 9**,** 2-8.

SZEWCZYK, M. M., ISHIKAWA, Y., ORGAN, S., SAKAI, N., LI, F., HALABELIAN, L., ACKLOO, S., COUZENS, A. L., ERAM, M., DILWORTH, D., FUKUSHI, H., HARDING, R., DELA SENA, C. C., SUGO, T., HAYASHI, K., MCLEOD, D., ZEPEDA, C., AMAN, A., SANCHEZ-OSUNA, M., BONNEIL, E., TAKAGI, S., AL-AWAR, R., TYERS, M., RICHARD, S., TAKIZAWA, M., GINGRAS, A. C., ARROWSMITH, C. H., VEDADI, M., BROWN, P. J., NARA, H. & BARSYTE-LOVEJOY, D. 2020a. Author Correction: Pharmacological inhibition of PRMT7 links arginine monomethylation to the cellular stress response. *Nat Commun,* 11**,** 2683.

SZEWCZYK, M. M., ISHIKAWA, Y., ORGAN, S., SAKAI, N., LI, F., HALABELIAN, L., ACKLOO, S., COUZENS, A. L., ERAM, M., DILWORTH, D., FUKUSHI, H., HARDING, R., DELA SENA, C. C., SUGO, T., HAYASHI, K., MCLEOD, D., ZEPEDA, C., AMAN, A., SANCHEZ-OSUNA, M., BONNEIL, E., TAKAGI, S., AL-AWAR, R., TYERS, M., RICHARD, S., TAKIZAWA, M., GINGRAS, A. C., ARROWSMITH, C. H., VEDADI, M., BROWN, P. J., NARA, H. & BARSYTE-LOVEJOY, D. 2020b. Pharmacological inhibition of PRMT7 links arginine monomethylation to the cellular stress response. *Nat Commun,* 11**,** 2396.

TAKIZAWA, T., NAKASHIMA, K., NAMIHIRA, M., OCHIAI, W., UEMURA, A., YANAGISAWA, M., FUJITA, N., NAKAO, M. & TAGA, T. 2001. DNA methylation is a critical cell-intrinsic determinant of astrocyte differentiation in the fetal brain. *Dev Cell,* 1**,** 749-58.

TANG, J., GARY, J. D., CLARKE, S. & HERSCHMAN, H. R. 1998. PRMT 3, a type I protein arginine N-methyltransferase that differs from PRMT1 in its oligomerization, subcellular localization, substrate specificity, and regulation. *J Biol Chem,* 273**,** 16935-45.

TANNER, G., BARROW, R., AJAIB, S., AL-JABRI, M., AHMED, N., POLLOCK, S., FINETTI, M., RIPPAUS, N., BRUNS, A. F., SYED, K., POULTER, J. A., MATTHEWS, L., HUGHES, T., WILSON, E., JOHNSON, C., VARN, F. S., BRUNING-RICHARDSON, A., HOGG, C., DROOP, A., GUSNANTO, A., CARE, M. A., CUTILLO, L., WESTHEAD, D. R., SHORT, S. C., JENKINSON, M. D., BRODBELT, A., CHAKRABARTY, A., ISMAIL, A., VERHAAK, R. G. W. & STEAD, L. F. 2024. IDHwt glioblastomas can be stratified by their transcriptional response to standard treatment, with implications for targeted therapy. *Genome Biol,* 25**,** 45.

TARADE, D. & OHH, M. 2018. The HIF and other quandaries in VHL disease. *Oncogene,* 37**,** 139-147.

TAYLOR, K. R., BARRON, T., HUI, A., SPITZER, A., YALCIN, B., IVEC, A. E., GERAGHTY, A. C., HARTMANN, G. G., ARZT, M., GILLESPIE, S. M., KIM, Y. S., MALEKI JAHAN, S., ZHANG, H., SHAMARDANI, K., SU, M., NI, L., DU, P. P., WOO, P. J., SILVA-TORRES, A., VENKATESH, H. S., MANCUSI, R., PONNUSWAMI, A., MULINYAWE, S., KEOUGH, M. B., CHAU, I., AZIZ-BOSE, R., TIROSH, I., SUVA, M. L. & MONJE, M. 2023. Glioma synapses recruit mechanisms of adaptive plasticity. *Nature,* 623**,** 366-374.

TERAIYA, M., PERREAULT, H. & CHEN, V. C. 2023. An overview of glioblastoma multiforme and temozolomide resistance: can LC-MS-based proteomics reveal the fundamental mechanism of temozolomide resistance? *Front Oncol,* 13**,** 1166207.

TESILEANU, C. M. S., DIRVEN, L., WIJNENGA, M. M. J., KOEKKOEK, J. A. F., VINCENT, A., DUBBINK, H. J., ATMODIMEDJO, P. N., KROS, J. M., VAN DUINEN, S. G., SMITS, M., TAPHOORN, M. J. B., FRENCH, P. J. & VAN DEN BENT, M. J. 2020. Survival of diffuse astrocytic glioma, IDH1/2 wildtype, with molecular features of glioblastoma, WHO grade IV: a confirmation of the cIMPACT-NOW criteria. *Neuro Oncol,* 22**,** 515-523.

TEWARY, S. K., ZHENG, Y. G. & HO, M. C. 2019. Protein arginine methyltransferases: insights into the enzyme structure and mechanism at the atomic level. *Cell Mol Life Sci,* 76**,** 2917-2932.

THE GLASS CONSORTIUM 2018. Glioma through the looking GLASS: molecular evolution of diffuse gliomas and the Glioma Longitudinal Analysis Consortium. *Neuro Oncol,* 20**,** 873-884.

THORPE, L. M., YUZUGULLU, H. & ZHAO, J. J. 2015. PI3K in cancer: divergent roles of isoforms, modes of activation and therapeutic targeting. *Nat Rev Cancer,* 15**,** 7-24.

TILAK, M., HOLBORN, J., NEW, L. A., LALONDE, J. & JONES, N. 2021. Receptor Tyrosine Kinase Signaling and Targeting in Glioblastoma Multiforme. *Int J Mol Sci,* 22.

TIMERMAN, D. & YEUNG, C. M. 2014. Identity confusion of glioma cell lines. *Gene,* 536**,** 221-2.

TRADEWELL, M. L., YU, Z., TIBSHIRANI, M., BOULANGER, M. C., DURHAM, H. D. & RICHARD, S. 2012. Arginine methylation by PRMT1 regulates nuclear-cytoplasmic localization and toxicity of FUS/TLS harbouring ALS-linked mutations. *Hum Mol Genet,* 21**,** 136-49.

TRIPATHI, P. H., AKHTAR, J., ARORA, J., SARAN, R. K., MISHRA, N., POLISETTY, R. V., SIRDESHMUKH, R. & GAUTAM, P. 2022. Quantitative proteomic analysis of GnRH agonist treated GBM cell line LN229 revealed regulatory proteins inhibiting cancer cell proliferation. *BMC Cancer,* 22**,** 133.

TRIPSIANES, K., MADL, T., MACHYNA, M., FESSAS, D., ENGLBRECHT, C., FISCHER, U., NEUGEBAUER, K. M. & SATTLER, M. 2011. Structural basis for dimethylarginine recognition by the Tudor domains of human SMN and SPF30 proteins. *Nat Struct Mol Biol,* 18**,** 1414-20.

TSIKAS, D., BOLLENBACH, A., HANFF, E. & KAYACELEBI, A. A. 2018. Asymmetric dimethylarginine (aDMA), symmetric dimethylarginine (sDMA) and homoarginine (hArg): the aDMA, sDMA and hArg paradoxes. *Cardiovasc Diabetol,* 17**,** 1.

TÜRKEŞ, G. P., E.T.; KıRAL, N.; DOĞAN, C.; & SAĞMEN, S. B. F., A. AND CÖMERT, S. 2018. A Rare Cause of Lung Metastasis -

UJIIE, D., OKAYAMA, H., SAITO, K., ASHIZAWA, M., THAR MIN, A. K., ENDO, E., KASE, K., YAMADA, L., KIKUCHI, T., HANAYAMA, H., FUJITA, S., SAKAMOTO, W., ENDO, H., SAITO, M., MIMURA, K., SAZE, Z., MOmMA, T., OHKI, S. & KONO, K. 2020. KRT17 as a prognostic biomarker for stage II colorectal cancer. *Carcinogenesis,* 41**,** 591-599.

UXA, S., CASTILLO-BINDER, P., KOHLER, R., STANGNER, K., MULLER, G. A. & ENGELAND, K. 2021. Ki-67 gene expression. *Cell Death Differ,* 28**,** 3357-3370.

VALDES-RIVES, S. A., CASIQUE-AGUIRRE, D., GERMAN-CASTELAN, L., VELASCO-VELAZQUEZ, M. A. & GONZALEZ-ARENAS, A. 2017. Apoptotic Signaling Pathways in Glioblastoma and Therapeutic Implications. *Biomed Res Int,* 2017**,** 7403747.

VALERIE, N. C., DZIEGIELEWSKA, B., HOSING, A. S., AUGUSTIN, E., GRAY, L. S., BRAUTIGAN, D. L., LARNER, J. M. & DZIEGIELEWSKI, J. 2013. Inhibition of T-type calcium channels disrupts Akt signaling and promotes apoptosis in glioblastoma cells. *Biochem Pharmacol,* 85**,** 888-97.

VALVONA, C. J., FILLMORE, H. L., NUNN, P. B. & PILKINGTON, G. J. 2016. The Regulation and Function of Lactate Dehydrogenase A: Therapeutic Potential in Brain Tumor. *Brain Pathol,* 26**,** 3-17.

VAN DEN BENT, M. J., BRANDES, A. A., RAMPLING, R., KOUWENHOVEN, M. C., KROS, J. M., CARPENTIER, A. F., CLEMENT, P. M., FRENAY, M., CAMPONE, M., BAURAIN, J. F., ARMAND, J. P., TAPHOORN, M. J., TOSONI, A., KLETZL, H., KLUGHAMMER, B., LACOMBE, D. & GORLIA, T. 2009. Randomized phase II trial of erlotinib versus temozolomide or carmustine in recurrent glioblastoma: EORTC brain tumor group study 26034. *J Clin Oncol,* 27**,** 1268-74.

VAN DEN BENT, M., EOLI, M., SEPULVEDA, J. M., SMITS, M., WALENKAMP, A., FRENEL, J. S., FRANCESCHI, E., CLEMENT, P. M., CHINOT, O., DE VOS, F., WHENHAM, N., SANGHERA, P., WELLER, M., DUBBINK, H. J., FRENCH, P., LOOMAN, J., DEY, J., KRAUSE, S., ANSELL, P., NUYENS, S., SPRUYT, M., BRILHANTE, J., COENS, C., GORLIA, T. & GOLFINOPOULOS, V. 2020. INTELLANCE 2/EORTC 1410 randomized phase II study of Depatux-M alone and with temozolomide vs temozolomide or lomustine in recurrent EGFR amplified glioblastoma. *Neuro Oncol,* 22**,** 684-693.

VANDERLINDE, R. E. 1985. Measurement of total lactate dehydrogenase activity. *Ann Clin Lab Sci,* 15**,** 13-31.

VASILE, F., DOSSI, E. & ROUACH, N. 2017. Human astrocytes: structure and functions in the healthy brain. *Brain Struct Funct,* 222**,** 2017-2029.

VAZ-SALGADO, M. A., VILLAMAYOR, M., ALBARRAN, V., ALIA, V., SOTOCA, P., CHAMORRO, J., ROSERO, D., BARRILL, A. M., MARTIN, M., FERNANDEZ, E., GUTIERREZ, J. A., ROJAS-MEDINA, L. M. & LEY, L. 2023. Recurrent Glioblastoma: A Review of the Treatment Options. *Cancers (Basel),* 15.

VELAND, N., HARDIKAR, S., ZHONG, Y., GAYATRI, S., DAN, J., STRAHL, B. D., ROTHBART, S. B., BEDFORD, M. T. & CHEN, T. 2017. The Arginine Methyltransferase PRMT6 Regulates DNA Methylation and Contributes to Global DNA Hypomethylation in Cancer. *Cell Rep,* 21**,** 3390-3397.

VERHAAK, R. G., HOADLEY, K. A., PURDOM, E., WANG, V., QI, Y., WILKERSON, M. D., MILLER, C. R., DING, L., GOLUB, T., MESIROV, J. P., ALEXE, G., LAWRENCE, M., O'KELLY, M., TAMAYO, P., WEIR, B. A., GABRIEL, S., WINCKLER, W., GUPTA, S., JAKKULA, L., FEILER, H. S., HODGSON, J. G., JAMES, C. D., SARKARIA, J. N., BRENNAN, C., KAHN, A., SPELLMAN, P. T., WILSON, R. K., SPEED, T. P., GRAY, J. W., MEYERSON, M., GETZ, G., PEROU, C. M., HAYES, D. N. & CANCER GENOME ATLAS RESEARCH, N. 2010. Integrated genomic analysis identifies clinically relevant subtypes of glioblastoma characterized by abnormalities in PDGFRA, IDH1, EGFR, and NF1. *Cancer Cell,* 17**,** 98-110.

VERKHRATSKY, A. & SEMYANOV, A. 2022. The great astroglial metabolic revolution: Mitochondria fuel astrocyte homeostatic support and neuroprotection. *Cell Calcium,* 104**,** 102583.

VHUIYAN, M. I., PAK, M. L., PARK, M. A., THOMAS, D., LAKOWSKI, T. M., CHALFANT, C. E. & FRANKEL, A. 2017. PRMT2 interacts with splicing factors and regulates the alternative splicing of BCL-X. *J Biochem,* 162**,** 17-25.

VILLA, G. R., HULCE, J. J., ZANCA, C., BI, J., IKEGAMI, S., CAHILL, G. L., GU, Y., LUM, K. M., MASUI, K., YANG, H., RONG, X., HONG, C., TURNER, K. M., LIU, F., HON, G. C., JENKINS, D., MARTINI, M., ARMANDO, A. M., QUEHENBERGER, O., CLOUGHESY, T. F., FURNARI, F. B., CAVENEE, W. K., TONTONOZ, P., GAHMAN, T. C., SHIAU, A. K., CRAVATT, B. F. & MISCHEL, P. S. 2016. An LXR-Cholesterol Axis Creates a Metabolic Co-Dependency for Brain Cancers. *Cancer Cell,* 30**,** 683-693.

VIVANCO, I., ROBINS, H. I., ROHLE, D., CAMPOS, C., GROMMES, C., NGHIEMPHU, P. L., KUBEK, S., OLDRINI, B., CHHEDA, M. G., YANNUZZI, N., TAO, H., ZHU, S., IWANAMI, A., KUGA, D., DANG, J., PEDRAZA, A., BRENNAN, C. W., HEGUY, A., LIAU, L. M., LIEBERMAN, F., YUNG, W. K., GILBERT, M. R., REARDON, D. A., DRAPPATZ, J., WEN, P. Y., LAMBORN, K. R., CHANG, S. M., PRADOS, M. D., FINE, H. A., HORVATH, S., WU, N., LASSMAN, A. B., DEANGELIS, L. M., YONG, W. H., KUHN, J. G., MISCHEL, P. S., MEHTA, M. P., CLOUGHESY, T. F. & MELLINGHOFF, I. K. 2012. Differential sensitivity of glioma- versus lung cancer-specific EGFR mutations to EGFR kinase inhibitors. *Cancer Discov,* 2**,** 458-71.

WAGNER, M. & WIIG, H. 2015. Tumor Interstitial Fluid Formation, Characterization, and Clinical Implications. *Front Oncol,* 5**,** 115.

WALL, M. L. & LEWIS, S. M. 2017. Methylarginines within the RGG-Motif Region of hnRNP A1 Affect Its IRES Trans-Acting Factor Activity and Are Required for hnRNP A1 Stress Granule Localization and Formation. *J Mol Biol,* 429**,** 295-307.

WANG, B., CHEN, D. & HUA, H. 2021. TBC1D3 family is a prognostic biomarker and correlates with immune infiltration in kidney renal clear cell carcinoma. *Mol Ther Oncolytics,* 22**,** 528-538.

WANG, C., DENG, L., HONG, M., AKKARAJU, G. R., INOUE, J. & CHEN, Z. J. 2001. TAK1 is a ubiquitin-dependent kinase of MKK and IKK. *Nature,* 412**,** 346-51.

WANG, C., SUN, M., SHAO, C., SCHLICKER, L., ZHUO, Y., HARIM, Y., PENG, T., TIAN, W., STOFFLER, N., SCHNEIDER, M., HELM, D., CHU, Y., FU, B., JIN, X., MALLM, J. P., MALL, M., WU, Y., SCHULZE, A. & LIU, H. K. 2024. A multidimensional atlas of human glioblastoma-like organoids reveals highly coordinated molecular networks and effective drugs. *NPJ Precis Oncol,* 8**,** 19.

WANG, E. J. C., J.; JAIN, S.; MORSHED, R.A.; HADDAD, A.F.; GILL, S.; BENIWAL, A.S. AND AGHI, M.K. 2021. Immunotherapy Resistance in Glioblastoma. *Frontiers in Genetics,* 12.

WANG, F., ZHANG, J., KE, X., PENG, W., ZHAO, G., PENG, S., XU, J., XU, B. & CUI, H. 2020a. WDR5-Myc axis promotes the progression of glioblastoma and neuroblastoma by transcriptional activating CARM1. *Biochem Biophys Res Commun,* 523**,** 699-706.

WANG, G. M., CIOFFI, G., PATIL, N., WAITE, K. A., LANESE, R., OSTROM, Q. T., KRUCHKO, C., BERENS, M. E., CONNOR, J. R., LATHIA, J. D., RUBIN, J. B. & BARNHOLTZ-SLOAN, J. S. 2022. Importance of the intersection of age and sex to understand variation in incidence and survival for primary malignant gliomas. *Neuro Oncol,* 24**,** 302-310.

WANG, J. & PAN, W. 2020. The Biological Role of the Collagen Alpha-3 (VI) Chain and Its Cleaved C5 Domain Fragment Endotrophin in Cancer. *Onco Targets Ther,* 13**,** 5779-5793.

WANG, J., CAZZATO, E., LADEWIG, E., FRATTINI, V., ROSENBLOOM, D. I., ZAIRIS, S., ABATE, F., LIU, Z., ELLIOTT, O., SHIN, Y. J., LEE, J. K., LEE, I. H., PARK, W. Y., EOLI, M., BLUMBERG, A. J., LASORELLA, A., NAM, D. H., FINOCCHIARO, G., IAVARONE, A. & RABADAN, R. 2016. Clonal evolution of glioblastoma under therapy. *Nat Genet,* 48**,** 768-76.

WANG, J., XIAO, Z., LI, P., WU, C., LI, Y., WANG, Q., CHEN, Y., ZHOU, H., LI, Z., WANG, Z., LAN, Q. & WANG, Y. 2023a. PRMT6-CDC20 facilitates glioblastoma progression via the degradation of CDKN1B. *Oncogene,* 42**,** 1088-1100.

WANG, L., CHAROENSUKSAI, P., WATSON, N. J., WANG, X., ZHAO, Z., CORIANO, C. G., KERR, L. R. & XU, W. 2013a. CARM1 automethylation is controlled at the level of alternative splicing. *Nucleic Acids Res,* 41**,** 6870-80.

WANG, L., LIANG, B., LI, Y. I., LIU, X., HUANG, J. & LI, Y. M. 2019a. What is the advance of extent of resection in glioblastoma surgical treatment-a systematic review. *Chin Neurosurg J,* 5**,** 2.

WANG, M., FUHRMANN, J. & THOMPSON, P. R. 2014. Protein arginine methyltransferase 5 catalyzes substrate dimethylation in a distributive fashion. *Biochemistry,* 53**,** 7884-92.

WANG, Q., HU, B., HU, X., KIM, H., SQUATRITO, M., SCARPACE, L., DECARVALHO, A. C., LYU, S., LI, P., LI, Y., BARTHEL, F., CHO, H. J., LIN, Y. H., SATANI, N., MARTINEZ-LEDESMA, E., ZHENG, S., CHANG, E., SAUVE, C. G., OLAR, A., LAN, Z. D., FINOCCHIARO, G., PHILLIPS, J. J., BERGER, M. S., GABRUSIEWICZ, K. R., WANG, G., ESKILSSON, E., HU, J., MIKKELSEN, T., DEPINHO, R. A., MULLER, F., HEIMBERGER, A. B., SULMAN, E. P., NAM, D. H. & VERHAAK, R. G. W. 2017. Tumor Evolution of Glioma-Intrinsic Gene Expression Subtypes Associates with Immunological Changes in the Microenvironment. *Cancer Cell,* 32**,** 42-56 e6.

WANG, S., TAN, X., YANG, B., YIN, B., YUAN, J., QIANG, B. & PENG, X. 2012. The role of protein arginine-methyltransferase 1 in gliomagenesis. *BMB Rep,* 45**,** 470-5.

WANG, W. J., HSU, J. M., WANG, Y. N., LEE, H. H., YAMAGUCHI, H., LIAO, H. W. & HUNG, M. C. 2019b. An essential role of PRMT1-mediated EGFR methylation in EGFR activation by ribonuclease 5. *Am J Cancer Res,* 9**,** 180-185.

WANG, W. Y., PAN, L., SU, S. C., QUINN, E. J., SASAKI, M., JIMENEZ, J. C., MACKENZIE, I. R., HUANG, E. J. & TSAI, L. H. 2013. Interaction of FUS and HDAC1 regulates DNA damage response and repair in neurons. *Nat Neurosci,* 16**,** 1383-91.

WANG, W. Y., PAN, L., SU, S. C., QUINN, E. J., SASAKI, M., JIMENEZ, J. C., MACKENZIE, I. R., HUANG, E. J. & TSAI, L. H. 2013b. Interaction of FUS and HDAC1 regulates DNA damage response and repair in neurons. *Nat Neurosci,* 16**,** 1383-91.

WANG, X., SUN, Y., ZHANG, D. Y., MING, G. L. & SONG, H. 2023. Glioblastoma modeling with 3D organoids: progress and challenges. *Oxf Open Neurosci,* 2**,** kvad008.

WANG, X., SUN, Y., ZHANG, D. Y., MING, G. L. & SONG, H. 2023b. Glioblastoma modeling with 3D organoids: progress and challenges. *Oxf Open Neurosci,* 2**,** kvad008.

WANG, Y., LONG, P., WANG, Y. & MA, W. 2020b. NTRK Fusions and TRK Inhibitors: Potential Targeted Therapies for Adult Glioblastoma. *Front Oncol,* 10**,** 593578.

WASSATI, H., LOO, S. W. & LOW, H. L. 2016. Lymphatic metastasis due to glioblastoma. *Neurosciences (Riyadh),* 21**,** 168-9.

WATANABE, T., NOBUSAWA, S., KLEIHUES, P. & OHGAKI, H. 2009. IDH1 mutations are early events in the development of astrocytomas and oligodendrogliomas. *Am J Pathol,* 174**,** 1149-53.

WEATHERS, S. P. & DE GROOT, J. 2015. VEGF Manipulation in Glioblastoma. *Oncology (Williston Park),* 29**,** 720-7.

WEBER, D. C., LIM, P. S., TRAN, S., WALSER, M., BOLSI, A., KLIEBSCH, U., BEER, J., BACHTIARY, B., LOMAX, T. & PICA, A. 2020. Proton therapy for brain tumours in the area of evidence-based medicine. *Br J Radiol,* 93**,** 20190237.

WEBER, S. C. & BRANGWYNNE, C. P. 2012. Getting RNA and protein in phase. *Cell,* 149**,** 1188-91.

WEI, H. F., X.; HU, Y.; GUO, M; FANG, Z.; WU, P.; TIAN, X.; GAO, S.; PENG, C.; YANG, Y. AND WANG, Z. 2019. A systematic survey of PRMT interactomes reveals the key roles of arginine methylation in the global control of RNA splicing and translation. *bioRxiv*.

WEIL, S., OSSWALD, M., SOLECKI, G., GROSCH, J., JUNG, E., LEMKE, D., RATLIFF, M., HANGGI, D., WICK, W. & WINKLER, F. 2017. Tumor microtubes convey resistance to surgical lesions and chemotherapy in gliomas. *Neuro Oncol,* 19**,** 1316-1326.

WELLER, M. & LE RHUN, E. 2020. How did lomustine become standard of care in recurrent glioblastoma? *Cancer Treat Rev,* 87**,** 102029.

WELLER, M., WICK, W., ALDAPE, K., BRADA, M., BERGER, M., PFISTER, S. M., NISHIKAWA, R., ROSENTHAL, M., WEN, P. Y., STUPP, R. & REIFENBERGER, G. 2015. Glioma. *Nat Rev Dis Primers,* 1**,** 15017.

WEN, P. Y., DRAPPATZ, J., DE GROOT, J., PRADOS, M. D., REARDON, D. A., SCHIFF, D., CHAMBERLAIN, M., MIKKELSEN, T., DESJARDINS, A., HOLLAND, J., PING, J., WEITZMAN, R. & CLOUGHESY, T. F. 2018. Phase II study of cabozantinib in patients with progressive glioblastoma: subset analysis of patients naive to antiangiogenic therapy. *Neuro Oncol,* 20**,** 249-258.

WERNICKE, A. G., TAUBE, S., SMITH, A. W., HERSKOVIC, A., PARASHAR, B. & SCHWARTZ, T. H. 2020. Cs-131 brachytherapy for patients with recurrent glioblastoma combined with bevacizumab avoids radiation necrosis while maintaining local control. *Brachytherapy,* 19**,** 705-712.

WEST, A. J., TSUI, V., STYLLI, S. S., NGUYEN, H. P. T., MOROKOFF, A. P., KAYE, A. H. & LUWOR, R. B. 2018. The role of interleukin-6-STAT3 signalling in glioblastoma. *Oncol Lett,* 16**,** 4095-4104.

WHITTSETTE, A. L., WANG, Y. J. & MU, T. W. 2022. The endoplasmic reticulum membrane complex promotes proteostasis of GABA(A) receptors. *iScience,* 25**,** 104754.

WHYTE, M. B., HINTON, W., MCGOVERN, A., VAN VLYMEN, J., FERREIRA, F., CALDERARA, S., MOUNT, J., MUNRO, N. & DE LUSIGNAN, S. 2019. Disparities in glycaemic control, monitoring, and treatment of type 2 diabetes in England: A retrospective cohort analysis. *PLoS Med,* 16**,** e1002942.

WIIG, H. & SWARTZ, M. A. 2012. Interstitial fluid and lymph formation and transport: physiological regulation and roles in inflammation and cancer. *Physiol Rev,* 92**,** 1005-60.

WILLIAM, D., MULLINS, C. S., SCHNEIDER, B., ORTHMANN, A., LAMP, N., KROHN, M., HOFFMANN, A., CLASSEN, C. F. & LINNEBACHER, M. 2017. Optimized creation of glioblastoma patient derived xenografts for use in preclinical studies. *J Transl Med,* 15**,** 27.

WONG, H. H., CHOU, C. Y. C., WATT, A. J. & SJOSTROM, P. J. 2023. Comparing mouse and human brains. *Elife,* 12.

WU, H. T., KUO, Y. C., HUNG, J. J., HUANG, C. H., CHEN, W. Y., CHOU, T. Y., CHEN, Y., CHEN, Y. J., CHEN, Y. J., CHENG, W. C., TENG, S. C. & WU, K. J. 2016b. K63-polyubiquitinated HAUSP deubiquitinates HIF-1alpha and dictates H3K56 acetylation promoting hypoxia-induced tumour progression. *Nat Commun,* 7**,** 13644.

WU, H., ZHENG, W., ERAM, M. S., VHUIYAN, M., DONG, A., ZENG, H., HE, H., BROWN, P., FRANKEL, A., VEDADI, M., LUO, M. & MIN, J. 2016a. Structural basis of arginine asymmetrical dimethylation by PRMT6. *Biochem J,* 473**,** 3049-63.

WU, K., LI, W., LIU, H., NIU, C., SHI, Q., ZHANG, J., GAO, G., SUN, H., LIU, F. & FU, L. 2023. Metabolome Sequencing Reveals that Protein Arginine-N-Methyltransferase 1 Promotes the Progression of Invasive Micropapillary Carcinoma of the Breast and Predicts a Poor Prognosis. *Am J Pathol,* 193**,** 1267-1283.

XIAO, Z. Z., WANG, Z. F., LAN, T., HUANG, W. H., ZHAO, Y. H., MA, C. & LI, Z. Q. 2020. Carmustine as a Supplementary Therapeutic Option for Glioblastoma: A Systematic Review and Meta-Analysis. *Front Neurol,* 11**,** 1036.

XIE, Z., CHEN, M., LIAN, J., WANG, H. & MA, J. 2023. Glioblastoma-on-a-chip construction and therapeutic applications. *Front Oncol,* 13**,** 1183059.

XIONG, T., WANG, Y., ZHANG, Y., YUAN, J., ZHU, C. & JIANG, W. 2023. lncRNA AC005224.4/miR-140-3p/SNAI2 regulating axis facilitates the invasion and metastasis of ovarian cancer through epithelial-mesenchymal transition. *Chin Med J (Engl),* 136**,** 1098-1110.

XIONG, Z., RAPHAEL, I., OLIN, M., OKADA, H., LI, X. & KOHANBASH, G. 2024. Glioblastoma vaccines: past, present, and opportunities. *EBioMedicine,* 100**,** 104963.

XU, R. X., LIU, R. Y., WU, C. M., ZHAO, Y. S., LI, Y., YAO, Y. Q. & XU, Y. H. 2015. DNA damage-induced NF-kappaB activation in human glioblastoma cells promotes miR-181b expression and cell proliferation. *Cell Physiol Biochem,* 35**,** 913-25.

XU, W., CHO, H., KADAM, S., BANAYO, E. M., ANDERSON, S., YATES, J. R., 3RD, EMERSON, B. M. & EVANS, R. M. 2004. A methylation-mediator complex in hormone signaling. *Genes Dev,* 18**,** 144-56.

XU, Z., JIANG, J., XU, C., WANG, Y., SUN, L., GUO, X. & LIU, H. 2013. MicroRNA-181 regulates CARM1 and histone arginine methylation to promote differentiation of human embryonic stem cells. *PLoS One,* 8**,** e53146.

XUE, Q., CAO, L., CHEN, X. Y., ZHAO, J., GAO, L., LI, S. Z. & FEI, Z. 2017. High expression of MMP9 in glioma affects cell proliferation and is associated with patient survival rates. *Oncol Lett,* 13**,** 1325-1330.

YALAMARTY, S. S. K., FILIPCZAK, N., LI, X., SUBHAN, M. A., PARVEEN, F., ATAIDE, J. A., RAJMALANI, B. A. & TORCHILIN, V. P. 2023. Mechanisms of Resistance and Current Treatment Options for Glioblastoma Multiforme (GBM). *Cancers (Basel),* 15.

YAMAMOTO, Y., SASAKI, N., KUMAGAI, K., TAKEUCHI, S., TOYOOKA, T., OTANI, N., WADA, K., NARITA, Y., ICHIMURA, K., NAMBA, H., MORI, K. & TOMIYAMA, A. 2018a. Involvement of Intracellular Cholesterol in Temozolomide-Induced Glioblastoma Cell Death. *Neurol Med Chir (Tokyo),* 58**,** 296-302.

YAMAMOTO, Y., TOMIYAMA, A., SASAKI, N., YAMAGUCHI, H., SHIRAKIHARA, T., NAKASHIMA, K., KUMAGAI, K., TAKEUCHI, S., TOYOOKA, T., OTANI, N., WADA, K., NARITA, Y., ICHIMURA, K., SAKAI, R., NAMBA, H. & MORI, K. 2018b. Intracellular cholesterol level regulates sensitivity of glioblastoma cells against temozolomide-induced cell death by modulation of caspase-8 activation via death receptor 5-accumulation and activation in the plasma membrane lipid raft. *Biochem Biophys Res Commun,* 495**,** 1292-1299.

YAN, L., YAN, C., QIAN, K., SU, H., KOFSKY-WOFFORD, S. A., LEE, W. C., ZHAO, X., HO, M. C., IVANOV, I. & ZHENG, Y. G. 2014. Diamidine compounds for selective inhibition of protein arginine methyltransferase 1. *J Med Chem,* 57**,** 2611-22.

YAN, X., FENG, L., XU, Z., CHEN, W., YAN, H., WU, P., DING, C., ZHU, X. & LU, Y. 2023. Histone acetylation gene-based biomarkers as novel markers of the immune microenvironment in glioblastoma. *J Gene Med,* 25**,** e3511.

YAN, Y., XU, Z., CHEN, X., WANG, X., ZENG, S., ZHAO, Z., QIAN, L., LI, Z., WEI, J., HUO, L., LI, X., GONG, Z. & SUN, L. 2019. Novel Function of lncRNA ADAMTS9-AS2 in Promoting Temozolomide Resistance in Glioblastoma via Upregulating the FUS/MDM2 Ubiquitination Axis. *Front Cell Dev Biol,* 7**,** 217.

YANG, F., XIE, Y., TANG, J., LIU, B., LUO, Y., HE, Q., ZHANG, L., XIN, L., WANG, J., WANG, S., ZHANG, S., CAO, Q., WANG, L., HE, L. & ZHANG, L. 2021. Uncovering a Distinct Gene Signature in Endothelial Cells Associated With Contrast Enhancement in Glioblastoma. *Front Oncol,* 11**,** 683367.

YANG, L., WANG, Y., LI, Y. J. & ZENG, C. C. 2018. Chemo-resistance of A172 glioblastoma cells is controlled by miR-1271-regulated Bcl-2. *Biomed Pharmacother,* 108**,** 734-740.

YANG, W., WANG, L., ROEHN, G., PEARLSTEIN, R. D., ALI-OSMAN, F., PAN, H., GOLDBRUNNER, R., KRANTZ, M., HARMS, C. & PASCHEN, W. 2013. Small ubiquitin-like modifier 1-3 conjugation [corrected] is activated in human astrocytic brain tumors and is required for glioblastoma cell survival. *Cancer Sci,* 104**,** 70-7.

YANG, Y., HADJIKYRIACOU, A., XIA, Z., GAYATRI, S., KIM, D., ZURITA-LOPEZ, C., KELLY, R., GUO, A., LI, W., CLARKE, S. G. & BEDFORD, M. T. 2015. PRMT9 is a type II methyltransferase that methylates the splicing factor SAP145. *Nat Commun,* 6**,** 6428.

YANG, Y., LIANG, Z., XIA, Z., WANG, X., MA, Y., SHENG, Z., GU, Q., SHEN, G., ZHOU, L., ZHU, H., XU, N. & LIANG, S. 2019. SAE1 promotes human glioma progression through activating AKT SUMOylation-mediated signaling pathways. *Cell Commun Signal,* 17**,** 82.

YE, L., GU, L., WANG, Y., XING, H., LI, P., GUO, X., WANG, Y. & MA, W. 2024. Identification of TMZ resistance-associated histone post-translational modifications in glioblastoma using multi-omics data. *CNS Neurosci Ther,* 30**,** e14649.

YEO, E. C. F., BROWN, M. P., GARGETT, T. & EBERT, L. M. 2021. The Role of Cytokines and Chemokines in Shaping the Immune Microenvironment of Glioblastoma: Implications for Immunotherapy. *Cells,* 10.

YI, M., MA, Y., CHEN, Y., LIU, C., WANG, Q. & DENG, H. 2020. Glutathionylation Decreases Methyltransferase Activity of PRMT5 and Inhibits Cell Proliferation. *Mol Cell Proteomics,* 19**,** 1910-1920.

YOSHIMOTO, T., BOEHM, M., OLIVE, M., CROOK, M. F., SAN, H., LANGENICKEL, T. & NABEL, E. G. 2006. The arginine methyltransferase PRMT2 binds RB and regulates E2F function. *Exp Cell Res,* 312**,** 2040-53.

YU, Z., CHEN, T., HEBERT, J., LI, E. & RICHARD, S. 2009. A mouse PRMT1 null allele defines an essential role for arginine methylation in genome maintenance and cell proliferation. *Mol Cell Biol,* 29**,** 2982-96.

YUAN, X., LARSSON, C. & XU, D. 2019. Mechanisms underlying the activation of TERT transcription and telomerase activity in human cancer: old actors and new players. *Oncogene,* 38**,** 6172-6183.

YUE, Y., LIU, J. & HE, C. 2015. RNA N6-methyladenosine methylation in post-transcriptional gene expression regulation. *Genes Dev,* 29**,** 1343-55.

YUILE, P., DENT, O., COOK, R., BIGGS, M. & LITTLE, N. 2006. Survival of glioblastoma patients related to presenting symptoms, brain site and treatment variables. *J Clin Neurosci,* 13**,** 747-51.

ZERROUQI, A., PYRZYNSKA, B., FEBBRAIO, M., BRAT, D. J. & VAN MEIR, E. G. 2012. P14ARF inhibits human glioblastoma-induced angiogenesis by upregulating the expression of TIMP3. *J Clin Invest,* 122**,** 1283-95.

ZHANG, H., DAI, Z., WU, W., WANG, Z., ZHANG, N., ZHANG, L., ZENG, W. J., LIU, Z. & CHENG, Q. 2021. Regulatory mechanisms of immune checkpoints PD-L1 and CTLA-4 in cancer. *J Exp Clin Cancer Res,* 40**,** 184.

ZHANG, H., GUO, X., FENG, X., WANG, T., HU, Z., QUE, X., TIAN, Q., ZHU, T., GUO, G., HUANG, W. & LI, X. 2017a. MiRNA-543 promotes osteosarcoma cell proliferation and glycolysis by partially suppressing PRMT9 and stabilizing HIF-1alpha protein. *Oncotarget,* 8**,** 2342-2355.

ZHANG, H., ZHANG, Y., FENG, Z., LU, L., LI, Y., LIU, Y. & CHEN, Y. 2022. Analysis of the Expression and Role of Keratin 17 in Human Tumors. *Front Genet,* 13**,** 801698.

ZHANG, J., STEVENS, M. F. & BRADSHAW, T. D. 2012. Temozolomide: mechanisms of action, repair and resistance. *Curr Mol Pharmacol,* 5**,** 102-14.

ZHANG, M., XU, Y., ZHU, G., ZENG, Q., GAO, R., QIU, J., SU, W. & WANG, R. 2024. Human C15orf39 Inhibits Inflammatory Response via PRMT2 in Human Microglial HMC3 Cell Line. *Int J Mol Sci,* 25.

ZHANG, Q., ZHANG, X., XIE, P. & ZHANG, W. 2024. Liquid biopsy: An arsenal for tumour screening and early diagnosis. *Cancer Treat Rev,* 129**,** 102774.

ZHANG, W., JIANG, J., XU, Z., YAN, H., TANG, B., LIU, C., CHEN, C. & MENG, Q. 2023. Microglia-containing human brain organoids for the study of brain development and pathology. *Mol Psychiatry,* 28**,** 96-107.

ZHANG, X., LIU, X., ZHOU, W., YANG, M., DING, Y., WANG, Q. & HU, R. 2018a. Fasudil increases temozolomide sensitivity and suppresses temozolomide-resistant glioma growth via inhibiting ROCK2/ABCG2. *Cell Death Dis,* 9**,** 190.

ZHANG, Y., CRUICKSHANKS, N., YUAN, F., WANG, B., PAHUSKI, M., WULFKUHLE, J., GALLAGHER, I., KOEPPEL, A. F., HATEF, S., PAPANICOLAS, C., LEE, J., BAR, E. E., SCHIFF, D., TURNER, S. D., PETRICOIN, E. F., GRAY, L. S. & ABOUNADER, R. 2017b. Targetable T-type Calcium Channels Drive Glioblastoma. *Cancer Res,* 77**,** 3479-3490.

ZHANG, Y., DUBE, C., GIBERT, M., JR., CRUICKSHANKS, N., WANG, B., COUGHLAN, M., YANG, Y., SETIADY, I., DEVEAU, C., SAOUD, K., GRELLO, C., OXFORD, M., YUAN, F. & ABOUNADER, R. 2018b. The p53 Pathway in Glioblastoma. *Cancers (Basel),* 10.

ZHANG, Y., VAN HAREN, M. J. & MARTIN, N. I. 2020. Peptidic transition state analogues as PRMT inhibitors. *Methods,* 175**,** 24-29.

ZHAO, D. Y., GISH, G., BRAUNSCHWEIG, U., LI, Y., NI, Z., SCHMITGES, F. W., ZHONG, G., LIU, K., LI, W., MOFFAT, J., VEDADI, M., MIN, J., PAWSON, T. J., BLENCOWE, B. J. & GREENBLATT, J. F. 2016. SMN and symmetric arginine dimethylation of RNA polymerase II C-terminal domain control termination. *Nature,* 529**,** 48-53.

ZHAO, T., LI, C., GE, H., LIN, Y. & KANG, D. 2022. Glioblastoma vaccine tumor therapy research progress. *Chin Neurosurg J,* 8**,** 2.

ZHAO, T., ZENG, J., XU, Y., SU, Z., CHONG, Y., LING, T., XU, H., SHI, H., ZHU, M., MO, Q., HUANG, X., LI, Y., ZHANG, X., NI, H. & YOU, Q. 2022. Chitinase-3 like-protein-1 promotes glioma progression via the NF-kappaB signaling pathway and tumor microenvironment reprogramming. *Theranostics,* 12**,** 6989-7008.

ZHENG, K., CHEN, S., REN, Z. & WANG, Y. 2023. Protein arginine methylation in viral infection and antiviral immunity. *Int J Biol Sci,* 19**,** 5292-5318.

ZHONG, J., CAO, R. X., ZU, X. Y., HONG, T., YANG, J., LIU, L., XIAO, X. H., DING, W. J., ZHAO, Q., LIU, J. H. & WEN, G. B. 2012. Identification and characterization of novel spliced variants of PRMT2 in breast carcinoma. *FEBS J,* 279**,** 316-35.

ZHOU, A., LIN, K., ZHANG, S., CHEN, Y., ZHANG, N., XUE, J., WANG, Z., ALDAPE, K. D., XIE, K., WOODGETT, J. R. & HUANG, S. 2016. Nuclear GSK3beta promotes tumorigenesis by phosphorylating KDM1A and inducing its deubiquitylation by USP22. *Nat Cell Biol,* 18**,** 954-966.

ZHOU, P., FERNANDES, N., DODGE, I. L., REDDI, A. L., RAO, N., SAFRAN, H., DIPETRILLO, T. A., WAZER, D. E., BAND, V. & BAND, H. 2003. ErbB2 degradation mediated by the co-chaperone protein CHIP. *J Biol Chem,* 278**,** 13829-37.

ZIKOU, A., SIOKA, C., ALEXIOU, G. A., FOTOPOULOS, A., VOULGARIS, S. & ARGYROPOULOU, M. I. 2018. Radiation Necrosis, Pseudoprogression, Pseudoresponse, and Tumor Recurrence: Imaging Challenges for the Evaluation of Treated Gliomas. *Contrast Media Mol Imaging,* 2018**,** 6828396.

ZIÓŁKOWSKA, K. K., R. AND BRZÓZKA, Z. 2011. Microfluidic devices as tools for mimicking the in vivo environment. *New J Chem,* 35**,** 979.

CHAPTER 9: APPENDICES

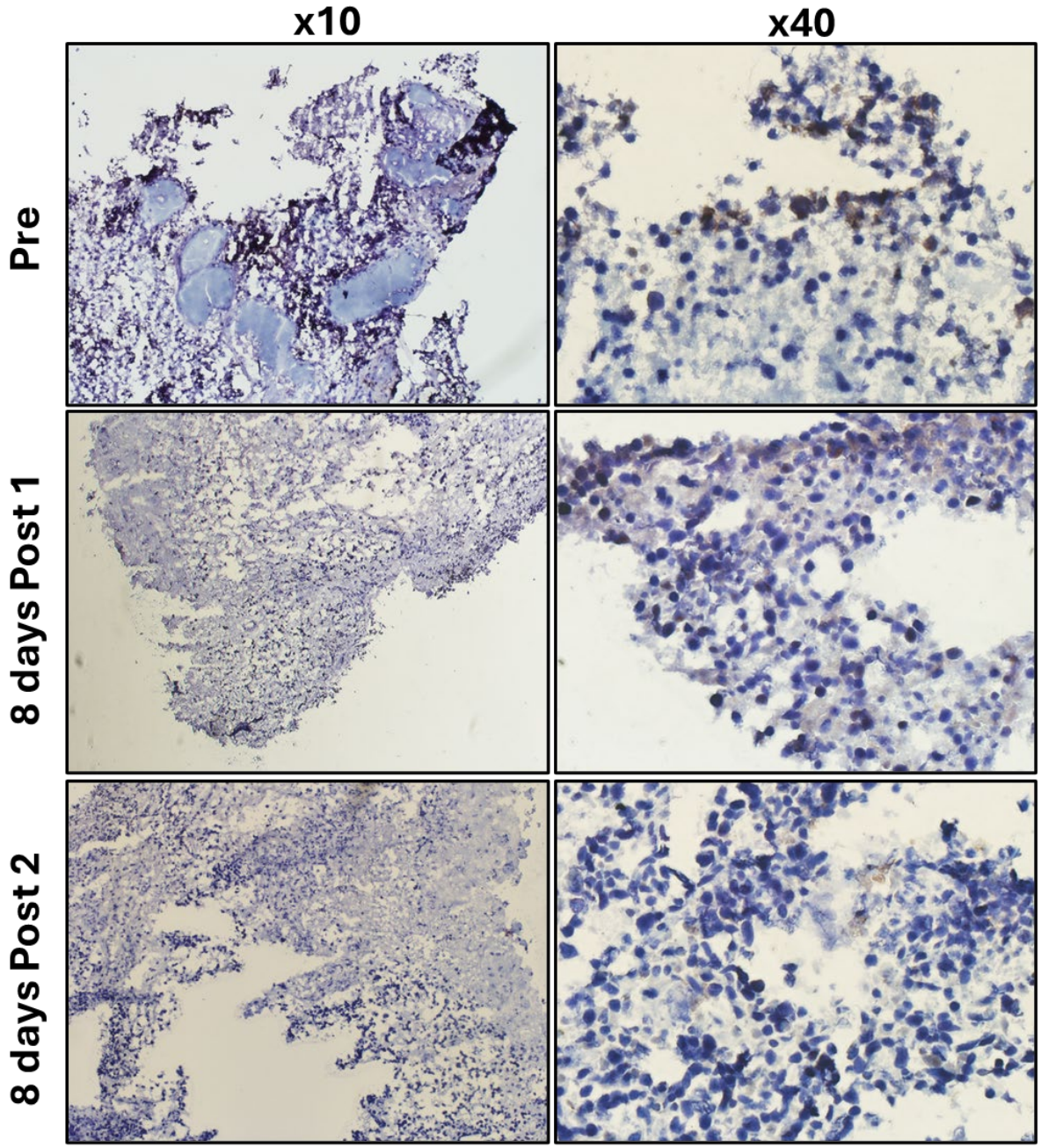

Appendix 1.: Representative images of Ki67 stained GBM tissue used for validation of Cell profiler pipeline.

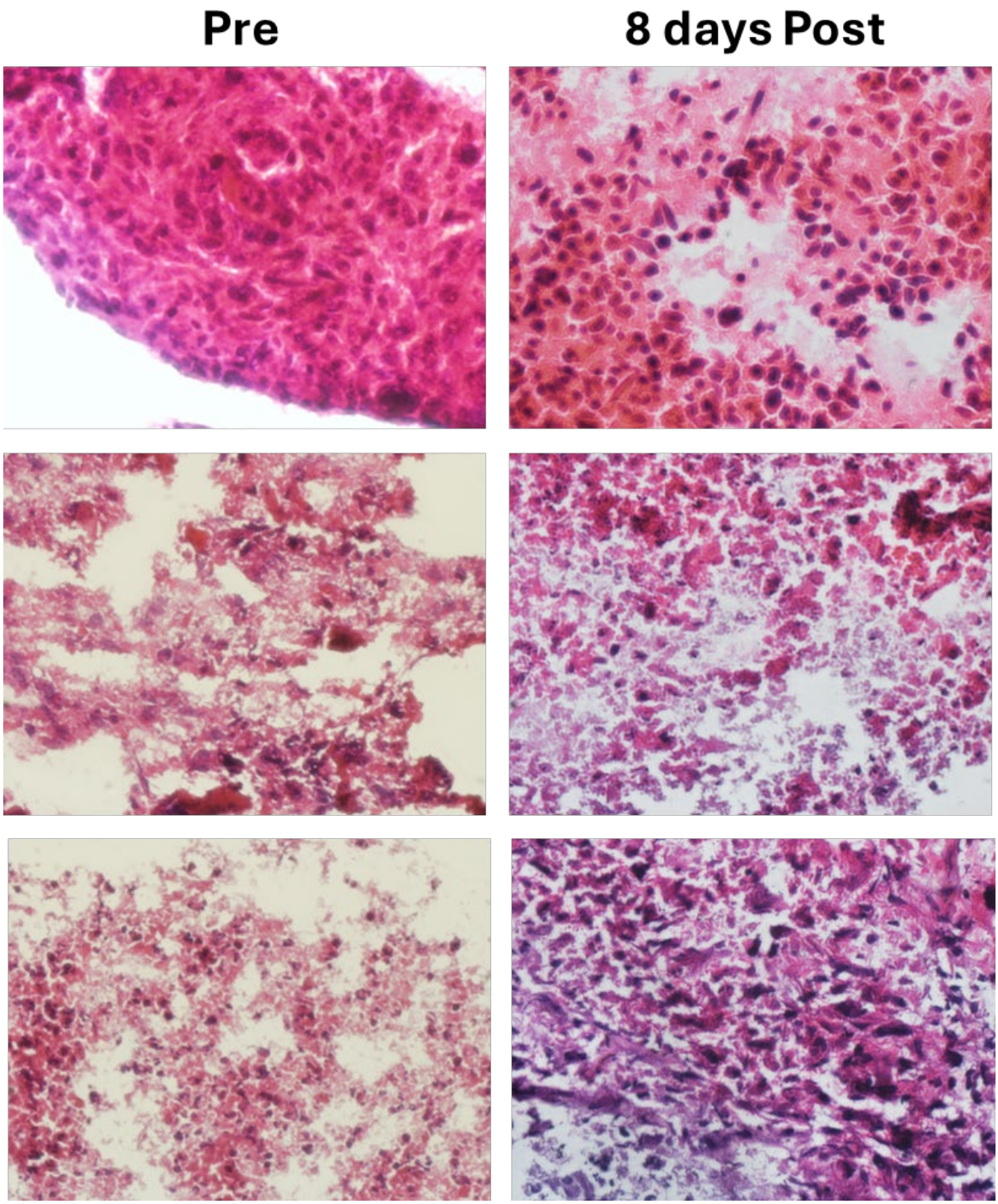

Appendix 2.: Representative images of H&E-stained GBM tissue pre- and 8-days post-perfusion.

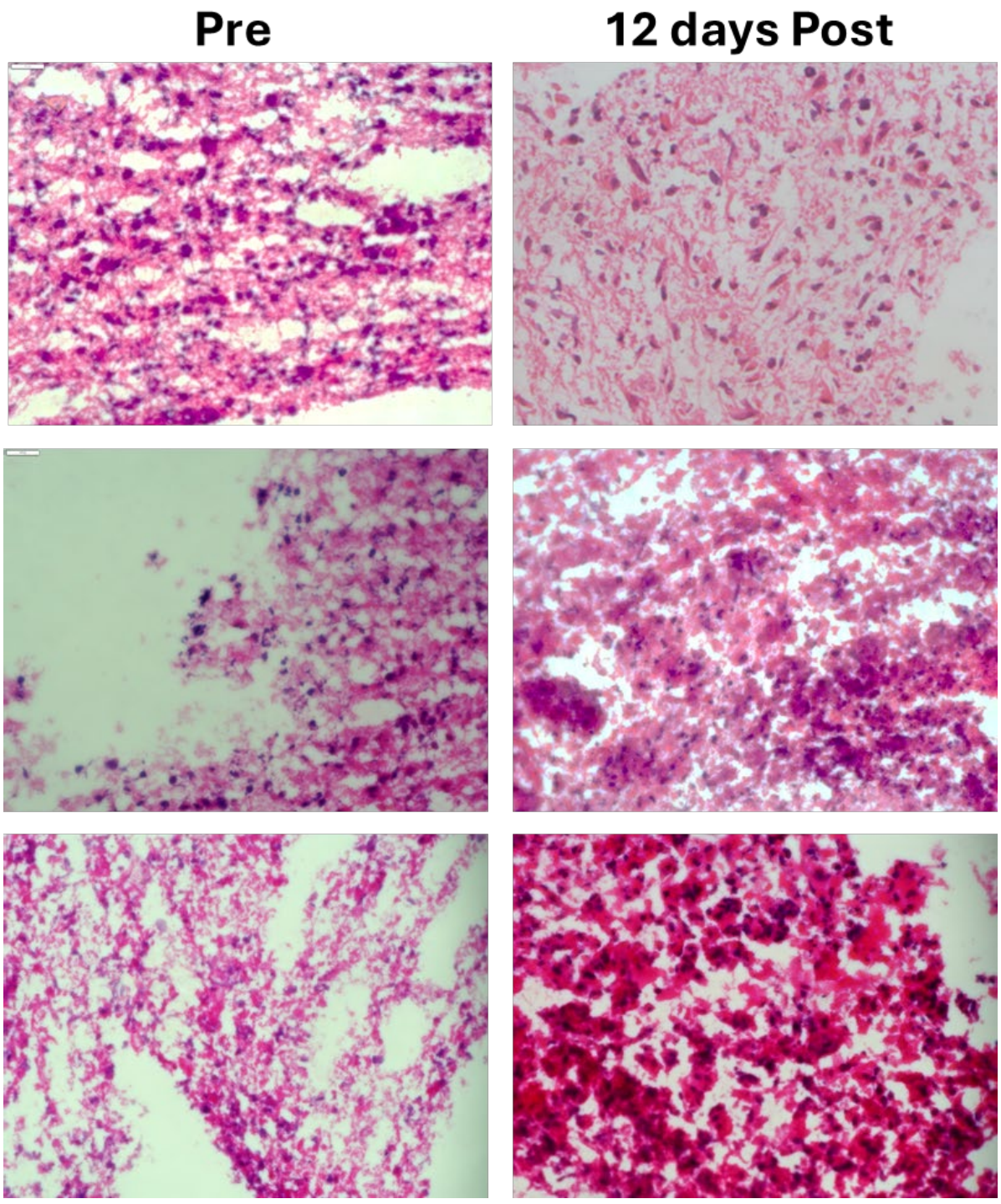

Appendix 3.: Representative images of H&E-stained GBM tissue pre- and 12-days post-perfusion

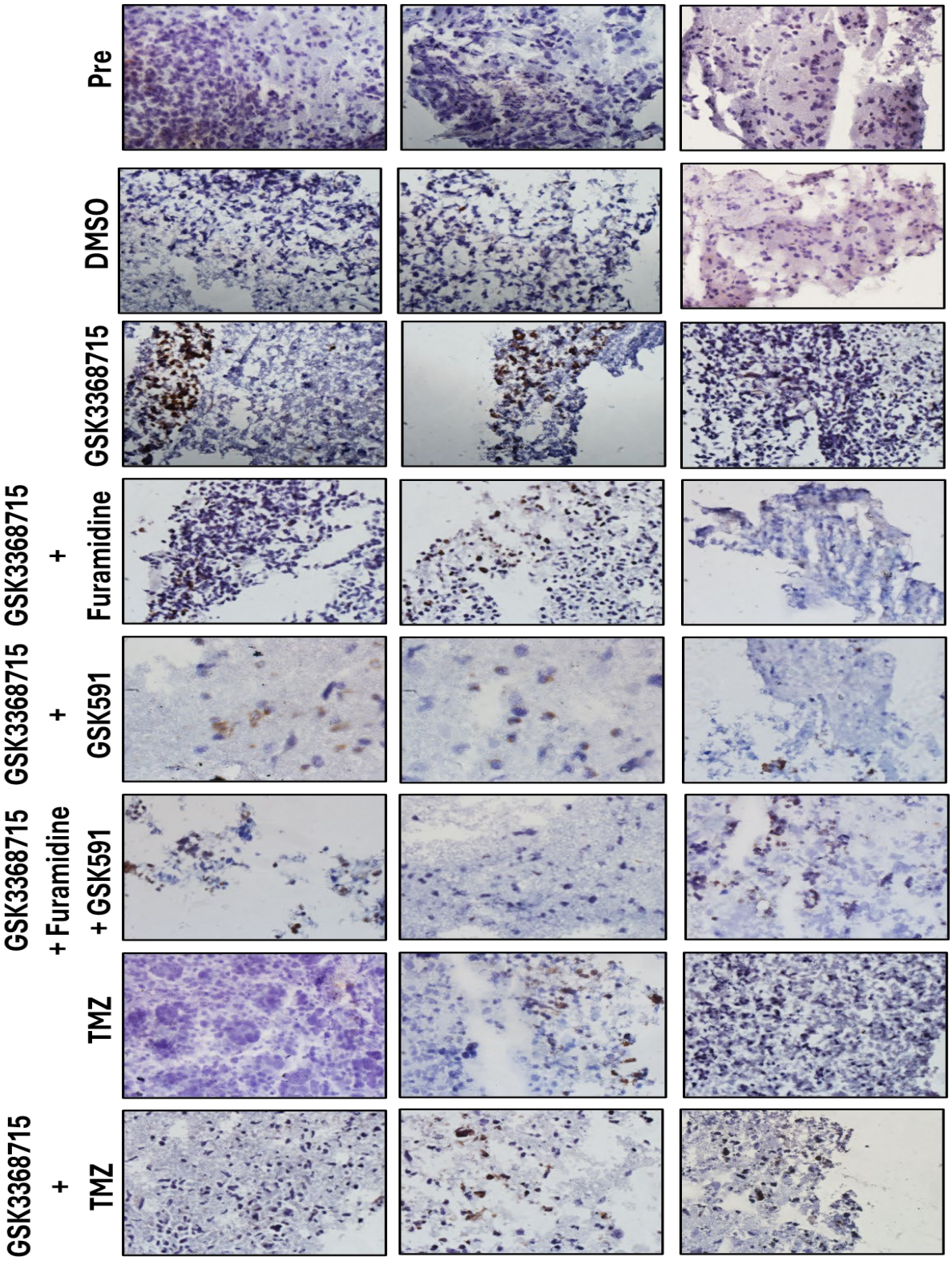

Appendix 4.: Representative images of cleaved PARP-stained GBM tissue pre- and 8-days post-perfusion and treated with 1µM GSK3368715, 10µM TMZ, 1µM GSK3368715 +10µM TMZ, 1µM GSK3368715 + 1µM Furamidine, 1µM GSK3368715 + 1µM Furamidine + 1µM GSK591.

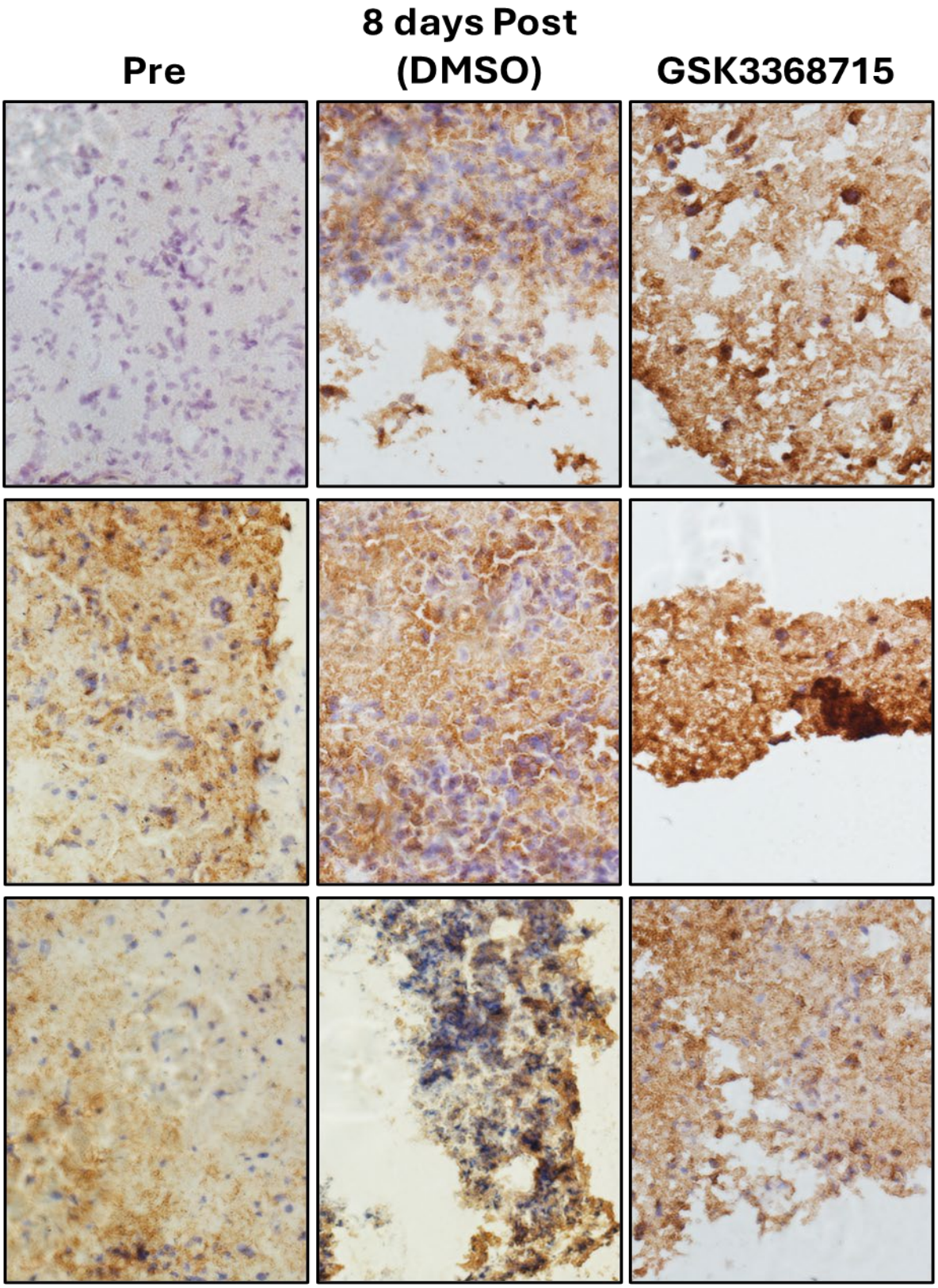

Appendix 5: Representative images of Annexin V-stained GBM tissue pre- and 8-days post-perfusion and treated with 1µM GSK3368715.

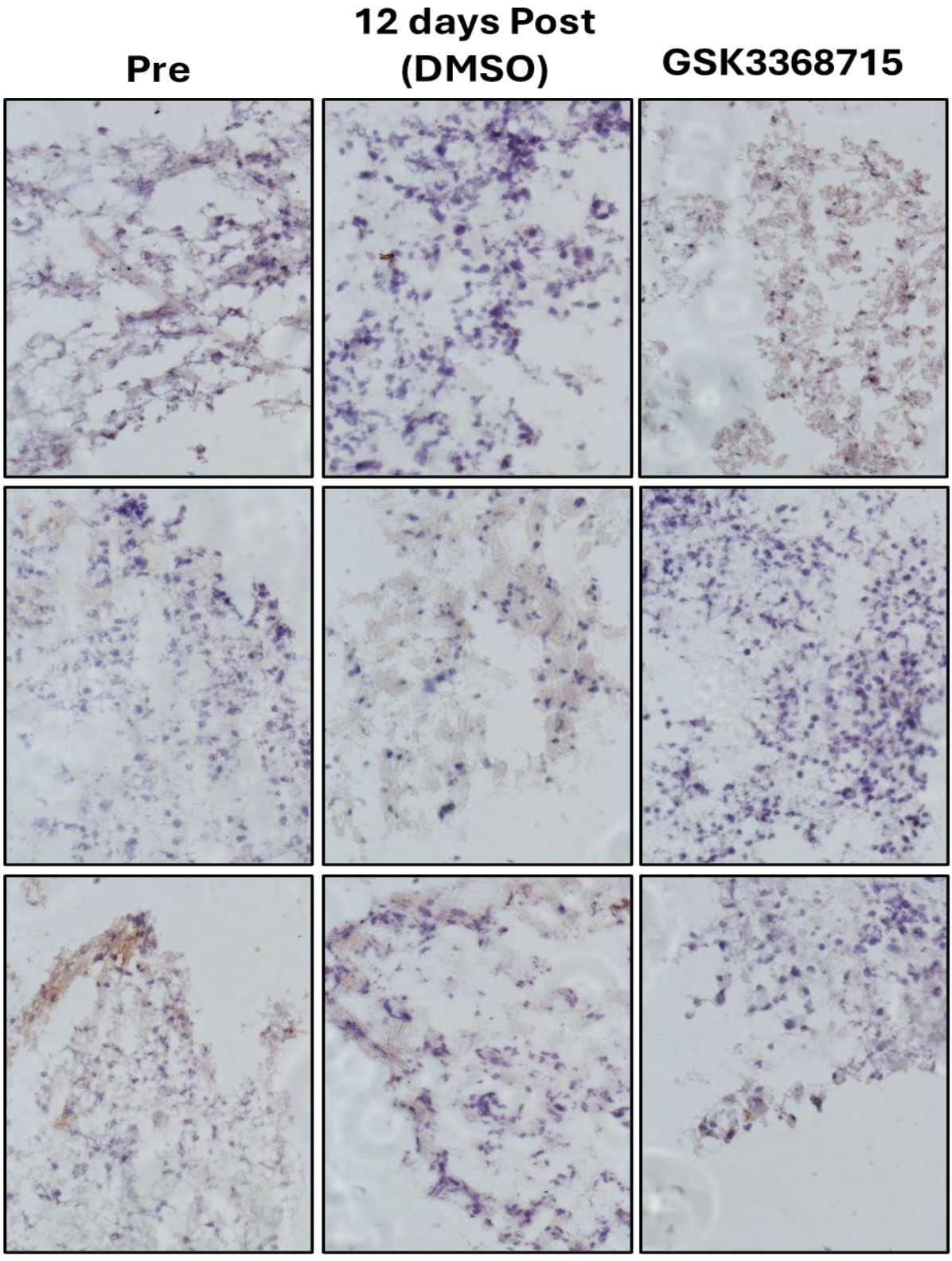

Appendix 6: Representative images of cleaved PARP-stained GBM tissue pre- and 12-days post-perfusion and treated with 1μM GSK3368715.

Gene Ontology showing enrichment of biological processes of upregulated differentially expressed genes (DEGs) common to 2 or more patients after 8-day in a microfluidics device, treated with 1 μM GSK3368715 vs the DMSO control

Enrichment FDR	nGenes	Pathway Genes	Fold Enrichment	Pathway	URL	Genes
1.24E-09	66	699	2.654022216	Chemotaxis	http://amigo.geneontology.org/amigo/term/GO:0006935	ANOS1 HGF ADGRA2 TRIO NTN1 SPI1 EDN1 SEMA5B PIK3CG HOXA2 CXCL12 CCL7 CCL2 CCL8 BST1 BIN2 VEGFA LOX FGF1 CSF3R CCRL2 EGR2 PREX1 LBP DOCK2 PLXNC1 EDNRB GPNMB CH25H FGF2 LYST GDF7 ACKR3 SLIT2 PIK3R1 CXCL14 PLA2G7 PTPRO KIF5A CXCL13 SLAMF8 FCER1G CCR5 CCR1 VEGFD MAPK7 GBX2 GFRA2 CXCL8 GPR183 S1PR1 FPR1 C3AR1 SCG2 GAP43 PTPRM CDK5R1 ADAMTSL1 CSF1R FPR3 EVL CSAR1 DPP4 PLXNB3 SUCNR1 TUBB3
1.24E-09	116	1639	1.989375796	Cell adhesion	http://amigo.geneontology.org/amigo/term/GO:0007155	PKD1 CD4 ANOS1 CNTN1 SLAMF7 IBSP VCAN VMP1 NTN1 CD84 SPI1 FCGR2B APBB1IP FAP PCDHB4 CD200 CORO2B APLP1 CD33 CADM4 PIK3CG ECM2 CXCL12 MAP3K8 CCL2 ALOX12 BST1 LPXN CD83 VEGFA CDH6 CD86 ITGA4 LOXL3 PLEK RND3 GBP1 CNN3 CSF3R PCDHB8 PCDHB10 PCDHB14 SASH3 TNFAIP6 PREX1 FGL2 LIF POSTN DUSP26 ADAMDEC1 PTPN22 APC HAVCR2 CD36 SERPINE2 STAB2 PLXNC1 PCDH8 GPNMB SMAD6 CYP1B1 ITGB7 CDH11 TMEFF2 ACKR3 NFKBIZ PIK3R1 MEGF10 NLGN4X CDHR1 PTPRO MERTK ABI3BP VSIG4 FZD7 CXCL13 ACAN PLPP3 DISC1 CCR1 FOLR2 FBN1 DCHS1 MFAP4 MAPK7 COL3A1 NPNT SIGLEC7 COL4A3 CXCL8 CTNND2 S1PR1 COL8A2 FRMD5 PTPRM PEAK1 SUSD5 RGMB CDK5R1 ADAMTSL1 SOX2 ABAT LSAMP SLITRK2 APOD PCDH18 DPP4 PLXNB3 PCDHGC3 PCDHGC5 BGLAP PCDHGC4 PCDHGA5 PCDHGA8 PCDHGA10 MMP12
1.24E-09	116	1646	1.98091551	Biological adhesion	http://amigo.geneontology.org/amigo/term/GO:0022610	PKD1 CD4 ANOS1 CNTN1 SLAMF7 IBSP VCAN VMP1 NTN1 CD84 SPI1 FCGR2B APBB1IP FAP PCDHB4 CD200 CORO2B APLP1 CD33 CADM4 PIK3CG ECM2 CXCL12 MAP3K8 CCL2 ALOX12 BST1 LPXN CD83 VEGFA CDH6 CD86 ITGA4 LOXL3 PLEK RND3 GBP1 CNN3 CSF3R PCDHB8 PCDHB10 PCDHB14 SASH3 TNFAIP6 PREX1 FGL2 LIF POSTN DUSP26 ADAMDEC1 PTPN22 APC HAVCR2 CD36 SERPINE2 STAB2 PLXNC1 PCDH8 GPNMB SMAD6 CYP1B1 ITGB7 CDH11 TMEFF2 ACKR3 NFKBIZ PIK3R1 MEGF10 NLGN4X CDHR1 PTPRO MERTK ABI3BP VSIG4 FZD7 CXCL13 ACAN PLPP3 DISC1 CCR1 FOLR2 FBN1 DCHS1 MFAP4 MAPK7 COL3A1 NPNT SIGLEC7 COL4A3 CXCL8 CTNND2 S1PR1 COL8A2 FRMD5 PTPRM PEAK1 SUSD5 RGMB CDK5R1 ADAMTSL1 SOX2 ABAT LSAMP SLITRK2 APOD PCDH18 DPP4 PLXNB3 PCDHGC3 PCDHGC5 BGLAP PCDHGC4 PCDHGA5 PCDHGA8 PCDHGA10 MMP12
1.24E-09	66	702	2.642680241	Taxis	http://amigo.geneontology.org/amigo/term/GO:0042330	ANOS1 HGF ADGRA2 TRIO NTN1 SPI1 EDN1 SEMA5B PIK3CG HOXA2 CXCL12 CCL7 CCL2 CCL8 BST1 BIN2 VEGFA LOX FGF1 CSF3R CCRL2 EGR2 PREX1 LBP DOCK2 PLXNC1 EDNRB GPNMB CH25H FGF2 LYST GDF7 ACKR3 SLIT2 PIK3R1 CXCL14 PLA2G7 PTPRO KIF5A CXCL13 SLAMF8 FCER1G CCR5 CCR1 VEGFD MAPK7 GBX2 GFRA2 CXCL8 GPR183 S1PR1 FPR1 C3AR1 SCG2 GAP43 PTPRM CDK5R1 ADAMTSL1 CSF1R FPR3 EVL CSAR1 DPP4 PLXNB3 SUCNR1 TUBB3
2.65E-09	131	1982	1.857827724	Locomotion	http://amigo.geneontology.org/amigo/term/GO:0040011	FGR SOX8 ANOS1 DCN HGF ADGRA2 TRIO VCAN NTN1 CD84 SPI1 CAMK2A FAP EDN1 SEMA5B CD200 HMOX1 BEX4 CADM4 PIK3CG HOXA2 CXCL12 CCL7 CCL2 CCL8 ALOX12 BST1 LPXN BIN2 SOD2 PHACTR1 NR2E1 VEGFA LOX SPARC FGF1 ITGA4 APC2 RND3 MARK1 GADD45A CD48 CSF3R CCRL2 EGR2 TNFAIP6 PREX1 SNAI1 LBP PLVAP RGN AKAP12 POSTN PTPN22 DOCK2 APC DOCK10 HTR2B SERPINE2 PLXNC1 SPRY2 EDNRB GPNMB CYP1B1 CH25H FGF2 ITGB7 NLRP12 LYST GDF7 TMEFF2 ACKR3 SLIT2 PIK3R1 MEGF10 CXCL14 PLA2G7 ADRA2A PTPRO DAB2 MERTK KIF5A CXCL13 FMNL2 SLAMF8 FCER1G CELF3 CCR5 PLPP3 DISC1 CCR1 VEGFD DCHS1 MAPK7 MAPRE2 GBX2 COL3A1 GFRA2 CXCL8 GPR183 LDB2 S1PR1 FPR1 C3AR1 FRMD5 SCG2 GAP43 CLEC7A PTPRM PEAK1 CDK5R1 ADAMTSL1 CHRM4 CSF1R SPATA13 FPR3 DNAH17 CLN3 APOD EVL CSAR1 DPP4 PLXNB3 SUCNR1 SOX18 CFAP44 TUBB3 MMP12 NEFL ADORA3 CCDC39
1.25E-08	41	343	3.359909121	Cell chemotaxis	http://amigo.geneontology.org/amigo/term/GO:0060326	HGF SPI1 EDN1 PIK3CG CXCL12 CCL7 CCL2 CCL8 BST1 BIN2 VEGFA LOX FGF1 CSF3R CCRL2 PREX1 LBP EDNRB CH25H FGF2 LYST ACKR3 SLIT2 CXCL14 PLA2G7 PTPRO CXCL13 SLAMF8 FCER1G CCR5 CCR1 VEGFD CXCL8 GPR183 S1PR1 C3AR1 SCG2 CSF1R CSAR1 DPP4 PLXNB3
4.53E-08	108	1590	1.909257148	Cell migration	http://amigo.geneontology.org/amigo/term/GO:0016477	FGR SOX8 DCN HGF ADGRA2 VCAN NTN1 CD84 SPI1 CAMK2A FAP EDN1 SEMA5B CD200 HMOX1 BEX4 PIK3CG CXCL12 CCL7 CCL2 CCL8 ALOX12 BST1 LPXN BIN2 SOD2 PHACTR1 NR2E1 VEGFA LOX SPARC FGF1 ITGA4 APC2 RND3 MARK1 GADD45A CD48 CSF3R CCRL2 TNFAIP6 PREX1 SNAI1 LBP PLVAP AKAP12 POSTN PTPN22 APC DOCK10 HTR2B SERPINE2 PLXNC1 SPRY2 EDNRB GPNMB CYP1B1 CH25H FGF2 ITGB7 NLRP12 LYST TMEFF2 ACKR3 SLIT2 PIK3R1 MEGF10 CXCL14 PLA2G7 ADRA2A PTPRO DAB2 MERTK CXCL13 FMNL2 SLAMF8 FCER1G CCR5 PLPP3 DISC1 CCR1 VEGFD MAPRE2 GBX2 COL3A1 CXCL8 GPR183 LDB2 S1PR1 C3AR1 FRMD5 SCG2 CLEC7A PTPRM CHRM4 CSF1R SPATA13 CLN3 APOD EVL CSAR1 DPP4 PLXNB3 SUCNR1 SOX18 MMP12 ADORA3
4.62E-08	81	1056	2.156050331	Regulation of locomotion	http://amigo.geneontology.org/amigo/term/GO:0040012	FGR DCN HGF ADGRA2 NTN1 SPI1 CAMK2A EDN1 SEMA5B CD200 HMOX1 BEX4 CADM4 PIK3CG CXCL12 CCL7 CCL2 CCL8 ALOX12 BST1 SOD2 PHACTR1 NR2E1 VEGFA SPARC FGF1 ITGA4 GADD45A TNFAIP6 PREX1 SNAI1 LBP PLVAP RGN AKAP12 POSTN PTPN22 APC DOCK10 SERPINE2 PLXNC1 SPRY2 GPNMB CYP1B1 FGF2 TMEFF2 ACKR3 SLIT2 PIK3R1 CXCL14 PLA2G7 ADRA2A PTPRO DAB2 CXCL13 SLAMF8 PLPP3 CCR1 VEGFD MAPRE2 COL3A1 CXCL8 GPR183 LDB2 S1PR1 C3AR1 FRMD5 SCG2 CLEC7A PTPRM CHRM4 CSF1R SPATA13 CLN3 APOD EVL CSAR1 DPP4 PLXNB3 SUCNR1 ADORA3
4.89E-08	75	946	2.228475794	Regulation of cell migration	http://amigo.geneontology.org/amigo/term/GO:0030334	FGR DCN HGF ADGRA2 NTN1 SPI1 CAMK2A EDN1 SEMA5B CD200 HMOX1 BEX4 PIK3CG CXCL12 CCL7 CCL2 CCL8 ALOX12 BST1 SOD2 PHACTR1 NR2E1 VEGFA SPARC FGF1 ITGA4 GADD45A TNFAIP6 PREX1 SNAI1 LBP PLVAP AKAP12 POSTN PTPN22 APC DOCK10 SERPINE2 PLXNC1 SPRY2 GPNMB CYP1B1 FGF2 TMEFF2 ACKR3 SLIT2 PIK3R1 CXCL14 PLA2G7 ADRA2A DAB2 CXCL13 SLAMF8 PLPP3 CCR1 VEGFD MAPRE2 COL3A1 CXCL8 GPR183 LDB2 S1PR1 C3AR1 FRMD5 CLEC7A PTPRM CSF1R SPATA13 CLN3 APOD EVL CSAR1 DPP4 PLXNB3 ADORA3
1.30E-07	33	258	3.595274281	Leukocyte chemotaxis	http://amigo.geneontology.org/amigo/term/GO:0030595	SPI1 EDN1 PIK3CG CXCL12 CCL7 CCL2 CCL8 BST1 VEGFA CSF3R PREX1 LBP EDNRB CH25H LYST SLIT2 CXCL14 PLA2G7 PTPRO CXCL13 SLAMF8 FCER1G CCR5 CCR1 VEGFD CXCL8 GPR183 S1PR1 C3AR1 SCG2 CSF1R CSAR1 DPP4

Gene Ontology showing enrichment of cellular component of upregulated differentially expressed genes (DEGs) common to 2 or more patients after 8-day in a microfluidics device, treated with 1 μM GSK3368715 vs the DMSO control

Enrichment FDR	nGenes	Pathway Genes	Fold Enrichment	Pathway	URL	Genes
3.25E-09	129	1965	1.845291366	Intrinsic component of plasma membrane	http://amigo.geneontology.org/amigo/term/GO:0031226	PKD1 CD4 CNTN1 TNFRSF9 IL17RB CD84 PLPP1 ABCC9 ASIC4 FCGR2B GPR137B ADCYAP1R1 PCDHB4 P2RX7 CD200 CSF2RB KCND1 HAS3 AQP9 OLFM2 CD33 CACNG7 GLRB P2RX3 CD83 GHR LIFR ITGA4 NCF2 KCNQ4 CD48 CSF3R KCNIP2 GRIA2 PCDHB8 PCDHB10 PCDHB14 CCRL2 ACVR2A RAMP3 HS3ST3B1 EDA2R CHRM3 TSPAN2 SYT6 DAGLA APLNR CD36 GPR55 HTR2B STAB2 PLXNC1 PCDH8 EDNRB GPNMB TLR4 FXYD6 SLC5A6 SLC40A1 VAMP1 ITGB7 LPAR6 GPR65 CD53 FCGR2A SLC26A1 NLGN4X CDHR1 GRIK4 ADRA2A PTPRO KCNE4 KCNK13 RASGRP3 MERTK SLC24A2 TSPAN7 KCNB1 FCER1G NPR2 CHRNB2 CCR5 PLPP3 LRRTM1 SLC15A2 CCR1 GRM2 GRIK2 SLC13A4 TMC1 NPNT SIGLEC7 GPR183 KCNAB3 GPR34 C3AR1 PTPRM TLR1 RGMB CHRNA9 KCNE3 KCNA2 CD163 GAS1 CHRM4 SLC26A11 CSF1R TMPRSS2 DIABLO KCNQ3 EVI2B SLITRK2 COL25A1 PCDH18 LRRC8B SLC22A4 C5AR1 FCGR1B PLXNB3 PCDHGC3 PCDHGC5 PCDHGC4 PCDHGA5 PCDHGA8 PCDHGA10 CLEC5A ADORA3
7.24E-09	123	1881	1.838036409	Integral component of plasma membrane	http://amigo.geneontology.org/amigo/term/GO:0005887	PKD1 CD4 TNFRSF9 IL17RB CD84 PLPP1 ABCC9 ASIC4 FCGR2B GPR137B ADCYAP1R1 PCDHB4 P2RX7 CD200 CSF2RB KCND1 HAS3 AQP9 OLFM2 CD33 CACNG7 GLRB P2RX3 CD83 GHR LIFR ITGA4 NCF2 KCNQ4 CSF3R KCNIP2 GRIA2 PCDHB8 PCDHB10 PCDHB14 CCRL2 ACVR2A RAMP3 HS3ST3B1 EDA2R CHRM3 TSPAN2 SYT6 DAGLA APLNR CD36 GPR55 HTR2B STAB2 PLXNC1 PCDH8 EDNRB GPNMB TLR4 FXYD6 SLC5A6 SLC40A1 VAMP1 ITGB7 LPAR6 GPR65 CD53 FCGR2A SLC26A1 NLGN4X CDHR1 GRIK4 ADRA2A PTPRO KCNE4 KCNK13 RASGRP3 MERTK SLC24A2 TSPAN7 KCNB1 FCER1G NPR2 CHRNB2 CCR5 PLPP3 LRRTM1 SLC15A2 CCR1 GRM2 GRIK2 SLC13A4 TMC1 NPNT SIGLEC7 GPR183 KCNAB3 GPR34 C3AR1 PTPRM TLR1 CHRNA9 KCNE3 KCNA2 CD163 CHRM4 SLC26A11 CSF1R TMPRSS2 DIABLO KCNQ3 EVI2B SLITRK2 COL25A1 PCDH18 LRRC8B SLC22A4 C5AR1 FCGR1B PLXNB3 PCDHGC3 PCDHGC5 PCDHGC4 PCDHGA5 PCDHGA8 PCDHGA10 CLEC5A ADORA3
1.54E-06	51	601	2.385247768	External encapsulating structure	http://amigo.geneontology.org/amigo/term/GO:0030312	ANOS1 DCN VCAN LTBP1 NTN1 APLP1 ECM2 CXCL12 HPX MGP VEGFA LOX SPARC FGF1 MMP8 A1BG F13A1 CFP FGL2 CHI3L1 POSTN ADAMDEC1 CD180 SERPINE2 LUM TMEFF2 ABI3BP ACAN COLEC12 C1QC LRRTM1 CTSS PTX3 TNFRSF11B SBSPON FBN1 MFAP4 COL3A1 NPNT COL4A3 SERPINB9 COL8A2 FGFBP3 NPPA LRRN1 ADAMTSL1 COL25A1 PRELP LINGO3 TRIL MMP12
1.54E-06	51	600	2.389223181	Extracellular matrix	http://amigo.geneontology.org/amigo/term/GO:0031012	ANOS1 DCN VCAN LTBP1 NTN1 APLP1 ECM2 CXCL12 HPX MGP VEGFA LOX SPARC FGF1 MMP8 A1BG F13A1 CFP FGL2 CHI3L1 POSTN ADAMDEC1 CD180 SERPINE2 LUM TMEFF2 ABI3BP ACAN COLEC12 C1QC LRRTM1 CTSS PTX3 TNFRSF11B SBSPON FBN1 MFAP4 COL3A1 NPNT COL4A3 SERPINB9 COL8A2 FGFBP3 NPPA LRRN1 ADAMTSL1 COL25A1 PRELP LINGO3 TRIL MMP12
2.16E-05	38	422	2.531097878	Receptor complex	http://amigo.geneontology.org/amigo/term/GO:0043235	CD4 APBB1IP ADCYAP1R1 LRP2 CSF2RB OLFM2 CACNG7 P2RX3 GHR LIFR ITGA4 CSF3R GRIA2 ACVR2A RAMP3 CD36 HTR2B PLXNC1 TLR4 ITGB7 GRIK4 ADRA2A NR3C2 MERTK CHRNB2 GRIK2 GPRC5B GFRA2 NPNT GPR160 TLR1 CHRNA9 CSF1R DIABLO TLR7 PLXNB3 LIME1 TRIL
5.50E-05	65	960	1.90318023	Cell surface	http://amigo.geneontology.org/amigo/term/GO:0009986	PKD1 CD4 ANOS1 ADGRA2 BTN3A1 TNFRSF9 FCGR2B FAP ADCYAP1R1 LRP2 CD200 TLR8 CD33 CXCL12 BTN3A3 CD83 VEGFA GHR SPARC LIFR CD86 ITGA4 CSF3R GRIA2 CCRL2 ACVR2A RAMP3 LBP PLVAP HAVCR2 CD36 HILPDA SERPINE2 STAB2 TLR4 ITGB7 CD53 CTSK ACKR3 IQGAP2 PAM NLGN4X FZD1 SLAMF8 FCER1G CHRNB2 CCR5 CCR1 TMC1 FOLR2 GPRC5B GFRA2 S1PR1 CLEC7A NRROS CD163 CD163L1 AQP11 RGMA CSF1R KCNQ3 C5AR1 DPP4 PLXNB3 CLEC5A
0.001034591	35	446	2.20582462	Collagen-containing extracellular matrix	http://amigo.geneontology.org/amigo/term/GO:0062023	DCN VCAN LTBP1 NTN1 APLP1 CXCL12 HPX MGP SPARC MMP8 A1BG F13A1 CFP FGL2 POSTN ADAMDEC1 SERPINE2 LUM TMEFF2 ABI3BP ACAN C1QC CTSS SBSPON FBN1 MFAP4 COL3A1 NPNT COL4A3 SERPINB9 COL8A2 FGFBP3 NPPA COL25A1 PRELP
0.001206444	69	1150	1.686510481	Secretory vesicle	http://amigo.geneontology.org/amigo/term/GO:0099503	FGR HGF CTSA CTTNBP2 EDN1 MOXD1 SNX10 MT3 CHGB LYZ STX1B ATP8B4 SCG3 CD33 BST1 BIN2 STX2 VEGFA SPARC QPCT NCF2 MMP8 A1BG RAB9B TNFAIP6 F13A1 CFP FGL2 KLK14 UNC13A CHI3L1 SYT6 DOCK2 CD36 HILPDA SERPINE2 RCBTB2 SYTL2 VAMP1 GLIPR1 SLC15A4 DPEP3 SYPL2 CD53 FCGR2A SYT2 LHFPL2 IQGAP2 PAM DOK3 TMEM163 FCER1G DISC1 CTSS PTX3 IQUB VEGFD RAB4B FTH1 MYRIP FPR1 C3AR1 SCG2 CLEC12A HSPA6 FUCA1 CLN3 C5AR1 CLEC5A
0.002000127	32	409	2.199198671	External side of plasma membrane	http://amigo.geneontology.org/amigo/term/GO:0009897	CD4 BTN3A1 TNFRSF9 FCGR2B LRP2 TLR8 CD33 CXCL12 BTN3A3 CD83 GHR LIFR CD86 CSF3R GRIA2 CCRL2 CD36 SERPINE2 STAB2 TLR4 CTSK ACKR3 FCER1G CHRNB2 CCR5 CCR1 TMC1 FOLR2 GFRA2 S1PR1 CD163 CD163L1
0.00304139	80	1444	1.557258062	Neuron projection	http://amigo.geneontology.org/amigo/term/GO:0043005	SARM1 NCDN ANK1 VCAN CAMK2A FCGR2B CTTNBP2 ADCYAP1R1 LRP2 EPB41L3 NCOA1 MT3 RGS17 CD200 STX1B KCND1 CACNG7 GLRB P2RX3 ITGA4 MARK1 CNN3 GRIA2 PREX1 TMOD2 UNC13A CHRM3 DTNA DAGLA DOCK10 HTR2B PCDH8 CPEB2 GCHFR VAMP1 ADCY10 SYT2 UNC80 GRIP2 PAM NLGN4X CDHR1 PTPRO NRSN1 MERTK SLA KIF5A KCNB1 CHRNB2 DISC1 LRRTM1 GRM2 GRIK2 TMC1 CTNND2 MYRIP NSG2 NPTX1 SYNPO GAP43 PLK3 CHRNA9 KCNE3 CDK5R1 KCNA2 AQP11 CHRM4 RGMA ABAT LRIT3 KCNQ3 CERKL CLN3 APOD KIF13B ATL1 BGLAP OMP TUBB3 NEFL

Gene Ontology showing enrichment of Molecular Function of upregulated differentially expressed genes (DEGs) common to 2 or more patients after 8-day in a microfluidics device, treated with 1 μM GSK3368715 vs the DMSO control

Enrichment FDR	nGenes	Pathway Genes	Fold Enrichment	Pathway	URL	Genes
0.000781718	88	1488	1.662331119	RNA polymerase II transcription regulatory region sequence-specific DNA binding	http://amigo.geneontology.org/amigo/term/GO:0000977	SOX8 CALCOCO1 ZNF112 SPI1 ZNF671 NCOA1 ZNF302 TFEC HOXA2 NKX3-2 E2F3 NR2E1 KAT2B ZBTB47 DLX2 EGR2 SNAI1 HOXD11 SOX5 DMTF1 IRF4 ZIC5 NR3C2 ZNF547 ZNF776 SIM2 ZNF382 ZNF577 KLF15 SALL2 ZNF606 ZNF610 ZNF528 GBX2 FOXD4 ZIK1 NHLH1 ZNF570 ZNF596 ZNF621 ZNF680 ZNF491 JUN ZNF154 ZNF571 ZNF594 ZFP3 HOXC10 BHLHE22 SOX2 ZNF329 ZNF708 SATB1 HOXB4 ZNF320 FOXD4L1 ZBTB37 ZNF397 ZSCAN30 ZNF395 FOXD4L3 ZNF626 ZNF793 ZNF527 ZNF493 ZSCAN26 ZNF665 HOXC6 ZNF461 ZNF181 ZNF334 PEG3 ZNF583 ZNF789 SOX18 MAFB MEF2B YY2 ZNF879 ZSCAN31 ZNF737 ZNF709 ZNF585B ZNF432 ZNF10 ZNF253 ZNF224
0.000781718	76	1253	1.704905514	RNA polymerase II cis-regulatory region sequence-specific DNA binding	http://amigo.geneontology.org/amigo/term/GO:0000978	SOX8 CALCOCO1 ZNF112 SPI1 ZNF671 ZNF302 TFEC HOXA2 NKX3-2 E2F3 NR2E1 ZBTB47 DLX2 EGR2 SNAI1 HOXD11 SOX5 DMTF1 IRF4 ZIC5 NR3C2 ZNF547 ZNF776 ZNF382 ZNF577 KLF15 SALL2 ZNF606 ZNF610 ZNF528 FOXD4 ZIK1 NHLH1 ZNF570 ZNF621 ZNF680 JUN ZNF154 ZNF571 ZNF594 HOXC10 BHLHE22 SOX2 ZNF708 SATB1 HOXB4 ZNF320 FOXD4L1 ZBTB37 ZNF397 ZSCAN30 ZNF395 FOXD4L3 ZNF626 ZNF793 ZNF527 ZNF493 ZSCAN26 ZNF665 HOXC6 ZNF461 ZNF181 ZNF334 ZNF583 ZNF789 SOX18 MAFB MEF2B YY2 ZNF879 ZSCAN31 ZNF737 ZNF585B ZNF432 ZNF253 ZNF224
0.000781718	85	1446	1.652298189	DNA-binding transcription factor activity, RNA polymerase II-specific	http://amigo.geneontology.org/amigo/term/GO:0000981	SOX8 ZNF112 SPI1 ZNF302 TFEC HOXA2 NKX3-2 E2F3 NR2E1 ZBTB47 DLX2 EGR2 SNAI1 HOXD11 SOX5 DMTF1 IRF4 ZIC5 NR3C2 ZNF547 ZNF776 SIM2 ZNF577 KLF15 SALL2 ZNF606 ZNF610 ZNF528 GBX2 SHOX2 FOXD4 ZIK1 NHLH1 ZNF570 ZNF596 ZNF621 ZNF680 ZNF491 JUN ZNF154 ZNF571 ZNF594 ZFP3 HOXC10 BHLHE22 SOX2 ZNF329 ZNF708 SATB1 HOXB4 ZNF320 FOXD4L1 ZBTB37 ZNF529 ZNF397 ZSCAN30 ZNF395 FOXD4L3 ZNF626 ZNF793 ZNF527 ZNF493 ZSCAN26 ZNF665 HOXC6 ZNF461 ZNF181 ZNF334 PEG3 ZNF583 ZNF789 MDM4 SOX18 MAFB MEF2B YY2 ZNF879 ZSCAN31 ZNF737 ZNF709 ZNF585B ZNF432 ZNF10 ZNF253 ZNF224
0.000781718	22	186	3.324662238	Extracellular matrix structural constituent	http://amigo.geneontology.org/amigo/term/GO:0005201	CD4 ANOS1 DCN VCAN LTBP1 MGP SPARC FGL2 CHI3L1 POSTN LUM ABI3BP ACAN SBSPON FBN1 MFAP4 COL3A1 NPNT COL4A3 COL8A2 COL25A1 PRELP
0.000781718	25	253	2.777520555	Glycosaminoglycan binding	http://amigo.geneontology.org/amigo/term/GO:0005539	ANOS1 DCN VCAN APLP1 ECM2 CCL7 CCL8 VEGFA FGF1 TNFAIP6 POSTN SERPINE2 STAB2 GPNMB FGF2 SLIT2 ABI3BP CXCL13 ACAN FBN1 SUSD5 FGFBP3 NELL2 COL25A1 PRELP
0.000781718	19	160	3.337885327	Cytokine binding	http://amigo.geneontology.org/amigo/term/GO:0019955	CD4 TNFRSF9 LTBP1 GHR LIFR ITGA4 IL1R2 GBP1 CSF3R CCRL2 CD36 IL18BP FGF2 ACKR3 CCR5 CCR1 NRROS CSF1R ACKR1
0.000881914	76	1272	1.679439158	Cis-regulatory region sequence-specific DNA binding	http://amigo.geneontology.org/amigo/term/GO:0000987	SOX8 CALCOCO1 ZNF112 SPI1 ZNF671 ZNF302 TFEC HOXA2 NKX3-2 E2F3 NR2E1 ZBTB47 DLX2 EGR2 SNAI1 HOXD11 SOX5 DMTF1 IRF4 ZIC5 NR3C2 ZNF547 ZNF776 ZNF382 ZNF577 KLF15 SALL2 ZNF606 ZNF610 ZNF528 FOXD4 ZIK1 NHLH1 ZNF570 ZNF621 ZNF680 JUN ZNF154 ZNF571 ZNF594 HOXC10 BHLHE22 SOX2 ZNF708 SATB1 HOXB4 ZNF320 FOXD4L1 ZBTB37 ZNF397 ZSCAN30 ZNF395 FOXD4L3 ZNF626 ZNF793 ZNF527 ZNF493 ZSCAN26 ZNF665 HOXC6 ZNF461 ZNF181 ZNF334 ZNF583 ZNF789 SOX18 MAFB MEF2B YY2 ZNF879 ZSCAN31 ZNF737 ZNF585B ZNF432 ZNF253 ZNF224
0.000881914	87	1515	1.614151945	DNA-binding transcription factor activity	http://amigo.geneontology.org/amigo/term/GO:0003700	SOX8 ZNF112 SPI1 ZNF671 ZNF302 TFEC HOXA2 NKX3-2 E2F3 NR2E1 ZBTB47 DLX2 EGR2 SNAI1 HOXD11 SOX5 DMTF1 IRF4 ZIC5 NR3C2 ZNF547 ZNF776 SIM2 ZNF382 ZNF577 KLF15 SALL2 ZNF606 ZNF610 ZNF528 GBX2 SHOX2 FOXD4 ZIK1 NHLH1 ZNF570 ZNF596 ZNF621 ZNF680 ZNF491 JUN ZNF154 ZNF571 ZNF594 ZFP3 HOXC10 BHLHE22 SOX2 ZNF329 ZNF708 SATB1 HOXB4 ZNF320 FOXD4L1 ZBTB37 ZNF529 ZNF397 ZSCAN30 ZNF395 FOXD4L3 ZNF626 ZNF793 ZNF527 ZNF493 ZSCAN26 ZNF665 HOXC6 ZNF461 ZNF181 ZNF334 PEG3 ZNF583 ZNF789 MDM4 SOX18 MAFB MEF2B YY2 ZNF879 ZSCAN31 ZNF737 ZNF709 ZNF585B ZNF432 ZNF10 ZNF253 ZNF224

Gene Ontology showing enrichment of KEGG pathways of upregulated differentially expressed genes (DEGs) common to 2 or more patients after 8-day in a microfluidics device, treated with 1 μM GSK3368715 vs the DMSO control

Enrichment FDR	nGenes	Pathway Genes	Fold Enrichment	Pathway	URL	Genes
0.000382386	40	495	2.271394587	Herpes simplex virus 1 infection	http://www.genome.jp/kegg-bin/show_pathway?hsa05168	ZNF112 ZNF671 ZNF302 SRSF5 CCL2 CFP CASP9 PIK3R1 ZNF547 ZNF382 ZNF577 ZNF606 ZNF610 ZNF528 ZIK1 ZNF570 ZNF596 ZNF621 ZNF680 ZNF154 ZNF571 ZNF708 ZNF320 SOCS3 ZNF529 ZNF793 ZNF527 ZNF665 ZNF461 ZNF181 ZNF334 ZNF583 ZNF879 ZNF737 ZNF709 ZNF585B ZNF432 ZNF10 ZNF253 ZNF224
0.007858332	25	294	2.390179253	Cytokine-cytokine receptor interaction	http://www.genome.jp/kegg-bin/show_pathway?hsa04060	CD4 TNFRSF9 IL17RB CSF2RB CXCL12 CCL7 CCL2 CCL8 GHR LIFR IL1R2 CSF3R ACVR2A LIF EDA2R GDF7 ACKR3 CXCL14 CXCL13 CCR5 CCR1 TNFRSF11B CXCL8 CLCF1 CSF1R
0.029153166	26	350	2.088060595	Neuroactive ligand-receptor interaction	http://www.genome.jp/kegg-bin/show_pathway?hsa04080	EDN1 ADCYAP1R1 P2RX7 GLRB P2RX3 GHR GRIA2 CHRM3 APLNR HTR2B EDNRB LPAR6 GRIK4 ADRA2A CHRNB2 GRM2 GRIK2 S1PR1 FPR1 APLN C3AR1 CHRNA9 CHRM4 FPR3 C5AR1 ADORA3
0.029153166	11	92	3.360799671	Rheumatoid arthritis	http://www.genome.jp/kegg-bin/show_pathway?hsa05323	CXCL12 CCL2 VEGFA CD86 TLR4 CTSK ATP6V1B2 ATP6V0D2 CXCL8 ATP6V0E2 JUN
0.043705288	11	99	3.123167557	Viral protein interaction with cytokine and cytokine receptor	http://www.genome.jp/kegg-bin/show_pathway?hsa04061	CXCL12 CCL7 CCL2 CCL8 ACKR3 CXCL14 CXCL13 CCR5 CCR1 CXCL8 CSF1R
0.050710264	11	103	3.001879497	Toll-like receptor signaling pathway	http://www.genome.jp/kegg-bin/show_pathway?hsa04620	TLR8 MAP3K8 CD86 LBP TLR4 CTSK PIK3R1 CXCL8 TLR1 JUN TLR7
0.09147972	13	151	2.419937776	Phagosome	http://www.genome.jp/kegg-bin/show_pathway?hsa04145	FCGR2B NCF2 CD36 TLR4 FCGR2A ATP6V1B2 ATP6V0D2 COLEC12 CTSS ATP6V0E2 CLEC7A TUBA8 TUBB3
0.09147972	10	100	2.810650801	AGE-RAGE signaling pathway in diabetic complications	http://www.genome.jp/kegg-bin/show_pathway?hsa04933	EDN1 CCL2 VEGFA PLCD4 PIK3R1 VEGFD COL3A1 COL4A3 CXCL8 JUN
0.09147972	32	530	1.697117465	Pathways in cancer	http://www.genome.jp/kegg-bin/show_pathway?hsa05200	HGF SPI1 CAMK2A EDN1 NCOA1 HMOX1 CSF2RB CXCL12 E2F3 VEGFA FGF1 APC2 GADD45A CSF3R CASP9 APC EDNRB FGF2 LPAR6 PIK3R1 RASGRP3 FZD7 FZD1 VEGFD COL4A3 CXCL8 GSTA4 JUN CSF1R DAPK1 GSTM2 EGLN2
0.097163682	15	191	2.207474451	Chemokine signaling pathway	http://www.genome.jp/kegg-bin/show_pathway?hsa04062	FGR PIK3CG CXCL12 CCL7 CCL2 CCL8 PREX1 DOCK2 PIK3R5 PIK3R1 CXCL14 CXCL13 CCR5 CCR1 CXCL8

Gene Ontology showing enrichment of biological processes of downregulated differentially expressed genes (DEGs) common to 2 or more patients after 8-day in a microfluidics device, treated with 1 μM GSK3368715 vs the DMSO control

Enrichment FDR	nGenes	Pathway Genes	Fold Enrichment	Pathway	URL	Genes
2.84E-32	40	118	14.77525359	Cotranslational protein targeting to membrane	http://amigo.geneontology.org/amigo/term/GO:0006613	RPS20 RPL18 RPS5 RPLP0 RPL3 RPS19 RPL18A RPL28 RPS12 RPL24 RPS15 SIL1 RPL21 RPS4Y1 RPL36 RPL27 RPS15A RPL35 RPS6 RPLP1 RPS24 RPS11 RPL13A RPL32 RPS3A RPS3 RPL8 RPL29 RPL9 RPS14 RPL27A RPL13 RPSA RPS21 RPL38 RPL4 RPLP2 RPL12 RPS29 UBA52
3.16E-32	39	112	15.17761541	SRP-dependent cotranslational protein targeting to membrane	http://amigo.geneontology.org/amigo/term/GO:0006614	RPS20 RPL18 RPS5 RPLP0 RPL3 RPS19 RPL18A RPL28 RPS12 RPL24 RPS15 RPL21 RPS4Y1 RPL36 RPL27 RPS15A RPL35 RPS6 RPLP1 RPS24 RPS11 RPL13A RPL32 RPS3A RPS3 RPL8 RPL29 RPL9 RPS14 RPL27A RPL13 RPSA RPS21 RPL38 RPL4 RPLP2 RPL12 RPS29 UBA52
7.95E-30	39	128	13.28041348	Protein targeting to ER	http://amigo.geneontology.org/amigo/term/GO:0045047	RPS20 RPL18 RPS5 RPLP0 RPL3 RPS19 RPL18A RPL28 RPS12 RPL24 RPS15 RPL21 RPS4Y1 RPL36 RPL27 RPS15A RPL35 RPS6 RPLP1 RPS24 RPS11 RPL13A RPL32 RPS3A RPS3 RPL8 RPL29 RPL9 RPS14 RPL27A RPL13 RPSA RPS21 RPL38 RPL4 RPLP2 RPL12 RPS29 UBA52
2.27E-29	39	132	12.87797671	Establishment of protein localization to endoplasmic reticulum	http://amigo.geneontology.org/amigo/term/GO:0072599	RPS20 RPL18 RPS5 RPLP0 RPL3 RPS19 RPL18A RPL28 RPS12 RPL24 RPS15 RPL21 RPS4Y1 RPL36 RPL27 RPS15A RPL35 RPS6 RPLP1 RPS24 RPS11 RPL13A RPL32 RPS3A RPS3 RPL8 RPL29 RPL9 RPS14 RPL27A RPL13 RPSA RPS21 RPL38 RPL4 RPLP2 RPL12 RPS29 UBA52
1.79E-27	39	147	11.56389745	Nuclear-transcribed mRNA catabolic process, nonsense-mediated decay	http://amigo.geneontology.org/amigo/term/GO:0000184	RPS20 RPL18 RPS5 RPLP0 RPL3 RPS19 RPL18A RPL28 RPS12 RPL24 RPS15 RPL21 RPS4Y1 RPL36 RPL27 RPS15A RPL35 RPS6 RPLP1 RPS24 RPS11 RPL13A RPL32 RPS3A RPS3 RPL8 RPL29 RPL9 RPS14 RPL27A RPL13 RPSA RPS21 RPL38 RPL4 RPLP2 RPL12 RPS29 UBA52
8.43E-26	39	162	10.49316621	Protein localization to endoplasmic reticulum	http://amigo.geneontology.org/amigo/term/GO:0070972	RPS20 RPL18 RPS5 RPLP0 RPL3 RPS19 RPL18A RPL28 RPS12 RPL24 RPS15 RPL21 RPS4Y1 RPL36 RPL27 RPS15A RPL35 RPS6 RPLP1 RPS24 RPS11 RPL13A RPL32 RPS3A RPS3 RPL8 RPL29 RPL9 RPS14 RPL27A RPL13 RPSA RPS21 RPL38 RPL4 RPLP2 RPL12 RPS29 UBA52
4.07E-25	39	169	10.05853802	Cytoplasmic translation	http://amigo.geneontology.org/amigo/term/GO:0002181	RPS20 RPL18 RPS5 RPLP0 RPL3 RPS19 RPL18A RPL28 RPS12 RPL24 RPS15 RPL21 RPL36 RPL27 RPS15A RPL35 RPS6 RPLP1 RPS24 RPS11 RPL13A RPL32 RPS3A RPS3 RPL8 RPL29 RPL22L1 RPL9 RPS14 RPL27A RPL13 RPSA RPS21 RPL38 RPL4 RPLP2 RPL12 RPS29 UBA52
4.45E-23	43	241	7.776933269	Protein targeting to membrane	http://amigo.geneontology.org/amigo/term/GO:0006612	RPS20 RPL18 RPS5 RPLP0 RPL3 ABCD1 RPS19 RPL18A RPL28 RPS12 RPL24 RPS15 SIL1 RPL21 RPS4Y1 RPL36 RPL27 RPS15A RPL35 RPS6 RPLP1 RPS24 RPS11 RPL13A RPL32 RPS3A RPS3 RPL8 RPL29 RPL9 RPS14 RPL27A RPL13 RPSA RPS21 RPL38 RPL4 RPLP2 CIB1 MYO1C RPL12 RPS29 UBA52
5.56E-23	41	217	8.235331436	Viral transcription	http://amigo.geneontology.org/amigo/term/GO:0019083	RPS20 RPL18 NUCKS1 RPS5 RPLP0 RPL3 RPS19 RPL18A RPL28 RPS12 RPL24 RPS15 RPL21 RPS4Y1 RPL36 RPL27 RPS15A RPL35 RPS6 RPLP1 RPS24 RPS11 RPL13A RPL32 RPS3A RPS3 RPL8 RPL29 RPL9 RPS14 PSMC3 RPL27A RPL13 RPSA RPS21 RPL38 RPL4 RPLP2 RPL12 RPS29 UBA52
5.23E-21	40	230	7.580347494	Translational initiation	http://amigo.geneontology.org/amigo/term/GO:0006413	RPS20 RPL18 RPS5 RPLP0 RPL3 RPS19 RPL18A HSPB1 RPL28 RPS12 RPL24 RPS15 RPL21 RPS4Y1 RPL36 RPL27 RPS15A RPL35 RPS6 RPLP1 RPS24 RPS11 RPL13A RPL32 RPS3A RPS3 RPL8 RPL29 RPL9 RPS14 RPL27A RPL13 RPSA RPS21 RPL38 RPL4 RPLP2 RPL12 RPS29 UBA52

Gene Ontology showing enrichment of cellular component of downregulated differentially expressed genes (DEGs) common to 2 or more patients after 8-day in a microfluidics device, treated with 1 μM GSK3368715 vs the DMSO control

Enrichment FDR	nGenes	Pathway Genes	Fold Enrichment	Pathway	URL	Genes
2.86E-35	42	123	14.8833652	Cytosolic ribosome	http://amigo.geneontology.org/amigo/term/GO:0022626	RPS20 RPL18 RPS5 RPLP0 RPL3 RPS19 RPL18A RPL28 RPS12 RPL24 RPS15 RPL21 RPS4Y1 RPL36 RPL27 RPS15A RPL35 RPS6 RPLP1 RPS24 RPS11 RPL13A RPL32 RPS3A RPS3 RPL8 RPL29 RPL9 RPL39L RPS14 RPL36AL RPL27A RPL13 RPSA RPS21 RPL38 RPL4 RPLP2 ISG15 RPL12 RPS29 UBA52
2.86E-35	52	218	10.39689863	Ribosomal subunit	http://amigo.geneontology.org/amigo/term/GO:0044391	RPS20 RPL18 MRPS34 RPS5 MRPL28 RPLP0 RPL3 RPS19 RPL18A RPL28 RPS12 RPL24 RPS15 MRPL37 MRPS15 RPL21 MRPS2 RPS4Y1 RPL36 RPL27 RPS15A RPL35 RPS6 RPLP1 RPS24 RPS11 RPL13A RPL32 RPS3A RPS3 MRPL17 RPL8 RPL29 RPL9 RPL39L RPS14 RPL36AL RPL27A RPL13 RPSA RPS21 RPL38 RPL4 MRPL11 RPLP2 MRPL14 ISG15 MRPL21 RPL12 RPS29 UBA52 MRPL12
7.96E-30	53	291	7.908525425	Ribosome	http://amigo.geneontology.org/amigo/term/GO:0005840	RPS20 RPL18 MRPS34 RPS5 MRPL28 RPLP0 RPL3 RPS19 RPL18A RPL28 RPS12 RPL24 RPS15 MRPL37 MRPS15 RPL21 MRPS2 RPS4Y1 RPL36 RPL27 RPS15A RPL35 RPS6 RPLP1 RPS24 RPS11 RPL13A RPL32 RPS3A RPS3 MRPL17 RPL8 RPL29 RPL22L1 RPL9 RPL39L RPS14 RPL36AL RPL27A RPL13 RPSA RPS21 RPL38 RPL4 MRPL11 RPLP2 MRPL14 ISG15 MRPL21 RPL12 RPS29 UBA52 MRPL12
7.77E-24	25	58	18.78749918	Cytosolic large ribosomal subunit	http://amigo.geneontology.org/amigo/term/GO:0022625	RPL18 RPLP0 RPL3 RPL18A RPL28 RPL24 RPL21 RPL36 RPL27 RPL35 RPLP1 RPL13A RPL32 RPL8 RPL29 RPL9 RPL39L RPL36AL RPL27A RPL13 RPL38 RPL4 RPLP2 RPL12 UBA52
6.21E-23	32	122	11.43265524	Large ribosomal subunit	http://amigo.geneontology.org/amigo/term/GO:0015934	RPL18 MRPL28 RPLP0 RPL3 RPL18A RPL28 RPL24 MRPL37 RPL21 RPL36 RPL27 RPL35 RPLP1 RPL13A RPL32 MRPL17 RPL8 RPL29 RPL9 RPL39L RPL36AL RPL27A RPL13 RPL38 RPL4 MRPL11 RPLP2 MRPL14 MRPL21 RPL12 UBA52 MRPL12
9.22E-18	66	792	3.632249641	Ribonucleoprotein complex	http://amigo.geneontology.org/amigo/term/GO:1990904	RPS20 RPL18 HSD17B10 MRPS34 SNRPA RPS5 MRPL28 RPLP0 RPL3 RPS19 RPL18A RPL28 RPS12 RPL24 RPS15 MRPL37 MRPS15 RPL21 MRPS2 SNRPD2 EMG1 RPS4Y1 RPL36 LSM4 RPL27 CTNNBL1 RPS15A RPL35 RPS6 RPLP1 RPS24 WRAP53 RPS11 RPL13A RPL32 RPS3A RPS3 ERG MRPL17 FAM207A RPL8 RPL29 RPL9 RPL39L RPS14 RPL36AL RPL27A RPL13 RPSA RPS21 PPIH RPL38 RPL4 MRPL11 RPLP2 MRPL14 TBL3 PXP3 ISG15 RRP7A MRPL21 RPL12 RPS29 UBA52 PWP2 MRPL12
1.48E-13	18	62	12.65428977	Cytosolic small ribosomal subunit	http://amigo.geneontology.org/amigo/term/GO:0022627	RPS20 RPS5 RPS19 RPS12 RPS15 RPS4Y1 RPS15A RPS6 RPS24 RPS11 RPS3A RPS3 RPS14 RPSA RPS21 ISG15 RPS29 UBA52
7.33E-13	21	100	9.153269586	Small ribosomal subunit	http://amigo.geneontology.org/amigo/term/GO:0015935	RPS20 MRPS34 RPS5 RPS19 RPS12 RPS15 MRPS15 MRPS2 RPS4Y1 RPS15A RPS6 RPS24 RPS11 RPS3A RPS3 RPS14 RPSA RPS21 ISG15 RPS29 UBA52
2.16E-07	36	512	3.064710803	Mitochondrial matrix	http://amigo.geneontology.org/amigo/term/GO:0005759	CPS1 TFB1M HSD17B10 MRPS34 MRPL28 ATP5F1D MCAT GSTZ1 ETFB NDUFS8 MRPL37 MRPS15 MTHFD1L MRPS2 ATP5F1E PRDX3 ECHS1 TST FPGS HADH MMAB MDH2 RPS3 MRPL17 FDXR NUDT2 NDUFB8 ECI1 CDK1 MRPL11 MRPL14 TXNRD2 MRPL21 ATAD3A ARL2 MRPL12
3.30E-06	32	471	2.961324711	Focal adhesion	http://amigo.geneontology.org/amigo/term/GO:0005925	RPL18 SLC9A3R2 PVR RPS5 RPLP0 EZR MISP RPL3 RPS19 CAV2 HSPB1 RPS15 MAP2K2 RPL27 RPLP1 GRB7 RPS11 RPL13A RPS3A RPS3 RPL8 RPL9 RPS14 RPL38 CSPG4 RPL4 RPLP2 PARVB RPL12 TGM2 ARL2 RPS29

Gene Ontology showing enrichment of Molecular Function of downregulated differentially expressed genes (DEGs) common to 2 or more patients after 8-day in a microfluidics device, treated with 1 μM GSK3368715 vs the DMSO control

Enrichment FDR	nGenes	Pathway Genes	Fold Enrichment	Pathway	URL	Genes
9.78E-37	52	201	11.27623831	Structural constituent of ribosome	http://amigo.geneontology.org/amigo/term/GO:0003735	RPS20 RPL18 MRPS34 RPS5 MRPL28 RPLP0 RPL3 RPS19 RPL18A RPL28 RPS12 RPL24 RPS15 MRPL37 MRPS15 RPL21 MRPS2 RPS4Y1 RPL36 RPL27 RPS15A RPL35 RPS6 RPLP1 RPS24 RPS11 RPL13A RPL32 RPS3A RPS3 MRPL17 RPL8 RPL29 RPL22L1 RPL9 RPL39L RPS14 RPL36AL RPL27A RPL13 RPSA RPS21 RPL38 RPL4 MRPL11 RPLP2 MRPL14 MRPL21 RPL12 RPS29 UBA52 MRPL12
2.47E-17	66	784	3.668313615	Structural molecule activity	http://amigo.geneontology.org/amigo/term/GO:0005198	RPS20 LAMC3 RPL18 MRPS34 RPS5 MRPL28 RPLP0 RPL3 MYL9 MYOM1 RPS19 RPL18A RPL28 RPS12 COL7A1 RPL24 RPS15 MRPL37 MRPS15 RPL21 MRPS2 TUBA4A KRT17 RPS4Y1 RPL36 RPL27 RPS15A RPL35 RPS6 RPLP1 RPS24 RPS11 RPL13A RPL32 RPS3A RPS3 MRPL17 LMNA RPL8 RPL29 RPL22L1 RPL9 RPL39L RPS14 RPL36AL RPL27A RPL13 RPSA RPS21 RPL38 MMRN2 SPTBN2 RPL4 MRPL11 CLTB RPLP2 MRPL14 COL18A1 PSMD13 KRT14 ZP3 MRPL21 RPL12 RPS29 UBA52 MRPL12
3.02E-06	82	1873	1.908240173	RNA binding	http://amigo.geneontology.org/amigo/term/GO:0003723	REXO5 RPS20 TFB1M RPL18 NUCKS1 TCOF1 HSD17B10 IGF2BP2 SNRPA RPS5 MRPL28 RPLP0 EZR LGALS1 MCAT RPL3 RANGAP1 RPS19 RPL18A HSPB1 RPL28 RPS12 RPL24 RPS15 FARSB MRPL37 MRPS15 CPSF3 RPL21 SNRPD2 EMG1 TST RPS4Y1 RPL36 BST2 LSM4 RPL27 CLUH RPS15A IGF2BP3 TACO1 RPL35 RPS6 RPS24 ZGRF1 NUDT7 WRAP53 GRB7 RPS11 RPL13A RPL32 RPS3A C7orf50 MDH2 MKI67 RPS3 RPL8 FLYWCH2 RPL29 RPL22L1 RPL9 APEH RPS14 RPL27A RPL13 RPSA PUSL1 RPS21 ISG20 RPL38 RPL4 MRPL11 MRPL14 TBL3 RRP7A MRPL21 RPL12 HMGN5 RPS29 NME1 PWP2 MRPL12
8.87E-06	13	81	6.995444138	RNA binding	http://amigo.geneontology.org/amigo/term/GO:0019843	RPS5 RPLP0 EMG1 TST RPS4Y1 TACO1 RPS11 RPS3 RPL8 RPL9 RPS14 MRPL11 RPL12
0.016606251	14	183	3.334524444	Carboxylic acid binding	http://amigo.geneontology.org/amigo/term/GO:0031406	CPS1 GSTP1 GSS P3H3 LRAT PRR7 THNSL2 AKR1C2 ACOXL ALKBH3 FABP4 SLC19A1 AKR1C1 UROS
0.02659821	8	69	5.053564996	Damaged DNA binding	http://amigo.geneontology.org/amigo/term/GO:0003684	ERCC1 POLQ NTHL1 RPA3 DDB2 RPS3 RECQL4 BLM
0.02659821	63	1743	1.575433666	Adenyl nucleotide binding	http://amigo.geneontology.org/amigo/term/GO:0030554	CPS1 EHD2 RFC2 POLQ CAMK2B PRKCQ MYO3B SMC1B KIF22 ACOT7 ATP5F1D DMC1 PNPLA3 GSS TRIB3 KIF3B ABCD1 PIM2 UBE2S GALK1 FARSB PTPA TTLL5 MTHFD1L SIL1 CIT SRMS MAP2K2 CHTF18 BRIP1 FPGS KIF12 MMAB AK7 KIF2C ABCA12 MKI67 TKFC UBE2Z RECQL4 STK32C PSMC3 PIP5KL1 MVD TK1 PBK CDK1 RBKS SLC19A1 SPHK1 HASPIN AURKB RAD51B DNAH14 POMK KIF24 PRKAR1B BLM ATAD3A MYO1C APRT NME1 IKBKE
0.02659821	3	6	21.79349904	Large ribosomal subunit rRNA binding	http://amigo.geneontology.org/amigo/term/GO:0070180	RPLP0 MRPL11 RPL12
0.032566988	62	1730	1.562077388	Adenyl ribonucleotide binding	http://amigo.geneontology.org/amigo/term/GO:0032559	CPS1 EHD2 RFC2 POLQ CAMK2B PRKCQ MYO3B SMC1B KIF22 ACOT7 ATP5F1D DMC1 PNPLA3 GSS TRIB3 KIF3B ABCD1 PIM2 UBE2S GALK1 FARSB PTPA TTLL5 MTHFD1L CIT SRMS MAP2K2 CHTF18 BRIP1 FPGS KIF12 MMAB AK7 KIF2C ABCA12 MKI67 TKFC UBE2Z RECQL4 STK32C PSMC3 PIP5KL1 MVD TK1 PBK CDK1 RBKS SLC19A1 SPHK1 HASPIN AURKB RAD51B DNAH14 POMK KIF24 PRKAR1B BLM ATAD3A MYO1C APRT NME1 IKBKE
0.034647825	15	235	2.782148814	Catalytic activity, acting on DNA	http://amigo.geneontology.org/amigo/term/GO:0140097	ERCC1 RFC2 POLQ NTHL1 DMC1 CHTF18 BRIP1 ZGRF1 RPS3 RECQL4 MGMT ISG20 RAD51B BLM NME1

Gene Ontology showing enrichment of KEGG pathways of downregulated differentially expressed genes (DEGs) common to 2 or more patients after 8-day in a microfluidics device, treated with 1 μM GSK3368715 vs the DMSO control

Enrichment FDR	nGenes	Pathway Genes	Fold Enrichment	Pathway	URL	Genes
2.59E-43	49	134	15.93852915	Ribosome	http://www.genome.jp/kegg-bin/show_pathway?hsa03010	RPS20 RPL18 RPS5 MRPL28 RPLP0 RPL3 RPS19 RPL18A RPL28 RPS12 RPL24 RPS15 MRPS15 RPL21 MRPS2 RPS4Y1 RPL36 RPL27 RPS15A RPL35 RPS6 RPLP1 RPS24 RPS11 RPL13A RPL32 RPS3A RPS3 MRPL17 RPL8 RPL29 RPL22L1 RPL9 RPS14 RPL36AL RPL27A RPL13 RPSA RPS21 RPL38 RPL4 MRPL11 RPLP2 MRPL14 MRPL21 RPL12 RPS29 UBA52 MRPL12
2.05E-23	42	232	7.890749654	Coronavirus disease	http://www.genome.jp/kegg-bin/show_pathway?hsa05171	RPS20 RPL18 RPS5 RPLP0 RPL3 RPS19 RPL18A RPL28 RPS12 RPL24 RPS15 RPL21 RPS4Y1 RPL36 RPL27 RPS15A RPL35 RPS6 RPLP1 RPS24 RPS11 RPL13A RPL32 RPS3A RPS3 RPL8 RPL29 RPL22L1 RPL9 RPS14 RPL36AL RPL27A RPL13 RPSA RPS21 RPL38 RPL4 MRPL11 RPLP2 ISG15 RPL12 RPS29 UBA52
9.57E-05	65	1527	1.8553732	Metabolic pathways	http://www.genome.jp/kegg-bin/show_pathway?hsa01100	UQCRC1 XYLT2 CPS1 MSMO1 ST6GALNAC2 HSD17B10 GSTP1 BLVRB PHGDH NANS ATP5F1D MCAT PNPLA3 GSTZ1 GSS PIGU FAH GALK1 NDUFS8 GMDS B4GALT2 GALNT12 MTHFD1L LRAT ATP5F1E NT5C COX6B1 ECHS1 TST ALDH3B2 NT5E FPGS ATIC HADH B4GALNT3 MMAB AK7 CYP1A1 MDH2 EBP NDUFB9 PTGES2 GSTO1 TKFC COX6B2 NUDT2 LARGE2 NDUFB8 PIP5KL1 MVD TK1 AGPAT2 DCXR RBKS RRM2 SPHK1 HSD11B2 B3GNT3 PGP POMK AKR1C1 UROS APRT NME1 ACY1
0.000134041	29	475	2.661100936	Pathways of neurodegeneration	http://www.genome.jp/kegg-bin/show_pathway?hsa05022	UQCRC1 CAMK2B HSD17B10 ATP5F1D KLC3 NDUFS8 WNT5B OPTN ATP5F1E COX6B1 MAP2K2 TRAF2 TUBA4A SEM1 TOMM40 WNT10A PSMB7 PSMB6 WNT9A NDUFB9 COX6B2 PSMC3 NDUFB8 PSMD1 SPTBN2 PSMD13 DNAH14 WNT7B UBA52
0.00048549	21	306	2.991264575	Huntington disease	http://www.genome.jp/kegg-bin/show_pathway?hsa05016	UQCRC1 AP2S1 ATP5F1D KLC3 NDUFS8 ATP5F1E COX6B1 TRAF2 TUBA4A SEM1 PSMB7 PSMB6 NDUFB9 COX6B2 PSMC3 NDUFB8 PSMD1 CLTB PSMD13 DNAH14 TGM2
0.001317833	23	383	2.617495969	Alzheimer disease	http://www.genome.jp/kegg-bin/show_pathway?hsa05010	UQCRC1 HSD17B10 ATP5F1D KLC3 NDUFS8 WNT5B ATP5F1E COX6B1 MAP2K2 TRAF2 TUBA4A SEM1 WNT10A PSMB7 PSMB6 WNT9A NDUFB9 COX6B2 PSMC3 NDUFB8 PSMD1 PSMD13 WNT7B
0.001795587	18	266	2.949496111	Parkinson disease	http://www.genome.jp/kegg-bin/show_pathway?hsa05012	UQCRC1 CAMK2B ATP5F1D KLC3 NDUFS8 ATP5F1E COX6B1 TUBA4A SEM1 PSMB7 PSMB6 NDUFB9 COX6B2 PSMC3 NDUFB8 PSMD1 PSMD13 UBA52
0.006607134	17	272	2.72418738	Prion disease	http://www.genome.jp/kegg-bin/show_pathway?hsa05020	UQCRC1 ATP5F1D KLC3 CAV2 NDUFS8 ATP5F1E COX6B1 TUBA4A SEM1 PSMB7 PSMB6 NDUFB9 COX6B2 PSMC3 NDUFB8 PSMD1 PSMD13
0.008967435	20	363	2.401487498	Amyotrophic lateral sclerosis	http://www.genome.jp/kegg-bin/show_pathway?hsa05014	UQCRC1 ATP5F1D KLC3 NDUFS8 OPTN ATP5F1E COX6B1 TRAF2 TUBA4A SEM1 TOMM40 PSMB7 PSMB6 NDUFB9 COX6B2 PSMC3 NDUFB8 PSMD1 PSMD13 DNAH14
0.016205455	6	46	5.68526062	Proteasome	http://www.genome.jp/kegg-bin/show_pathway?hsa03050	SEM1 PSMB7 PSMB6 PSMC3 PSMD1 PSMD13

Appendix 7: Top 10 Gene Ontology (GO) terms analysis (ShinyGO (Ge SX, Jung D & Yao R, Bioinformatics 36:2628–2629, 2020; http://bioinformatics.sdstate.edu/go/)) of significantly (p<0.05) differentially expressed genes (DEGs) (FC >1.5/<-1.5), common to 2 or more patients, in RNA-seq analysis of 4 patient GBM samples, 8-days post-chip and treated with 1 μM GSK3368715 vs DMSO control. Upregulated biological processes, cellular components, molecular function and KEGG pathways. Downregulated biological processes, cellular components, molecular function and KEGG pathways.

A) ShinyGO 2+ samples

KEGG

Enrichment FDR	nGenes	Pathway Genes	Fold Enrichment	Pathways (click for details)
5.00E-02	19	98	2.1	Choline metabolism in cancer
2.40E-02	27	141	2.1	Alcoholic liver disease
4.30E-02	24	132	2	Spliceosome
4.30E-02	25	141	1.9	Ubiquitin mediated proteolysis
4.30E-02	25	141	1.9	Autophagy
2.60E-02	38	232	1.8	Thermogenesis
2.60E-02	40	246	1.8	Shigellosis
4.30E-02	39	249	1.7	Salmonella infection
1.40E-03	76	485	1.7	Herpes simplex virus 1 infection
1.40E-03	193	1527	1.4	Metabolic pathways

GO: Biological Process

Enrichment FDR	nGenes	Pathway Genes	Fold Enrichment	Pathways (click for details)
4.50E-05	64	348	2	Reg. of small GTPase mediated signal transduction
3.20E-05	91	553	1.8	Small GTPase mediated signal transduction
3.70E-06	114	705	1.7	Microtubule cytoskeleton organization
2.50E-04	85	536	1.7	Reg. of GTPase activity
4.40E-08	155	970	1.7	Microtubule-based proc.
2.50E-05	108	686	1.7	Organelle localization
1.80E-05	104	662	1.7	Cell projection assembly
5.50E-05	101	647	1.7	Plasma membrane bounded cell projection assembly
5.10E-05	103	661	1.7	Reg. of cell projection organization
3.70E-06	147	900	1.6	Organelle assembly
2.90E-08	224	1553	1.6	Cytoskeleton organization
2.90E-08	240	1690	1.5	Cell projection organization
5.50E-05	153	1092	1.5	Chromosome organization
1.20E-07	231	1649	1.5	Plasma membrane bounded cell projection organization
4.50E-05	165	1192	1.5	Pos. reg. of cellular component organization
4.50E-05	189	1496	1.4	Cell cycle proc.
6.10E-06	249	1896	1.4	Reg. of intracellular signal transduction
1.20E-05	258	1987	1.4	Cell cycle
1.70E-05	253	1960	1.4	Cellular protein localization
2.60E-05	253	1974	1.4	Cellular macromolecule localization

GO: Cellular Component

Enrichment FDR	nGenes	Pathway Genes	Fold Enrichment	Pathways (click for details)
6.30E-04	7	11	6.9	Microtubule organizing center attachment site
5.60E-04	21	80	2.8	Actomyosin
1.60E-04	34	162	2.3	Centriole
6.30E-04	40	214	2	Lamellipodium
4.40E-08	113	658	1.9	Centrosome
1.10E-09	144	968	1.8	Microtubule organizing center
6.90E-05	79	481	1.8	Nuclear speck
6.30E-04	65	416	1.7	Spindle
1.60E-04	74	471	1.7	Focal adhesion
1.60E-04	75	478	1.7	Cell-substrate junction
4.70E-04	82	542	1.6	Actin cytoskeleton
1.60E-06	140	922	1.6	Nuclear body
1.60E-04	101	686	1.6	Cilium
1.40E-04	128	907	1.5	Anchoring junction
1.20E-06	194	1391	1.5	Microtubule cytoskeleton
6.30E-04	119	872	1.5	Mitochondrial envelope
2.50E-04	179	1379	1.4	Nuclear protein-containing complex
3.20E-04	175	1352	1.4	Organelle envelope
3.20E-04	175	1352	1.4	Envelope
1.70E-05	234	1816	1.4	Mitochondrion

GO: Molecular Function

Enrichment FDR	nGenes	Pathway Genes	Fold Enrichment	Pathways (click for details)
9.90E-05	15	39	4.1	Pre-mRNA binding
9.90E-05	46	235	2.1	Catalytic activity, acting on DNA
1.30E-05	60	316	2	MRNA binding
7.90E-04	43	233	2	Guanyl-nucleotide exchange factor activity
2.60E-05	67	378	1.9	Protein serine kinase activity
5.80E-04	50	283	1.9	Protein-macromolecule adaptor activity
1.00E-06	91	525	1.9	GTPase regulator activity
1.00E-06	91	525	1.9	Nucleoside-triphosphatase regulator activity
5.70E-06	84	490	1.8	GTPase activator activity
5.80E-04	59	353	1.8	Molecular adaptor activity
1.10E-04	77	477	1.7	Actin binding
4.30E-04	74	470	1.7	Protein serine/threonine kinase activity
7.80E-08	162	1050	1.7	Cytoskeletal protein binding
6.50E-05	110	742	1.6	Phosphotransferase activity, alcohol group as acceptor
2.20E-05	125	849	1.6	Kinase activity
2.20E-05	144	1014	1.5	Transferase activity, transferring phosphorus-containing groups
2.80E-07	229	1662	1.5	ATP binding
6.00E-07	234	1730	1.5	Adenyl ribonucleotide binding
6.00E-07	235	1740	1.5	Adenyl nucleotide binding
3.90E-05	237	1873	1.4	RNA binding

B) ShinyGO 3+ samples

KEGG

Enrichment FDR	nGenes	Pathway Genes	Fold Enrichment	Pathways (click for details)
2.60E-02	6	33	6.9	Base excision repair
1.00E-02	8	49	6.2	Amino sugar and nucleotide sugar metabolism

GO: Biological Process

Enrichment FDR	nGenes	Pathway Genes	Fold Enrichment	Pathways (click for details)
2.50E-02	4	6	25.4	Pos. reg. of protein localization to cell cortex
2.50E-02	7	35	7.6	Base-excision repair, gap-filling
4.50E-02	27	463	2.2	Cilium organization
2.50E-02	34	600	2.2	Autophagy
2.50E-02	34	600	2.2	Process utilizing autophagic mechanism
2.70E-02	35	639	2.1	DNA repair
2.50E-02	48	980	1.9	Organelle assembly
2.50E-02	49	1005	1.9	Cellular response to DNA damage stimulus
2.70E-02	48	1003	1.8	Reg. of cellular catabolic proc.
2.70E-02	80	1960	1.6	Cellular protein localization
3.00E-02	80	1974	1.5	Cellular macromolecule localization

GO: Cellular Component

Enrichment FDR	nGenes	Pathway Genes	Fold Enrichment	Pathways (click for details)
2.50E-02	3	6	19	GATOR1 complex
2.80E-03	11	80	5.2	Cytoplasmic stress granule
4.70E-02	6	44	5.2	AP-type membrane coat adaptor complex
1.40E-02	14	162	3.3	Centriole
3.30E-03	21	275	2.9	Cytoplasmic region
3.40E-02	13	172	2.9	Spindle pole
2.50E-02	18	272	2.5	Cytoplasmic ribonucleoprotein granule
3.40E-02	18	288	2.4	Ribonucleoprotein granule
1.40E-02	28	481	2.2	Nuclear speck
3.40E-02	23	410	2.1	Spindle
2.50E-03	49	932	2	Nuclear body
2.80E-02	34	696	1.9	Cilium
2.50E-02	41	868	1.8	Microtubule organizing center
2.50E-02	58	1379	1.6	Nuclear protein-containing complex
2.50E-02	58	1391	1.6	Microtubule cytoskeleton

GO: Molecular Function

Enrichment FDR	nGenes	Pathway Genes	Fold Enrichment	Pathways (click for details)
3.10E-02	3	4	28.5	Oxidized base lesion DNA N-glycosylase activity
4.90E-02	3	7	16.3	Phosphatidylinositol-3,5-bisphosphate 3-phosphatase activity
4.90E-02	3	7	16.3	Class I DNA-(apurinic or apyrimidinic site) endonuclease activity
4.10E-02	4	13	11.7	DNA N-glycosylase activity
4.90E-02	5	27	7	Phosphatidylinositol-3,5-bisphosphate binding
4.90E-02	6	39	5.9	Pre-mRNA binding
4.90E-02	8	69	4.4	Damaged DNA binding
4.10E-02	11	109	3.8	Phosphatidylinositol bisphosphate binding
4.10E-02	14	176	3	Phosphatidylinositol phosphate binding
4.10E-02	18	262	2.6	Phosphatidylinositol binding
2.90E-02	78	1873	1.6	RNA binding

C) ShinyGO 4 samples

No enrichment in any category

D) GOrilla 2+ samples

GO: Biological Process				
GO term	Description	P-value	FDR q-value	Enrichment (N, B, n, b)
GO:0045008	depyrimidination	2.56E-06	2.10E-02	711.00 (2133,3,2,2)
GO:0006285	base-excision repair, AP site formation	7.49E-06	3.07E-02	533.25 (2133,4,2,2)
GO:0006284	base-excision repair	4.92E-05	1.35E-01	304.71 (2133,7,2,2)
GO:0006244	pyrimidine nucleotide catabolic process	4.92E-05	1.01E-01	304.71 (2133,7,2,2)
GO:0072529	pyrimidine-containing compound catabolic process	4.92E-05	8.07E-02	304.71 (2133,7,2,2)
GO:0046386	deoxyribose phosphate catabolic process	4.92E-05	6.73E-02	304.71 (2133,7,2,2)
GO:0009223	pyrimidine deoxyribonucleotide catabolic process	4.92E-05	5.77E-02	304.71 (2133,7,2,2)
GO:0009219	pyrimidine deoxyribonucleotide metabolic process	4.92E-05	5.04E-02	304.71 (2133,7,2,2)
GO:0009264	deoxyribonucleotide catabolic process	4.92E-05	4.48E-02	304.71 (2133,7,2,2)
GO:0009394	2'-deoxyribonucleotide metabolic process	7.37E-05	6.04E-02	266.62 (2133,8,2,2)
GO:0009262	deoxyribonucleotide metabolic process	7.37E-05	5.49E-02	266.62 (2133,8,2,2)
GO:0019692	deoxyribose phosphate metabolic process	7.37E-05	5.03E-02	266.62 (2133,8,2,2)
GO:0006304	DNA modification	2.47E-04	1.56E-01	177.75 (2133,12,2,2)
GO:0031098	stress-activated protein kinase signaling cascade	3.19E-04	1.87E-01	6.42 (2133,15,155,7)
GO:0016072	rRNA metabolic process	3.63E-04	1.98E-01	1.88 (2133,28,930,23)
GO:0021762	substantia nigra development	3.66E-04	1.87E-01	6.24 (2133,5,342,5)
GO:0006220	pyrimidine nucleotide metabolic process	3.73E-04	1.80E-01	152.36 (2133,14,2,2)
GO:0072527	pyrimidine-containing compound metabolic process	5.15E-04	2.34E-01	133.31 (2133,16,2,2)
GO:0009166	nucleotide catabolic process	8.92E-04	3.85E-01	106.65 (2133,20,2,2)
GO: Molecular Function				
GO term	Description	P-value	FDR q-value	Enrichment (N, B, n, b)
GO:0019104	DNA N-glycosylase activity	7.49E-06	1.49E-02	533.25 (2133,4,2,2)
GO:0016799	hydrolase activity, hydrolyzing N-glycosyl compounds	1.66E-05	1.65E-02	426.60 (2133,5,2,2)
GO:0016798	hydrolase activity, acting on glycosyl bonds	2.47E-04	1.64E-01	177.75 (2133,12,2,2)
GO:0003906	DNA-(apurinic or apyrimidinic site) endonuclease activity	4.50E-04	2.24E-01	8.74 (2133,4,244,4)
GO:0000703	oxidized pyrimidine nucleobase lesion DNA N-glycosylase activity	9.38E-04	3.73E-01	1,066.50 (2133,1,2,1)
GO:0004844	uracil DNA N-glycosylase activity	9.38E-04	3.11E-01	1,066.50 (2133,1,2,1)
GO:0097506	deaminated base DNA N-glycosylase activity	9.38E-04	2.66E-01	1,066.50 (2133,1,2,1)
GO:0017065	single-strand selective uracil DNA N-glycosylase activity	9.38E-04	2.33E-01	1,066.50 (2133,1,2,1)
GO:0003723	RNA binding	9.46E-04	2.09E-01	1.80 (2133,243,190,39)
GO: Cellular Component				
GO term	Description	P-value	FDR q-value	Enrichment (N, B, n, b)
GO:0031371	ubiquitin conjugating enzyme complex	1.02E-04	1.18E-01	96.95 (2133,2,22,2)
GO:0032991	protein-containing complex	2.72E-04	1.58E-01	1.14 (2133,682,987,361)
GO:0043232	intracellular non-membrane-bounded organelle	7.01E-04	2.71E-01	1.50 (2133,407,259,74)
GO:0043228	non-membrane-bounded organelle	7.84E-04	2.27E-01	1.49 (2133,408,259,74)

E) GOrilla 3+ samples

GO: Biological Process				
GO term	Description	P-value	FDR q-value	Enrichment (N, B, n, b)
GO:0045008	depyrimidination	3.04E-05	1.44E-01	204.00 (612,3,2,2)
GO:0006244	pyrimidine nucleotide catabolic process	3.04E-05	7.22E-02	204.00 (612,3,2,2)
GO:0072529	pyrimidine-containing compound catabolic process	3.04E-05	4.81E-02	204.00 (612,3,2,2)
GO:0046386	deoxyribose phosphate catabolic process	3.04E-05	3.61E-02	204.00 (612,3,2,2)
GO:0009394	2'-deoxyribonucleotide metabolic process	3.04E-05	2.89E-02	204.00 (612,3,2,2)
GO:0009223	pyrimidine deoxyribonucleotide catabolic process	3.04E-05	2.41E-02	204.00 (612,3,2,2)
GO:0009219	pyrimidine deoxyribonucleotide metabolic process	3.04E-05	2.06E-02	204.00 (612,3,2,2)
GO:0009264	deoxyribonucleotide catabolic process	3.04E-05	1.81E-02	204.00 (612,3,2,2)
GO:0009262	deoxyribonucleotide metabolic process	3.04E-05	1.60E-02	204.00 (612,3,2,2)
GO:0019692	deoxyribose phosphate metabolic process	3.04E-05	1.44E-02	204.00 (612,3,2,2)
GO:0006285	base-excision repair, AP site formation	8.96E-05	3.87E-02	153.00 (612,4,2,2)
GO:0006284	base-excision repair	1.86E-04	7.35E-02	122.40 (612,5,2,2)
GO:0006304	DNA modification	3.39E-04	1.24E-01	102.00 (612,6,2,2)
GO:0006220	pyrimidine nucleotide metabolic process	3.39E-04	1.15E-01	102.00 (612,6,2,2)
GO:1901292	nucleoside phosphate catabolic process	3.39E-04	1.07E-01	102.00 (612,6,2,2)
GO:0009166	nucleotide catabolic process	3.39E-04	1.01E-01	102.00 (612,6,2,2)
GO:0072527	pyrimidine-containing compound metabolic process	5.65E-04	1.58E-01	87.43 (612,7,2,2)
GO:0046434	organophosphate catabolic process	5.65E-04	1.49E-01	87.43 (612,7,2,2)
GO:0120039	plasma membrane bounded cell projection morphogenesis	8.09E-04	2.02E-01	6.94 (612,7,63,5)
GO:0032990	cell part morphogenesis	8.09E-04	1.92E-01	6.94 (612,7,63,5)
GO:0048858	cell projection morphogenesis	8.09E-04	1.83E-01	6.94 (612,7,63,5)
GO:0048812	neuron projection morphogenesis	8.09E-04	1.75E-01	6.94 (612,7,63,5)
GO:0034404	nucleobase-containing small molecule biosynthetic process	8.29E-04	1.71E-01	76.50 (612,8,2,2)
GO:0007275	multicellular organism development	8.80E-04	1.74E-01	2.60 (612,18,170,13)
GO: Molecular Function				
GO term	Description	P-value	FDR q-value	Enrichment (N, B, n, b)
GO:0016799	hydrolase activity, hydrolyzing N-glycosyl compounds	8.96E-05	8.90E-02	153.00 (612,4,2,2)
GO:0019104	DNA N-glycosylase activity	8.96E-05	4.45E-02	153.00 (612,4,2,2)
GO:0016798	hydrolase activity, acting on glycosyl bonds	3.39E-04	1.12E-01	102.00 (612,6,2,2)
GO: Celullar Component: no enrichment in this category				

F) GOrilla 4 samples

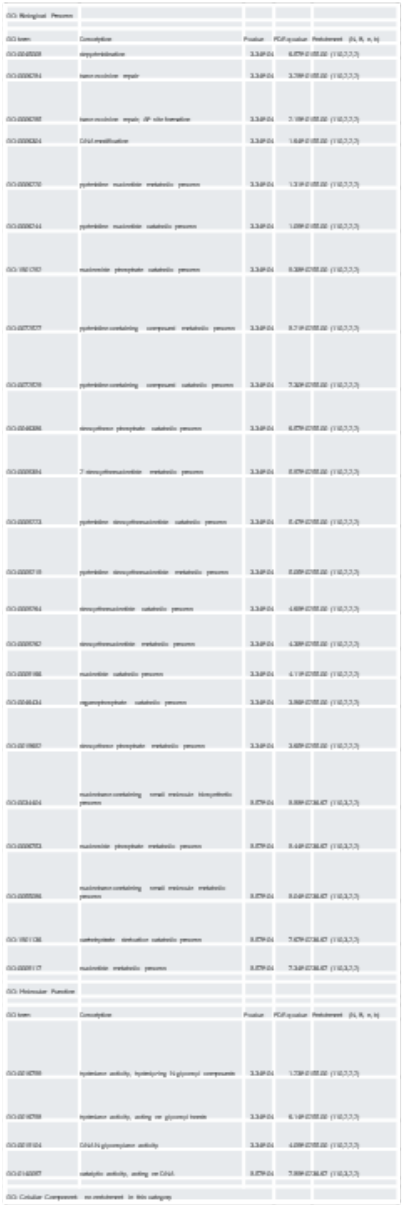

Appendix 8: Gene Ontology (GO) analysis of alternatively spliced genes common to 2 or more patients, in RNA-seq analysis of 4 patient GBM samples, 8-days post-chip and treated with 1 μM GSK3368715 vs DMSO control. GO was performed for biological processes, cellular components, molecular function and KEGG pathways. ShinyGO analysis: A) 2 patients, B) 3 patients, C) 4 patients, Gorilla analysis: D) 2 patients, E) 3 patients and F) 4 patients.

Fedoriw et al. 2019	*Nakaya et al. 2013*
ACIN1	*AACS*
AKAP8	*ABLIM1*
AKAP8L	*ANK2*
ALG8	*ANK3*
ANKZF1	*ANKRD11*
ARHGAP32	*ANKRD36*
ATXN2L	*APBB2*
BCLAF1	*APP*
BPTF	*ARHGAP26*
CIRBP	*ARHGEF7*
CNBP	*AUTS2*
CNN2	*BCAS3*
COL4A3BP	*BIN1*
DAZAP1	*BRF1*
DCXR	*BRSK2*
DDX17	*BTBD9*
DDX5	*C1orf61*
DNM2	*CACNA1A*
DONSON	*CACNB4*
DROSHA	*CAMK2B*
DSTYK	*CAMTA1*
DTX2	*CCDC57*
EIF3H	*CDC42BPA*

EIF4G1	*CLASP1*
EIF4G3	*CLEC16A*
EP400	*CLSTN1*
EWSR1	*CNKSR2*
FAM104A	*CSMD1*
FBXO44	*CTBP2*
FOXRED1	*CTNND1*
G3BP2	*DAZAP1*
GIGYF2	*DDX17*
GIPC1	*DENND1A*
GMIP	*DGKi*
HNRNPA2B1	*DGKZ*
HNRNPH1	*DIP2C*
ILF3	*DNM1*
KANK2	*DOCK9*
KCNAB2	*DYNC1I1*
LAS1L	*EIF4G3*
LSM14A	*EPB41L1*
MBD6	*EPB41L2*
MEF2B	*EPHB1*
MINK1	*EphB1*
MROH6	*EPN2*
MSI2	*EPS15L1*
MTCH1	*ESYT2*

NCOR2	*FBRSL1*
NDUFS2	*FOXN3*
NOP56	*FRMD4A*
PARD3	*GRB10*
PDLIM7	*GRIA2*
PLEKHA6	*GRIK2*
PML	*HDAC4*
QKI	*HDAC9*
RBFOX2	*HNRNPA2B1*
RBM39	*IMMP2L*
RBMX	*KALRN*
RCCD1	*KCNAB2*
REXO2	*KCNMA1*
RGS3	*KDM4C*
SERBP1	*KIAA1217*
SF1	*KIF1B*
SIRT7	*KLC1*
SLAIN2	*LDB2*
SLTM	*LPP*
SMARCD1	*LSAMP*
SNRPB	*MAGI1*
SNRPN	*MAP4K4*
SRRT	*MAPK10*
SRSF1	*MAPT*

SRSF5	*MAST4*
SVIL	*MBD5*
TAF6	*MEG3*
TARDBP	*MEGF11*
TBC1D10C	*MIAT*
TCF3	*MICAL2*
TMC6	*MPRIP*
TNIP1	*MSI2*
TRA2B	*MSRA*
TRIP6	*MYO18A*
U2AF1	*NADK*
USP54	*NBPF1*
WRN	*NCOR2*
YBX3	*NDRG4*
ZC3H13	*NFASC*
ZFC3H1	*NFIB*
ZGPAT	*NFIX*
ZNF451	*NRG1*
ZNF568	*NRXN1*
ZSWIM8	*NRXN2*
	NRXN3
	NTRK3
	PARD3
	PCDH7

	PDXK
	PI4KA
	PKD1
	PLEKHA6
	PPP2R2B
	PRODH
	PTK2
	PTPRD
	PTPRS
	QKI
	R3HDM1
	RAB11FIP3
	RALGDS
	RAP1GAP
	RAP1GAP2
	RNF220
	ROBO1
	RXRA
	SDK1
	SEMA4D
	SGIP1
	SIPA1L1
	SLC39A11
	SNTG1

	SPTAN1
	SRGAP3
	SSBP3
	SYNE1
	TBC1D22A
	TBC1D5
	TBCD
	THRB
	TNK2
	TNRC6A
	TRERF1
	TRPM3
	TSNARE1
	UBR3
	WNK1
	ZBTB16
	ZBTB38

Appendix 9: Gene lists of significantly (p<0.05) alternative spliced genes in 2 or more patients (D31-D34) which correspond with known FUS splicing targets (Nakaya et al. 2013), or in proteins which shown arginine methylation switches after GSK3368712 treatment (Fedoriw et al. 2019).

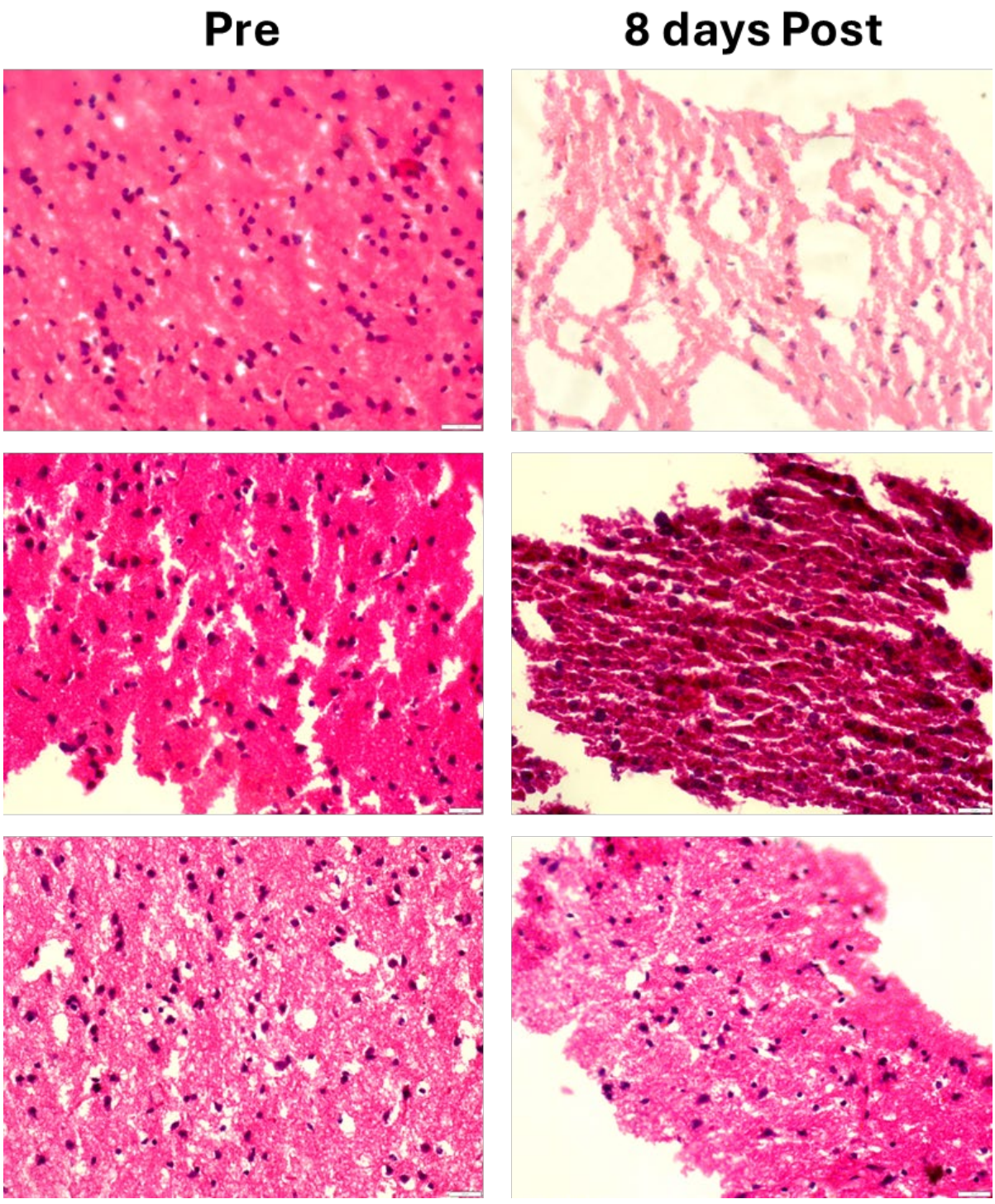

Appendix 10: Representative images of H&E-stained healthy mouse brain tissue pre- and 8-days post-perfusion.

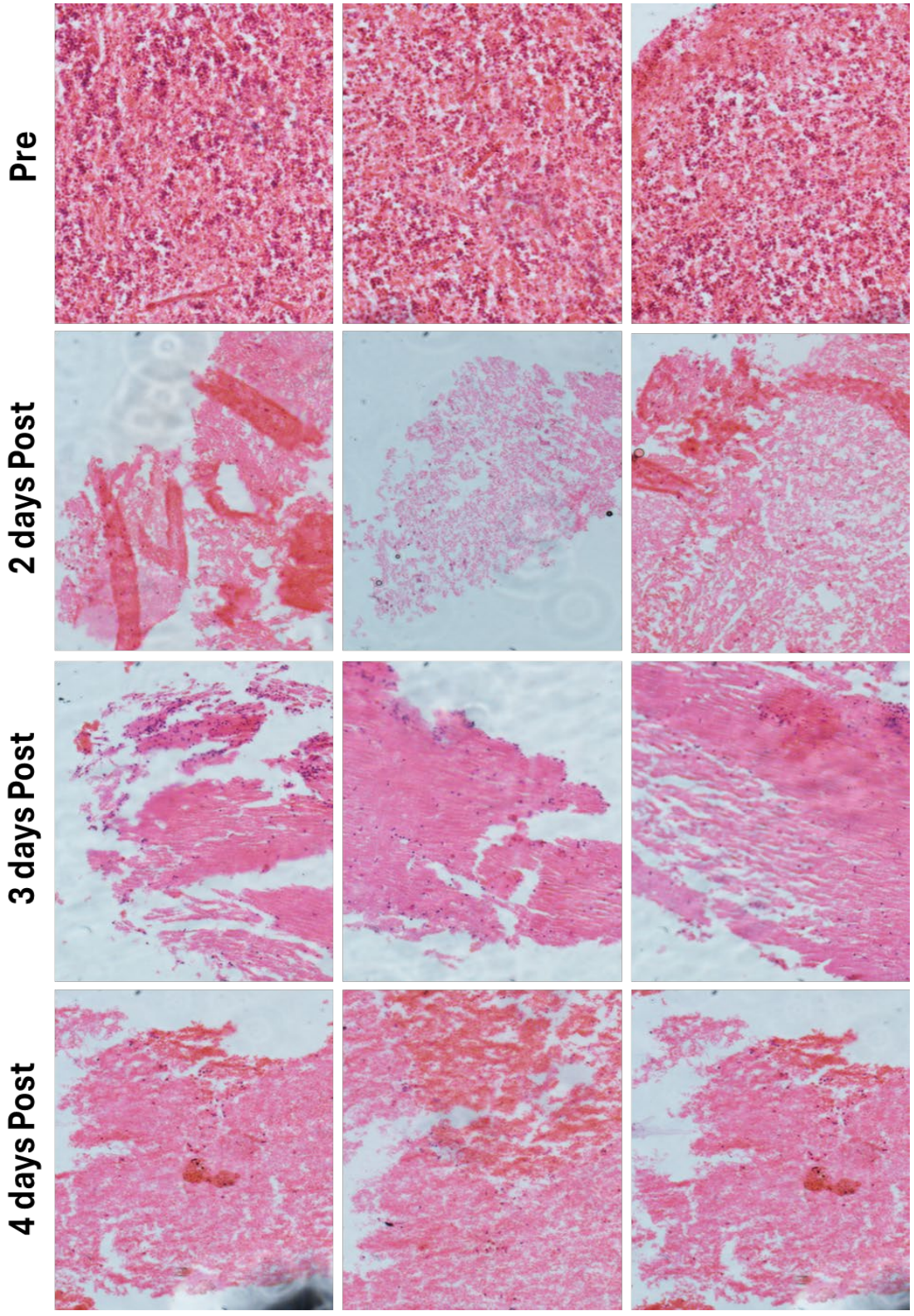

Appendix 11: Representative images of H&E-stained fish brain tissue pre- and 8-days post-perfusion.

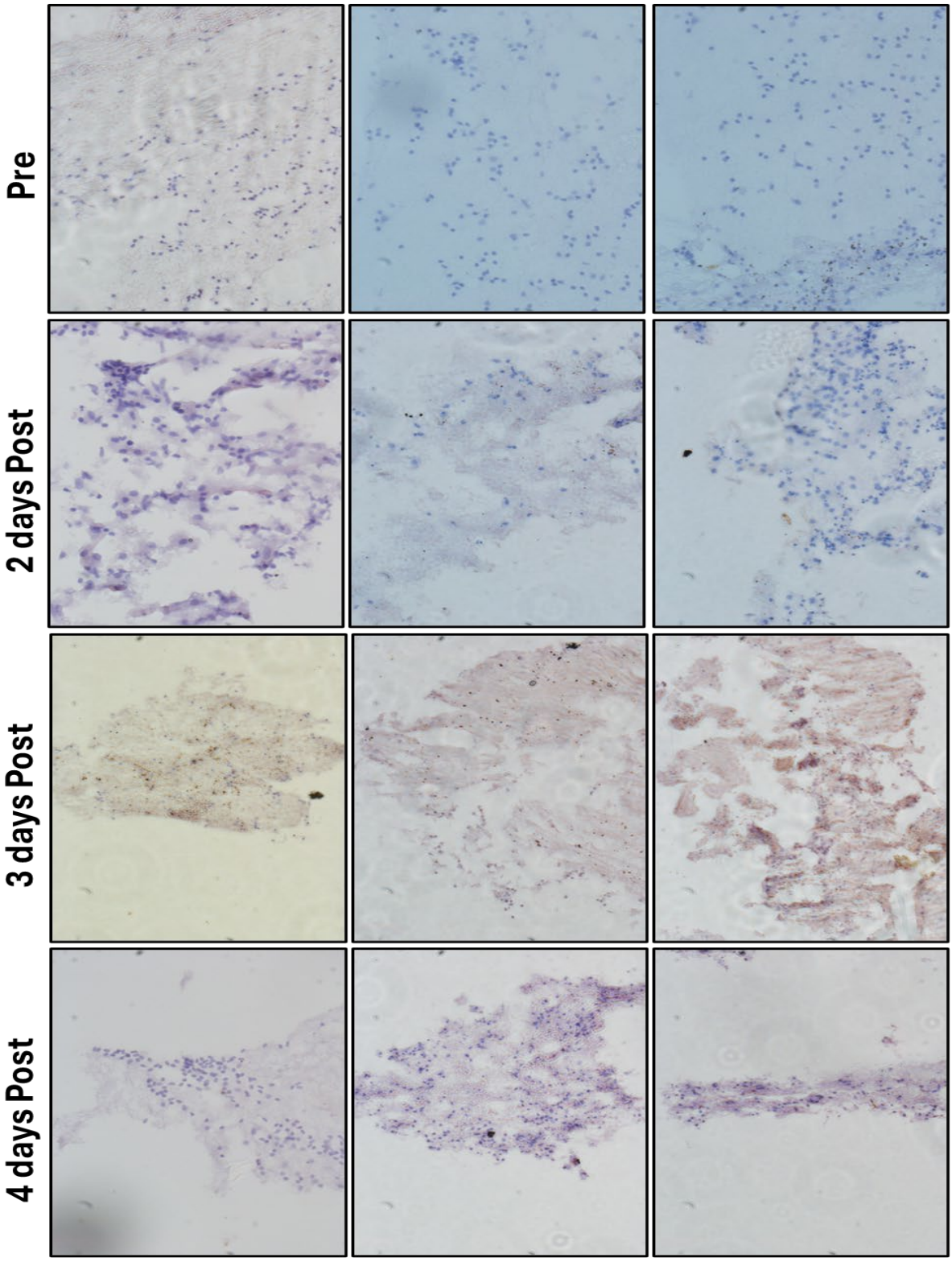

Appendix 12: Representative images of Annexin V-stained fish brain tissue pre- and 8-days post-perfusion and treated with 1µM GSK3368715.

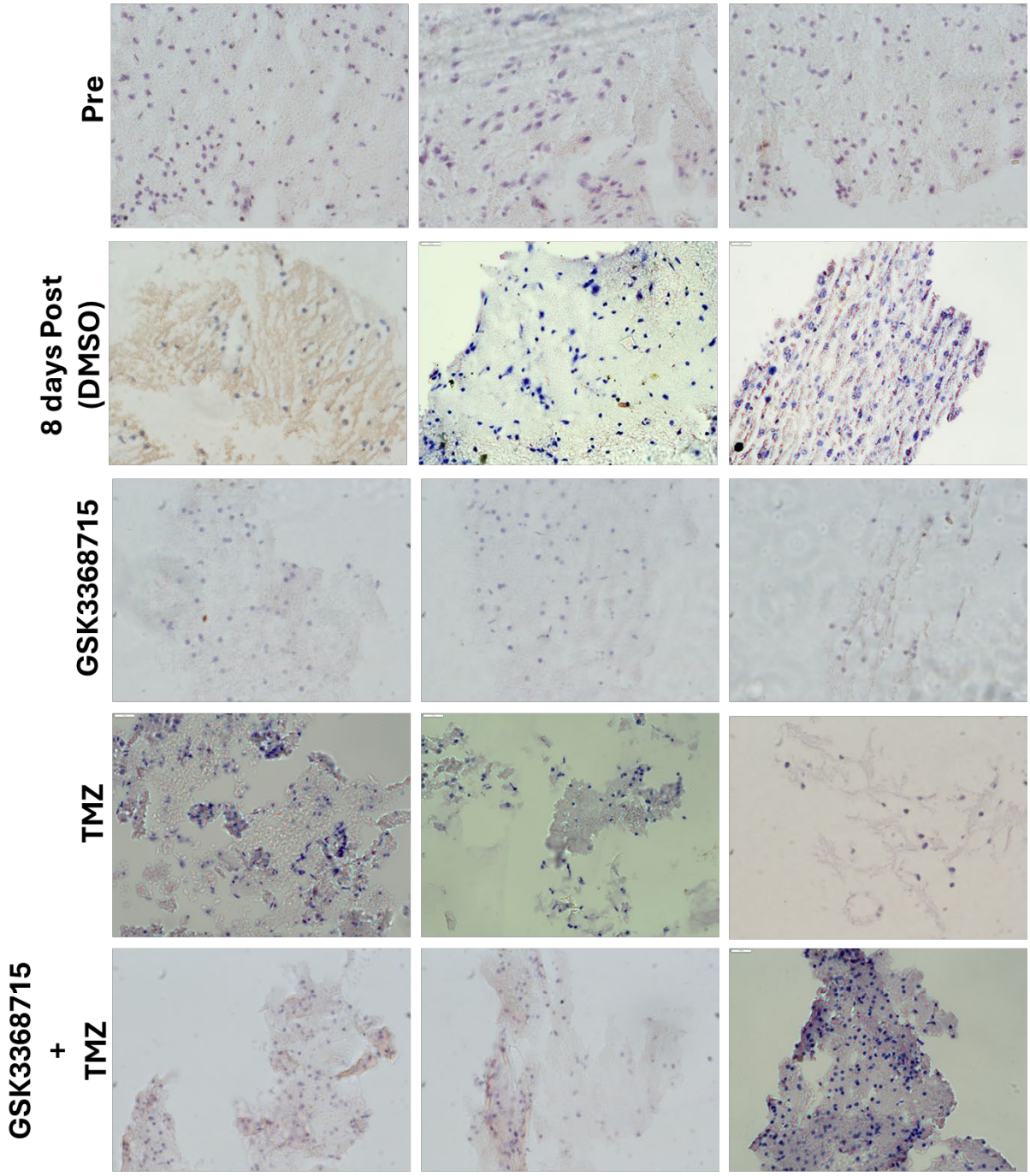

Appendix 13: Representative images of cleaved PARP-stained healthy mouse brain tissue pre- and 8-days post-perfusion and treated with 1µM GSK3368715.

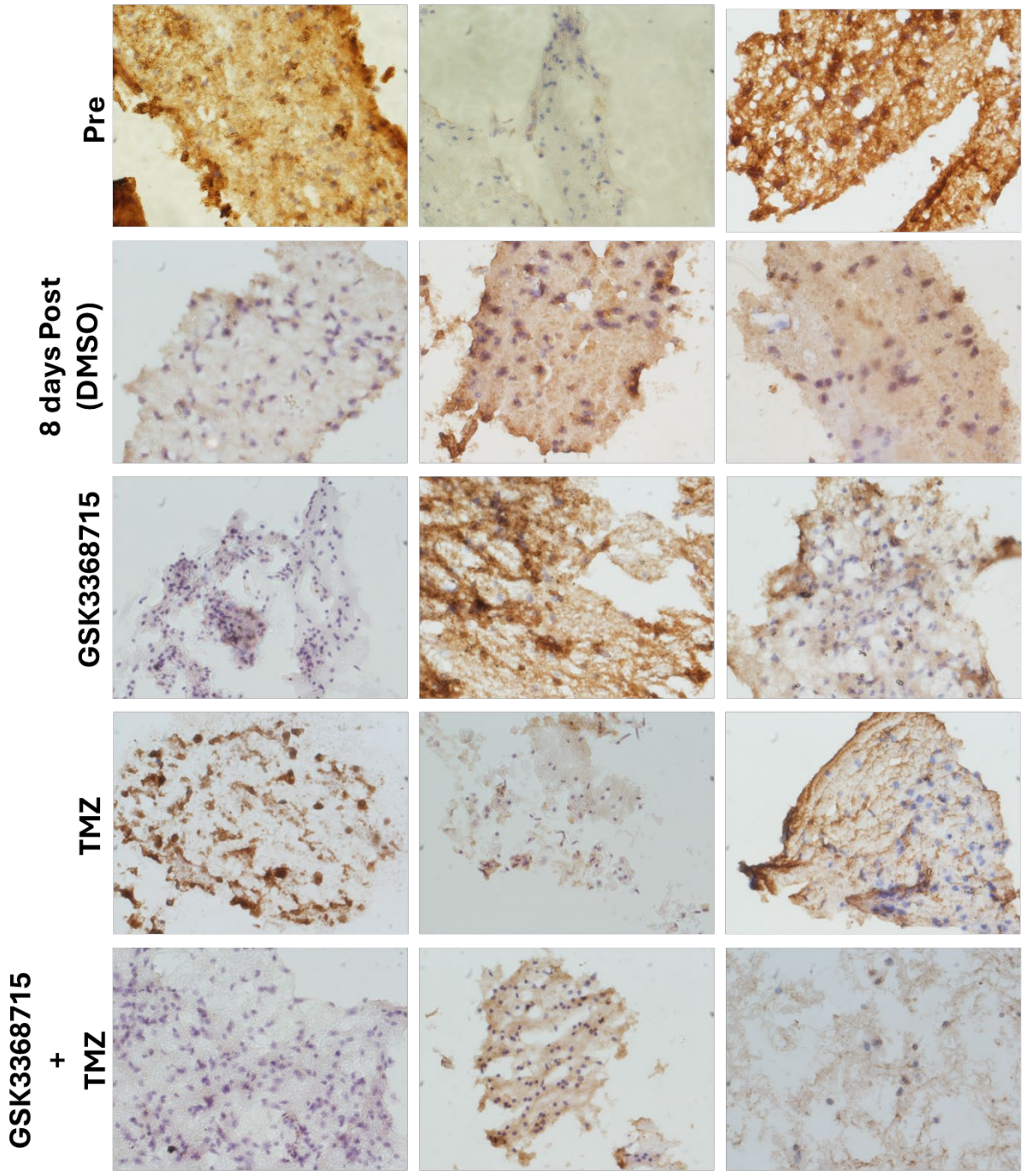

Appendix 14: Representative images of Annexin V-stained healthy mouse brain tissue pre- and 8-days post-perfusion and treated with 1µM GSK3368715.